Author:
Daly, James

Title:
Molecular insights into the role of endosomal recycling in health and disease

Molecular Insights into the Role of Endosomal Recycling in Health and Disease

James Lorente Daly

School of Biochemistry

University of Bristol

March 2021

A dissertation submitted to the University of Bristol in accordance with the requirements for award of degree of PhD in the Faculty of Life Sciences

Word Count: 60,124

Table of Contents

List of Figures

List of Tables

Abstract

The endosomal network is a crucial sorting hub in eukaryotic cells, responsible for integrating transmembrane proteins and lipids, termed ‘cargoes’, from multiple input pathways and sorting them for a crucial subsequent fate decision. Cargoes in the endosomal network can either be degraded within the lysosome, or recycled back to an acceptor compartment such as the plasma membrane or *trans*-Golgi network (TGN). Endosomal sorting complexes that facilitate this process play as central role in the maintenance of cellular homeostasis by regulating a delicate balance between cargo degradation and recycling. Perturbations to endosomal recycling are increasingly associated with disease, many of which are neurodegenerative in their aetiology.

Recent methodological advances have expanded the understanding of the flux of cargoes through the endosomal network, with hundreds of transmembrane proteins depending upon sequence-dependent sorting for their delivery to the plasma membrane. In this thesis, I utilised proteomics and RNA-sequencing techniques to investigate two key complexes involved in orchestrating endosomal recycling: the retromer complex, and the endosomal SNX-BAR sorting complex promoting exit-1 (ESCPE-1). I identified a multivariate phenotype of endolysosomal dysfunction upon retromer depletion, consistent with complex neurodegenerative phenotypes reported in the literature. By developing a methodology to specifically label *trans*-Golgi network proteins by proximity biotinylation, I also performed a screen to identify retrograde endosome-to-TGN cargo proteins for ESCPE-1, which highlighted Neuropilin-1 as a novel cargo.

The coronavirus disease 2019 (COVID-19) pandemic emerged in 2019 and swept across the globe, causing > 116,000,000 cases and > 2,500,000 deaths worldwide at the time of writing. As part of a collaborative project, we identified Neuropilin-1 as an important host factor for infection by the causative virus, SARS-CoV-2. We showed that SARS-CoV-2 directly binds to Neuropilin-1, and blocking this interaction suppresses infection in cell culture, therefore establishing Neuropilin-1 as an important therapeutic target in the study of COVID-19.

Acknowledgements

Firstly, I would like to thank Pete Cullen for his excellent supervision and support throughout my PhD. Your expertise and wide range of interests have made my PhD project far more diverse than I could have imagined at the start, which has made it a great learning experience. From always thinking about the bigger picture of the projects, to bringing in ski goggles as an elaborate metaphor to get me to 'push off the slope' and not shy away from big experiments, your supervision has made my PhD truly enjoyable and exciting.

I must thank the members of the Cullen lab, past and present, for all their help and advice over the course of my PhD: Adam, Ash, Boris, Carlos, Chris, Frances, Jenn, Kerrie, Kirsty, Molly, Neil, Paul and Rachel. I have been incredibly fortunate to learn and work in such a supportive lab, surrounded by colleagues with so much expertise that they are always willing to share. The day-to-day discussions and lab meetings, along with the Dodding and Carroll labs, have really broadened my interests in cell biology. Thank you all for your friendship and for always taking the time to listen to questions that I had. Thank you also to those who have helped with data acquisition and analysis – Kate Heesom, Maz Wilson, Phil Lewis, Hugh Tanner, Lorna Hodgson, and Andrea Ballabio and the staff at TIGEM.

I especially owe Boris a huge amount of gratitude for his friendship, mentorship, and scientific contributions throughout my PhD project, from supervising me during my rotation in the lab through to the frantic cloning and immunoprecipitation marathon during the COVID-19 project in my final year. Thank you for always being approachable and taking the time to listen, discuss and think about my data over a coffee or a beer whenever I was stuck.

I never would have imagined that my PhD research would become of relevance in the study of an emerging pandemic. I owe an enormous amount to everybody involved in the COVID-19 project, particularly Boris, Carlos, Katja, Yohei and Pete, for lending so much support and expertise, and trusting in me to be involved. Despite the pressure of working on a pandemic virus and trying to keep up with the relentless pace of the literature, I will always cherish the memories of tangible excitement in our email exchanges and zoom calls, the camaraderie in the lab, and the socially distanced beers in the office discussing big ideas and learning virology from Yohei while the world around us was at a standstill.

Finally, I would like to thank my family and my partner Molly. Particularly in a difficult 2020, your support, love, and belief in me has driven me forwards throughout this PhD, even from a distance. I would not be where I am today without your encouragement.

Author’s Declaration

I declare that the work in this dissertation was carried out in accordance with the requirements of the University's *Regulations and Code of Practice for Research Degree Programmes* and that it has not been submitted for any other academic award. Except where indicated by specific reference in the text, the work is the candidate's own work. Work done in collaboration with, or with the assistance of, others, is indicated as such. Any views expressed in the dissertation are those of the author.

SIGNED: James Daly DATE: 06/07/2021

Abbreviations

ACE2	Angiotensin-Converting Enzyme 2
ALIX	Apoptosis-Linked Gene-2 Interacting Protein X
ANOVA	Analysis of Variance
AP	Adaptor Protein
APEX	Ascorbate Peroxidase
APOB	Apolipoprotein B
APP	Amyloid Precursor Protein
APPL	Adaptor Protein Containing PH Domain, PTB Domain and Leucine Zipper Motif
Arf	ADP-Ribosylation Factor
ARFRP1	Arf-related protein 1
Arl	Arf-Like
Arp2/3	Actin Related Protein 2/3
ATCC	American Type Culture Collection
ATP	Adenosine Triphosphate
ATP7A	Copper Transporting ATPase 1
Aβ	Amyloid β
β2AR	β2-adrenergic receptor
BACE1	Beta-Secretase 1
BAR	Bin/Amphiphysin/Rvs
BCA	Bicinchoninic Acid
BP	Biotin-Phenol
BSA	Bovine Serum Albumin
Caco-2	Human Colon Adenocarcinoma Cell Line
Calu-3	Human Lung Adenocarcinoma Cell Line
Cas9	CRISPR-Associated Protein 9
CASP1	Caspase-1
CCC	COMMD/CCDC22/CCDC93
CCDC	Coiled Coil Domain Containing
CD-MPR	Cation-Dependent Mannose-6-Phosphate Receptor
CendR	C-End Rule
CI-MPR	Cation-Independent Mannose-6-Phosphate Receptor
CK2	Casein Kinase II
CLEAR	Coordinated Lysosomal Expression and Regulation
CME	Clathrin-Mediated Endocytosis
COG	Conserved Oligomeric Golgi
COMMD	Copper and Metabolism Gene Murr1 Domain-Containing
CORVET	Class C Core Vacuole/Endosome Tethering
CoV	Coronavirus
COVID-19	Coronavirus Disease 2019
CPY	Carboxypeptidase Y
CRIM1	Cysteine-Rich Motor Neuron 1 Protein
CRISPR	Clustered Regularly Interspaced Short Palindromic Repeats
CTSD	Cathepsin D
CUB	Complement C1r/C1s, Uegf, Bmp1

DAB	3,3’-Diaminobenzidine
DAPI	4’, 6-Diamidino-2-Phenylindole Dihydrochloride
DIC	Differential Interference Contrast
DMEM	Dulbecco’s Modified Eagle Medium
DMSO	Dimethyl Sulphoxide
DMT1-II	Divalent Metal Transporter 1 Isoform II
DNA	Deoxyribonucleic Acid
EDTA	Ethylenediaminetetraacetic Acid
EEA1	Early Endosome Antigen 1
EGF	Epidermal Growth Factor
EGFR	Epidermal Growth Factor Receptor
EM	Electron Microscopy
ER	Endoplasmic Reticulum
ERC	Endocytic Recycling Compartment
ERGIC	ER-Golgi Intermediate Compartment
ESCPE	Endosomal SNX-BAR Sorting Complex Promoting Exit
ESCRT	Endosomal Sorting Complex Required for Transport
F-Actin	Filamentous Actin
FERARI	Factors for Endosome Recycling and Retromer Association
FERM	Protein 4.1/Ezrin/Radixin/Moesin
FYVE	FAB1, YotB, Vac1, EEA1
GAE	γ-adaptin ear
GAP	GTPase Activating Protein
GARP	Golgi-Associated Retrograde Protein
GAT	GGA and TOM
gB	Glycoprotein B
GCC	GRIP and coiled-coil domain-containing protein
GDF	GDI Dissociation Factor
GDI	GDP Dissociation Inhibitor
GDP	Guanosine Diphosphate
GEF	Guanine Nucleotide Exchange Factor
GFP	Green Fluorescent Protein
GGA	Golgi-Localised, γ-Ear-Containing, Arf-Binding Protein
GIPC1	GAIP C-terminus interacting protein
GLUT1	Glucose Transporter Type 1
GPI	Glycosylphosphatidylinositol
GRIP	Golgin-97, RanBP2alpha, Imh1p and p230/Golgin-245
gRNA	Guide RNA
GSEA	Gene Set Enrichment Analysis
GTP	Guanosine Triphosphate
H4	Human Neuroglioma/Astrocytoma Cell Line
HA	Hemagglutinin
HCMV	Human Cytomegalovirus
HCV	Hepatitis Virus C
HDAC6	Histone Deacetylase 6
HEAT	Huntingtin/EF3/PP2A/TOR1
HEK293T	Human Embryonic Kidney 293 Large T Antigen

HeLa	Henrietta Lacks
HGF	Hepatocyte Growth Factor
HIV	Human Immunodeficiency Virus
H/N	Influenza Hemagglutinin/Neuraminidase
HOPS	Homotypic Fusion and Protein Sorting
Hpi	Hours Post-Infection
HRP	Horseradish Peroxidase
HS	Heparan Sulphate
Hsc	Heat Shock Cognate
HSPG	Heparan Sulphate Proteoglycan
HSRV	Human Respiratory Syncytial Virus
HTLV	Human T-Lymphotropic Virus
IF	Immunofluorescence
IMDM	Iscove's Modified Dulbecco's Medium
IP	Immunoprecipitation
IPA	Ingenuity Pathway Analysis
iPSC	Induced Pluripotent Stem Cell
ITC	Isothermal Titration Calorimetry
Kb	Kilobase
K_d	Dissociation Constant
KD	Knockdown
kDa	Kilodaltons
KEGG	Kyoto Encyclopaedia of Genes and Genomes
KIBRA	Kidney and Brain Protein
KO	Knockout
LAMP	Lysosome Associated Membrane Glycoprotein
LB	Luria-Bertani
LC-MS/MS	Liquid Chromatography with Tandem Mass Spectrometry
LDL	Low Density Lipoprotein
LDLR	Low Density Lipoprotein Receptor
LDS	Lithium Dodecyl Sulphate
LIMP-II	Lysosomal Integral Membrane Protein II
LRRK2	Leucine-Rich Repeat Serine/Threonine-Protein Kinase 2
M21	Human Melanoma Cell Line
M6P	Mannose-6-Phosphate
mAb	Monoclonal Antibody
MAGEL2	MAGE-like protein 2
MAM	Meprin, A-5 Protein and Receptor Protein-Tyrosine Phosphatase Mu
MDCK	Madin-Darby Canine Kidney
MERS-CoV	Middle Eastern Respiratory Syndrome Coronavirus
MIT	Microtubule Interacting and Trafficking Molecule
MITF	Microphthalmia Associated Transcription Factor
MOI	Multiplicity of Infection
MT-MMP	Matrix Metalloprotease
mTORC1	Mechanistic Target of Rapamycin Complex 1
MUST	MAGEL2-USP7-TRIM27
MYO6	Myosin VI
N	Nucleocapsid Protein

NEAA	Nonessential Amino Acids
NMR	Nuclear Magnetic Resonance
NRP	Neuropilin
PACS1	Phosphofurin Acidic-Cluster Sorting Protein 1
PAR1	Protease Activated Receptor 1
PCR	Polymerase Chain Reaction
PDB	Protein Data Bank
PDZ	Postsynaptic Density 95/Discs Large/Zonula Occludens-1
PDZbm	PDZ Binding Motif
PEI	Polyethylenimine
PFA	Paraformaldehyde
PH	Pleckstrin Homology
P_i	Inorganic Phosphate
PI	Phosphatidylinositol
PI4KIIα	Phosphatidylinositol 4-Kinase Type 2-Alpha
PI4Kβ	Phosphatidylinositol 4-Kinase Beta
PIKFYVE	1-Phosphatidylinositol 3-Phosphate 5-Kinase
PIP	Phosphoinositide
PPC-1	Primary Prostate Carcinoma-1
PTB	Phosphotyrosine Binding
PTP1B	Protein-Tyrosine Phosphatase 1B
PVDF	Polyvinylidene Fluoride
PX	Phox Homology
PXA-RGS-PXC	PX- Associated Domain A, Regulator of G-Protein, PX-Associated Domain C
RBD	Receptor Binding Domain
RCP	Rab-Coupling Protein
RILP	Rab7-Interacting Lysosomal Protein
RIPA	Radioimmunoprecipitation Assay
RME-8	Required for Receptor-Mediated Endocytosis-8
RMSD	Root Mean Square Deviation
RNA	Ribonucleic Acid
RNA-Seq	RNA-Sequencing
Rpm	Revolutions Per Minute
RTK	Receptor Tyrosine Kinase
S	Spike Protein
SARS-CoV	Severe Acute Respiratory Syndrome Coronavirus
SARS-CoV-2	Severe Acute Respiratory Syndrome Coronavirus 2
SD	Standard Deviation
SDM	Site-Directed Mutagenesis
SDS	Sodium Dodecyl Sulphate
SDS-PAGE	Sodium Dodecyl Sulphate-Polyacrylamide Gel Electrophoresis
SEM	Standard Error of the Mean
SEMA4C	Semaphorin 4C
SFN	14-3-3 Protein Sigma
SH3	Src Homology 3
shRNA	Short Hairpin RNA
SILAC	Stable Isotope Labelling by Amino Acids in Cell Culture
siRNA	Small Interfering RNA

SNARE	Soluble N-ethylmaleimide Sensitive Factor Attachment Protein Receptor
SNX	Sorting Nexin
SOC	Super Optimal Broth with Catabolite Repression
SorLA	Sortilin-Related Receptor
SORT1	Sortilin
ST6GAL1	Beta-Galactosidase Alpha-2,6-Sialyltransferase 1
STED	Stimulated Emission Depletion
STxB	Shiga Toxin Subunit B
TAE	Tris-Acetate-EDTA
TBC1D	Tre-2, BUB2p, Cdc16p-1-Domain
TBST	Tris-Buffered Saline with 0.1% Tween
TCA	Trichloroacetic acid
TFE3	Transcription Factor E3
TFEB	Transcription factor EB
TfR	Transferrin Receptor
TGM2	Transglutaminase-2
TGN	*trans*-Golgi Network
TGN46	*trans*-Golgi Network Glycoprotein 46
TIP47	Tail-Interacting 47 kDa Protein
TM	Transmembrane
TM9SF	Transmembrane 9 Superfamily
TMPRSS2	Transmembrane Protease Serine 2
TRIM27	Tripartite Motif-Containing Protein 27
t-SNARE	Target SNARE
TX-100	Triton X-100
UIM	Ubiquitin Interacting Motif
USP7	Ubiquitin Carboxyl-Terminal Hydrolase 7
VAMP	Vesicle-Associated Membrane Protein
VAP	VAMP-Associated Protein
v-ATPase	Vacuolar Adenosine Triphosphatase
VEGF	Vascular Endothelial Growth Factor
VEGFR	Vascular Endothelial Growth Factor Receptor
VHS	Vps27, Hrs, STAM
VPS	Vacuolar Protein Sorting
VPS35L	VPS35 Endosomal Protein-Sorting Factor-Like
v-SNARE	Vesicle SNARE
VSV	Vesicular Stomatitis Virus
VTI	Vesicle Transport through Interaction with t-SNARES Homolog
WASH	Wiskott-Aldrich Syndrome Protein and SCAR Homolog
WB	Western Blot
WT	Wild-Type
x g	Relative Centrifugal Force
YWHA	Tyrosine 3-Monooxygenase/Tryptophan 5-Monooexygenase Activation

Chapter 1: Introduction

1.1 Principles of Interorganellar Communication

The defining feature of the eukaryotic cell, both visually and functionally, is its compartmentalisation into spatially separated, membrane-bound structures. The internal organisation of the endomembrane system prompted the diversification of intricate organelles with highly specialised functions, ranging from storage and decryption of genetic information in the nucleus, to conductance of electrical currents across the mitochondrial inner membrane, to meticulous processing of proteins through the biosynthetic pathway. However, organelles do not operate in isolation. Just as organs of the body are remarkably complex, but ultimately rely on communication and feedback from each other to operate successfully, so too do organelles at the subcellular level. One of the most remarkable developments in the evolution of complex life is undoubtedly the development of interorganellar communication, a series of processes that allow eukaryotic cells to attain a level of complexity that is greater than the sum of their parts.

1.1.1 Membrane Identity of Organelles

Intracellular membranes are composed mainly of phospholipids, whereby amphiphilic lipid molecules coalesce into a fluid bilayer based on electrostatic attractions and repulsions with the surrounding aqueous environment. The endoplasmic reticulum (ER) is the principal site of lipid biogenesis and processing (Van Meer et al., 2008). The main components of mammalian cell membranes are phosphoglycerides and sphingomyelin, which comprise a polar hydrophilic headgroup and a hydrophobic acyl chain. The length and degree of saturation within the acyl chain of lipids dictate the biophysical properties of the bilayer (Bigay and Antonny, 2012). Moreover, the polarity of lipid headgroups influences how lipid bilayers interact with proteins possessing complementary electrostatic charges (Jackson et al., 2016). Additional classes of lipids, such as cholesterol, can associate with the bilayer to alter its characteristics, including its permeability to small molecules. Biochemically, eukaryotic organelle membranes are fundamentally distinct, with different intrinsic lipid and protein compositions which characterise their structures and functions (Behnia and Munro, 2005). The degree of flexibility and asymmetry within a phospholipid bilayer, as defined by its lipid composition and packing, dictates membrane curvature, which in turn impacts membrane functionality. For example, the plasma membrane is tightly packed and rich in cholesterol, resulting in a relatively flat, stiff and impermeable membrane that serves its structural purpose as the boundary of the cell (Bigay and Antonny, 2012).

The thickness of biological membranes, which is also an emergent property of their lipid composition, influences how transmembrane proteins partition into different organelles

(Sharpe et al., 2010). For example, the membranes of the Golgi apparatus are thinner than the plasma membrane. Consequently, the transmembrane domains of Golgi-resident glycosylation enzymes are shorter to reflect the dimensions of the bilayers they reside in (Bretscher and Munro, 1993). Remarkably, substitution of all 17 residues within the transmembrane domain of the glycosyltransferase alpha-2,6-sialyltransferase enzyme with leucine residues does not affect its retention within the Golgi apparatus, whereas addition of additional leucine transmembrane residues resulted in export to the plasma membrane (Munro, 1991). It is therefore more energetically favourable for Golgi-resident proteins to partition into thinner membranes, as opposed to thicker bilayers where there is an electrostatic repulsion between hydrophilic residues flanking the transmembrane domain and the hydrophobic lipid bilayer. This adaptation of transmembrane domain length therefore ensures that proteins localise to the correct subcellular membrane.

In addition to defining geometric parameters, acting as a physical boundary between cellular compartments and imposing a diffusion barrier for macromolecules, certain lipids influence the specialised cell biology of organelles by interacting with and recruiting a plethora of proteins. One class of lipid in particular plays a crucial role in the recruitment of effectors that further define membrane identity: phosphoinositides.

1.1.2 Phosphoinositides

Phosphoinositides (PIPs) are a dynamic class of phospholipids that localise to the cytosolic-facing leaflet of phospholipid bilayers. While only comprising a minor component of total cellular lipid content, PIPs can reach high local membrane concentrations (Martin, 1998). All PIPs derive from the progenitor lipid phosphatidylinositol (PI), which comprises a diacylglycerol molecule attached to an anionic inositol sugar headgroup (Balla, 2013). PI is synthesised in the ER from the precursor molecules cytidine diphosphate diacylglycerol and D-myo-inositol by the PI synthase enzyme (Blunsom and Cockcroft, 2020). In the inositol headgroup structure, each of the 6 carbon atoms is conjugated to a free hydroxyl group, besides one which is engaged in the phosphodiester linkage connecting PI to diacylglycerol (denoted as position 1) (Agranoff, 2009). Of the remaining hydroxyl groups, positions 3, 4 and 5 can be phosphorylated by a range of lipid kinases to generate 7 potential combinations of PIP: PI(3)P, PI(4)P, PI(5)P, PI(3,4)P_2, PI(4,5)P_2, PI(3,5)P_2 and PI(3,4,5)P_3 (De Matteis and Godi, 2004).

Despite their minor contribution to total lipid content, PI and PIPs play a huge role in the establishment and maintenance of membrane identity. Since their discovery as membrane markers, the development of PI sensors has revealed the broad distribution of PIPs around the cell. The plasma membrane is comprised of PI(4)P, PI(3,4)P_2, PI(4,5)P_2, and PI(3,4,5)P_3;

the Golgi apparatus is rich in PI(4)P; autophagosomes and endosomes are primarily enriched in PI(3)P, accompanied by PI(3,5)P_2 as the network matures to late endosomes and lysosomes (Cullen, 2011; Schink et al., 2016) **(Figure 1.1)**. More recently, PI(4,5)P_2 has been detected on mitochondrial and peroxisomal membranes, (Chu et al., 2015; Rosivatz and Woscholski, 2011). The endoplasmic reticulum, despite its role in PI synthesis, is devoid of a defining PIP population (Schink et al., 2016).

PIPs are not static, despite their assignation to distinct membrane compartments. PIPs can be rapidly generated in response to dynamic subcellular events, such as the formation of PI(3,4)P_2 in the late stages of clathrin vesicle formation during endocytosis (Schink et al., 2016). To mediate the rapid biogenesis and turnover of PIPs, an ensemble of PI kinases and phosphatases are also spatially restricted to specific membrane subcompartments (De Matteis and Godi, 2004). The incessant interplay of phosphorylation and dephosphorylation of phosphoinositides imparts an additional level of regulation in the maintenance of membrane identity. Moreover, PIPs can be cleaved from the membrane by phospholipases in response to various stimuli to liberate free inositol phosphate and diacylglycerol molecules that act as potent secondary messengers in signal transduction pathways (Schink et al., 2016). The association of mutations in kinases, phosphatases and phospholipases involved in PI dynamics with a range of diseases serves as a clear demonstration of the importance of PI biology to cellular physiology (McCrea and De Camilli, 2009).

A range of evolutionarily conserved protein domains possess the capacity to bind to PIPs, including PH (Pleckstrin Homology), PX (Phox Homology) and FYVE (FAB1, YOTB, Vac1, EEA1) domains (Cullen, 2011). While some integral PIP-binding proteins exist, the majority are peripherally associated, and therefore PIP binding serves to recruit these proteins from the cytosol to the target membrane. Importantly, the affinity of most PIP-binding proteins for their PIPs tends to be relatively weak, in the low micromolar range (Schink et al., 2016). Consequently, avidity effects and the coincidence detection of other proteins on the target membrane are crucial factors in PIP effector recruitment, particularly in the endosomal network (Carlton and Cullen, 2005). Ultimately, this hierarchical system of spatially restricted PI kinases and phosphatases implementing subdomains of localised PIP populations, which in turn recruit specialised protein effectors, defines organelle biology and membrane identity.

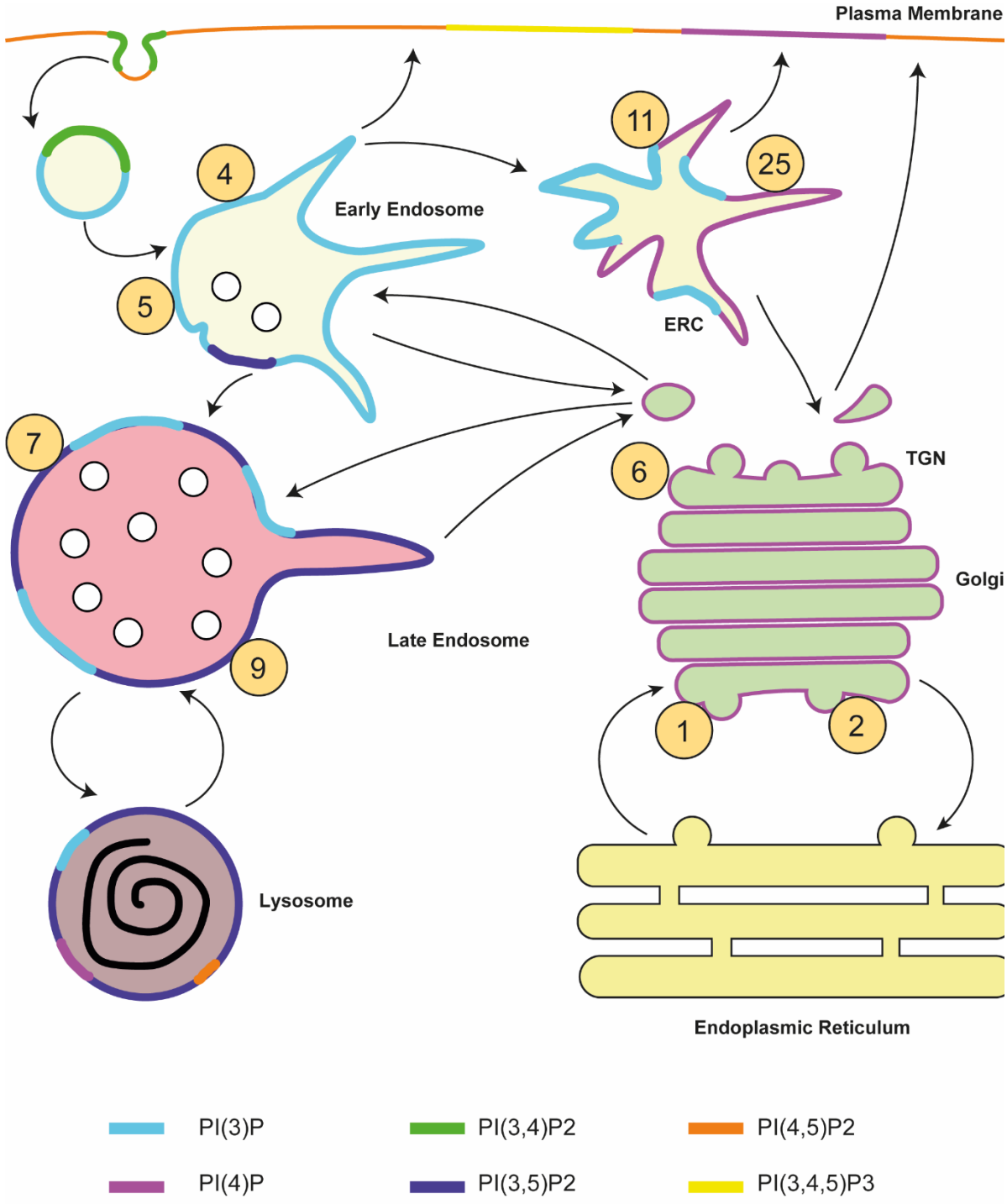

Figure 1.1 Membrane Identity in the Biosynthetic and Endosomal Pathways

The organelles of the biosynthetic and endosomal pathways display unique lipid and Rab identities that are constantly remodelled by effector proteins. Different PIP species are indicated by coloured membranes, and key Rab proteins that define the organelles are represented by numbered labelled orange circles. While these Rabs are the best characterised, many more are reported to localise to these organelles and play distinct roles in maintaining organelle identity and membrane trafficking. Figure adapted from (Jean and Kiger, 2012) and (Wallroth and Haucke, 2018).

1.1.3 Rab GTPases

Another set of critical determinants of membrane identity and transport are Rab guanosine-triphosphatases (GTPases) (Zerial and McBride, 2001). Comprising a family of over 60 members in mammals, Rab GTPases act as molecular switches that recruit guanosine triphosphate (GTP) and catalyse its hydrolysis to guanosine diphosphate (GDP), releasing an inorganic phosphate (P_i) group in the reaction (Stenmark, 2009). Rabs are active in their GTP-bound state, and recruit a host of effector proteins in response to their activation (Stenmark, 2009). Rabs are soluble cytosolic proteins, and therefore must be prenylated to associate with membranes. The enzyme responsible for this post-translational modification is Rab geranylgeranyl transferase, which covalently attaches either one, or more commonly, two lipophilic geranylgeranyl moieties to the C-terminus of Rab proteins (Pereira-Leal et al., 2001). Once attached, Rabs utilise the geranylgeranyl modifications as hydrophobic anchors to peripherally associate with organelle membranes. Many Rabs can be expressed as different isoforms, which can display specificity for different tissues (Zerial and McBride, 2001).

Despite their intrinsic hydrolytic capacity Rabs do not act autonomously, and require a range of accessory factors that control their activity: GTPase activating proteins (GAPs) stimulate the catalytic activity of Rabs to convert GTP to GDP and release P_i; guanine nucleotide exchange factors (GEFs) replace hydrolysed GDP with GTP to allow a subsequent round of hydrolysis; GDP dissociation inhibitors (GDIs) occupy and sequester the geranylgeranyl lipid moieties of Rabs in the cytosol, inhibiting their anchorage to membranes; finally, GDI dissociation factors (GDFs) promote the release of Rabs from GDIs, thereby regulating their association with cellular membranes (Stenmark, 2009). The interplay of these accessory factors establishes an exquisite level of control over Rab biology, creating a constantly shifting regulatory cycle of membrane recruitment and nucleotide switching between ‘active’ (GTP-bound) and ‘inactive’ (GDP-bound) conformations.

Similarly to PIPs, Rabs localise to specific organelle membranes, and in some cases, distinct subdomains within a membrane **(Figure 1.1)**. Once localised and activated, GTP-bound Rabs recruit an array of effector proteins to nucleate the formation of a network of proteins and intricate feedback loops in a cascade (Zerial and McBride, 2001). Importantly, many Rab effector proteins also recognise PIPs, and are therefore recruited to the correct membrane by a coincidence detection mechanism, a reoccurring theme in cell biology that further hones the spatiotemporal specificity of effector association with membranes (Carlton and Cullen, 2005). Moreover, certain PI kinases and phosphatases are also Rab effectors, such as Vps34, which in complex with Vps15, Beclin1 and UVRAG is recruited by Rab5, and therefore modify the surrounding lipid environment in response to the developing Rab cascade of protein recruitment (Christoforidis et al., 1999; Tremel et al., 2021). Rabs (and other smaller families such as Arf GTPases) play an essential and ubiquitous role in all processes of membrane

trafficking between subcellular compartments, from organelle biogenesis, to vesicle formation and trafficking, to tethering and fusion steps.

1.1.4 Membrane Trafficking: Enrichment, Fission, Transport and Fusion

The exchange of lipids and proteins (collectively termed 'cargoes') between organelles is largely mediated by the process of membrane trafficking. Membrane trafficking pathways in the eukaryotic cell principally relate to the biosynthetic pathway, whereby all transmembrane and certain soluble proteins are processed and exported to their target compartment **(Section 1.2.1)**; and the myriad endocytic pathways, where cargo proteins internalised from the cell surface or received from intracellular compartments such as the *trans*-Golgi network or autophagosomes are sorted, and either recycled to an accepting compartment or degraded in the lysosome **(Section 1.3).** A more recently established pathway involves the biogenesis of mitochondrial-derived vesicles to mediate trafficking of mitochondrial cargoes to lysosomes and peroxisomes (Sugiura et al., 2014). For each membrane trafficking route, the cargoes and molecular machinery mediating the process differ, but broadly they adhere to the same principles and order of events **(Figure 1.2)**.

Firstly, cargoes are selectively recognised and enriched at a membrane exit site. In the case of transmembrane cargoes, this is mediated by coat complexes that peripherally associate with the target membrane (often through coincidence detection of PIPs and Rab effectors) and recognise a characteristic sequence motif in a solvent-exposed domain of cargo, either directly or via accessory proteins (Bonifacino and Glick, 2004). An example of sequence-based recognition is provided by the COPI coat machinery, which recognises cytosolic KKxx or KxKxx dilysine motifs in transmembrane cargoes to mediate retrograde intra-Golgi and Golgi-to-ER cargo sorting (Jackson et al., 2012; Ma and Goldberg, 2013). Once captured by a coat complex or adaptor, the lateral diffusion of cargo becomes impaired, and as a result cargo begin to accumulate at distinct, coated sites in the membrane. This enrichment of cargo, coupled with higher-order oligomerisation of coat complexes, imposes biophysical tension on the membrane that induces localised curvature (Bonifacino and Glick, 2004).

Once scission occurs, components of the vesicle coat are recognised by adaptors for cytoskeletal motors to facilitate their polarised trafficking towards an accepting compartment. The cytoplasm is a crowded environment, and as a result the first membrane that a vesicle encounters is unlikely to be the intended target. To circumvent this issue, filamentous proteins extend from the target organelle to specifically recognise and tether incoming vesicles (Cai et al., 2007). Once tethered within close proximity, membrane fusion and release of cargo is

mediated by N-ethylmaleimide-sensitive factor attachment protein receptor (SNARE) proteins. In the model of SNARE-mediated membrane fusion, a monomeric vesicle-associated SNARE (v-SNARE) protein on an incoming membrane associates with a trimeric assembly of cognate target membrane SNAREs (t-SNAREs) (Rothman, 1994). Association of these SNAREs into a tight four-helix bundle serves to ensure specificity and provide the free energy required to bring the two membranes into close apposition, excluding water molecules from the space in between. Once solvent is displaced, lipid molecules in the outer leaflets of the two bilayers begin to flow between each other, widening the fusion zone through a hemi-fusion intermediate, and ultimately resolve as a continuous membrane and releasing the luminal and transmembrane contents of the vesicle (Bonifacino and Glick, 2004).

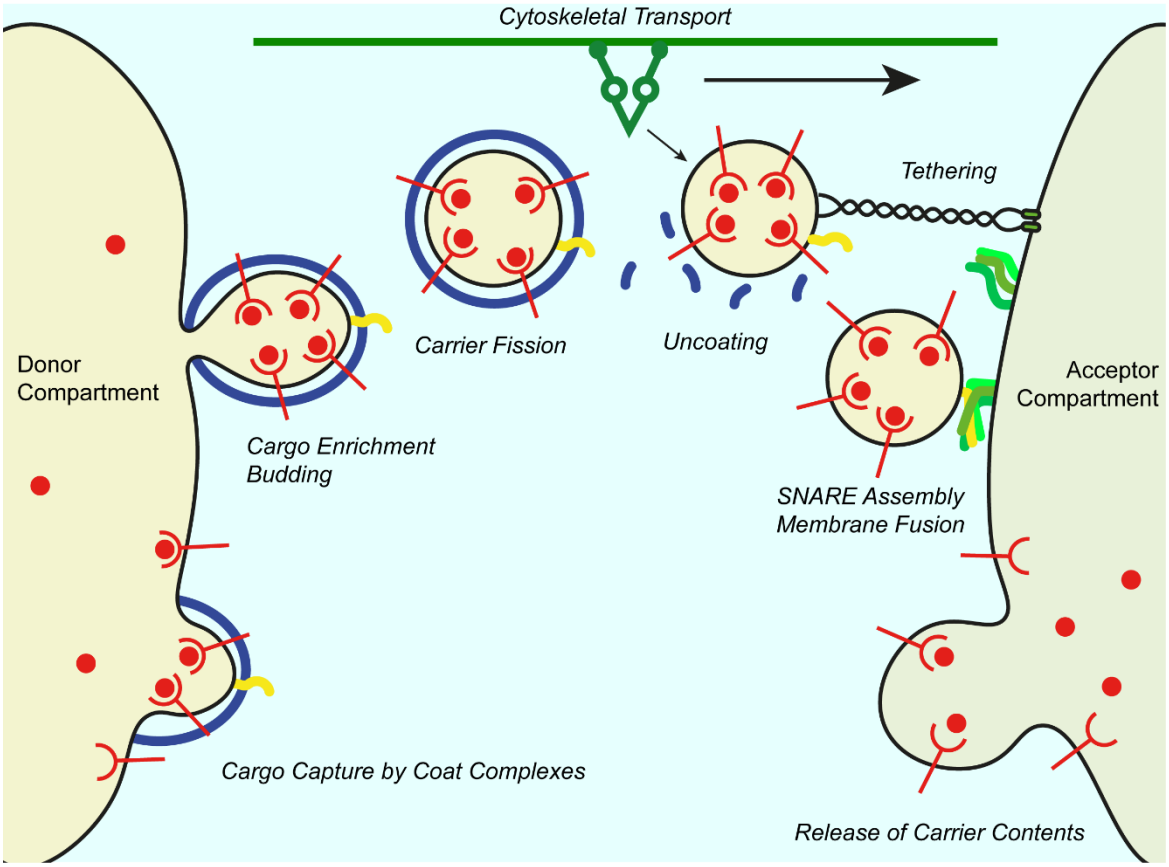

Figure 1.2 Principles of Membrane Trafficking

The key steps of membrane trafficking are displayed, beginning with cargo capture and concentration on the donor compartment by coat complexes. Cargo accumulation and biophysical forces imposed by coat complexes induce membrane curvature, which ultimately leads to membrane carrier fission. Coat complexes can subsequently be released to facilitate their reuse. Association with cytoskeletal motors drives the directional trafficking of cargo. Incoming membrane carriers are recognised and captured by tethering proteins, and once in proximity undergo SNARE-dependent fusion with the acceptor compartment to release their contents into the accepting compartment. Figure adapted from (Bonifacino and Glick, 2004) and (Behnia and Munro, 2005).

1.2 Cargo Sorting through the Biosynthetic and Endocytic Pathways

In each membrane trafficking pathway, the cargoes destined for transport must be separated from the surrounding environment of the organelle and incorporated into transport carriers. The process of cargo sorting is crucial both for ensuring the correct cargoes are transported, and for protecting the identity of the donor organelle by preventing the mistrafficking of resident proteins and lipids. In the case of trafficked proteins, the molecular code that governs sorting usually resides within the amino acid sequence of the cargo itself. This control of protein localisation is crucial for the maintenance of cellular homeostasis. Towards the end of the biosynthetic pathway, a more complex cargo sorting decision must be made to dictate cargo trafficking, with multiple routes and machineries available.

1.2.1 The *trans*-Golgi Network – a Crossroad in the Secretory Pathway

Morphologically, the structures of the Golgi apparatus and its associated tubuloreticular compartments of the ER-Golgi intermediate compartment (ERGIC) and *trans*-Golgi network (TGN) are strikingly recognisable (Golgi, 1898; Mogelsvang et al., 2004). As roughly one third of the proteome traverses the flattened, fenestrated cisternae of the Golgi apparatus, proteins receive a wide range of posttranslational modifications that prime them for their biological functions (Guo et al., 2014). The *trans*-facing side of the Golgi apparatus is continuous with a highly pleiomorphic tubular compartment, termed the *trans*-Golgi network (Griffiths and Simons, 1986). Once cargo arrive at the TGN, multiple destinations lie ahead, and therefore a major sorting decision must be made. Cargo can be exported to the endosomal network, to the plasma membrane, or to more specialised compartments such as secretory vesicles in pre-synaptic boutons (Gu et al., 2001). Additionally, the TGN plays a specialised role in establishing planar cell polarity, by ensuring export of proteins to the correct subdomains of the plasma membrane (Bonifacino, 2014). Molecular machinery such as Rabs and cargo adaptors on TGN-derived anterograde carriers can further define fusion specificity in the context of establishing planar cell polarity by interacting with the exocyst complex, which specifically tethers incoming vesicles to the correct plasma membrane subdomain (Heider and Munson, 2012).

The TGN is a PI(4)P-rich compartment, generated by the kinase activity of PI4KIIα and PI4Kβ (Weixel et al., 2005). Arf1 is a major GTPase involved in cargo sorting at the TGN. Like Rabs, Arf1 is at the centre of a complex cascade of GTPase effector proteins that constantly remodels itself to regulate membrane trafficking events (Gillingham and Munro, 2007). The

PI(4)P and GTPase membrane identity of the TGN membrane establishes a template for coincidence detection by cargo adaptor proteins, of which the heterotetrametric adaptor complexes (APs) are best described. Of the 5 distinct AP complexes in mammals, AP-1 and AP-4 are involved in cargo sorting at the TGN (Sanger et al., 2019). AP-1 directs cargo for transport into the endosomal network or basolateral membrane, whereas AP-4 mediates trafficking to specialised compartments such as autophagosomes (Bonifacino, 2014; Sanger et al., 2019). AP-1 can recognise two characteristic motifs in the cytosolic tails of a wide range of transmembrane cargoes: YxxØ (referred to as a tyrosine motif, where Ø represents a bulky hydrophobic amino acid), and [D/E]xxxL[L/I] (referred to as a dileucine motif) (Bonifacino and Traub, 2003). Following the engagement of cargo through these motifs, AP-1 recruits clathrin to sites of cargo enrichment. Clathrin coats are formed by an assembly of light and heavy clathrin chains into triskelion structures, which associate into a basket-like coat of hexagons and pentagons, termed a clathrin-coated vesicle (CCV) (Kirchhausen and Harrison, 1981; Robinson, 2015). AP-4 has been reported to mediate the TGN export of the autophagy regulator ATG9A and the Alzheimer's-associated protein amyloid precursor protein (APP), amongst others, but a conserved sorting motif amongst these cargoes is not apparent (Burgos et al., 2010; Mattera et al., 2017). AP-4 does not recruit clathrin, and therefore the fundamental mechanism of AP-4 mediated TGN export remains elusive (Guo et al., 2014).

Another class of cargo adaptor for TGN-to-endosome export is the Golgi-localised, γ-ear-containing, Arf-binding proteins (GGAs), of which there are three members in mammals. GGA proteins are organised into modular domains, comprising the VHS (Vps27, Hrs, STAM) domain, GAT (GGA and TOM) domain, and GAE (γ-adaptin ear) domains (Guo et al., 2014). Like AP-1 and AP-4, GGAs are also cooperatively recruited to the TGN by PI(4)P and Arf1. The VHS domain recognises acidic-cluster dileucine motifs in cargo cytosolic tails conforming to a DxxLL sequence, which despite its similarity to the dileucine motifs of AP-1 cargoes, is specifically bound by GGAs (Bonifacino and Traub, 2003). Phosphorylation of serine residues upstream of this sequence by casein kinase II (CK2) can enhance GGA binding and therefore provide further spatiotemporal control of GGA cargo sorting **(Figure 1.3)** (Bonifacino and Traub, 2003; Braulke and Bonifacino, 2009). Examples of cargoes for the GGA family include the cation-dependent and -independent mannose-6-phosphate receptors (CD-MPR and CI-MPR, respectively) (Puertollano et al., 2001). The GAE domain contains a flexible linker that binds and recruits clathrin (Guo et al., 2014). Super-resolution imaging reveals that AP-1 and GGA2 both colocalise with clathrin, but are spatially segregated from each other at the TGN and therefore are likely responsible for sorting cargoes into separate vesicles (Y. Huang et al., 2019). Providing additional crosstalk between TGN cargo sorting machinery, epsinR is an

adaptor that can bind both to AP-1 and GGAs to recruit clathrin coats, and mediates the trafficking of the SNARE protein VTI1B (Hirst et al., 2004).

Accumulating evidence suggests that TGN-derived transport carriers destined for the endosomal network and the apical plasma membrane are morphologically distinct from each other. In contrast to cargo export to the endosomal network and basolateral membrane, which relies on the well-established hierarchical sequence of cargo recognition by adaptors, coat complex recruitment, scission and transport, TGN trafficking to the apical plasma membrane is far less understood. Detailed microscopical studies have revealed that the vesicular stomatitis virus G (VSV-G) protein, LAMP1 (a transmembrane lysosomal marker) and the transferrin receptor (TfR, a transmembrane cell surface receptor) are incorporated into pleiomorphic tubulovesicular structures that transit to the plasma membrane. Moreover, these structures appear to be devoid of a coat complex (Chen et al., 2017; Polishchuk et al., 2000). In contrast, CD-MPR-containing carriers, while also occasionally appearing as tubulovesicular, contained clathrin-coated subdomains (Polishchuk et al., 2006). Strikingly, a chimeric construct comprising the luminal and transmembrane domains of LAMP1 fused to the cytosolic domain of CD-MPR still transited to the plasma membrane, despite the endosomal export signals present in the CD-MPR tail. Moreover, mutation of CD-MPR to abrogate its acidic-cluster dileucine motif caused TGN accumulation, but not export to the plasma membrane (Chen et al., 2017).

Taken together, this evidence suggests that TGN-to-plasma membrane trafficking is more than simply a ‘bulk flow’ model whereby proteins that are not sorted to the endosomal network are exported, but rather that information governing the sorting of cell surface proteins can reside within their luminal and transmembrane domains **(Figure 1.3)**. Plasma membrane cargoes are known to partition away from Golgi-resident transmembrane proteins (Bretscher and Munro, 1993; Patterson et al., 2008). Chimeric constructs replacing the transmembrane domains of plasma membrane resident proteins with those of the *trans*-Golgi glycosylation enzymes beta-1,4-galactosyltransferase and alpha-2,6-sialyltransferase are efficiently retained in the Golgi (Munro, 1991; Nilsson et al., 1991). Moreover, glycosylphosphatidyl-inositol (GPI)-anchored proteins exported to the plasma membrane do not possess a transmembrane or cytosolic domain and therefore are incapable of interacting with a coat complex through a canonical recognition mechanism (Surma et al., 2012). Instead, these proteins associate with the membrane through a GPI lipid moiety, and the depletion of cholesterol has been demonstrated to inhibit their anterograde trafficking to the cell surface (Hannan and Edidin, 1996). A model for cargo segregation within the Golgi therefore posits that the biophysical properties arising from the length and charge of cargo transmembrane and luminal domains (or in the case of GPI-anchored proteins, their lipid moiety) results in

their enrichment into discrete glycosphingolipid and cholesterol rich microdomains, termed lipid rafts. The coalescence and accumulation of proteins and lipids within rafts induces curvature and ultimately fission from the TGN membrane (Surma et al., 2012).

Soluble proteins also require cargo sorting to ensure their accurate export from the TGN, either for delivery to the endosomal network or for secretion from the cell surface. In the case of many acid hydrolases, a group of catabolic enzymes that degrade the luminal contents of the lysosome, the solution is relatively simple. A mannose-6-phosphate (M6P) tag is covalently attached to acid hydrolases during their progression through the Golgi apparatus. This tag can then be recognised by the M6P receptors, CD-MPR and CI-MPR. Consequently, the sorting decision of M6P-tagged hydrolase receptors is outsourced, depending instead on the cytosolic tail motifs of the receptors rather than the hydrolases themselves (Braulke and Bonifacino, 2009). A recently established model for the regulated secretion of soluble proteins is more complex and involves Cab45, a soluble calcium-binding protein that oligomerises in response to Ca^{2+} influx through the SPCA1 ion channel on the TGN membrane. Cab45 oligomers bind and cluster soluble cargoes for secretion, such as lysozyme, but not the acid hydrolyse cathepsin D, and therefore selectively sequesters soluble secretory cargo to facilitate their incorporation into transport carriers at the TGN **(Figure 1.3)** (Crevenna et al., 2016; Pakdel and Von Blume, 2018). Moreover, SPCA1 couples its activity with the synthesis of sphingomyelin, which may contribute to lipid raft formation for plasma membrane trafficking (Deng et al., 2018).

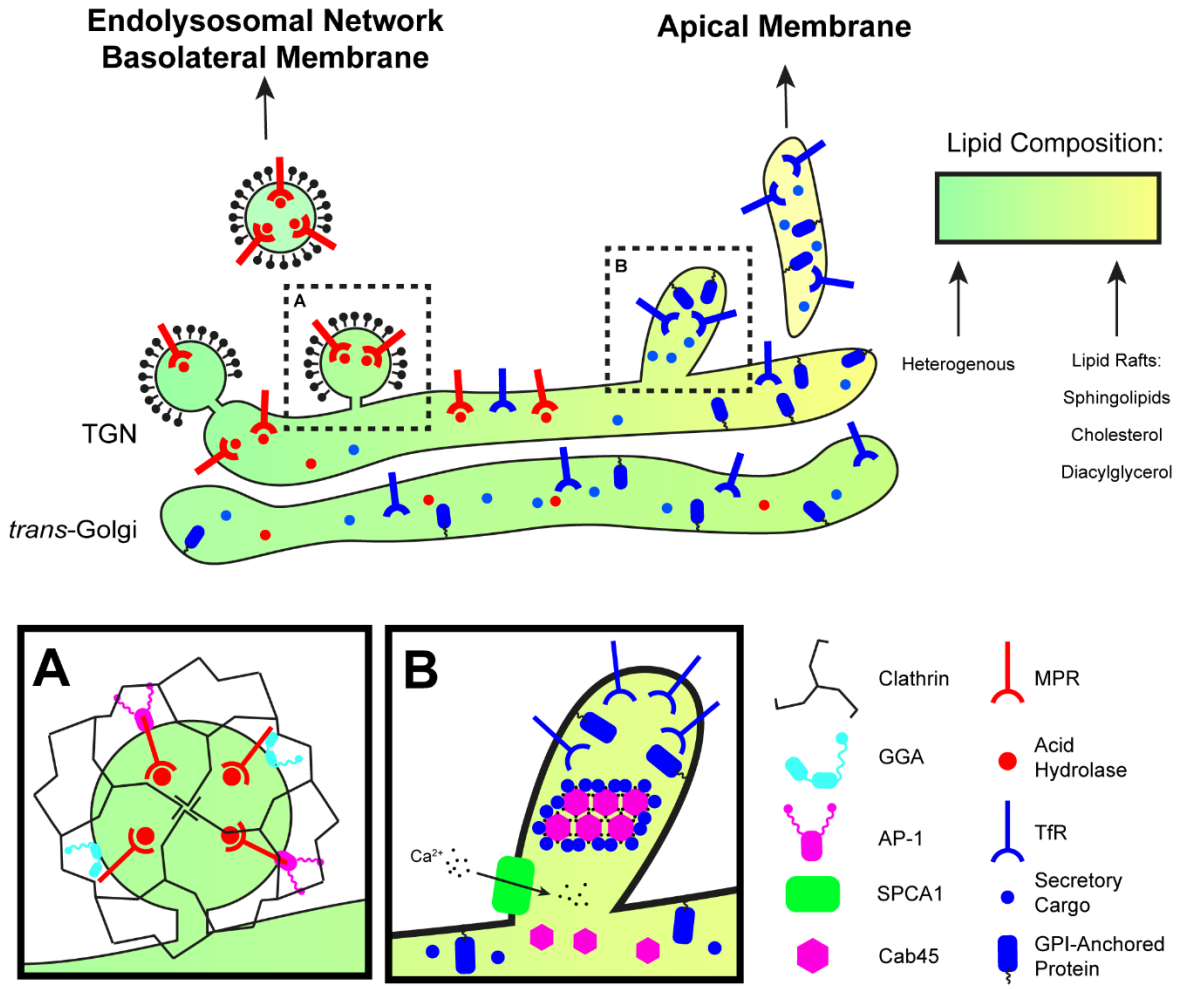

Figure 1.3 Cargo Sorting at the TGN

Examples of cargo export to the endolysosomal network/basolateral membrane via clathrin-coated pits, and anterograde transport to the apical plasma membrane are displayed. Although AP-1 and GGA are spatiotemporally distinct from each other, here they are displayed in the same CCV for clarity. The thicker membrane of budding apical membrane carriers reflects a distinct lipid identity that facilitates cargo recruitment.

1.2.2 Endocytosis and Biogenesis of Early Endosomes

The cell uses multiple endocytic pathways to internalise cargo proteins and extracellular contents. Endocytosis can occur in response to a wide range of cues, such as receptor-ligand binding, to modulate cell adhesion to the extracellular matrix, to uptake nutrients from the surrounding environment, or to mediate protein turnover (Kaksonen and Roux, 2018). The predominant pathway for internalisation is clathrin-mediated endocytosis (CME), which was reported to transport approximately 95% of surface-labelled proteins into TfR-positive vesicles (Bitsikas et al., 2014). Clathrin-independent mechanisms have also been established, including caveolin coat dependent endocytosis, GTPase recruitment of the actin cytoskeleton

and curvature sensing proteins to stabilise tubulovesicular membrane invaginations, and larger-scale uptake through phagocytosis and macropinocytosis (Mayor et al., 2014).

Following their internalisation from the plasma membrane, endocytic vesicles fuse with the early endosome, a pleiomorphic vacuolar organelle with dynamic tubular extensions (Helenius et al., 1983). Prior to this fusion step, endocytic vesicles attain Rab5-GTP, which begins recruiting effectors (Woodman, 2000). A subset of endocytic vesicles transiently acquire the Rab5 effectors APPL1 (adaptor protein containing PH domain, PTB domain and leucine zipper motif 1) and APPL2, which in turn possess phosphotyrosine binding (PTB) domains that interact with various receptor tyrosine kinases (RTKs) (Lin et al., 2006; Mao et al., 2006). APPL-positive endosomal compartments represent a dynamic compartment that is distinct from early endosomes and may serve as a platform for intracellular signalling of internalised receptors. Ultimately, APPL1 and APPL2 are lost from these compartments and they progress to fuse with early endosomes.

Recently, an elegant model for the fusion of endocytic vesicles with early endosomes has been established. The defining hallmarks of early endosomes are the presence of both Rab5 and PI(3)P, the coincidence detection of which recruits a plethora of effectors, including the coiled-coil tethering protein EEA1 (Simonsen et al., 1998). The presence of EEA1 on early endosomes, but its absence from incoming endocytic vesicles which are Rab5-positive but devoid of PI(3)P, confers the directionality of membrane fusion (Rubino et al., 2000). In an unbound state, the N-terminus of EEA1 rigidly projects into the cytosol by approximately 200 nm and is capable of binding Rab5-GTP on incoming endocytic vesicles and early endosomes in *trans*. Rab5-GTP binding induces allosteric changes in the EEA1 structure, introducing a large degree of flexibility within the coiled-coils (Murray et al., 2016). This large-scale re-structuring of EEA1, termed an ‘entropic collapse’, liberates free energy that pulls the incoming vesicle into closer proximity to the early endosome, to a point where SNAREs can mediate the subsequent fusion steps. In the case of homotypic fusion of early endosomes, the main SNAREs involved in early endosome fusion are Syntaxin-6, Syntaxin-13 and Vti1a (t-SNAREs on the accepting membrane), and vesicle-associated membrane protein 4 (VAMP4, v-SNARE on the incoming membrane) (Brandhorst et al., 2006). Additional factors facilitate early endosome fusion independently of EEA1, including the Rabenosyn-5, which is required for Cathepsin D sorting into the endosomal network and therefore may be responsible for receiving anterograde TGN-to-endosome vesicles, and the CORVET complex, which is involved in multiple early endosome fusion events (Nielsen et al., 2000; Perini et al., 2014). This variety of fusion complexes reflects the dynamicity of the early endosome.

1.2.3 The Endosomal Network

Like the TGN, the endosomal network constitutes a major sorting station within eukaryotic cells that integrates membrane inputs from multiple locations to make a fate decision: broadly, cargoes within the endosomal network can either be degraded in the lysosome or recycled back to an accepting compartment **(Figure 1.1)** (Cullen and Steinberg, 2018). The process of endosomal recycling is responsible for maintaining the subcellular localisation of thousands of integral membrane proteins. These dynamic organelles are collectively referred to as a 'network' due to their multiplicity within a cell; unlike organelles with a single copy number such as the endoplasmic reticulum or Golgi apparatus, endosomes are stationed throughout the cytoplasm (early endosomes are typically peripheral, whilst late endosomes become perinuclear), and are constantly remodelled by fusion and fission events. The endosomal network can be broadly categorised into 3 well-defined components: early endosomes (alternatively referred to as sorting endosomes), which predominantly receive incoming membrane carriers and begin the mechanistic process of cargo sorting; late endosomes (alternatively referred to as multivesicular bodies), which undergo a transition in molecular markers from early endosomes and ultimately proceed to fuse with lysosomes to degrade their components; and the endocytic recycling compartment (ERC, alternatively referred to as recycling endosomes), a secondary sorting station that receives cargo from early endosomes and directs their subsequent trafficking steps **(Figure 1.1)** (Cullen and Steinberg, 2018). These subcompartments of the endosomal network possess fundamentally distinct characteristics that dictate their functions.

Early endosomes are highly diverse in their size and morphology. Broadly, endosomes comprise a vacuolar portion, which contains most of the luminal volume and is the localised site of endosomal cargo sorting, and tubular projections, which contribute most of the membrane surface area (Huotari and Helenius, 2011). Early endosomes display a mildly acidic pH of 5.9-6.8 (Maxfield and Yamashiro, 1987). Cargoes destined for endosomal recycling are enriched into the tubular subdomains, which ultimately separate and traffic away from endosomes to mediate recycling. Cargoes that have been targeted for degradation are internalised into intraluminal vesicles (ILVs) of 50-80 nm in diameter (Van Meel and Klumperman, 2008). The number of ILVs within endosomes can be appreciated as a marker of their identity. Early endosomes are visualised as having 1-8 ILVs, whereas later endosomes display 8-30 ILVs as degradative cargoes accumulate (Van Meel and Klumperman, 2008). Early endosomes undergo homotypic fusion with each other, which results in a funnel-like hierarchy, whereby endosomes grow in size and decrease in number as they mature (Villaseñor et al., 2016). Consequently, late endosomes are typically much larger than early endosomes, with a size of 250 – 1000 nm (Huotari and Helenius, 2011). Late endosomes

have a lower pH range of 4.9-6.0, and acquire a distinct ionic identity in response to acidification (Maxfield and Yamashiro, 1987). Ultimately, endosomes fuse with lysosomes to deliver their contents which forms a transient degradative organelle, termed the endolysosome, with a pH of 4.5, the lowest of any organelle (Huotari and Helenius, 2011; Maxfield and Yamashiro, 1987). Endolysosomes are subsequently resolved back to lysosomes (Luzio et al., 2007).

1.2.4 Endosomal Maturation

The endosomal network can be imagined as a conveyor belt moving centripetally towards the lysosome, which constitutes a point of no return for cargoes, which if not recycled are ultimately degraded by lysosomal acid hydrolases. Endosomal maturation is therefore a highly regulated process that ensures an adequate amount of time is allowed for endosomal cargo sorting and recycling to occur before reaching this terminus. The large-scale morphological changes associated with endosomal maturation occur quickly: early endosomes fuse with each other and receive incoming membranes for a time window of approximately 5-15 minutes prior to their maturation into late endosomes; late endosomes then progress towards fusion with lysosomes within 10-40 minutes (Huotari and Helenius, 2011; Maxfield and McGraw, 2004). The key regulators of this maturation process are the Rab GTPases and PIPs, which recruit a cascade of effectors that modulate endosome membrane identity.

Multiple Rab GTPases localise throughout the endosomal network, the best characterised of which include Rab4 and Rab5 on early endosomes, Rab11 and Rab25 on the ERC, and Rab7 and Rab9 on late endosomes **(Figure 1.1)** (Galvez et al., 2012). Many additional Rabs also localise to these organelles or the intermediate trafficking compartments that exchange material between them (Galvez et al., 2012). The key regulators of endosomal maturation are Rab5 and Rab7, and a coordinated switch between them facilitates this process (Huotari and Helenius, 2011). The Rab5/Rab7 conversion has been described as a ‘cut-out switch’ model analogous to an electrical circuit breaker, whereby as Rab5 levels and effector recruitment reach their peak, a negative feedback loop is initiated that rapidly shuts off Rab5 signalling and recruits Rab7 and its effectors (Del Conte-Zerial et al., 2008).

Lipids also play a crucial role in endosome maturation. PI(3)P pools generated by the class III PI-3 kinase VPS34 recruit the GAP protein TBC1D2A, which may modulate the activities of Rab5 and Rab7 (Jaber et al., 2016; Law et al., 2017). A class III PI-5 kinase, PIKFYVE, is also recruited during the process of endosomal maturation through the binding of its FYVE domain to PI(3)P (Sbrissa et al., 1999; Wallroth and Haucke, 2018). PIKFYVE generates pools of PI(3,5)P_2 that are required for the subsequent processes of late endosomal cargo sorting and degradation (Jefferies et al., 2008). Endosomal maturation ultimately results in the

homotypic fusion of late endosomes and heterotypic fusion with lysosomes (Huotari and Helenius, 2011). This process is mediated by the HOPS complex, which acts as a tether and coordinates the SNARE assembly required for membrane fusion (Balderhaar and Ungermann, 2013; Solinger and Spang, 2013).

A decrease in intraluminal pH accompanies the shifting identity of maturing endosomes. This acidification is mediated by a vacuolar ATPase (v-ATPase) multi-protein complex comprising a transmembrane pore for shuttling protons from the cytosol to the endosomal lumen (the V_0 domain), and a cytosolic ATP-driven rotor that provides energy for proton pumping (the V_1 domain) (Forgac, 2007). v-ATPases regulate the intralumenal pH of a range of organelles and can even be targeted to the plasma membrane to acidify the extracellular space in certain cell types (Forgac, 2007). Accordingly, the a subunit of the V_0 domain, of which there are four isoforms in mammals, confers organelle targeting specificity, with a2 responsible for early endosomal targeting (Marshansky and Futai, 2008). Moreover, the endosomal v-ATPase partitions into detergent-resistant lipid subdomains, highlighting a potential role of lipid composition in regulating v-ATPase recruitment and thus lumen acidification (Huotari and Helenius, 2011). The progressive decrease in pH facilitates the dissociation of receptors from their ligands within the endosomal lumen, allowing receptors to be recycled to undergo further iterations of ligand binding. Progressing further through the network to endolysosomes and lysosomes, the decreasing pH becomes necessary to facilitate the catalytic activity of acid hydrolase enzymes which operate below pH 5 (Wartosch et al., 2015).

1.2.5 The Endocytic Recycling Compartment

The ERC is a tubular network of predominantly Rab11-positive membranes that represents a distinct, indirect route for endosomal cargo recycling to target organelles. The ERC receives cargoes from early and late endosomes and sorts them for recycling to the plasma membrane or TGN (Maxfield and McGraw, 2004). However, the precise details of this process, and why it takes place away from the central Rab5/Rab7 endosome axis remains enigmatic. Direct endocytic recycling from Rab5/7 positive endosomes is termed ‘fast recycling’ whereas indirect sorting through the ERC is referred to as ‘slow recycling’ (Cullen and Steinberg, 2018). Rab11 regulates the cell surface localisation of a wide range of proteins (Welz et al., 2014). Expression of a constitutively active Rab11 mutant had no impact on TfR internalisation and initial trafficking from Rab5-positive early endosomes, but led to a perturbation in recycling to the plasma membrane from the ERC, highlighting its role as a secondary sorting station (Ullrich et al., 1996). Rab11 also interacts with the Sec15 subunit of the exocyst complex, and therefore may be involved in polarised transport to the plasma membrane (Zhang et al., 2004). Accordingly, the Rab11 isoform Rab25 directly interacts with integrin β1, and the Rab11

effector Rab-coupling protein (RCP) engages α5β1-integrin heterodimers (Caswell et al., 2008, 2007). Rab11-dependent recycling in the ERC may therefore represent a sorting hub that conducts controlled, polarised endocytic recycling to facilitate dynamic processes such as persistent cell migration (Paul et al., 2015).

1.2.6 The Degradative Route: Internalisation of Cargo into ILVs

A key step in the fate decision of early endosomal cargoes is the identification and sequestration of proteins to be degraded. A model cargo for this process is the activated epidermal growth factor receptor (EGFR). EGFR localises to the plasma membrane, and once bound to its extracellular ligand EGF, becomes activated by a range of phosphorylation events within its tyrosine kinase domain (Bakker et al., 2017). This recruits numerous effector proteins that potentiate pro-growth and pro-survival signalling within the cell. In response to high extracellular concentrations of its ligand, EGFR signalling is attenuated through its internalisation into ILVs and degradation in the lysosome (Bakker et al., 2017). The initiation of this degradative pathway begins at the plasma membrane, with the covalent attachment of ubiquitin to the cytosolic domains of cargo destined for degradation. In the case of EGFR, and a range of other activated RTKs, ubiquitylation is performed by the ubiquitin ligase enzyme c-CBL, which is recruited to activated receptors by its binding partner GRB2 (Levkowitz et al., 1998). Cargoes can be marked for degradation by either mono- or polyubiquitylation. Various cargo adaptors for CME are capable of recognising ubiquitylated cargo via ubiquitin-interaction motifs (UIMs) (Clague et al., 2012). Accordingly, ubiquitylated cargo can be rapidly recognised and internalised into endocytic vesicles for delivery to the early endosome. The use of ubiquitylation as a destruction signal bypasses the requirement for a distinct sorting motif for degradation within cargo tails, instead establishing a binary code that allows cargo turnover to be a flexible and responsive pathway.

The machineries primarily responsible for the sorting of cargo for degradation are the endosomal sorting complex required for transport (ESCRT) proteins, which are classed into four complexes: ESCRT-0, ESCRT-I, ESCRT-II and ESCRT-III (Henne et al., 2011). Together, the ESCRT complexes serve to recognise ubiquitylated cargo on early endosomes, corral them into a spatially restricted subdomain, catalyse their deubiquitylation and facilitate their internalisation into ILVs. ESCRT-0 is a heterodimer comprised of hepatocyte growth factor-regulated tyrosine kinase substrate (HRS) and signal transducing adapter molecule 1 (STAM1) (Henne et al., 2011). Localised to early endosomal membranes through the PI(3)P-binding FYVE domain of HRS, ESCRT-0 binds ubiquitinylated proteins via the UIMs and VHS domains present in HRS and STAM1 (Raiborg et al., 2001; Ren and Hurley, 2010). ESCRT-0 oligomerises into higher order complexes to densely cluster ubiquitylated cargoes with high

avidity on the endosomal membrane (Mayers et al., 2011). This establishes a degradative subdomain on early endosomes, to which further effectors are recruited (Cullen and Steinberg, 2018). ESCRT-0 also recruits clathrin, which in contrast to its role in vesicular membrane trafficking, forms a relatively flat, scaffolding lattice on the endosomal membrane that plays a role in degradative cargo sorting (Raiborg et al., 2006; Sachse et al., 2002).

ESCRT-1 is recruited to the sites of cargo internalisation via interactions with HRS and ubiquitin (Katzmann et al., 2003). ESCRT-1 subsequently recruits ESCRT-II, which also recognises ubiquitin, and the association of these complexes serves to further corral ubiquitylated cargoes by limiting their lateral diffusion within the membrane (Cullen and Steinberg, 2018; Kostelansky et al., 2006). ESCRT-II recruits ESCRT-III (Henne et al., 2011). The ESCRT-III component CHMP4 oligomerises into a spiral lattice, analogous to an elastic spring, that imposes membrane tension and begins to invaginate the endosomal membrane to form an ILV (Chiaruttini and Roux, 2017). ESCRT-0, -1 and -II components disengage from nascent vesicles through a poorly understood mechanism. Finally, the hexameric AAA-ATPase VPS4 mediates the scission of ILV neck by unfolding ESCRT-III components and threading them through a central cavity in the hexamer, bringing the membranes of the ILV neck into direct apposition (Adell et al., 2017; Schöneberg et al., 2016) **(Figure 1.4)**.

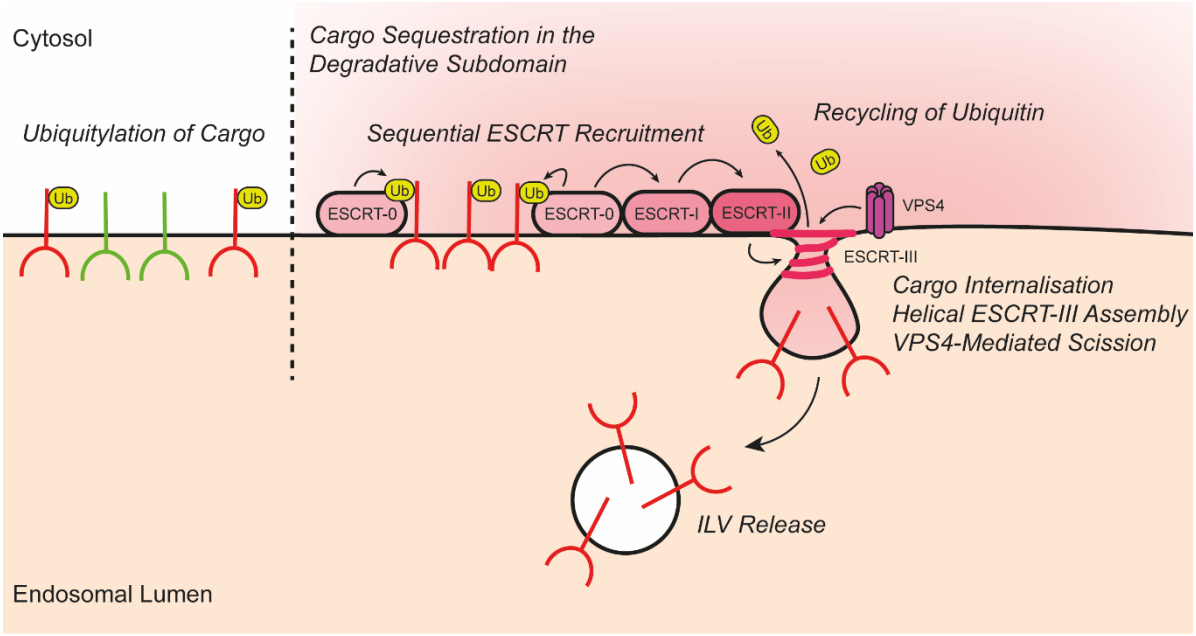

Figure 1.4 Degradative Cargo Sorting by the ESCRT Complexes

In the canonical ESCRT model, cargo destined for degradation are labelled with a ubiquitin tag, which is recognised by ESCRT-0. The polymerisation of ESCRT-0, and sequential recruitment of ESCRT-1, -II and -III sequesters cargo within a degradative subdomain on the endosomal membrane. ESCRT-III assembles into a spiral lattice that invaginates the endosomal membrane and constricts the neck of the nascent vesicle. VPS4 mediates the final scission stage, and the recycling of ESCRT-III components and ubiquitin.

In addition to the well-described mechanism of ESCRT-dependent degradation of ubiquitylated cargoes, a mechanism of ubiquitin-independent degradative sorting has been proposed, based on the ability of the ESCRT-III adaptor apoptosis-linked gene-2 interacting protein X (ALIX) to bind to the protease activated receptor 1 (PAR1) and sort its internalisation into ILVs (Dores et al., 2012). ESCRT-independent pathways for internalisation may also exist (Babst, 2011; Edgar et al., 2014). The ESCRT complexes are also employed in various other membrane remodelling events in cell biology, including abscission of the cytokinetic bridge during mitosis (Henne et al., 2011).

1.2.7 The Catabolic Endolysosome

The lysosome has historically been viewed as the catabolic centre of the cell, where protein and lipid cargoes are degraded into their constituent parts. The lysosome is equipped with a host of enzymes, broadly termed acid hydrolases, that encompass proteases, lipases, nucleases and more (Bainton, 1981; de Duve, 2005). The lysosomal membrane and its associated resident proteins must be protected from hydrolysis to ensure lysosomal integrity. Accordingly, lysosomal-associated membrane glycoprotein 1 (LAMP1) and LAMP2, which together constitute approximately 50% of the lysosomal membrane proteome, possess densely glycosylated luminal domains that form an intraluminal glycocalyx of 5-12 nm in thickness (Schulze et al., 2009; Wilke et al., 2012). Acid hydrolases therefore cannot access the membrane, or the luminal domains of transmembrane proteins within this dense meshwork of glycosylation, which prevents the lysosome from digesting its own resident proteins and lipids. ILVs, and the cargoes they possess, lack this protection and are therefore degraded by the hydrolytic enzymes of the lysosome.

More recently, electron microscopy (EM) and biochemical analysis has revealed a functional and morphological distinction between inactive lysosomes, termed ‘terminal storage lysosomes’, and endolysosomes that have recently undergone fusion with late endosomes. This emerging model suggests that terminal storage lysosomes are densely packed with acid hydrolase enzymes with a neutral pH, taking on the role of a storage granule (Bright et al., 2016). Catabolism occurs upon fusion with late endosomes, either by a kiss-and-run or complete fusion of the two organelles (Bright et al., 2005). This fusion and formation of an endolysosome mixes the luminal contents of the two organelles, leading to acid hydrolase activation in the low pH environment of the lumen. It is within these hybrid organelles that cargo degradation occurs. Following the biogenesis of this organelle, the endolysosome undergoes a condensation process to resolve itself back into a lysosome and recycle any remaining membrane proteins (Luzio et al., 2007). It is possible that the final recycling events occurring at the endolysosomal membrane serve to rescue any remaining endosomal

machinery, such as SNAREs (as has been observed with VAMP7) and acid hydrolase receptors (Huotari and Helenius, 2011; Ko et al., 2001; Luzio et al., 2007).

It is now well established that in addition to the classical view of lysosomes as the passive 'dustbin' of the cell, lysosomes play a central role in nutrient sensing and cell signalling. Much of this signalling axis is centred around the mechanistic target of rapamycin complex 1 (mTORC1) complex, which translocates from the cytosol to the lysosomal membrane in response to amino acid stimulation (Ballabio and Bonifacino, 2020; Carroll, 2020). mTORC1 phosphorylates a wide range of substrates, including transcription factors that up-regulate gene networks involved in cell growth and proliferation. These recent discoveries reframe the lysosome as a highly active and responsive organelle, and this signalling function is implicated in a wide range of processes, from oncogenesis to ageing (Ballabio and Bonifacino, 2020).

1.3 Mechanistic Endosomal Recycling

Endosomes mature rapidly, ultimately leading to the degradation of their contents upon fusion with lysosomes. To escape this degradative fate, cargo must be actively recycled away from endosomes and back to an accepting compartment. The flux of cargo through the endosomal network is vast, incorporating thousands of transmembrane proteins entering upon various different conditions and stimuli (Cullen and Steinberg, 2018). Many receptors undergo multiple iterative rounds of ligand binding, internalisation/export into the endosomal network, and recycling during their lifetime. Endosomal recycling eases the burden of constitutive protein production and processing to replace degraded cargoes and facilitates the adaptive complexity of eukaryotic cells in responding to their environment. Degrading the entirety of incoming endosomal cargo would therefore be catastrophic: to do so would blunt the responsiveness of the cell to extracellular cues through the loss of plasma membrane receptors; impair timely synaptic transmission and plasticity; induce lysosomal dysfunction due to the impaired delivery of acid hydrolases, which in turn results in the accumulation of toxic intracellular aggregates; amongst many other complex detrimental consequences. To ensure endosomal recycling is tightly regulated, a wide range of cargo adaptors and coat complexes serve to recognise the highly diverse repertoire of endosomal cargo to ensure their efficient mechanistic recycling away from degradation (Cullen and Steinberg, 2018).

1.3.1 Geometry-Based versus Sequence-Dependent Endosomal Recycling Models

Following initial observations that internalised endosomal cargoes were subsequently recycled, a prevailing model explained this process based on the geometric parameters of early endosomes, and the transmembrane cargo that they sort. Early endosomal tubules have

a high surface-area-to-volume ratio that can accommodate freely diffusing transmembrane proteins, while excluding luminal content containing components such as dissociated ligands that require degradation. Cargoes that were not actively sorted for degradation would therefore be recycled away from the endosome along with the bulk membrane flow during the maturation process (Maxfield and McGraw, 2004). This 'geometry-based sorting' model is supported by the evidence that the removal of the cytosolic tail of TfR does not impair its endocytic recycling, implying that specific tail sequences were not required for this process (Jing et al., 1990). Moreover, a fluorescently labelled plasma membrane lipid reporter was internalised and recycled with the same kinetics as TfR (Mayor et al., 1993). While bulk flow may account for some endosomal recycling of transmembrane cargoes, the identification of the endosomal sorting complexes and the cargo they associate with has facilitated the identification of a diverse range of cytosolic cargo sorting motifs (Bonifacino and Traub, 2003; Cullen and Steinberg, 2018; Weeratunga et al., 2020). TfR itself appears to participate in sequence-dependent recycling, despite earlier reports of its capacity to traffic without a cytosolic domain (Chen et al., 2013; Dai et al., 2004). Endosomal recycling is therefore a largely active process that relies on the concerted action of multiple multi-protein complexes to specifically identify, sequester, and traffic the cargoes present on the endosomal membrane.

1.3.2 The Retromer Complex: From Yeast to Metazoans

The discovery of the retromer complex arose following a series of genetic screens in the yeast model organism *Saccharomyces cerevisiae*. Deletion of a wide range of proteins caused missorting of the yeast acid hydrolase carboxypeptidase Y (CPY) (Bankaitis et al., 1986; Bonangelino et al., 2002; Rothman et al., 1989). The delivery of CPY to the yeast vacuole relies on the constitutive bidirectional traffic of the hydrolase receptor Vps10p between the TGN and endosomes (Cooper and Stevens, 1996). Many of the uncharacterised hits from these screens were named as vacuolar protein sorting (VPS) proteins. Two complexes, one comprising Vps26, Vps29 and Vps35, and the other composed of Vps5 and Vps17, were found to mediate the retrograde endosome-to-TGN sorting of Vps10p and the efficient vacuolar delivery of CPY (Horazdovsky et al., 1997; Seaman et al., 1997). These two subcomplexes interact to assemble a heteropentameric recycling coat complex associated with vacuolar and tubular portions of endosomes, termed the retromer complex (Seaman et al., 1998).

The retromer components are evolutionarily conserved from yeast to metazoans, although three paralogues of VPS26 have diverged (VPS26A, VPS26B and VPS26C) and gene duplications of Vps5 (into SNX1 and SNX2) and Vps17 (into SNX5, SNX6 and SNX32) have arisen (Carlton et al., 2004; Koumandou et al., 2011; Wassmer et al., 2007). Of the three

VPS26 paralogues, VPS26A and VPS26B can be incorporated into the human retromer complex (Kerr et al., 2005). VPS26A and VPS26B may confer different characteristics to the complex, such as dictating which cargo it recognises (Bugarcic et al., 2011). However, recent proteomic analysis of VPS26A and VPS26B revealed a largely overlapping interactome (McMillan et al., 2016). The third VPS26 paralogue, VPS26C, does not integrate into the retromer complex, but rather incorporates into the structurally analogous retriever complex (Koumandou et al., 2011; McNally et al., 2017). In mammals, the Vps5 and Vps7 homologues SNX1/2 and SNX5/6/32 respectively form members of the sorting nexin (SNX)-Bin/Amphiphysin/Rvs (BAR) family. In contrast to the yeast heteropentameric complex, the retromer heterotrimer and SNX-BAR dimer do not biochemically interact in humans (Kvainickas et al., 2017; Simonetti et al., 2017). Accordingly, the core human heterotrimer of VPS26A/VPS26B-VPS35-VPS29 is herein referred to as 'retromer', and the heterodimeric SNX1/2-SNX5/6/32 complex is referred to as the 'endosomal SNX-BAR sorting complex for promoting exit-1' (ESCPE-1) **(section 1.3.7)** (Simonetti et al., 2019). Retromer and ESCPE-1 may cooperate in the sensing and retrieval of endosomal cargo, but increasing evidence suggests that they also independently recycle separate protein populations (Kvainickas et al., 2017; Simonetti et al., 2019, 2017; Yong et al., 2020).

Structural biology can provide meaningful insights into mechanistic endosomal cargo sorting by revealing the specific molecular details of adaptor complex assembly and the mechanism of cargo binding. Several studies have now elucidated structural details of the retromer complex and its association with cargo and adaptors **(Figure 1.5)**. VPS35 is the largest subunit, and forms a central platform for the assembly of VPS26A/B and VPS29 at its C- and N-termini, respectively (Collins et al., 2005; Norwood et al., 2011; Shi et al., 2006). VPS35 forms a slightly kinked α-solenoid structure that assembles into 17 anti-parallel HEAT (Huntingtin/EF3/PP2A/TOR1) repeats (Collins, 2008; Hierro et al., 2007; Lucas et al., 2016). Both VPS26A and VPS26B form an arrestin-like antiparallel β-sandwich fold, an extended C-terminus that engages VPS35, and an exposed hydrophilic core region (Collins et al., 2008; Shi et al., 2006). VPS29 forms a metallo-phosphoesterase-like fold, but has been demonstrated not to display phosphatase activity *in vitro* (Hierro et al., 2007).

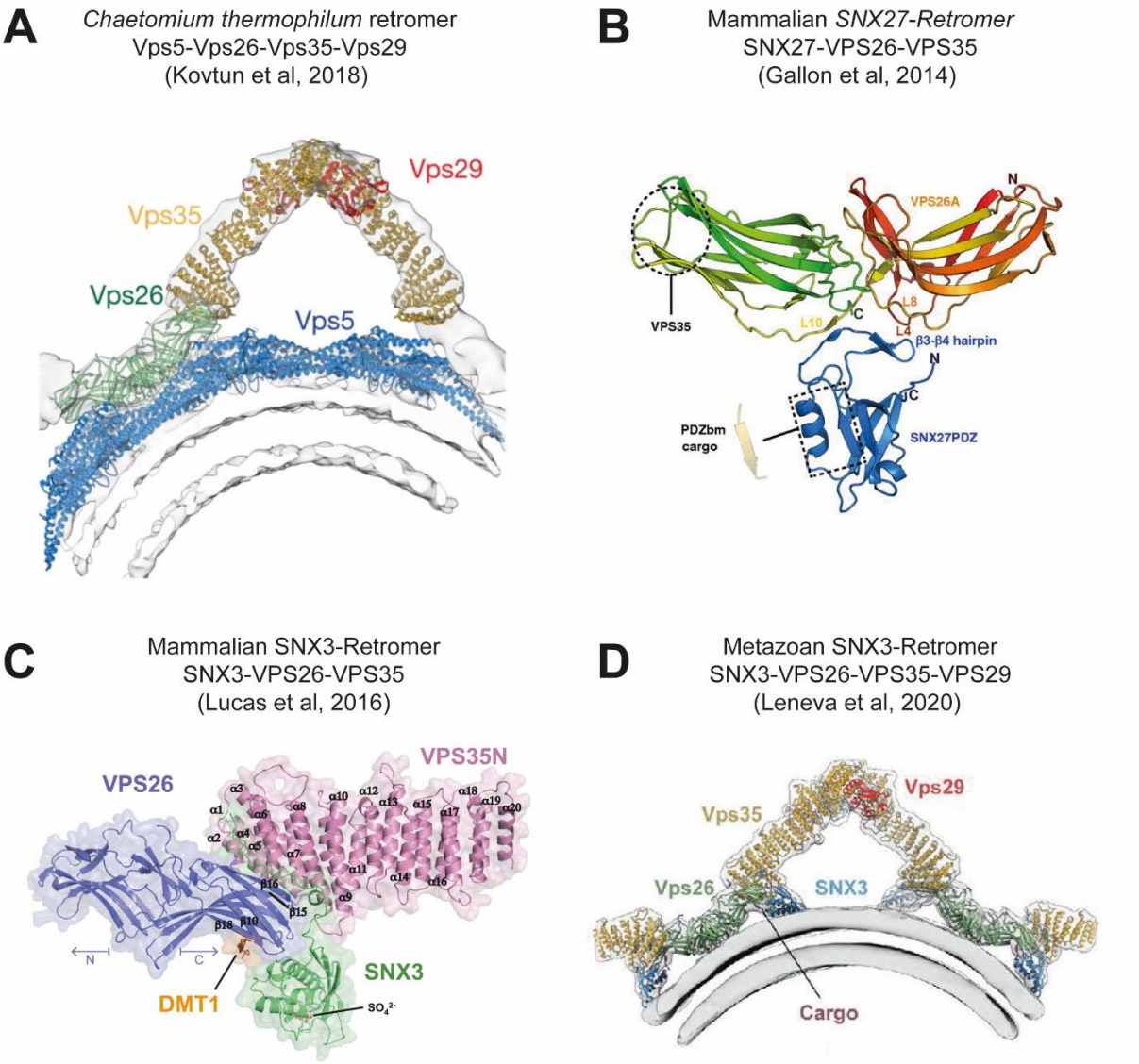

Figure 1.5 Structures of the Retromer Complex

Multiple structures for retromer have been reported, in complex with Vps5 (the fungal SNX-BAR protein) **(A)**, SNX27 **(B)** and SNX3 **(C and D)**. Retromer does not appear to contact membranes directly, and rather requires SNX association for its recruitment. The recent structure of metazoan SNX3-retromer suggests an intrinsic membrane remodelling capacity of the complex, and an ability to assemble into polymeric filamentous structures, similarly to the *Chaetomium thermophilum* retromer. Figures adapted from (Kovtun et al., 2018) protein data bank (PDB) ID: 6H7W, (Gallon et al., 2014) PDB ID: 4P2A, (Lucas et al., 2016) PBD ID: 5F0L, (Leneva et al., 2020) PDB ID: 7BLO.

Cryo-EM techniques have provided the most recent structural insights into the assembly of retromer into higher-order structures. The *Chaetomium thermophilum* retromer (a fungal pentameric complex analogous to yeast) structure was recently solved utilising recombinant Vps26, Vps29 and Vps35 with Vps5 on liposomes **(Figure 1.5A)** (Kovtun et al., 2018). This assembly formed a coat structure on the membrane approximately 15 nm thick. The core

retromer trimer does not contact the membrane itself and requires recruitment through Vps5 binding to Vps26. Interestingly, within this coat structure, two Vps26/Vps29/Vps35 heterotrimers project away from the membrane and associate into an arch-like dimer, mediated by a binding interface between opposing C-termini of Vps35 subunits. Vps29 is exposed at the apex of the arch, which may allow it to recruit important accessory factors such as the Rab7-GAP TBC1D5 in humans (Jia et al., 2016; Kovtun et al., 2018). Furthermore, the cryo-EM structure of murine retromer is largely in agreement with the ability of retromer to form higher-order structures (Kendall et al., 2020). Retromer was found to form dimers, tetramers, and oligomeric chains of heterotrimers. Moreover, local resolution variability around the VPS35-VPS35 dimer interface implies a degree of flexibility at this hinge region. Flexibility of the retromer dimer arch may therefore confer plasticity to the structure that allows retromer to adopt different conformations in response to the binding of diverse cargo and adaptors. Furthermore, the adaptive oligomerisation of retromer complexes may cluster cargo within a distinct retrieval subdomain on the endosome (Kendall et al., 2020). Reconstituted retromer components were also found to form low-order oligomers on a supported lipid bilayer (Deatherage et al., 2020).

Depletion of retromer components induces the redistribution of a vast range of cell surface cargoes (Steinberg et al., 2013). The emerging model of retromer in endosomal recycling is that it plays a role as a ‘master-regulator’, through its myriad interactions with effectors such as sorting nexin (SNX) cargo adaptors, and TBC1D5 (Cullen and Steinberg, 2018). In this role, retromer orchestrates the sensing and timing of cargo for recycling, and additionally modulates Rab7 activity to define the properties of the late endosomes **(see Chapter 3.1.2 for more detailed introduction)**.

1.3.3 Sorting Nexins as Cargo Adaptors

The SNX family comprises 33 proteins in mammals, characterised by the presence of a PX domain that engages PI species, most commonly PI(3)P (Gallon and Cullen, 2015). While the PX domain of SNXs is conserved, the additional domains can vary considerably, and classify the family into 5 main groups: SNX-PX, SNX-BAR, SNX-FERM (Protein 4.1/Ezrin/Radixin/Moesin), SNX-PXA-RGS-PXC (PX-Associated Domain A, Regulator of G-Protein Signalling, PX-Associated Domain C) and SNX-MIT (Microtubule Interacting and Trafficking Molecule), and further domain organisation can differentiate members of these subfamilies even further (Gallon and Cullen, 2015; Teasdale and Collins, 2012). SNXs have diverse roles in regulating membrane trafficking events, ranging from endocytosis and endosomal recycling to regulating ER-lipid droplet contact sites (Datta et al., 2019; Worby and Dixon, 2002). Many SNXs possess the ability to recognise specific cargo through coincidence

detection mechanisms, which has far-reaching implications in the endosomal network in particular (Gallon and Cullen, 2015).

1.3.4 Retromer's Cargo Adaptors: SNX3 and SNX27

Despite references to the mammalian retromer as a 'cargo-selective complex', its ability to autonomously bind cargo appears to be limited. Moreover, the retromer heterotrimer does not engage membranes directly, and therefore requires recruitment to endosomes by effector proteins. Retromer can engage and recycle the Sortilin-related receptor SorLA, a Vps10p homologue that acts as a sorting receptor for APP, through a mechanism solely dependent on VPS26 (Fjorback et al., 2012). Beyond this example, retromer appears to require association with sorting nexin (SNX) adaptors to achieve cargo selectivity. In particular, the recruitment of SNX3 and SNX27 broadly expands the repertoire of cargoes that retromer can engage.

SNX3 is a member of the SNX-PX family, and besides its PX domain does not contain any additional structured regions. SNX3 is recruited to early endosomes through its engagement with PI(3)P, and binds VPS26 through three separate sites (Lucas et al., 2016). Together, this assembly is referred to as SNX3-retromer. SNX12 is a paralogue of SNX3 that can also engage the retromer complex, though its role as a cargo adaptor remains uncharacterised (Pons et al., 2012). SNX3-retromer facilitates retrograde endosome-to-TGN cargo transport. SNX3 association induces a conformational change within VPS26 that opens a binding site at the SNX3-VPS26 interface that can engage cargo tails conforming to a Øx(L/M/V) motif. In particular, the structural basis of SNX3-retromer binding to the iron transporter DMT1-II (Divalent Metal Transporter 1 Isoform II) has been resolved **(Figure 1.5C)** (Lucas et al., 2016). Additional reported SNX3-retromer cargoes include the Wntless receptor, TfR, and polycystin-2 (Chen et al., 2013; Feng et al., 2017; Harterink et al., 2011; Tilley et al., 2018). SNX3-retromer has been also implicated in CI-MPR retrograde recycling, by engaging its cytosolic ^{2369}WLM^{2371} motif and generating retrograde vesicles that are specifically recognised by the TGN golgin GCC88 (golgin-97, RanBP2alpha, Imh1p and p230/golgin-245 (GRIP) and coiled-coil domain-containing protein (GCC) protein 88) (Cui et al., 2019; Seaman et al., 2007). However, in a recent study a dissociation constant (K_d) value for SNX3-retromer binding to the cytosolic tail of CI-MPR could not be obtained by isothermal titration calorimetry (ITC) (Yong et al., 2020).

EM analysis revealed that SNX3-retromer decorates early endosomes and spherical CCVs, implying an independent mechanism of spherical transport carrier biogenesis compared to canonical tubulovesicle formation by BAR proteins (Harterink et al., 2011). Proteomic interrogation of the SNX3 interactome revealed its association with a MON2/DOPEY2/ATP9A

complex. ATP9A is a flippase enzyme that translocates phospholipids from the luminal to the cytosolic leaflet of the endosomal membrane, a process that generates localised sites of membrane curvature that contributes to SNX3-retromer vesicle formation (McGough et al., 2018). However, a recent cryo-EM study has revealed the assembled metazoan SNX3-retromer structure, which forms arch-like dimers that assemble into coated lattices on tubular membranes **(Figure 1.5D)** (Leneva et al., 2020). This finding challenges the understanding of SNX3-retromer function and opens further important questions about the direct role of retromer in endosomal recycling.

Another retromer-associated cargo adaptor is SNX27, which is also recruited to endosomal membranes through PI(3)P binding **(Figure 1.5B)**. SNX27 is a SNX-FERM family member, and through its C-terminal FERM domain can recognise cargo bearing ΦxNPxY and ΦxNxxY cytosolic motifs (Φ represents any hydrophobic amino acid residue), with a preference for phosphorylated tyrosine residues (Ghai et al., 2013). Furthermore, SNX27 uniquely possesses a N-terminal postsynaptic density 95/discs large/zonula occludens-1 (PDZ) domain capable of binding type I PDZ binding motifs (PDZbms) present at the C-termini of cargo. The presence of acidic or phosphorylated residues upstream of the PDZbm can significantly increase affinity of the SNX27 interaction (Clairfeuille et al., 2016). Through these distinct modes of binding, SNX27 engages a wide range of cargo, including APP, P-Selectin and GPR88 through its FERM domain, and GLUT1, β2-adrenergic receptor (β2AR) and the potassium channel Kir3.3 through its PDZ domain (Cullen and Steinberg, 2018; Ghai et al., 2013; Lauffer et al., 2010; Steinberg et al., 2013). SNX27 associates with retromer through a β-hairpin loop within the PDZ domain that interacts with arrestin-like fold within VPS26 (Gallon et al., 2014). Surface biotinylation of cargoes coupled with quantitative proteomics revealed that SNX27-retromer regulates the endosome-to-plasma membrane recycling of over 400 cargoes (Steinberg et al., 2013). Intriguingly, SNX27 is also capable of binding to SNX1 and SNX2 through its FERM domain, independently of retromer. Furthermore, depletion of SNX27 or retromer components induces lysosomal localisation of transmembrane cargoes, whereas depletion of ESCPE-1 complexes results in re-distribution to EEA1-positive early endosomes (Steinberg et al., 2013). Collectively this evidence suggests that SNX27-retromer is responsible for retrieving its cargo away from the degradative fate, then coupling to ESCPE-1 through SNX27 may facilitate tubulovesicle biogenesis for endosome-to-plasma membrane recycling. Consistent with this view, the SNX27-retromer cargo β2AR can be visualised in tubular profiles emanating from endosomes (Temkin et al., 2011).

1.3.5 The SNX-BAR Family

Of the 33 sorting nexins, 12 harbour a BAR domain: SNX1, SNX2, SNX4, SNX5, SNX6, SNX7, SNX8, SNX9, SNX18, SNX30, SNX32 and SNX33 (van Weering et al., 2010). Of these proteins, SNX1, SNX2, SNX5, SNX6 and SNX32 associate in different dimeric combinations to comprise ESCPE-1, SNX4, SNX7 and SNX30 can dimerise to mediate autophagic membrane trafficking, and SNX8 appears to function autonomously in retrograde endosome-to-TGN trafficking (Antón et al., 2020; Dyve et al., 2009; Simonetti et al., 2019; van Weering et al., 2010). SNX9 is a well-characterised facilitator of endocytosis, and alongside its evolutionarily related subfamily members SNX18 and SNX33 is implicated in the abscission steps of cytokinesis (Bendris and Schmid, 2017; Ma and Chircop, 2012).

BAR domain-containing proteins are modulators of membrane shape that electrostatically adhere to negatively charged membrane leaflets through a curved, positively charged surface (Simunovic et al., 2019). As members of the sorting nexin family, SNX-BAR proteins are recruited to biological membranes through the recognition of PIPs by their PX domains. SNX-BAR proteins induce membrane curvature through three mechanisms: the adherence of the curved BAR domain to the membrane, the insertion of shallow amphipathic helices that disrupt local lipid organisation, and by driving an entropy-driven crowding effect that is enhanced by SNX-BAR oligomerisation into lattices **(Figure 1.6)** (Simunovic et al., 2019). The SNX-BAR proteins are specifically classified as containing N-BAR domains, which induce positive membrane curvature in the direction of the cytosol (Van Weering et al., 2012).

Oligomerisation into higher-order lattice structures is an essential feature of SNX-BAR proteins in membrane tubulation, and is mediated by a combination of lateral electrostatic and hydrophobic interactions between dimers (Van Weering et al., 2012). An estimated 30-40% BAR protein coverage of tubules is sufficient to stabilise the structure (Simunovic et al., 2016). Cargo can be incorporated into SNX-BAR-generated tubules by endosomal sorting complexes. Following cargo enrichment, scission is mediated by a complex symphony of biochemical and biophysical forces imposing tension at the base of the tubule (Derivery et al., 2009; Rowland et al., 2014; Simunovic et al., 2017). The resulting tubulovesicular carriers harbouring cargo proteins are subsequently trafficked to an accepting organelle compartment. Taken together, SNX-BAR proteins play a spatiotemporally regulated role in endocytic recycling, by selectively recognising lipid identity, membrane curvature, and in a newly emerging concept, cargoes themselves.

1.3.6 Endosomal SNX-BAR Sorting Complex Promoting Exit-1 (ESCPE-1)

ESCPE-1, comprised of heterodimeric combinations of either SNX1 or SNX2 with either SNX5, SNX6 or their paralogue SNX32 which is expressed exclusively in brain tissue, has been recently characterised as a cargo-selective endosomal sorting complex (Simonetti et al., 2019). Recent evidence has highlighted the capacity for ESCPE-1 to bind CI-MPR with far higher affinity than retromer, with reported K_d values of 25 μM and 18 μM for the SNX5 binding to the cytosolic tail of CI-MPR (Simonetti et al., 2019; Yong et al., 2020). SNX5, SNX6 and SNX32 contain specialised PX domains that do not engage PIPs, but form a hydrophobic groove that recognises cargo tails conforming to a $\Phi x \Omega x \Phi x_n \Phi$ motif (where Φ corresponds to any hydrophobic residue, Ω corresponds to an aromatic residue, and x_n corresponds to a flexible linker of variable length) **(Figure 1.6)** (Simonetti et al., 2019; Weeratunga et al., 2020). The functional PX domains of SNX1 and SNX2 mediate the detection of PI(3)P and PI(3,5)P_2 required to localise ESCPE-1 to endosomal membranes. Moreover, SNX1 and SNX2 can homodimerize in the absence of the cargo-selective subunits to tubulate membranes (Van Weering et al., 2012).

CRISPR-Cas9 knockout KO of ESCPE-1 components, but not retromer components, induces a redistribution of CI-MPR from the TGN to EEA1-positive endosomes, indicative of a defective retrieval of this cargo (Kvainickas et al., 2017; Simonetti et al., 2017). ESCPE-1 therefore appears to predominantly control CI-MPR retrograde trafficking. Since this discovery, surface biotinylation of a range of ESCPE-1 cargoes and structural resolution of the cargoes CI-MPR and Semaphorin 4C (SEMA4C) in complex with SNX5 has broadly expanded our understanding of the cargoes dependent upon ESCPE-1 for their surface localisation **(see Chapter 5.1.1 for more detailed introduction)** (Simonetti et al., 2019).

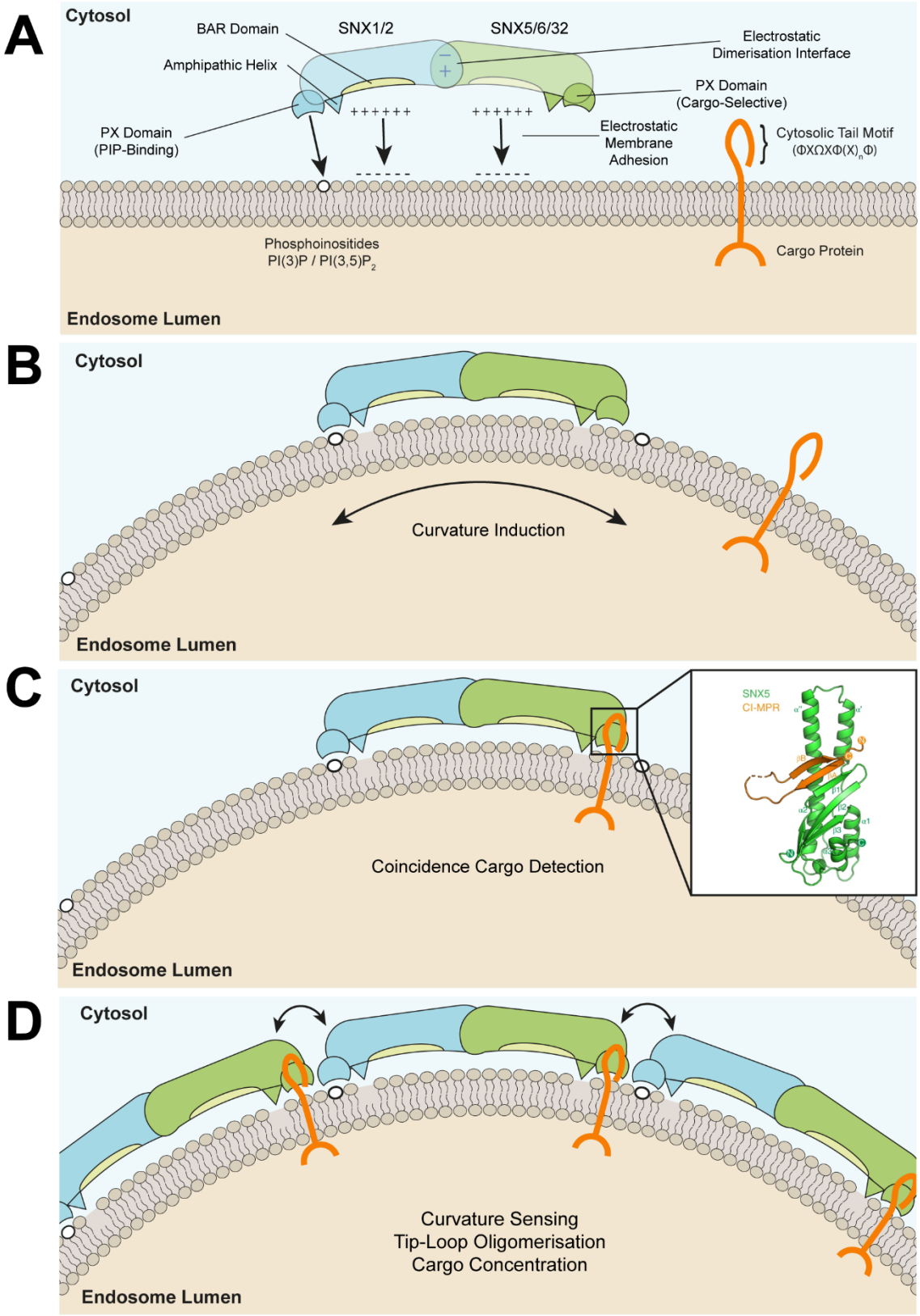

Figure 1.6 Model of ESCPE-1 Membrane Association and Cargo Selectivity

(A) ESCPE-1 subunits dimerise through an electrostatic interface. SNX1/2 recruit the complex to endosomal membranes through their PX domains. **(B)** Amphipathic helix insertion and the curved shape of the BAR domain begin to remodel the membrane to induce curvature. **(C)** The specialised SNX5/6/32 PX domain engages cargo tails conforming to a $\Phi x \Omega x \Phi x_n \Phi$ motif. The crystal structure of SNX5 bound

to the CI-MPR tail is adapted from (Simonetti et al., 2019), PDB ID 6N5X **(D)** Further ESCPE-1 complexes sense and induce curvature. The polymerisation of ESCPE-1 into a lattice and the concentration of cargo further remodels the membrane into a tubular structure.

1.3.7 Additional Cargo Selective Endosomal Sorting Complexes

In recent years, additional endosomal sorting complexes have been characterised that mediate endocytic recycling independently of retromer and ESCPE-1 and the clathrin-associated adaptors. The retriever complex is structurally similar to retromer, comprised of a core heterotrimer of VPS26C, VPS35 Endosomal Protein-Sorting Factor-Like (VPS35L), and the shared retromer subunit VPS29 (McNally et al., 2017). Molecular modelling predicts the presence of a HEAT repeat fold within the central VPS35L subunit, similarly to VPS35. The VPS26C subunit of retriever engages the SNX-FERM protein SNX17, which acts as a cargo adaptor that recognises ΦxNPx[F/Y]/ΦxNxx[F/Y] motifs within cargo tail sequences, such as integrin-β1 (Böttcher et al., 2012; Steinberg et al., 2012). SNX17 suppression causes the depletion of > 220 transmembrane proteins from the cell surface, highlighting SNX17-retriver as a key player in endosome-to-plasma membrane recycling (McNally et al., 2017). Whether retriever can assemble into higher order filamentous structures, like retromer, and the potential implications of this oligomerisation on its function remains an important open question.

An additional complex acts cooperatively with SNX17-retrivever to mediate endosomal cargo sorting, comprised of a scaffold of coiled-coil domain containing protein 22 (CCDC22) and CCDC93 in complex with homo- or heterodimers of copper metabolism gene MURR1 domain-containing (COMMD) proteins, of which there are 10 family members. This complex, termed the CCC (COMMD/CCDC22/CCDC93) complex, also facilitates integrin-β1 recycling, and various combinations of incorporated COMMD subunits may control cargo selectivity, such as for the low density lipoprotein receptor (LDLR) and the copper-transporting ATPase 1 (ATP7A) (Cullen and Steinberg, 2018). The CCC complex may also regulate endosomal dynamics by facilitating the recruitment of the PI(3)P phosphatase myotubularin-related related protein 2 (MTMR2) (Singla et al., 2019). A bioinformatic study posits the existence of a ‘COMMander’ complex comprising both retriever and CCC complexes together, but this has yet to be biochemically verified (Mallam and Marcotte, 2017).

Most recently, an additional sorting complex has been characterised that mediates Rab11-dependent recycling of TfR, termed Factors for Endosome Recycling and Retromer Association (FERARI) (Solinger et al., 2020). FERARI is a multisubunit tethering complex that anchors Rab11-positive compartments in proximity to SNX1-positive tubules on Rab5 endosomes, facilitating transfer of cargo between these structures (Solinger et al., 2020).

However, a quantitative proteomic analysis of the cargoes dependent on FERARI has yet to be performed, and the sorting motifs that dictate this mechanism are unclear.

1.3.8 The WASH Complex and the Role of Actin in Endosomal Cargo Sorting

A key regulator that establishes cohesion between endosomal sorting complexes and regulates spatiotemporal dynamics of endocytic recycling is the Wiskott-Aldrich Syndrome protein and SCAR homolog (WASH) complex. This pentameric complex, comprising the subunits WASHC1-5, is partially recruited onto the endosomal membrane through multivalent interactions between the extended tail domain of WASHC2 (previously named FAM21) and VPS35 molecules (Jia et al., 2012). Through this association, which is mediated by modular repeats of leucine, phenylalanine and acidic (LFa) sequences in the WASHC2 tail, the WASH complex may be able to sense the density of retromer and cargo proteins on the endosomal membrane. Moreover, the WASH complex in turn facilitates the recruitment of the CCC complex to endosomes, thereby providing and link that integrates multiple endosomal sorting machineries to the same discrete subdomain (McNally and Cullen, 2018; Phillips-Krawczak et al., 2015).

Importantly, the WASH complex acts as a nucleation promoting factor for the actin related protein 2/3 (Arp2/3) complex, which generates filamentous, branched actin (F-actin) (Derivery et al., 2009). The WASH complex thus regulates the specific, localised polymerisation of actin on the endosomal membrane. This localised actin cortex plays an important role in endocytic recycling, providing a meshwork that aids the capture of cargo proteins by endosomal sorting machinery by limiting their lateral diffusion within the endosomal membrane (Simonetti and Cullen, 2019). The importance of actin in mediating cargo capture has been demonstrated for β2AR, whereby exchange of its PDZbm for an actin-binding domain is sufficient to rescue its recycling to the plasma membrane (Puthenveedu et al., 2010).

The WASH complex is also involved in regulating endosomal tubule dynamics, as its suppression results in elongated, persistent tubular protrusions that fail to undergo severance (Derivery et al., 2009). In contrast, complete depletion of the WASH complex induces a morphological collapse of the endosomal network into the perinuclear region, highlighting a fundamental role for the complex in regulating endosomal homeostasis (Gomez et al., 2012). WASH may locally induce actin polymerisation that generates a local ‘pushing’ force that biophysically opposes the ‘pulling’ force on endosomal tubules mediated by microtubule motors (Cullen and Steinberg, 2018). WASH activity is modulated by ER-endosome contact sites that form between SNX2 and VAMP-Associated Protein (VAP), whereby PI(4)P extrusion

from the endosomal membrane attenuates localised actin polymerisation, potentially providing a timing mechanism for endosomal tubule fission (Dong et al., 2016).

1.3.9 Subdomain Organisation at the Endosomal Membrane

With the characterisation of multiple endosomal sorting machineries and their coordination with localised branched actin polymerisation, a sophisticated model of endosomal subdomain organisation is emerging **(Figure 1.7)**. Imaging of enlarged endosomes reveals the discrete punctate localisations of components of the endocytic retrieval machinery including retromer, ESCPE-1 and WASH, arguing for regulated subdomain organisation (Derivery et al., 2012; Norris et al., 2017; Simonetti et al., 2017). Spatially and functionally opposed to this 'retrieval' subdomain is a 'degradative' subdomain, comprising ESCRT complexes and a flattened clathrin bilayer which also functions to capture cargo by limiting their diffusion, and then mediates sorting into budding ILVs at the edges of the clathrin coat (Klumperman and Raposo, 2014; Norris and Grant, 2020).

A key regulator of endosomal subdomain architecture appears to be the Hsc70 chaperone required for receptor-mediated endocytosis-8 (RME-8). RME-8 is a SNX1 effector protein, and depletion of either of these proteins leads to a dysregulation of subdomain architecture that causes an expansion of the degradative portion of the endosome (Norris et al., 2017). An interesting hypothesis is that the intrinsic ATPase activity of RME-8 is required to disassemble the clathrin coat at the interface between endosomal subdomains, thereby protecting the integrity of the recycling subdomain by preventing encroachment of ESCRT and clathrin polymerisation (Norris et al., 2017). However, this model still requires experimental support. An additional function of RME-8, possibly also relating to its ATPase activity, may pertain to the catalysis of endosomal tubule fission, as RME-8 suppression induces striking tubulation of the endosomal network (Freeman et al., 2014). A similar role in maintaining subdomain integrity has been proposed for retromer, which locally stimulates Rab7a GTP-hydrolysis through the recruitment of the Rab7-GAP TBC1D5. Suppression of retromer causes an expansion of the Rab7a-GTP population, which is normally discretely constrained, across the late endosome, leading myriad cellular consequences, including defective mitophagy turnover and mTORC1 signalling (Jimenez-Orgaz et al., 2017; Kvainickas et al., 2019).

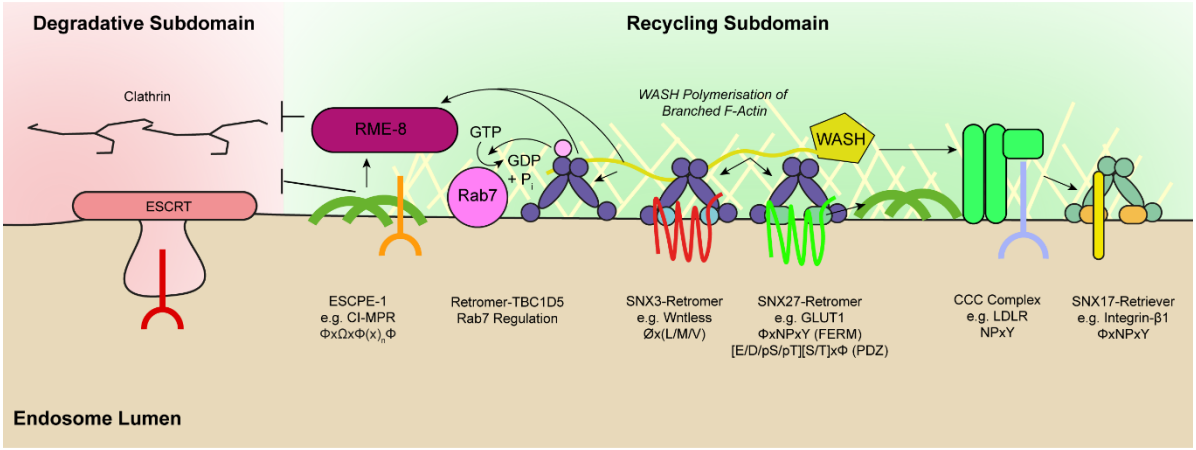

Figure 1.7 Subdomain Organisation of the Endosome

The endosomal membrane is compartmentalised into discrete microdomains with degradative or recycling functions. The ESCRT-populated degradative subdomain is coated by a flattened clathrin bilayer. Endosomal sorting complexes assemble and contribute to the integrity of the recycling subdomain. Branched actin polymerisation, RME-8 and SNX1 activity maintain the border between domains. Endosomal cargoes destined for recycling are efficiently captured within this domain for sequence-dependent sorting. There is an interconnectivity between sorting machinery that contributes to the cohesion of this subdomain, represented by arrows.

1.3.10 Coupling Endosomal Recycling to Cytoskeletal Dynamics

The cytoskeleton regulates the positioning of endolysosomal compartments in response to a wide range of cellular cues. Moreover, cytoskeletal dynamics contribute to the formation, fission and subsequent trafficking of cargo-enriched endosomal tubulovesicular carriers to an accepting compartment. The SNX5/6 subunits of ESCPE-1 associate with $p150^{glued}$, a component of the dynactin complex that activates dynein-driven, minus-end directed microtubule transport (Wassmer et al., 2009). Similarly, SNX4 also engages dynein via the kidney and brain protein (KIBRA) as an intermediate (Traer et al., 2007). Microtubule motor suppression also perturbs SNX8 endosomal tubule scission, and increases the mixing of different SNX-BAR proteins within the same tubules (Hunt et al., 2013). Similarly, the kinesin motor KIF13A interacts with Rab11 to coordinate tubule formation on recycling endosomes (Delevoye et al., 2014). The pulling force generated by microtubule motors may contribute to the extrusion of the endosomal membrane into a tubular structure. Microtubule motors and BAR-domain containing proteins can mediate tubule scission *in vitro*, and thus these components likely cooperate to make this process highly efficient within the cellular environment (Simunovic et al., 2017).

Following the separation of cargo-loaded membrane carriers from the endosomal network, the cytoskeleton mediates directional trafficking to an acceptor compartment. The degree to which endosomal cargo sorting machinery remains associated with recycling membrane carriers following dissociation form the endosomal network is not completely clear, although some

degree of coat protein identity must be required to maintain the connection to the cytoskeleton. Ultimately, the specific interaction with microtubule motors and the engagement of tethering factors determines the specificity for fusion with an accepting compartment. Interestingly, dual, live-imaging analysis of SNX27-retromer and SNX3-retromer cargoes β2AR and Wntless, which predominantly traffic from early endosomes to the plasma membrane or TGN respectively, reveals that they enrich at the same sites of endosomal membrane budding and fission (Varandas et al., 2016). This raises the possibility of further downstream sorting events dictating the trafficking direction used by cargo following their initial sorting on the endosomal membrane.

1.4 Retrograde Endosomal Recycling

From endosomes, cargo can be sorted to distinct subcellular localisations, including the plasma membrane, TGN, or the ERC. Due to technical challenges, endosome-to-TGN (referred to herein as 'retrograde' trafficking) is perhaps the least characterised endosomal recycling route. For example, recent methodological advances have facilitated the characterisation of hundreds of cell surface-localised cargoes that depend upon the activity of SNX27-retromer and SNX17-retriever (McNally et al., 2017; Steinberg et al., 2013). By contrast, fewer cargoes have been mechanistically characterised as transiting through the retrograde route, and the molecular signals that dictate this process are less clear. Retrograde trafficking is a crucial process for the maintaining lysosomal homeostasis, and facilitating the polarised recycling of endosomal cargoes to discrete plasma membrane subdomains **(see Chapter 4.1.1 for more detailed introduction)** (Johannes and Popoff, 2008).

The prototypical cargoes for retrograde recycling are the receptors that mediate the delivery of soluble lysosomal proteins into the endosomal lumen, including CI-MPR, CD-MPR and the Vps10p-related proteins Sortilin, SorLA and SorCS1-3 (Johannes and Popoff, 2008). While a subpopulation of these receptors transits anterogradely from the TGN to the plasma membrane, their role in the constitutive delivery of lysosomal proteins demands a dedicated retrograde retrieval mechanism that directs them back to the TGN from the endosomal membrane. The M6P receptors CI-MPR and CD-MPR optimally bind their ligands in the TGN at pH ~6.5, then dissociate in the endosomal network as the lumen acidifies, with no detectable binding below pH 5 (Dahms et al., 2008). It remains unclear whether the ligand-binding status of the luminal portion of these receptors is conformationally transmitted through to the cytosolic domain to modulate coat recruitment and mediate the timing of anterograde and retrograde transport, or whether constitutive cycling of these receptors and rapid dissociation of their ligands is sufficient to maintain the supply of lysosomal proteins.

1.4.1 Mechanisms of Retrograde Endosomal Sorting

Multiple protein sorting machineries have been implicated in retrograde cargo sorting, with some degree of reported redundancy and conflicting data regarding their respective contributions. In addition to its role in constructing flat lattices that border the degradative endosomal subdomain, clathrin is also implicated in retrograde endosomal recycling. Clathrin, alongside its adaptor proteins AP-1 and epsinR, has been implicated in the retrograde retrieval of CI-MPR, *trans*-Golgi network glycoprotein 46 (TGN46) and the Shiga toxin subunit B (STxB) (Mallard et al., 1998; Meyer et al., 2000; Saint-Pol et al., 2004). Most recently, a nanobody-based retrograde surface uptake assay also demonstrated that suppression of AP-1, epsinR or GGA1-3 proteins reduce the rate of CD-MPR transport the TGN (Buser et al., 2018; Buser and Spiess, 2019). Additionally, phosphofurin acidic-cluster sorting protein 1 (PACS1) binds to acidic patches in the cytosolic tails of retrograde cargoes such as CI-MPR and furin, and this binding is modulated by CK2 phosphorylation (Scott et al., 2006; Wan et al., 1998). PACS1 links binds to GGA3 and AP-1 and therefore may link capture and sort cargo proteins for clathrin-dependent retrograde traffic (Crump et al., 2001; Scott et al., 2006).

Rab9, which localises to late endosomes, has also been implicated as a coordinator of retrograde trafficking of CI-MPR. Expression of a dominant-negative form of Rab9 reduces the rate of MPR sialylation following neuraminidase treatment at the cell surface and increases levels of lysosomal enzymes in the cell culture media, suggestive of impaired delivery to the endolysosomal network (Lombardi et al., 1993; Riederer et al., 1994). More recently, live imaging has suggested Rab9 may be involved in delivery of TGN46 and CI-MPR from the TGN to the endosomal network (Kucera et al., 2016). Tail-interacting 47 kDa protein (TIP47) was reported as a Rab9 effector that selectively binds the cytoplasmic tails of MPRs and furin to mediate retrograde sorting, although more recent data have revealed a primary localisation and function of this protein in regulating lipid droplet biogenesis (Bulankina et al., 2009; Díaz and Pfeffer, 1998).

Following its discovery in yeast, the retromer complex has become an established regulator of retrograde transport. Early EM studies pinpointed retromer as predominantly juxtaposed to the base of endosomal tubules, supporting a model that retromer either buds vesicular carriers as a complex with SNX3, or sorts cargo into SNX-BAR-generated tubulovesicular projections. However, the recent cyro-EM structure of metazoan SNX3-retromer assembled as a coat structure that can incorporate Wntless binding at the SNX3-VPS26 interface suggests that SNX3-retromer may also form tubulovesicular structures for retrograde trafficking (Leneva et al., 2020). Moreover, Wntless is sorted into SNX1-negative membrane protrusions, suggesting independence from ESCPE-1 in this recycling process (Harterink et al., 2011). The degree to

which retromer acts autonomously versus co-operatively with other sorting machinery in the tubulovesicular retrograde trafficking of cargo therefore remains unclear.

The SNX-BAR complexes of ESCPE-1, SNX4-SNX7/30 and SNX8 are also linked to retrograde recycling. The cargo-selective and mechanical roles of ESCPE-1 can be functionally separated by the specific suppression of the SNX5, SNX6 and SNX32 subunits, which mediate direct cargo binding (Simonetti et al., 2019). In this instance, SNX1 or SNX2 homodimers may still mediate 'bulk' tubular recycling, but ESCPE-1-specific cargo fail to incorporate into these carriers. Upon SNX5+6 suppression, the retrograde trafficking of CI-MPR is perturbed, leading to an accumulation on early endosomal compartments (Kvainickas et al., 2017; Simonetti et al., 2017). SNX4 and SNX8 have been linked to the retrograde trafficking of the ricin and STxB toxins respectively, although mechanistic details of endogenous cargo recycling through this route is lacking (Dyve et al., 2009; Skånland et al., 2007).

Taken together, there is a complex multiplicity of mechanisms and routes for retrograde endosomal recycling **(Figure 1.7)**. Many of the seminal studies establishing this pathway have focussed on CI-MPR as a model cargo, which has been reported to directly or indirectly interact with almost all of the established retrograde machineries. A single SNX5 point mutant that perturbs CI-MPR recycling is sufficient to block retrograde trafficking, suggesting that ESCPE-1 constitutes a dominant component of the recycling of this receptor (Simonetti et al., 2019). The multiplicity of cargo-selective mechanisms for CI-MPR could therefore be reconciled by a model whereby CI-MPR interacting proteins, such as retromer, PACS1, GGAs and AP-1 contribute to the capture of CI-MPR on the endosomal membrane, and the handover into ESCPE-1 generated tubules, where sequence dependent binding occurs most strongly to retain the receptor within these structures. Possible support for this model arrives from the observation that CI-MPR reaches the TGN with faster kinetics in VPS35 KO cells through a surface uptake assay, perhaps indicating that retromer captures and concentrates CI-MPR to temporally regulate its ESCPE-1-dependent recycling (Cullen and Steinberg, 2018). As methodologies investigating this pathway continue to improve, untangling the intricate separate contributions of retrograde recycling machinery towards this process remains an interesting avenue for future research.

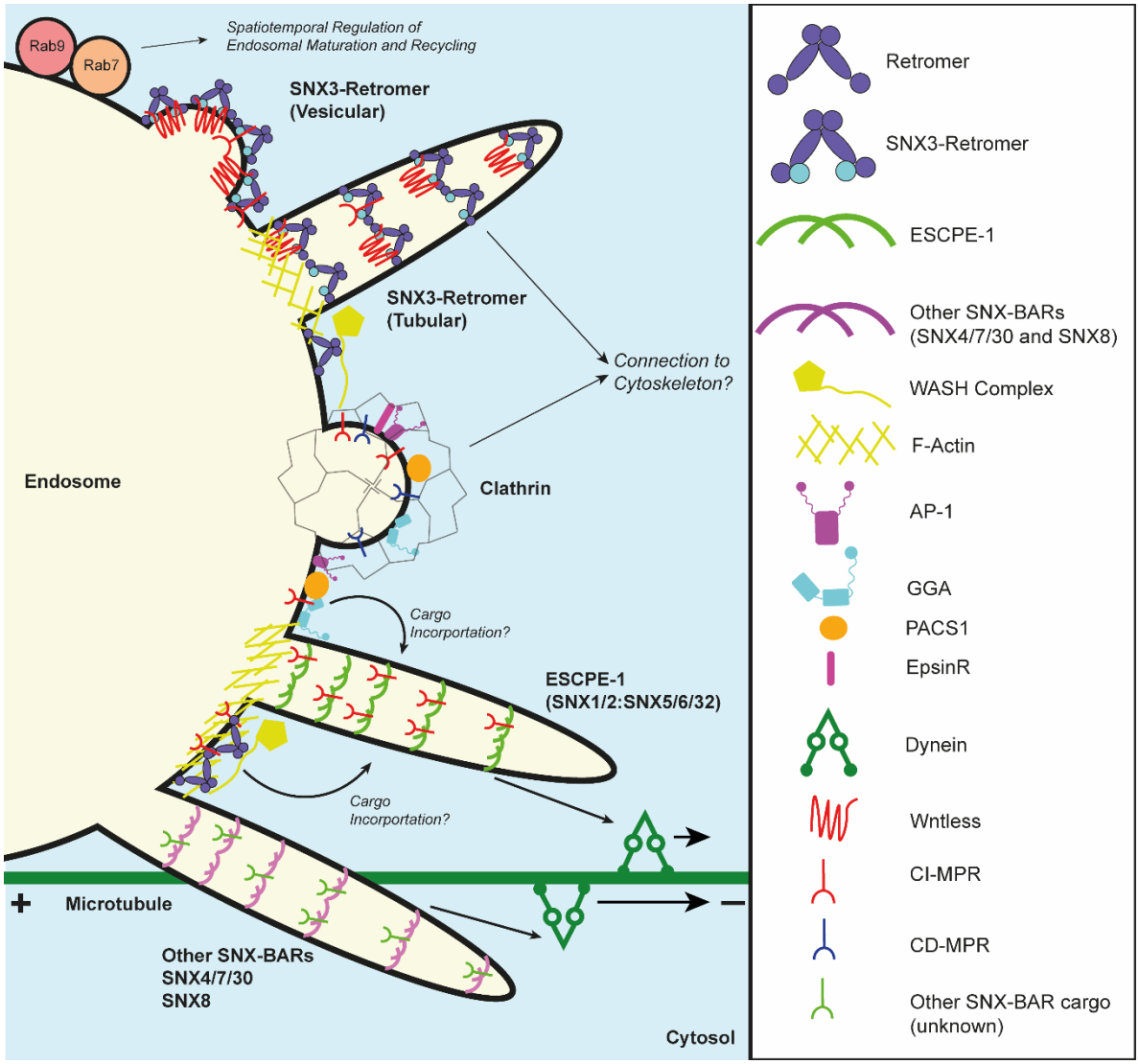

Figure 1.8 Mechanistic Retrograde Recycling

The multiple reported pathways for retrograde cargo sorting are displayed, along with the respective sorting machineries that capture and enrich cargo through specific sequence recognition. Curved arrows represent the possibility of cargo captured by retromer, or alternative machinery such as GGAs and PACS1, being incorporated into ESCPE-1-positive tubular structures.

1.4.2 Tethering Retrograde Cargo at the TGN

Similarly to the host of machineries that sorts endocytic cargoes into retrograde recycling carriers, multiple proteins act cooperatively at the TGN to capture, tether and fuse incoming vesicles to complete the recycling process. Golgins are a family of extended, coiled-coil proteins of varying lengths that associate with Golgi membranes and protrude into the cytosol to form a ‘tentacular’ matrix (Munro, 2011). Golgins utilise N-terminal sequences to mediate cargo specificity in the capture of incoming transport vesicles throughout the Golgi, including COPII-coated anterograde carriers arriving from the ER, intra-Golgi vesicles, and retrograde transport vesicles arriving from the endosomal network (Gillingham and Munro, 2019).

Four golgins localise to the TGN membrane: Golgin-97, Golgin-245, and the golgin-97, RanBP2alpha, Imh1p and p230/golgin-245 (GRIP) and coiled-coil domain-containing protein (GCC) proteins GCC88 and GCC185 (Cheung and Pfeffer, 2016). Recent proteomic methodologies have defined the cargo selectivity of these golgins by coupling their ectopic relocation to mitochondria with spatial proteomics (Shin et al., 2020, 2017). Through these approaches, it appears as though Golgin-97 and Golgin-245 possess widely overlapping cargo preferences, and associate with the bridging factor TBC1D23, which in turn directly binds the extended WASHC2 tail on incoming retrograde transport carriers to mediate cargo selectivity (Shin et al., 2017). Moreover, TBC1D23 interacts with a complex of WD repeat-containing protein 11 (WDR11), FAM91A1 and C17orf75 to capture AP-1-derived vesicles (Navarro Negredo et al., 2018). Through this mechanism, ectopic expression of Golgin-97 on mitochondria induces the redistribution of retrograde carriers positive for the cargo sorting machineries AP-1, retromer, SNX3, ESCPE-1 and SNX4, as well as cargoes including CI-MPR, CD-MPR, TGN46 and furin. By contrast, GCC88 redistributes fewer proteins, some of which are also captured by Golgin-97, such as TGN46, highlighting a degree of redundancy in the capture of various retrograde cargoes (Shin et al., 2020).

The rod-like extension of golgins several hundred nanometres into the cytosol serves as the first point of contact that tethers retrograde carriers in proximity to the TGN membrane. Following engagement of incoming membrane carriers, the precise mechanism that draws them into direct proximity of the TGN membrane is unknown, but may be mediated by golgin ‘bending’ at hinge regions where coiled-coils are disrupted, or the ‘hopping’ of vesicles between Rab-binding sites on the golgin coils to bring them into closer proximity to the membrane (Ramirez and Lowe, 2009).

To mediate the final stages of membrane tethering and fusion, the Golgi-associated retrograde protein (GARP) complex, comprising the subunits VPS51, VPS52, VPS53 and VPS54, plays a crucial role (Bonifacino and Hierro, 2011). GARP regulates the delivery of multiple retrograde cargoes to the TGN, including CI-MPR, CD-MPR, TGN46 and STxB, and has most recently been implicated in mediating the retention of Golgi glycosylation machinery within the TGN compartment (Khakurel et al., 2020; Pérez-Victoria et al., 2008). GARP associates with the t-SNAREs Syntaxin-6, Syntaxin-16 and VTI1A (vesicle transport through interaction with t-SNARES homolog 1A) on the TGN membrane, and the v-SNARE VAMP4 on incoming membrane carriers to couple vesicle tethering and fusion at the TGN (Pérez-Victoria and Bonifacino, 2009).

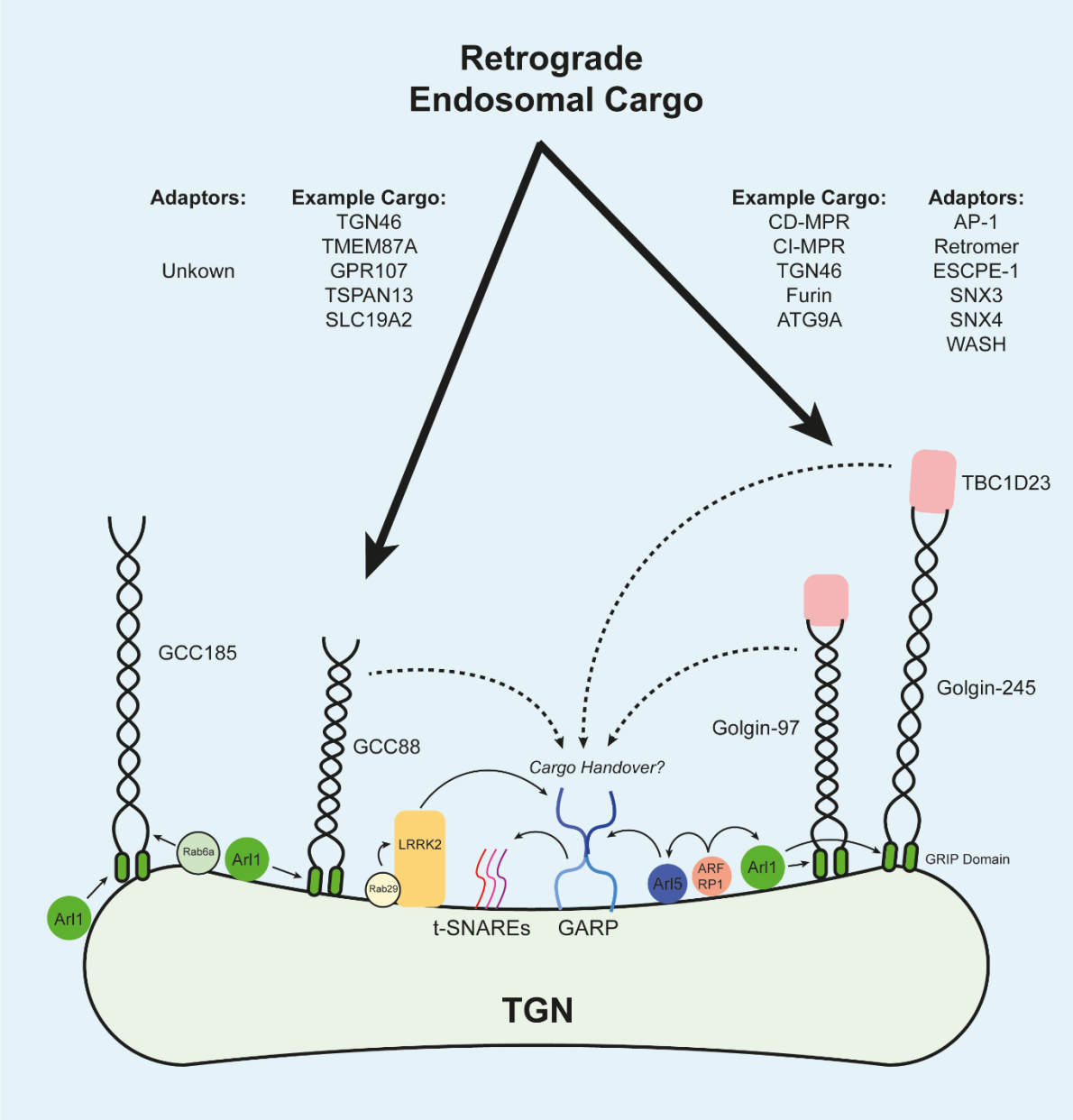

Figure 1.9 Assembly of the Retrograde Tethering and Fusion Machinery at the TGN

Retrograde endosomal transport carriers are recognised and tethered by TGN-localised golgin proteins that protrude into the cytosol. Example cargoes and adaptors for distinct golgins are provided based on (Shin et al., 2020). Following tethering, membrane carriers are brought into close proximity to the TGN membrane. GARP coordinates SNARE assembly for mediating the final fusion step, where cargo proteins and lipids are released into the TGN. A range of GTPases and effector molecules that coordinate this assembly are also displayed.

Recent studies have provided insights into the assembly of the cargo recognition machinery at the TGN **(Figure 1.8)**. Arf-related protein 1 (ARFRP1) mediates the recruitment of the Arf-like (Arl) GTPases Arl1 and Arl5 (Ishida and Bonifacino, 2019). Arl1 recruits Golgin-97/245 and GCC88 by engaging their GRIP domains (Ishida and Bonifacino, 2019; Lu and Hong, 2003). Additionally, Rab6a functions cooperatively with Arl1 to recruit GCC185 to the TGN (Burguete et al., 2008). Moreover, Arl5 mediates the localisation of GARP to the TGN (Ishida

and Bonifacino, 2019; Rosa-Ferreira et al., 2015). A recent study demonstrated that the Parkinson's disease associated protein leucine-rich repeat serine/threonine-protein kinase 2 (LRRK2) is recruited to the TGN by its effector Rab29. LRRK2 subsequently interacts with GARP and enhances its association with Syntaxin-6 to facilitate retrograde transport (Beilina et al., 2020). SNX1 also interacts with Rab6-interacting protein-1 (RAB6IP1), and silencing of this protein suppresses retrograde transport of CI-MPR, providing an additional mechanism of docking retrograde transport carriers in proximity to the TGN membrane (Wassmer et al., 2009).

1.5 Endosomal Recycling and Disease

The endolysosomal network maintains a delicate balance between cargo recycling and degradation that is crucial for cellular and organismal homeostasis. This importance is underscored by the embryonic lethality resulting from depletion of coat proteins and cargo adaptors facilitating this process, such as AP-1 and retromer (Dell'Angelica and Bonifacino, 2019). Due to the vast numbers of proteins that depend upon efficient endosomal recycling, the consequences of endosomal dysfunction can be widespread and unpredictable and are most commonly linked to neurodegenerative diseases through highly complex phenotypes (Schreij et al., 2016).

1.5.1 Neurodegeneration

Neurodegenerative diseases are a group of pathologies characterised by the progressive loss of specific neuronal cell populations within the brain. Various components of the endocytic recycling machinery have been genetically linked to rare forms of neurodegenerative disease, such as familial Parkinson's and Alzheimer's disease, amyotrophic lateral sclerosis and hereditary spastic paraplegia (Schreij et al., 2016). In these examples, perturbed endosomal recycling can have myriad negative consequences leading to neurodegeneration, such as impaired synaptic transmission due to inefficient endosomal recycling at the synapse, and the reduced catabolic capacity that arises from lysosomal dysfunction leading to the intracellular accumulation of damaged organelles and pathogenic aggregates. In sporadic cases of neurodegeneration, defective endosomal recycling is still a pathogenic hallmark, although its causes are less clear (Small et al., 2017). A unifying phenotype in neurodegeneration appears to be the accumulation of swollen endosomes and defective lysosomal function within neurons, referred to by some as endosomal 'traffic jams' **(see Chapter 3.3.2 for extended discussion)** (Small et al., 2017). Importantly, in Alzheimer's disease patient samples these hallmarks are observable prior to the accumulation and extracellular deposition of pathogenic aggregates, suggesting that endosomal dysfunction can be a key driving factor in the

development of neurodegeneration (Cataldo et al., 2000). On the basis of this evidence, endosomal recycling is now considered broadly neuroprotective, and emerging pharmacological strategies aim to stabilise and enhance endosomal recycling to treat neurodegeneration (McMillan et al., 2017; Mecozzi et al., 2014; Muzio et al., 2020).

1.5.2 Pathogenic Exploitation of the Endosomal Network

The catabolic endosomal and autophagic clearance pathways represent an innate cellular defence against invading pathogens. Many pathogens have evolved to subvert the endosomal network to circumvent lysosomal degradation and proliferate within cells. For example, many viruses are internalised into the cells through endocytic pathways after binding of host receptors, then rely on endosomal maturation and acidification to trigger their uncoating and genome release, thereby preventing exposure of the genome to nuclease enzymes present in the mature lysosome (Yamauchi and Greber, 2016). Moreover, various bacterial pathogens exploit endosomal recycling to promote survival. For example, the bacterium *Chlamydia trachomatis* secretes a protein, IncE, that localises to the surface of intracellular inclusion bodies. This bacterial protein directly binds the cargo-selective SNX5/6 subunits of ESCPE-1, restricting their usual role in endosomal cargo sorting (Elwell et al., 2017; Mirrashidi et al., 2015; Paul et al., 2017). The *Legionella pneumophila* effector protein RidL directly binds the VPS29 subunit of retromer, displacing the Rab7-GAP TBC1D5 and perturbing retromer-dependent trafficking (Bärlocher et al., 2017; Finsel et al., 2013). Bacterial toxins that traverse the retrograde recycling route, such as STxB and ricin, have even been crucial tools in the study of endosomal recycling (Mallard et al., 1998; Skånland et al., 2007; Stechmann et al., 2010).

The precise details of how this subversion of endosomal recycling machinery promotes pathogen survival remain unclear, but a general view is that this hijacking process sequesters bacteria away from the degradative pathway, or impairs the degradative capacity of the lysosome itself. As more examples of pathogenic exploitation of the endosomal network emerge, inhibiting these processes may become an increasingly viable therapeutic strategy in the future.

1.6 Aims

The molecular characterisation of endosomal sorting complexes has led to improved understanding of the importance of timely and efficient recycling of cargo proteins in health and disease. In this thesis, I aim to take a primarily proteomic approach to further understand the roles of two of these complexes: retromer and ESCPE-1. In **Chapter 3**, I aim to validate recent data regarding the distinct roles of retromer and ESCPE-1 in a neuroglioma cell culture

model. Moreover, using whole cell proteomics and transcriptomics, I aim to understand the global effects that retromer depletion exerts on the cell to further characterise this complex as a master regulator of endolysosomal homeostasis. In **Chapter 4** and **Chapter 5**, I am to build on the recent molecular characterisation of ESCPE-1-mediated cargo binding by developing a proteomic tool to label endogenous proteins at the TGN, and observe how these proteins remodel upon SNX5+6 suppression. This approach aims to expand the currently limited knowledge of sequence-specific retrograde cargoes for ESCPE-1. Finally, in **Chapter 6**, results and techniques from the preceding chapters are applied to understand the mechanism of infection by the pandemic severe acute respiratory syndrome coronavirus 2 (SARS-CoV-2).

Chapter 2: Materials and Methods

2.1 Materials

2.1.1 Antibodies

Table 2.1 List of Primary Antibodies Used in this Study

Antibody Target	Species	Clonality	WB Dilution	IF Dilution	Supplier	Clone	Category Number
ACE2	Mouse	Monoclonal	1/1000		Proteintech	2F12A4	66699-1-Ig
Calnexin	Rabbit	Polyclonal	1/1000	1/400	Abcam		ab22595
Cathepsin D	Rabbit	Polyclonal	1/1000		Proteintech		21327-1-AP
CI-MPR	Rabbit	Monoclonal	1/1000	1/400	Abcam	EPR6599	ab124767
EEA1	Mouse	Monoclonal		1/200	BD Biosciences	Clone 14	610456
EEA1	Goat	Monoclonal		1/200	Santa Cruz Biotechnology	N-19	sc-6415
EphA2	Rabbit	Monoclonal	1/1000	1/200	Cell Signalling	D4A2	6997
FLAG	Mouse	Monoclonal		1/100	Sigma-Aldrich	M2	F1804
GALNT2	Rabbit	Polyclonal	1/1000	1/400	Abcam		ab102650
GAPDH	Rabbit	Polyclonal	1/2000		Sigma-Aldrich		G9545
GFP	Mouse	Monoclonal	1/2000	1/400	Roche	7.1, 13.1	11814460001
GFP	Rabbit	Polyclonal	1/2000	1/400	Genetex		GTX113617
Giantin	Rabbit	Polyclonal	1/2000	1/1000	Biolegend		Poly19243
Golgin-97	Mouse	Monoclonal	1/1000	1/200	Thermo Fischer Scientific	CDF4	A-21270
HA	Mouse	Monoclonal		1/100	Proteintech	1C1D2	66006-1-Ig
Integrin α5 (CD49e)	Mouse	Monoclonal	1/1000		BD Biosciences	VC5	555651
KIAA2013	Rabbit	Polyclonal		1/200	Proteintech		27886-1-AP
LAMP1	Mouse	Monoclonal		1/400	Developmental Studies Hybridoma Bank	H4A3	AB_2296838
mCherry	Rabbit	Polyclonal	1/2000		Abcam		ab167453
MET	Rabbit	Monoclonal	1/1000	1/200	Cell Signalling	D1C2	8198
Myc	Mouse	Monoclonal	1/1000		Merck	4A6	05-724-25
N-Cadherin	Mouse	Monoclonal	1/1000		Cell Signalling	13A9	14215
N-Cadherin	Rabbit	Monoclonal	1/1000		Cell Signalling	D4R1H	13116
NRP1	Mouse	Monoclonal	1/1000		Proteintech	2H3F6	60067-1-Ig
NRP1	Rabbit	Monoclonal	1/1000	1/50	Abcam	EPR3113	ab81321
NRP1 mAb#1	Mouse	Monoclonal		1/10	Gift from T.Teesalu		
NRP1 mAb#2	Mouse	Monoclonal		1/10	Gift from T.Teesalu		

NRP1 mAb#3	Mouse	Monoclonal		1/10	Gift from T.Teesalu		
Rab27a	Mouse	Monoclonal	1/500		Proteintech	1C4B8	66058-1-Ig
Rab27b	Rabbit	Polyclonal	1/500		Proteintech		13412-1-AP
SARS-CoV-2 N	Rabbit	Polyclonal		1/2000	Rockland		200-401-A50
SARS-CoV-2 Spike (S1 epitope)	Rabbit	Polyclonal	1/1000		Sino Biologicals		40592-T62
SARS-CoV-2 Spike (S2 epitope)	Mouse	Monoclonal	1/1000		Genetex	1A9	GTX632604
SNX1	Rabbit	Polyclonal	1/1000	1/200	Abcam		ab995
SNX2	Mouse	Monoclonal	1/1000	1/200	BD Biosciences	Clone 13	5345661
SNX3	Rabbit	Polyclonal	1/1000	1/200	Proteintech		10772-1-AP
SNX4	Rabbit	Monoclonal	1/1000		Abcam	EPR16954	ab198504
SNX5	Rabbit	Polyclonal	1/1000		Proteintech		17918-1-AP
SNX5	Rabbit	Monoclonal	1/1000		Abcam	EPR14358	ab180520
SNX6	Mouse	Monoclonal	1/500	1/300	Santa Cruz Biotechnology	D-5	365965
SNX8	Mouse	Monoclonal	1/1000		Origene	OTI4F8	CF502136
Sortilin	Rabbit	Polyclonal	1/1000		Abcam		ab16640
TGN46	Sheep	Polyclonal	1/500	1/400	Bio-Rad		AHP500G
TMCO3	Rabbit	Polyclonal		1/400	Genetex		GTX120621
TMEM230	Rabbit	Polyclonal	1/1000	1/200	Proteintech		21466-1-AP
Tom20	Mouse	Monoclonal	1/1000	1/400	BD Biosciences	Clone 29	612278
Tubulin	Rabbit	Polyclonal	1/2000		Abcam		ab6046
VPS26A	Rabbit	Polyclonal	1/1000		Abcam		ab23892
VPS29	Rabbit	Polyclonal	1/1000		Abcam		ab98929
VPS35	Goat	Polyclonal		1/200	Abcam		ab10099
VPS35	Rabbit	Monoclonal	1/1000		Abcam	EPR11501(B)	ab157220
VPS35	Rabbit	Polyclonal		1/400	Abcam		ab97545
β-Actin	Mouse	Monoclonal	1/2000		Sigma-Aldrich	AC-15	A1978

Abbreviations: IF: Immunofluorescence; WB: Western blot.

Table 2.2 List of Secondary Antibodies

Secondary Antibody	Species	IF/WB	Dilution	Supplier	Category Number
Alexa Fluor 488 anti-goat IgG	Donkey	IF	1/400	Invitrogen	A-11055
Alexa Fluor 488 anti-mouse IgG	Donkey	IF	1/400	Invitrogen	A32753
Alexa Fluor 488 anti-rabbit IgG	Donkey	IF	1/400	Invitrogen	A32731

Alexa Fluor 546 anti-mouse IgG	Goat	IF	1/250	Invitrogen	A-11030
Alexa Fluor 568 anti-goat IgG	Donkey	IF	1/400	Invitrogen	A-11057
Alexa Fluor 568 anti-mouse IgG	Donkey	IF	1/400	Invitrogen	A10037
Alexa Fluor 568 anti-rabbit IgG	Donkey	IF	1/400	Invitrogen	A10042
Alexa Fluor 594 anti-mouse IgG	Goat	IF	1/250	Invitrogen	A32742
Alexa Fluor 594 anti-rabbit IgG	Goat	IF	1/250	Invitrogen	A32740
Alexa Fluor 647 anti-goat IgG	Donkey	IF	1/400	Invitrogen	A32849
Alexa Fluor 647 anti-mouse IgG	Donkey	IF	1/400	Invitrogen	A32787
Alexa Fluor 647 anti-rabbit IgG	Donkey	IF	1/400	Invitrogen	A32795
Alexa Fluor 680 anti-goat IgG	Donkey	WB	1/20000	Invitrogen	A-21084
Alexa Fluor 680 anti-mouse IgG	Donkey	WB	1/20000	Invitrogen	A-21057
Alexa Fluor 800 anti-rabbit IgG	Donkey	WB	1/20000	Invitrogen	A32735

2.1.2 Plasmids

Table 2.3 List of Plasmids Used in this Study

Plasmid Name	Plasmid Backbone	Source
APEX2-TGN46	XLG3	Cloned by Dr Boris Simonetti
CI-MPR Signal Peptide-GFP	pEGFP-C1	From the lab
CI-MPR Signal Peptide-GFP-Nrp1	pEGFP-C1	Cloned by PCR from Nrp1-mCherry and CI-MPR Signal Peptide-GFP
EphA2-GFP	pEGFP-N1	Gift from Professor Jim Norman
GFP	pEGFP-N1	From the lab
GFP	pEGFP-C1	From the lab
GFP-5PX-SNX1	pmCherry-C1	Cloned by Dr Boris Simonetti
GFP-EphA2$^{559-976}$	pEGFP-C1	Cloned by PCR from EphA2-GFP
GFP-NRP1 tail	pmCherry-C1	Cloned by Dr Boris Simonetti
GFP-Puromycin Resistance	pEGFP-C1	From the lab
GFP-S1	pEGFP-C1	Cloned by Dr Boris Simonetti
GFP-S1$^{493-685}$	pEGFP-C1	Cloned by Dr Boris Simonetti
GFP-S1^{R685D}	pEGFP-C1	Cloned by site directed mutagenesis from GFP-S1
GFP-S1ΔRRAR	pEGFP-C1	Cloned by site directed mutagenesis from GFP-S1
GFP-SNX1	pmCherry-C1	From the lab
GFP-SNX2	pmCherry-C1	From the lab
GFP-SNX32	pmCherry-C1	From the lab
GFP-SNX4	XLG3	From the lab
GFP-SNX5	pmCherry-C1	From the lab
GFP-SNX5	XLG3	From the lab
GFP-SNX5 F136D	pmCherry-C1	Cloned by Dr Boris Simonetti
GFP-SNX6	pmCherry-C1	From the lab
GFP-SNX6	XLG3	From the lab

GFP-SNX8	XLG3	From the lab
HRP-TGN46	XLG3	Cloned by Dr Boris Simonetti
Lentivirus Packaging Vector	pCMV-dR8.91	From the lab
Lentivirus VSV-G Envelope	pMDG2	From the lab
mCherry	pmCherry-C1	From the lab
mCherry	pmCherry-N1	From the lab
mCherry-CI-MPR	pmCherry-C1	Cloned by Dr Boris Simonetti
mCherry-NRP1 b1	pmCherry-C1	Cloned by PCR from NRP1-GFP
mCherry-NRP1 b1b2	pmCherry-C1	Cloned by PCR from NRP1-GFP
mCherry-NRP1 b1^{T316R}	pmCherry-C1	Cloned by site directed mutagenesis from mCherry-NRP1 b1
mCherry-SNX5	pmCherry-C1	From the lab
mCherry-SNX6	pmCherry-C1	From the lab
NRP1-GFP	pEGFP-N1	Gift from Yohei Yamauchi
NRP1-GFP T316R	pEGFP-N1	Cloned by site directed mutagenesis from NRP1-GFP
NRP1-HRP	pLNT-SFFV	Gift from Dr Tom Nightingale
NRP1-mCherry	pmCherry-N1	Cloned by restriction from NRP1-GFP
Nrp1-mCherry	pmCherry-N1	Gift from Donatella Valdembri
NRP1-tail-GFP	pEGFP-N1	Cloned by Dr Boris Simonetti
NRP1-tail-GFP N898D	pEGFP-N1	Cloned by Dr Boris Simonetti
NRP1-tail-GFP N900D	pEGFP-N1	Cloned by Dr Boris Simonetti
NRP1-tail-GFP N901D	pEGFP-N1	Cloned by Dr Boris Simonetti
NRP1-tail-GFP Y899D	pEGFP-N1	Cloned by Dr Boris Simonetti
NRP2-GFP	pEGFP-N1	Gift from Dr Yohei Yamauchi
NRP2-mCherry	pmCherry-N1	Cloned by restriction from NRP2-GFP
pSpCas9(BB)-2A-Puro	pX459	From the lab
pX330-U6-Chimeric_BB-CBh-hSpCas9	pX330	From the lab
ST6GAL1-APEX2	XLG3	Cloned by Dr Boris Simonetti
ST6GAL1-HRP	XLG3	Cloned by Dr Boris Simonetti
VPS35-GFP	pEGFP-N1	From the lab
VPS35-GFP D620N	pEGFP-N1	From the lab
VPS35-GFP KKK-555/6/9-EEE	pEGFP-N1	Cloned by Dr Adam Jellett
VPS35-GFP-frb	pLVX-Puro	Cloned by Dr Ash Evans
XLG3	XLG3	From the lab

2.1.3 Oligonucleotides

Table 2.4 List of Oligonucleotides Used for Cloning in this Study

Primer Name	5'-3' Sequence
EphA2 Tail F EcoRI	TATGAATTCACACCGCAGGAGGAAGAAC
EphA2 Tail R KpnI	ATAGGTACCCTAGTACAAGAAAGCTGGGTCC
NRP1 b1 F EcoRI	TATGAATTCAAAATGTATGGAAGCTCTGGG

NRP1 b1 R KpnI	TATGGTACCTTAATCTGTTATCTTGCAACCGTA
NRP1 b1 T316R SDM F	CCTCTCCGGGCCTCCACCCATTCTCAGGG
NRP1 b1 T316R SDM R	CCCTGAGAATGGGTGGAGGCCCGGAGAGG
NRP1 b1b2 F EcoRI	TATGAATTCAAAATGTATGGAAGCTCTGGG
NRP1 b1b2 R KpnI	TATGGTACCTTACACTTCACAGCCCAGCAGC
Nrp1 F FseI	TATGGCCGGCCAAAATGTGGCGGGACCATAAA
Nrp1 R SacII	ATACCGCGGTCACGCCTCTGAGTAATTACTCTGT
NRP1 KO F	CACCGATCGACGTTAGCTCCAACG
NRP1 KO R	AAACCGTTGGAGCTAACGTCGATC
S1 R685D SDM F	CGGTGGATCCTTAATCTGCCCGCCGAGGAG
S1 R685D SDM R	CTCCTCGGCGGGCAGATTAAGGATCCACCG
S1ΔRRAR SDM F	CTTAACGTGCCCGCTAAGGAGAATTAGTCTGAGTCTGATAAC
S1ΔRRAR SDM R	GTTATCAGACTCAGACTAATTCTCCTTAGCGGGCACGTTAAG
VPS35 KO F	CACCGTGGTGTGCAACATCCCTTG
VPS35 KO R	AAACCAAGGGATGTTGCACACCAC

Abbreviations: F: Forward Primer; R: Reverse Primer; SDM: Site-Directed Mutagenesis

Table 2.5 List of Small Interfering RNA (siRNA) Duplexes Used for Knockdowns

Target	Sequence (5'-3')	Source
ON-Target Plus Nontargeting Control Pool	UGGUUUACAUGUCGACUAA, UGGUUUACAUGUUGUGUGA, UGGUUUACAUGUUUUCUGA, UGGUUUACAUGUUUUCCUA,	GE Healthcare
Rab27b	SMARTPool of 4 siRNAs	Horizon (M-004228-00-0005)
SNX5	CUACGAAGCCCGACUUUGA	Eurofins MWG
SNX6	UAAAUCAGCAGAUGGAGUA	Eurofins MWG
VPS35	GUUGUUAUGUGCUUAGUA, AAAUACCACUUGACACUUA	GE Healthcare

2.1.4 CRISPR/Cas9 guide RNAs (gRNAs)

Table 2.6 List of CRISPR gRNA Sequences Used in this Study

Target	Sequence (5'-3')	Plasmid	Source
NRP1	GATCGACGTTAGCTCCAACG	PX459	This study
SNX1	GGCCGGGGGATCAGAACCCG	PX330	From the lab
SNX2	GCAGCACTGTCTCCACCCTAG	PX330	From the lab
SNX4	GCGGTCGGCAAGGAAGCGGA, GATTTTGTCTCTACAAAGGA	PX330	From the lab
SNX5	GCTCTGAAACGTGGGCAGTG	PX330	From the lab
SNX6	GATGTGCTGCCACACGACAC	PX330	From the lab

SNX8	GCACAAGTTCCCCTACCGTA, GGAGTCAGCACAGTGCGTCG, GGGCCGAGCGGATCGCATCG	PX330	From the lab
VPS35	GTGGTGTGCAACATCCCTTG	PX330	From the lab
VPS35	GTGGTGTGCAACATCCCTTG	PX459	This study

2.1.5 Cell Lines

Table 2.7 List of Cell Lines Used in this Study

Cell Line	Description	Source
Caco-2	Human colon adenocarcinoma	ATCC
Calu-3	Human lung adenocarcinoma	ATCC
H4	Human neuroglioma/astrocytoma	ATCC
Henrietta Lacks (HeLa)	Human cervical adenocarcinoma	ATCC
Human Embryonic Kidney (HEK293T)	Human embryonic kidney cells, artificially immortalised with sheared adenovirus DNA, expressing the large T antigen of Simian virus 40	ATCC
Vero E6	Green monkey, spontaneously immortalised	ATCC

Abbreviation: ATCC: American Type Culture Collection

2.1.6 Cell Culture Reagents

Hela, HEK293T, H4 and Vero E6 cells were routinely cultured in Dulbecco's Modified Eagle Medium (DMEM), containing 4.5 g/L glucose (Sigma, D5796), supplemented with 10% (v/v) foetal bovine serum (FBS, Sigma, F7524), 100 U/mL penicillin and 0.1 mg/mL streptomycin. Calu-3 cells were grown in Eagle's Minimal Essential Medium + GlutaMAX (Gibco, 35050061) supplemented with 10% FBS, 0.1 mM non-essential amino acids (NEAA), 1 mM sodium pyruvate, 100 U/mL penicillin and 0.1 mg/mL streptomycin. Caco-2 cells were maintained in DMEM + GlutaMAX, 10% FCS, 0.1 mM NEAA and 100 U/mL penicillin and 0.1 mg/mL streptomycin.

After seeding single cells to generate CRISPR-Cas9 KO clones, HeLa and H4 cells were incubated with Iscove's Modified Dulbecco's Medium (IMDM; Thermo Fischer, 12440053) until confluent. For transfections, nucleic acids were mixed with transfection reagents in OptiMEM reduced serum media (Gibco, 31895062). Cell culture grade phosphate-buffered saline (PBS) was used to wash cells (Thermo Fisher, 14190144).

To detach cells from culture, trypsin-ethylenediaminetetraacetic acid (EDTA; Sigma, T4174) was diluted in PBS to a final concentration of 0.5 g/L porcine trypsin, 0.2 g/L EDTA.

2.1.7 Reagents for Stable Isotope Labelling by Amino Acids in Cell Culture (SILAC)

Media for SILAC cell culture was assembled in DMEM for SILAC (Thermo Scientific, 89985), devoid of L-lysine and L-arginine, supplemented with 10% dialysed FBS (Sigma, F0392), 100 U/mL penicillin and 0.1 mg/mL streptomycin. This media was supplemented with SILAC amino acids to isotopically label proteins.

Table 2.8 List of Amino Acids used for SILAC Experiments

Amino Acid	Composition	Source	Catalogue Number
R_0 (Light Arginine)	L-Arginine monohydrochloride	Sigma	A6969
K_0 (Light Lysine)	L-Lysine monohydrochloride	Sigma	L8662
R_6 (Medium Arginine)	L-Arginine HCl 13C	Silantes	201203902
K_4 (Medium Lysine)	L-Lysine 2HCL (4.4'.5.5'-D4-L-Lysine 2HCl) 2H	Silantes	211103913
R_{10} (Heavy Arginine)	L-Arginine HCl 13C,15N	Silantes	201603902
K_8 (Heavy Lysine)	L-Lysine HCl 13C,15N	Silantes	211603902

2.1.8 Buffers

PBS: 170 mM NaCl, 3 mM KCl, 1 mM Na_2HPO_4, 1.8 mM KH_2HPO_4, pH 7.4.

Tris-buffered saline with 0.1% tween (TBST): 150 mM NaCl, 50 mM Tris-HCl, pH 7.6, 0.1% (v/v) Tween (Sigma, P1379).

Triton-based cell lysis buffer: 1% (v/v) Triton X-100 (TX-100; Sigma, T8787) and 1 x complete protease inhibitor tablet (Roche, 04693124001) were suspended in 10 mL PBS, pH 7.4.

GFP/RFP nanotrap buffer: 0.5% (v/v) IGEPAL CA-360 (Sigma, I8896), 20 mM Tris-HCl, 1 x complete protease inhibitor tablet were suspended in 10 mL PBS, pH 7.4.

Radioimmunoprecipitation assay (RIPA) buffer: 150 mM NaCl, 0.1% (v/v) sodium dodecyl sulphate (SDS), 0.5% (w/v) sodium deoxycholate, 1% (v/v/) TX-100), 1 x complete protease inhibitor tablet were suspended in 10 mL 50 mM Tris-HCl, pH 7.5.

Tris-Acetate-EDTA (TAE) buffer: 0.8 M tris-acetate, 20 mM EDTA, pH 7.8.

2.1.9 Bacterial Cell Culture

XL1-Blue supercompetent *E.coli* cells (genotypes: recA1, endA1, gyrA96, thi^{-1}, hsdR17, supE 44, relA1 and lac [F´ proAB $lacI^{q}ZΔM15$ Tn*10* (Tet^{r})] were purchased from Agilent (200236). These cells were used for transformation of all constructs cloned in this study.

Bacterial growth media: Luria-Bertani (LB) medium (10g NaCl, 10 g tryptone, 5 g yeast extra ct in 1 L sterilised water); LB agar (20 g agar, 10 g NaCl, 10 g tryptone, 5 g yeast extract in 1 L sterilised water); super optimal broth with catabolite repression (SOC) media (20 g tryptone , 5 g yeast extract in 1 L sterilised water; Sigma, S1797).

Antibiotics for bacterial selection: 100 µg/mL ampicillin (Sigma, A9518), 50 µg/mL kanamycin (Sigma, B5264)**.**

2.1.10 Sterilised Water

The PURELAB Elga water system was used to sterilise water for the preparation of all solutions and buffers used in this study, except for the use of nuclease-free water in molecular cloning.

2.2 Molecular Biology and Cloning

2.2.1 Cloning Strategies

Table 2.3 lists the plasmids used in this study. Constructs were generated by conventional cloning methods: polymerase chain reaction (PCR) and/or restriction digestion was used to isolate sequences of interest from template DNA, followed by ligation into a plasmid backbone digested with compatible restriction enzymes. For SDM, primers were designed containing homology to the template DNA, but with desired mutations to be incorporated.

2.2.2 Polymerase Chain Reaction

All PCR reactions were performed in a T100 Thermal Cycler machine (Bio-Rad).

For gene amplification, a PCR mix comprising 1X Q5 high-fidelity master mix (New England Biolabs, M0492), 0.5 µM forward and reverse primers, and < 1 µg of template DNA was

assembled in nuclease-free water (Promega, P1193). A typical program for standard PCR is shown below:

Table 2.9 Typical Amplification PCR Program

Step	Temperature (ºC)	Duration
Initial Denaturation	98	30 seconds
25-35 Cycles: Denaturation Annealing Extension	 98 50-72 72	 10 seconds 30 seconds 30 seconds/kb
Final Extension	72	2 minutes
Hold	4	Until stopped

Annealing temperature was calculated based on the melting temperature of primers. Abbreviation: kb: kilobase.

For site-directed mutagenesis (SDM), primers were designed using the online Agilent 'QuikChange' tool. A SDM PCR mix comprising 1X Q5 high-fidelity master mix (New England Biolabs, M0492), 0.5 µM forward and reverse primers, and 25 ng of template DNA was assembled in nuclease-free water. A typical program for SDM PCR is shown below:

Table 2.10 Typical Program for Site-Directed Mutagenesis

Step	Temperature (ºC)	Duration
Initial Denaturation	98	30 seconds
18 Cycles: Denaturation Annealing Extension	 98 55 72	 10 seconds 30 seconds 1 minute + 1 minute/kb
Final Extension	72	10 minutes
Hold	4	Until stopped

Following SDM PCR, the methylated template DNA was digested by addition of 1 µl of DpnI per 50 µL of PCR sample, followed by 1 hour of incubation at 37ºC.

2.2.3 Restriction Digestion

Restriction enzymes were purchased from New England Biolabs and utilised to excise DNA fragments from a template sequence. Digestion mixes were assembled comprising 1 µg template DNA, 1 µL of each restriction enzyme, 5 µL of restriction buffer compatible with the enzyme(s) used in the reaction, adjusted to a total reaction volume of 50 µL with nuclease-free water. Samples were mixed well, then incubated at 37ºC for the appropriate length of time recommended by the manufacturer for each restriction enzyme.

2.2.4 Ligation Reactions

Digested DNA fragments and digested plasmid backbones were mixed at a 3:1 ratio, alongside 1 µL T4 DNA ligase (Thermo Fisher, EL0014) and 1.5 µL DNA ligase buffer (Thermo Fisher, EL0014) in a total volume of 15 µL. This mixture was incubated for 15 minutes at room temperature.

2.2.5 Agarose Gel Electrophoresis

To analyse the size and purity of DNA following molecular cloning steps, DNA was resolved according to size on 1% (w/v) agarose gels. 0.5 g agarose was added to 50 mL TAE buffer **(Chapter 2.1.8)** and heated to dissolve the agarose. Once dissolved, the solution was cooled slightly, then 0.5 µL SYBR Safe DNA Gel Stain (Invitrogen, S33102) was added to label DNA. This solution was poured into a casting tank, and a comb was added to insert wells for DNA loading. Once the gel solidified, the comb was removed, and the gel was submerged in 1X TAE in a Mini-Sub Cell GT Cell (Bio-Rad). DNA samples were mixed with 6X gel loading dye (New England Biolabs, B7024) to a 1X concentration, and loaded into the wells alongside a 2-log DNA ladder (New England Biolabs, N3200). A constant voltage of 100 V was applied across the gel tank to migrate DNA towards the anode according to size. Once resolved, DNA bands were visualised using a D-DiGit gel scanner (LI-COR). If downstream cloning steps were required, DNA bands were excised from the gel.

2.2.6 Purification of DNA Fragments

To purify excised DNA fragments after PCR or restriction digests, the illustra GFX PCR DNA and Gel Band Purification Kit (GE healthcare, 28903470) was used according to the manufacturer's instructions.

2.2.7 Transformation

XL1-Blue supercompetent *E.coli* cells **(Chapter 2.1.9)** were thawed on ice. For each transformation, 20-50 µL of cells was added to a 1.5 mL microcentrifuge tube. 50 ng of circular DNA was added to the cells, and this mixture was incubated on ice for 30 minutes. The cells were then heat shocked in a 42ºC water bath for 45 seconds to facilitate DNA uptake, then returned to ice for 2 minutes to reduce cell damage. 1 mL of SOC medium **(Chapter 2.1.9)**, pre-warmed to 37ºC, was added to the mixture, then cells were moved to a 37ºC incubator with shaking at 180 revolutions per minute (rpm) for 30-60 minutes. 100 µl of the culture was then spread on an LB agar plate containing the appropriate antibiotic for plasmid selection and incubated in a 37ºC incubator overnight.

2.2.8 Purification of Plasmid DNA

Following transformation, colonies were picked with a pipette tip and added to LB medium containing the appropriate selection antibiotic and incubated in a 37ºC incubator with shaking at 180 rpm. For small scale miniprep purifications, colonies in 5 mL of LB medium were incubated at 37ºC with shaking at 180 rpm for 16 hours, prior to purification using a QIAprep Spin Miniprep Kit (Qiagen, 27106) according to the manufacturer's instructions. For large scale maxiprep purifications, a starter culture of 2 mL was grown for 6 hours, then added to 250 mL LB medium containing the appropriate selection antibiotic in a flask and moved to a 37ºC incubator with shaking at 180 rpm for 16 hours, then purified using a HiSpeed Plasmid Maxi Kit (Qiagen, 12662) according to the manufacturer's instructions. Following purification, DNA concentration was measured using a NanoDrop 1000 machine (Thermo Fisher). For sequencing, DNA concentration was adjusted to a concentration of 90 ng/µL in a volume of 15 µL and sent to Eurofins MWG Operon for Sanger sequencing.

2.2.9 RNA Extraction

H4 cells were grown to confluence in a 6-well plate. Media was removed and cells were washed twice with ice cold PBS. Cells were lysed and RNA was purified using the RNeasy kit (Qiagen, 74134) according to the manufacturer's instructions. RNA concentration was measured using a NanoDrop 1000 machine (Thermo Fisher).

2.3 Mammalian Cell Culture

2.3.1 Cell Culture

HeLa, HEK293T, H4, Calu-3, Caco-2 and Vero E6 cells were grown in their respective media solutions **(Chapter 2.1.6)** in a 37°C incubator with a 5% CO_2 atmosphere (LEEC). All cell

culture work was performed in a sterile category 2 vertical laminar flow cabinet (Holten Laminair, Thermo Fisher). All category 3 lab involving live SARS-CoV-2 was performed by Dr Katja Klein, Dr Maia Kavanagh Williamson, and Dr Andrew Davidson.

To passage cells, media was removed, and cells were washed twice with sterile PBS. Trypsin-EDTA was then added to detach adherent cells from the cell culture dish **(Chapter 2.1.6)**. After cell detachment, media was added to dilute the tryspin-EDTA, then an appropriate fraction of the cell suspension was transferred to a new cell culture dish. For seeding specific cell numbers, the concentration of cells within this suspension calculated using a cell counting chamber (Hawksley, BS748).

2.3.2 DNA Transfection

For transient transfection of HeLa and H4 cells, FuGENE 6 (Promega, E2693), and DNA were added to 50 µl of minimal OptiMEM media at a 3 µl:1 µg ratio and incubated for 5 minutes at room temperature. The DNA:FuGENE mixture was added dropwise to cells in a 12- or 6-well plate seeded according to the manufacturer's guidelines. Cells were incubated for 4 hours at 37°C, then washed twice with PBS to reduce toxicity. Fresh media was added to wells, and cells were incubated for 24-48 hours before fixation for immunofluorescence or lysis for Western blotting.

A 10 µg/µL stock solution of 25 kDa linear polyethylenimine (PEI; Polysciences, 23966-2) in distilled water was made. PEI transfection was used to introduce DNA into HEK293T cells, typically prior to immunoprecipitation experiments or to produce lentiviral particles. $10x10^6$ HEK293T cells were seeded into a 15 cm plate the day before transfection. To create the transfection mixture, 5 mL of OptiMEM was mixed with 5 µL of 10 µg/µL PEI. This mixture was filtered through a 0.2 µm filter into a sterile falcon tube. A separate mixture of 15 µg transfection DNA with 5 mL OptiMEM was also created and mixed. The PEI and DNA solutions were then combined and incubated for 10 minutes at room temperature. Following incubation, media was aspirated from the plate and cells were washed twice in PBS. The PEI:DNA mixture was added to the plate, and cells were returned to the incubator for 4 hours. After this incubation period, the transfection mixture was removed, cells were washed and then fresh DMEM was added. Transfected cells were harvested 24-48 hours after transfection.

2.3.3 siRNA Transfection

siRNA-mediated knockdown (KD) of HeLa and H4 cells was achieved using a 4-day protocol including 2 transfections. On the first day, cells in a 6-well plate were 'reverse transfected' by mixing 6 µl of DharmaFECT 1 (Dharmacon, T-2001-01) with 200 µl of OptiMEM for 5 minutes, then added to 20 µl of 2 µM siRNA in an empty well. This mixture was incubated for 20 minutes

at room temperature. Meanwhile, cells were detached with trypsin and counted, then following 20 minutes of siRNA:DharmaFECT incubation, 700,000 cells were added to the well containing the transfection mix, in a total volume of 2 mL and returned to the incubator overnight.

The following morning, cells were detached with trypsin and re-seeded into a fresh 6-well plate and allowed to adhere for one hour. A 'fast forward' transfection mix comprising 20 µl of 2 µM siRNA, 12 µl HiPerFect (Qiagen, 301705), and 200 µl of OptiMEM was assembled in a sterile microcentrifuge tube. Once cells adhered in the new plate, this mixture was added dropwise to the cells, mixed by gently swirling the plate, and cells were returned to the incubator.

On the third day of the protocol, the siRNA-containing media was exchanged for fresh DMEM to reduce toxic effects. On the fourth day cells were either fixed for immunofluorescence or lysed for Western blotting.

2.3.4 Lentivirus Production and Transduction

Lentiviral transduction was used to generate cell lines stably expressing constructs of interest. Lentiviral particles were produced in HEK293T cells using a PEI transfection. HEK293T cells were seeded the day before transfection as described in **Chapter 2.3.2**. A transfection mixture of 40 µg of lentiviral expression plasmid (construct of interest in a XLG3 or pLVX-puro backbone), 30 µg of lentiviral packaging plasmid (pCMV-dR8.91) and 10 µg of vesicular stomatitis virus (VSV)-G envelope plasmid (pMDG2) in 5 mL OptiMEM was assembled and passed through a 0.2 µm filter **(Chapter 2.1.2)**. This DNA mixture was combined with 25 µL of 10 µg/µL PEI in a total volume of 10 mL and incubated for 5 minutes, then added dropwise to HEK293T cells and returned to the incubator. 4 hours later, the transfection mixture was removed and replaced with fresh DMEM. After 48 hours of lentivirus production, medium was carefully removed and transferred to a falcon tube, then centrifuged for 5 minutes at 4000 x g to remove detached HEK293T cells. The supernatant was removed and passed through a 0.45 µm filter. The resulting lentivirus mixture could then be frozen at -80ºC.

500,000 HeLa or H4 cells were seeded in a 6-well plate 1 hour prior to lentiviral transduction. Once attached, varying titres of lentivirus mixture were added to different wells to produce a range of different expression levels. Cells were returned to the incubator for 48 hours. After 48 hours, cells were passaged, then passaged twice more on subsequent days to ensure that all live lentivirus was removed before processing for further experiments.

2.3.5 CRISPR-Cas9 Knockout (KO)

To deplete protein levels and generate KO HeLa and H4 cells, clustered regularly interspaced short palindromic repeats (CRISPR)-Cas9 was used. The pX330 and pX459 plasmids encoding *S.pyogenes* Cas9 nuclease and a gRNA of interest were transfected into HeLa or H4 cells using FuGENE 6 as described in **Chapter 2.3.2**. pX459 was transfected alone, due to the puromycin resistance marker present in the plasmid. When transfecting the pX330 plasmid, cells were co-transfected with a GFP-puromycin resistance plasmid to facilitate selection of transfected cells **(Chapter 2.1.2)**.

24 hours after transfection, media was removed and replaced with fresh DMEM containing 3 µg/mL puromycin dihydrochloride (Calbiochem, 540411) for selection. An untransfected well of cells was also incubated with puromycin as a control. Cells were returned to the incubator for a further 24 hours. Once all control cells were dead, any surviving cells transfected with pX330/GFP-puromycin resistance or pX459 were presumed to be KO cells expressing the resistance plasmids. The media was changed and replaced with fresh DMEM. Cells could then be seeded for the selection of KO clones, or grown further for imaging or biochemical experiments.

To seed CRISPR KO cells for clonal selection, cells were detached using trypsin following puromycin selection and counted. 100 cells were added to 25 mL of IMDM **(Chapter 2.1.6)**. This mixture was seeded into a 96-well plate at a volume of 200 µL per well, a density of < 1 cell per well. Cells were incubated to grow until large colonies have formed, which were then expanded and screened for successful KO by Western blotting using an antibody against the protein target.

2.4 Protein Biochemistry

2.4.1 Cell Lysis

Triton-based buffer was used to lyse cells for routine whole cell lysate experiments, GFP/mCherry nanotrap buffer was used to lyse cells for immunoprecipitation experiments, and RIPA buffer was used to lyse cells for biotinylation experiments **(Chapter 2.1.8)**. Cells were removed from the incubator and placed on ice. Media was removed, and cells were washed twice in ice cold PBS, ensuring to remove all liquid from the final wash to avoid diluting the lysate. Appropriate amounts of lysis buffer were added according to the size of the culture well/plate, followed by gentle rocking to ensure coating of all cells with lysis buffer. A cell scraper was used to remove cells from the base of the culture well/plate, and this lysate solution was pipetted to homogenise cell debris and transferred into a fresh microcentrifuge

tube. Lysates were centrifuged at 15,000 x g for 10 minutes at 4ºC to pellet insoluble material, then the supernatant was transferred to a fresh microcentrifuge tube. 4X NuPAGE lithium dodecyl sulphate (LDS) Sample Buffer (Thermo Fisher, NP0008), supplemented with 3% β-mercaptoethanol (Sigma, M3148), was added to lysates at a 1:3 dilution to create a 1X final concentration.

2.4.2 GFP/mCherry-Nanotrap Immunoprecipitation

HEK293T cells expressing green fluorescent protein (GFP)/mCherry or GFP/mCherry-tagged constructs were grown to confluency in a 15 cm plate following transfection **(Chapter 2.3.2)**. Cells were washed twice with ice cold PBS, then lysed in GFP/mCherry nanotrap buffer **(Chapter 2.4.1)**. The centrifuged lysate was transferred to a fresh microcentrifuge tube, and an appropriate amount of this lysate was reserved for the 'input' fraction as a representation of protein levels in the total cell lysate.

20 µl of GFP-trap or RFP-trap agarose beads (Chromotek, GTA20, RTA20) were added to a fresh microcentrifuge tube and washed three times with the lysis buffer described above. Following each wash step, the suspended beads were pelleted by centrifugation at 350 x g for 30 seconds. Following the HEK293T cell lysates were then added to the tube to mix with the beads, and the immunoprecipitation reaction was left rotating for 1 hour at 4ºC.

Following incubation, beads were centrifuged at 350 x g for 30 seconds. The unbound cell lysate supernatant was discarded, and beads were subsequently washed twice in a modified wash buffer containing IGEPAL CA-360 (50 mM Tris-HCl, 0.25% IGEPAL, 1 x protease inhibitor cocktail in PBS), and once in wash buffer devoid of IGEPAL CA-360 (50 mM Tris-HCl, 1 x protease inhibitor cocktail in PBS). Finally, beads were resuspended in 4X LDS sample buffer supplemented with 3% β-mercaptoethanol and diluted to a final 2X concentration.

For immunoprecipitation of the VSV-Spike pseudotyped virus, mCherry, mCherry-b1 and mCherry-b1 T316R were transfected into HEK293T cells the day before immunoprecipitation. Lysates were cleared by centrifugation at 15,000 x g for 10 minutes at 4°C. From the resulting supernatant, an input fraction was reserved, and the rest incubated with RFP-trap beads to rotate for 1 hour at 4°C. Following enrichment of mCherry constructs, the beads were washed three times as above to remove residual cell lysate and detergent. VSV-Spike pseudotyped virus was added to the isolated mCherry beads in a category 2 cell culture laminar flow hood and incubated rotating for a further 1 hour at 4°C. Following virus immunoprecipitation, the beads were again washed three times in a laminar flow hood, then resuspended in 2X LDS sample loading buffer for elution.

2.4.3 HRP-TGN46 Biotinylation

The protocol for HRP-TGN46 biotinylation is adapted from the APEX2 biotinylation protocol outlined by the Ting group in (Hung et al., 2016). $10x10^6$ HRP-TGN46-expressing cells were seeded in a 15 cm plate the day before biotinylation. The next day, cells were incubated in DMEM media supplemented with 500 µM biotin-phenol (BP; Iris Biotech Gmbh, LS-3500) and incubated for 30 minutes at 37°C. Plates were removed to a fume hood at room temperature due to the toxicity of sodium azide in the quenching buffer. Hydrogen peroxide (H_2O_2) (ThermoFisher, 10687022) was added at a final concentration of 1 mM and evenly distributed by rocking the cell plate. To block cell surface labelling, sodium ascorbate (Sigma-Aldrich, A7631) was added to the H_2O_2 solution to incubate cells at a final concentration of 1 mM H_2O_2, 50 mM sodium ascorbate as described in (Kostelnik et al., 2019). After 45 seconds of H_2O_2 incubation, the media was removed and replaced with ice cold, freshly prepared quencher solution consisting of 1 mM sodium ascorbate, 500 µM (±)-6-Hydroxy-2,5,7,8-tetramethylchromane-2-carboxylic acid (Trolox, Sigma-Aldrich, 238813) and 1 mM sodium azide (VWR, 0639-250G) in PBS to ensure that the biotinylation reaction did not proceed beyond 1 minute. The quencher solution was left for 1 minute, then discarded, and this washing process was repeated 5 times. Following washes, cells were lysed in RIPA buffer **(Chapter 2.1.8)** and lysates spun at 15,000 x g for 10 minutes at 4°C. 50 µL aliquots of streptavidin beads were prepared and washed 3 times in RIPA buffer, centrifuging beads between washes at 350 x g for 30 seconds. The cell lysates were then mixed with the streptavidin beads and rotated for 1 hour at 4°C.

After the binding step was completed, streptavidin beads were centrifuged at 350 x g for 30 seconds and the supernatant containing unbound proteins was removed. The beads were then washed 7 times (twice in RIPA buffer, once with 1 M KCl, once with 0.1 M Na_2CO_3, once with 2 M Urea 10 mM Tris-HCl pH 8.0, and twice again with RIPA buffer). All buffers were kept ice cold throughout the process. After the final wash step, all supernatant was removed and beads were resuspended in 3X NuPAGE sample buffer supplemented with 2.5% β-mercaptoethanol, 2 mM free biotin and 20 mM DTT.

2.4.4 Protein Precipitation from Culture Medium

Proteins were precipitated from cell culture medium utilising trichloroacetic acid (TCA) according to the protocol outlined in (Koontz, 2014). H4 cells were grown to confluency in a 12-well plate. Following overnight incubation in DMEM without FBS supplementation, cell culture media was removed with a pipette and transferred to microcentrifuge tubes, then centrifuged at 300 x g for 10 minutes at 4°C, then the supernatant was transferred to a fresh

microcentrifuge tube and centrifuged at 2,000 x g for a further 10 minutes 4°C to pellet dead cells. The cells were subsequently lysed and processed for Western blotting for use as loading controls.

100 µL of 0.15% sodium deoxycholate was added to the media samples, followed by vortexing and incubation at room temperature for 10 minutes. 50 µL of 100% TCA was added to the samples, followed by vortexing and incubation on ice for 30 minutes to precipitate protein content. The samples were centrifuged at 10,000 x g for 15 minutes to pellet precipitated protein, then the supernatant was removed and discarded. The remaining pellet was resuspended in 50 µL 2X LDS sample buffer.

2.4.5 SDS-PAGE and Western Blotting

Protein samples were resolved by sodium dodecyl sulphate-polyacrylamide gel electrophoresis (SDS-PAGE). To ensure even loading of protein samples, a bicinchoninic acid (BCA) assay (Pierce, 23225) or 660 nm assay (Pierce, 22662) was used to determine protein concentration according to the manufacturer's instructions. Cell lysate samples were boiled at 95°C for 10 minutes in LDS sample buffer prior to loading. For immunoprecipitation and streptavidin affinity isolation experiments, samples were regularly vortexed during boiling to ensure pellet resuspension. NuPAGE 4-12% gradient Bis-Tris precast gels (Life Technologies, NPO336) were used for SDS-PAGE. NuPAGE MOPS SDS Running Buffer (Thermo Fisher, NP001-2) was diluted in distilled water to a 1X concentration and used as running buffer. Boiled protein samples were evenly pipetted into the wells of the gel. An initial voltage of 100 V was applied to resolve samples, which was increased to a maximum of 200 V to fully resolve proteins.

Following SDS-PAGE, proteins were transferred onto a polyvinylidine fluoride (PVDF) membrane (Immobilon-FL membrane, pore size 0.45 µm; Millipore, IPFL00010). The PVDF membrane was activated by soaking in methanol. The membrane and gel were placed in apposition between 2 foam pads and 4 squares of filter paper in a blotting cassette. The assembled components were soaked in transfer buffer (25 mM Tris, 192 mM glycine, 20% (v/v) methanol) and inserted into a mini-Trans Blot Cell (Bio-Rad, 1703930) electrophoresis tank filled with transfer buffer. Proteins were transferred by applying a constant voltage of 100 V across the cassette for 90 minutes.

After transfer, the PVDF membrane was blocked in 5% (w/v) milk powder in TBST **(Chapter 2.1.8)** for 30-60 minutes. Primary antibodies were diluted in 2% (w/v) bovine serum albumin (BSA) TBST according to the concentrations listed in **Table 2.1**. The membrane was incubated in primary antibody mixture overnight in a falcon tube at 4°C. Following incubation, the primary

antibody solution was discarded or frozen, and the membrane was washed 3 times with TBST, with each wash incubated for 5 minutes. Fluorescently conjugated secondary antibodies were diluted in 5% (w/v) milk powder in 0.1% (v/v) SDS TBST according to the concentrations listed in **Table 2.2**, then added to the membrane and incubated rocking at room temperature for 30 minutes. For streptavidin labelling, IRDye 800CW streptavidin (LI-COR, 926-32230) was added to 5% (w/v) milk powder in 0.1% (v/v) SDS TBST at a 1/5000 concentration and incubated for 30 minutes. The membrane was washed 3 times in TBST as previously described. Fluorescence was then detected by scanning with a LI-COR Odyssey scanner (LI-COR Biosciences). If re-probing was required, Restore PLUS Western Blot Stripping Buffer (Thermo Scientific, 46430) was used to remove bound antibodies. The membrane was then washed with three times in TBST before adding primary antibodies and beginning the procedure again.

2.5 Microscopy

2.5.1 Immunofluorescence Staining

HeLa and H4 cells were seeded onto sterile 13 mm coverslips the day before fixation. DMEM was removed, followed by two washes with PBS, then cells were fixed in 4% paraformaldehyde (Pierce, 28906) for 20 minutes at room temperature. Cells were then washed three times with PBS, then permeabilised with 0.1% (v/v) TX-100 for 5 minutes. For immunofluorescence staining against LAMP1 **(Table 2.1)**, cells were permeabilised in 0.1% (w/v) saponin (Sigma-Aldrich, 47036) for 5 minutes instead of TX-100. Cells were washed three more times in PBS, then incubated with 1% BSA in PBS for 15 minutes.

Antibody solutions were made in a 1% BSA PBS solution according to the concentrations listed in **Table 2.1**. 50 µL of primary antibody mixture was spotted onto Parafilm (Sigma-Aldrich, P7793). Coverslips were incubated face down on the antibody mixtures for 1 hour, covered in darkness at room temperature. A secondary antibody mixture was assembled in 1% BSA PBS according to the concentrations in **Table 2.2**. To label DNA, 0.5 µg/mL 4', 6-diamidino-2-phenylindole dihydrochloride (DAPI; Sigma-Aldrich, D8417) was added to the secondary antibody mixture. To label biotinylated proteins, 0.5 µg/mL Alexa Fluor 568-conjugated streptavidin (Invitrogen, S11226) was added to the secondary antibody mixture. Coverslips were washed three times in PBS, then placed face down on the 50 µL spots of the secondary antibody mixture on Parafilm for a further 30 minutes at room temperature in darkness. The coverslips were washed three final times in PBS, then mounted face down onto microscope slides spotted with Fluoromount-G (Invitrogen, 00-4958-02).

2.5.2 Surface Uptake Assay

To specifically label surface-localised Neuropilin-1 and trace its internalisation into cells, a GFP-Nrp1 construct was created, with the GFP tag localised extracellularly **(Chapter 5.2.5)**. To perform the surface uptake assay, HeLa cells were transiently transfected with GFP-Nrp1 using FuGENE 6, then incubated at 37ºC for 24-48 hours to express the construct. A 1% BSA PBS solution containing an anti-GFP antibody **(Table 2.1)** was prepared and 50 µL of this mixture was spotted onto Parafilm per coverslip. Live cells were removed from the incubator and placed face down on this antibody mixture, then incubated for 1 hour at 4ºC in darkness, to allow antibody binding to the extracellular GFP epitope, but preventing temperature-dependent membrane trafficking activity. After this incubation, coverslips were washed three times in PBS, then returned to pre-warmed 37ºC DMEM to begin the surface uptake timecourse. At varying timepoints, coverslips were fixed, then the immunofluorescence protocol detailed in **Chapter 2.5.1** was followed.

2.5.3 Confocal Microscopy

Confocal microscope images were taken on a Leica SP5-II confocal laser scanning microscope attached to a Leica DMI 6000 inverted epifluorescence microscope (Leica Microsystems), with a 63x CX PL APO lambda blue UV oil immersion lens, numerical aperture 1.4 (Leica Microsystems, 506192). For stimulated emission depletion (STED) microscopy, images were taken using a Leica SP8 confocal laser scanning microscope attached to a Leica DMi8 inverted epifluorescence microscope (Leica Microsystems) with a 63x HC PL APO CS2 oil immersion lens, numerical aperture 1.4 (Leica Microsystems, 506351). STED was achieved using 592 nm and 660 nm depletion lasers. Images were acquired using the Leica Application Suite AF software (version 2.7.3.9723).

2.5.4 Electron Microscopy

100,000 wild-type or HRP-TGN46-expressing HeLa cells were seeded in glass bottom 35 mm dishes (MatTek, P35G-1.5-14-CGRD) the day before sample processing. Cells were fixed in solution of 2.5% glutaraldehyde (Sigma-Aldrich, G5882), 3 mM $CaCl_2$, 0.1 M cacodylate (Na(CH3)2AsO2) buffer, pH 7.4, for 5 minutes at room temperature, then 1 hour on ice. All solutions and incubation steps from this point onwards until the embedding stage were kept ice cold. Samples were washed 5 times in 0.1 M cacodylate buffer, leaving each wash on ice for 2 minutes. Samples were incubated in a quenching buffer of 20 mM glycine and 0.1 M cacodylate for 5 minutes, then washed in 0.1 M cacodylate buffer a further 5 times, at 2 minutes per wash. A 1X 3,3'-diaminobenzidine (DAB), 10 mM H_2O_2 solution was assembled by dissolving 50 mg of DAB in 10 mL of 0.1M HCl, then diluting 1 mL of this solution in 9 mL of 0.1 M cacodylate and 10 µL of 30% (w/w) H_2O_2.

To obtain differential interference contrast (DIC) images of DAB polymerisation, a Leica DM IRBE inverted epifluorescence microscope (Leica Microsystems) was used. An initial picture was taken prior to DAB labelling. The 0.1 M cacodylate washing buffer was removed and replaced with the 1 mL of 1X DAB 10 mM H_2O_2 solution. DAB polymerisation was observed through the eyepiece in real time, and DIC images were taken. The reaction was stopped by removing the solution and washing 5 times with 0.1 M cacodylate buffer, at 2 minutes per wash. The final wash was removed, and cells were incubated in 1% OsO_4 for 30 minutes. This solution was removed, then samples were washed with distilled water 3 times, at 1 minute per wash. Finally, samples were incubated overnight in a filtered solution of 2% uranyl acetate in distilled water at 4ºC.

The next day, samples were dehydrated by sequential 3-minute incubations of 20%, 50%, 70%, 90%, 100%, 100% ice cold ethanol, followed by a final 3-minute wash of 100% ethanol at room temperature. The final ethanol wash was removed and EPON resin (TAAB, T031) was poured onto the samples, then samples were left rocking for 3 hours. The resin was discarded, then fresh EPON resin was poured onto samples. The samples were incubated at 60ºC overnight to set the resin. A small volume of fresh EPON was poured into the middle of the sample, then used to adhere an EPON stub. The sample was returned to 60ºC for a further 24 hours. The coverslip was removed from the resin by sequential plunging into liquid nitrogen and boiling water. The embedded resin was cut into < 100 nm slices for transmission electron microscopy using a Leica UC6 + FCS cryo ultra microtome (Leica Microsystems). Samples were imaged on a FEI Tecnai 12 120 kV BioTwin Spirit transmission electron microscope (FEI Company).

2.5.5 Image Analysis

Colocalisation and fluorescence intensity analysis was performed using Volocity 6.3 software (PerkinElmer) with automatic Costes background thresholding (Costes et al., 2004). Immunofluorescence images were prepared in Volocity 6.3. Lysosomal positioning quantification was performed in ImageJ as described in (Starling et al., 2016). Electron microscopy figures were prepared in ImageJ.

2.6 Proteomics and RNA-Sequencing (RNA-Seq)

All processing and quantification of proteomics samples were performed by Dr Kate Heesom and Dr Mariangela Wilson, and Dr Phil Lewis performed statistical analysis of raw proteomics data in the Proteomics Facility, Faculty of Life Sciences at the University of Bristol. Proteomics and RNA-Seq data are presented as tables in **Appendix A**.

2.6.1 Stable Isotope Labelling of Amino Acids in Culture (SILAC)-Based Proteomics

HeLa cells were cultured for at least 6 doublings in three different isotopically labelled media compositions: R_0K_0 (light), R_6K_4 (medium), $R_{10}K_8$ (heavy) **(Chapter 2.1.7)**. The prolonged culture of cells in these media compositions results in the differential labelling of proteins with the respective arginine and lysine isotopes.

After performing the biotinylation protocol and streptavidin affinity purification outlined in **Chapter 2.4.3**, the streptavidin beads corresponding to different SILAC conditions were pooled together prior to washing steps. Biotinylated proteins were eluted in a volume of 40 µL 3X NuPAGE sample buffer supplemented with 2.5% β-mercaptoethanol, 2 mM free biotin and 20 mM DTT. The eluate was loaded onto a gel, and proteins were resolved by SDS-PAGE, then visualised by staining with SimplyBlue SafeStain (Thermo Fisher, LC6060). The gel was cut into 10 individual slices, which were digested with trypsin prior to nano-liquid chromatography with tandem mass spectrometry (LC-MS/MS). Peptides were fractionated by LC using an UltiMate 3000 RSLCnano system (Thermo Fisher, ULTIM3000RSLCNANO) and ionised and quantified with an Orbitrap Fusion Lumos Tribrid Mass Spectrometer (Thermo Fisher, IQLAAEGAAPFADBMBHQ). Parameters for quantifying mass spectrometry data were adjusted to include a maximum missed cleavage range of 4 cleavages, and include variable peptide modifications of oxidation, acetylation and biotinylation by biotin-phenol (which adds a $C_{18}H_{23}N_3O_3S$ adduct to peptides).

2.6.2 Tandem Mass Tagging (TMT)-Based Proteomics

To prepare TMT samples for whole cell lysate analysis of H4 cells, cells were grown to confluency in a 10 cm plate, then lysed with TX-100 lysis buffer and quantified with a BCA assay. The concentrations and volumes were normalised to a 200 µL volume of 2 mg/mL protein for each sample. To prepare samples for growth media 'secretome' analysis, H4 cells were grown in a 6-well plate in DMEM media without FBS for 16 hours. The medium was removed, and centrifuged at 300 x g for 10 minutes at 4°C, then the supernatant was transferred to a fresh microcentrifuge tube and centrifuged at 2,000 x g for a further 10 minutes 4°C and cells were lysed and quantified with a BCA assay as described in **Chapter 2.4.4**. The media volumes were normalised based on BCA assay quantification.

Samples were digested in trypsin then labelled with the TMT10plex isobaric reagent set (Thermo Fisher, 90110). Samples were subjected to high pH reversed-phase chromatography with an Ultimate 3000 liquid chromatography system (Thermo Fisher), then the resulting fractions were analysed by nano-LC-MS/MS.

2.6.3 RNA-Seq

For RNA-Seq analysis, H4 samples were grown and RNA was extracted and quantified as described in **Chapter 2.2.9**. Concentrations of all samples were normalised to 50 ng/µL and shipped to collaborators at the Telethon Institute of Genetics and Medicine, Naples, Italy, in dry ice. RNA-seq analysis quantified 33,694 gene transcripts, and the differential gene expression between experimental samples was quantified by staff at the Telethon Institute of Genetics and Medicine.

2.6.4 Statistical Analysis of Proteomics and RNA-Seq Data

Raw files from mass spectrometry were quantified using Proteome Discoverer software v2.1 (Thermo Fisher). Peptides were searched against the UniProt human proteome database using the SEQUEST algorithm. For statistical analysis of differential protein abundance between conditions, standard t-tests were used. Volcano plots were plotted using either the VolcaNoseR webapp (Goedhart and Luijsterburg, 2020), or Orange software (University of Ljubljana). Typically, thresholds of $\log_2$ fold change of ±1 (corresponding to a 2-fold enrichment or depletion), and a $-\log_{10}$ p-value of 1.3 (corresponding to 0.05) were set, although these thresholds were adjusted based on assessment of data distributions for various experiments. For generation of the HRP-TGN46-labelled proteome, described in **Chapter 4.2.4**, proteins that were only identified in the HRP-TGN46 biotinylation condition in ≥ 4 out of 5 repeats that were not identified in negative control conditions and thus could not be statistically analysed, were assumed to be significant hits

Gene ontology experiments were performed using the PANTHER classification system (Mi et al., 2019). Protein IDs for enriched or depleted proteins were compared against the total human genome. Gene ontology terms, falling under the categories of ‘Cellular Component’, ‘Biological Process’ or ‘Molecular Function’ that were significantly enriched or depleted relative to the expected number for the sample size of proteins were identified by a Fisher’s exact test with the Bonferroni correction for multiple testing by PANTHER software. The raw gene ontology output data is presented in **Appendix A**.

Gene set enrichment analysis (GSEA) of RNA-Seq data was performed using the GSEA software (UC San Diego and Broad Institute) and MSigDB database of gene sets. Specifically, the cellular compartment gene ontology gene sets (c5.go.cc.v7.2.symbols.gmt) and Kyoto Encyclopaedia of Genes and Genomes (KEGG) pathway gene sets (c2.cp.kegg.v7.2.symbols.gmt) were used for analysis (Mootha et al., 2003; Subramanian et al., 2005). Gene set networks from GSEA were visualised using Cytoscape 3.3 software with

the Enrichment Map plug-in (Merico et al., 2010). Ingenuity pathway analysis (Qiagen) was used to identify potential upstream transcription factors in the RNA-Seq dataset.

2.7 Data Analysis and Statistics

All statistical analysis was performed on data from a minimum of 3 independent experimental repeats. GraphPad Prism 9 (La Jolla, CA) software was used for statistical analysis of Western blot and confocal microscopy data. Unpaired, two-way t-tests were used for the comparison of two experimental conditions. For the statistical comparison of multiple conditions within an experiment, ordinary one-way analysis of variance (ANOVA) with Dunnett's multiple comparisons test was used when there was one experimental variant, and two-way ANOVA with Šídák's multiple comparisons test was used when there were two experimental variants. For the quantification of lysosomal positioning, a fourth order polynomial nonlinear regression curve was fit to the cumulative fluorescence intensity values for each experimental condition, and the statistical difference between these fits was measured by the extra sum of F-squares test as described in (Starling et al., 2016).

All graphs were prepared in GraphPad Prism 9, apart from graphs depicting proteomics and RNA-Seq datasets. Individual datapoints represent independent experimental repeats. Graphs are plotted representing the mean value ± the standard error of the mean (SEM) for each experimental condition. *n* represents the number of independent experimental repeats. In all graphs, * = $p \leq 0.05$, ** = $p \leq 0.01$, *** = $p \leq 0.001$, **** = $p \leq 0.0001$.

2.8 Data Deposition

Coordinates and structure factors for the NRP1 b1 - S1 CendR peptide complex **(Chapter 6.2.3)** have been deposited at the Protein Data Bank (PDB) with accession code 7JJC.

2.9 Additional Methods Used by Collaborators

In **Chapter 6**, data from a collaborative publication are presented. For experimental methods that were not performed by myself, such as live SARS-CoV-2 culturing, sequencing and infection experiments, and biochemical methods directly testing the NRP1-S1 interaction, such as isothermal titration calorimetry and X-ray crystal structure determination, please refer to the supplementary materials for (Daly et al., 2020).

Chapter 3: Investigating the Role of Retromer in Regulating Lysosomal Homeostasis

3.1 Introduction

3.1.1 Retromer as an Endosomal Cargo Sorting Complex

Since its discovery in yeast as a heteropentameric complex responsible for the retrograde recycling of the Vps10p receptor, accumulating evidence has implicated retromer as a regulator of endosomal cargo sorting **(Chapters 1.3.2-1.3.4)** (Seaman, 2021). While originally reported to bind and mediate the retrograde trafficking of Vps10p-like receptors, such as CI-MPR, Sortilin and SorLA, the role of retromer in endosomal recycling has greatly expanded to include a repertoire of hundreds of cargoes (Seaman, 2007; Steinberg et al., 2013). In most cases, sorting nexins such as such as SNX3, SNX27 and ESCPE-1 appear to mediate cargo selectivity, either co-operatively with or independently from retromer. Retromer may potentially play different roles in endocytic recycling, switching from a cargo adaptor to a master regulator of sorting as endosomes mature. Retromer appears to predominantly direct trafficking to the plasma membrane and TGN from early endosomal compartments in conjunction with the PI(3)P-sensing adaptors SNX27 and SNX3, respectively. On late endosomes, retromer recruitment depends on a dynamic interplay with Rab7 and in this scenario retromer may act as a spatiotemporal regulator of later endocytic trafficking events (Cullen and Steinberg, 2018).

An initial sorting signal for retromer was reported to be Øx[L/M/V], with examples including the ^{2369}WLM^{2371} motif of CI-MPR, the ^{787}FLV^{789} motif of Sortilin, and the ^{555}YLL^{557} motif of DMT1-II (Seaman et al., 2007; Tabuchi et al., 2010). However, in a surface uptake assay, CI-MPR was reported to retrogradely traffic to the TGN at an enhanced rate in the absence of retromer (Kvainickas et al., 2017; Simonetti et al., 2017). Taking this into account, an emerging hypothesis is that retromer may sense cargo occupancy on the late endosomal membrane through transient, low affinity interactions, such as recognition of the Øx[L/M/V]motif in cargo tails (Cullen and Steinberg, 2018). This low affinity sensing may be sufficient to enrich cargos within the recycling subdomain of the endosome, where lateral diffusion becomes impaired by additional factors such as branched, filamentous actin polymerised by the WASH complex **(Chapter 1.3.9)**. Once enriched within this subdomain, cargo can be 'handed over' to more specific machinery, such as ESCPE-1, for sequence-dependent recycling. Retromer may utilise this cargo sensing as a 'checkpoint' to regulate endosome-lysosome fusion once cargo recycling is complete (Cullen and Steinberg, 2018).

3.1.2 The Emerging Role of Retromer as a Master Regulator of Endolysosomal Biology

In addition to sensing the presence of cargo proteins on the endosomal membrane and coordinating downstream endocytic recycling events, retromer may also play a broader role in regulating the properties of late endosomes and lysosomes. Rab7a-GTP interacts with retromer to facilitate recruitment to the late endosomal membrane (Rojas et al., 2008; Seaman et al., 2009). Retromer in turn influences the nucleotide cycling of Rab7a through the recruitment of the Rab7 GAP protein TBC1D5 by the VPS29 subunit (Jia et al., 2016; Seaman et al., 2009). Therefore, following its Rab7a-dependent recruitment, retromer accumulates on the late endosomal membrane then acts as a sensor that feeds back to coordinate Rab7a GTP hydrolysis at the appropriate timing, similarly to the 'cut-out switch' model of Rab5/Rab7 conversion during endosomal maturation **(Chapter 1.2.4)** (Del Conte-Zerial et al., 2008). This spatiotemporal regulation of Rab7a activity appears to be important in constricting active Rab7a-GTP to a distinct microdomain on the late endosomal membrane (Kvainickas et al., 2019).

Insights into the significance of this regulatory role for retromer can be provided by investigating the phenotypic consequences of retromer depletion. Upon retromer depletion, Rab7a becomes hyperactivated in a GTP-locked state, and accordingly the entire cellular pool of Rab7a is recruited to endosomal and lysosomal compartments (Jimenez-Orgaz et al., 2017). Moreover, this phenomenon is dependent upon TBC1D5, as rescue of VPS29 KO cells with a point mutant unable to engage TBC1D5 phenocopied Rab7a hyperactivation (Jimenez-Orgaz et al., 2017). In agreement with this study, *Vps29* homozygous-null *Drosophila* flies demonstrate impaired endolysosomal morphology and synaptic activity, a phenotype which can be rescued by TBC1D5 overexpression (Ye et al., 2020). Retromer-dependent Rab7a nucleotide cycling was found to be crucial for the turnover of damaged mitochondria through mitophagy (Jimenez-Orgaz et al., 2017). Furthermore, the expansion of Rab7a-GTP from a controlled microdomain to encompass the entire late endosomal network appears to perturb the recruitment of the amino-acid sensing ragulator and mTORC1 complex machinery (Kvainickas et al., 2019). Lysosomes in VPS35 KO HeLa cells display an impaired degradative capacity, which may in part arise from these defects in Rab7a dynamics (Y. Cui et al., 2019).

In addition to influencing endosomal dynamics through tuning Rab7a signalling output, retromer itself can be transcriptionally regulated in response to lysosomal signalling (Curnock et al., 2019). In nutrient-replete conditions the mTORC1 complex phosphorylates transcription factor EB (TFEB) (Settembre et al., 2012). In this state, TFEB is constrained within the cytosol by 14-3-3 proteins that bind its phosphorylated S211 residue (Martina et al., 2012). Under

starvation conditions this spatial control is lost, and TFEB translocates to the nucleus, where it regulates lysosomal biogenesis (Sardiello et al., 2009; Settembre et al., 2012). Through this mechanism, TFEB increases the catabolic capacity of the cell to meet energy demands when exogenous nutrient supply is low (Sardiello et al., 2009). Additionally, mTORC1-independent mechanisms of TFEB regulation have been proposed, such as signalling via protein kinase C (Li et al., 2016). Specifically, TFEB recognises palindromic promoter sequences in its target genes, termed Coordinated Lysosomal Expression and Regulation (CLEAR) elements (Sardiello et al., 2009). Recently it was found that the retromer subunit genes *VPS26A* and *VPS35* contained putative CLEAR elements, and these were up-regulated in response to TFEB overactivation or nutrient starvation (Curnock et al., 2019). In turn, retromer mediates the endocytic recycling of various nutrient transporters to the cell surface to increase nutrient availability (Curnock et al., 2019). Together, these recent data implicate retromer as a highly dynamic complex that is both regulated by and a coordinator of intricate signalling events within the endolysosomal network.

3.1.3 Retromer and Neurodegenerative Disease

The retromer complex has been associated with neurodegeneration since observations of its deficiency in Alzheimer's disease, followed by the discovery of familial Parkinson's disease mutations affecting the complex (Muhammad et al., 2008; Small et al., 2005; Vilariño-Güell et al., 2011; Wen et al., 2011; Zimprich et al., 2011). VPS35 depletion is embryonic lethal in mice, indicating its widespread importance in development (Wen et al., 2011). As such, the familial mutations observed in Parkinson's disease appear to be subtle perturbations to retromer activity, rather than complete loss-of-functions (McGough et al., 2014; McMillan et al., 2016). It may be that retromer function and endolysosomal homeostasis in general is particularly important in neurons, which have exceptionally long lifespans and energy demands, to sustain the balance between protein recycling and turnover, hence why retromer mutation or decreased expression manifests as neurodegenerative phenotypes. Retromer depletion or dysfunction has been associated with increased seeding of pathogenic aggregates such as α-synuclein, amyloid-β (Aβ) and Tau (Bi et al., 2013; Carosi et al., 2020; Simoes et al., 2020; Sullivan et al., 2011; Tang et al., 2015).

Due to the multiple lines of evidence linking retromer perturbation to neurodegeneration, the complex is now considered to be neuroprotective, and a potential therapeutic target (McMillan et al., 2017). Small molecule chaperones that stabilise the retromer complex appear to increase protein levels of the complex, and enhanced APP trafficking to reduce amyloidogenic processing (Mecozzi et al., 2014). More recently, a retromer-stabilising compound attenuated amyotrophic lateral sclerosis pathology in mouse models (Muzio et al., 2020). Enhancing

retromer function to protect against neurodegeneration is therefore likely to be an exciting and rapidly developing therapeutic avenue in the future.

3.1.4 Aim

Given the clear association of retromer with endolysosomal dysfunction and neurodegenerative disease phenotypes, in this chapter I aim to translate some of the recent insights into retromer function to a neuroglioma cell culture model. Through the use of quantitative proteomics and RNA sequencing, I will attempt to attain a global, integrated overview of the role of retromer in regulating lysosomal homeostasis, and the cellular consequences of its absence.

3.2 Results

3.2.1 Investigating Endosomal Recycling in a H4 Neuroglioma Cell Line Model

An increasing wealth of evidence implicates retromer and endolysosomal homeostasis as neuroprotective (McMillan et al., 2017). To validate recent insights into retromer and ESCPE-1 function in a cell culture model that is more relevant to neurodegeneration, I began to use H4 neuroglioma cells to study retromer function. H4 cells are a glia-derived cell line that represent a compromise between utilising primary neurons or induced pluripotent stem cells (iPSCs) which can provide highly relevant insight into neurodegenerative phenotypes, and the ease of use of immortalised cell culture lines. H4 cells can therefore be transfected and genetically manipulated more easily than neuronal cultures, and have been used to study various aspects of neurodegeneration including α-synuclein and Aβ aggregation and trafficking (Danzer et al., 2012; Edgar et al., 2015; Klucken et al., 2012).

To validate the recently described role of ESCPE-1 in retrograde CI-MPR sorting in this cell line, H4 cells were transfected with CRISPR-Cas9 gRNAs targeting *VPS35* and dual guides targeting both of the cargo-selective ESCPE-1 subunits *SNX5* and *SNX6* (*SNX5+6*). In wild-type cells, CI-MPR localises both to the TGN and endosomal compartments, where it shuttles M6P-tagged proteins into the endolysosomal network (Mullins and Bonifacino, 2001). As recently demonstrated in HeLa cells, SNX5+6 suppression induced a dispersal of CI-MPR signal from the TGN **(Figures 3.1A and 3.1B)**. When the core retromer subunit VPS35 was suppressed, CI-MPR displayed a dramatic increase in signal intensity, though its partial colocalisation with Golgin-97 appeared unperturbed **(Figures 3.1A-C)**. To investigate this striking phenotype in further detail, VPS35 KO H4 cells were co-stained for the TGN marker Golgin-97, the early endosomal marker EEA1 and the lysosomal marker LAMP1. CI-MPR

retained its bipartite distribution between Golgin-97 and EEA1-positive compartments in VPS35 KO cells, indicating that its retrograde trafficking is unperturbed **(Figure 3.1D)**. LAMP1 labelling revealed a dramatic redistribution of LAMP1-positive compartments from the perinuclear region to the cell periphery in VPS35 KO cells **(Figure 3.1D)**.

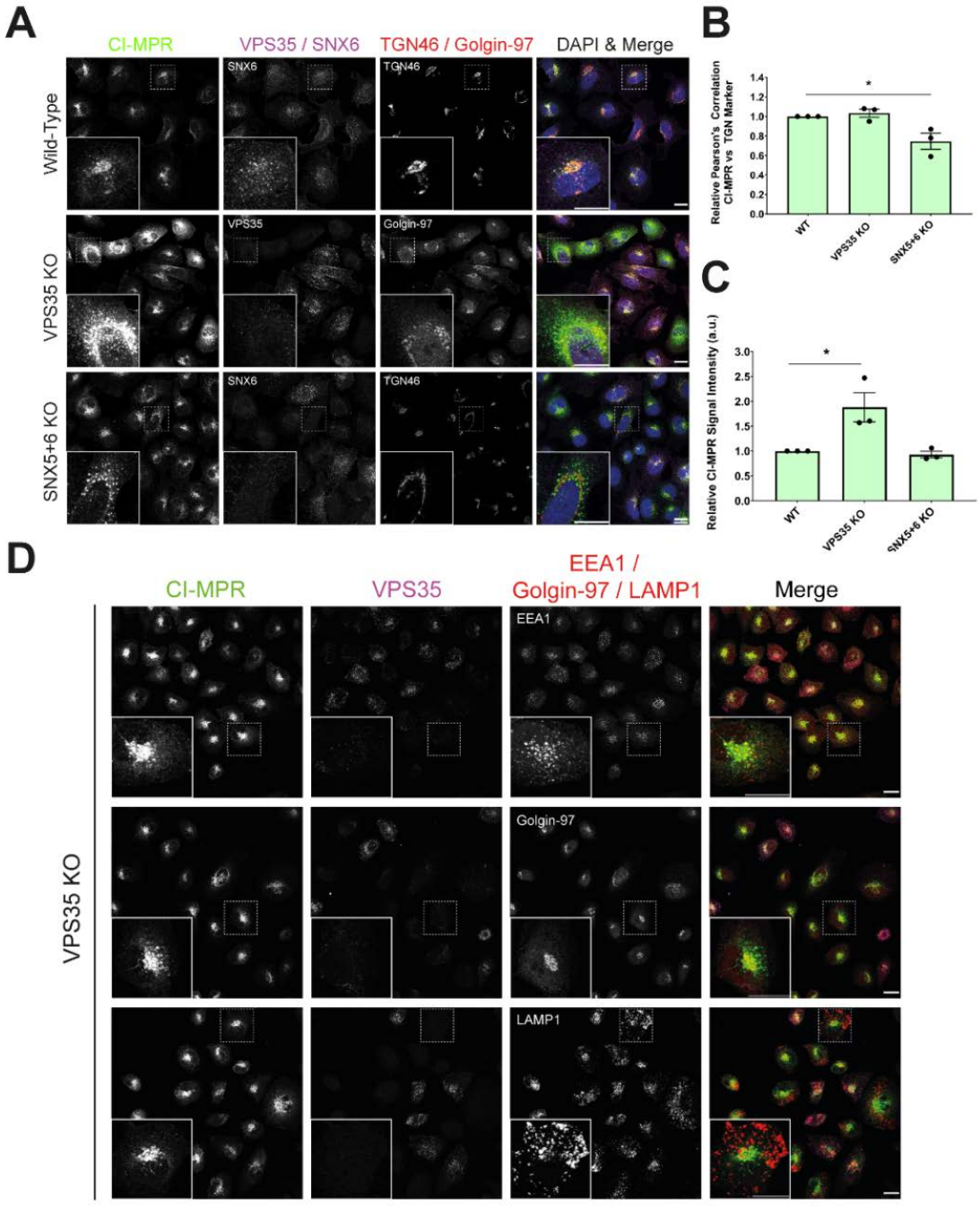

Figure 3.1 Retromer Suppression Induces a Dramatic Increase in CI-MPR Intensity and Redistributes LAMP1.

(A) Confocal microscopy of CI-MPR colocalisation with TGN markers. H4 cells were transiently transfected with CRISPR gRNAs targeting *VPS35* or *SNX5+6*. KO cells were selected with puromycin and validated by VPS35/SNX6 staining. Scale bar = 20 µm, insets 5 µm. **(B)** Quantification of relative CI-MPR vs TGN marker colocalisation between VPS35 KO/SNX5+6 KO cells and wild-type (WT) H4 cells. n = 3, 67 WT cells (with Golgin-97), 62 VPS35 KO cells (with Golgin-97), 47 WT cells (with TGN46), 51 SNX5+6 KO cells (with TGN46). Ordinary one-way ANOVA with Dunnett's

multiple comparisons test, WT vs VPS35 KO p = 0.8716, WT vs SNX5+6 KO p = 0.0270. **(C)** Quantification of CI-MPR signal intensity in WT, VPS35 KO and SNX5+6 KO H4 cells. n = 3, 38 WT cells, 38 VPS35 KO cells, 38 SNX5+6 KO cells. Ordinary one-way ANOVA with Dunnett's multiple comparisons test, WT vs VPS35 KO p = 0.0206, WT vs SNX5+6 KO p = 0.9433. **(D)** Confocal microscopy of CI-MPR staining and early endosome, TGN and lysosomal markers in VPS35 KO H4 cells. Scale bar = 20 µm, insets 5 µm.

3.2.2 Generation of VPS35 KO and SNX5+6 Double KO Clonal H4 Cell Lines

To investigate these phenotypes in more detail, VPS35 and SNX5+6 KO clonal H4 cell lines were generated. Successful knockout lines were validated by the absence of either VPS35 or SNX5 and SNX6 signal observed by Western blotting. VPS35 KO clones recapitulated the increased CI-MPR signal intensity phenotype by immunofluorescence **(Figures 3.2A and 3.2B)**. SNX5+6 double KO clonal H4 cells displayed a similar phenotype to that observed in HeLa cells, whereby CI-MPR appears more dispersed from the perinuclear region of the cell **(Figures 3.2C and 3.2D)**.

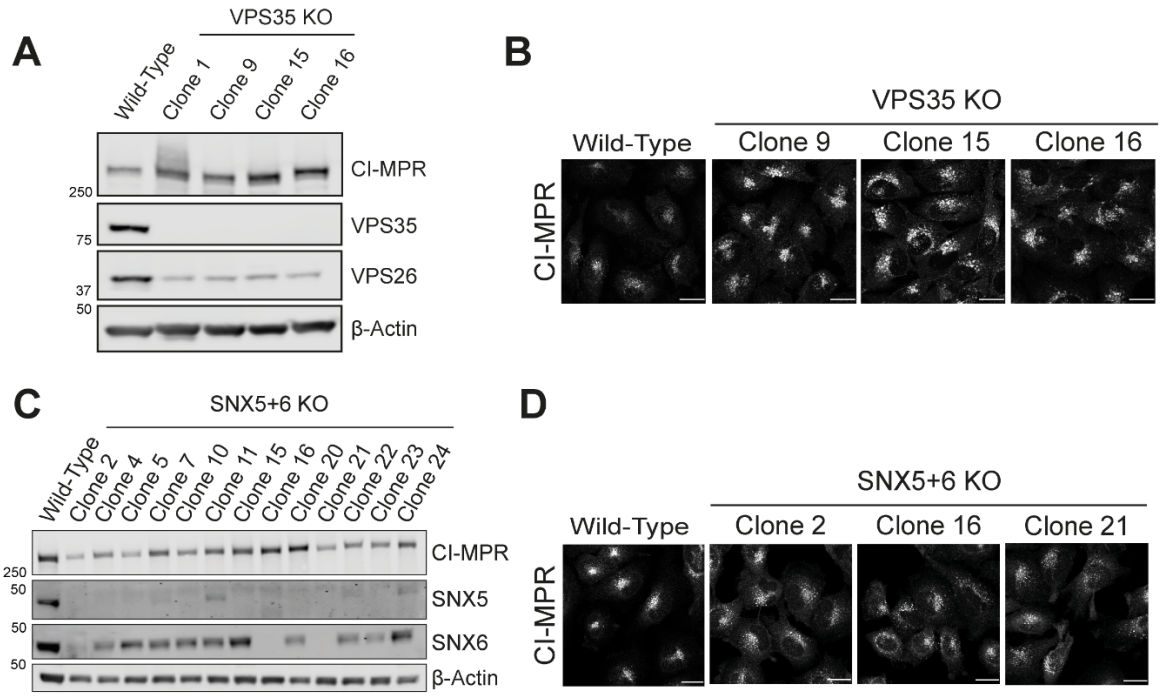

Figure 3.2 Generation of VPS35 KO and SNX5+6 KO H4 Clonal Cell Lines
(A) Western blot validation of H4 VPS35 KO clones. Knockout clones were validated by the absence of endogenous VPS35 immunolabelling. **(B)** Immunofluorescence labelling of CI-MPR in VPS35 KO clones. Scale bar = 20 µm. **(C)** Western blot validation of H4 SNX5+6 double KO clones. Knockout clones were validated by the absence of both endogenous SNX5 and SNX6 immunolabelling. **(D)** Immunofluorescence labelling of CI-MPR in SNX5+6 double KO clones. Scale bar = 20 µm.

A quantitative comparison of various endolysosomal marker proteins revealed a clear trend of increased abundance in VPS35 KO H4 cells **(Figure 3.3A)**. The acid hydrolase receptors

CI-MPR and Sortilin, and LAMP1 were markedly more abundant in VPS35 KO H4 cells relative to wild-type H4 cells **(Figures 3.3B-D)**. Moreover, SNX5+6 double KO cells did not display a significant increase in these markers, in agreement with increased CI-MPR signal intensity only being visualised in VPS35 KO cells by confocal microscopy **(Figures 3.3B-D)**. Strikingly, the lysosomal acid hydrolase protein Cathepsin D (CTSD) was notably more abundant in VPS35 KO H4 cells. CTSD is synthesised as a precursor protein that is exported into the endolysosomal network by acid hydrolase receptors (including CI-MPR), where it becomes proteolytically processed to its activated form in acidic lysosomal compartments (Laurent-Matha et al., 2006). Interestingly, in addition to its lower molecular weight, enzymatically active isoform, the precursor isoforms of pro-CTSD were also clearly more abundant in VPS35 KO H4 cells, potentially suggestive of perturbations to lysosomal homeostasis such as pH **(Figures 3.3E and 3.3F)**. Similar phenotypes of immature CTSD accumulation upon retromer suppression have also been reported in HeLa cells (Carosi et al., 2020; Y. Cui et al., 2019; Seaman, 2004).

3.2.3 Retromer Suppression Induces Dramatic Endolysosomal Defects in H4 Cells

Further microscopy analysis revealed drastic morphological defects in endosomal and lysosomal compartments in VPS35 KO H4 cells **(Figure 3.4A)**. In addition to enlarged, bright CI-MPR punctae, EEA1-positive endosomes were also clearly swollen, often with a visible luminal cross section that typically cannot be resolved in wild-type cells by standard confocal microscopy. Moreover, LAMP1 signal intensity was dramatically increased, and lysosomal compartments appeared swollen and more peripheral as previously visualised in **Figure 3.1**. These data suggest that the entire endolysosomal network, spanning from EEA1-positive early endosomes to LAMP1-positive lysosomes appears to be perturbed in H4 cells upon retromer KO. CD-MPR, believed to be a retromer-independent retrograde cargo, could also be visualised on swollen endosomal membranes **(Figure 3.4B)** (Y. Cui et al., 2019).

To further attribute this phenotype to a broad endolysosomal dysfunction, rather than a specific trafficking defect of CI-MPR, wild-type or VPS35 KO H4 cells were transfected with CRISPR-Cas9 gRNAs targeting *SNX5* and *SNX6*. As previously observed, in wild-type cells, SNX5+6 suppression caused a characteristic dispersal of CI-MPR into predominantly vesicular compartments **(Figure 3.5)**. In VPS35 KO cells, the swollen CI-MPR signal was clustered in the perinuclear region and partially colocalised with SNX6 and EEA1. Upon SNX5+6 double KO in these cells, enlarged CI-MPR-positive compartments also became more peripheral, suggesting that the two phenotypes are separate and can be additively combined **(Figure 3.5)**. These data need to be repeated in order to perform a quantitative analysis of this effect,

and I aim to characterise the morphology of these dysfunctional endolysosomal compartments at the ultrastructural level through an ongoing collaboration with Dr James Edgar (University of Cambridge, United Kingdom).

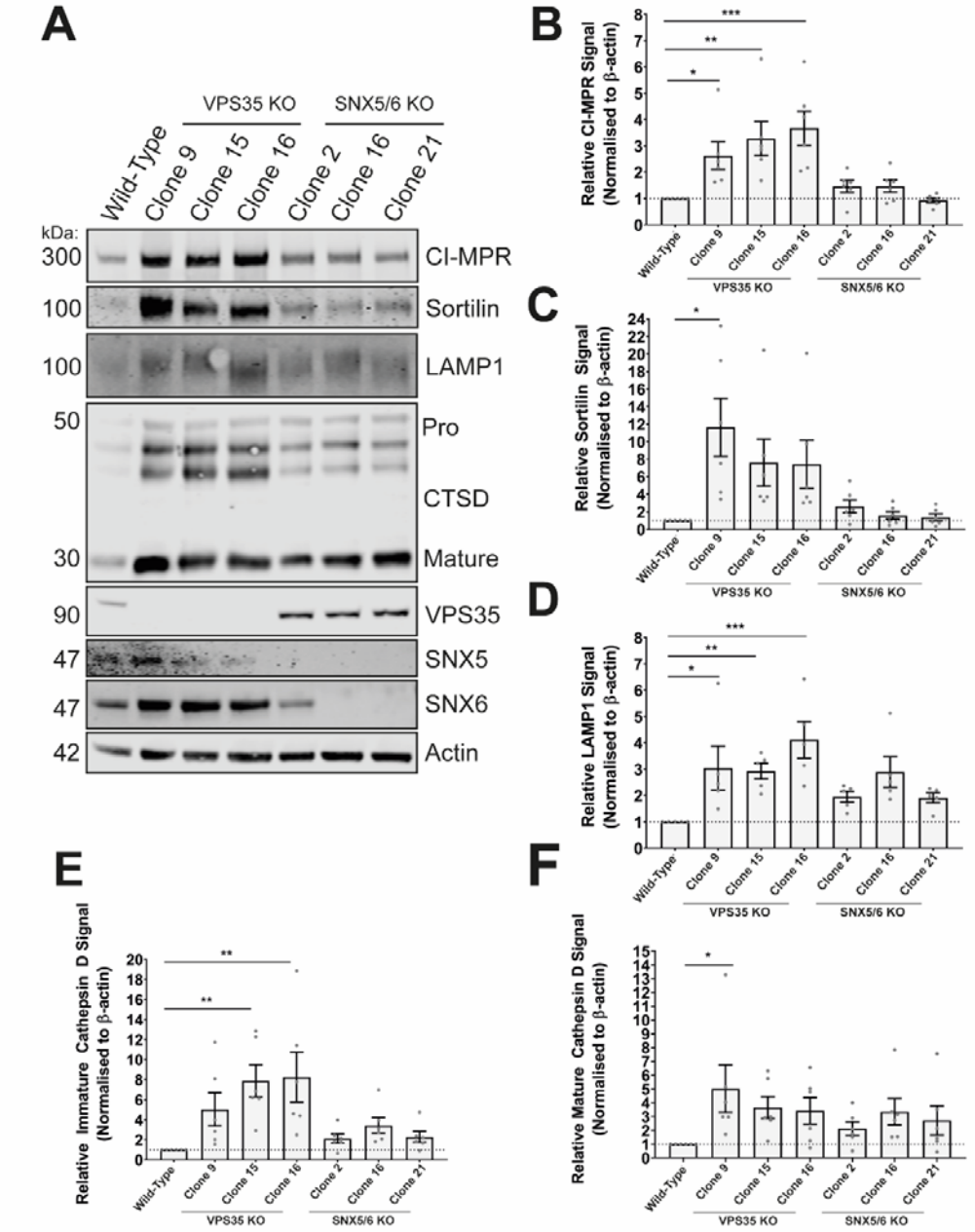

Figure 3.3 VPS35 KO H4 Display an Enrichment of Endolysosomal Proteins

(A) Representative Western blot of whole cell lysates from wild-type, VPS35 KO and SNX5+6 double KO H4 cells. **(B-F)** Quantification of total protein abundances of CI-MPR **(B)**, Sortilin **(C)**, LAMP1 **(D)**, Pro-*CTS*D **(E)** and mature *CTS*D **(F)**. n = 6 independent repeats for CI-MPR, Sortilin and CTSD quantification, and 5 independent repeats for LAMP1 quantification. Ordinary one-way ANOVA with Dunnett's multiple comparisons tests. * = $p < 0.05$, ** = $p < 0.01$, *** = $p < 0.001$

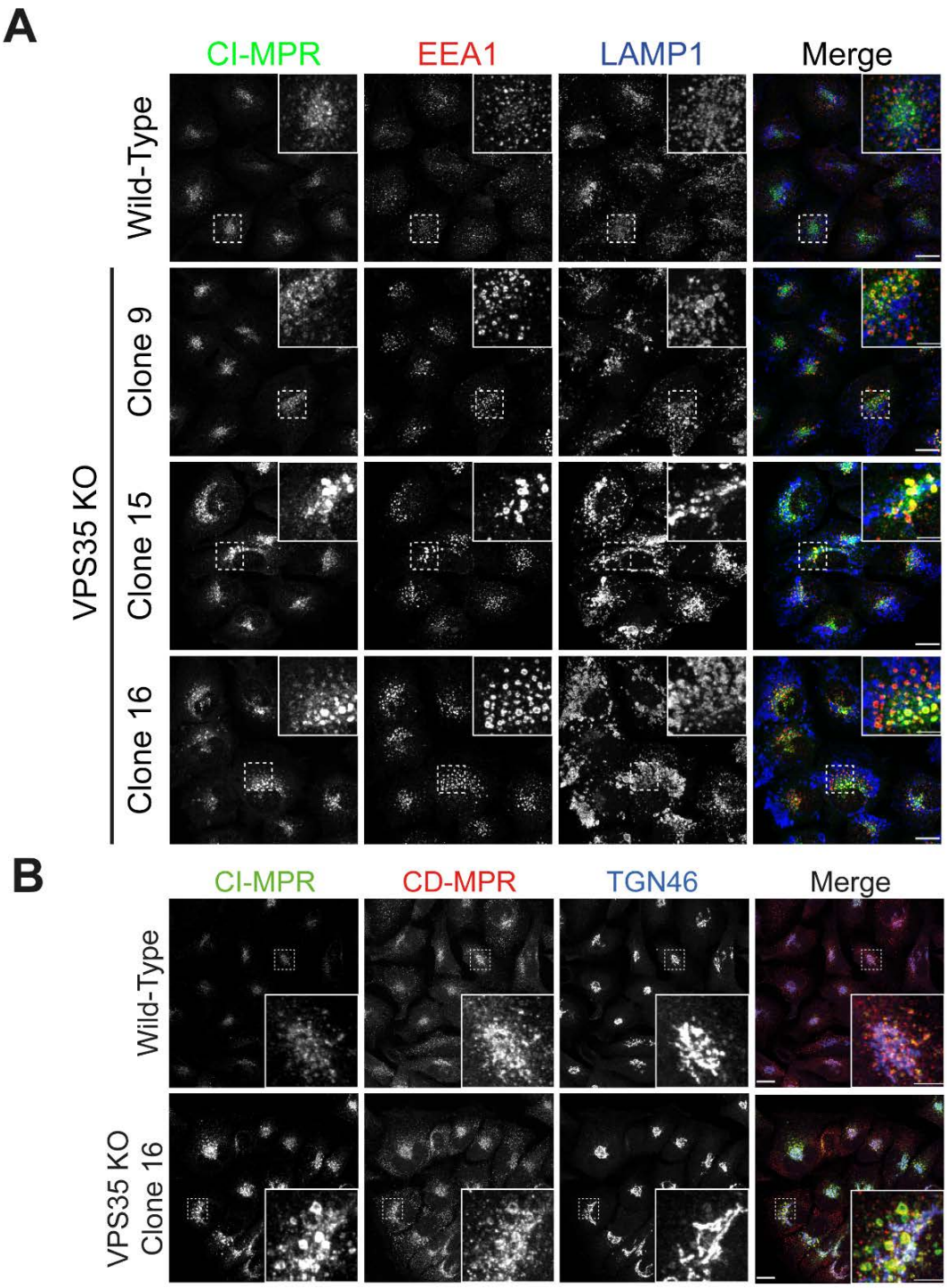

Figure 3.4 VPS35 KO H4 Cells Display Altered Endolysosomal Morphology

(A) Immunofluorescence staining of CI-MPR, EEA1 and LAMP1 in wild-type and VPS35 KO H4 cells. Scale bar = 20 µm, insets = 5 µm. **(B)** Immunofluorescence labelling of CI-MPR and CD-MPR in wild-type and VPS35 KO clone 16 H4 cells. Scale bar = 20 µm, insets = 5 µm.

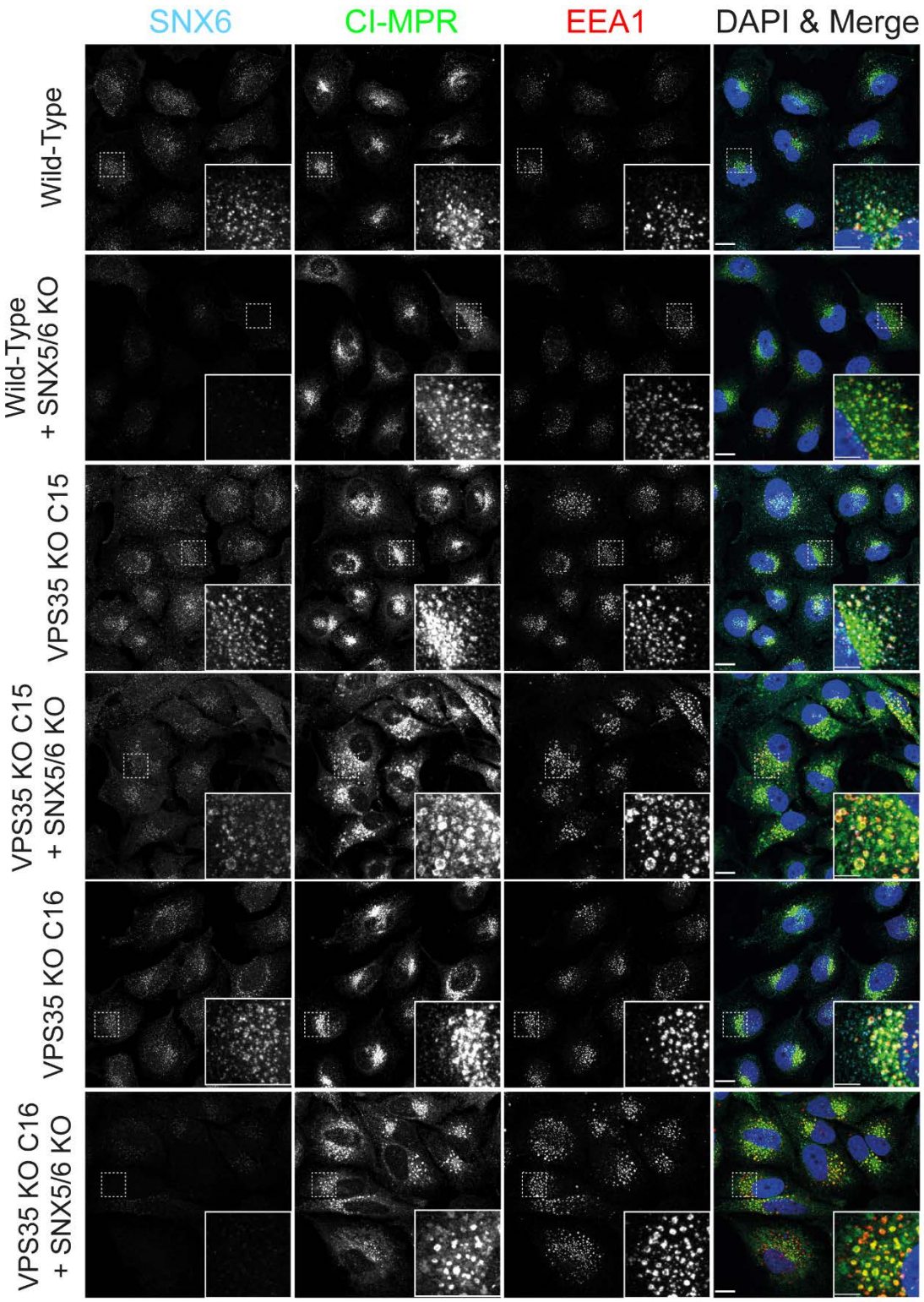

Figure 3.5 Simultaneous Depletion of both VPS35 and SNX5+6 Displays Additive Effects on CI-MPR Trafficking

Wild-type, VPS35 KO clone 15 and VPS35 KO clone 16, either untreated or transfected with SNX5- and SNX6-targeting CRISPR-Cas9 gRNAs were labelled with antibodies targeting SNX6, CI-MPR and EEA1. SNX5+6 KO cells were validated by a reduction in SNX6 labelling. Scale bar = 20 µm, insets 5 µm

The VPS35 KO H4 cell lines established in this chapter have been subjected to a 'knocksideways' approach of retromer inactivation **(See Appendix B)** (Evans et al., 2020). VPS35 KO cells were stably rescued with a VPS35-GFP-FRB construct that localises to endosomes and dimerises with a peroxisomal 'hook' protein containing FKBP upon the addition of the small molecule rapalog (Robinson and Hirst, 2013). The high affinity FRB-rapalog-FKBP interaction functionally inactivates the retromer complex by removing it from the endosomal membrane and redistributing it to peroxisomes where it cannot engage its effector proteins (Evans et al., 2020). This approach can temporally resolve endosomal trafficking defects, such as the increasing missorting of the glucose transporter type 1 (GLUT1) after 1 hour of retromer inactivation. Acute retromer inactivation did not, however, induce a CI-MPR trafficking defect, nor did it appear to induce the striking increase in signal intensity seen by longer timepoints of suppression (Evans et al., 2020). Taken together, these results suggest that the endolysosomal defects characterised by CI-MPR and LAMP1 labelling in H4 cells result from a more chronic perturbation to endolysosomal health, rather than an acute trafficking defect.

3.2.4 VPS35-GFP Expression Rescues Endolysosomal Morphology

To directly implicate the loss of retromer function as the cause for endolysosomal dysfunction, a VPS35-GFP rescue construct was stably transduced into the VPS35 KO clones **(Figures 3.6A and 3.6B)**. Re-expression of VPS35-GFP rescued the increase in CI-MPR and LAMP1 signal intensity in VPS35 KO clone 16 **(Figures 3.6C-E),** and CI-MPR was successfully resolved from swollen compartments back to a more punctate staining pattern reminiscent of wild-type cell morphology. Furthermore, lysosomal positioning returned from the cell periphery to the perinuclear region in rescue cells. To quantify lysosomal distribution, an image analysis protocol was used that compartmentalises cells into segments, concentrically expanding by 10% increments from the cell centre to the periphery **(Figure 3.6F)**. By quantifying the cumulative LAMP1 signal from the centre to the periphery, a curve of lysosomal positioning can be fitted by nonlinear regression (Starling et al., 2016). From a wild-type baseline, shifting of the curve to the left or right indicates more perinuclear or peripheral lysosomal positioning, respectively. VPS35 KO induced a large shift towards a more peripheral distribution, which was significantly different to both wild-type and VPS35-GFP rescue cells **(Figure 3.6G)**. VPS35-GFP distribution was closer to the wild-type distribution but still significantly different indicating partial, but not complete, rescue of lysosome positioning **(Figure 3.6G)**.

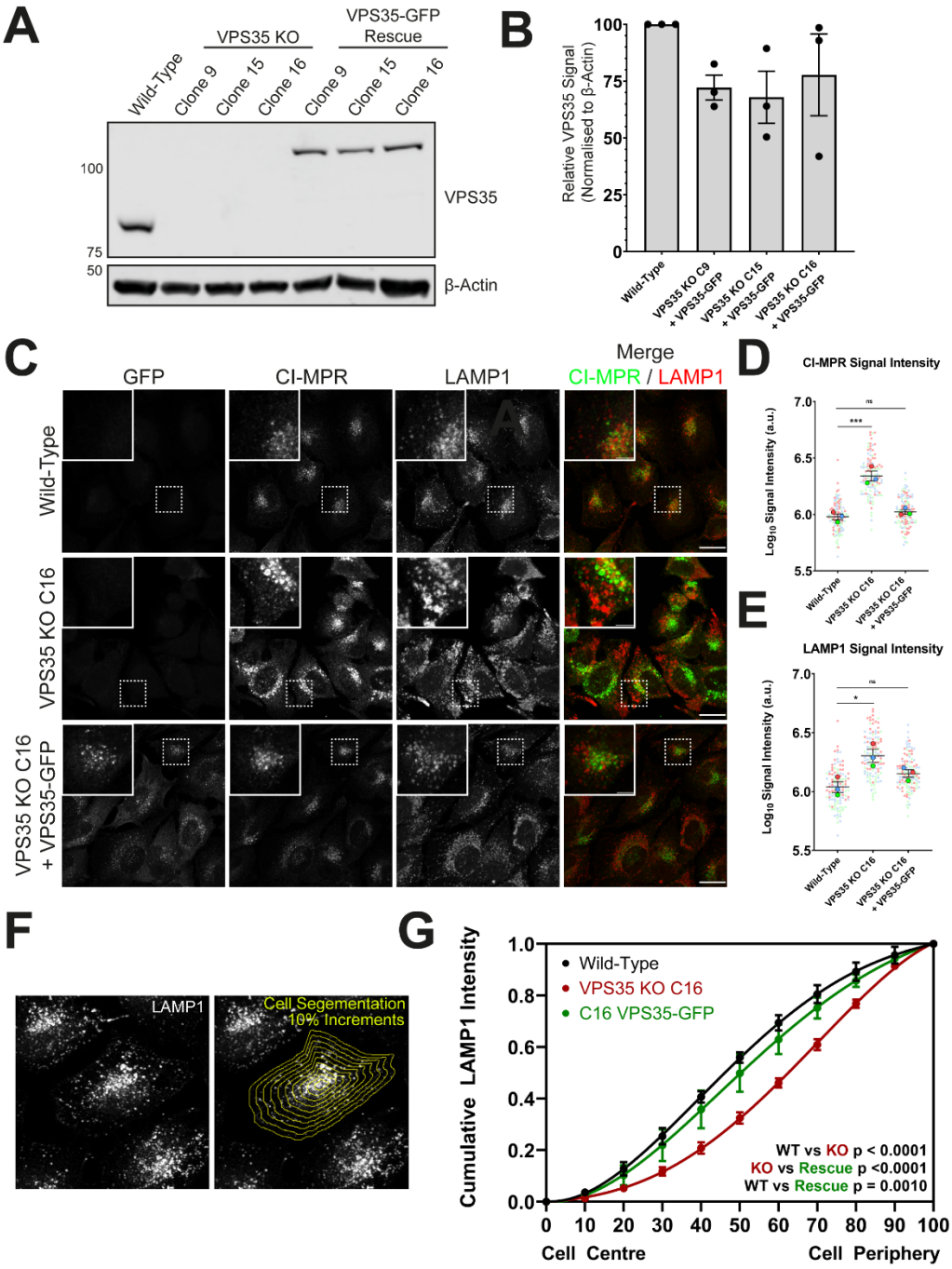

Figure 3.6 VPS35-GFP Re-Expression Rescues Endolysosomal Defects in VPS35 KO H4 Cells.

(A) Western blot validation of VPS35-GFP expression in VPS35 KO H4 cells. The presence of the VPS35-GFP construct is indicated by increased molecular weight of VPS35, corresponding to GFP. **(B)** Quantification of VPS35-GFP protein levels relative to endogenous VPS35 in wild-type H4 cells. n = 3 independent repeats, mean + SEM, one-way ANOVA with Dunnett's multiple comparison's test, p = 0.2471 (Clone 9 rescue), p = 0.1679 (Clone 15 rescue), p = 0.3977 (Clone rescue). **(C)** Immunofluorescence staining of CI-MPR and LAMP1 in wild-type, VPS35 KO clone 16, and clone 16 VPS35-GFP rescue H4 cells. Scale = 20 µm, insets = 5 µm. **(D)** Superplot of Log_{10} CI-MPR signal intensity. n = 3 independent repeats, 117 cells quantified per condition, mean + SEM, one-way ANOVA with Dunnett's multiple comparison test performed on experiment mean values, wild-type vs VPS35 KO clone 16 p = 0.0004, wild-type vs clone 16 VPS35-GFP rescue p = 0.5658. **(E)** Superplot of Log_{10} LAMP1 signal intensity. n = 3 independent repeats, 117 cells quantified per condition, mean

+ SEM, one-way ANOVA with Dunnett's multiple comparison test performed on experiment mean values, wild-type vs VPS35 KO clone 16 p = 0.0104, wild-type vs clone 16 VPS35-GFP rescue p = 0.2037. **(F)** Representative images of cell segmentation to determine lysosomal positioning. **(G)** Quantification of cumulative LAMP1 signal intensity, relative to the total cell LAMP1 signal intensity. n = 3 independent repeats, 39 cells quantified per condition, mean + SEM. Curves were fit by a fourth order polynomial nonlinear regression. p-values are shown on the graph, and is determined by the extra sum of F-squares test following nonlinear regression.

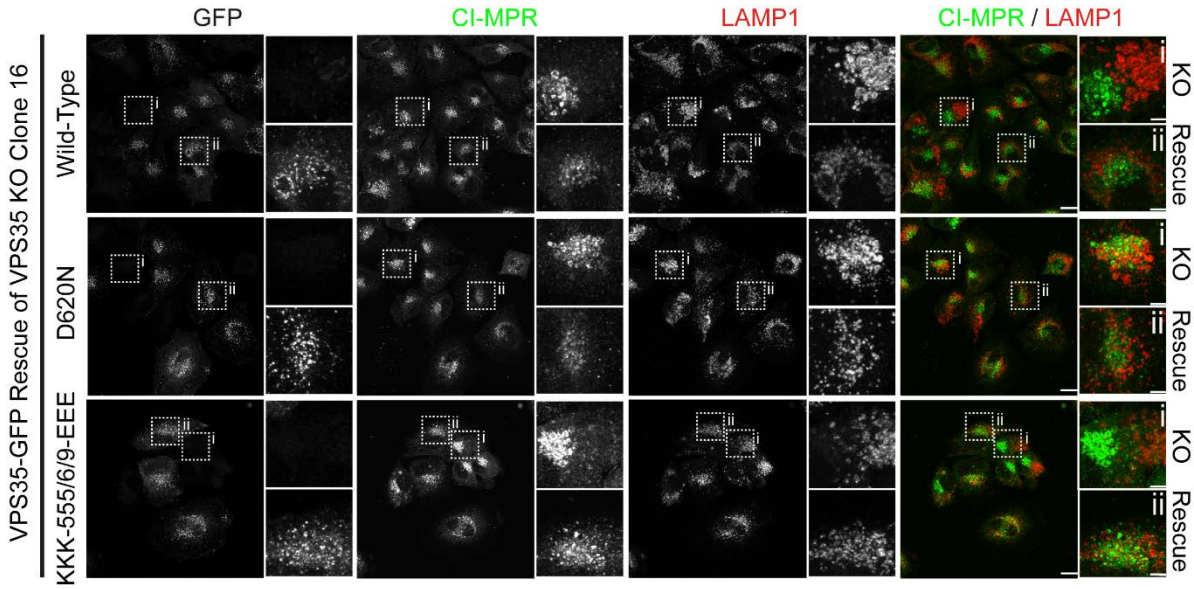

Figure 3.7 VPS35-GFP Mutants with Impaired WASH Binding Appear to Rescue CI-MPR and LAMP1 Compartment Morphology.

VPS35 KO Clone 16 H4 cells were transiently transfected with wild-type, D620N mutant, or KKK-555/6/9-EEE mutant VPS35-GFP constructs. CI-MPR and LAMP1 were labelled by immunofluorescence. Insets represent untransfected knockout cells (i) and GFP-positive rescue cells (ii). Data representative of one experiment. Scale bar = 20 µm, insets = 5 µm.

Finally, to investigate whether the lysosomal positioning phenotype was reflective of perturbed endosomal recycling, VPS35 KO cells were rescued with VPS35-GFP constructs corresponding to either the wild-type VPS35 sequence, the D620N mutant associated with autosomal dominant Parkinson's disease that perturbs binding to the WASH complex, and a newly characterised charge-swapping mutant that completely abolishes affinity for the WASH complex (KKK-555/6/9-EEE) (Jellett, 2018; McGough et al., 2014). Retromer recruitment of the WASH complex to endosomal membranes influences myriad aspects of endosomal cargo sorting, including the sensing of cargo density, association with additional endosomal machineries such as the CCC complex, and coordinating localised actin polymerisation to spatially localise and enrich cargo into forming recycling carriers (Cullen and Steinberg, 2018). Despite their impaired ability to interact with the WASH complex, these mutant VPS35 constructs appeared to rescue LAMP1 positioning from the cell periphery to the perinuclear

region, and also rescue the CI-MPR signal intensity phenotype **(Figure 3.7)**. Further repeats and quantification of this experiment are required, but these preliminary data suggest that endolysosomal dysfunction in VPS35 KO H4 cells might be independent from its capacity as an endosomal recycling complex via WASH association, but rather rely on its spatiotemporal regulation of Rab7a nucleotide cycling (Kvainickas et al., 2019).

3.2.5 Quantitative Proteomics Reveals an Enriched Cohort of Intracellular and Extracellular Proteins in VPS35 KO H4 Cells

The data presented thus far have indicated a role for retromer in regulating lysosomal homeostasis, however I have only focused on a relatively small selection of marker proteins by confocal microscopy and Western blotting. To obtain a broader, global view of the total cellular proteome in response to retromer depletion, a quantitative mass spectrometry experiment was designed whereby the whole cell lysates of wild-type, VPS35 KO or VPS35-GFP rescue cells were labelled by tandem mass tagging (TMT) and analysed by quantitative mass spectrometry **(Figure 3.8A, Chapter 2.6.2)**. Furthermore, due to the peripheral positioning of lysosomes, I investigated whether lysosomal contents were more abundantly released into the cell culture medium in VPS35 KO cells, possibly through mechanisms of lysosomal exocytosis. Lysosomal exocytosis is increasingly considered to be a compensatory mechanism for lysosomal stress and may mediate cell-to-cell transfer of pathogenic aggregates such as α-synuclein and amyloid precursor protein (APP) fragments (Alvarez-Erviti et al., 2011; Ballabio and Bonifacino, 2020; Medina et al., 2011; Miranda et al., 2018). To obtain a cell culture 'secretome', the media of wild-type, VPS35 KO and VPS35-GFP rescue cells were harvested, centrifuged to pellet large cellular debris, and quantified by TMT mass spectrometry **(Figure 3.8A)**.

To ensure that proteomic hits were specific to the loss of retromer, the abundances of proteins in VPS35 KO H4 cells relative to VPS35-GFP rescue cells were analysed. In the whole cell lysate, 110 proteins were significantly enriched in VPS35 KO cells (log_2 fold change > 0.26, $p < 0.05$), and 98 proteins were significantly depleted (log_2 fold change < -0.26, $p < 0.05$) **(Figure 3.8B, Table 3.1)**. VPS35 was the most depleted protein in VPS35 KO cells, along with significant reduction of VPS26A/B and VPS29 levels, confirming suppression of the entire retromer complex. A range of additional proteins were also depleted in retromer KO cells, including Syntaxin-8 (STX8), a late endosomal SNARE protein that can engage VAMP7 or VAMP8 to mediate homotypic late endosome fusion or heterotypic late endosome fusion with lysosomes (Prekeris et al., 1999; Pryor et al., 2004). VAMP7 SNARE function is regulated by VARP, a retromer effector recruited to late endosomes through interaction with VPS29 (Hesketh et al., 2014). Considering the abundance of swollen endolysosomal compartments

in VPS35 KO cells, the loss of Syntaxin-8 at the whole cell lysate level may be reflective of perturbed endolysosomal fusion dynamics in the absence of retromer. Surprisingly, transcription factor E3 (TFE3) was significantly depleted in VPS35 KO cells. TFE3 is a member of the microphthalmia (MiTF/TFE) family of transcription factors that, along with TFEB, regulates the transcription of *VPS35* and *VPS26A* in response to nutrient deprivation (Curnock et al., 2019).

The acid hydrolase receptors CI-MPR (IGF2R) and Sortilin (SORT1) were significantly enriched in VPS35 KO cells, in agreement with their observed accumulation in **Figure 3.3**. Interestingly Rab27b and myosin VI (MYO6), two proteins involved in organelle positioning were significantly enriched **(Figure 3.8B)**. Rab27b is a regulator of the lysosomal exocytosis pathway that translocates late endosomes towards the cell periphery for docking at the plasma membrane (Ostrowski et al., 2010). Myosin VI engages with multiple cargoes to remodel the cortical actin meshwork at the cell periphery, and depletion of myosin VI leads to perinuclear accumulation of Rab5-positive endosomes (Masters et al., 2017). Apolipoprotein B (APOB), a major component of low density lipoprotein (LDL) was also significantly enriched in VPS35 KO cells. APOB has been genetically linked to coronary heart disease, and elevated APOB levels have been linked to early onset Alzheimer's disease (Richardson et al., 2020; Wingo et al., 2019). These proteins represent interesting hits for future studies relating loss of retromer expression to increased lysosomal stress and neurodegenerative disease.

In contrast to the total cell proteome, the 'secretome' dataset displayed a vast enrichment of proteins in the VPS35 KO condition, that were rescued by VPS35-GFP re-expression **(Figure 3.8C, Table 3.2)**. A potential cause for this discrepancy in distribution may be that the total proteome dataset was normalised to total peptide count between conditions, a routine analysis step for whole cell proteomics due to the sheer abundance of proteins, which may have masked some changes between conditions. 493 proteins were considered significantly enriched in the VPS35 KO 'secretome' (log_2 fold change > 1, $p < 0.05$), and 1 protein was depleted (log_2 fold change < 1, $p < 0.05$). Strikingly, this list of enriched proteins was populated with lysosomal proteins, including the acid hydrolase enzymes CTSB, CTSD, ASAH1 and DNASE2 as top hits **(Figure 3.8C)**. Multiple lysosomal hydrolases have been identified as risk genes for Parkinson's disease, resulting in aberrant pathogenic aggregate processing (Bartels et al., 2020). In additional to soluble proteins, transmembrane lysosomal proteins were also detected, including GPNMB, LAMP1 and CI-MPR. The presence of enriched transmembrane proteins in the cell culture medium may be indicative of exosome release, whereby ILVs are released upon late endosome fusion with the plasma membrane (Blanchette and Rodal, 2020).

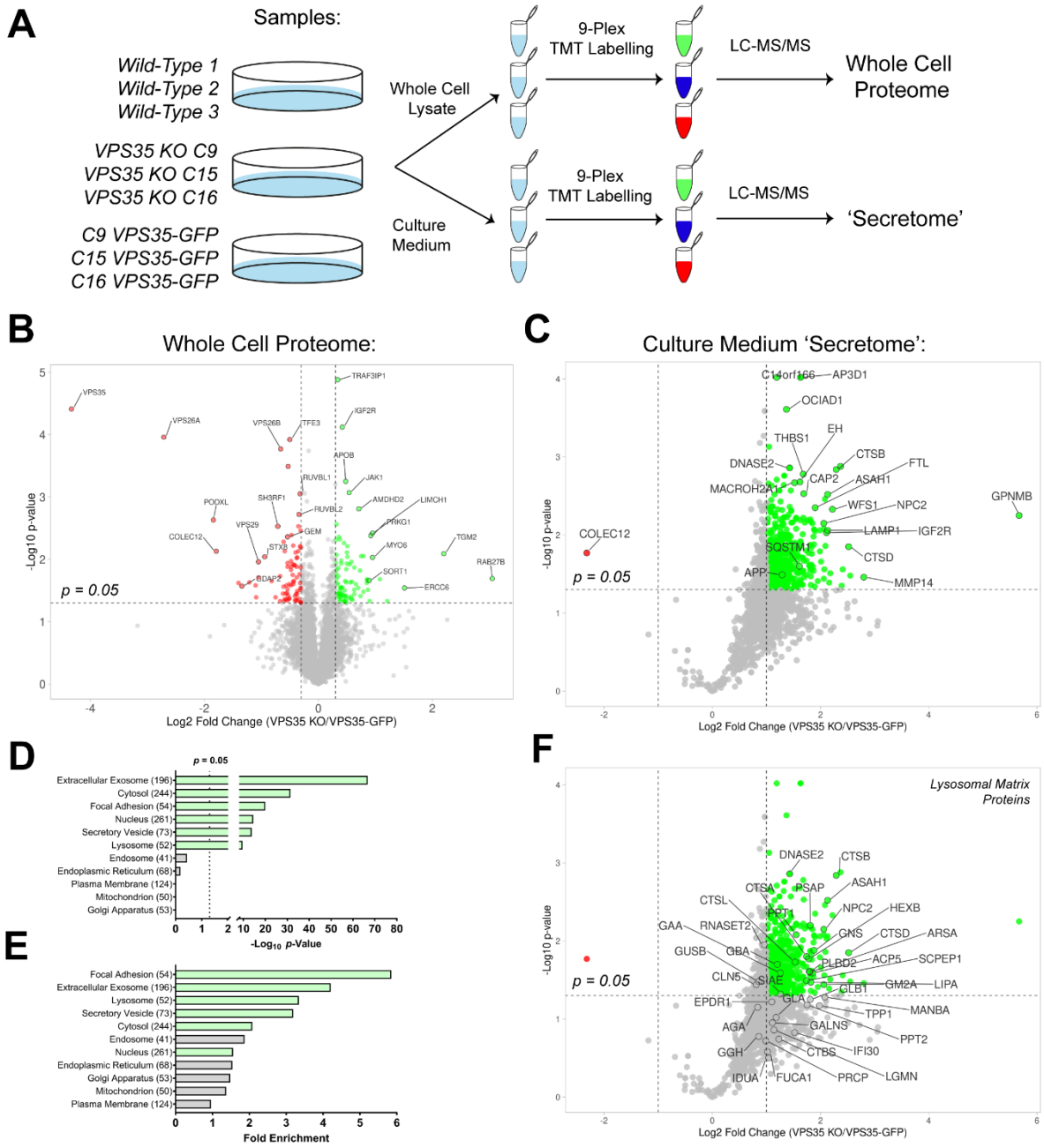

Figure 3.8 Quantitative Proteomic Analysis of VPS35 KO H4 Cells.

(A) Schematic of TMT labelling of wild-type, VPS35 KO clones 9, 15 and 16, and VPS35-GFP rescue clones 9, 15 and 16 to generate whole cell proteome and 'secretome' datasets. **(B)** Volcano plot of quantified protein abundances presented as a ratio of Log_2 VPS35 KO/VPS35-GFP abundance. Thresholds are set at p = 0.05, and fold change +/- 1.2. Retromer subunits VPS26A/B, VPS29 and VPS35 are labelled, along with CI-MPR (IGF2R) and Sortilin (SORT1). Additionally, the top 20 proteins ranked by Manhattan distance are labelled. **(C)** Volcano plot of quantified protein abundances from cell culture medium presented as a ratio of Log_2 VPS35 KO/VPS35-GFP abundance. Thresholds are set at p = 0.05, and fold change +/- 2. CI-MPR (IGF2R), COLEC12, SQSTM1 and APP are manually labelled, in addition to the top 20 proteins ranked by Manhattan distance. **(D)** and **(E)** Gene ontology analysis of cellular components significantly enriched in the VPS35 KO/VPS35-GFP rescue 'secretome' analysis, ranked by ascending p-value (D) or descending fold change (E). Significantly enriched cellular component categories are coloured in green. Brackets indicate the number of proteins identified for each category. **(F)** Volcano plot of quantified protein

abundances from cell culture medium, presented as in (C). All quantified lysosomal matrix proteins presented in (Schröder et al., 2010) are labelled.

Impaired APP processing and increased extracellular release of APP and Aβ fragments have been reported upon VPS35 depletion (Sullivan et al., 2011). Accordingly, APP was significantly enriched in the VPS35 KO 'secretome', perhaps indicative of altered amyloidogenic processing **(Figure 3.8C)**. VPS35 suppression was recently reported to greatly impair autophagic flux, leading to increased LC3 lipidation and tau aggregation (Carosi et al., 2020). Indeed, the autophagic cargo receptor Sequestome-1 (SQSTM1) was prominently enriched in VPS35 KO cells culture media, potentially indicating that autophagic material is also released from the cell surface **(Figure 3.8C)**. COLEC12, a scavenger receptor with a reported potential function in binding and clearing Aβ fibrils, was the only significantly depleted protein in the VPS35 KO 'secretome' and was also significantly depleted at the total proteome level **(Figures 3.8A and 3.8C)** (Nakamura et al., 2006).

Gene ontology analysis of enriched extracellular proteins revealed a significant enrichment of 'focal adhesion', 'extracellular exosome', 'lysosome', 'secretory vesicle', 'cytosol' and 'nucleus' cellular component categories **(Figures 3.8D and 3.8E, Table 3.3)**. Of a list of 37 identified lysosomal matrix proteins, 20 were significantly enriched in the VPS35 KO 'secretome' **(Figure 3.8F)** (Schröder et al., 2010). Together, these data establish a broad enrichment of proteins annotated as lysosomal or exosomal in the culture media of VPS35 KO H4 cells. What is not clear from these data, however, is whether the broad enrichment of lysosomal proteins arises from transcriptional upregulation, such as TFEB-dependent activation of CLEAR network genes, or protein accumulation due to impaired degradative capacity of lysosomes.

3.2.6 RNA Sequencing of VPS35 KO H4 Cells Reveals Transcriptional Reconfigurations

To directly investigate whether the enrichment of lysosomal proteins in VPS35 KO H4 cells was due to a coordinated transcriptional response, RNA sequencing (RNA-seq) of wild-type, VPS35 KO and VPS35-GFP H4 cells was performed in collaboration with Professor Andrea Ballabio (Telethon Institute of Genetics and Medicine, Naples, Italy) **(Figure 3.9A, Chapter 2.6.3)**. An even distribution of gene transcripts was altered in VPS35 KO cells relative to VPS35-GFP rescue cells **(Figure 3.9B, Table 3.4)**. 76 transcripts were considered significantly enriched in VPS35 KO cells (log_2 fold change > 1, FDR < 0.1), and 76 transcripts were also significantly depleted in VPS35 KO cells (log_2 fold change < -1, FDR < 0.1). Again, *VPS35* was the most depleted gene transcript in VPS35 KO cells. *VPS26A, VPS26B* and *VPS29* transcript abundances were unaltered, suggesting that the loss of additional retromer

components at the proteomic level is due to impaired stability of these proteins in the absence of VPS35, rather than transcriptional repression **(Figure 3.9B)**.

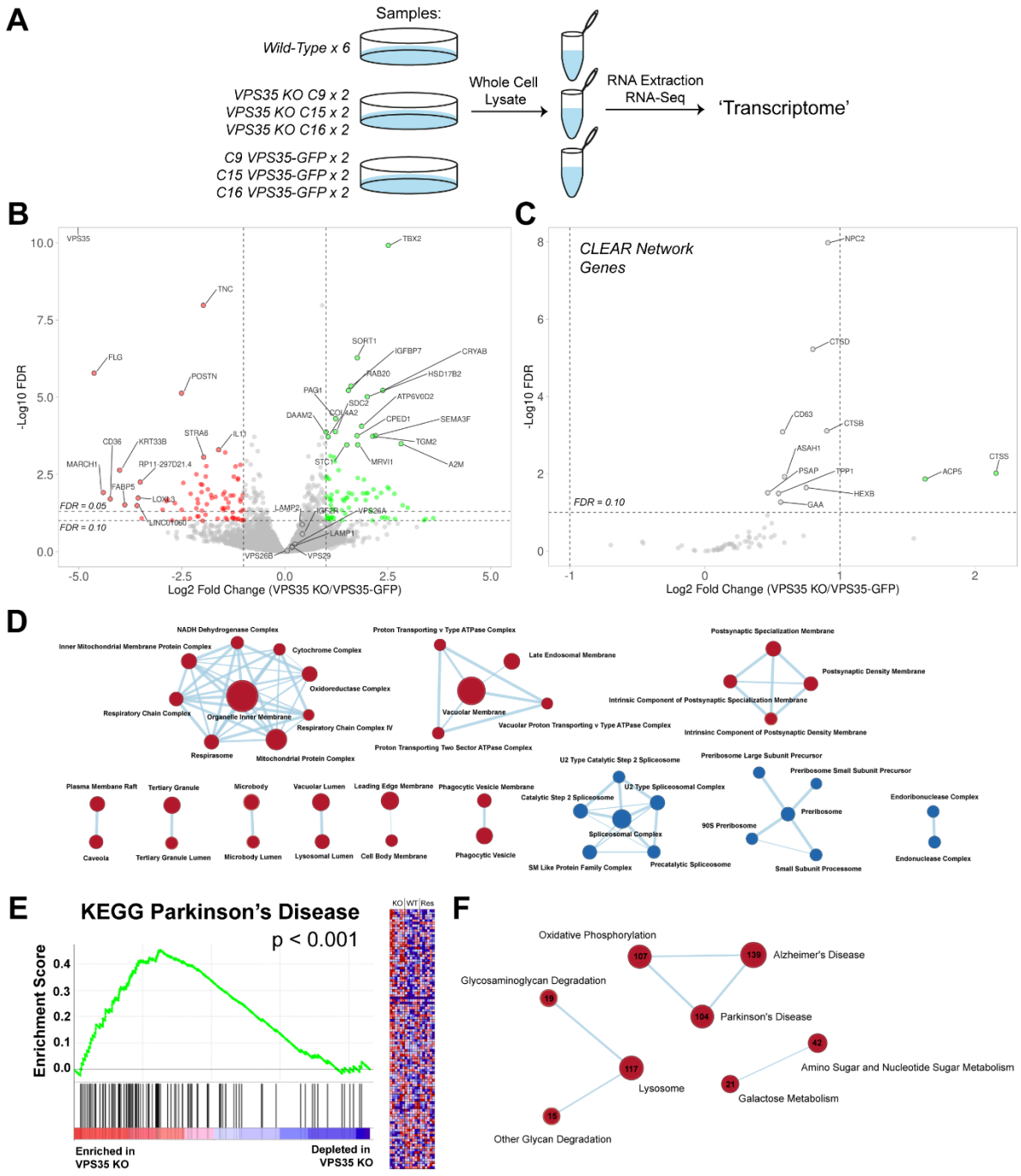

Figure 3.9 RNA-Seq analysis of the VPS35 KO Transcriptome in H4 Cells.

(A) Schematic of the RNA-seq experimental design. 6 wild-type samples, 6 VPS35 KO samples (2 each of VPS35 KO clones 9, 15 and 16) and 6 VPS35-GFP rescue samples (2 each of VPS35-GFP rescue clones 9, 15 and 16) were analysed. **(B)** Volcano plot displaying quantified gene transcript abundances as a ratio of Log_2 VPS35 KO/VPS35-GFP abundance. Thresholds are set at FDR = 0.1 and 0.05, and Log_2 fold change +/- 2. *VPS35* is cropped from the graph due to its extreme values (Log_2 fold change = -8.575, -log10 p-value = 264.9). The top 30 hits are labelled by ranking according to Manhattan distance. Retromer components *VPS26A/B and VPS29*, *IGF2R* and *LAMP1* are

additionally labelled. **(C)** Volcano plot displaying quantified gene transcript abundances of CLEAR network genes regulated by TFEB. Thresholds are set at FDR = 0.1 and Log2 fold change +/- 2. Genes with FDR < 0.1 are labelled. **(D)** Network analysis of significantly enriched cellular component gene sets. Red circles denote enriched categories, and blue circles denote depleted categories in VPS35 KO H4 cells. Circle size represents the number of enriched/depleted genes belonging to each gene set within the dataset. **(E)** Representative enrichment plot and heat map of genes enriched in the 'Parkinson's Disease' KEGG pathway. **(F)** Network analysis of significantly enriched KEGG pathway gene sets, presented as in (D). Circles are annotated with the number of enriched genes within each gene set.

Interestingly, *SORT1* was enriched with high confidence in VPS35 KO cells, in accordance with the increased abundance visualised by proteomics and Western blotting **(Figure 3.9B)**. The v-ATPase subunit *ATP6V0D2* is also upregulated, potentially in response to the lysosomal dysfunction observed in VPS35 KO cells. *RAB20*, reported to regulate phagosome maturation is prominently upregulated, although this Rab was not detected by proteomics (Schnettger et al., 2017). The most statistically significant hit is *TBX2*, a transcription factor that may in turn influence further downstream transcriptional activation. Despite these enriched transcripts, many proteins that were significantly altered at the proteomic level were not drastically changed at the transcriptional level. For example, *CI-MPR*, *LAMP1* and *LAMP2* displayed slight, but not statistically significant increases in transcript abundance in VPS35 KO cells **(Figure 3.9B)**.

TFEB regulates the transcription of a network of genes to mediate lysosomal biogenesis in response to nutrient starvation or lysosomal stress, and has also been reported to be a regulator of the lysosomal exocytosis pathway (Medina et al., 2011; Settembre et al., 2012). To investigate whether TFEB target genes are upregulated in VPS35 KO cells, their RNA transcript abundances were analysed **(Figure 3.9C, Table 3.5)** (Sardiello et al., 2009). Only two genes, *ACP5* and *CTSS*, were significantly enriched beyond the established thresholds. 9 additional targets were increased with high confidence (FDR < 0.1) but did not exceed a $\log_2$ fold change threshold of > 1. Therefore, through this analysis it does not appear that the entire TFEB network of lysosomal genes is upregulated and responsible for the increased proteomic abundance of lysosomal proteins. However, the fold change thresholds used in the analysis of RNA-seq (and proteomics) data are by nature somewhat arbitrary. The excellent coverage obtained often makes RNA-seq datasets amenable to gene set enrichment analysis (GSEA), which interrogates the behaviour of cohorts of genes within experiments, rather than simply analysing how individual genes were altered (Subramanian et al., 2005).

GSEA revealed significant enrichment of a range of different cellular compartment categories **(Table 3.6)**. Network analysis of enriched gene sets demonstrated a large network of genes associated with the mitochondrial respiratory chain complexes, a network of endosomal and lysosomal genes including late endosomal membrane, lysosomal lumen and v-ATPase genes,

and a network of postsynaptic density genes were enriched in VPS35 KO cells relative to wild-type and VPS35-GFP rescue cells **(Figure 3.9D)**. Conversely, gene networks associated with spliceosome, ribosome and endonuclease complexes were significantly depleted in VPS35 KO cells. In addition, GSEA was performed to investigate the enrichment of Kyoto Encyclopaedia of Genes and Genomes (KEGG) pathway genes. This analysis revealed significant enrichment of genes associated with neurodegenerative Parkinson's ($p < 0.001$), Alzheimer's ($p = 0.002$) and Huntington's ($p = 0.023$) diseases, consistent with the observed reduction of retromer expression in patients with Alzheimer's and Parkinson's disease (MacLeod et al., 2013; Small et al., 2005) **(Figure 3.9E, Table 3.7)**. Network analysis of these enriched pathways highlighted considerable overlap of Parkinson's- and Alzheimer's-associated genes with oxidative phosphorylation **(Figure 3.9F)**. This observation may therefore reflect a transcriptional upregulation of mitochondrial respiratory chain complexes in response to oxidative stress, perhaps due to impaired clearance of damaged mitochondria by mitophagy in the absence of functional retromer (Jimenez-Orgaz et al., 2017).

Together these data indicate a transcriptional reconfiguration of VPS35 KO H4 cells that appears to predominantly upregulate mitochondrial and endolysosomal genes. The overlap of these gene sets with characterised pathways associated with neurodegenerative disease further strengthens the neuroprotective role of retromer and highlights mitochondrial and endolysosomal dysfunction as key contributors to neurodegenerative pathology. However, not all lysosomal proteins that are enriched in the total cell proteome appear to be upregulated at the transcriptional level, and therefore the accumulation of endolysosomal proteins is likely to arise from a complex interplay between defective catabolic turnover of proteins in the lysosome and transcriptional reprogramming of VPS35 KO cells.

3.2.7 Correlative Analysis of Proteomics and Transcriptomic Data Highlights Upregulated Proteins in Response to VPS35 Depletion

Proteins that were upregulated both at the proteomic and transcriptional level represent the highest confidence hits that were reconfigured following VPS35 KO. To identify these proteins, the VPS35 KO/VPS35-GFP rescue abundance ratios quantified in the total cell proteome and 'secretome' were plotted against their corresponding 'transcriptome' abundance ratios. Applying this approach to the total cell proteome revealed a slight correlation between protein and transcript abundance, but that only a select few proteins were highly enriched or depleted at both the protein and transcript level **(Figure 3.10A)**. As expected, VPS35 was the most depleted protein in both experiments, alongside 14-3-3 protein sigma (SFN) **(Figure 3.10B)**. SFN is a member of the tyrosine 3-monooxygenase/tryptophan 5-monooexygenase activation protein (YWHA) 14-3-3 protein family that specifically bind the transcription factors TFEB,

TFE3 and MITF in response to mTORC1-mediated phosphorylation to sequester them in the cytosol in nutrient-replete conditions (Slade and Pulinilkunnil, 2017; Xu et al., 2019). The strong reduction of SFN transcription and protein abundance may indicate a decreased inhibitory regulation of these transcription factors in VPS35 KO cells, leading to their nuclear translocation and upregulation of lysosomal genes.

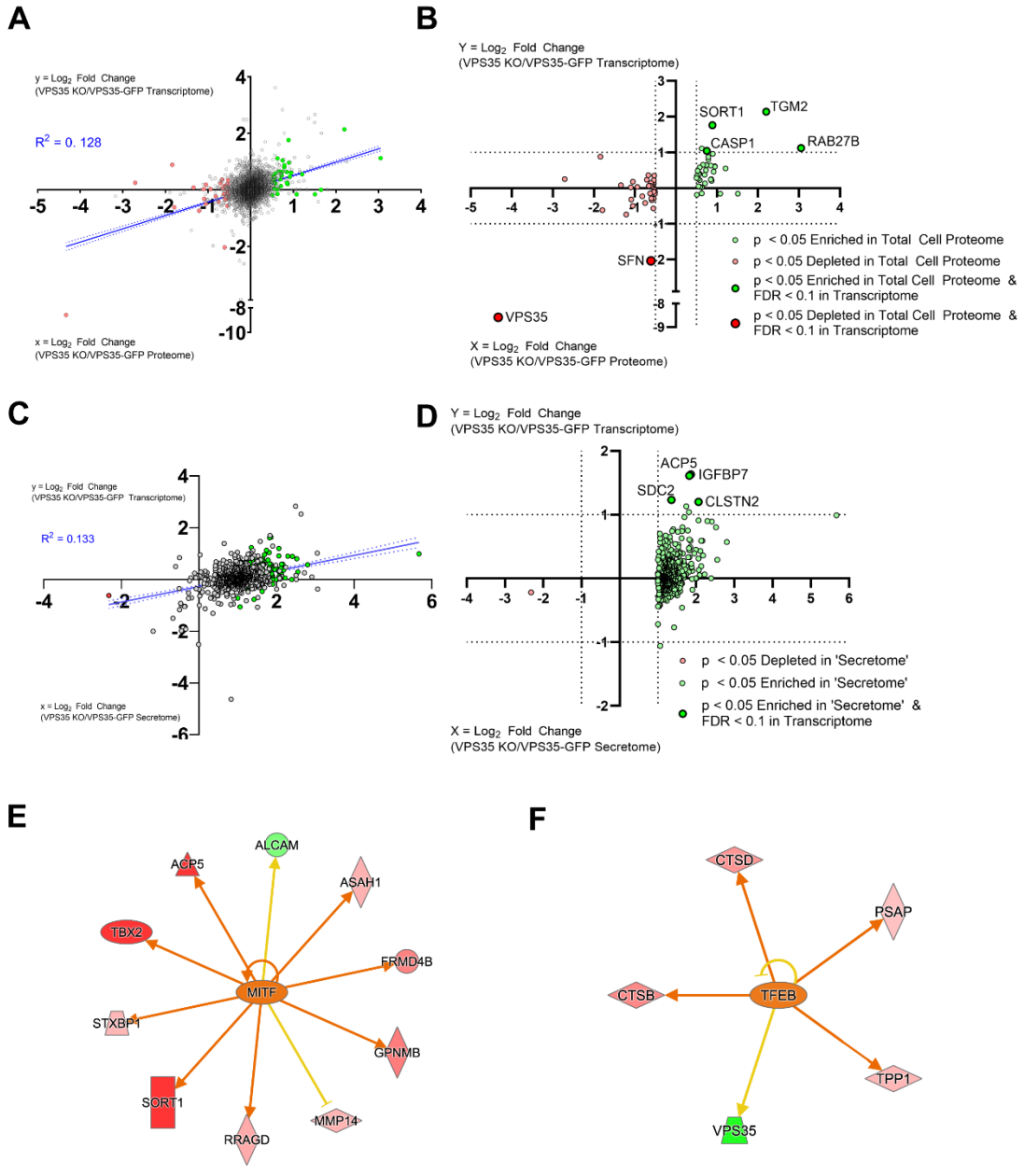

Figure 3.10 Correlative Analysis of the VPS35 KO Total Cell Proteome, 'Secretome' and 'Transcriptome'

(A) and **(B)** Scatter plot of proteins based on their Log_2 VPS35 KO/VPS35-GFP total cell proteome (x axis) and corresponding transcript (y axis) abundance ratios. **(C)** and **(D)** Scatter plot of proteins based on their Log_2 VPS35 KO/VPS35-GFP 'secretome' (x axis) and corresponding transcript (y axis) abundance ratios. Proteins significantly enriched in the total cell proteome are coloured green, and significantly depleted proteins are coloured red. For (A) and (C), a simple linear regression is

fitted, and the R^2 value displayed. In (B) and (D), Proteins with a proteomic p value > 0.05 are removed, and proteins that are significantly enriched/depleted, with a concomitant significant increase/decrease in gene transcript abundance by RNA-Seq are bold and labelled. **(E)** and **(F)** Ingenuity pathway analysis of predicted transcriptional regulators based on the RNA-seq dataset. Target genes are coloured red based on their increased transcript abundance, or green based on decreased transcript abundance. Orange arrows represent logical agreements with transcription factor activation, whereas yellow arrows logical clashes with predicted transcription factor activity.

Four proteins were significantly upregulated by both RNA-seq and proteomics analysis in VPS35 KO cells: Caspase-1 (CASP1), Sortilin (SORT1), transglutaminase-2 (TGM2), and Rab27b **(Figure 3.10B)**. CASP1 is activated by the inflammasome complex, and induces mitochondrial stress and oxidative damage (Yu et al., 2014). Interestingly, a model of neuroinflammation was recently proposed in microglial cells whereby manganese treatment decreased VPS35 expression, which in turn dysregulated its mitochondrial effector protein Mul1, leading to mitochondrial damage, CASP1 activation and increased exosome release (Sarkar et al., 2019). TGM2 is a transamidase enzyme that catalyses the covalent crosslinking of glutamine residues of bound peptides to primary amines. TGM2 is predominantly a cytosolic protein, although is also believed to act extracellularly where its crosslinking activity stabilises extracellular matrix (Gundemir et al., 2012). Additionally, many other diverse functions for TGM2 have been reported, including acting as a GTPase and a kinase. TGM2 has been implicated in a range of neurodegenerative diseases, most prominently Huntington's disease, but also Alzheimer's, Parkinson's and amyotrophic lateral sclerosis (Ruan and Johnson, 2007). TGM2 demonstrates higher activity in tissue samples from Huntington's patients, and its mRNA expression is increased in Alzheimer's and Parkinson's patient brain samples, similarly to the VPS35 KO H4 cell culture model (Citron et al., 2002, 2001). Aβ, Tau and α-synuclein are *in vitro* substrates for TGM2-catalysed crosslinking, raising the fascinating hypothesis that TGM2 plays a role in facilitating pathogenic aggregate formation (Andringa et al., 2004; Dudek and Johnson, 1994). However, *in vivo* evidence supporting this hypothesis remains unclear (Szondy et al., 2017).

The observed upregulation of Sortilin is particularly interesting, given its role as an acid hydrolase receptor responsible for delivery of enzymes to the endolysosomal network **(Figure 3.10B)**. Sortilin has been reported to be a direct retromer cargo, in particular through its ^{787}FLV^{789} cytosolic sequence, which bears resemblance to the ^{2369}WLM^{2371} motif of CI-MPR and the ^{555}YLL^{557} motif of DMT1-II, reported to be SNX3-retromer cargoes (Y. Cui et al., 2019; Lucas et al., 2016; Seaman et al., 2007). Mutation of the ^{787}FLV^{789} motif perturbs retrograde Sortilin trafficking through a surface uptake assay, and immunoprecipitation of retromer by Sortilin appears to also depend on its YxxØ-conforming ^{792}YSVL^{795} motif (Canuel et al., 2008b; Seaman et al., 2007). Sortilin is implicated in the delivery of a range of lysosomal proteins,

including PSAP, GM2A, SMPD1, and CTSD (Canuel et al., 2008a; Lefrancois et al., 2003). Notably, the M6P-independent Sortilin substrate GM2A is significantly enriched in the VPS35 KO 'secretome' alongside a range of M6P-tagged proteins **(Figure 3.9F)**. Sortilin has also been reported to chaperone the trafficking of transmembrane cargoes, including GLUT4 and the aspartyl protease β-site APP cleaving enzyme 1 (BACE1) which is involved in processing APP into its pathogenic Aβ isoform (Finan et al., 2011; Pan et al., 2017). Sortilin expression is also increased in Alzheimer's patient brain samples, which also display a reduction in VPS35 levels, mirroring its increase in VPS35 KO H4 cells (Finan et al., 2011; Small et al., 2005).

Finally, Rab27b was the most abundantly enriched protein in the VPS35 KO total cell proteome and was concomitantly upregulated at the transcript level **(Figure 3.10B)**. Rab27b was identified through a suppression screen as a regulator of the lysosome and lysosome-related organelle exocytosis pathway, where it acts sequentially with its paralogue Rab27a (Imai et al., 2004; Mizuno et al., 2007; Ostrowski et al., 2010; Shen et al., 2016). Rab27b appears to play a role in the translocation of late endosomes to the cell periphery, as its suppression induces perinuclear endosomal clustering (Ostrowski et al., 2010). Once in proximity to the plasma membrane, Rab27a coordinates the formation of a SNARE complex that docks, and ultimately fuses late endosomes to the plasma membrane (Ostrowski et al., 2010). Recent studies have linked Rab27b to Parkinson's disease, with higher expression levels reported in patient brain samples (Underwood et al., 2020a). In particular Rab27b appears to promote the cell-to-cell transmission of pathogenic alpha-synuclein aggregates through a lysosomal exocytosis and re-uptake mechanism (Underwood et al., 2020a, 2020b). The discovery of Rab27b upregulation in response to VPS35 depletion raises the fascinating possibility that the lysosomal exocytosis pathway is upregulated as a compensatory mechanism to deal with lysosomal dysfunction, leading cells to release undigested lysosomal material at the cell surface.

Similarly, 4 proteins were identified in the 'secretome' dataset that also displayed upregulated mRNA abundance: SDC2, ACP5, IGFBP7 and CLSTN2 **(Figures 3.10C and 3.10D)**. SDC2 is a member of the syndecan family of heparan sulphate proteoglycan (HSPG) surface receptors. SDC2 has previously been identified by a screen for SNX27 interactors, and its cell surface localisation is dependent upon SNX27 expression despite containing a type II PDZ-binding motif, rather than a type I sequence more often associated with SNX27 (Maday et al., 2008; Steinberg et al., 2013). Syndecans and other HSPGs play important roles in mediating uptake of extracellular Aβ through electrostatic interactions, and enhanced syndecan expression has been shown in Alzheimer's patient brain samples (Letoha et al., 2019; Liu et al., 2016; Small et al., 1996). The precise role for SDC2 in this process however is unclear. ACP5 is a phosphatase that cleaves the M6P tag from proteins upon their delivery into acidic

lysosomes (Sun et al., 2008). Alongside increased CI-MPR and Sortilin levels, ACP5 upregulation may form part of a compensatory network to deliver more M6P-tagged proteins to the lysosome. IGFBP7 is a soluble, secreted protein that binds insulin growth factors I and II and can modulate intracellular signalling through the IGF1R receptor (Evdokimova et al., 2012).

Calsyntenin-2 (CLSTN2) is a poorly characterised transmembrane protein that regulates synaptic morphology (Ranneva et al., 2020). Interestingly, Calsyntenin-2, and the other members of the calsyntenin family, undergo similar proteolytic cleavage events to APP, including presenilin-1-dependent intramembrane cleavage of CLSTN2 C-terminal fragments (Hata et al., 2009). Increased CLSTN2 in the VPS35 KO 'secretome' may therefore be reflective of increased amyloidogenic APP processing. It is also worth noting that the most abundantly enriched protein in the VPS35 KO 'secretome' dataset, GPNMB was just below the $\log_2$ fold change threshold of > 1 by RNA-Seq ($\log_2$ fold change = 0.99, FDR = 0.004) **(Figure 3.10C)**. GPNMB is a transmembrane protein that localises to endosomes and melanosomes, and can be cleaved by the protease ADAM10 at the cell surface to shed an extracellular ectodomain. *In vitro*, incubating microglial cells with Aβ induces enhanced *GPNMB* transcription, and GPNMB is significantly enriched in Alzheimer's patient brain and cerebrospinal fluid samples (Hüttenrauch et al., 2018; Rose et al., 2010).

Finally, to investigate whether the activity of a specific transcription factor could be inferred based on the upregulation of mRNA transcripts, ingenuity pathway analysis (IPA) was performed on the RNA-seq dataset. 76 transcriptional regulators were identified as potentially being altered in VPS35 KO cells ($p < 0.05$) **(Table 3.8)**. Of these, activation of the transcription factor MITF, a member of the MiTF/TFE family, could potentially underlie the increased transcription and protein abundance of Sortilin, ACP5 and GPNMB amongst others **(Figure 3.10E)**. MITF may also upregulate STXBP1, which forms part of a SNARE complex with the Rab27a effector protein Slp4-a in the exocytosis of Weibel-Palade bodies (Van Breevoort et al., 2014). Sortilin has been suggested to be a TFEB target, and overexpression of TFEB induces SORT1 upregulation (Bajaj et al., 2019; Song et al., 2013). However, IPA only linked 4 genes to TFEB activity, and Sortilin was absent from this group **(Figure 3.10F)**. The roles of TFEB and MITF in coordinating the transcriptional reconfiguration in response to VPS35 depletion are not clearly defined, but these dynamic regulators of lysosomal biogenesis are interesting candidates for further investigation.

3.2.8 Rab27b Suppression Alone Does Not Prevent Extracellular Release of Lysosomal Proteins

Of the hits identified by correlative proteomic and transcriptomic analysis, Rab27b upregulation is particularly interesting due to its potential role in increasing lysosomal exocytosis and transmission of pathogenic aggregates implicated in neurodegeneration. To validate Rab27b overexpression, whole cell lysates from wild-type, VPS35 KO and VPS35-GFP rescue H4 cells were immunoblotted for Rab27a and Rab27b abundance **(Figure 5.12A)**. Unlike Rab27b, Rab27a was not enriched in either the total cell proteome or the 'transcriptome' of VPS35 KO cells, suggestive of differential regulation of the two Rab27 paralogues. Rab27a expression appeared variable between VPS35 KO clones, generally displaying a decreased abundance relative to wild-type cells **(Figure 5.12B)**. However, this abundance did not appear to be rescued by VPS35-GFP re-expression, and therefore this phenotype may not be retromer-specific. Rab27b levels were dramatically increased in VPS35 KO clones, displaying > 10-fold higher quantified abundance than wild-type cells, and appeared to be rescued by VPS35-GFP expression, in accordance with the proteomic and RNA-seq datasets **(Figure 5.12C)**. However, Rab27b signal in wild-type or VPS35-GFP rescue cells was difficult to detect, causing calculated fold-change values to vary greatly, and due to this inconsistent quantification only VPS35 KO clone 15 passed the statistical significance threshold.

Next, I investigated whether Rab27b suppression could inhibit the release of lysosomal contents into the extracellular medium in VPS35 KO cells. Wild-type and VPS35 KO clones were treated with siRNA targeting either a scramble (Scr) or *Rab27b* sequence. At the whole cell lysate level, this did not induce a clear intracellular accumulation of lysosomal proteins, although Sortilin was significantly more abundant in wild-type H4 cells and two VPS35 KO clones upon Rab27b knockdown **(Figure 5.13A-E)**. To probe protein abundance in the cellular culture medium, large cellular debris was removed by centrifugation, and trichloroacetic acid (TCA) was used to precipitate proteins from the supernatant (Koontz, 2014). Rab27b suppression did not prevent the release of lysosomal proteins into the culture medium, suggesting perhaps that this pathway can occur independently of Rab27b **(Figure 5.13F-J)**. Further work investigating the role of Rab27b in VPS35 KO cells, for example using constitutively active and dominant negative constructs and image analysis of lysosomal positioning in response to Rab27b activity, will be required to understand the significance of Rab27b upregulation in response to VPS35 depletion.

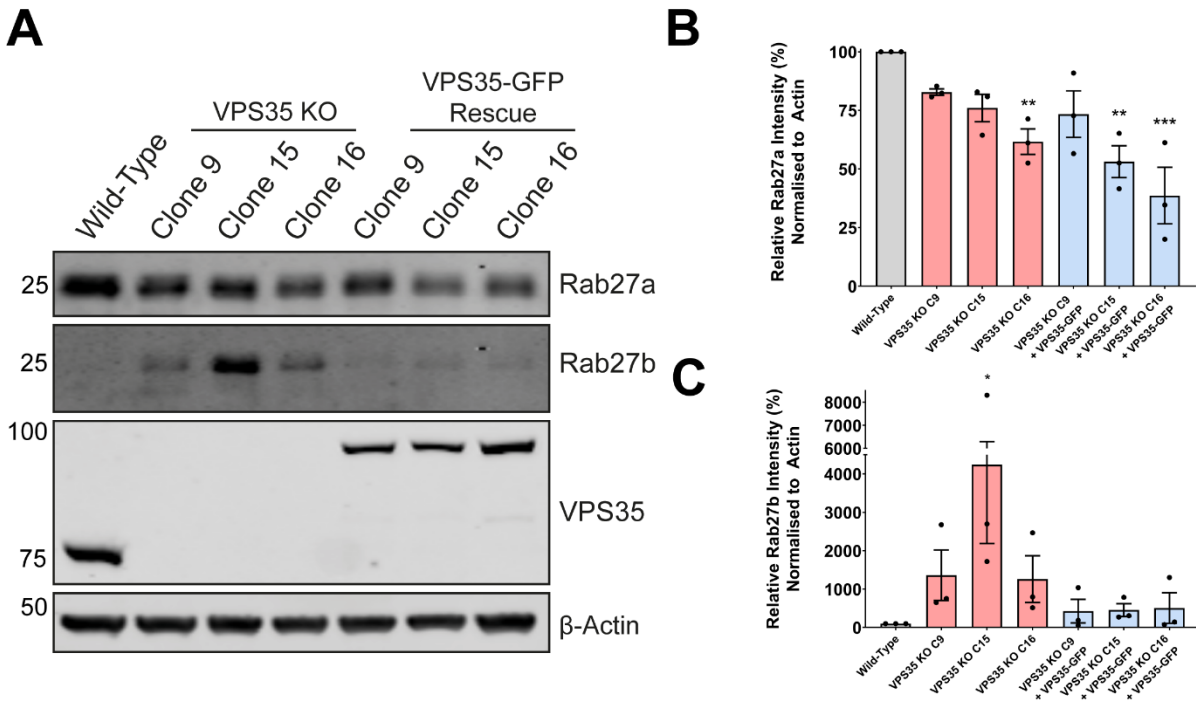

Figure 3.11 Rab27b is Upregulated in VPS35 KO H4 Cells

(A) Representative Western blot of whole cell lysates from wild-type, VPS35 KO or VPS35-GFP rescue clones, immunoblotted with anti-Rab27a and anti-Rab27b antibodies. **(B)** and **(C)** Quantification of Rab27a (B) and Rab27b (C) signal intensity, normalised to β-Actin. n = 3 independent experiments, mean + SEM, ordinary one-way ANOVA with Dunnett's multiple comparison's tests. * $p < 0.05$, ** $p < 0.01$, *** $p < 0.001$.

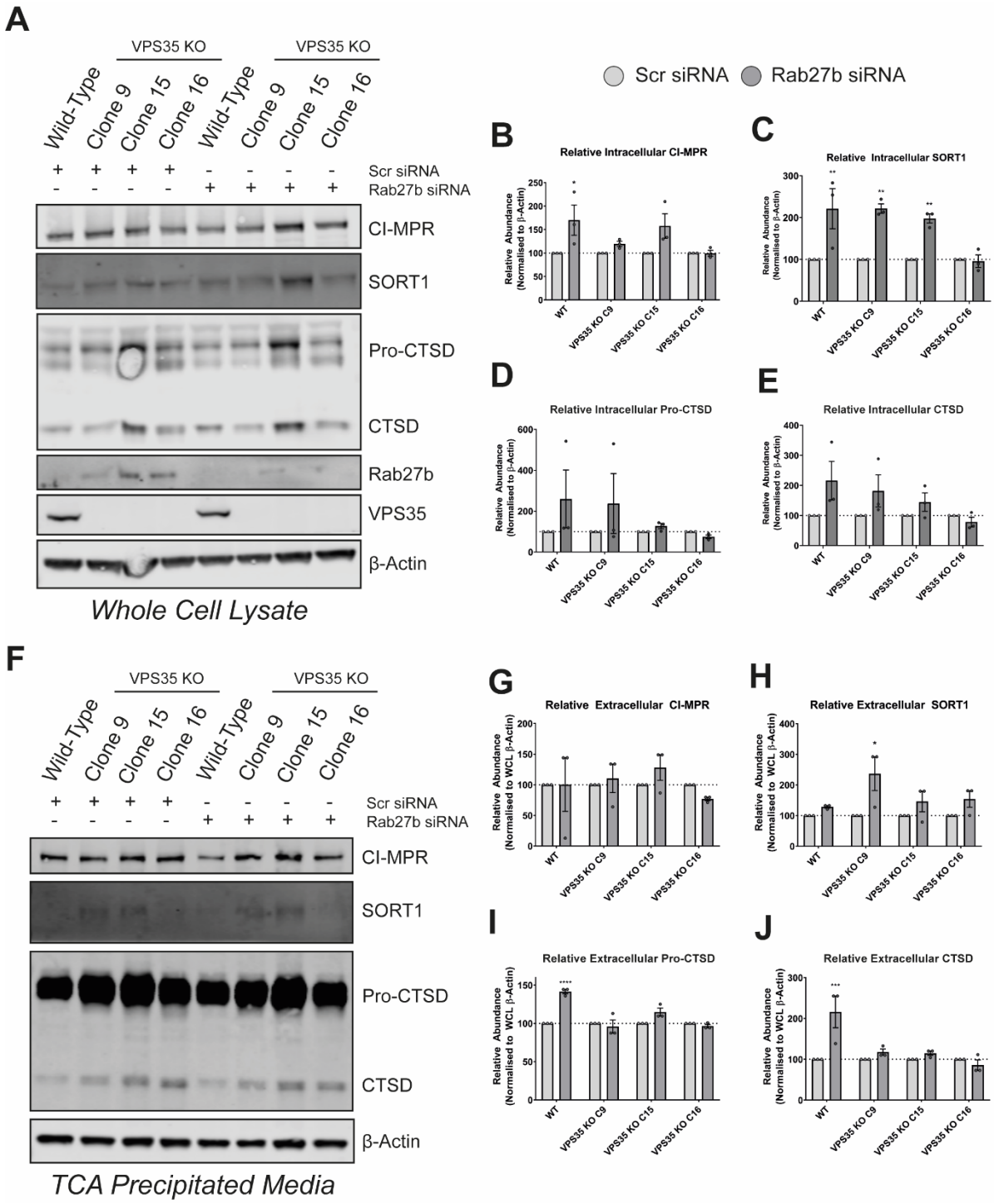

Figure 3.12 Rab27b Suppression Alone does not Suppress Extracellular Accumulation of Lysosomal Proteins

(A) Representative Western blot of whole cell lysates from wild-type or VPS35 KO H4 clonal cells treated with either scramble- or Rab27b-targeting siRNA. **(B-E)** Quantification of intracellular CI-MPR (B), Sortilin (C), Pro-cathepsin D (D) and mature Cathepsin D (E). **(F)** Representative Western blot of cell culture media following TCA precipitation from wild-type or VPS35 KO H4 clonal cells treated with either scramble- or Rab27b-targeting siRNA. **(G-J)** Quantification of CI-MPR (G), Sortilin (H), Pro-CTSD (I) and mature CTSD (J). n = 3 independent experiments, mean + SEM, ordinary one-way ANOVA with Dunnett's multiple comparisons tests, * $p < 0.05$, ** $p < 0.01$, *** $p < 0.001$, **** $p < 0.0001$.

3.3 Discussion

3.3.1 The Role of Retromer in Regulating Lysosomal Homeostasis

In the H4 cell culture model, VPS35 suppression imposes dramatic alterations to the endolysosomal network, characterised by enlargement of early and late endosomal compartments, and redistribution of LAMP1-positive lysosomes to the cell periphery. A range of eventualities could contribute to this phenotype, although a direct mechanistic link remains unclear. Lysosome positioning arises from a dynamic interplay between centripetal inward movement mediated by Rab7 and its effector RILP to direct dynein-mediated minus-end directed microtubules transport; and centrifugal outwards movement mediated by Arl8 and its effectors SKIP and the BORC complex to direct kinesin-mediated plus-end microtubule transport (Jordens et al., 2001; Pu et al., 2015). Given the reported hyperactivation of Rab7a-GTP in VPS35 KO cells, it could be expected that dynein-dependent minus end transport would prevail upon retromer suppression. However, in addition to this simplistic view of bidirectional lysosomal transport, further regulatory mechanisms add considerable complexity to the picture. For example, the ER protein protrudin mediates coincidence detection of Rab7 and PI(3)P at ER-endosome membrane contact sites to facilitate the loading of the kinesin-1 adaptor FYCO1 onto late endosomes for peripheral transport (Raiborg et al., 2015). Moreover, nutrient availability regulates lysosomal positioning, with lysosomes more peripheral under nutrient-replete conditions of mTORC1 activity through a mechanism dependent on the Arl8-BORC1 transport axis, and lysosomes cluster perinuclearly during starvation conditions through a nutrient sensing pathway dependent on Folliculin and Rab34 association with RILP (Pu et al., 2017; Starling et al., 2016). Moreover, the upregulation of Rab27b may promote peripheral actin-based transport through association with myosin Va (Chen et al., 2002; Rojo Pulido et al., 2011). The redistribution of lysosomes upon retromer depletion could therefore feasibly arise from a complex interplay between differential motor recruitment and the cellular metabolic response to nutrients.

Impaired fusion and/or resolution of endolysosomes may also contribute to the swollen appearance of LAMP1-positive compartments in VPS35 KO cells. Constitutively active Rab7 mutants induce peripheral, clustered lysosomal distribution and display impaired motility and turnover from endolysosomal membranes (Jimenez-Orgaz et al., 2017; McCray et al., 2010). Rab7 hyperactivation in VPS35 KO cells therefore may induce defects in endolysosomal fusion/fission dynamics. For example. hyperactivated Rab7a could lead to aberrant recruitment of the HOPS complex to mediate homotypic and heterotypic late endosome and lysosome tethering and fusion events. Alternatively, the observed decrease in Syntaxin-8 levels, and the defective recruitment of the retromer effector VARP, may suggest impaired

endosome-lysosome fusion in VPS35 KO cells (Hesketh et al., 2014). If fusion is impaired, then perhaps the swollen LAMP1-positive compartments observed in VPS35 KO H4 cells represent late endosomes rather than lysosomes, due to impaired delivery of LAMP1 to their native subcellular localisation.

Following fusion, endolysosomes undergo a reformation process that involves the final removal of cargoes from the membrane to retain a pool of dense-core lysosomes that can undergo further cycles of fusion and fission (Luzio et al., 2007). The reformation of autolysosomes, a fusion intermediate between autophagosomes and lysosomes, was reported to be dependent on mTORC1 signalling in response to the release of catabolites from the autolysosome lumen (Yu et al., 2010). Moreover, expression of constitutively active Rab7, or supplementation of cells with a non-hydrolysable GTP analogue inhibited autolysosome reformation, suggesting that Rab7 GTP hydrolysis occurs during this process (Yu et al., 2010). Dysfunctional proteins related to hereditary spastic paraplegia have also been demonstrated to induce a lysosomal swelling phenotype, posited to arise from defective lysosomal reformation (Allison et al., 2017; Chang et al., 2014; Hirst et al., 2015). Taken together, a hypothesis regarding the distinctive morphology of LAMP1 compartments in VPS35 KO cells is that they represent ‘locked’ endolysosomal fusion intermediates that are incapable of reforming into late endosomes and lysosomes. Ultrastructural electron microscopy analysis of VPS35 KO H4 cells in the future may be able to characterise these compartments and add support to whether they represent swollen endosomes that do not fuse with lysosomes, or endolysosomes that are unable to resolve.

3.3.2 Retromer and the Endosomal ‘Traffic Jam’ Model of Neurodegeneration

Impaired endolysosomal function and morphology are increasingly being recognised as hallmarks of neurodegenerative disease (Colacurcio et al., 2018; Vidyadhara et al., 2019). Moreover, many of the risk genes associated with familial forms of neurodegenerative diseases relate to endolysosomal biology. An emerging model is that perturbations to endosomal recycling and maturation cause ‘traffic jams’ that lead to luminal accumulations of pathogenic aggregates such as α-synuclein, Aβ and Tau (Small et al., 2017). Enlarged and/or peripheral lysosomal morphology has frequently been observed in retromer-depleted cells, with an unclear mechanistic basis (Arighi et al., 2004; Kvainickas et al., 2019; Steinberg et al., 2013). The missorting of retromer cargo proteins into the degradative pathway may cause an influx of proteins that exceeds the rate at which the ESCRT machinery can facilitate intraluminal degradation, leading to accumulation of cargos on and within endosomes. Moreover, retromer dysfunction is increasingly linked to endosomal defects that precipitate

the biogenesis of pathogenic aggregates, most commonly through the lens of the mistrafficking of individual cargo proteins (Carosi et al., 2021; Small and Petsko, 2015). The phenotypic similarity of VPS35 KO H4 cells to those harbouring hereditary spastic paraplegia mutations also suggests that multiple neurodegenerative diseases converge upon endosomal traffic jams from different angles (Allison et al., 2017; Hirst et al., 2015).

Considered within the context of recent literature regarding retromer's role in regulating Rab7a nucleotide cycling, the data presented in this chapter suggest broad dysfunction of the endolysosomal network upon retromer suppression, leading to perturbed morphology, transcriptional reprogramming, and increased exocytosis of a cohort of lysosomal proteins including lysosomal hydrolases and APP **(Figure 3.13)**. Further work will be required to support this model, such as a more thorough investigation of Rab7 dynamics, and time resolution of these multifaceted phenotypes through a knocksideways approach.

A complex 'chicken-and-egg' paradox arises regarding the role of retromer in endosomal traffic jams: what is the causative event that initiates endolysosomal dysfunction in neurodegeneration? For example, in the context of Alzheimer's disease does decreased retromer activity induce the mistrafficking of receptors genetically implicated in the onset of neurodegeneration (such as the APP receptor SorLA) lead to increased APP processing into Aβ which in turn initiates the hallmarks of endosomal blockage, such as swelling and reduced degradative capacity? Or do the broad defects in endosomal homeostasis occur first, providing optimal conditions for amyloidogenic Aβ processing on the endosomal membrane and reduced proteolytic degradation of pathogenic aggregates? The answer will likely be a complex interplay of the two scenarios and is not addressed by the data in this chapter. However, in early stage sporadic Alzheimer's disease, patient neurons display visibly enlarged endosomes prior to extracellular deposition of Aβ, suggesting that endolysosomal dysfunction can lie upstream of pathogenic aggregate formation (Cataldo et al., 2000). To further strengthen the link between the findings in this chapter and neurodegeneration, it will be necessary to observe retromer depletion phenotypes in neuronal cell models, for example primary neurons from model organisms or human iPSCs.

A

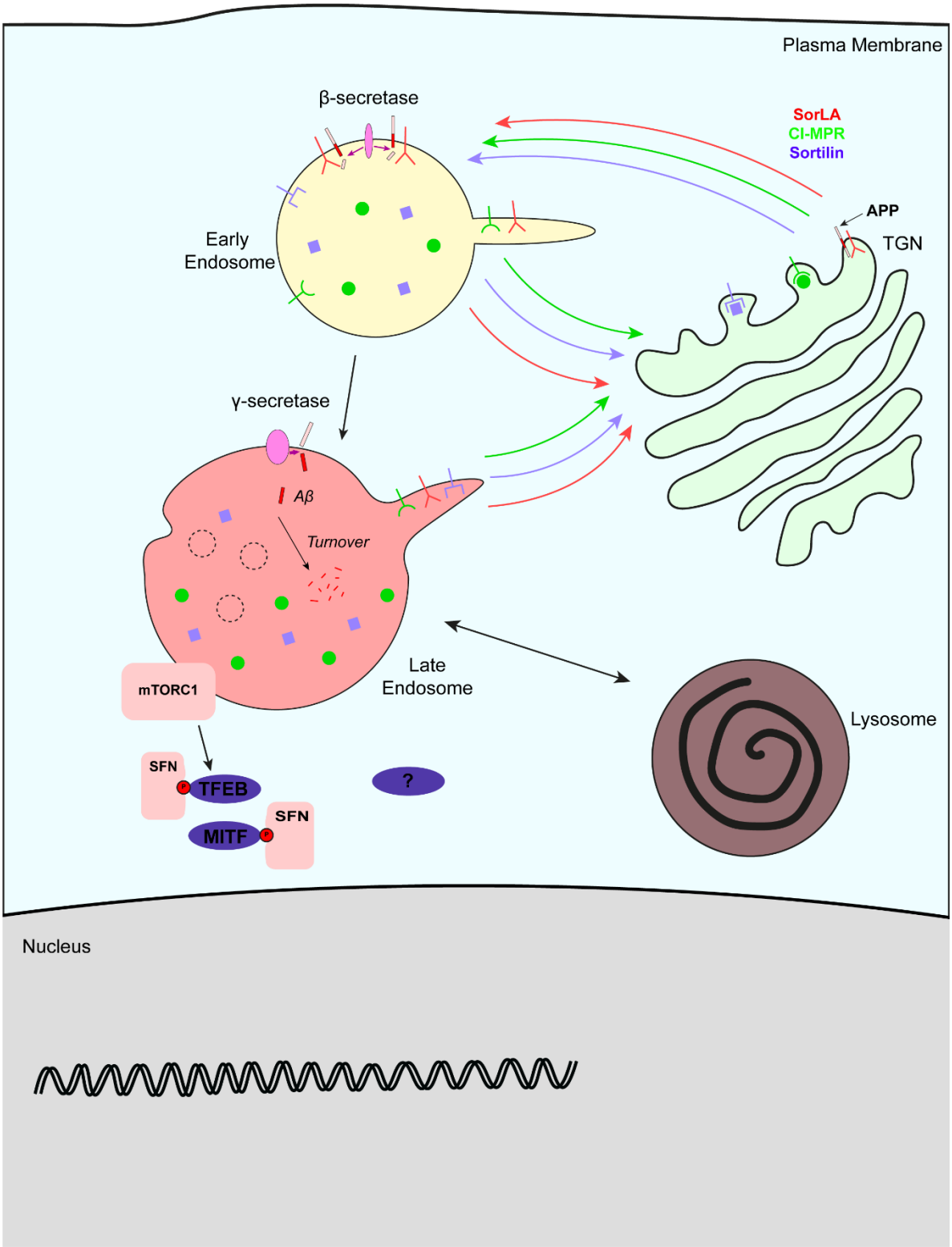

(Figure continues on next page)

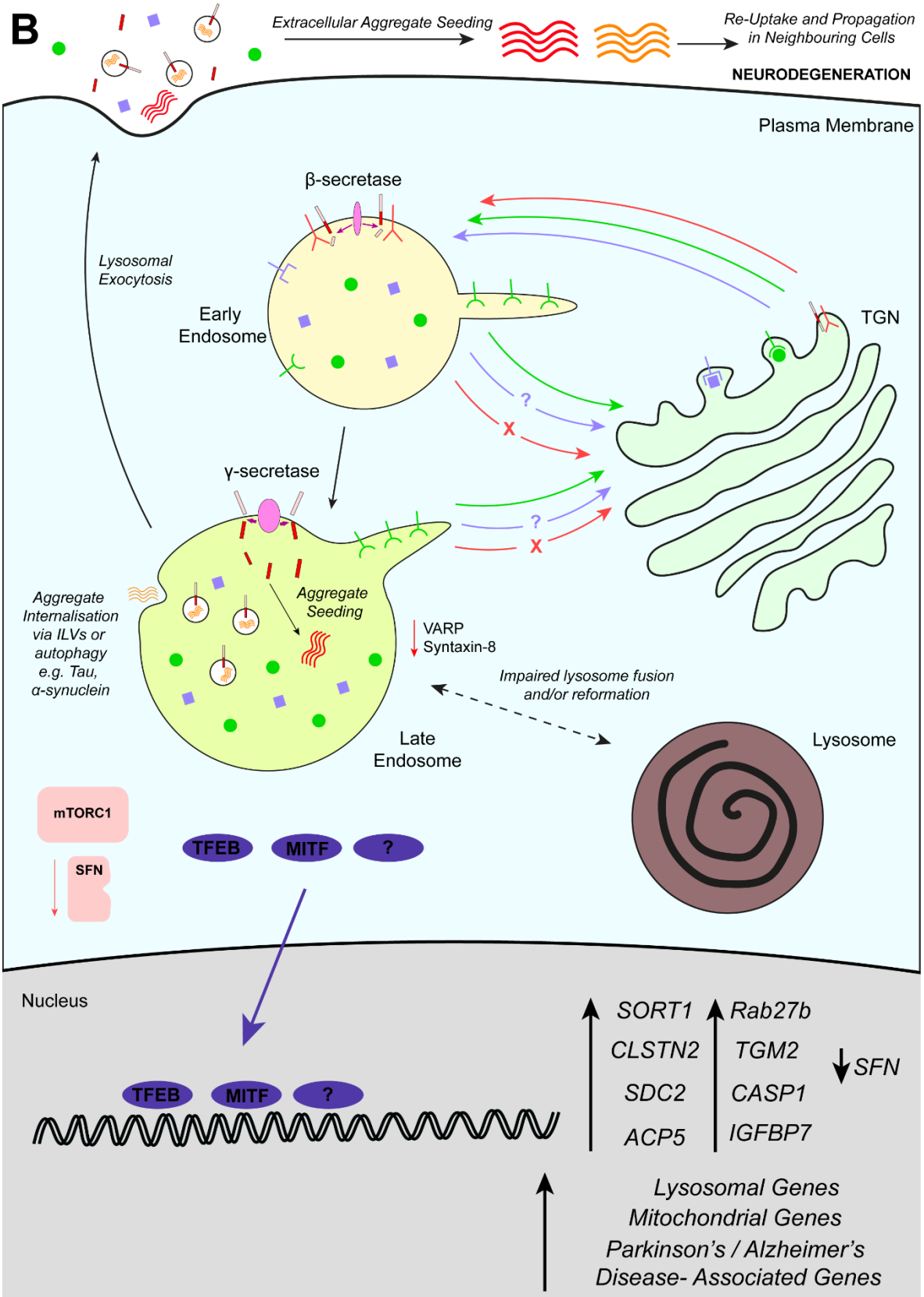

Figure 3.13 Model of Endosomal Traffic Jams Leading to Increased Lysosomal Exocytosis in VPS35 KO Cells

(A) Model of typical endolysosomal function in wild-type cells. A steady supply of lysosomal proteins is maintained through anterograde and retrograde recycling at the interface between the biosynthetic pathway and endosomal network. APP is efficiently processed and turned over within the lysosome.

In nutrient-replete conditions, mTORC1 activity restricts TFEB/MITF function. **(B)** In VPS35 KO cells, APP is aberrantly processed, in part due to mistrafficking of the SorLA receptor. Aβ fragments accumulate within the lysosome, where they may begin to coalesce into fibrillar structures. Other cytosolic pathogenic aggregates, such as α-synuclein and Tau, may be internalised via ILVs or autophagic delivery and inefficiently degraded. Fusion and reformation with lysosomes may be impaired due to decreased VARP recruitment and Syntaxin-8 levels. As a compensatory mechanism, lysosomal contents are released at the cell surface, where pathogenic aggregates may continue to be seeded. mTORC1 dissociates from the lysosomal membrane and SFN expression is transcrpitonally suppressed, allowing increased nuclear translocation of TFEB and MITF, and potentially additional unidentified transcription factors, into the nucleus to upregulate a cohort of genes relating to lysosomal and mitochondrial biology, and Alzheimer's and Parkinson's disease pathology.

3.3.3 Lysosomal Exocytosis as a Compensatory Mechanism in VPS35 KO H4 Cells

The enrichment of soluble and transmembrane lysosomal proteins within the VPS35 KO 'secretome' is suggestive of lysosomal exocytosis. Retromer suppression has been associated with increased release of Aβ through exosome in cell culture models (Sullivan et al., 2011). Mass spectrometry of cerebrospinal fluid also recently revealed increased abundance of Tau in VPS35 KO mice and Alzheimer's disease patient samples compared to controls (Simoes et al., 2020). In a recent study, *Vps35* mutant flies demonstrated APP accumulation in presynaptic neurons of the neuromuscular junction, and increased APP in extracellular postsynaptic vesicles (Walsh et al., 2020). Moreover, the *Vps35*^{D238N} mutation, equivalent to the VPS35^{D620N} Parkinson's-linked mutation observed in humans, effectively rescued the APP accumulation phenotype, in agreement with the observation in **Figure 3.7** that VPS35 re-expression can rescue lysosomal morphology independently of WASH interaction (Walsh et al., 2020). Interestingly, a *Snx1/Snx6* double mutant also increased intra- and extra-neuronal APP abundance, although to a lesser extent, potentially implicating ESCPE-1 in this pathway (Walsh et al., 2020).

Lysosomal exocytosis has been proposed as a compensatory mechanism in response to lysosomal dysfunction (Bécot et al., 2020). For example, chemical perturbation of lysosomal homeostasis with ammonium chloride or bafilomycin A1 in SH-SY5Y cells leads to increased α-synuclein exocytosis and paracrine transfer to neighbouring cells (Alvarez-Erviti et al., 2011). This pathway may be particularly beneficial to neurons, whereby extracellular release of lysosomal contents alleviates endolysosomal stress, and the released material can be internalised and degraded by microglial cells in the brain. While this mechanism may be neuroprotective in the short-term, continued extracellular release of undegraded lysosomal material over the lifetime of an organism may contribute to the propagation and extracellular deposition and spread of pathogenic aggregates in later life as the ability of microglia to degrade this material diminishes. The discovery of Rab27b as one of the most abundantly

enriched hits in VPS35 KO H4 cells, both at the transcript and protein level, provides a potential mechanistic insight into why this process may be upregulated upon retromer suppression **(Figure 3.14)**. Preliminary experiments suppressing Rab27b demonstrated little impact on extracellular release of lysosomal contents, although due to time constraints these experiments were not optimised. An exciting testable hypothesis is whether, in a co-culture experiment, VPS35 KO H4 cells transfected with aggregate-prone proteins such as α-synuclein display a greater propensity to transfer pathogenic aggregates to surrounding cells.

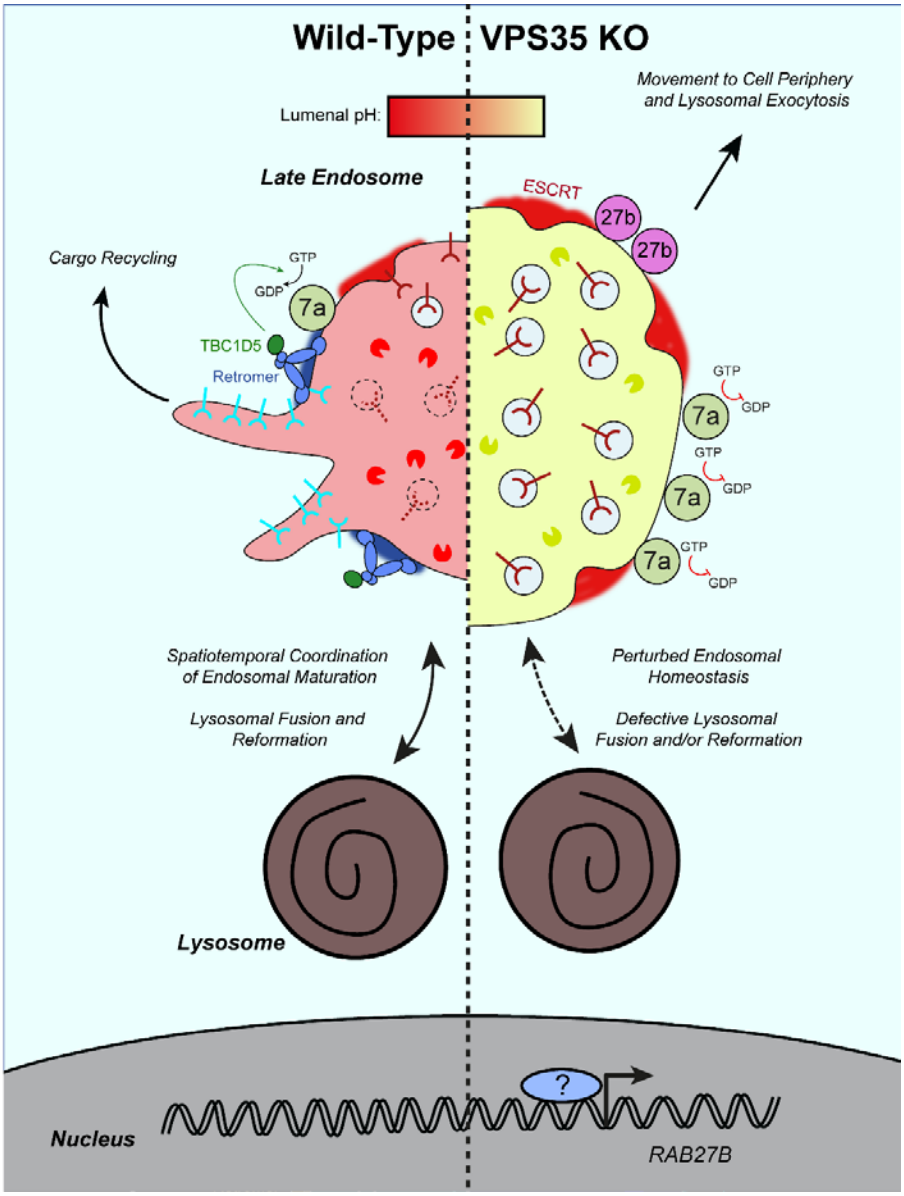

Figure 3.14 Model for Rab27b-Mediated Lysosomal Exocytosis

In VPS35 KO cells, Rab27b is upregulated as part of a transcriptional response to manage endolysosomal stress. Rab27b localises to late endosomal membranes and directs their trafficking to the plasma membrane for fusion, in conjunction with its paralogue Rab27a. Over time, Rab27b can contribute to the pathogenic spreading of undigested material between cells.

It should be noted that in this chapter I did not perform an exosome purification protocol, and therefore it cannot be concluded whether the lysosomal contents in the 'secretome' were soluble in the media, or present in extracellular vesicles. An exosome purification may be necessary to make more definitive conclusions regarding enhanced lysosomal exocytosis in VPS35 KO H4 cells.

3.3.4 Insights into the Role of Retromer in Lysosomal Acid Hydrolase Delivery and Activation

A striking phenotype in VPS35 KO H4 cells is the polar distinction between LAMP1-positive compartments at the cell periphery, and CI-MPR/EEA1-positive compartments in the perinuclear region. If the swollen LAMP1 compartments visualised in these cells are indeed 'locked' endolysosomal compartments, then retrieval steps still appear to be in place to recycle acid hydrolase receptors from the endosomal membrane to the TGN, for example ESCPE-1-mediated retrograde recycling (Kvainickas et al., 2017; Simonetti et al., 2017). The complete separation of CI-MPR and LAMP1 signal is also reminiscent of fibroblasts cultured from hereditary spastic paraplegia patients (Chang et al., 2014).

A historical view in the literature has been that upon retromer suppression, or expression of the Parkinson's disease-linked D620N VPS35 mutant, the unprocessed isoform of CTSD is secreted from the cell via an anterograde TGN-to-plasma membrane pathway due to missorting of its receptor CI-MPR **(Figures 3.15A and 3.15B)** (Bugarcic et al., 2011; Follett et al., 2014; Rojas et al., 2008; Seaman, 2004). CTSD is involved in α-synuclein degradation, and therefore its delivery to and activation within the endosomal network is important in preventing aggregate formation (Sevlever et al., 2008). Indeed, the immature precursor isoform of CTSD was predominantly observed in TCA-precipitated media in **Figure 3.12**. However, given the recent characterisation of ESCPE-1-mediated retrograde trafficking of CI-MPR in the absence of retromer, and the diverse range of lysosomal matrix proteins in the VPS35 KO 'secretome', some of which are not M6P-tagged CI-MPR substrates, it may be possible to posit an alternative hypothesis for this phenomenon: that increased extracellular acid hydrolase release occurs through a lysosomal exocytosis pathway upon VPS35 suppression **(Figure 3.15C)**. These hydrolases, such as CTSD, may be predominantly in an inactivate precursor state, due to dysregulated lysosomal homeostasis impairing their pH-dependent proteolytic activation. Density purification of lysosomes from VPS35 KO HeLa cells recently revealed an increased lysosomal abundance of immature CTSD precursors, suggesting that M6P-tagged hydrolases can indeed continue to be delivered to the endolysosomal network in the absence of retromer, but then subsequently fail to be efficiently activated (Carosi et al., 2020). The transcriptional upregulation of Sortilin may form part of a

compensatory mechanism to supply the lysosome with more enzymes to boost catabolic capacity, however this may contribute to further congestion of endosomal 'traffic jams'.

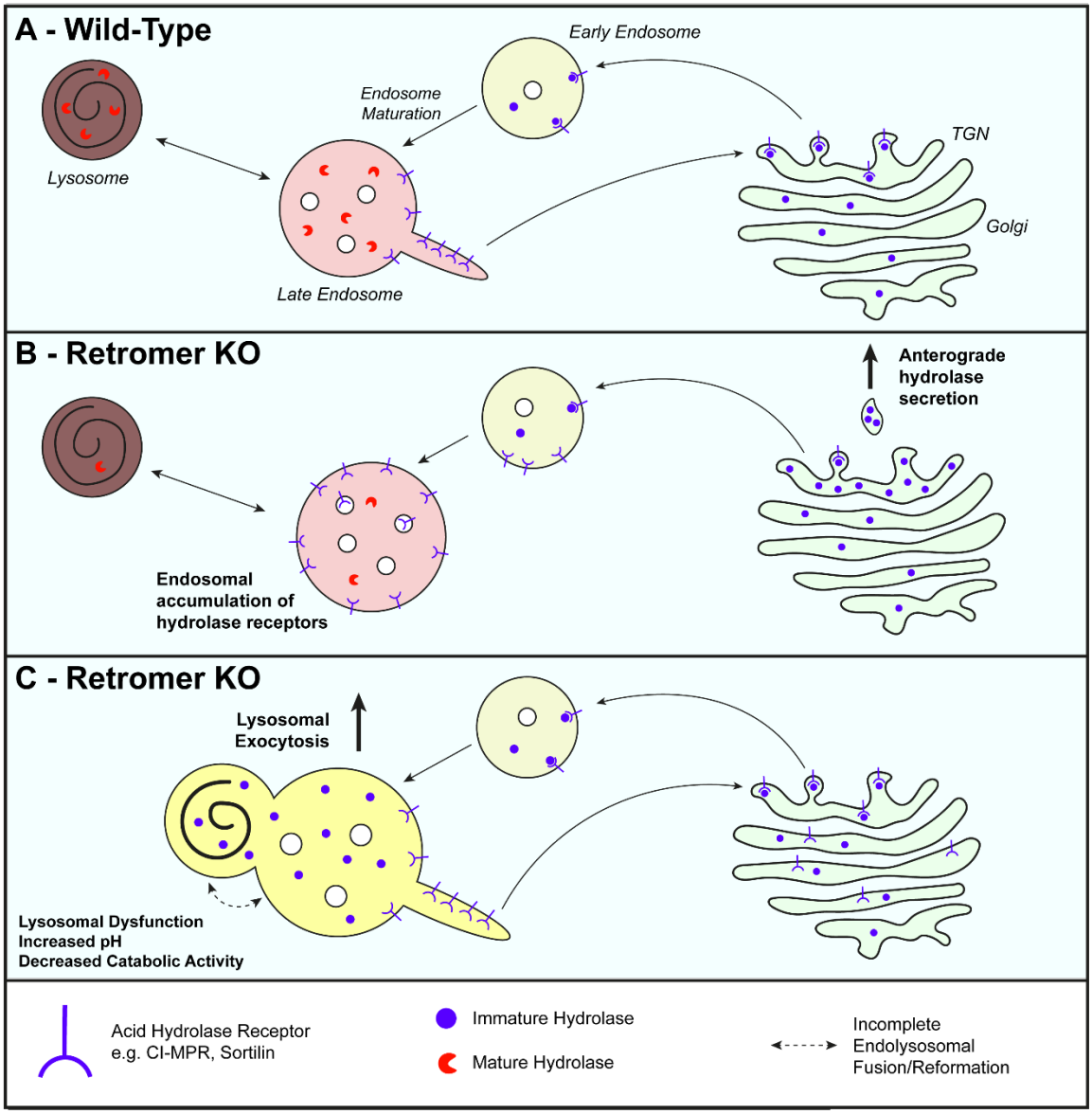

Figure 3.15 Models for Acid Hydrolase Release in VPS35 Depleted Cells

(A) In wild-type cells, a steady state of acid hydrolases is supplied to the endolysosomal network through constitutive acid hydrolase receptor recycling. **(B)** In a model of anterograde hydrolase secretion, defective sequence-dependent acid hydrolase receptor recycling due to the loss of retromer leads to an accumulation of acid hydrolase precursors in the biosynthetic pathway, leading to secretion into the extracellular space**. (C)** In a model of lysosomal exocytosis of acid hydrolases, retromer dysfunction induces severe endosomal dysfunction through Rab7 hyperactivation. While acid hydrolase receptors appear to be retrieved and can deliver acid hydrolases to the endolysosomal network, proteolytic activation of hydrolase receptors is impaired. Through a compensatory exocytic mechanism, lysosomal contents, including immature hydrolases, are released at the cell surface. Acid hydrolase receptors such as Sortilin may be upregulated through a compensatory mechanism.

3.3.5 A Transcriptional Response to Retromer Suppression

GSEA analysis of RNA-seq transcription profiles in VPS35 KO H4 cells revealed a significant enrichment of lysosomal transcripts. TFEB has been reported to act as a master regulator of lysosomal biogenesis by enhancing the transcription of genes harbouring CLEAR elements in their promotor regions. Moreover, TFEB was recently shown to translocate to the nucleus upon VPS35 KO in HeLa cells (Curnock et al., 2019). The reported decrease in mTORC1 activity in VPS35 KO cells, and the downregulation of the 14-3-3 protein SFN would suggest enhanced TFEB transcriptional activity (Kvainickas et al., 2019). RNA-seq analysis indicated a general increased trend in transcription of TFEB target genes, although only two transcripts were enriched > 2-fold in VPS35 KO cells. In the future, it will be interesting to investigate whether TFEB is indeed activated in VPS35 KO H4 cells, and if so, why some genes within the CLEAR network are selectively upregulated over others.

Another MiTF/TFE transcription family member may also be involved in the VPS35 KO compensatory response. MITF, like TFEB, was not detected in the proteomics datasets within this chapter, but its activity can potentially be inferred through pathway analysis of RNA-seq data. According to this analysis, MITF activity could potentially underlie the pronounced upregulation of Sortilin in VPS35 KO H4 cells, alongside other proteins of interest. Studies into MITF, and how its transcriptional targets differ to TFEB, may provide additional insights into how cells transcriptionally respond to endolysosomal dysfunction.

Chapter 4: Developing a Proteomics Methodology to Label Endogenous TGN-Resident Proteins

4.1 Introduction

4.1.1 The Technical Challenge of Tracing Retrograde Endosomal Cargo Sorting

Investigating the mechanistic basis of endosomal cargo recycling is an ongoing endeavour that underpins our understanding of a wide range of diseases (Cullen and Steinberg, 2018). Studying the spatiotemporal regulation of disease-related proteins through this dynamic network could potentially lead to future innovative therapies that correct defects in endolysosomal biology in disease contexts, particularly in relation to neurodegeneration (Small et al., 2017). Affinity-based pulldown experiments have been an important strategy in identifying novel cargoes for endosomal recycling complexes. This approach broadly involves tagging a constituent member of a recycling complex and purifying the tag from whole cell lysates with high affinity, thereby co-isolating interaction partners of the complex. This methodology has revealed multiple protein-protein interactions between endosomal sorting machineries and their cargoes (McGough et al., 2018; McMillan et al., 2016; Seaman et al., 2009; Simonetti et al., 2017; Singla et al., 2019; Steinberg et al., 2013). However, a caveat of this approach is that the protein-protein interactions involved in cargo recycling are typically transient, of low affinity, and may depend on coincidence detection of phosphoinositide identity, cargo density and effector proteins. As a result, the somewhat reductionist system of affinity-based pulldowns, which removes many of these auxiliary factors, is only likely to identify the strongest cargo interactors and fail to identify others.

In recent years surface biotinylation has proven to be an indispensable tool that circumvents much of this problem by indirectly identifying the vast numbers of cargo that are recycled from the endosomal network to the plasma membrane **(Figure 4.1A)**. This technique allows the unbiased labelling of the cell surface proteome in wild-type cells, and a quantitative comparison of how this proteome is altered when recycling machinery is depleted. For example, surface biotinylation revealed over 400 proteins lost from the cell surface when SNX27-retromer endosome-to-plasma membrane recycling was disrupted and 220 proteins lost from the surface when the functionally similar SNX17-retriever recycling pathway is disrupted (McNally et al., 2017; Steinberg et al., 2013).

In comparison, far less is known about the numbers of cargoes that undergo retrograde endosome-to-TGN trafficking **(Chapter 1.4.1)**. This pathway is of crucial importance to cells for controlling a range of biological pathways. For example, the retrograde recycling of acid hydrolase receptors is required to maintain a consistent delivery of hydrolytic enzymes to the lysosome (Brown et al., 1986). Mutations disrupting this pathway are associated with

lysosomal storage disorders, and retrograde cargoes influencing this process have therefore been considered therapeutic targets (Koeberl et al., 2011; Parenti et al., 2015). It is also crucial to return internalised endosomal cargoes to the TGN in order to facilitate polarised re-secretion to the plasma membrane, with examples including the establishment of morphogen gradients through the Wntless receptor, and directed trafficking of matrix metalloproteases and integrins to mediate directional cell migration (Harterink et al., 2011; Johannes and Popoff, 2008; Shafaq-Zadah et al., 2016; Wang et al., 2004).

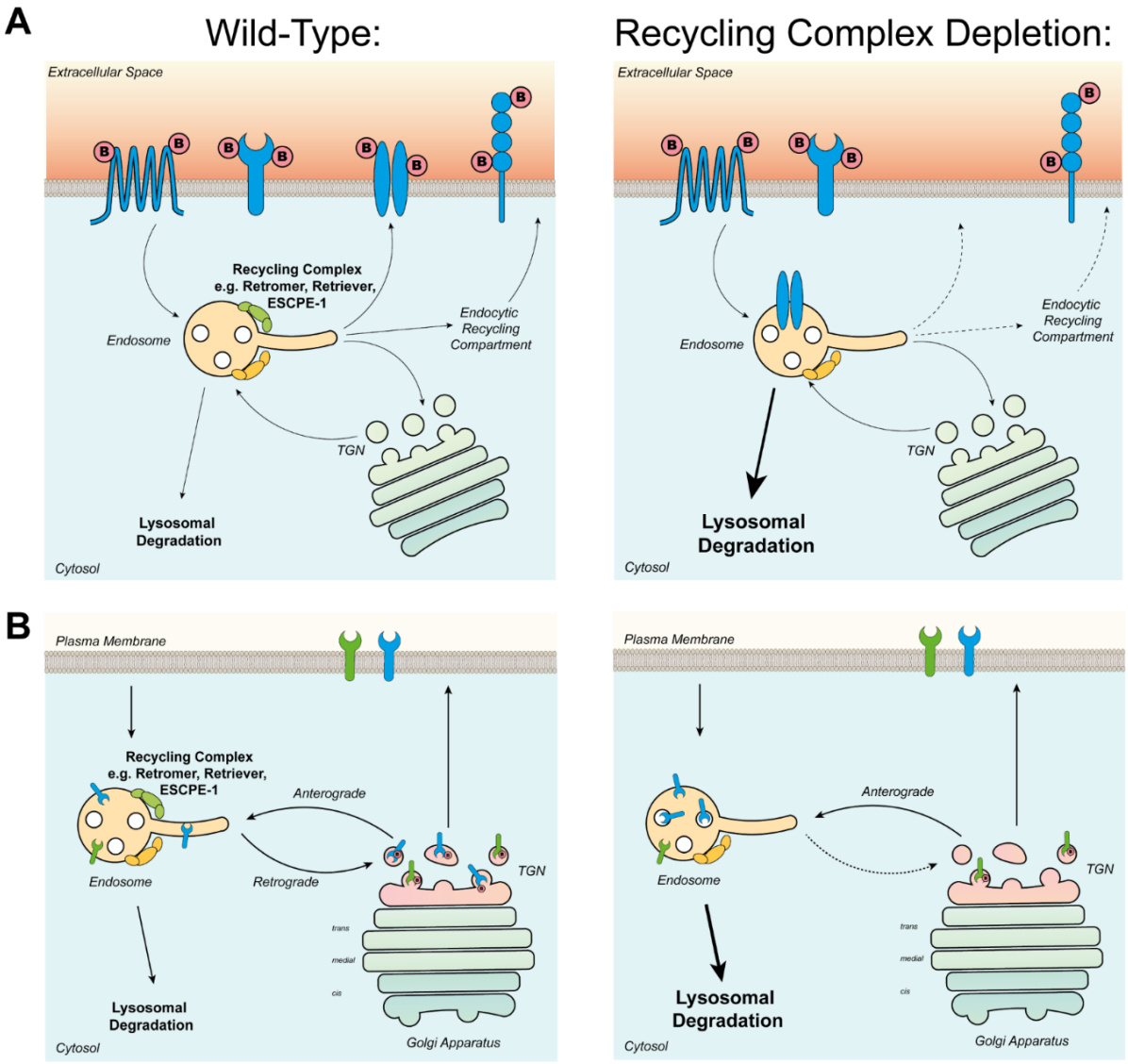

Figure 4.1 Spatially Restricted Proteomic Labelling Facilitates Unbiased Detection of Endosomal Recycling Cargoes

(A) Schematic overview of surface biotinylation methodology. Depletion of an endosomal recycling complex induces the intracellular endolysosomal accumulation of cargoes that depend on the targeted complex for cell surface delivery. This can be indirectly quantified as a decrease in the cell surface biotinylation of missorted cargoes. **(B)** Conceptual schematic of an analogous approach to specifically biotinylate TGN-resident proteins. Dispersal of cargoes from the TGN resulting from impaired retrograde trafficking can therefore be quantified as a decrease in cargo biotinylation.

Ideally, a similar experimental approach to surface biotinylation could facilitate the attainment of a TGN proteome in wild-type cells, followed by a quantitative comparison of how this proteome is remodelled upon perturbation of retrograde recycling **(Figure 4.1B)**. However, obtaining a selective proteome of the TGN represents a major technical challenge. The plasma membrane is an excellent target for biotinylation because of the exposure of transmembrane proteins to the extracellular culture medium, but the TGN in contrast is a small and dynamic membrane-enclosed intracellular compartment, and therefore far less accessible. Advances in methods of organelle purification in metazoan cells by differential centrifugation can effectively distinguish the Golgi compartments from the earlier secretory pathway, but often fail to differentiate the TGN from the Golgi and related compartments such as the endosomal network (Geladaki et al., 2019; Gilchrist et al., 2006; Waugh et al., 2011). Furthermore, the inherent multivariate localisations of TGN-resident proteins across these compartments make them difficult to interpret.

A recent experimental advance circumvented some of these issues through the ectopic targeting of TGN-resident golgin proteins to mitochondria, in order to capture retrograde membrane carriers on a completely distinct subcellular compartment (Shin et al., 2020). Investigating the redistributed proteins in the mitochondrial fraction provided insights into the distinct vesicle populations captured by different golgins at the endpoint of the pathway, but for many retrograde cargoes the upstream endosomal mechanisms of capture and incorporation into retrograde membrane carriers remain unclear. An innovative methodology for labelling proteins at the cell surface with a benzylguanine derivative, then covalently conjugating them to a TGN-localised SNAP-tag has also been used to detect novel retrograde cargo proteins. This approach, while highly sensitive, identified only a limited list of 20 retrograde proteins including various integrins and the transferrin receptor, but did not identify validated historical cargoes such as TGN46 and the mannose-6-phosphate receptors (Shafaq-Zadah et al., 2016; Shi et al., 2012).

Proximity-based biotinylation techniques have recently proved to be extremely useful in understanding the subcellular localisation of protein populations (Samavarchi-Tehrani et al., 2020). One method in particular utilises an engineered ascorbate peroxidase enzyme (APEX2) to generate rapid bursts of membrane-impermeable biotin-phenoxyl free radicals that irreversibly tag nearby endogenous proteins (Hung et al., 2016). This technique is therefore able to provide a high spatiotemporal resolution of labelling, compared with other similar techniques, such as BioID and its derivatives, which exhibit excellent spatial signal-to-noise but rely on a longer residency timeframe for proteins to be biotinylated (Sears et al., 2019).

Coupled with streptavidin affinity isolation of biotinylated proteins followed by mass spectrometry, APEX2 labelling has established proteomic maps of a range of subcellular compartments, such as the matrix, intermembrane space and outer membrane of mitochondria, the ER membrane, the synaptic cleft and endosomal membranes (Hung et al., 2017; Lobingier et al., 2017; Loh et al., 2016; Rhee et al., 2013).

4.1.2 Aim

In this chapter, I aim to develop a proximity biotinylation methodology, using either APEX2 or horseradish peroxidase (HRP), to label endogenous TGN-resident proteins. This will be a novel approach, as to my knowledge proximity biotinylation of this kind has yet to be applied to this cellular compartment. I aim to use quantitative proteomics to validate the specificity of protein labelling and assess the suitability of this technique for investigating retrograde endosome-to-TGN cargo recycling. Ultimately, I aim to develop a methodology that is complementary to surface biotinylation, therefore allowing integration with pre-existing proteomic datasets to provide a clearer global picture of the endosomal network as a nexus of cargo sorting within the cell.

4.2 Results

4.2.1 Design of a TGN-Localised Peroxidase Construct

To expand our insight into endosome-to-TGN retrograde cargo recycling, we hypothesised that a proximity biotinylation methodology targeted to the lumen of the TGN could facilitate the unbiased detection of retrograde cargo proteins within their native subcellular environment **(Figure 4.2A)**. A peroxidase-based biotinylation approach would be particularly suited to this objective as the membrane-impermeability of biotin-phenoxyl radicals could mediate extensive labelling of transmembrane cargoes within their luminal/extracellular domains, without labelling soluble and peripherally associated proteins on the cytosolic face of the TGN membrane (Hung et al., 2016).

Four candidate constructs were generated, comprising a peroxidase enzyme (either APEX2 or HRP), targeted to the TGN by fusion to either TGN46 or beta-galactosidase alpha-2,6-sialyltransferase 1 (ST6GAL1) on their luminal termini **(Figure 4.2B)**. TGN46 was chosen as a representative single-pass type I transmembrane protein that predominantly localises to the TGN, and is perhaps the best marker of this dynamic compartment (Luzio et al., 1990). Subpopulations of TGN46 also localise to the plasma membrane, where they can be endocytosed and retrogradely trafficked to the TGN through mechanisms independent of retromer and ESCPE-1 (Kvainickas et al., 2017; Seaman et al., 2009; Simonetti et al., 2017).

Moreover, unlike most retrograde cargoes, TGN46 displays promiscuity in its recruitment to the TGN by the golgin proteins Golgin-97, Golgin-245 and GCC88 (Shin et al., 2020). This redundancy may mitigate the possibility that the HRP-TGN46 probe becomes missorted by targeted perturbations of endosomal recycling machinery. To ensure faithful targeting to the biosynthetic pathway, HRP was inserted after the N-terminal signal peptide of TGN46. Conversely, ST6GAL1 is a single-pass type II *trans*-Golgi enzyme with a short cytosolic tail, that relies on the conserved oligomeric Golgi (COG) and Golgi-associated retrograde protein (GARP) complexes for *trans*-Golgi retention (Khakurel et al., 2020).

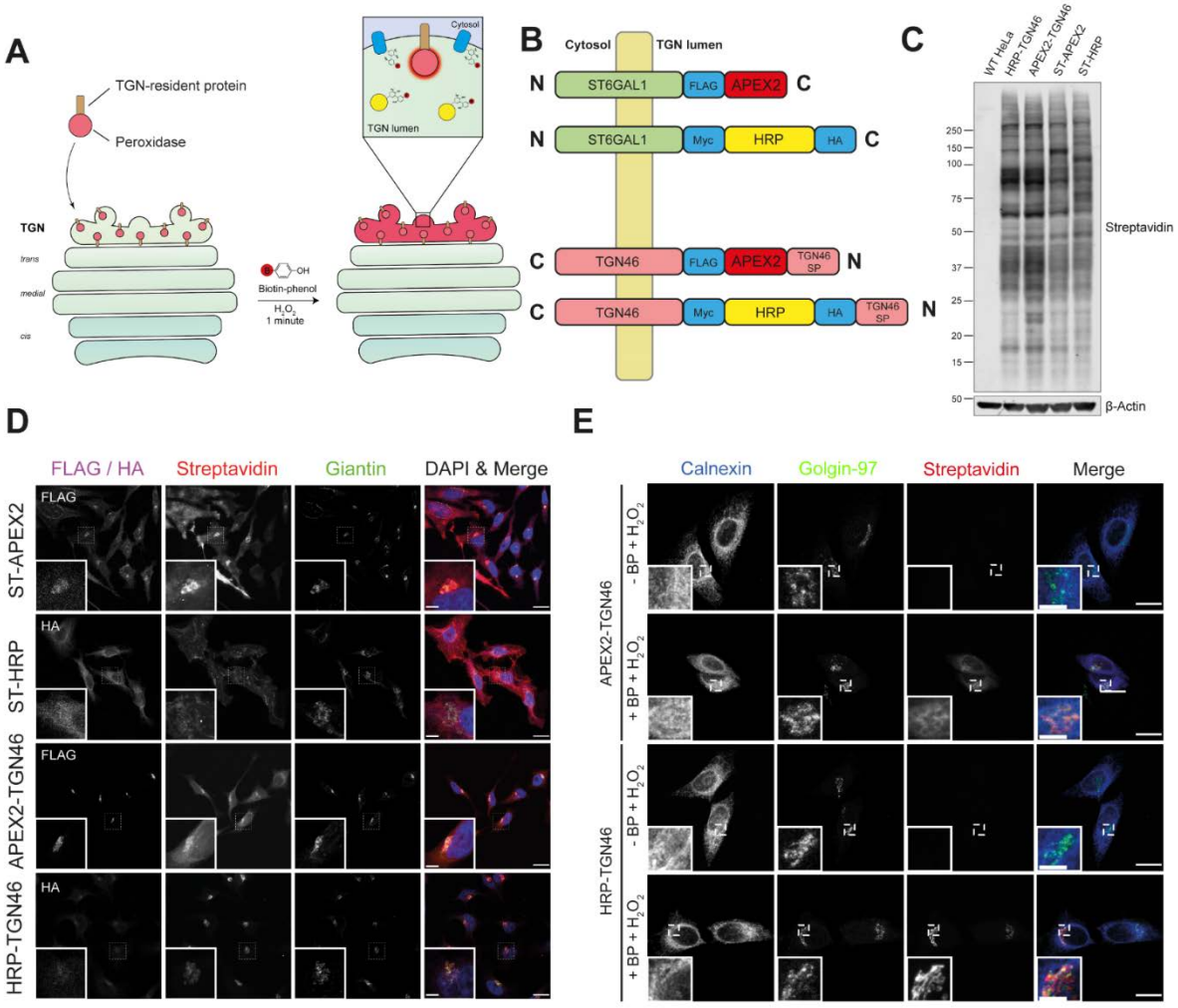

Figure 4.2 Design of a Range of Chimeric TGN-Resident Constructs Linked to Luminal Peroxidase Enzymes

(A) Conceptual schematic of proximity biotinylation to label endogenous TGN-resident proteins. **(B)** Schematic of ST6GAL1- and TGN46-based construct designs. SP = Signal peptide. **(C)** SDS-PAGE of whole cell lysates from HeLa cell lines stably expressing the designed constructs. Total biotinylation was visualised with fluorescent streptavidin labelling. **(D)** Immunofluorescence staining of HeLa cells stably expressing the designed constructs from low viral titres. Biotinylation was performed in the presence of biotin-phenol and H_2O_2, then fixed cells were labelled with streptavidin to visualise biotinylation specificity. Scale bars = 20 µm, 5 µm insets. **(E)** Comparison of APEX2-TGN46 and HRP-TGN46 secretory pathway biotinylation. HeLa stells stably expressing either APEX2-TGN46 or HRP-

TGN46 were biotinylated and labelled with fluorescent streptavidin, anti-calnexin (ER) and anti-Golgin-97 (TGN) antibodies. Scale bars = 20 µm, 5 µm insets.

APEX2 and HRP are both capable of catalysing the generation of highly reactive biotin-phenoxyl radicals for proximity labelling, with HRP reported to exhibit faster reaction kinetics (Lam et al., 2014). A notable difference between the two peroxidases is the sensitivity of HRP to pH, redox potential and calcium concentration, due to the presence of four functionally essential disulphide bonds and two Ca^{2+} binding sites within HRP. Consequently, HRP efficiently folds and retains activity within the oxidising and calcium-rich secretory pathway but fails to assemble in the reducing cytosol and most other cellular environments (Hung et al., 2016). Furthermore, the pH optimum for HRP activity is between 6.0 and 6.5, which fits the slightly acidic nature of the Golgi and TGN (Schomburg et al., 1994). In contrast, the ER is slightly less acidic, with a pH of 7.2 (Paroutis et al., 2004). HRP activity at pH 7.5 is reported to be 84% of its maximum, so HRP is likely to be slightly less efficient in the ER (Schomburg et al., 1994). In brief, the peroxidase-catalysed biotinylation of endogenous proteins involves the incubation of live cells in culture medium supplemented with the membrane-permeable precursor biotin-phenol (BP). Upon the addition of hydrogen peroxide, APEX2 and HRP rapidly generate highly reactive biotin-phenoxyl free radical molecules, which irreversibly tag vicinal proteins with biotin through the formation of covalent bonds with electron dense residues such as tyrosine **(Figure 4.2A)**. Crucially, biotin-phenoxyl radicals are membrane impermeable and therefore should not escape the TGN lumen, and exhibit a very short half-life (< 1 ms) and labelling radius (< 20 nm) (Hung et al., 2016).

These four constructs **(Figure 4.2B)** were lentivirally transduced into HeLa cells, and their activity was confirmed by performing a biotinylation reaction with biotin-phenol and H_2O_2, **(Chapter 2.4.3)**, resolving lysates by SDS-PAGE and labelling with fluorescent streptavidin **(Figure 4.2C)**. Cell lines were also validated by confocal microscopy, where intensity and localisation of fluorescent streptavidin and FLAG/HA tag labelling were used as indicators of construct localisation and expression levels **(Figure 4.2D)**. Accordingly, cell lines that were homogenously transduced and expressing low levels of the four candidate constructs were selected. All constructs appeared to exhibit streptavidin labelling colocalising with the Golgi marker Giantin, but the ST6GAL1-based constructs additionally displayed diffuse labelling resembling the plasma membrane, perhaps due to overexpression inducing construct leakage through the secretory pathway. Of the TGN46-based constructs, APEX2-TGN46 labelled the TGN, as defined by colocalisation with the TGN marker Golgin-97, but additionally exhibited colocalisation with the ER marker Calnexin **(Figure 4.2E)**. In contrast, HRP-TGN46 exhibited

a more specific labelling of the TGN with minimal background ER labelling and was therefore selected for further study as the construct with the highest degree of biotinylation specificity.

4.2.2 Analysis of HRP-TGN46 Localisation and Activity

Following selection of HRP-TGN46 as a methodology to biotinylate endogenous TGN proteins **(Figure 4.3A)**, the specificity of streptavidin labelling was further interrogated. Fluorescent streptavidin labelling exhibited colocalisation with Golgin-97, and partial colocalisation with the prototypical retrograde cargo protein CI-MPR, as visualised by confocal and stimulated emission depletion (STED) microscopy **(Figures 4.3B, C and D)**. Moreover, Amplex Red, a precursor chemical that is converted into the red fluorescent dye resourifin by peroxidase enzymes in the presence of H_2O_2, further validated the selectivity of HRP-TGN46 labelling (Martell et al., 2012) **(Figure 4.3E)**.

Peroxidase enzymes have historically been used as reagents for electron microscopy by catalysing the polymerisation of 3,3'-diaminobenzidine (DAB) into electron-dense polymers that produce sensitive contrast when stained with OsO_4 (Martell et al., 2012). Moreover, soluble HRP has previously been used to define the morphology and dynamics of the secretory pathway, displaying strong intralumenal contrast in the ER, Golgi and TGN (Connolly et al., 1994). HeLa cells either lacking or expressing HRP-TGN46 were fixed and incubated with a solution of DAB and H_2O_2 for 10 minutes. In HRP-TGN46-expressing cells, electron density resembling the Golgi/TGN could soon be observed in the perinuclear region by differential interference contrast microscopy, whereas labelling was not observed in untransduced HeLa cells **(Figure 4.4A, Chapter 2.5.4)**. To achieve a higher resolution of HRP-TGN46 labelling, fixed cells were incubated with DAB and H_2O_2 for 10 minutes, then processed for transmission electron microscopy. Again, untransduced HeLa cells displayed no labelling of Golgi cisterna or perinuclear vacuolar compartments (**Figure 4.4B)**. In contrast, HRP-TGN46-expressing cells exhibited clear labelling of Golgi cisterna, in addition to density on the luminal membrane face of pleimorphic structures associated with the Golgi stacks, resembling previously observed soluble HRP labelling (Connolly et al., 1994) **(Figure 4.4C)**. Moreover, small, spherical vesicles peripherally associated with the Golgi stacks of ~50-75 nm in diameter were clearly labelled, possibly representing anterograde/retrograde intra-Golgi carriers. In some cells, DAB density was additionally observed in the nuclear envelope and tubular ER structures, indicating with this more sensitive microscopy approach that despite HRP-TGN46 displaying clear TGN labelling by confocal microscopy, some labelling may still occur in the early secretory pathway**.**

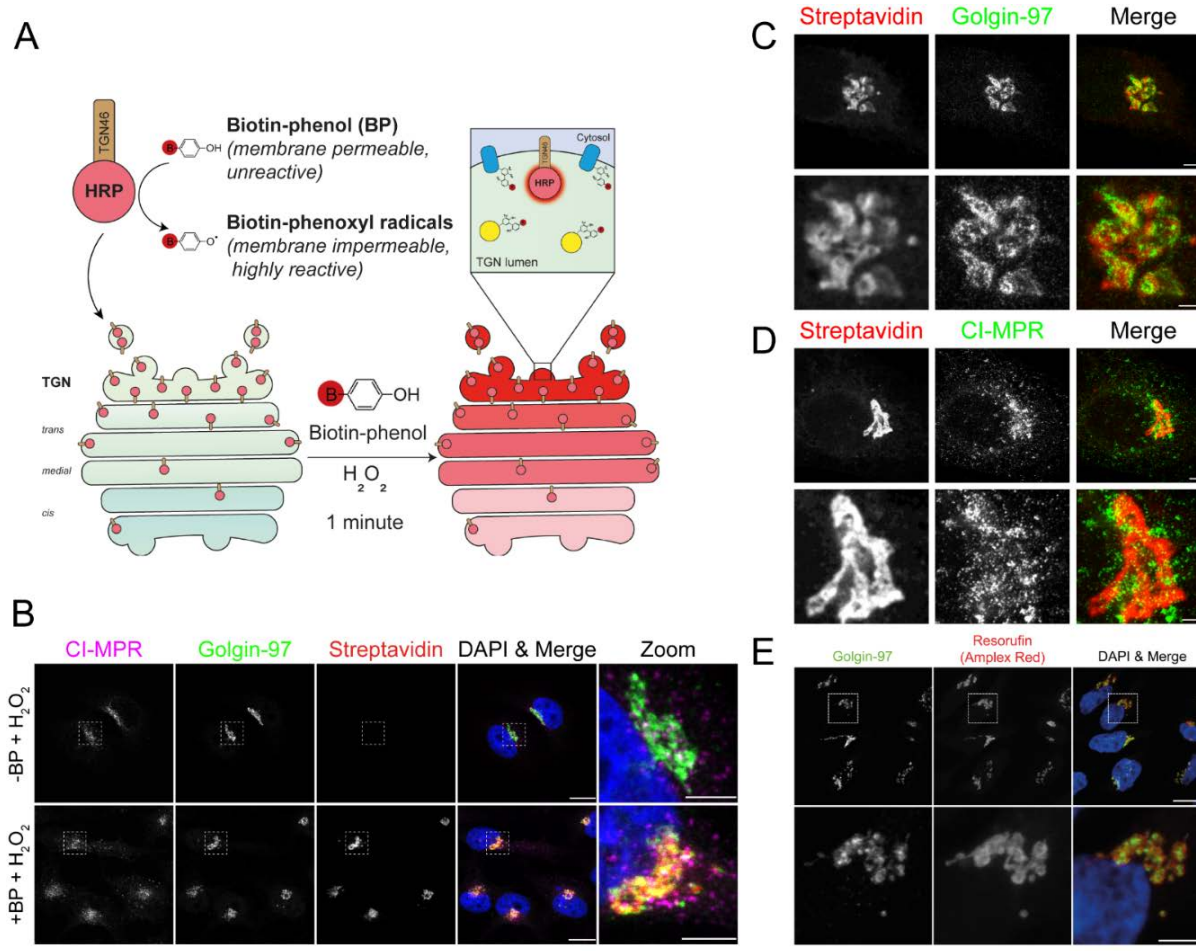

Figure 4.3 HRP-TGN46 Labelling Colocalises with Markers of the TGN

(A) Schematic of HRP-TGN46 biotinylation labelling of endogenous TGN-resident proteins. **(B)** Fluorescent streptavidin labelling of HRP-TGN46-expressing HeLa cells incubated with H_2O_2 in the absence or presence of biotin-phenol. The TGN marker Golgin-97 and retrograde endosomal cargo CI-MPR are labelled by immunofluorescence. Scale bars = 20 µm, 5 µm insets. **(C)** and **(D)** STED microscopy of HRP-TGN46-expressing HeLa cells following biotinylation, stained with fluorescent streptavidin and immunofluorescence labelling of Golgin-97 (C) and CI-MPR (D). Scale bars = 5 µm, 2 µm insets. **(E)** Live HRP-TGN46-expressing HeLa cells were labelled with Amplex Red prior to fixation. Fluorescent resorufin is generated by HRP in the presence of H_2O_2. Scale bars = 20 µm, 5 µm insets.

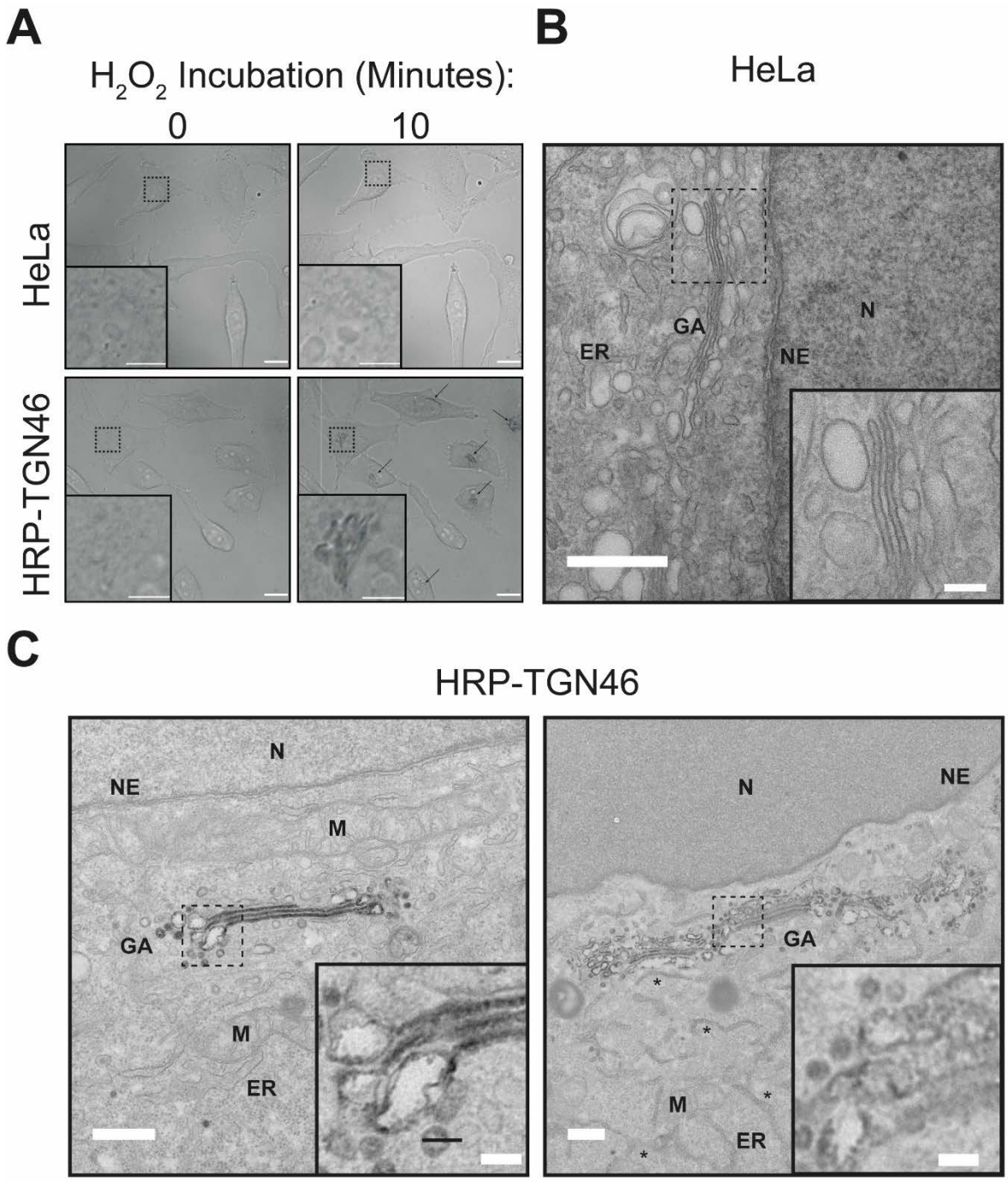

Figure 4.4 Validation of HRP-TGN46 Localisation and Function by Electron Microscopy

(A) Differential interference contrast imaging of HRP-TGN46 expressing cells before and after incubation with DAB and H_2O_2. Arrows indicate electron-dense contrast after 10 minutes localising to the Golgi/TGN. Scale bar: Scale bar: 20 µm, zoom scale bar: 5 µm. **(B)** and **(C)** Transmission electron microscopy of HeLa (B) and HRP-TGN46-expressing (C) cells incubated with diaminobenzidine and H_2O_2 for 10 minutes. Scale bar: 500 nm, zoom scale bar: 100 nm. ER = Endoplasmic Reticulum, GA = Golgi Apparatus, M = Mitochondrion, N = Nucleus, NE = Nuclear Envelope. Asterisks indicate DAB density in the ER.

4.2.3 Validation of HRP-TGN46 Proximity Biotinylation

The molecular weight of HRP-TGN46 was determined by immunoblotting against the HA tag, revealing a specific band of approximately 130 kDa **(Figure 4.5A)**. Streptavidin affinity isolation of whole cell lysates following biotinylation in the presence or absence of H_2O_2 revealed specific labelling of endogenous proteins of the biosynthetic pathway, including the Golgi-localised glycosylation enzyme GALNT2, the retrograde endosomal cargo CI-MPR, and the cell surface proteins integrin-α5 and N-Cadherin **(Figure 4.5B)**. The identification of plasma membrane proteins may represent the labelling within the secretory pathway during transit to the cell surface. Supporting evidence for this notion is provided by the predominant labelling of the higher molecular weight precursor of N-Cadherin, which traverses the secretory pathway prior to proteolytic processing and transport to the cell surface (Wahl et al., 2003), despite the mature isoform being the more abundant in the whole cell lysate input **(Figure 4.5B)**. Moreover, labelling of the precursor isoform of the lysosomal hydrolase Cathepsin D, which navigates the biosynthetic pathway prior to endosomal export, but the absence of its mature lysosomal isoform further emphasised the specificity of labelling to the membrane-bound confines of the biosynthetic pathway (Godbold et al., 1998) **(Figure 4.5B)**.

Finally, the robust identification of Calnexin by HRP-TGN46 confirms a degree of biotinylation occurring within the ER **(Figure 4.5B)**. Upon further confocal microscopy analysis, streptavidin labelling colocalising with Calnexin in addition to Golgin-97 can be observed in visibly 'high-expressing' HRP-TGN46 cells among the heterogenous population that display strong fluorescent streptavidin signal intensity. HRP retains its enzymatic activity after short timepoints of PFA fixation, and ER labelling could still be observed after performing the biotinylation reaction in pre-fixed cells (Hopkins et al., 2000) **(Figure 4.5C)**. ER labelling thus likely reflects the presence of HRP-TGN46 in the early biosynthetic pathway as it undergoes processing and anterograde trafficking, rather than the diffusion of biotin-phenoxyl radicals backwards through the pathway **(Figure 4.5D)**. While background ER labelling effectively lowers the spatial resolution of this proximity biotinylation methodology, originally designed to focus directly on the TGN compartment, the interconnectivity of the biosynthetic pathway makes this by-product difficult to avoid without significantly perturbing cellular function with reagents such as cycloheximide. Importantly, proteins completely unrelated to the biosynthetic pathway, such as cytosolic and mitochondrial proteins, were not labelled by HRP-TGN46 **(Figure 4.5B)**.

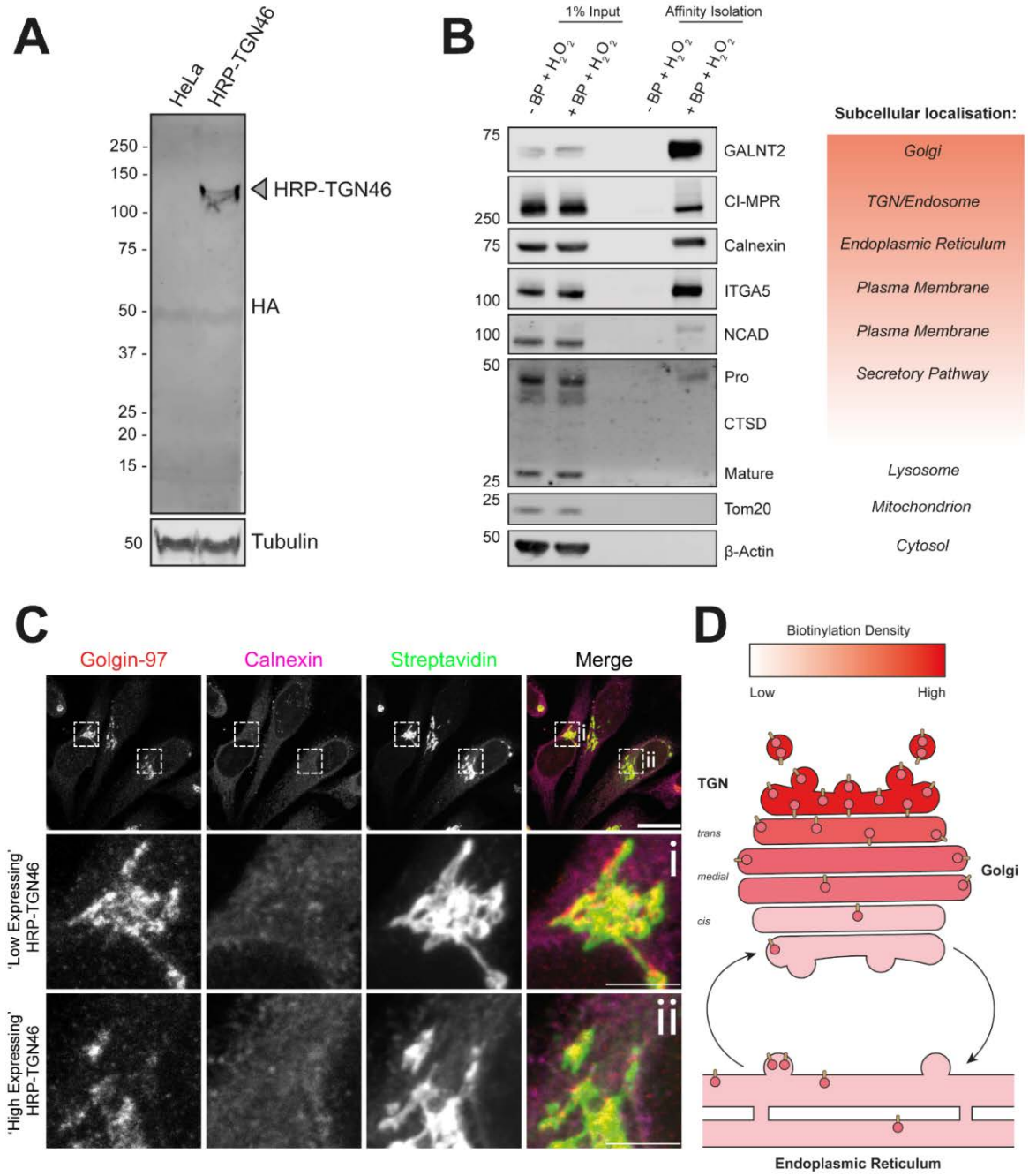

Figure 4.5 Biochemical Validation of Biosynthetic Pathway Labelling by HRP-TGN46

(A) Identification of HRP-TGN46 from concentrated whole cell lysates with an anti-HA antibody. **(B)** Streptavidin affinity isolation of biotinylated proteins from total cell lysate of HRP-TGN46-expressing cells incubated with H_2O_2 in the presence or absence of BP, and their corresponding known subcellular localisation. **(C)** HRP-TGN46-expressing cells were fixed in PFA prior to labelling with BP and H_2O_2. 'Low expressing' cells display minimal visible labelling of the ER, whereas 'high expressing' cells exhibit streptavidin colocalisation with Calnexin. Scale bars = 20 µm, 5 µm zoom. **(D)** Schematic depicting HRP-TGN46 labelling as a gradient across the secretory pathway.

A recent study using HRP for proximity proteomics within intracellular vesicles incubated cells in 50 mM sodium ascorbate during the labelling protocol (Kostelnik et al., 2019). Ascorbate is a membrane impermeable peroxidase substrate, and therefore competitively inhibits labelling at the cell surface (Stoorvogel et al., 1996). To investigate whether plasma membrane proteins identified by HRP-TGN46 were being labelled at the cell surface, the effect of ascorbate incubation on protein labelling was tested. Using a HRP construct extracellularly tagged to the predominantly cell surface-localised transmembrane protein Neuropilin-1 (NRP1-HRP, a gift from Dr Tom Nightingale), ascorbate incubation dramatically reduced the amount of plasma membrane fluorescent streptavidin labelling **(Figure 4.6A)**. Conversely, ascorbate inhibition had no visible effect on HRP-TGN46 labelling, indicating that biotinylation predominantly occurs intracellularly **(Figure 4.6B)**.

To confirm these observations at the biochemical level, streptavidin affinity isolation was used to purify proteins biotinylated by HRP-TGN46 in the presence or absence of 50 mM sodium ascorbate **(Figures 4.6C-I)**. Ascorbate inhibition induced a nearly 25% reduction in both CI-MPR and NRP1 labelling, indicating that a minor fraction of the proteins was being labelled at the cell surface **(Figures 4.6D and 4.6E)**. The labelling of mature N-Cadherin, which is detected at low levels by HRP-TGN46, was more clearly reduced by ascorbate blocking **(Figures 4F and 4.6G)**. Calnexin and GALNT2, which should not reside at the cell surface in abundance, were unaffected by ascorbate inhibition. **(Figure 4.6H and 4.6I)**. Together these data indicate that some HRP-TGN46 labelling occurs at the plasma membrane, but cell surface-localised proteins such as NRP1 are predominantly biotinylated within intracellular compartments.

4.2.4 Defining the HRP-TGN46 Proximity Proteome

To establish an extensive profile of proteins labelled by HRP-TGN46 proximity biotinylation, stable isotope labelling of amino acids in cell culture (SILAC) was employed to sensitively quantify the abundance of proteins enriched following streptavidin affinity isolation by mass spectrometry **(Chapter 2.6.1)**. HeLa cells either lacking or expressing HRP-TGN46 were grown in three different isotopically-labelled media conditions: light (R_0K_0), medium (R_6K_4), and heavy ($R_{10}K_8$), then labelled in the presence or absence of H_2O_2 **(Figure 4.7A)**. Accordingly, only the medium condition, comprising HRP-TGN46-expressing cells incubated with both biotin-phenol and H_2O_2 demonstrated streptavidin labelling by SDS-PAGE and confocal microscopy **(Figures 4.7A and 4.7B)**. The SILAC approach was independently repeated 5 times in order establish a comprehensive list of proteins biotinylated by HRP-TGN46. The heavy SILAC condition, (untransduced HeLa cells incubated with both biotin-phenol and H_2O_2) displayed an enrichment of 10 proteins over the light condition (HRP-

TGN46-expressing cells lacking biotin-phenol) some of which were endogenous biotin-binding proteins **(Figure 4.7D)**. These proteins were assumed to be false positives and removed from subsequent analysis.

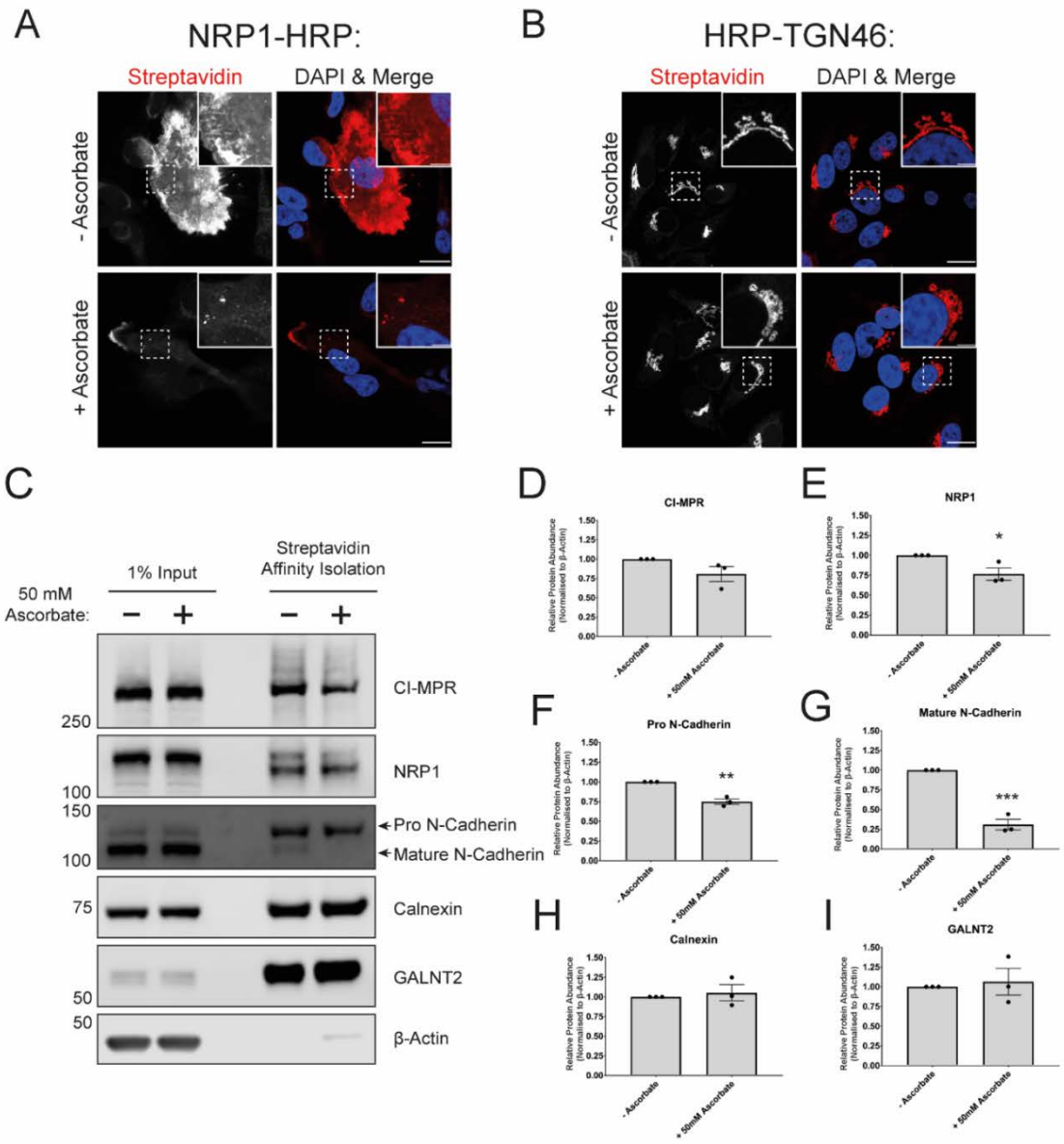

Figure 4.6 HRP-TGN46 Biotinylation in the Presence of Ascorbate Blocks Cell Surface Labelling

(A) and **(B)** Confocal microscopy of HeLa cells expressing either NRP1-HRP **(A)** or HRP-TGN46 **(B)**, labelled in the absence or presence of 50 mM sodium ascorbate and stained with fluorescent streptavidin. Scale bar = 20 µm, inset = 5 µm. **(C)** Representative streptavidin affinity isolation of biotinylated proteins labelled by HRP-TGN46 in the absence or presence of 50 mM sodium ascorbate. **(D-I)** Quantification of marker protein abundances following streptavidin pulldown in the presence or absence of 50 mM ascorbate. n = 3, Unpaired t-test: CI-MPR p = 0.1148, NRP1 p = 0.0385, Calnexin p = 0.6413, GALNT2 p = 0.7253, Pro N-Cadherin p = 0.0018, Mature N-Cadherin p = 0.0005.

591 proteins were significantly enriched by HRP-TGN46 labelling only in the presence of biotin-phenol (log_2 fold change > 2, $p < 0.05$), representing proteins reproducibly isolated and quantified by mass spectrometry following HRP-TGN46 labelling **(Figure 4.7E)**. Additionally, 656 proteins were robustly quantified in the medium condition in ≥ 4 independent repeats but were not identified in the negative control condition omitting biotin-phenol, and therefore no ratiometric comparison could be calculated. When compared based on protein abundance and coverage, proteins that were abundantly quantified with a higher peptide coverage were more likely to be identified in the negative control condition, where they likely constituted part of the whole cell lysate 'carry-over' between bead washes in the streptavidin affinity isolation protocol **(Figure 4.7F)**. Low abundance proteins, however, were less likely to be detected in the negative control, hence providing no statistical measure of enrichment. Inspection of this list of ratio-lacking proteins revealed that it was populated with proteins validated as localising to the biosynthetic pathway. As these proteins were therefore likely to be true vicinal targets of HRP-TGN46, these two protein groups were combined to produce a list of 1247 proteins considered to be reproducibly enriched by proximity biotinylation and together considered the HRP-TGN46-labelled proteome **(Table 4.1)**.

Unbiased gene ontology analysis of the HRP-TGN46-labelled proteome highlighted a significant enrichment of cellular component categories corresponding to the biosynthetic pathway and the interface of the TGN with the endolysosomal network; including 'Endoplasmic Reticulum' (386 proteins), 'Golgi Apparatus' (308 proteins), 'Lysosome' (133) proteins, 'Plasma Membrane' (563 proteins), and 'Endosome' (125 proteins) **(Figures 4.8A and 4.8B, Table 4.2)**. 34 proteins were annotated as TGN residents. Nuclear proteins, which are not expected to be labelled by HRP-TGN46, were significantly underrepresented in the proteome, emphasising the specificity of labelling. Moreover, biological processes pertaining to biosynthetic pathway function were highly enriched in the proteome, including 'Protein Glycosylation' (46 proteins), 'Cell Adhesion' (67 proteins), 'Protein Folding' (30 proteins), and 'Golgi Vesicle Transport' (29 proteins) **(Figure 4.8C, Table 4.3)**. To further validate specificity, the HRP-TGN46-labelled proteome was compared with the previously published APEX2-labelled proteomic profiles of the mitochondrial matrix and intermembrane space (Hung et al., 2014; Rhee et al., 2013), highlighting a 4% and 10% representation of these proteomes, respectively **(Figure 4.8D)**. A recent study utilised sensitive affinity chromatography to unbiasedly characterise a list of 35 mannose-6-phosphate tagged glycoproteins in HeLa cells (Čaval et al., 2019). As an estimation of coverage of these proteins, which reside in the TGN during their processing, 26 (74%) were identified in the HRP-TGN46-labelled proteome **(Figures 4.8E and 4.8F, Table 4.4)**. Moreover, validated retrograde cargo proteins, such as

Furin, CI-MPR, CD-MPR (M6PR), SORT1 and SORL1 were all enriched in the proximity proteome **(Figure 4.8E)**.

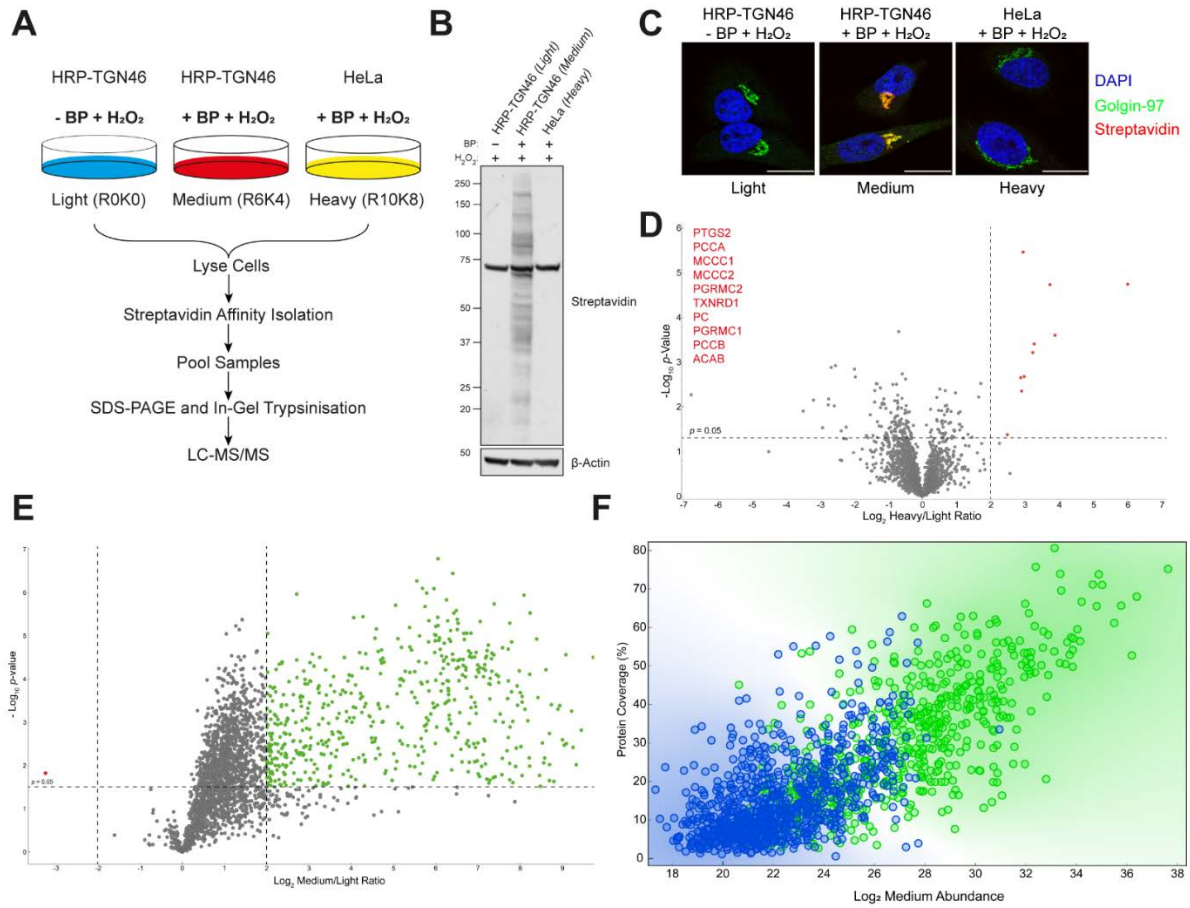

Figure 4.7 Defining the HRP-TGN46-Labelled Proteome

(A) Schematic of SILAC experimental design to label the HRP-TGN46 proximity proteome. **(B)** Validation of construct expression and biotinylation efficiency by Western blotting of whole cell lysate samples. **(C)** Confocal microscopy of HRP-TGN46-expressing or WT HeLa cells incubated in SILAC medium and incubated with H_2O_2 in the presence or absence of BP as indicated in (A). Scale bars = 20 µm. **(D)** Volcano plot of proteins altered between the 'heavy' and 'light' SILAC conditions. Proteins coloured in red were significantly enriched ($p < 0.05$) in the 'heavy' condition. Protein names listed in red are either direct biotin-binding proteins, or components of a biotin-binding protein complex. **(E)** Volcano plot of proteins altered between the 'medium' and 'light' conditions. Proteins coloured in green were significantly enriched ($p < 0.05$) by TGN46-HRP biotinylation. n = 5 independent repeats. **(F)** Scatter plot comparing proteins that were significantly enriched in the medium condition (green) and proteins that were quantified in ≥ 4 independent repeats with no calculatable ratio (blue) based on their medium condition abundances and protein coverage. n = 5 independent repeats.

To explore the potential for HRP-TGN46 labelling as a discovery tool, 'orphan' proteins within the dataset were identified that had, to my knowledge, no pre-existing evidence of subcellular localisation according the Uniprot database. As examples, antibodies recognising endogenous KIAA2013, an uncharacterised single-pass transmembrane protein, and TMCO3, a probable ion multi-pass antiporter, were both found to colocalise with Golgin-97, highlighting the potential of the HRP-TGN46 proteome as a discovery tool to annotate proteins in the

biosynthetic pathway **(Figure 4.8G)**. It should be noted that, since performing this experiment, KIAA2013 has been validated as a Golgi-localised protein on the Protein Atlas database (Uhlen et al., 2015).

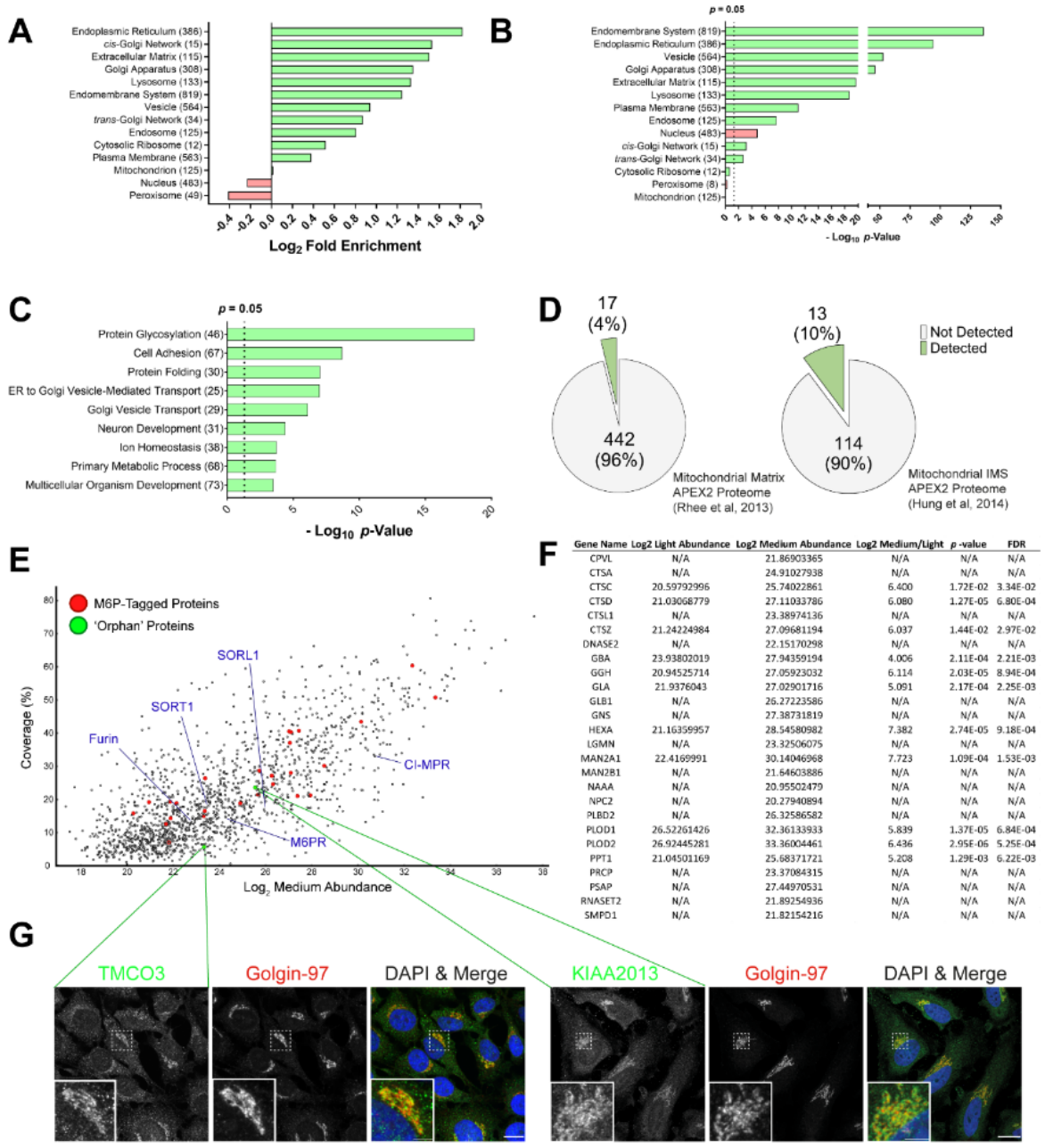

Figure 4.8 Analysis of the HRP-TGN46-Labelled Proteome

(A) and **(B)** Graphical representation of overrepresentation of cellular compartments within the HRP-TGN46-proteome according to their calculated or fold-enrichment (A) and p-value (B). Overrepresented gene ontology terms are coloured green, and underrepresented terms are coloured red. Brackets represent the number of identified proteins belonging to each category. **(C)** Graphical representation of the top 10 most significantly enriched gene ontology biological process categories in the HRP-TGN46-labelled proteome, ranked by p-value. Brackets represent the number of identified proteins belonging to each category. **(D)** Pie chart presentation of overlap between the

HRP-TGN46-labelled proteome (green), with the previously published APEX2 proximity proteomes of the mitochondrial matrix and intermembrane space. **(E)** Scatter plot of all HRP-TGN46 labelled proteins, with known mannose-6-phosphate-tagged proteins overlaid in red, example TGN retrograde cargoes highlighted by blue labels, and representative 'orphan' proteins in green. n = 5 independent repeats. **(F)** Table of mannose-6-phosphate-tagged proteins identified by HRP-TGN46 labelling, with raw abundance and ratiometric values displayed. Proteins that were not identified in the 'light' condition but were quantified in ≥ 4 independent repeats in the 'medium' condition were considered significant. **(G)** Immunofluorescence staining and confocal microscopy of two candidate 'orphan' proteins identified from the HRP-TGN46 dataset Scale bars = 20 µm, 5 µm zoom.

4.3 Discussion

In this chapter, I have established HRP-TGN46 proximity biotinylation as a methodology for labelling endogenous proteins within the TGN and wider secretory pathway. Analysis of the proteins reproducibly identified by quantitative mass spectrometry revealed a broad yet specific proteome, encompassing the secretory pathway and including the main compartments of interest for the study of retrograde endosomal recycling.

4.3.1 A Methodology to Label Endogenous Proteins Within the Biosynthetic Pathway

Like most approaches aimed at scrutinising the highly pleiomorphic and dynamic TGN compartment, this methodology has associated caveats. Mainly, HRP-TGN46 appears to label the entire biosynthetic pathway leading to the TGN, despite attempts to express the construct at low levels. This echoes historical problems with effectively resolving the compartments of the secretory pathway by ultracentrifugation. An additional limitation is that TGN46, itself a retrograde cargo, invariably passes through the plasma membrane and endosomal compartments to some degree and may label proteins there. Confocal and electron microscopy validation has established that labelling occurs most strongly in the TGN compartment, with some plasma membrane labelling occurring. Endosomal labelling was not observed, although labelling may occur below visible thresholds. Such 'off-target' labelling at the cell surface or endosomal network may therefore reduce the resolution of the proximity proteome, but do not appear to be primary sites of biotinylation.

The described methodology also provides a range of advantages compared to other similar methods of isolating or labelling TGN-resident proteins. While less specific, the proteome established in this chapter is far more expansive than the proteins labelled by SNAP-tagging (Shi et al., 2012). Moreover, HRP-TGN46 labelling does not only measure the localisation of proteins internalised from the cell surface, but also includes proteins that intracellularly cycle between the TGN and endosomal compartments, such as acid hydrolase receptors. HRP-TGN46 labelling is also a faster and more convenient methodology compared to differential centrifugation, once cell lines are established and validated, which will be beneficial when

screening various recycling complexes for retrograde cargoes. Taken together, the development of this method will allow me to begin to investigate retrograde endosomal recycling in molecular detail, beginning with the cargo-selective role of ESCPE-1.

4.3.2 Alternative Uses of HRP-TGN46 as a Tool to Investigate Secretory Pathway Biology

In addition to the usage of HRP-TGN46 labelling to investigate mechanistic retrograde endosomal recycling, there are other areas of research that could benefit from this methodology. In addition to the two 'orphan' proteins validated by immunofluorescence in this chapter, it may be possible to assign more proteins to the biosynthetic pathway that have previously undefined subcellular localisations. For poorly characterised proteins with disease-associated mutations, this subcellular localisation could be of biological interest. It will also be interesting to compare the proximity proteomes of various TGN-resident proteins, in addition to TGN46. Such comparison may provide additional proteomic insights into how the TGN is sub-compartmentalised to sort cargo to different destinations within the cell (Stalder and Gershlick, 2020).

Moreover, the HRP-TGN46-labelled proteome could be conceivably refined further to home in on the TGN compartment. For example, by tagging HRP into the ER and early Golgi compartment and obtaining a proteomic profile of these subcellular localisations, the resulting datasets could be used to filter proteins out of the HRP-TGN46 proteome. This approach could potentially enrich TGN-resident proteins with clearer signal-to-noise. A HRP construct tagged with a KDEL sequence was recently used to biotinylate the ER, and could potentially be used for this purpose (Hung et al., 2014). Proximity labelling of the biosynthetic pathway in this way may also be able to provide temporal insights into protein trafficking. For example, combination of proximity labelling with the incubation of compounds or microorganisms that disrupt endosomal or biosynthetic membrane trafficking pathways in live cells, such as the retrograde transport inhibitor retro-2 or the bacterium *Chlamydia trachomatis* which manipulates myriad aspects of Golgi biology, could highlight how these organelles are re-modelled on a scale of minutes to hours (Asrat et al., 2014; Stechmann et al., 2010).

In the timeframe of my PhD project, these potential applications of HRP-TGN46 labelling were not explored further, but remain interesting options for the future. In the next chapter, I will apply this methodology to address biological questions pertaining to retrograde endosomal recycling.

Chapter 5: Designing a HRP-TGN46-based Proteomic Screen to Identify Novel Retrograde Cargoes for ESCPE-1

5.1 Introduction

In **Chapter 4**, I described the development of a methodology for labelling endogenous proteins within their native environment of the biosynthetic pathway. To apply this approach to obtain new insights into endosomal membrane trafficking, I chose to focus on retrograde recycling performed by ESCPE-1, a recently characterised cargo-selective sorting complex. A surface biotinylation screen has identified 61 transmembrane proteins whose steady-state plasma membrane residence is dependent on ESCPE-1 sequence-dependent recycling (Simonetti et al., 2019). However, besides the well-characterised CI-MPR cargo, our understanding of retrograde sequence-dependent ESCPE-1 trafficking remains limited.

5.1.1 Biochemical Characterisation of Sequence-Dependent Cargo Recruitment by ESCPE-1

Following the identification of SNX5, SNX6 and SNX32 as cargo selective components of the SNX-BAR endosomal recycling complex, now referred to as ESCPE-1, the biochemical mechanism underpinning cargo recruitment was elucidated **(Chapter 1.3.6)** (Simonetti et al., 2019; Yong et al., 2020). SNX5, SNX6 and SNX32 contain a helical insertion within their PX domains that is not present in their counterpart subunits SNX1 or SNX2 (Teasdale et al., 2001). A lipid-binding screen of sorting nexin PX domains revealed that SNX5, SNX6 and SNX32 are unable to bind phosphoinositides (Chandra et al., 2019). This specialised PX domain is therefore likely to have functionally diverged from its lipid binding role, and SNX5, SNX6 and SNX32 rely on dimerisation with either SNX1 or SNX2, which contain canonical phosphoinositide-binding PX domains, for recruitment to endosomal membranes (Chandra et al., 2019).

Structural and biochemical data revealed that the cytosolic tail of CI-MPR forms a β-hairpin structure that directly binds the specialised PX domain of SNX5 **(Figure 1.6)**. Specifically, the tail of CI-MPR forms a β-hairpin encoding two binding sites, termed βA and βB, interspaced by a flexible linker that does not contact SNX5 (Simonetti et al., 2019). The identification and sequence analysis of additional ESCPE-1 cargos conforming to this binding mode, including IGF1R and SEMA4C, facilitated the refinement of the βA motif into a consensus sequence - ΦxΩxΦ – whereby Φ represents a hydrophobic residue, and Ω constitutes a central aromatic residue. The hydrophobicity of this sequence allows the docking of the β-sheet into a hydrophobic groove comprised of the unique amino acids in the SNX5/6/32 PX domains, and the central aromatic residue forms a key stacking interaction with the F136 residue of SNX5 (or F137 in SNX6). The βB sequence, which is folded back by the hairpin into direct proximity to the βA motif, appears to be more variable, with hydrophobicity providing the key contribution

to affinity (Simonetti et al., 2019). Moreover, this conserved binding conformation is exploited by the intracellular pathogen *Chlamydia trachomatis* and its effector protein IncE, which recruits ESCPE-1 to intracellular inclusion membranes to promote survival (Paul et al., 2017). Taken together, this allowed the refinement of the SNX5/6/32 consensus binding site as ΦxΩxΦx$_n$Φ, whereby x$_n$[OBJ:OBJ].

An additional recent study confirmed the direct SNX5-CI-MPR interaction by isothermal titration calorimetry and nuclear magnetic resonance (NMR) spectroscopy (Yong et al., 2020). Moreover, no direct binding affinity between retromer, or a SNX3-retromer complex and CI-MPR could be observed, highlighting ESCPE-1 as a key cargo-selective mediator of CI-MPR retrograde trafficking. Further analysis led to the bioinformatic prediction of two SNX5/6/32-binding motifs: Ψx[FY]x[RK] and Ωx[FY], whereby Ψ and Ω denote aliphatic and aromatic hydrophobic amino acids, respectively (Yong et al., 2020). These motifs are similar, but slightly distinct to the ΦxΩxΦx$_n$Φ consensus, perhaps indicating some variability in cargo binding mechanisms.

5.1.2 The Enigmatic Role of ESCPE-1 in Retrograde Recycling

Despite the initial discovery of SNX-BAR proteins as components of the yeast pentameric retromer complex, and the now emerging role of ESCPE-1 in sequence-dependent recycling, there remains a limited understanding of cargo proteins transiting through the endosome-to-TGN retrograde pathway. At present CI-MPR remains the only biochemically characterised cargo that is selectively recycled by ESCPE-1 through this pathway, with other receptors such as IGF1R seemingly undergoing ESCPE-1-mediated endosome-to-plasma membrane recycling (Simonetti et al., 2019). In addition, the number of retrograde cargoes reliant on other recycling complexes, such as the retromer cargo SorLA or the SNX3-retromer cargo Wntless, also remains limited (Fjorback et al., 2012; Harterink et al., 2011). It is possible that given this conserved retrograde recycling mechanism, considerably more cargo proteins are likely to be actively recycled by complexes such as ESCPE-1 but have eluded detection due to trafficking assays incompletely resolving this pathway.

5.1.3 Aim

In this chapter, I aim to further extend the HRP-TGN46 labelling methodology developed in **Chapter 4** by identifying novel ESCPE-1 dependent cargoes, and thereby expand the biological significance of ESCPE-1-mediated retrograde cargo sorting. Furthermore, I aim to extend this methodology to begin to investigate other potentially cargo selective SNX-BAR complexes and their roles in retrograde sorting.

5.2 Results

5.2.1 ESCPE-1 is a Cargo-Selective Endosomal Sorting Complex for Retrograde Transport

The recent characterisation of the mechanism of SNX5/6 engagement of cargo through the hydrophobic PX domain provided new insights into ESCPE-1 cargo sorting **(Figure 5.1A)**. Comparative proteomics of GFP-SNX5 versus GFP-SNX5 F136D, which introduces negative charge into the hydrophobic pocket and thus impairs cargo recruitment, highlighted a suite of proteins selectively immunoprecipitated by GFP-SNX5; including CI-MPR, IGF1R, SEMA4C and TMEM230 (Simonetti et al., 2019). TMEM230 is an attractive candidate for a putative retrograde cargo protein, due to its reported localisation in the TGN, and the identification of *TMEM230* mutations in familial Parkinson's disease (Deng et al., 2016). TMEM230 also colocalises with retromer-positive endosomal compartments, and Parkinson's disease mutants enhance CI-MPR degradation, implicating a role for TMEM230 in regulating endolysosomal biology (Kim et al., 2017).

To validate the role of ESCPE-1 in retrograde sorting of TMEM230, wild-type HeLa cells or a clonal SNX5+6 double KO HeLa cell line (previously validated in Simonetti et al., 2017) were stained for CI-MPR and TMEM230 localisation. TMEM230 antibody staining labelled vesicular compartments throughout the cell, but predominantly labelled a perinuclear compartment colocalising with TGN46 **(Figure 5.1B)**. SNX5+6 KO caused a significant depletion of this TGN46-colocalising pool of TMEM230, similarly to the established cargo CI-MPR, highlighting TMEM230 as a retrograde cargo for ESCPE-1 **(Figure 5.1C)**. Unlike CI-MPR, TMEM230 did not clearly accumulate on a particular endosomal compartment once dispersed from the TGN.

Before moving onto using HRP-TGN46 labelling to screen for additional ESCPE-1 retrograde cargoes, the independence of TGN46 from ESCPE-1-dependent trafficking was validated. TGN46 contains a ^{410}IAFVL^{414} cytosolic sequence that could potentially conform to a βA SNX5/6/32 binding motif, although efficient retrograde trafficking has been shown to primarily depend on the transmembrane domain and a ^{428}SDYQRL^{433} sequence near the C-terminus (Reaves et al., 1998). SNX5+6 KO HeLa cells retained tight colocalisation between TGN46 and Golgin-97, a TGN-resident peripheral membrane protein that does not depend on retrograde recycling for its localisation (Munro, 2011) **(Figure 5.1D)**. These data confirm the suitability of HRP-TGN46 as a probe to investigate ESCPE-1 retrograde trafficking.

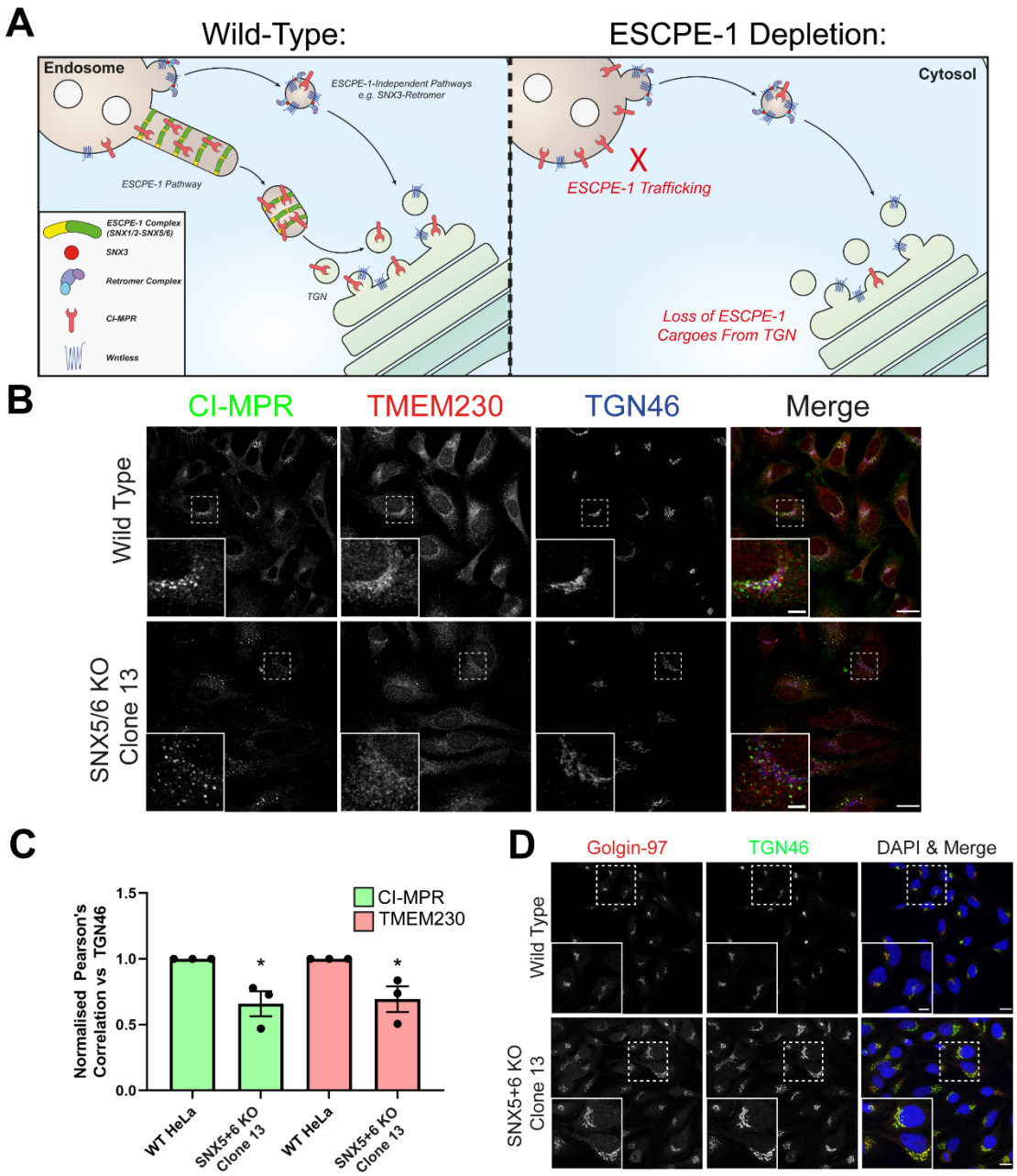

Figure 5.1 ESCPE-1 Selectively Regulates Endosome-to-TGN Traffic of Transmembrane Proteins Including CI-MPR and TMEM230

(A) Schematic overview of ESCPE-1-dependent and -independent retrograde trafficking pathways. Depletion of ESCPE-1 causes a dispersion of CI-MPR to endosomal compartments. See **Figure 1.8** for a more detailed overview of mechanistic retrograde recycling. **(B)** Immunofluorescence imaging of CI-MPR and TMEM230 co-localisation with TGN46 in wild-type and SNX5+6 KO HeLa cells. Scale = 20 µm, insets = 5 µm. **(C)** Normalised Pearson's correlation quantification of CI-MPR and TMEM230 colocalisation with TGN46. Independent experiments were performed with different intensity settings, therefore mean values for each independent repeat were normalised to the WT condition. n = 3, unpaired t-test, CI-MPR p = 0.0234, TMEM230 p = 0.354. **(D)** Confocal microscopy of Golgin-97 and TGN46 colocalisation in WT or SNX5+6 KO HeLa cells. Scale bar = 20 µm, insets 10 µm.

5.2.2 HRP-TGN46 Screening Identifies Potential ESCPE-1 Retrograde Cargoes

A SILAC approach was designed to identify retrograde cargoes for ESCPE-1, comparing HRP-TGN46 biotinylation in Scramble (Scr) siRNA-treated cells, and SNX5+6 siRNA-treated cells **(Figure 5.2A)**. siRNA knockdown (KD) was chosen as a suppression method as it can be performed on large, heterogenous cell populations 2-3 days prior to the experiment, allowing for minimal phenotypic compensation. Moreover, isolating a clonal SNX5+6 KO line by CRISPR-Cas9 may result in different levels of HRP-TGN46 expression to the control cell population, and therefore induce slight changes to biotinylation efficiency between conditions that could bias results. Due to the functional redundancy between SNX5 and SNX6 in cargo recognition, both subunits must be suppressed to perturb ESCPE-1 cargo selectivity (Kvainickas et al., 2017; Simonetti et al., 2017). The neuronal SNX32 paralogue is not expressed in HeLa cells, and therefore SNX5+6 suppression is sufficient to abrogate the cargo-selective binding capacity of ESCPE-1. In the absence of SNX5+6, SNX1 and SNX2 homodimers may still facilitate tubular recycling, although the cargo selectivity of this process will be lost. Double SNX5+6 knockdown of between 50 and 80% was reproducibly achieved, and this level of suppression did not perturb HRP-TGN46 labelling at the whole cell lysate level **(Figures 5.2B-D)**. 4 independent repeats of quantitative SILAC-based proteomic analysis of HRP-TGN46 labelled proteins were performed. The suppression of ESCPE-1 subunits could be confirmed in the resulting pre-filtered proteomic dataset **(Figure 5.2E)**.

The SNX5+6 depletion proteomics dataset was filtered to only include proteins that were considered reproducibly labelled by HRP-TGN46 in **Chapter 4 (Table 4.1)**. The resulting 1073 proteins displayed a normal distribution, although the fold changes in protein abundance were far lower than in **Figure 4.7E** when biotinylated proteins were compared to a control condition with no biotinylation **(Figure 5.3A)**. Based on the data distribution, a fold change threshold of < 1.2 was set, and p-value cut-offs of 0.05 and 0.1 were drawn **(Figure 5.3A)**. Proteins exceeding these thresholds were investigated further and are presented in **Table 5.1**.

76 proteins were depleted beyond the established thresholds in the SNX5+6 siRNA HRP-TGN46-labelled proteome compared to Scramble siRNA-treated cells. Among these hits, gene ontology analysis revealed significant enrichment of exosome, plasma membrane, Golgi apparatus and vesicular proteins **(Figure 5.3B, Table 5.2)**. Moreover, biological processes and molecular functions of proteins involved in cellular adhesion and migration, transmembrane receptor kinase activity and virus receptor activity were significantly enriched **(Figure 5.3B, Tables 5.3 and 5.4)**. Of the 76 identified proteins, 37 proteins were soluble, and 39 were transmembrane **(Table 5.1)**. The topologies of poorly annotated transmembrane

proteins were predicted using the TMHMM 2.0 program (Krogh et al., 2001). Bioinformatic sequence analysis further classified transmembrane proteins based on the presence of cytosolic sequences potentially conforming to a SNX5/6 binding βA ΦxΩxΦ motif, of which 20 proteins were identified **(Figure 5.3C, Table 5.1)**. Based on previous biochemical validation of SNX5/6 cargoes adhering to this motif, these 20 proteins are the most likely to be direct ESCPE-1 cargoes, although in some cases these sequences may not be accessible to cytosolic effector proteins due to secondary structure (Simonetti et al., 2019). Transmembrane proteins lacking a fitting motif may still be valid ESCPE-1 cargoes but may either associate with the complex indirectly, through an unidentified biochemical mechanism, or depend on ESCPE-1 for sequence-independent retrograde trafficking.

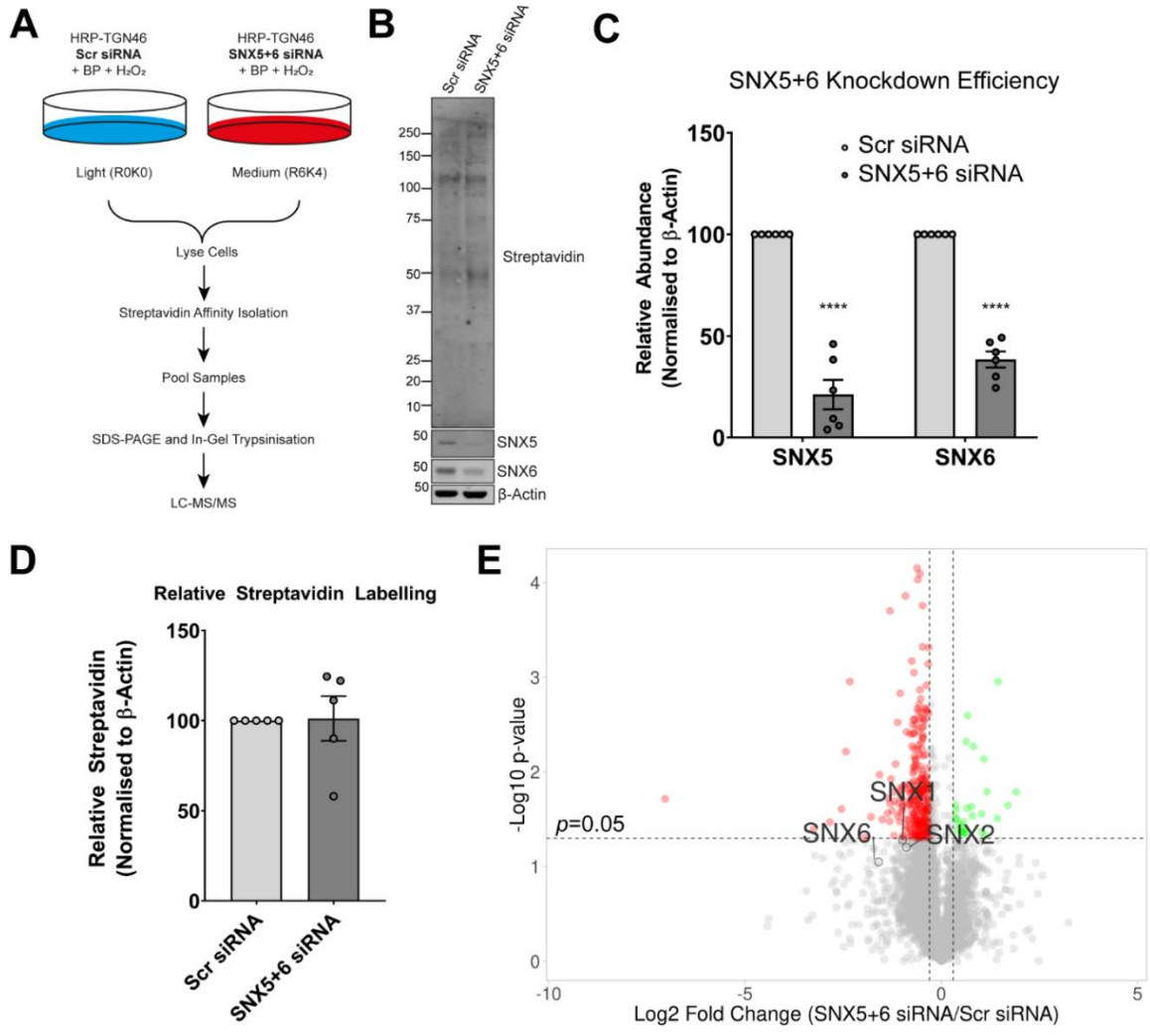

Figure 5.2 Designing a HRP-TGN46 Labelling Screen to Investigate ESCPE-1-dependent Retrograde Trafficking

(A) Schematic of SILAC approach used to elucidate ESCPE-1 dependent cargoes following HRP-TGN46 biotinylation. **(B)** Western blot of whole cell lysates from HRP-TGN46-expressing HeLa cells treated with Scr siRNA or SNX5+6 siRNA. **(C)** Quantification of SNX5+6 knockdown by siRNA, normalised to β-Actin levels. n = 6, 2-way ANOVA with Šídák's multiple comparisons test, $p < 0.0001$ (SNX5), $p < 0.0001$ (SNX6). **(D)** Quantification of total streptavidin labelling normalised to β-Actin

levels. n = 5, unpaired t-test, p = 0.9272. **(E)** Volcano plot of all quantified proteins presented as a fold change ratio of SNX5+6 siRNA treated cells/Scr siRNA treated cells. Thresholds are set at a fold change of Log_2 0.26 (1.2-fold change) and -Log_{10} p-value of 1.3 (p = 0.05). ESCPE-1 components SNX1, SNX2 and SNX6 are labelled. SNX5 was not identified. n = 4 independent experiments.

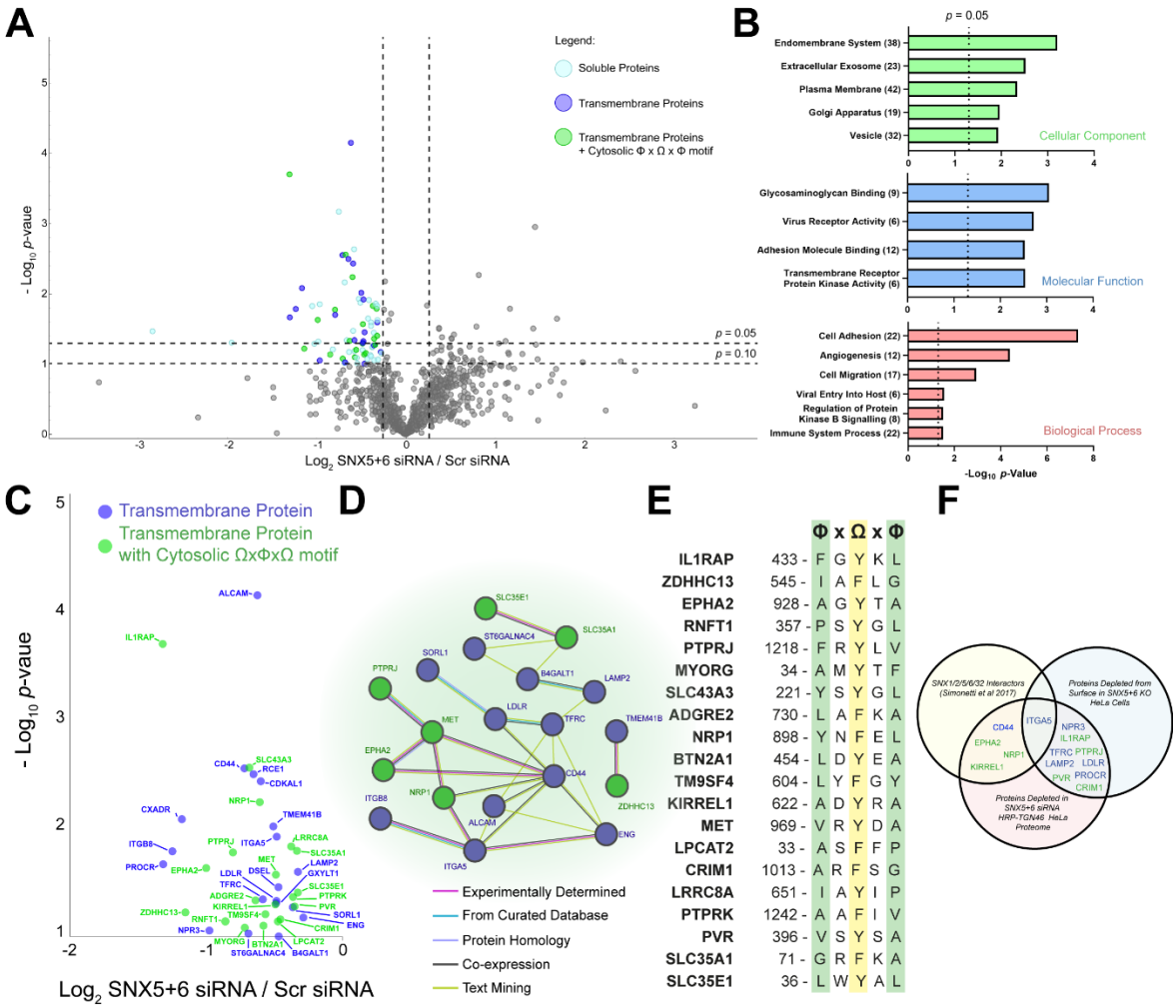

Figure 5.3 ESCPE-1 Suppression Causes a Shift in the HRP-TGN46-Labelled Proteome that Identifies Potential Transmembrane Cargoes

(A) Volcano plot displaying HRP-TGN46 target proteins and their fold change as a ratio of SNX5+6 siRNA abundance/Scr siRNA abundance. 76 proteins are highlighted as passing a p < 0.1 threshold and Log_2 fold change < -0.26, and are classified as 'soluble', 'transmembrane', or 'transmembrane with cytosolic ΦxΩxΦ motif' by colour. **(B)** Gene ontology analysis of the 76 proteins idenitified in (A). Graphs represent the statistical significance of category enrichment, with a dotted line representing p = 0.05. Brackets represent the number of proteins in each category. **(C)** Volcano plot focused into the 39 transmembrane proteins identified in (A). Proteins containing a potential putative SNX5/6 binding motif are coloured green, and those lacking a potential motif are coloured blue. **(D)** STRING network analysis of the 39 transmembrane proteins presented in (C). The legend indicates the level of evidence for each protein-protein association. **(E)** Alignment of potential cytosolic motifs in identified proteins conforming to a ΦxΩxΦ consensus sequence. Only one candidate motif is displayed for each protein, for proteins with multiple candidate motifs, the sequences are presented in **Table 5.1**. **(F)** Venn diagram displaying the overlap of established ESCPE-1 interactors and proteins depleted from the cell surface in SNX5+6 KO cells with the 76 ESCPE-1-dependent proteins identified in (A) (Simonetti et al., 2017).

STRING network analysis of depleted transmembrane hits revealed a cluster of proteins with varying degrees of association evidence **(Figure 5.3D)**. Notably, an experimentally determined network of Neuropilin-1 (NRP1) and its interaction partners integrin-α5 (ITGA5) and the receptor tyrosine kinase (RTK) MET was identified, with the cluster extending further to include the RTK EphA2, the tyrosine phosphatase PTPRJ, CD44 and integrin-β8 (ITGB8). Within this network, NRP1, MET, EphA2 and PTPRJ contain putative cytosolic SNX5/6-interacting motifs **(Figure 5.3E)**. As most of the proteins identified as potential ESCPE-1 dependent cargo appear to predominantly be cell surface localised, I compared the overlap between the SNX5+6 KD HRP-TGN46 proteome and a surface biotinylation proteome derived from SNX5+6 KO HeLa cells (unpublished data collected by Dr Boris Simonetti) **(Figure 5.3F)**. 10 of the depleted proteins were also significantly lost from the cell surface, including Integrin-α5, PTRJ and CRIM1. The majority of proteins identified by HRP-TGN46 were not identified from surface biotinylation, highlighting that this is largely a distinct proteomic population. Furthermore, cross referencing this list of proteins with previously identified interactors of the ESCPE-1 components SNX1, SNX2, SNX5, SNX6 and SNX32 by GFP-trap revealed the presence of NRP1, EphA2, CD44 and ITGA5 in these experiments, alongside KIRREL1 (Simonetti et al., 2017) **(Figure 5.3F)**. This network of proteins therefore represented the highest confidence candidates for ESCPE-1 mediated retrograde recycling.

NRP1 is a versatile co-receptor that associates with a diverse range of RTKs and integrin complexes at the cell surface, and can coordinate their signalling, internalisation and intracellular membrane trafficking in response to extracellular cues (Guo and Vander Kooi, 2015). By associating with both RTKs and their extracellular ligands, NRP1 modulates mitogenic signalling; for example by associating with both hepatocyte growth factor (HGF) and its primary receptor MET; and binding of vascular endothelial growth factor A (VEGF-A) and its receptor VEGFR2 (Guo and Vander Kooi, 2015; X. Huang et al., 2019; Zhang et al., 2010). Interestingly cysteine-rich motor neuron 1 protein (CRIM1), another depleted transmembrane protein with a cytosolic ΦxΩxΦ motif, has been reported to act as a VEGFA receptor and modulate VEGFR2 activity (Fan et al., 2014; Wilkinson et al., 2007). NRP1 is also intricately linked to cellular adhesion and motility through its association with α5β1-integrin dimers and coordinates their intracellular trafficking. NRP1 has also been reported to immunoprecipitate integrin-β8, although this interaction was not annotated in the STRING analysis (Hirota et al., 2015) **(Figure 5.3D)**. Accordingly, NRP1 is fundamentally important for a range of developmental processes, including angiogenesis and axonal guidance.

5.2.3 Investigating the Biochemical Basis of NRP1 Recruitment by ESCPE-1 *(experiments performed in collaboration with Dr Boris Simonetti)*

To investigate whether NRP1 directly interacts with ESCPE-1 through a canonical mechanism, the biochemical basis of this association was investigated in further. GFP-SNX5, GFP-SNX6 and GFP-SNX32 immunoprecipitated endogenous NRP1 from HEK293T cells **(Figure 5.4A)**. GFP-SNX1 and GFP-SNX2, which do not have a cargo-selective PX domain, failed to robustly immunoprecipitate NRP1, similarly to CI-MPR **(Figure 5.4A)**. The potential ^{899}YNFEL^{903} SNX5/6 binding motif in the tail of NRP1 is conserved in its homologue Neuropilin-2 isoform a (referred to herein as NRP2) (Rossignol et al., 2000). Accordingly, both NRP1-GFP and NRP2-GFP immunoprecipitated mCherry-SNX5 when co-expressed in HEK293T cells, suggesting that NRP2 may also be an ESCPE-1 cargo **(Figure 5.10B)**. Furthermore, the NRP1 binding interface was narrowed down to its cytosolic tail, which when N-terminally tagged with GFP could immunoprecipitate both mCherry-SNX5 and mCherry-SNX6 **(Figure 5.4C)**. Notably, more mCherry-SNX6 was immunoprecipitated by the NRP1 tail compared to mCherry-SNX5.

To confirm that the PX domain of SNX5/6 is the cargo-selective element that engages NRP1, the association of NRP1 with a chimeric GFP-tagged construct comprising the full sequence of SNX1 with its PX domain swapped for that of SNX5 (GFP-5PX-SNX1) was tested (Simonetti et al., 2019). As previously demonstrated, GFP-SNX1 did not immunoprecipitate NRP1, but when its PX domain was switched with SNX5, NRP1 pulldown was observed **(Figure 5.4D)**. The recently reported crystal structure of SNX5 in complex with a section of the CI-MPR cytosolic tail highlighted F136 as a crucial residue in the SNX5 PX domain that forms a stacking interaction with the central Y2351 residue of the CI-MPR ^{2349}VSYKY^{2353} βA motif (Simonetti et al., 2019). Mutation of this residue to aspartic acid, which disrupts the cargo-selective hydrophobic surface of the PX domain, was sufficient to disrupt binding to CI-MPR, IGF1R, SEMA4C and TMEM230, amongst other cargoes (Simonetti et al., 2019). Accordingly, the SNX5 F136D mutation dramatically disrupted association with NRP1 **(Figure 5.4E)**.

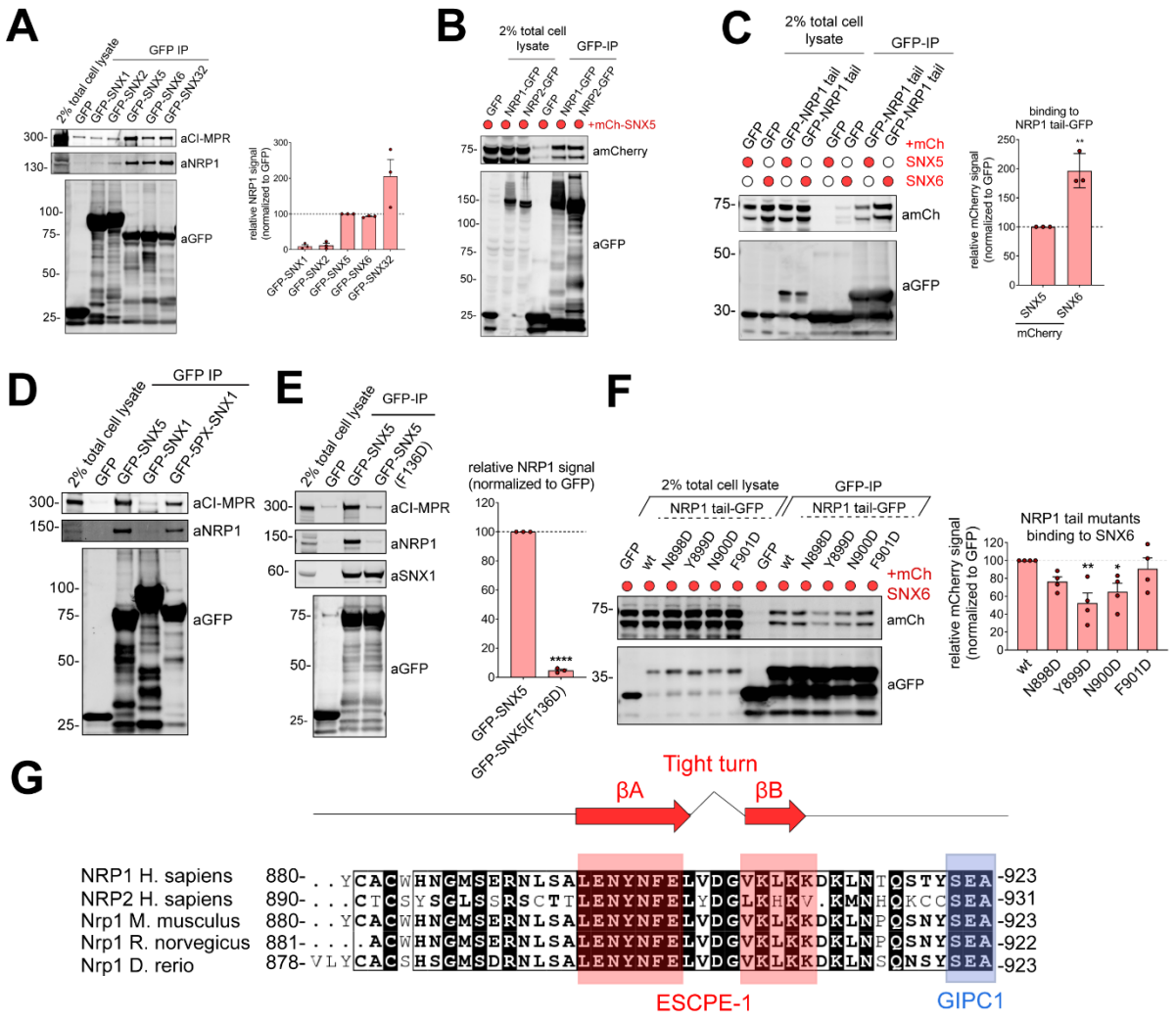

Figure 5.4 Biochemical Validation of the NRP1-SNX5/6 Interaction

(A) GFP-tagged ESCPE 1 subunits were transiently transfected in HEK293T cells, then isolated by GFP nanotrap. Co-immunoprecipitation of endogenous NRP1 was quantified as a normalised fraction relative to the amount pulled down by GFP-SNX5. n = 3 independent experiments. **(B)** GFP, NRP1-GFP and NRP2-GFP were co-expressed with mCherry-SNX5 by transient transfection in HEK293T cells and isolated by mCherry nanotrap. **(C)** GFP or GFP-NRP1 tail were co-expressed with either mCherry, mCherry-SNX5 or mCherry-SNX6 by transient transfection in HEK293T cells and isolated by GFP nanotrap. Co-immunoprecipitation of mCherry-SNX5 and mCherry-SNX6 is presented as a normalised fraction relative to the amount of mCherry-SNX5 pulldown. n = 3 independent experiments, unpaired t-test, p = 0.0048. **(D)** GFP, GFP-SNX5, GFP-SNX1 or a GFP-SNX5/1 chimera comprising SNX1 with the PX domain swapped for the SNX5 PX domain (GFP-5PX-SNX1) were expressed in HEK293T cells and subjected to GFP-nanotrap. Immunoisolates were blotted for endogenous CI-MPR and NRP1. **(E)** GFP, GFP-SNX5 and GFP-SNX5 F136D were transiently transfected in HEK293T cells, then isolated by GFP nanotrap. Co-immunoprecipitation of endogenous NRP1 was quantified as a normalised fraction relative to the amount pulled down by GFP-SNX5. n = 3 independent experiments, unpaired t-test, p < 0.0001. **(F)** GFP, NRP1 tail-GFP and NRP1 tail-GFP constructs with site directed aspartic acid mutagenesis were co-expressed with mCherry-SNX6 by transient transfection in HEK293T cells and subjected to GFP-nanotrap. Co-immunoprecipitation of mCherry-SNX6 constructs is presented as a normalised fraction relative to the amount isolated by WT NRP1 tail-GFP. n = 4 independent experiments. Ordinary one-way ANOVA with Dunnett's multiple comparisons tests, p = 0.2267 (N898D), p = 0.0061 (Y899D), p = 0.0447 (N900D), p = 0.8751 (F901D). **(G)** Sequence alignment of cytosolic tails from human NRP1 and NRP2, and Nrp1 from *M. musculus*, *R. norvegicus* and *D. rerio*. Indicated βA and βA motifs are

highlighted in red, and the C-terminal GIPC-binding PDZ binding motif is highlighted in blue. Data in this figure were collected by Dr Boris Simonetti.

Isothermal titration calorimetry established that a synthetic peptide comprising the NRP1 cytosolic tail residues (^{894}SALENYNFELVDGVKLKKDKLNTQS ^{918}) directly bound to recombinant SNX5 and SNX6, with affinities of 19.8 μM and 14.3 μM respectively (unpublished data in collaboration with Professor Brett Collins, data not shown). To identify the NRP1 sequence responsible for this direct binding, a site-directed mutagenesis screen across the ^{898}NYNF^{901} sequence of cytosolic tail was performed, where either Y899 or F901 could comprise a central aromatic residue interacting with SNX5/6. Residues were mutated to aspartic acid residues to disrupt hydrophobicity. Of these substitutions, Y899D gave the most pronounced perturbation in immunoprecipitation of mCherry-SNX6, a 48% decrease **(Figure 5.4F)**. These data suggest that Y899 is likely to form a central stacking interaction with the F136 residue of SNX5 (or the F137 residue of SNX6) (Simonetti et al., 2019). The SNX5/6-interacting βA motif is therefore likely to span ^{896}LENYNF^{901} as a ΦxxΩxΦ sequence, with Y899 forming the critical hydrophobic stacking interaction, which is a slight variation from the predicted ΦxΩxΦ consensus.

Structural analysis of ESCPE-1 cargoes has demonstrated that the hydrophobic βB sequence downstream of the βA motif folds back into a β-hairpin structure that enhances cargo binding to SNX5 (Simonetti et al., 2019). This is demonstrated by the cytosolic tails of CI-MPR and SEMA4C, whereby short ^{2368}EWLMEEI^{2374} and ^{743}LKI^{745} sequences respectively contribute to hydrophobic interactions with residues Y132, L133 and F136 of SNX5 (Simonetti et al., 2019). The C-terminal sequence downstream of the ^{896}LENYNF^{901} motif in NRP1 was therefore assessed for regions of hydrophobicity potentially corresponding to a βB motif. A short hydrophobic ^{907}VKL^{909} sequence in the NRP1 tail could represent a candidate βB motif, which may be slightly varied to ^{916}LKHKV^{920} in the NRP2 tail **(Figure 5.4G)**. Both potential βA and βB motif regions of the NRP1 tail are remarkably well conserved across vertebrates. Taken together, these data identify NRP1 as a direct endosomal cargo for SNX5 and SNX6, supporting the possibility that this receptor may be retrogradely recycled by ESCPE-1.

5.2.4 Neuropilin-1 Localises to ESCPE-1-Positive Endosomes and the TGN

The membrane trafficking of NRP1 was investigated in further detail. Antibody staining for endogenous NRP1 revealed partial colocalisation with Golgin-97, in addition to plasma membrane and an intracellular pool that did not colocalise with early endosomal markers **(Figure 5.5A)**. In SNX5+6 or SNX1+2 KO clonal HeLa cells, the Golgin-97 colocalisation was reduced, but plasma membrane and vesicular NRP1 staining appeared unaffected **(Figures 5.5A and 5.5B)**. To investigate this potential retrograde trafficking defect in further detail, a construct was cloned comprising GFP tagged to mouse Neuropilin-1 (Nrp1). Mouse and human Neuropilin-1 have highly similar tail sequences, with only two different amino acids that are located away from the ^{896}LENYNF^{901} SNX5/6 binding motif **(Figure 5.4G)**. GFP was inserted after a signal peptide belonging to CI-MPR to ensure membrane insertion of the construct. This produces a N-terminally tagged GFP-Nrp1 construct, with the short cytosolic tail unobstructed engage to intracellular effectors **(Figure 5.5C)**.

Overexpression of the ESCPE-1 cargo CI-MPR is sufficient to cause extensive endosomal membrane tubulation (Simonetti et al., 2017). Co-transfection of GFP-Nrp1 and mCherry-CI-MPR in HeLa cells induced SNX1-positive tubular profiles that colocalised with both GFP and mCherry signal, raising the possibility that these could be retrograde-directed membrane carriers that typically recycle CI-MPR to the TGN **(Figure 5.7D)**. GFP-Nrp1 demonstrates a tripartite subcellular localisation, of plasma membrane, TGN46- and EEA1-positive compartments in HeLa cells **(Figure 5.5E)**. When transfected into SNX5+6 KO HeLa cells, the TGN46-positive pool of GFP-Nrp1 was unperturbed **(Figure 5.5E)**. However, due to the transient overexpression of the construct, it is unclear whether this TGN-localised population represents newly synthesised or actively recycling GFP-Nrp1.

5.2.5 ESCPE-1 Depletion Perturbs Retrograde Neuropilin-1 Recycling

In order to circumvent the issue of distinguishing between newly synthesised and actively recycling GFP-Nrp1 signal, a surface uptake assay was designed. When localised at the plasma membrane, the GFP tag of the GFP-Nrp1 construct faces into the extracellular space. This tag can be labelled with highly specific anti-GFP antibodies in live, unpermeabilised cells, before returning them to culture medium at 37ºC to resume membrane trafficking events **(Figure 5.6A)**. Labelling the anti-GFP antibody by indirect immunofluorescence therefore only indicates the subcellular localisation of GFP-Nrp1 molecules that have been internalised from the cell surface **(Chapter 2.5.2)**.

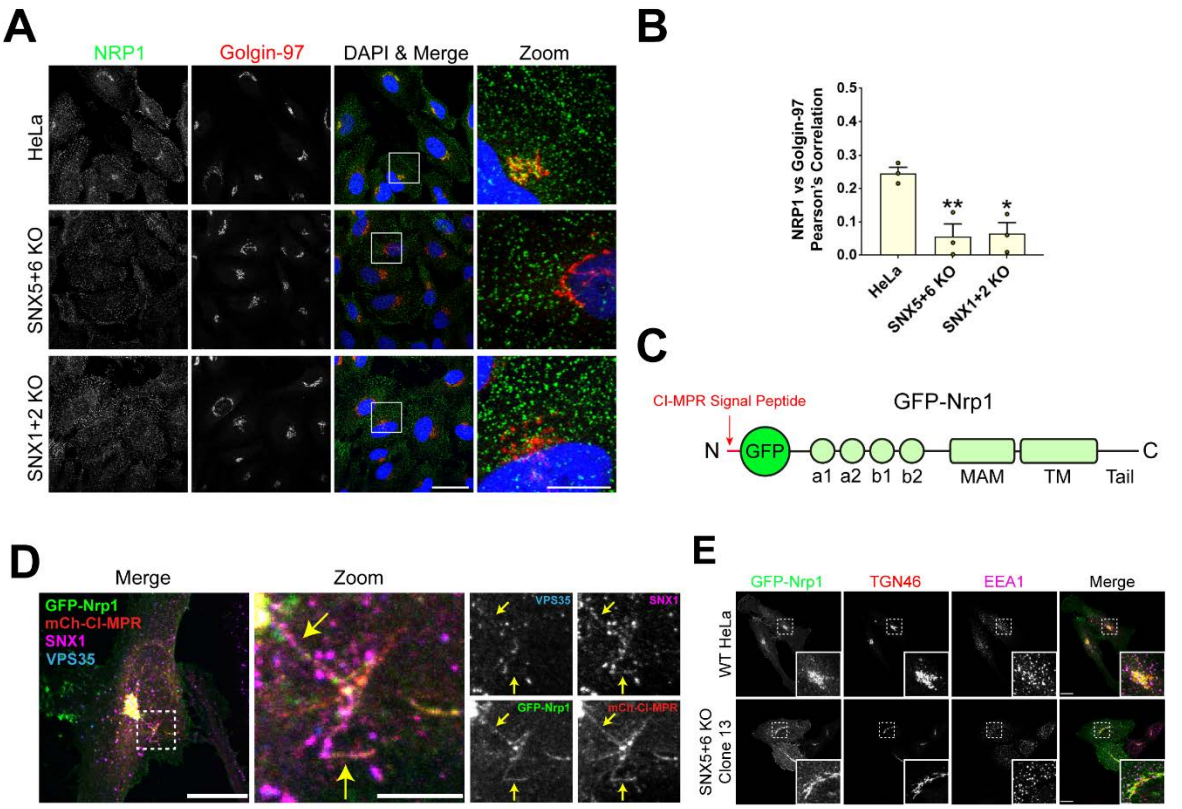

Figure 5.5 NRP1 Co-localises with SNX1-Positive Endosomes and Disperses from the TGN Upon SNX5+6 Depletion

(A) Immunofluorescence staining of endogenous NRP1 in HeLa WT HeLa cells, SNX5+6 KO HeLa cells and SNX1+2 KO HeLa cells. Scale = 50 µm, insets 5 µm. **(B)** Pearson's correlation quantification of the colocalisation of NRP1 and Golgin-97 upon ESCPE-1 depletion. Ordinary one-way ANOVA with Dunnett's multiple comparison's tests. WT vs SNX5+6 KO p = 0.0084, WT vs SNX1+2 KO p = 0.0103. **(C)** Schematic of a GFP-Nrp1 construct used to investigate Nrp1 subcellular localisation. **(D)** Confocal microscopy of HeLa cells co-transfected with mCherry-CI-MPR and GFP-Nrp1, co-stained with anti-SNX1 and anti-VPS35 antibodies. Yellow arrows denote mCherry-CI-MPR- and GFP-Nrp1-positive tubules emanating from a SNX1-positive endosome. Scale = 20 µm, zoom 5 µm. **(E)** Confocal microscopy of GFP-Nrp1 localisation in WT HeLa and SNX5+6 KO HeLa cells. Scale = 20 µm, insets 5 µm. Data for figures 5.7A and 5.7B were collected by Dr. Boris Simonetti.

At a 0-minute timepoint, anti-GFP signal labelled the cell surface, and did not colocalise with the TGN-resident GFP-Nrp1 signal **(Figure 5.6B)**. Following antibody surface uptake, internal anti-GFP signal was primarily visualised in vesicular compartments, which from 30 minutes onwards began to partially colocalise with TGN46 in the perinuclear region **(Figure 5.6B)**. Moreover, anti-GFP signal was observed in SNX6-positive tubular endosomal buds, potentially indicative of ESCPE-1 mediated membrane trafficking **(Figure 5.6C)**. As HeLa cells were incubated for longer timepoints prior to fixation and staining, colocalisation between anti-GFP signal and TGN46 continued to increase up to 8 hours post-uptake **(Figures 5.7A and 5.7B)**. When the experiment was performed in SNX5+6 KO HeLa cells, the anti-GFP signal failed to accumulate in the TGN **(Figures 5.7A and 5.7B)**. Taken together, these results suggest that ESCPE-1 regulates the retrograde trafficking of Neuropilin-1 from the endosomal

network to the TGN. Due to time constraints, I was unable to perform the additional experimental repeats and statistical analysis that would be required to confirm this hypothesis. Future work will be needed to validate the preliminary conclusions observed from this assay.

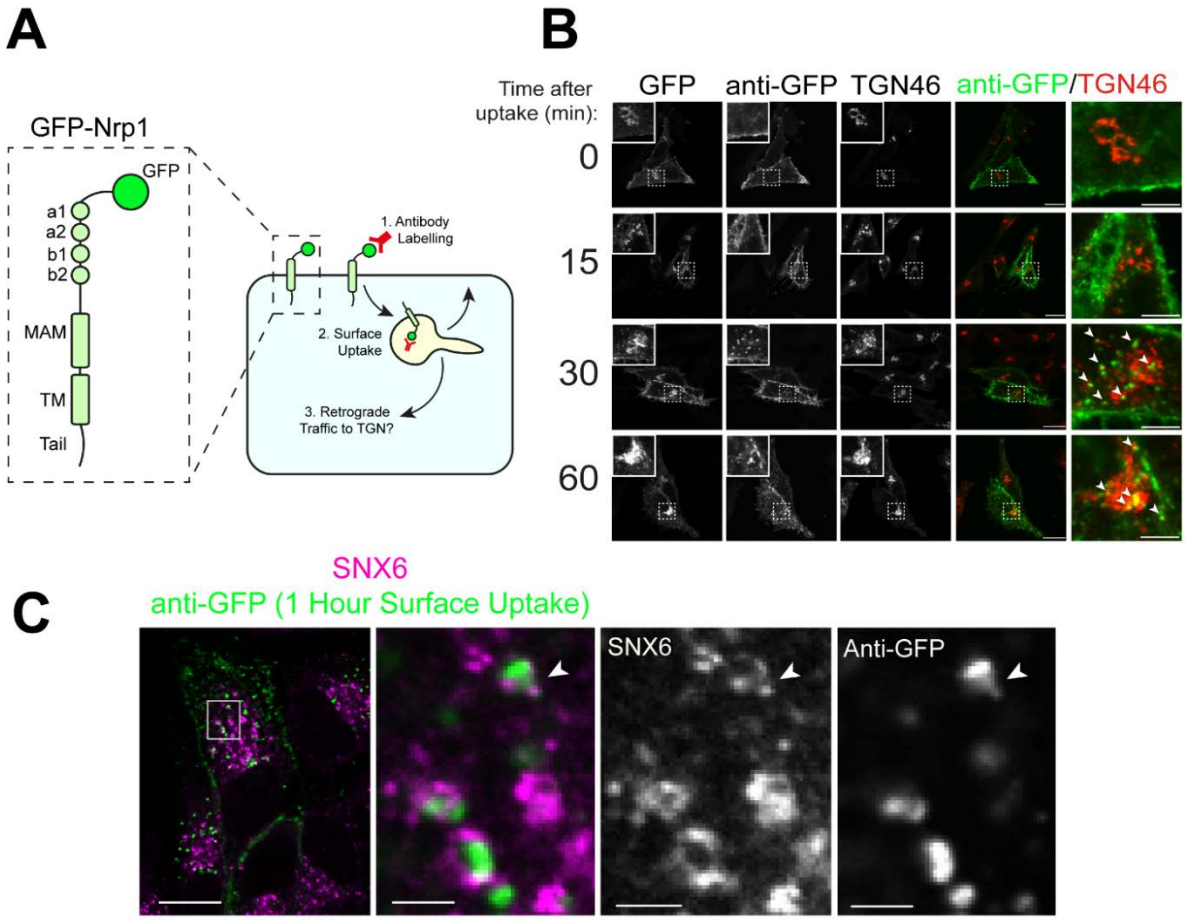

Figure 5.6 Design of a Surface Uptake Assay to Validate Retrograde NRP1 Trafficking

(A) Conceptual schematic depicting surface uptake of the GFP-Nrp1 construct using anti-GFP labelling. **(B)** Timecourse of GFP-Nrp1 internalisation by confocal microscopy and partial colocalisation with TGN46. Scale bars = 20 µm, zoom 5 µm. White arrows indicate points of colocalisation between anti-GFP and TGN46. **(C)** Confocal microscopy of SNX6 colocalisation with anti-GFP 1 hour after surface uptake. White arrows indicate anti-GFP signal in a SNX6-positive tubular bud. Scale bars = 10 µm, zoom 2 µm. Data for Figure 5C were collected by Dr. Boris Simonetti.

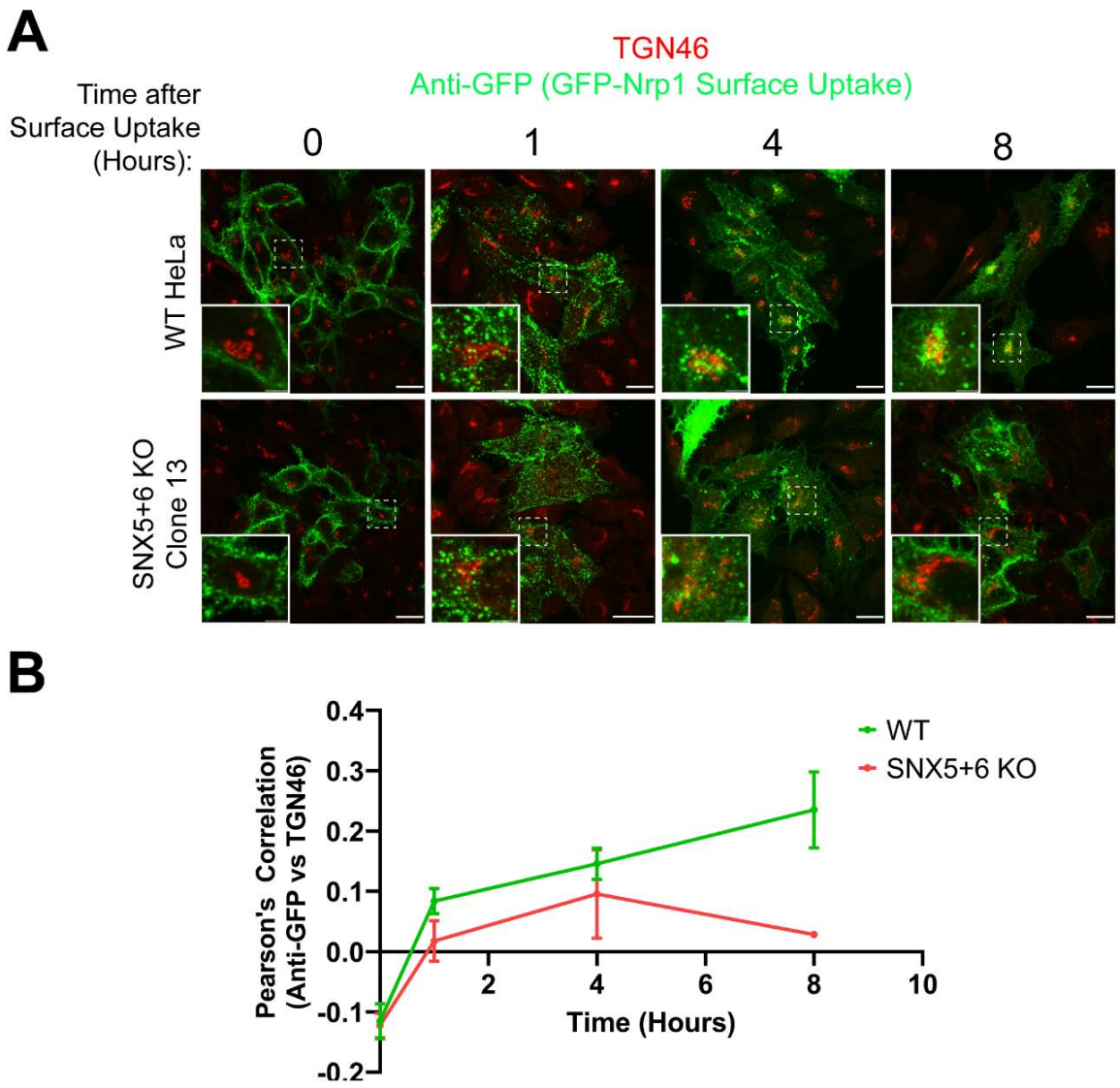

Figure 5.7 SNX5+6 KO Perturbs Retrograde Trafficking of GFP-Nrp1 in a Surface Uptake Assay.

(A) Surface uptake assay labelling GFP-Nrp1 with anti-GFP in WT or SNX5+6 KO HeLa cells. Scale bar = 20 µm, insets = 5 µm. **(B)** Pearson's correlation quantification of anti-GFP signal vs TGN46 staining. n = 2 independent repeats.

5.2.6 EphA2 and MET May Represent Additional ESCPE-1 Cargoes

Following the validation of NRP1 as an ESCPE-1 cargo, I sought to investigate other prominent hits identified in the SNX5+6 siRNA HRP-TGN46 proteome. EphA2 and MET represent potentially important cargoes due to their roles as receptor tyrosine kinases. EphA2 belongs to the Eph receptor family that responds to ephrin ligands in *cis* or *trans* to initiate intracellular signalling cascades that modulate cytoskeletal rearrangements, cell motility and cell survival (Kania and Klein, 2016). EphA2 is an established therapeutic target that is frequently overexpressed in cancer (Xiao et al., 2020). MET (alternatively referred to as c-

MET) is a RTK that initiates mitogenic signalling pathways and has historically been strongly linked to cancer biology (Organ and Tsao, 2011). Endocytosed RTKs can remain activated on internal membranes following activation, and the understanding of how endosomal recycling dynamics can spatiotemporally regulate RTK signalling output is an emerging field of research (Miaczynska, 2013).

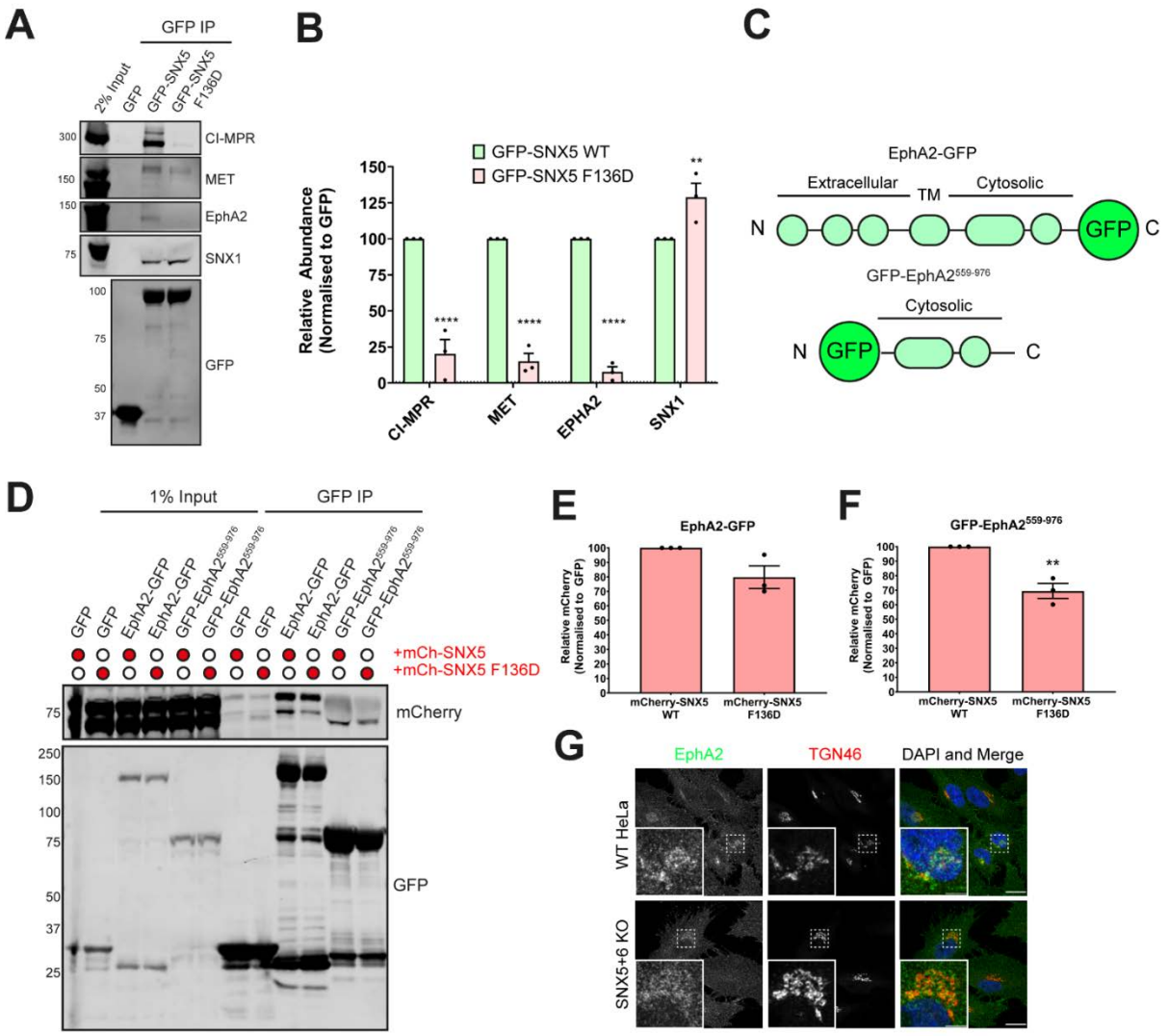

Figure 5.8 Validation of EphA2 as a Potential ESCPE-1 Cargo

(A) and **(B)** GFP, GFP-SNX5 and GFP-SNX5 F136D were transiently transfected into HEK293T cells then subjected to GFP-nanotrap. Immunoisolates were blotted for endogenous CI-MPR, MET and EphA2 levels and quantified. n = 3, 2-way ANOVA with Šídák's multiple comparisons tests, CI-MPR $p < 0.0001$, MET $p < 0.0001$, EphA2 $p < 0.0001$, SNX1 $p = 0.0073$. **(C)** Schematic of GFP-tagged EphA2 constructs used to further validate EphA2-SNX5 association. **(D)** GFP, EphA2-GFP and GFP-EphA2$^{559-976}$ were co-expressed with either mCherry-SNX5 or mCherry-SNX5 F136D by transient transfection, then subjected to GFP nanotrap. **(E)** and **(F)** Quantification of relative mCherry-SNX5 and mCherry-SNX5 F136D co-immunoprecipitated by EphA2-GFP (E) or GFP-EphA2$^{559-976}$ (F), presented as a fraction of the amount of quantified mCherry-SNX5. n = 3, unpaired t-test, EphA2-GFP $p = 0.0608$, GFP-EphA2$^{559-976}$ $p = 0.0042$. **(G)** Confocal microscopy of endogenous EphA2 localisation in WT or SNX5+6 KO HeLa cells. Scale = 20 µm, insets = 5 µm.

In HEK293T cells, GFP-SNX5 immunoprecipitated endogenous MET and EphA2, though the pulldown was not as strong as observed for CI-MPR **(Figure 5.8A)**. Introduction of the F136D mutation to GFP-SNX5 abrogated binding to MET, EphA2 and CI-MPR, suggesting involvement of the cargo-selective SNX5 PX domain in this association **(Figures 5.8A and 5.8B)**. To investigate EphA2 binding from the reverse direction, the ability of an EphA2-GFP construct (a gift from Professor Jim Norman) and a GFP-EphA2$^{559-976}$ tail construct to associate with SNX5 was determined **(Figure 5.8C)**. EphA2-GFP robustly immunoprecipitated mCherry-SNX5 when co-expressed in HEK293T cells **(Figure 5.8D)**. When co-expressed with mCherry-SNX5 F136D, a reproducible reduction of SNX5 association was observed, though this change was not statistically significant **(Figure 5.8E)**. Furthermore, the isolated GFP-EphA2$^{559-976}$ tail immunoprecipitated mCherry-SNX5, an association that was significantly reduced with the SNX5 F136D mutation **(Figure 5.8D)**.

These data suggest that EphA2 also associates with SNX5 but, unlike other cargoes such as CI-MPR and NRP1, the F136D mutation does not completely abrogate binding. There may therefore be bridging proteins involved in this interaction, or additional contacts between EphA2 and SNX5. Further biochemical analysis, such as site directed mutagenesis of potential βA and βB consensus sequences within the EphA2 tail, will be needed to further narrow down the binding interface. Finally, endogenous EphA2 staining in HeLa cells revealed a TGN46-colocalising intracellular population **(Figure 5.8E)**. However, this localisation appeared unaffected by SNX5+6 KO **(Figure 5.8E)**. Notably, HGF stimulation of cell-cell repulsion induces EphA2 internalisation and trafficking to a perinuclear intracellular compartment (Gundry et al., 2017). Similar to NRP1, it may therefore be necessary to establish more intricate methodologies such as surface uptake assays and ligand stimulation to study EphA2 and MET retrograde traffic in the future in more detail.

5.2.7 Development of CRISPR-Cas9 Cell Lines for Future HRP-TGN46 Screening of Retrograde Trafficking

The siRNA-based proteomics screen for ESCPE-1 cargoes has highlighted a range of potential new retrograde cargo proteins, some of which are functionally linked. However, these experiments failed to identify CI-MPR as significantly decreased from the HRP-TGN46-labelled proteome upon SNX5+6 suppression. TMEM230, investigated earlier in this chapter as an ESCPE-1 cargo, was also not detected. However, TMEM230 biotinylation was not quantified in wild-type cells by HRP-TGN46 labelling in **Chapter 4**, and therefore its shift in localisation could not be measured. This lack of quantification is likely due to TMEM230 containing only a short 12 amino acid luminal loop sequence that is available for biotinylation.

The CI-MPR dispersal phenotype upon SNX5+6 depletion has been consistently validated by myself and others (Evans et al., 2020; Itai et al., 2018; Kvainickas et al., 2017; Priya et al., 2017; Simonetti et al., 2017; Wassmer et al., 2007). CI-MPR was slightly less abundant in the SNX5+6 siRNA suppression proteome (Log_2 -0.16 SNX5+6 siRNA/Scr siRNA ratio), although this difference was not statistically sinfiicant ($p = 0.40$).

A potential explanation for this absence of detection may be insufficient suppression of SNX5+6 by siRNA suppression. CI-MPR is one of only 5 transmembrane proteins identified by GFP-trap proteomics by all three ESCPE-1 cargo-selective subunits: SNX5, SNX6 and SNX32 (alongside SDC2, ATP2A2, VAPA and VAPB) (Simonetti et al., 2017). Moreover, mutation of the cargo selective F136 residue of SNX5 to an alanine was sufficient to abrogate NRP1 binding, but not CI-MPR binding, which requires introduction of a more disruptive aspartic acid residue (Simonetti, 2017). As such, CI-MPR likely represents one of the highest affinity ESCPE-1 cargoes, and hence insufficient SNX5+6 suppression may not produce quantifiable changes in localisation by HRP-TGN46 labelling across a heterogenous population. The fold changes observed in cargoes such as NRP1 upon SNX5+6 siRNA suppression was also fairly small (Log_2 -0.60 SNX5+6 siRNA/Scr siRNA ratio), and residual SNX5/6 expression may therefore have been sufficient to maintain CI-MPR abundance below the cut-off thresholds.

To further develop the HRP-TGN46 methodology, I aimed to develop a CRISPR-Cas9-based system whereby clonal cell lines depleted of recycling complexes are compared relative to a rescue cell line. This approach would ensure complete depletion of endogenous proteins and circumvent issues of comparing a clonal cell line to a heterogenous wild-type HRP-TGN46-expressing population, as differences in HRP-TGN46 expression levels may bias biotinylation levels. I generated a SNX5+6 KO clonal cell expressing HRP-TGN46 and rescued this KO line through stable re-expression of GFP-SNX5 **(Figure 5.9A)**. In SNX5+6 KO cells following HRP-TGN46 labelling, CI-MPR was significantly dispersed away from the Golgin-97- and streptavidin-positive TGN compartment, and this phenotype was rescued by GFP-SNX5 **(Figures 5.9B and 5.9C)**. The absence of SNX5+6 did not impact fluorescent streptavidin signal intensity, or its colocalisation with Golgin-97 **(Figures 5.9D and 5.9E)**. Future work will be required to test whether this comparative KO vs rescue approach can produce more sensitive proteomic analysis of ESCPE-1 dependent retrograde cargo sorting.

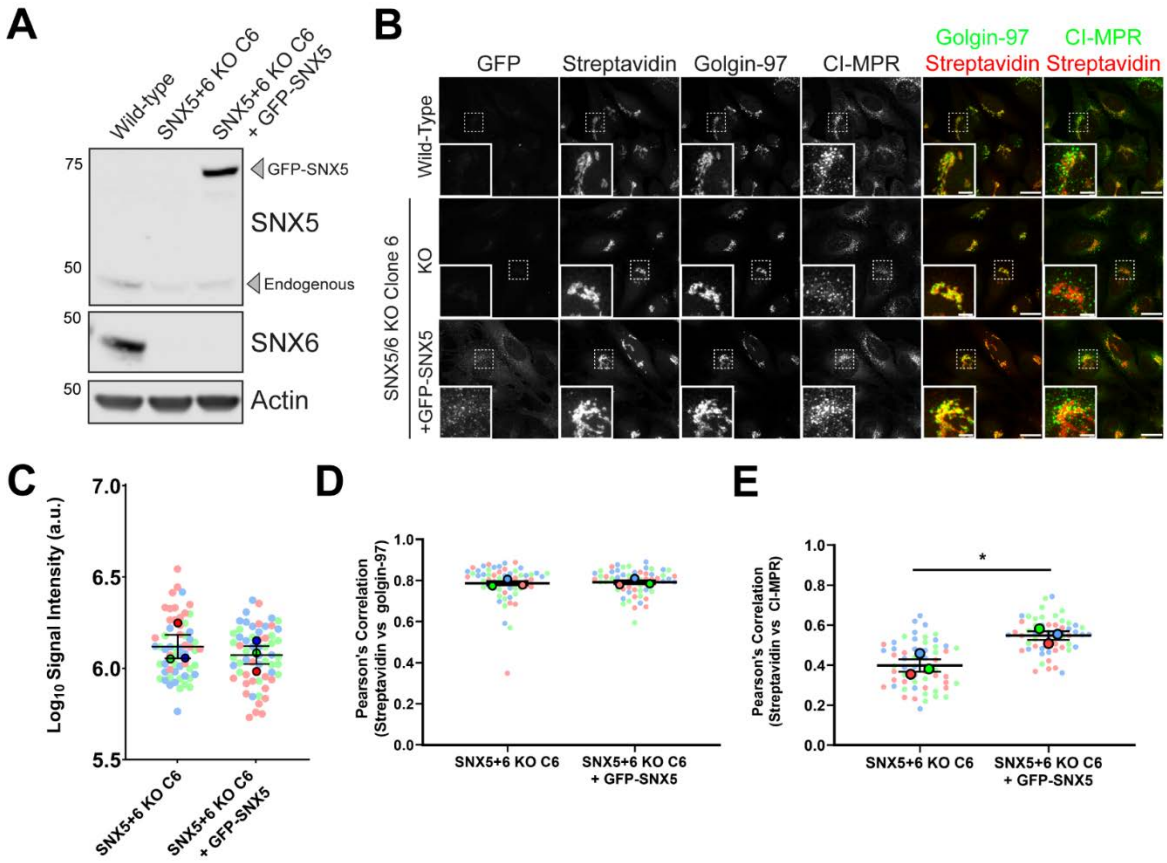

Figure 5.9 Generation and Validation of Clonal SNX5+6 KO and Rescue Clonal Cell Lines Expressing HRP-TGN46

(A) Western blot validation SNX5+6 KO and rescue with GFP-SNX5 in a background of HRP-TGN46-expressing HeLa cells. **(B)** Confocal microscopy of HRP-TGN46 streptavidin labelling following biotinylation, and colocalisation with Golgin-97 and CI-MPR. Scale bar = 20 µm, insets = 5 µm. **(C)** Superplot of fluorescent streptavidin signal intensity in WT, SNX5+6 KO and SNX5+6 KO + GFP-SNX5 HRP-TGN46-expressing HeLa cells. n = 3, unpaired t-test p = 0.6002. **(E)** Superplot of Pearson's correlation of streptavidin vs Golgin-97 in WT, SNX5+6 KO and SNX5+6 KO + GFP-SNX5 HRP-TGN46-expressing HeLa cells. n = 3, unpaired t-test p = 0.7259. **(E)** Superplot of Pearson's correlation of streptavidin vs CI-MPR in WT, SNX5+6 KO and SNX5+6 KO + GFP-SNX5 HRP-TGN46-expressing HeLa cells. n = 3, unpaired t-test p = 0.0167. In (C-E), individual data points are coloured according to independent repeats, and the mean values are bold.

The HRP-TGN46 methodology could also be expanded to study additional endosomal recycling complexes in the future. In addition to the SNX1/2-SNX5/6/32 complex that constitutes ESCPE-1, other SNX-BAR proteins have been implicated in retrograde endosomal cargo sorting. SNX4 can tubulate membranes *in vitro* either through the formation of homodimers, or through the association with the SNX-BAR proteins SNX7 or SNX30 (Van Weering et al., 2012). In yeast, Snx4 plays an early role in the retrograde recycling of the transmembrane autophagy protein Atg27 in a two-step model, whereby Snx4 mediates vacuole-to-endosome retrieval of Atg27, then retromer directs endosome-to-Golgi recycling (Suzuki and Emr, 2018). In humans, a SNX4-SNX7 heterodimer regulates ATG9A trafficking,

and is required for efficient autophagosome biogenesis, although this recycling step does not appear be endosome-to-TGN directed (Antón et al., 2020; Ravussin et al., 2021). SNX4 also facilitates Transferrin receptor sorting from early endosomes to the endocytic recycling compartment (Traer et al., 2007). Recently, proteomic analysis of proteins redirected to mitochondria upon Golgin-97 relocalisation revealed SNX4 as a significant hit, raising the possibility of SNX4-mediated endosome-to-TGN trafficking (Shin et al., 2020). SNX4 has also been implicated in the retrograde trafficking of the ricin toxin (Skånland et al., 2007). SNX4-SNX7/30 could therefore potentially represent a second cargo selective 'ESCPE' retrograde complex to be investigated by the HRP-TGN46 methodology.

To establish a methodology to analyse SNX4-mediated retrograde traffic, two HRP-TGN46-expressing SNX4 KO HeLa clones were generated, along with corresponding stable GFP-SNX4 rescue lines **(Figure 5.9A)**. Effective streptavidin labelling of the TGN could be achieved in these cells (**Figure 5.9C)** and hence they may represent a suitable methodology to interrogate SNX4-mediated retrograde trafficking in the future.

SNX8 is a poorly characterised SNX-BAR protein that forms homodimers and localises to Rab5- and Rab7-positive endosomes (van Weering et al., 2012). SNX8 has been reported to play a rate-limiting role in the retrograde trafficking of internalised StxB to the TGN (Dyve et al., 2009). Polymorphisms within the *SNX8* gene have been linked to Alzheimer's disease, and SNX8 expression was decreased in the brain samples of Alzheimer's disease patients (Rosenthal et al., 2012; Xie et al., 2019). SNX8 suppression increases β-amyloid levels, suggestive of a neuroprotective role for SNX8 in amyloidogenic processing (Xie et al., 2019). To investigate whether SNX8 regulates cargo residency at the TGN, two HRP-TGN46-expressing SNX8 HeLa KO clonal cell lines were generated, alongside corresponding stable GFP-SNX8 rescue cell lines **(Figure 5.9B)**. TGN morphology and TGN46 labelling appeared unaffected by SNX8 KO or rescue, suggesting that TGN46 is unaffected by the loss of SNX8, and the HRP-TGN46 methodology may be useful to investigate a potential role for SNX8 in controlling retrograde endosomal cargo sorting **(Figure 5.9C)**. With the establishment of these tools, HRP-TGN46 labelling can be expanded in the future to investigate the broader role of SNX-BAR proteins in orchestrating retrograde endosomal cargo sorting.

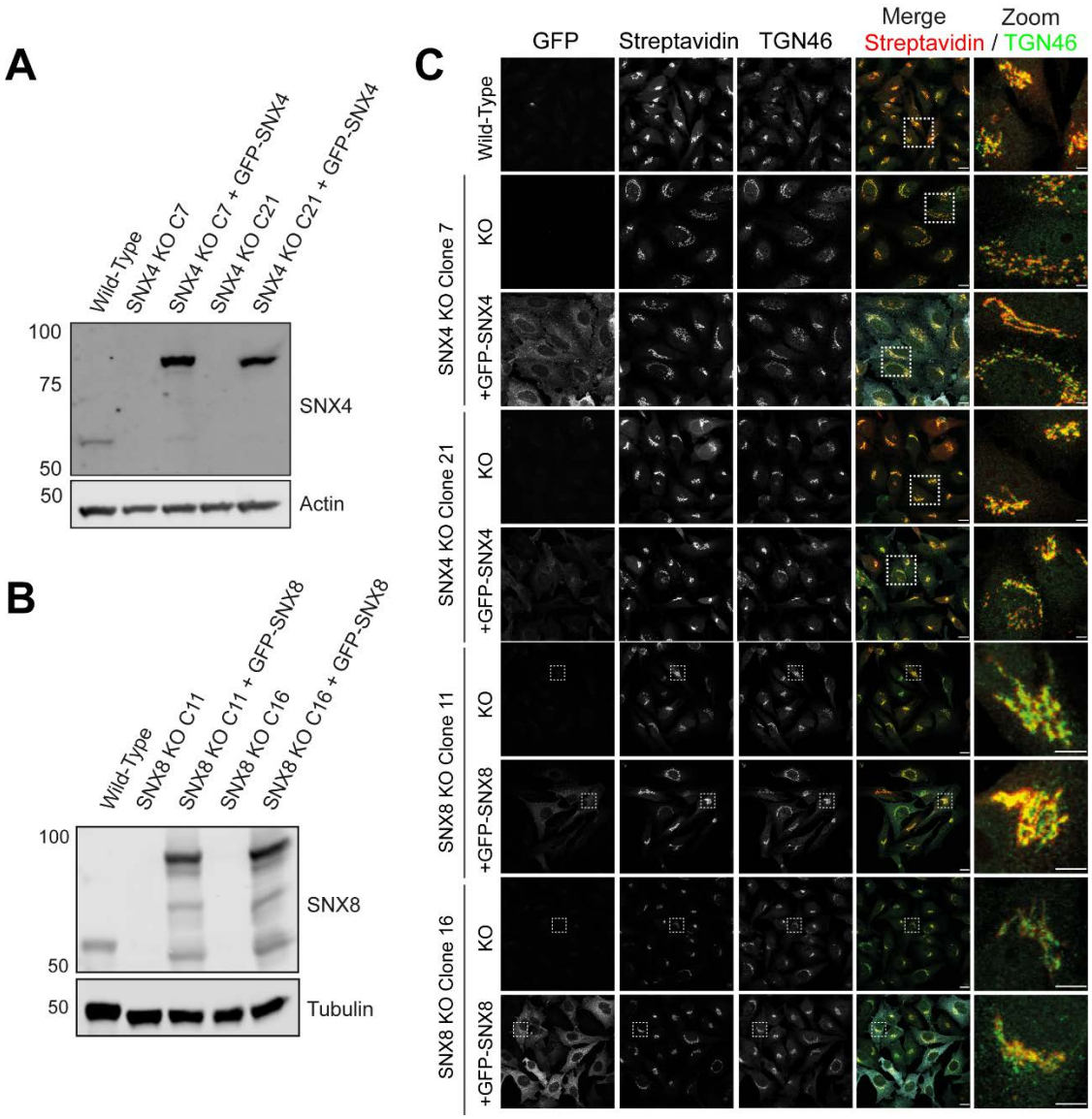

Figure 5.10 Generation and Validation of SNX4 KO and SNX8 KO HRP-TGN46-Expressing Cell Lines

(A) Western blot validating two clonal SNX4 KO HeLa cell lines and corresponding GFP-SNX4 rescues in a HRP-TGN46-expressing background. **(B)** Western blot validating two clonal SNX8 KO HeLa cell lines and corresponding GFP-SNX8 rescues in a HRP-TGN46-expressing background. In (A) and (B), the endogenous SNX4/SNX8 bands are visible in the wild-type sample, whereas a band GFP-tagging induces a band shift **(C)** Confocal microscopy of streptavidin labelling colocalisation with TGN46 in SNX4 and SNX8 KO and rescue cell lines. Scale bar = 20 µm, zoom = 5 µm.

5.3 Discussion

In this chapter, I have employed the HRP-TGN46 methodology developed in **Chapter 4** to investigate ESCPE-1-dependent retrograde cargo sorting. While CI-MPR, a positive control used throughout the development of the method, was not significantly perturbed in SNX5+6 suppressed cells, a suite of potential retrograde cargoes was identified that warrants further investigation. This represents an advance in the understanding of sequence-dependent ESCPE-1 retrograde recycling, but the validation of many hits in the future is likely to prove difficult and require specialised methodologies such as surface uptake trafficking assays. Of these hits, NRP1 in particular has been biochemically validated as a direct SNX5/6 cargo, which further advances the knowledge of the cargo selectivity of ESCPE-1.

5.3.1 A Preliminary Model for ESCPE-1-dependent NRP1 Retrograde Trafficking

The diverse functions of the Neuropilin family are conferred by their modular extracellular structure, which facilitates protein-protein interactions with a range of soluble ligands and transmembrane receptors in *cis* and *trans* conformations (Guo and Vander Kooi, 2015). Due to a relatively short and structurally uncharacterised cytosolic tail lacking a kinase domain, NRP1 acts as a co-receptor that engages and internalises with its binding partners upon activation (Pang et al., 2014; Soker et al., 1998). NRP1 has a wide range of extracellular interactors, including growth factors, axonal guidance molecules, RTKs, integrins (Chaudhary et al., 2014; Guo and Vander Kooi, 2015).

NRP1 has been particularly well-characterised in the context of endocytosis and trafficking of α5β1-integrin (Valdembri et al., 2009). α5β1-integrin constitutes the predominant fibronectin receptor and coordinates cellular adhesion by organising fibronectin into fibrillar extracellular structures. Moreover, α5β1-integrin is also largely responsible for the turnover of cleaved fragments of the extracellular fibronectin meshwork through endocytosis (Shi and Sottile, 2008). NRP1 associates with α5β1-integrin through its extracellular domain and this complex colocalises, internalises and traffics together (Valdembri et al., 2009). NRP1 suppression induces defective formation of extracellular fibronectin fibrils and perturbs focal adhesion turnover through a mechanism dependent on its cytosolic tail (Seerapu et al., 2013; Valdembri et al., 2009).

NRP1-α5β1-integrin endocytosis is mediated by the endocytic adaptor protein GAIP C-terminus interacting protein (GIPC1), a PDZ domain-containing protein which recognises the ^{921}SEA^{923} PDZ binding motif present at the C-terminus of NRP1 (Cai and Reed, 1999; Valdembri et al., 2009). GIPC1 recruits APPL1 and myosin-VI to facilitate minus end-directed

trafficking along actin filaments to converge with the early endosomes (Valdembri et al., 2009). Once in the endosomal network integrins have multiple characterised recycling routes back to the plasma membrane, including a Rab4-dependent 'short-loop', a Rab11-dependent 'long-loop', and a SNX17-retriever based pathway mediated by recognition of NPxY motifs in cytosolic integrin tails (McNally et al., 2017; Paul et al., 2015; Steinberg et al., 2012). NRP1 itself may also be recycled to the plasma membrane by multiple pathways. For example, NRP1 levels are decreased at the cell surface in retromer or SNX17-suppressed cells (McNally et al., 2017; Steinberg et al., 2013). Such redundancy and availability of direct recycling pathways raises the question of why NRP1 and integrin-α5 appear to be depleted from the TGN upon SNX5+6 suppression.

The matrix metalloprotease MT1-MMP regulates the cleavage of extracellular fibronectin fibrils to regulate integrin-dependent fibronectin turnover through endocytosis (Shi and Sottile, 2011). Following surface uptake, MT1-MMP has been reported to traffic retrogradely to the TGN (Wang et al., 2004). This controlled traffic to the TGN, the major sorting station for the establishment of cell polarity, may facilitate directional re-delivery of MT1-MMPs to the cell surface in migrating cells (Johannes and Popoff, 2008). It would therefore follow that integrins, and perhaps NRP1, could be subject to similar directional plasma membrane re-delivery. Indeed, integrin-α5 and integrin-β1 were identified as retrograde cargoes by a SNAP-tagging proteomics approach at the TGN (Shi et al., 2012). Retrograde traffic of integrin-β1 was found to be required for persistent cell migration in polarised cells (Shafaq-Zadah et al., 2016). α3β1-integrin has also been implicated in retrograde endosome-to-TGN traffic (Riggs et al., 2012).

In polarised endothelial cells where NRP1 is highly expressed, active α5β1-integrin is localised to the basolateral plasma membrane, where fibronectin is extracellularly deposited (Mana et al., 2016). In addition to facilitating turnover of extracellular fibronectin, α5β1-integrin also plays an important role in the binding and export of newly synthesised fibronectin dimers from the biosynthetic pathway, as integrin-α5 depletion causes an accumulation of fibronectin at the TGN (Mana et al., 2016). Suppression of machinery involved in basolateral post-Golgi carrier traffic, including the PI(4)P kinase PIK4B, the phosphatase PTPRF, the PTPRF-interacting protein PPFIA1, or Rab11b causes an accumulation of active α5β1-integrin in TGN46-positive compartments, and PPFIA1 silencing cause vascular defects in zebrafish models (Mana et al., 2016).

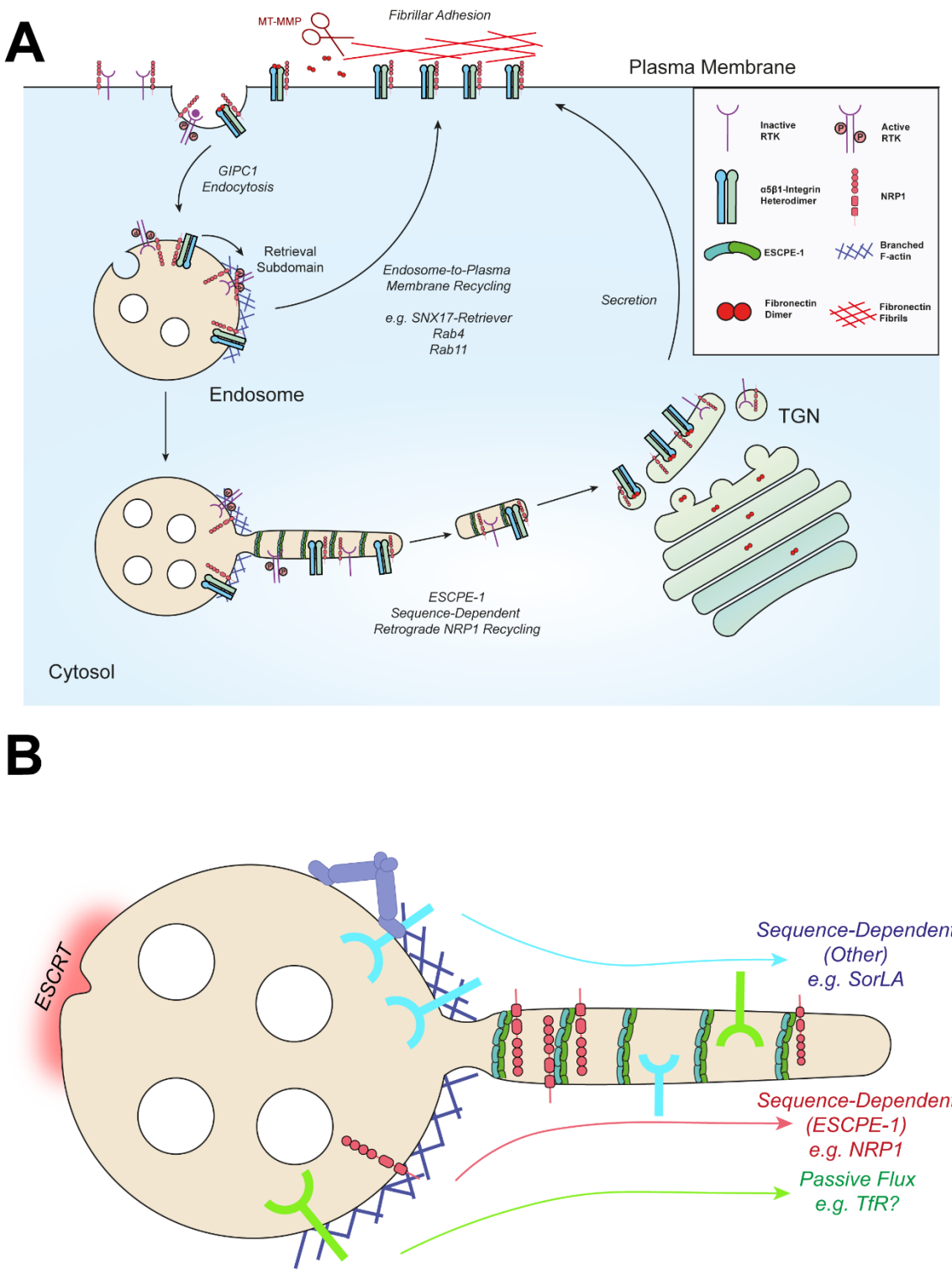

Figure 5.11 Models for ESCPE-1 Mediated Retrograde Trafficking

(A) Schematic of a model of ESCPE-1-dependent NRP1 recycling to facilitate polarised integrin trafficking to plasma membrane subdomains. MT-MMP = Matrix Metalloprotease **(B)** Schematic of incorporation of cargo into ESCPE-1-positive tubules through sequence-dependent and -independent routes.

Given the role of NRP1, particularly through its cytosolic tail, in mediating active integrin endocytosis and efficient fibronectin fibrillogenesis, and the newly-characterised interaction with SNX5/6 defined in this chapter, a potential hypothesis regarding the ESCPE-1 dependent retrograde trafficking of NRP1 could be that it chaperones activated integrins to the TGN to mediate polarised fibronectin secretion (Mana et al., 2020; Valdembri et al., 2009) **(Figure 5.11A)**. Immunoprecipitation of integrin-β1 identified components of the retromer complex, and the ESCPE-1 subunits SNX2 and SNX6, highlighting the possibility of retromer and ESCPE-1 regulating retrograde integrin trafficking (Shafaq-Zadah et al., 2016). Moreover, the interaction between NRP1 and integrin-β8 plays a critical role in sprouting angiogenesis in the central nervous system, expanding the scope of this model beyond α5β1-integrin (Hirota et al., 2015). Endoglin (ENG), another transmembrane glycoprotein that was depleted in SNX5+6 siRNA-treated cells, is similar to NRP1 in that it associates extracellularly with integrin-α5, contains a GIPC1-binding motif and acts as a co-receptor for transforming growth factor β receptors, adding another integrin- and RTK-regulating cargo to this dataset (Niland and Eble, 2019; Rossi et al., 2019; Tian et al., 2012).

Interestingly, the NRP1 co-receptor VEGFR2 has also been reported to reside in the TGN in endothelial cells, where it becomes mobilised upon stimulation (Manickam et al., 2011). VEGFR2 is not expressed in HeLa cells and thus was not identified by HRP-TGN46 labelling. However, the NRP1 co-receptor MET is significantly depleted from the HRP-TGN46-labelled proteome upon SNX5+6 suppression. Further work will therefore be needed to elucidate whether MET co-traffics to the TGN with NRP1 or engages ESCPE-1 directly through its own candidate βA motif. In a recent methodological advance that selectively biotinylated proteins at the apical or basolateral surface of polarised Madin-Darby canine kidney (MDCK) cells in a transwell, MET was more abundantly labelled at the basolateral membrane, potentially suggestive of polarised sorting through the TGN (Caceres et al., 2019).

In the development and application of the HRP-TGN46 labelling methodology, HeLa cells were chosen as a cell line for ease of genetic manipulation, the ability to grow sufficient material for sensitive mass spectrometry of biotinylated proteins, and to compare the resulting datasets with pre-exisiting surface biotinylation datasets so as to obtain a global view of membrane trafficking. However, to fully explore the model proposed herein it will be necessary to investigate the role of ESCPE-1 retrograde trafficking in polarised cells, whereby additional phenotypes may arise due to increased dependence on apical-basolateral cargo sorting at the TGN. Interestingly, plating HeLa cells on arrow shaped fibronectin micropatterns was sufficient to induce polarisation, with integrin-β1 predominantly localised to the leading edge of the cell (Shafaq-Zadah et al., 2016). Suppression of Rab6 or Syntaxin-16, components of retrograde trafficking machinery, disrupted this polarised integrin distribution, suggesting that retrograde

trafficking is important for mediating polarised integrin sorting from the TGN (Shafaq-Zadah et al., 2016). An additional study also demonstrated that disruption of Syntaxin-6, a TGN- and endosome-localised SNARE protein and binding partner of Syntaxin-16, also impairs α5β1-integrin recycling (Tiwari et al., 2011). Depletion of the endosomal SNARE protein VAMP3, or its TGN-resident counterpart SNARE protein Syntaxin-6 also disrupts chemotactic cell migration of HeLa cells cultured in Matrigel and impairs α3β1-integrin delivery to the cell surface (Riggs et al., 2012). α3β1-integrin acts as the receptor for laminin, an extracellular matrix component that is specifically sorted to the basolateral membrane of Madin-Darby canine kidney (MDCK) cells, suggesting that this model could be applicable to retrograde sorting of different integrin dimer compositions and their ligands to dictate polarised extracellular matrix assembly (Caplan et al., 1987).

Gene ontology analysis of proteins depleted from the HRP-TGN46-labelled proteome upon SNX5+6 suppression highlighted ‘Cell Adhesion’, ‘Angiogenesis’ and ‘Cell Migration’ as the most significantly enriched biological processes. In contrast to many other endosomal recycling complexes, which are typically linked to neurodegenerative diseases through decreased expression or inactivating mutations, components of ESCPE-1 have been linked to various cancers through overexpression (Hu et al., 2018; Schreij et al., 2016; Q. Zhou et al., 2020). Syntaxin-6, is also upregulated in many cancer types and its overexpression promotes a pro-migratory phenotype (Riggs et al., 2012). It will therefore be interesting to investigate in the future whether the upregulation of ESCPE-1-dependent trafficking induces tumorigenic phenotypes, such as invasive migration via enhanced integrin trafficking, or aberrant growth and angiogenesis via NRP1 and RTK signalling.

5.3.2 Additional Putative ESCPE-1 Cargoes for Future Validation

The HRP-TGN46 proteomics screen identified additional transmembrane proteins containing cytosolic βA consensus motif. For example, TM9SF4 is a member of the transmembrane 9 superfamily (TM9SF) of proteins that is implicated in the chaperoning of proteins through the early secretory pathway via specific recognition of their transmembrane domains (Perrin et al., 2015; Vernay et al., 2018). Moreover, distinct functions for TM9SF4 have been reported, for example as an autophagy regulator on mTOR-positive lysosomes, and as a v-ATPase interactor (Lozupone et al., 2015; Sun et al., 2018). Further work is required to extensively characterise the cellular functions of TM9SF4, but its multiple reported localisations across the biosynthetic pathway and endolysosomal network may be suggestive of a sequence-dependent retrograde trafficking mechanism. Of note, the short cytosolic tail of TM9SF4 (^{620}TGTIGFYAAYMFVRKIYAAVKID^{642}) contains 3 sequences conforming to a βA motifs that

could interact with SNX5/6. Like NRP1, this short tail will be amenable to *in vitro* biochemical analysis in the future.

The poliovirus receptor (PVR) was also identified as a potential ESCPE-1 binding cargo. In addition to its role as a viral receptor, PVR has a natural biological function as a cell adhesion molecule that strongly anchors to vitronectin (Lange et al., 2001). PVR is expressed in endothelial cells and is a facilitator of transendothelial migration - the exit of lymphocytes from blood by crossing the endothelial cell barrier (Bowers et al., 2017). Interestingly, the basolateral epithelial sorting of PVR was shown to be dependent on a ^{398}YSAV^{401} sequence that interacts with the AP-1B subunit μ1B, which overlaps with the putative ^{396}VSYSA^{400} ESCPE-1 binding site (Ohka et al., 2001). Moreover, the Golgi-localised cytidine-5'-monophospho-N-acetylneuraminic acid (CMP-sialic acid) transporter SLC35A1 contains a putative ^{71}GRFKA^{75} cytosolic SNX5/6-binding motif. Dispersion of this transporter from the Golgi could conceivably cause defective posttranslational protein modifications upon ESCPE-1 suppression. Future analysis will be required to biochemically validate these potential retrograde cargoes.

5.3.3 Sequence-Independent Retrograde Cargo Sorting by ESCPE-1

In addition to proteins containing putative cytosolic SNX5/6-interacting motifs which could constitute direct cargoes, and associated interacting proteins such as integrins, a range of transmembrane proteins lacking a candidate βA motif were identified by HRP-TGN46 in SNX5+6 suppressed cells. Some of these proteins already have well-characterised recycling mechanisms. For example, the transferrin receptor (TfR, gene name *TFRC*) was decreased upon SNX5+6 suppression. TfR has been a historically well characterised endosome-to-plasma membrane recycling cargo (Chen et al., 2013; Dai et al., 2004; Traer et al., 2007). However, TfR has additionally been linked to retrograde transport, suggestive of multiple routes back to the plasma membrane (Shi et al., 2012; Snider and Rogers, 1985). SorLA (SORL1), is a retromer-dependent cargo that cycles APP between the TGN and endosomal network, and disrupting this association relocalises APP to the endosomal network where APP processing is enhanced (Fjorback et al., 2012). Interestingly, SNX32 was one of 11 proteins, and the only ESCPE-1 subunit, identified in a proteome-wide association study for causal Alzheimer's disease risk proteins, potentially indicating that ESCPE-1 may play a regulatory role in APP processing (Wingo et al., 2021). The low density lipoprotein receptor (LDLR) relies on CCC- and WASH-complex mediated recycling for retrieval to the cell surface and efficient LDL uptake (Bartuzi et al., 2016).

The identification of these transmembrane proteins lacking an interacting motif but with previously established recycling mechanisms raises the possibility of sequence-independent

tubular retrograde recycling by ESCPE-1 **(Figure 5.11B)**. It is only recently that SNX-BAR proteins were considered to be cargo-selective. Prior to these discoveries it was believed that they play a predominantly mechanical role in forming membrane tubules on the endosomal membrane, into which other endosomal recycling complexes incorporate their cargo (Burd and Cullen, 2014; Seaman, 2012). In models of ESCPE-1 sequence-independent recycling, cargo corralled on the endosomal recycling subdomain may either exhibit a degree of passive flux into ESCPE-1-generated tubular carriers emanating from the membrane, or the same membrane carriers could contain cargo selectively incorporated by multiple different recycling complexes. For example, NRP1 and LDLR may be identified by the same screen due to both ESCPE-1 and CCC-/WASH-complex cargoes being incorporated into the same membrane buds that are dependent on SNX-BAR mechanical tubulation. Plasma membrane resident cargo, such as TfR and LDLR, retrogradely trafficked through this pathway will still likely reach the cell surface via anterograde TGN export, albeit perhaps at a slower rate than direct recycling. Therefore, if passive ‘leakage’ does occur through this pathway, it is unlikely to be of detriment to the cell. The significance of sequence-dependent versus -independent ESCPE-1 recycling is likely to be a significant future avenue of research in the understanding of mechanistic endosomal recycling.

Chapter 6: Neuropilin-1 is a Host Factor for SARS-CoV-2 Infection

6.1 Introduction

Before beginning, it is necessary to preface this chapter by acknowledging the collaborative nature of the data presented herein. Hypothesis generation, experimental design, and independent experimental repeats were all performed jointly with the multidisciplinary team that I was fortunate enough to work on this project with. In particular, the molecular cloning, cell culture and immunoprecipitation experiments were mainly performed by myself, Dr Boris Simonetti and Dr Carlos Antón-Plágaro in Professor Peter Cullen's laboratory. Infection experiments and culturing of the live SARS-CoV-2 virus depended upon the expertise of the laboratories of Dr Yohei Yamauchi, Dr Andrew Davidson, and Dr David Matthews at the University of Bristol. Isothermal titration calorimetry and X-ray crystallography data arose from a collaboration with Professor Brett Collins at the University of Bristol. Additionally, the expertise of the laboratories of Professor Urs Greber, Dr Peter Horvath, Dr Richard Sessions, Professor Ari Helenius, Professor Julian Hiscox and Professor Tambet Teesalu contributed greatly to this work. The publication of this project, which comprises the results section of this thesis chapter, was co-written by myself, Dr Boris Simonetti, Dr Andrew Davidson, Professor Pete Cullen and Dr Yohei Yamauchi **(See Appendix B)** (Daly et al., 2020). As such, the results section is written in plural form, and I do not take individual credit for the data and conclusions within this chapter; rather I would like to take the opportunity to credit and thank all of those who contributed to the study.

6.1.1 The Emergence of SARS-CoV-2 and the COVID-19 Pandemic

In December 2019, an infectious pneumonia outbreak of unknown origin was widely reported in Wuhan, Hubei province, China. Rapid isolation of the aetiological agent revealed a novel coronavirus capable of human-to-human transmission (Wu et al., 2020; P. Zhou et al., 2020). Coronaviruses (CoVs) are small (80-120 nm), positive-sense, single stranded RNA viruses that are classified into four groups; α-, β-, γ- and δ-coronaviruses (J. Cui et al., 2019). In recent history, two major zoonotic outbreaks have been caused by β-coronaviruses: Severe Acute Respiratory Syndrome (SARS, caused by SARS-CoV, 2002-2003), and Middle Eastern Respiratory Syndrome (MERS, caused by MERS-CoV, 2013-present) (J. Cui et al., 2019). Early sequencing and characterisation of the novel coronavirus confirmed its identity as a β-coronavirus with 79.6% genome similarity to SARS-CoV and was subsequently named as SARS-CoV-2 (Gorbalenya et al., 2020; P. Zhou et al., 2020). SARS-CoV-2 is the seventh coronavirus known to infect humans (Andersen et al., 2020). The viral pneumonia caused by SARS-CoV-2, (termed Coronavirus Disease 2019, COVID-19), has since instigated an ongoing global pandemic, thus far responsible for > 116,000,000 cases and > 2,500,000

deaths at the time of writing (World Health Organization, 2021). As this pandemic continues, there remains an urgent requirement for an understanding of the molecular biology underlying SARS-CoV-2 infection, and the development of effective antiviral therapies for the treatment of COVID-19.

6.1.2 The Spike Protein is a Key Player in SARS-CoV-2 Infection

Like all β-coronaviruses, the genome of SARS-CoV-2 is organised into 6 functional open reading frames that encode crucial, conserved proteins for infection and replication: ORF1a, ORF1b, Spike, Envelope, Membrane and Nucleocapsid. Additionally, putative open reading frames within the SARS-CoV-2 genome encode various accessory proteins (Chan et al., 2020). All coronaviruses utilise the clove-shaped, homotrimeric Spike protein (S) that protrudes from the surface of virions as receptors for host cell attachment and entry (Li, 2016). Consequently, the S trimer is the major antigenic target for neutralizing antibodies raised during the immune response to coronavirus infections (Jiang et al., 2020). The S protein is translated as a single polypeptide that is processed by host proteases to produce two non-covalently associated proteins: S1 and S2. The S1 subunit confers the receptor-binding ectodomain, whereas S2 is responsible for mediating membrane fusion upon proteolytic activation, and also contains a transmembrane domain and short cytosolic tail (Li, 2016). The S protein therefore plays a central role in the mechanism of virus entry and replication: by mediating receptor recognition and internalisation into the host cell, then subsequently triggering membrane fusion to facilitate release of viral RNA and replication machinery into the cytosol (Fehr and Perlman, 2015).

Structural studies have revealed a high degree of similarity between SARS-CoV-S and SARS-CoV-2-S (Walls et al., 2020; Wrapp et al., 2020). Given the sequence homology between these closely related viruses, the primary host receptor for SARS-CoV-2-S was quickly demonstrated to be angiotensin converting enzyme 2 (ACE2) (P. Zhou et al., 2020). Moreover, the structural details of the interface between the receptor binding domain (RBD) of SARS-CoV-2-S1 and ACE2 have been elucidated (Yan et al., 2020). Additionally, the S2 subunit is primed for cell fusion by the cell surface-localised transmembrane protease serine 2 (TMPRSS2) (Hoffmann et al., 2020b). The tissue tropism of SARS-CoV-2 is believed to be largely conferred by the cell type-specific expression of ACE2 and TMPRSS2 on the surface of cells lining the respiratory tract. However, SARS-CoV-2 demonstrates a wider, multi-organ tissue tropism compared to SARS-CoV, potentially indicating an acquired ability to engage novel host factors with broader expression profiles (Hui et al., 2020; Puelles et al., 2020).

A key difference between SARS-CoV-S and SARS-CoV-2-S appears to be the emergence of a multibasic furin cleavage motif at the S1/S2 boundary in the latter (Walls et al., 2020). This novel sequence has been proposed to facilitate proteolytic processing of S by furin in virus-producing cells or at the cell surface prior to infection, rather than occurring after viral entry, as is the case with SARS-CoV cleavage in the endolysosomal network by cathepsins (Simmons et al., 2005). Furin is an essential transmembrane endopeptidase that predominantly resides within the TGN and relies on a retrograde transport sorting mechanism to maintain its subcellular localisation (Chia et al., 2011; Mallet and Maxfield, 1999). The relevance of furin cleavage sites to coronavirus pathogenicity has been established since early studies on the mouse hepatitis virus demonstrated that furin cleavage is required for infected cell-cell fusion events, a well-documented pathogenic hallmark of coronavirus infections (de Haan et al., 2004; Frana et al., 1985). The multiple localisations of furin across the TGN, plasma membrane and endosomal network can facilitate the proteolytic processing of viruses either upon entry into cells or exit from infected cells. Moreover, due to the ubiquity of furin across mammalian tissues, the acquisition of a furin cleavage site is associated with expanded tissue tropism and higher pathogenicity, as is the case for highly pathogenic strains of avian influenza and Newcastle disease virus, both of which become dramatically more pathogenic upon the acquisition of a furin cleavage site (Andersen et al., 2020; Braun and Sauter, 2019; Izaguirre, 2019).

Preventing furin cleavage with proprotein convertase inhibitors significantly reduces efficiency of SARS-CoV-2 infection, and removal of the furin cleavage site abolishes the capacity of SARS-CoV-2 to form syncytia in cell culture (Hoffmann et al., 2020a; Shang et al., 2020). Moreover, a SARS-CoV-2 virus with a natural deletion of the furin cleavage site demonstrates attenuated pathogenicity in hamster disease models, consistent with less alveolar damage (Lau et al., 2020). The acquired furin cleavage site within the S protein of SARS-CoV-2 therefore appears to contribute significantly to the pathogenesis of COVID-19.

6.1.3 Neuropilin Receptors and the C-end Rule

The family of neuropilin proteins, comprising Neuropilin-1 (NRP1) and Neuropilin-2 (NRP2), are type I transmembrane cell surface receptors with diverse functions in cell biological pathways. Broadly, neuropilins serve as co-receptors for both soluble extracellular ligands and transmembrane proteins, both in *cis* and *trans* conformations at the cell surface (Guo and Vander Kooi, 2015). Neuropilins play roles in pleiotropic biological mechanisms, including regulating angiogenesis and vascular permeability in the cardiovascular system, coordinating axon migration and guidance in the nervous system, and regulating the immune synapse as

part of the primary immune response (Guo and Vander Kooi, 2015; Roy et al., 2017; Schwarz and Ruhrberg, 2010).

The diverse functions of neuropilins are conferred by their modular extracellular structure, which facilitate protein-protein interactions with a wide variety of substrates. The structures of both NRP1 and NRP2 consist of a short cytosolic tail, a transmembrane spanning domain, and five extracellular domains: two N-terminal CUB (complement C1r/C1s, Uegf, Bmp1) domains named a1 and a2; two tandem coagulation factor domains named b1 and b; and a MAM (meprin, A-5 protein and receptor protein-tyrosine phosphatase mu) domain. These domains are evolutionarily conserved and typically observed in proteins involved in cell adhesion (Lee et al., 2003). Moreover, soluble NRP1 and NRP2 splice isoforms comprising the a1a2b1b2 domains alone and lacking a transmembrane anchor, can be secreted (Gagnon et al., 2000; Rossignol et al., 2000). Soluble NRP1/2 isoforms can modulate signalling by associating with ligands extracellularly and preventing their engagement with cell surface NRP1/2 (Guo and Vander Kooi, 2015). The cytosolic tails of NRP1 and NRP2 are poorly characterised, beyond an established PDZ binding motif that recruits the endocytic adaptor GIPC1 **(Chapter 5.3.1)** (Valdembri et al., 2009). Based on the evidence presented in **Chapter 5**, the cytosolic tail of NRP1 directly engages ESCPE-1 to mediate intracellular trafficking of the receptor. Interestingly, NRP2 has two distinct splice isoforms that vary in their cytosolic tail sequences. NRP2a comprises a full length tail sequence with high homology to NRP1, including an analogous putative ESCPE-1-binding motif, whereas NRP2b lacks this sequence and the C-terminal PDZ binding motif, and differentially regulates RTK signalling (Gemmill et al., 2017; Rossignol et al., 2000).

A phage screen designed to identify protein sequences that mediated attachment and penetration of prostate cancer cell lines led to the discovery of a consensus C-terminal [R/K]xx[R/K] internalisation motif in cell-penetrating peptides (Teesalu et al., 2009). Affinity chromatography of internalised peptides conforming to this motif revealed NRP1 as their putative receptor. This phenomenon was termed the ‘C-end Rule’ (or ‘CendR’) due to its dependence on the C-terminal basic consensus sequence (Teesalu et al., 2009). A range of endogenous neuropilin ligands conform to this motif and engage a conserved binding pocket in the extracellular b1 domain. For example, this binding mechanism has been structurally characterised for NRP1 in complex with VEGF-A, and NRP2 in complex with VEGF-C (Parker et al., 2015, 2012c). The same basic motifs are often capable of binding both NRP1 and NRP2, and therefore receptor selectivity is likely conferred by secondary contact sites between ligand and receptor (Parker et al., 2015; Wang et al., 2015). Furthermore, ‘cryptic’ CendR motifs within a polypeptide chain can be unmasked by proteolytic cleavage events, as in the case of

Semaphorin 3F and VEGF-C binding to neuropilins (Guo et al., 2013; Parker et al., 2015). Notably, the CendR motif [R/K]xx[R/K], is almost identical to the minimal consensus motif required for cleavage by furin: RxxR (Krysan et al., 1999). Indeed, Semaphorin 3F only binds to neuropilins following productive furin processing to liberate a C-terminal ^{776}RNRR^{779} sequence (Guo et al., 2013; Parker et al., 2013).

Upon the discovery of this phenomenon, it was noted that the glycoproteins of many viruses may harbour cryptic CendR motifs that become liberated after proteolytic cleavage events during viral processing. This potential list of viruses includes H5N1 avian influenza virus, Ebola virus, and human immunodeficiency virus 1 (HIV-1) (Teesalu et al., 2009). Indeed, neuropilins have been implicated as receptors for a range of different viruses. For example, the human T-cell lymphotropic virus type I (HTLV-1) elicits molecular mimicry of the C-terminal region of VEGF-A to bind to NRP1 (Lambert et al., 2009). Moreover, a CendR motif in the Epstein-Barr virus glycoprotein B directly binds NRP1 to mediate infection (Wang et al., 2015). Neuropilins are therefore emerging host factors that can directly bind to viral glycoproteins to facilitate infection.

6.1.4 Aim

Following the development of the COVID-19 pandemic and the publication of the genetic sequence of SARS-CoV-2, our collaborative team began discussions aiming to investigate how SARS-CoV-2 cell biology might interface with the endosomal network. Following the identification of NRP1 in a screen for retrograde ESCPE-1-dependent cargoes in **Chapter 5**, and the observation that the SARS-CoV-2 S contains a novel CendR motif absent in its closest known relative in humans, we aimed to investigate whether NRP1 contributes to SARS-CoV-2 infection and could potentially comprise a novel therapeutic target in the study and treatment of COVID-19.

6.2 Results

6.2.1 Identification of a C-end Rule Motif in the SARS-CoV-2 Spike Protein

The C terminus of the SARS-CoV-2 S1 protein generated by furin cleavage has an amino acid sequence (^{682}RRAR^{685}) that conforms to the C-end rule **(Figures 6.2A and 6.2B)** (Teesalu et al., 2009). To explore the possibility that the SARS-CoV-2 S1 protein may associate with neuropilins, we generated a GFP–tagged S1 construct (GFP-S1) **(Figure 6.2C)**. When expressed in human embryonic kidney 293T (HEK293T) cells engineered to express the

SARS-CoV-2 ACE2, GFP-S1 immunoprecipitated endogenous NRP1 and ACE2 **(Figure 6.1A)**. We transiently co-expressed NRP1-mCherry and either GFP-S1 or GFP-S1 ΔRRAR (a deletion of the terminal ^{682}RRAR^{685} residues) in HEK293T cells. NRP1 immunoprecipitated the S1 protein, and deletion of the CendR motif reduced this association **(Figure 6.1B)**. Comparable binding was also observed with mCherry-NRP2, a receptor with high homology to NRP1 **(Figures 6.2D and 6.2E)**. In both cases, residual binding was observed with the ΔRRAR mutant, indicating an additional CendR-independent association between neuropilins and the S1 protein.

6.2.2 NRP1 Enhances SARS-CoV-2 Infection in Cell Culture

To probe the functional relevance of this interaction, we generated HeLa wild-type and NRP1 KO cell lines stably expressing ACE2, designated as HeLa^{wt}+ACE2 and HeLa^{NRP1KO}+ACE2, respectively (the level of ACE2 expression was comparable between these lines) **(Figure 6.2F)**. Using a clinical isolate SARS-CoV-2 (SARS-CoV-2/human/Liverpool/REMRQ001/2020), we performed viral infection assays and fixed the cells at 6, and 16 hours post-infection (hpi). SARS-CoV-2 infection was reduced in HeLa^{NRP1KO}+ACE2 relative to HeLa^{wt}+ACE2 **(Figure 6.1C)**. HeLa cells lacking ACE2 expression were not infected **(Figure 6.2G)**. In Caco-2 cells, a human colon adenocarcinoma cell line endogenously expressing ACE2 and widely used in COVID-19 studies, the suppression of NRP1 expression by short hairpin RNA (shRNA) greatly reduced SARS-CoV-2 infection at both 7 and 16 hpi, respectively, whereas that of vesicular stomatitis virus (VSV) pseudotyped with VSV-G was unaffected **(Figure 6.1D, 6.2H and 6.3A)**. To determine if NRP1 was required for early virus infection, we established a sequential staining procedure using antibodies against SARS-CoV-2 S and nucleocapsid (N) proteins to distinguish extracellular and intracellular viral particles **(Figure 6.3B)**. Although NRP1 depletion did not affect SARS-CoV-2 binding to the Caco-2 cell surface **(Figure 6.2E)**, virus uptake was halved in NRP1-depleted cells compared to control cells after 30 min of internalization **(Figure 6.1F)**. Thus, NRP1 enhances SARS-CoV-2 entry and infection.

We also observed that SARS-CoV-2–infected HeLa^{wt}+ACE2 cells displayed a multinucleated syncytia cell pattern, as reported by others **(Figure 6.1C)** (Hoffmann et al., 2020a). Using an image analysis algorithm and supervised machine learning **(Figure 6.3C-F)** (Hollandi et al., 2020), we quantified syncytia of infected HeLa^{wt}+ACE2 and HeLa^{NRP1KO}+ACE2 cells. At 16 hpi, the majority of HeLa^{wt}+ACE2 cells formed syncytia, whereas in HeLa^{NRP1KO}+ACE2 cells, this phenotype was reduced **(Figure 6.3G)**. When infected with a SARS-CoV-2 isolate lacking the furin cleavage site (SARS-CoV-2 ΔS1/S2) **(Figure 6.2A)**, the differences in infection and

syncytia formation were less pronounced **(Figures 6.3H and 6.3I)**. However, a significant decrease in infection of HeLa^{NRP1KO}+ACE2 was still observed at 16 hpi, indicating that NRP1 may additionally influence infection through a CendR-independent mechanism **(Figure 6.3H)**.

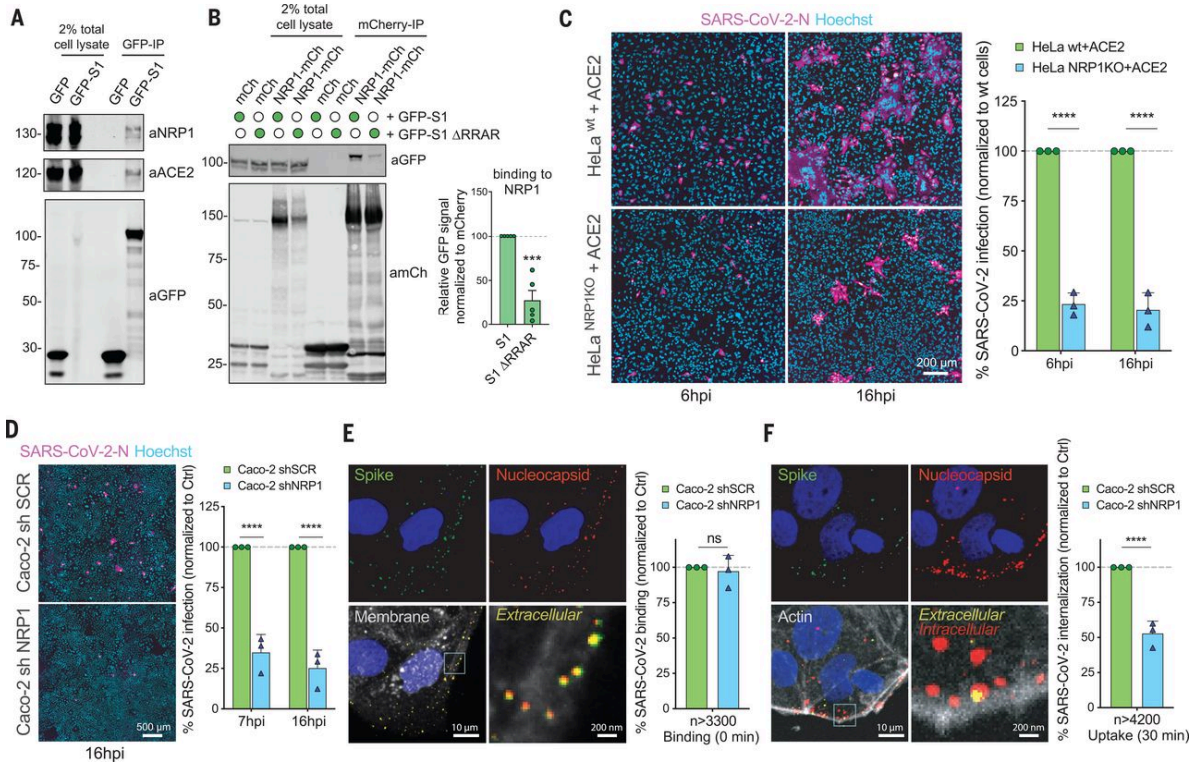

Figure 6.1 NRP1 Interacts with S1 and Enhances SARS-CoV-2 Infection

(**A**) HEK293T cells transduced to express ACE2 were transfected to express GFP or GFP-tagged S1 and lysed after 24 hours. The lysates were subjected to GFP-nanotrap, and the immune isolates were blotted for ACE2 and NRP1 (n = 3 independent experiments). (**B**) HEK293T cells were cotransfected to express GFP-tagged S1 or GFP-S1 ΔRRAR and mCherry or mCherry-tagged NRP1 and subjected to GFP-nanotrap (n = 5 independent experiments). Two-tailed unpaired t test; p = 0.0002. (**C**) HeLa^{wt}+ACE2 and HeLa$^{NRP1\ KO}$+ACE2 cells were infected with SARS-CoV-2. Cells were fixed at 6 or 16 hpi and stained for N protein (magenta) and Hoechst (cyan), and virus infectivity was quantified (n = 3 independent experiments). Two-tailed unpaired t test; p = 0.00002 and 0.00088. Scale bar, 200 µm. (**D**) Caco-2 cells expressing shRNA against NRP1 or a nontargeting control (SCR) were infected with SARS-CoV-2 and fixed at 7 or 16 hpi. The cells were stained for N protein (magenta) and Hoechst (cyan), and infectivity was quantified (n = 3 independent experiments). Two-tailed unpaired t test; p = 0.0005 and 0.00032. Scale bar, 500 µm. (**E**) Caco-2 shSCR or shNRP1 cells were inoculated with a multiplicity of infection (MOI) = 50 of SARS-CoV-2 and incubated in the cold for 60 min, and fixed. A two-step antibody staining procedure was performed with antibodies against S and N to distinguish external (green) and total (red) virus particles, and the binding of particles per cell was quantified for > 3300 particles per condition (n = 3 independent experiments). Two-tailed unpaired t test; p = 0.6859. (**F**) Caco-2 shSCR or shNRP1 cells were bound with SARS-CoV-2 as in (E), followed by incubation at 37°C for 30 min. The cells were fixed and stained as in (E). Viral uptake was quantified for > 4200 particles per condition (n = 3 independent experiments). Two-tailed unpaired t-test; p = 0.00079. Scale bars [(E) and (F)], 10 µm and 200 nm (magnified panels). The square regions were enlarged. The bars, error bars, and circles and triangles represent the

mean, SEM (B) and SD [(C) to (F)], and individual data points, respectively. ***p < 0.001, ****p < 0.0001. ns, not significant.

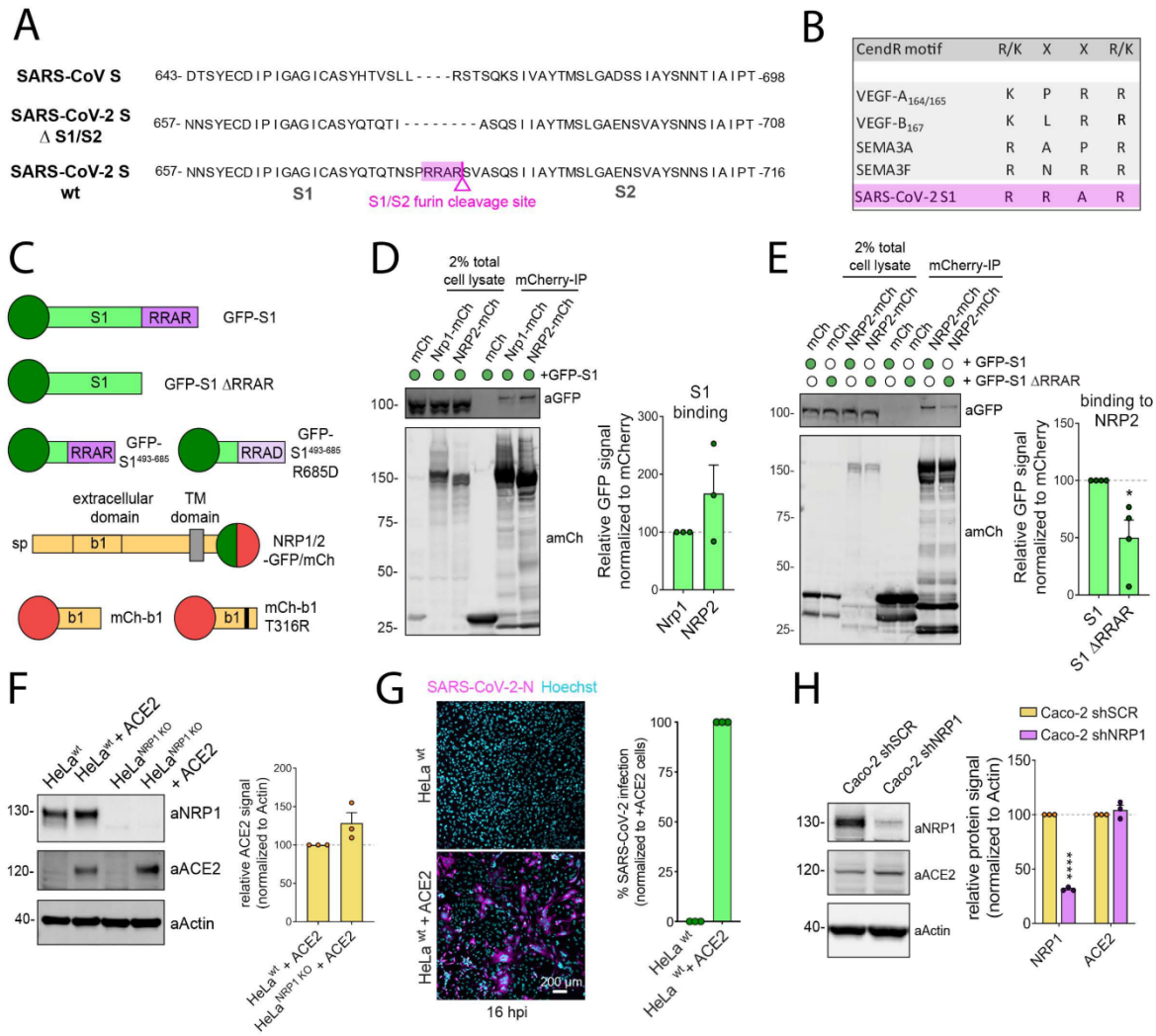

Figure 6.2 The SARS-CoV-2 S1 Protein Contains a CendR Motif

(A) Alignment of the S protein sequence of SARS-CoV and SARS-CoV-2. SARS-CoV-2 S possesses a furin cleavage site at the S1/S2 boundary that is absent in the SARS-CoV-2 ΔS1/S2 mutant. **(B)** Table highlighting the similarity between the C-terminal sequence of SARS-CoV-2 S1 and the CendR motifs of established NRP1 ligands. **(C)** Summary of constructs used in this study. TM = transmembrane. **(D)** SARS-CoV-2 S1 interacts with NRP2. HEK293T cells were co-transfected to express mCherry, mCherry-tagged Nrp1 or mCherry-tagged NRP2, and GFP-tagged S1, then subjected to mCherry-nanotrap (n = 3). Two-tailed unpaired t-test; p = 0.2421. **(E)** CendR motif dependent interaction of the SARS-CoV-2 S1 with NRP2. HEK293T cells were co-transfected to express GFP-tagged S1 or GFP-S1 ΔRRAR and mCherry or mCherry-tagged NRP2, then subjected to mCherry-nanotrap. (n = 4). Two-tailed unpaired t-test; p = 0.0175. **(F)** Quantification of ACE2 levels in HeLa^{wt}+ACE2 and HeLa^{NRP1KO} +ACE2 cells (n = 3). Two-tailed unpaired t-test; p =0.1065. **(G)** HeLa^{wt} and HeLa^{wt} +ACE2 were infected with SARS-CoV-2, fixed 16 hpi and infection was quantified (n = 3). Scale bar = 200 µm. **(H)** Caco-2 cells were transfected with a control shRNA (shSCR) an anti-NRP1 shRNA (shNRP1). Following western blotting of cell lysates, NRP1 and ACE2 bands were quantified (n = 3). Two-way ANOVA and Sidak's test; NRP1: p < 0.0001, ACE2: p = 0.374. The bars, error bars and circles represent the mean, SEM and individual data points, respectively. ∗p < 0.0001.

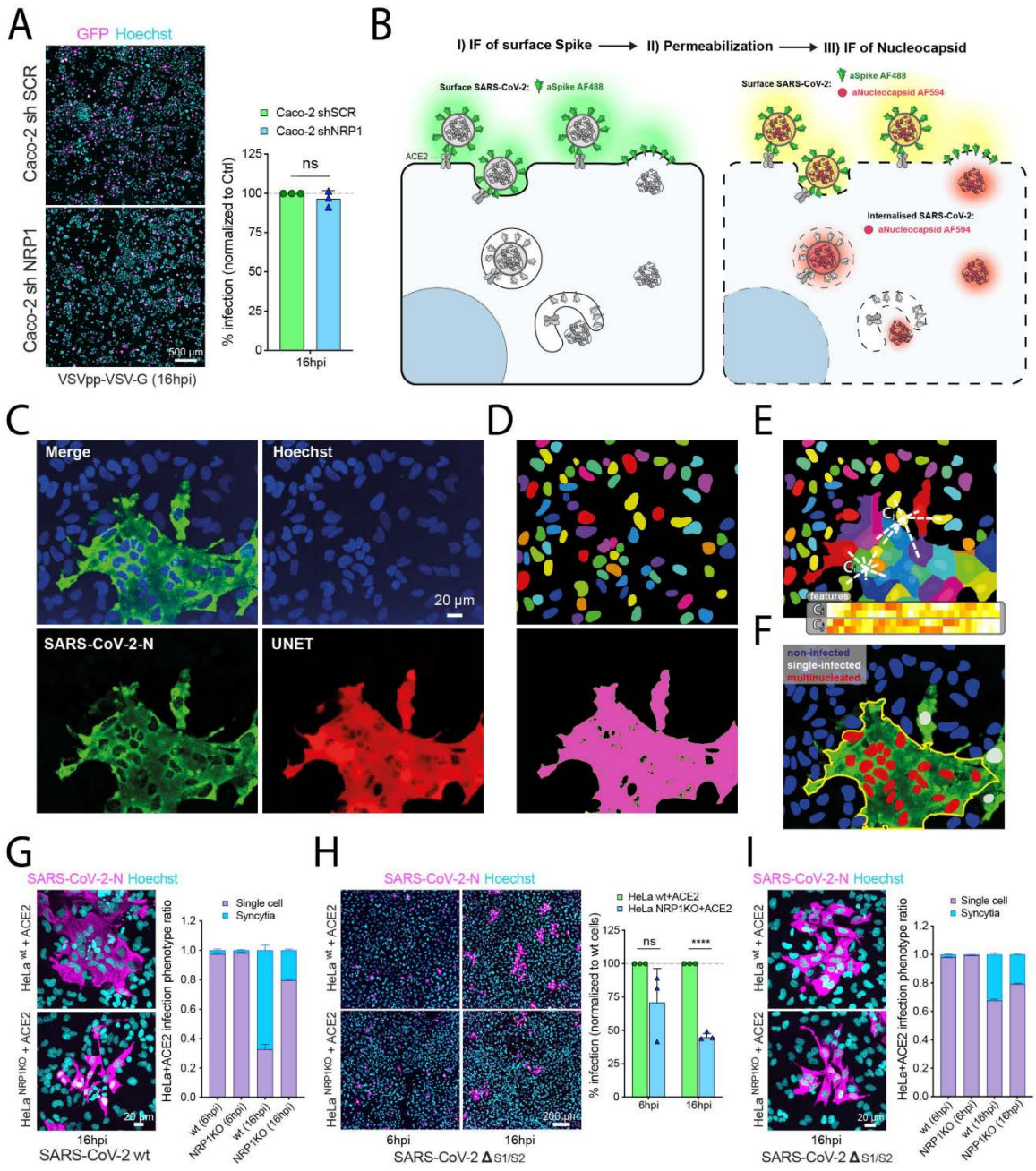

Figure 6.3 Image Processing and Phenotyping of SARS-CoV-2 Infected Cells

(A) Caco-2 shSCR and shNRP1 cells were infected with VSV pseudotyped with VSV-G for 16 hours, fixed, and detected by GFP reporter expression (n = 3). Two-tailed unpaired t-test. p =0.3187. Scale bar =500 µm. **(B)** Schematic of the two-step staining procedure used to distinguish external from internal virus particles. **(C)** Original image of SARS-CoV-2 N signal (green) and enhanced image (red) using UNET deep learning algorithm. **(D)** Single-cell segmentation of the nuclei using the nucleAIzer deep learning algorithm, and the cytoplasmic region based on global thresholding of the UNET enhanced image. **(E)** Morphology, shape and intensity features of single-cells and their microenvironment are extracted. Features include morphology, intensity and texture descriptor numbers. Ci: features of the i-th cell, Cj: features of the j-th cell. **(F)** Machine learning-based phenotyping of single cells into non-infected, single-nuclei infected and multinucleated cells. **(G)** Ratio of syncytia and single cell infection phenotypes in HeLa^{wt}+ACE2 and HeLa$^{NRP1\ KO}$+ACE2 cells infected with SARS-CoV-2. Cells were fixed at 16 hpi and stained for N protein (magenta) and Hoechst (cyan), and cell phenotypes were quantified (n = 3). Scale bar = 20 µm. **(H)** HeLa^{wt}+ACE2 and HeLa$^{NRP1\ KO}$+ACE2 cells were infected with SARS-CoV-2 ΔS1/S2. Cells were fixed at 6 or 16 hpi

and stained as in (G), and virus infectivity was quantified (n = 3). Two-tailed unpaired t-test; p =0.12 and p < 0.0001. Scale bar=200 µm. **(I)** Ratio of syncytia and single cell infection phenotypes in HeLa^{wt}+ACE2 and HeLa$^{NRP1\ KO}$+ACE2 cells infected with SARS-CoV-2 ΔS1/S2. Cells were fixed and stained as in (G). Scale bar = 20 µm. The bars, error bars, circles and triangles represent the mean, SD and individual data points, respectively. ∗p < 0.05, ∗∗p < 0.01, ∗∗∗p < 0.001, ∗∗∗∗p < 0.0001.

6.2.3 Biochemical Validation of the NRP1-S1 Interaction

The extracellular regions of NRP1 and NRP2 are composed of two CUB domains (a1 and a2), two coagulation factor domains (b1 and b2), and a MAM domain (Guo and Vander Kooi, 2015). Of these, the b1 domain contains the specific binding site for CendR peptides **(Figure 6.5A)** (Parker et al., 2012c). Accordingly, the mCherry-b1 domain of NRP1 immunoprecipitated GFP-S1, and a shortened GFP-S1 construct spanning residues 493 to 685 **(Figure 6.2C and 6.5B)**. Isothermal titration calorimetry (ITC) established that the b1 domain of NRP1 directly bound a synthetic S1 CendR peptide (^{679}NSPRRAR^{685}) with an affinity of 20.3 µM at pH 7.5, which was enhanced to 13.0 µM at pH 5.5 **(Figure 6.4A)**. Binding was not observed to an S1 CendR peptide in which the C-terminal arginine was mutated to alanine (^{679}NSPRRAA^{685}) **(Figure 6.4A)**. We co-crystallized the NRP1 b1 domain in complex with the S1 CendR peptide **(Figure 6.4B)**. The resolved 2.35-Å structure revealed four molecules of b1 with electron density of the S1 CendR peptide clearly visible in the asymmetric unit **(Figure 6.5C)**. S1 CendR peptide binding displayed strong similarity to the previously solved structure of NRP1 b1 domain in complex with its endogenous ligand VEGF-A$_{164}$ **(Figure 6.4C and 6.5D)** (Parker et al., 2012c). The key residues responsible for contacting the C-terminal R685 of the CendR peptide — Y297, W301, T316, D320, S346, T349 and Y353 — are almost identical between the two structures **(Figure 6.4B and 6.5D)**. The R682 and R685 side chains together engage NRP1 via stacked cation-π interactions with NRP1 side chains of Y297 and Y353. By projecting these findings onto the structure of the NRP1 ectodomain, the b1 CendR binding pocket appears to be freely accessible to the S1 CendR peptide **(Figure 6.5E)** (Janssen et al., 2012).

Site-directed mutagenesis of the S1 R685 residue to aspartic acid drastically reduced GFP-S1$^{493\text{-}685}$ immunoprecipitation by mCherry-b1, confirming the critical role of the C-terminal arginine **(Figure 6.4C)**. Mutagenesis of the T316 residue within the mCherry-b1 domain of NRP1 to arginine also reduced association with GFP-S1$^{493\text{-}685}$, consistent with its inhibitory impact on VEGF-A$_{164}$binding **(Figure 6.4D)** (Parker et al., 2012c). Accordingly, incubation of mCherry-b1 with VSV particles pseudotyped with trimeric S resulted in immunoprecipitation of processed forms of S1, which was dependent on the T316 residue **(Figure 6.5F)**. Next, we transiently expressed either GFP, full-length NRP1 wt-GFP, or full length NRP1-GFP harbouring the T316R mutation in HeLa^{NRP1KO}+ACE2 cells. GFP expression and ACE2

expression levels were comparable and both constructs retained similar cell surface localization **(Figures 6.5G and 6.5H)**. SARS-CoV-2 infection was significantly enhanced in cells expressing NRP1 wt-GFP compared to GFP control, whereas it was not enhanced in cells expressing the T316R mutant **(Figure 6.4E)**. Thus, the SARS-CoV-2 S1 CendR and NRP1 interaction promotes infection.

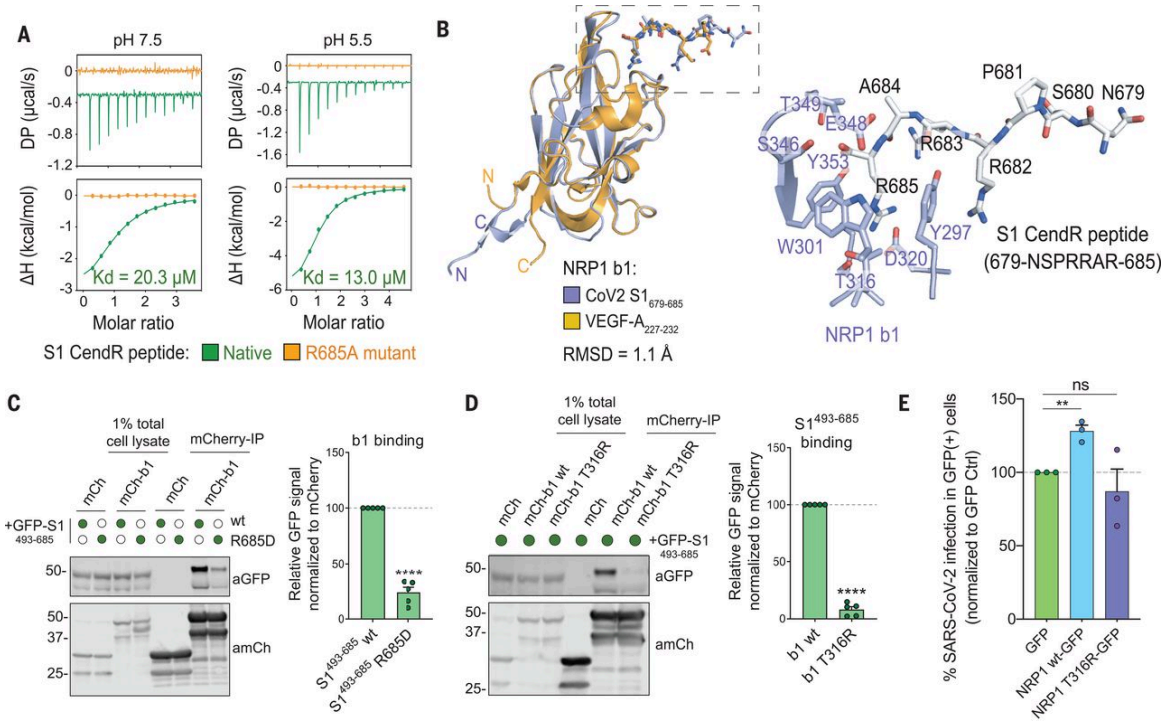

Figure 6.4 Molecular Basis for CendR Binding of SARS-CoV-2 S1 with NRP1

(**A**) Binding of NRP1 b1 with native (green line) and mutant (orange line) form of S1 CendR peptide (corresponding to residues 679 to 685) by ITC at two different pH conditions (n = 3 independent experiments). All ITC graphs represents the integrated and normalized data fit with 1-to-1 ratio binding. (**B**) (Left) NRP1 b1–S1 CendR peptide complex superposed with NRP1 b1–VEGF-A fusion complex (PDB ID: 4DEQ). Bound peptides are shown in stick representation. RMSD, root mean square deviation. (Right) Enlarged view highlighting the binding of S1 CendR peptide b1. Key binding residues on b1 are shown in stick representation. Abbreviations for the amino acid residues are as follows: A, Ala; D, Asp; E, Glu; N, Asn; P, Pro; R, Arg; S, Ser; T, Thr; W, Trp; and Y, Tyr. (**C**). HEK293T cells were cotransfected with combinations of GFP-tagged $S1^{493-685}$ and $S1^{493-685}$ R685D, and mCherry or mCherry-NRP1 b1, and subjected to mCherry-nanotrap (n = 5 independent experiments). Two-tailed unpaired t test; p < 0.0001. (**D**). HEK293T cells were cotransfected with combinations of GFP-tagged $S1^{493-685}$ and mCherry, mCherry-NRP1 b1 or mCherry-NRP1 b1 T316R mutant, and subjected to mCherry-nanotrap (n = 5 independent experiments). Two-tailed unpaired t test; p < 0.0001. (**E**) $HeLa^{NRP1KO}$ + ACE2 cells transfected with GFP, NRP1 wt-GFP, or NRP1 T316R-GFP constructs were infected 24 hours later with SARS-CoV-2. At 16 hpi, the cells were fixed and stained for SARS-CoV-2-N, and viral infection was quantified in the GFP-positive subpopulation of cells (n = 3 independent experiments). The percentage of infection was normalized to that of GFP-transfected cells. Two-tailed unpaired t-test; p = 0.002. The bars, error bars, and circles represent the mean, SEM [(C) and (D)] and SD (E), and individual data points, respectively. **p < 0.01, ****p < 0.0001. ns, not significant.

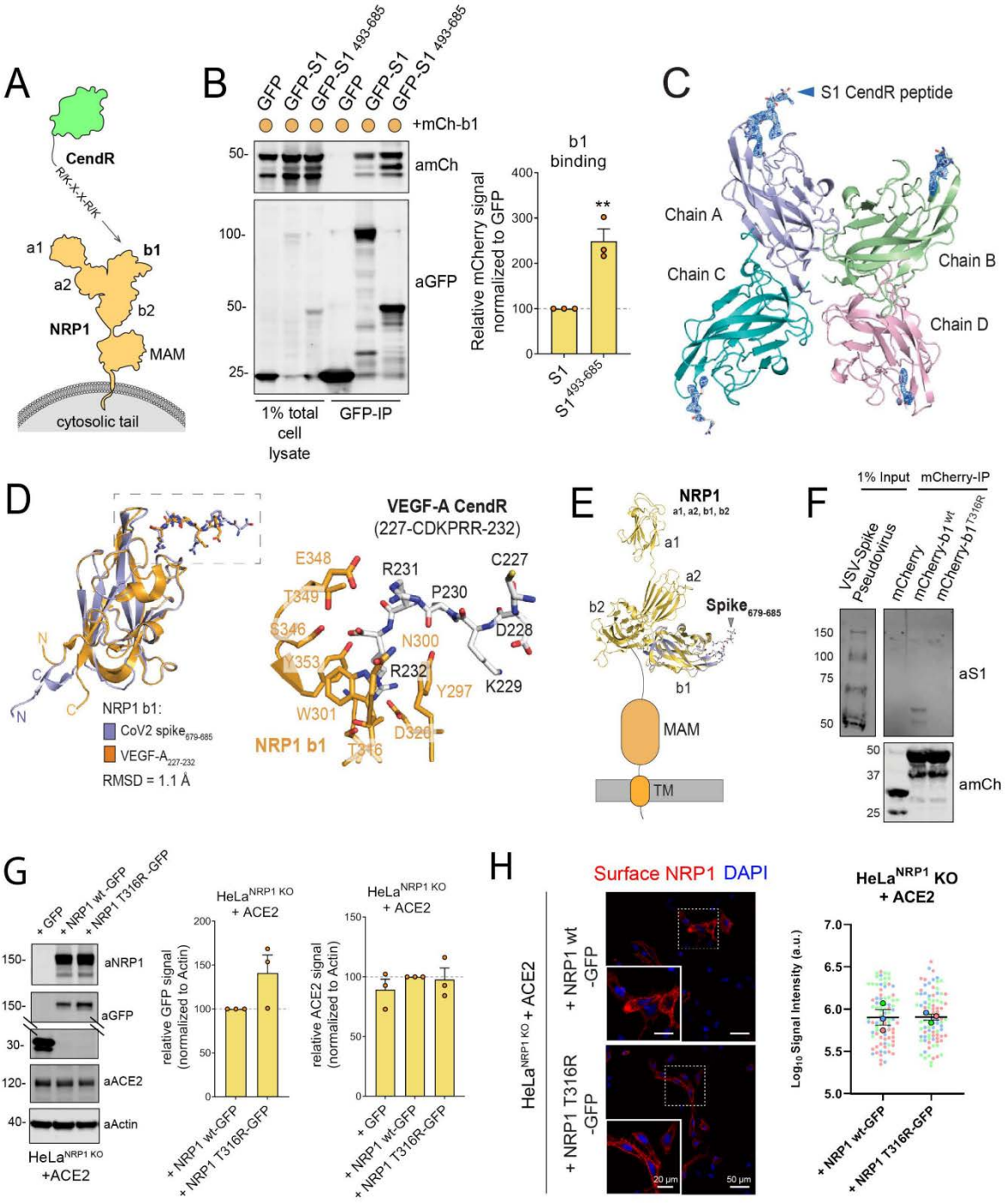

Figure 6.5 Extended Molecular Insights into the S1-NRP1 Interaction

(**A**) Schematic of CendR motif binding to the NRP1 b1 domain. (**B**) HEK293T cells were co-transfected with combinations of mCherry-b1, and GFP, GFP-tagged S1 or $S1^{493-685}$ and subjected to GFP nanotrap (n = 3). Two-tailed unpaired t-test; p = 0.0050. (**C**) Ribbon representation of NRP1 b1 –S1 CendR peptide complex. The electron density shown corresponds to a simulated-annealing OMIT Fo – Fc map of S1 CendR peptide contoured at 3σ. For clarity, the S1 CendR peptide binds to chain C of NRP1 B1 domain showing the electron density from N679 to R685 was selected for structural analysis and figure display. (**D**) Left: NRP1 b1 – S1 CendR peptide complex superposed with NRP1 b1 – VEGF-A fusion complex (PDB ID: 4DEQ). Right: enlarged view highlighting the binding of VEGF-A227-232 to NRP1 b1. Bound peptides and key binding residues on b1 are shown in stick representation. (**E**) NRP1 b1 – S1 CendR peptide complex superposed with NRP1 a1a2b1b2 structure (PDB ID: 4GZ9). (**F**) HEK293T cells were co-transfected with mCherry, mCherry-NRP1 b1

or mCherry-NRP1 b1 T316R and the mCherry-tagged proteins were captured on mCherry-beads. VSV-S pseudoparticles were then added and subjected mCherry nanotrap (n = 3). (**G**) HeLa$^{NRP1\ KO}$+ACE2 cells were transfected with GFP, NRP1 wt-GFP or NRP1 T316R-GFP and lysed 24 h later (n = 3). GFP levels: Two-tailed unpaired t-test, p = 0.1167. ACE2levels: one-way ANOVA and Dunnett's test; +NRP1 wt-GFP vs + GFP, p = 0.5293; +NRP1 wt-GFP vs + NRP1 T316R-GFP, p = 0.9672. (**H**) IF staining of HeLa^{NRP1KO} + ACE2 transfected with NRP1 wt-GFP and NRP1 T316R-GFP. Non-permeabilised cells were labelled with anti-NRP1 mAb#3, and signal intensity was quantified using Volocity software (n = 3, 88 cells per condition). Two-tailed unpaired t-test; p = 0.9829. Scale bar = 50 µm and 20 µm (zoom panel). The bars, error bars and circles represent the mean, SEM and individual data points, respectively. $*p < 0.05$, $**p < 0.01$, $***p < 0.001$, $****p < 0.0001$.

6.2.4 Inhibition of the NRP1-S1 Interaction Suppresses SARS-CoV-2 Infection in Cell Culture

To establish the functional relevance of the S1 CendR-NRP1 interaction, we screened monoclonal antibodies (mAb#1, mAb#2, mAb#3) raised against the NRP1 b1b2 ectodomain. All three bound to the NRP1 b1b2 domain, displayed staining by immunofluorescence in NRP1-expressing PPC-1 (human primary prostate cancer) cells but not in M21 (human melanoma) cells that do not express NRP1 **(Figure 6.7A)**, and stained the extracellular domain of NRP1-GFP expressed in cells **(Figure 6.7B)** (Teesalu et al., 2009). Of these antibodies, mAb#3, and to a lesser extent mAb#1, bound to the CendR-binding pocket with high specificity, as defined by reduced ability to bind to a b1b2 mutant that targets residues (S346, E348, T349) at the opening of the binding pocket **(Figure 6.6A)** (Parker et al., 2012c). Incubation of Caco-2 cells with mAbs#1 and 3 reduced SARS-CoV-2 infection compared to a control mAb targeting avian influenza A virus (H11N3) hemagglutinin **(Figure 6.6B)**. Consistent with this, mAb#3 inhibited binding of GFP-S1$^{493-685}$ and mCherry-b1 **(Figure 6.6C)**. As a comparison, Caco-2 and Calu-3 cells were incubated with soluble ACE2, which inhibited SARS-CoV-2 infection in both cases **(Figure 6.7C)**.

Next, we turned to the small molecule EG00229, a selective NRP1 antagonist that binds the b1 CendR binding pocket and inhibits VEGF-A binding **(Figure 6.6D)** (Jarvis et al., 2010). ITC established that EG00229 bound to the NRP1 b1 domain with a dissociation constant (K_d) of 5.1 and 11.0 µM at pH 7.5 and 5.5, respectively **(Figure 6.6E)**. EG00229 inhibited the direct binding between b1 and the S1 CendR peptide, and the immunoprecipitation of GFP-S1$^{493-685}$ by mCherry-b1 **(Figure 6.6E and 6.7D)**. Finally, incubation of Caco-2 cells with EG00229 reduced the efficiency of SARS-CoV-2 infection at 7 and 16 hpi **(Figure 6.6F)**. Thus, the SARS-CoV-2 interaction with NRP1 can be targeted to reduce viral infectivity in relevant human cell lines **(Figure 6.8)**.

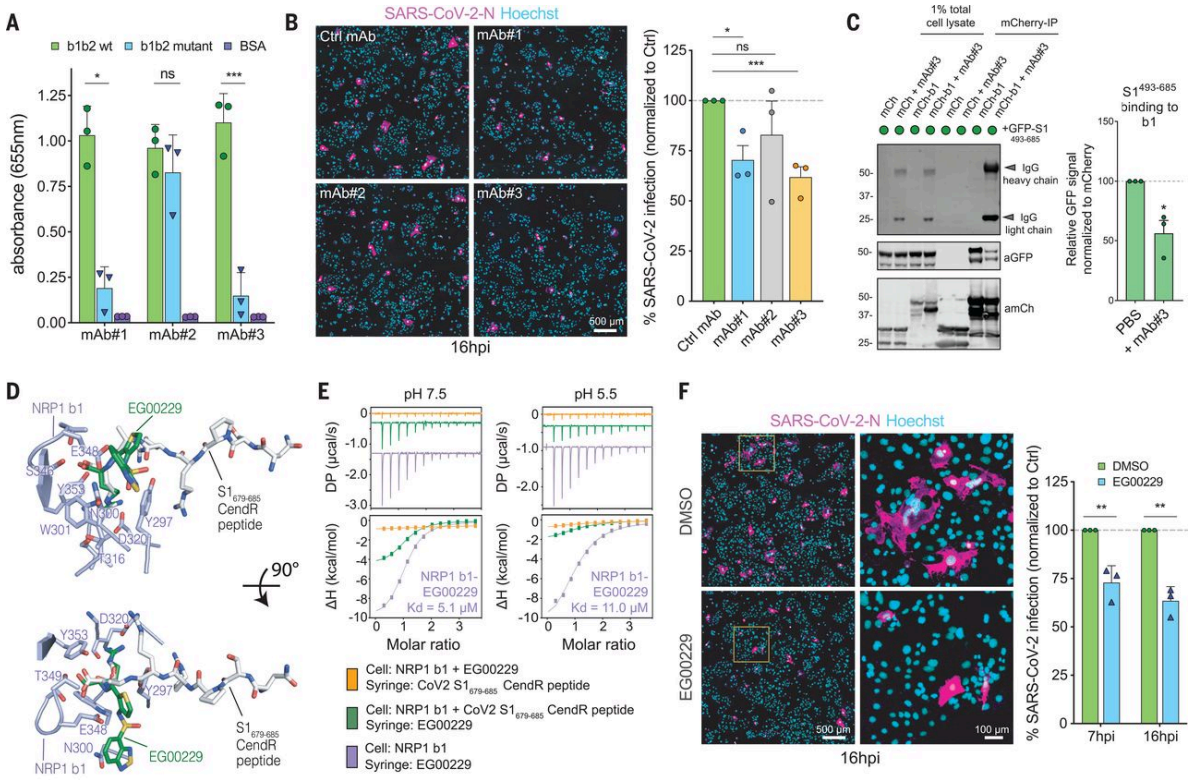

Figure 6.6 Selective Inhibition of the S1-NRP1 Interaction Reduces SARS-CoV-2 Infection

(**A**) Enzyme-linked immunosorbent assay of anti-NRP1 monoclonal antibodies (mAb#1, mAb#2, mAb#3) at 3 µg/mL using plates coated with NRP1 b1b2 wild type, b1b2 mutant (S346A, E348A, T349A), or bovine serum albumin (BSA), used as a control (n = 3 independent experiments). Binding is represented as arbitrary units of absorbance at 655 nm. Two-tailed unpaired t test; p = 0.0207, 0.2430, 0.0007. (**B**) Cells were first treated with anti-H11N3 (100 µg/ml) (Ctrl) mAb, mAb#1, mAb#2, or mAb#3 for 1 hour before infection with SARS-CoV-2. Cells were fixed at 16 hpi and stained for N protein (magenta) and Hoechst (cyan) (n = 3 independent experiments). Two-tailed unpaired t test; p = 0.015, 0.36, 0.0003. Scale bar, 500 µm. (**C**) HEK293T cells were cotransfected with combinations of mCherry or mCherry-b1 and GFP-tagged $S1^{493-685}$ and subjected to mCherry-nanotrap with or without coincubation with mAb#3 (n = 3 independent experiments). Two-tailed unpaired t test; p = 0.0143. (**D**) NRP1 b1–S1 CendR peptide complex superimposed with NRP1 b1–EG00229 inhibitor complex (PDB ID:3I97). Key binding residues on b1, bound peptides, and EG00229 are shown in stick representation. (**E**) ITC analysis of EG00229 binding to b1 domain of NRP1 at two different pH conditions. Preincubation with EG00229 blocks S1 CendR peptide binding (orange line), and the CendR peptide can reduce binding of EG00229 (green line) (n = 3 independent experiments). All ITC graphs represent the integrated and normalized data fit with 1-to-1 ratio binding. (**F**). Cells were first treated with 100 µM EG00229 or dimethyl sulfoxide (DMSO) before infection with SARS-CoV-2. Cells were fixed at 7 and 16 hpi and stained for N protein (magenta) and Hoechst (cyan) (n = 3 independent experiments). The square regions were enlarged. Scale bars, 500 µm and 100 µm (magnified panels). Two-tailed unpaired t test; p = 0.0059 and 0.0013. The bars, error bars, and circles and triangles represent the mean, SEM (C) and SD [(A), (B), and (F)], and individual data points, respectively. *p < 0.05, **p < 0.01, ***p < 0.001.

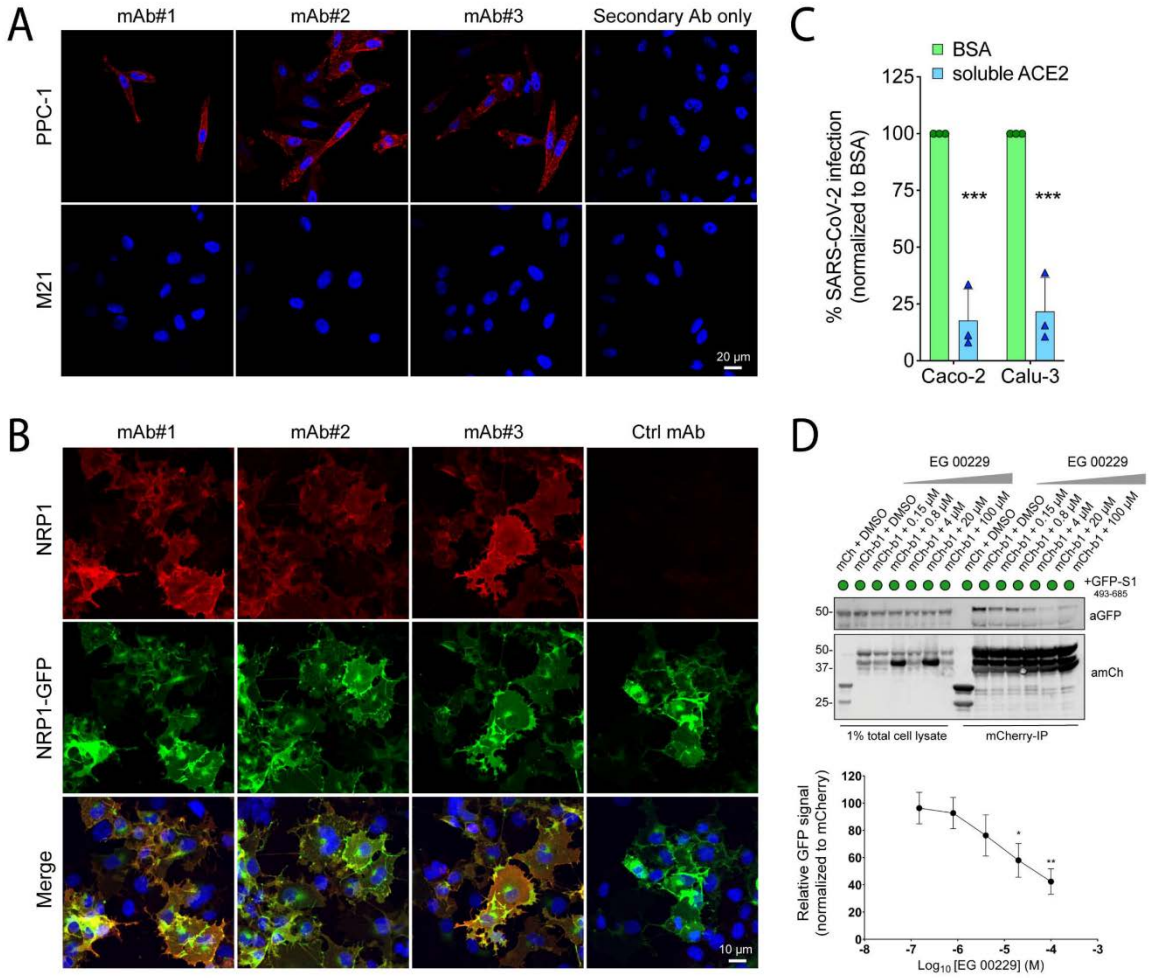

Figure 6.7 Validation of Selective Inhibitors for SARS-CoV-2 Infection

(A) Fluorescence confocal images of non-permeabilised NRP1-positive PPC-1 and NRP1-negative M21 cells incubated with mAb#1, #2 and #3 (n = 2). Antibody staining (red) and DAPI (blue) are shown. Scale bar = 20 µm. **(B)** Fluorescent spinning-disk confocal images of Cos7 cells expressing human NRP1-GFP using mAb#1, #2, #3 and ctrl mAb against influenza HA. Non-permeabilised, fixed cells in 96-well plates were incubated with the mAbs (1:10 dilution) for 1 h and immunostained with the secondary antibody AlexaFluor 594 goat anti-mouse IgG. Z- stack images were acquired using a 20x objective and maximum projections are shown (n = 3). Blue: Hoechst; Green: GFP; Red: antibody signal. Scale bar=10 µm. **(C)** Inhibition of SARS-CoV-2 infection by treatment with recombinant soluble ACE2 in Caco-2 and Calu-3 cells. Cells were pre-treated with soluble ACE2 (10 µg/mL) for 1 h prior to SARS-CoV-2 infection. At 16 hpi the cells were fixed and stained for N protein and infection was quantified (n = 3). Two-tailed unpaired t-test; p =0.0005 and 0.0008. **(D)** EG00229 inhibits GFP-S1493-685 immunoprecipitation. HEK293T cells were co-transfected with GFP-tagged S1493-685 and mCherry or mCherry-b1, and subjected to a mCherry-nanotrap in the presence of the indicated concentrations of EG00229 or DMSO (n = 6). Ordinary one-way ANOVA with Dunnett's multiple comparisons test, p = 0.9996 (0.15 µM), 0.9866 (0.8 µM), 0.4265 (4 µM), 0.0473 (20 µM) and 0.0041 (100 µM). The bars, error bars, circles and triangles represent the mean, SD (**C**) and SEM (**D**) respectively. $*p < 0.05$, $**p < 0.01$, $***p < 0.001$, $****p < 0.0001$.

.

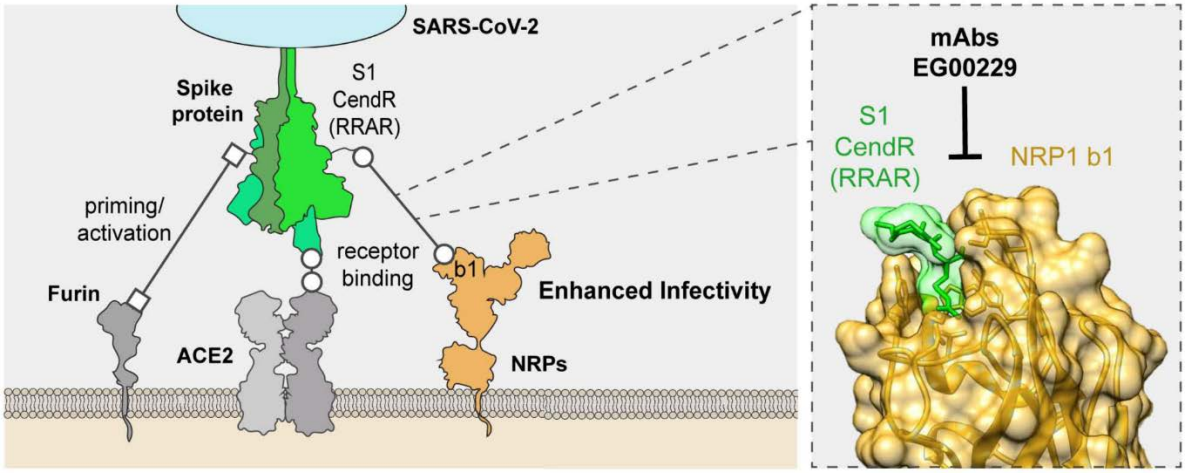

Figure 6.8 Model of NRP1 Binding in SARS-CoV-2 Infection

The S1 protein of SARS-CoV-2 associates with neuropilins through CendR peptide recognition by the neuropilin b1 domain. This interaction promotes SARS-CoV-2 entry and infection in physiologically relevant cell lines. The ability to target this specific interaction may provide a route for COVID-19 therapies.

6.3 Discussion

Cell entry of SARS-CoV-2 depends on priming by host cell proteases (Hoffmann et al., 2020a, 2020b; Millet and Whittaker, 2018). Our data indicate that a component of SARS-CoV-2 S protein binding to cell surface neuropilins occurs via the S1 CendR motif generated by the furin cleavage of S1/S2. Though not affecting cell surface attachment, this interaction promotes entry and infection by SARS-CoV-2 in physiologically relevant cell lines widely used in the study of COVID-19. The molecular basis for the effect is unclear, but neuropilins are known to mediate the internalization of CendR ligands through an endocytic process resembling macropinocytosis (Pang et al., 2014; Simons et al., 2016; Teesalu et al., 2009). Notably, gene expression analysis has revealed an up-regulation of NRP1 and NRP2 in lung tissue from COVID-19 patients (Ackermann et al., 2020). A SARS-CoV-2 virus with a natural deletion of the S1/S2 furin cleavage site demonstrated attenuated pathogenicity in hamster models (Lau et al., 2020). NRP1 binding to the CendR peptide in S1 is thus likely to play a role in the increased infectivity of SARS-CoV-2 compared with SARS-CoV. The ability to target this specific interaction may provide a route for COVID-19 therapies.

6.3.1 A Secondary Site in the S1-NRP1 Interaction Interface

The CendR sequence of the S1 protein directly interacts with the binding pocket present in the NRP1 b1 domain, and this interaction can be inhibited by small molecule compounds or monoclonal antibodies. However, truncation of the ^{682}RRAR^{685} sequence from GFP-S1 did not

completely abolish its affinity for NRP1 or NRP2. Moreover, saturating concentrations of EG00229 also failed to completely block immunoprecipitation of GFP-S1 by the mCherry-b1 domain of NRP1. Accordingly, the inhibitory effects of blocking SARS-CoV-2 infection with EG00229 or monoclonal antibodies blocking the b1 binding pocket, while significant, were not equal to the effects observed by NRP1 KO or suppression. Together these data suggest the presence of an additional interaction interface between S1 and NRP1 that contributes affinity to the association. The shortened GFP-S1$^{493-685}$ construct demonstrated higher levels of immunoprecipitation by mCherry-b1, suggesting that the additional interface may lie within this C-terminal 192 amino acid sequence.

Secondary contact sites between neuropilins and their ligands have been reported. In the case of mouse VEGF-A_{164} binding to NRP1, a glutamic acid side chain 10 residues upstream of the CendR motif contacts a loop on the external rim of the b1 binding pocket through a hydrogen bond (Parker et al., 2012c). Abolition of this interaction by site-directed mutagenesis causes an ~20% decrease in affinity between VEGF-A_{164} and NRP1 (Parker et al., 2012c). This modest, but significant contribution to affinity could be consistent with the ~25% residual GFP-S1 ΔRRAR binding observed by immunoprecipitation. However, in the case of the Epstein-Barr virus glycoprotein B (gB), truncation of the C-terminal ^{428}RRRR^{431} CendR motif greatly reduces NRP1 association, but the additional removal of a N-terminal 66 amino acid sequence over 300 residues upstream is required to completely abolish the interaction, highlighting that secondary interaction sites do not necessarily reside directly upstream of the CendR sequence (Wang et al., 2015). A recent molecular modelling study suggested that the a2b1b2 extracellular fragment of NRP1 could interact with trimeric spike protein, either independently or coincidentally with ACE2 binding, and that this interaction may enhance the separation of the S1 and S2 domains (Li and Buck, 2021). As expected, this modelled binding occurred away from the RBD, and thus the S1-NRP1 interaction may not preclude ACE2 binding. Multiple potential interfaces for S1:NRP1 association were postulated by the molecular model, including sequences between the RBD and CendR motif (residues 542-685) (Li and Buck, 2021). These potential interfaces represent particularly interesting candidates for further study of the secondary binding interface between S1 and NRP1.

6.3.2 NRP1 May Provide a Route to the Central Nervous System

An independent study also demonstrated that blocking NRP1 could limit SARS-CoV-2 infection in cell culture, and this effect depended upon the integrity of the SARS-CoV-2-S furin cleavage site (Cantuti-Castelvetri et al., 2020). Moreover, the study reported a potential role for NRP1 in facilitating SARS-CoV-2 entry into the central nervous system. 80 nm silver

nanoparticles, of similar size to coronavirus virions, were coated with short peptide sequences harbouring the post-cleaved CendR sequence of S1. These particles are effectively internalised by cells in culture and by olfactory epithelial cells of mice in a NRP1-dependent mechanism that depends on conformity of the peptide to a CendR motif (Cantuti-Castelvetri et al., 2020). Remarkably, when sprayed into the nasal passages of mice, the CendR-coated particles traversed the olfactory epithelium and entered neurons and blood vessels of the cortex. Infection of the olfactory epithelium was also observed by histopathology in human COVID-19 autopsy samples (Cantuti-Castelvetri et al., 2020). Intercellular transport of CendR ligands by NRP1 has previously been reported in spheroid cell cultures, though its mechanistic basis remains unclear (Pang et al., 2014). These data raise the possibility that NRP1-dependent infection of the olfactory epithelium and the olfactory neurons that project into this epithelium could contribute to the widely reported COVID-19 symptom of anosmia (Cantuti-Castelvetri et al., 2020).

Additional studies have since reported roles of NRP1 in SARS-CoV-2 infection of the central nervous system. Stimulation of neurons with VEGF-A promotes a pro-nociceptive electrophysiological signalling response associated with neuropathic pain. Recombinant SARS-CoV-2-S or EG00229 could effectively inhibit this pain response by outcompeting VEGF-A for NRP1 binding (Moutal et al., 2021). Accordingly, injection of rats with VEGF-A in the presence of recombinant SARS-CoV-2-S or EG00229 led to decreased responses to pain compared to controls, measured as slower paw withdrawal to painful stimuli. These data suggest that the SARS-CoV-2-S protein, at least when recombinantly administered, may promote an analgesic effect by blocking NRP1 signalling (Moutal et al., 2021). Moreover, a recent study reported that SARS-CoV-2 infected astrocytes in COVID-19 patient postmortem samples (Crunfli et al., 2020). NRP1 was expressed in higher levels in astrocytes of infected individuals compared to controls, while ACE2 expression in this cell type was not detected. An anti-NRP1 blocking antibody was also able to prevent entry of VSV particles pseudotyped with SARS-CoV-2-S into astrocytes, arguing for a potential NRP1-dependent, ACE2-independent mechanism of entry (Crunfli et al., 2020). NRP1-mediated infection may therefore play a role in the manifestation of neurological symptoms of COVID-19, although more data are required to strengthen this hypothesis (Aghagoli et al., 2020; Chen et al., 2020).

6.3.3 A Potential Role for NRP2 in SARS-CoV-2 Infection

Immunoprecipitation experiments revealed that GFP-S1 could also interact with NRP2-mCherry through a mechanism largely dependent on the ^{682}RRAR^{685} CendR motif. There appears to be some degree of redundancy in ligand binding between NRP1 and NRP2

(Nakamura et al., 2000; Parker et al., 2012b; Sarabipour and Mac Gabhann, 2018). Moreover, the reported ability of NRP1 and NRP2 to heterodimerise further complicates the understanding of ligand selectivity (Sawma et al., 2014). The b1 domain responsible for coordinating CendR ligand binding is highly homologous between both receptors, and therefore short basic CendR sequences likely bind both receptors with similar affinities, with additional selectivity conferred by secondary contact interfaces elsewhere on the receptor surface. However, more information regarding a potential secondary interface between NRP1 and S1 is required to subsequently observe whether this site would also be conserved in NRP2. Overall, more biochemical evidence will be required to directly implicate NRP2 as a host factor for SARS-CoV-2. Understanding the selectivity, or lack thereof, of the SARS-CoV-2-S protein for NRP1 or NRP2 may impact the design of selective inhibitors to block this interaction. Recently, hospitalised COVID-19 patients treated with selective NRP2 inhibitor originally developed for the treatment of sarcoidosis displayed a modest improvement compared to placebo-treated control patients (aTyr Pharma Inc, 2021).

6.3.4 The Role of NRP1 in Syncytia Formation

Multinucleated cells have been reported in COVID-19 autopsy samples, and may provide a virion-independent mechanism of cell spreading that facilitates tissue penetration during infection (Bradley et al., 2020; Xu et al., 2020). Syncytia formation potentially occurs through the binding of cell-surface localised SARS-CoV-2-S proteins to receptors on neighbouring cells, such as ACE2 and NRP1 (Leroy et al., 2020). In the case of SARS-CoV-2, and a range of other β-coronaviruses, a suboptimal COPI motif appears to facilitate the ‘leakage’ of some S molecules through the biosynthetic pathway towards the plasma membrane, where cell-cell fusion subsequently occurs (Cattin-Ortolá et al., 2020).

Furin cleavage appears to play an important role in mediating cell-cell fusion. For example, introduction of a furin cleavage site in S1-S2 boundary and/or at the S2’ site in SARS-CoV-S enhances syncytia formation (Belouzard et al., 2009; Hoffmann et al., 2020a). The SARS-CoV-2 ΔS1/S2 virus used in this chapter contains a naturally occurring deletion of the furin cleavage site that arises from passage in VeroE6 cells (Davidson et al., 2020). Infection with this virus predominantly induces single cell infections in HeLa + ACE2 cells. CRISPR-Cas9 KO of furin reduces SARS-CoV-2 infectivity but does not completely prevent syncytia formation through a cell-cell fusion assay (Papa et al., 2021). This may suggest potential redundancy with other proprotein convertase enzymes, a family of 9 proteins including furin with similar consensus cleavage motifs. Moreover, the presence of TMPRSS2 in ‘acceptor’ cells enhances the efficiency of their fusion with SARS-CoV-2-S-expressing ‘donor’ cells, highlighting the importance of TMPRSS2 priming for cell-cell fusion (Buchrieser et al., 2020;

Papa et al., 2021). Taken together, there appear to be multiple routes for SARS-CoV-2-S proteolytic activation to mediate infection and cell-cell fusion, with furin often playing an important role.

A striking phenotype upon SARS-CoV-2 infection of HeLa$^{NRP1\ KO}$ + ACE2 cells is the dramatic reduction in syncytia formation. The similarity of this phenotype to the effect seen in HeLa^{wt} + ACE2 cells infected with the SARS-CoV-2 ΔS1/S2 virus suggests that the recognition of the CendR sequence by NRP1 is particularly important in the cell-cell fusion phenomenon. The mechanistic basis for this process remains unclear. If experimentally verified, a possible mechanism could be that NRP1 on an 'acceptor' cell binding to the S1 CendR sequence on an adjacent 'donor' cell enhances separation of S1 from S2, priming the S2 protein at the cell surface to mediate fusion of the 'donor' and 'acceptor' plasma membranes (Li and Buck, 2021). Moreover, the ability of CendR ligands to be intercellularly transported through three-dimensional spheroidal cell cultures may relate to the cell-cell fusion phenotype observed upon SARS-CoV-2 infection (Pang et al., 2014).

Interestingly, overexpression of NRP1 in cells expressing the Epstein Barr virus glycoprotein gB, or the HTLV-1 glycoprotein SU, both of which interact with NRP1 through a CendR-dependent mechanism, enhances cell-cell fusion (Ghez et al., 2006; Wang et al., 2015). Epstein-Barr virus is a double-stranded DNA virus of the *Herpesviridae* family, whereas HTLV-1 and SARS-CoV-2 are single-stranded RNA virus of the *Retroviridae* and *Coronaviridiae* families respectively, belonging to a distinct taxonomic realm. Multiple other evolutionarily distant viruses have been reported to induce cell-cell fusion, including HIV-1 (*Retroviridae*), Ebola virus (*Filoviridae*), influenza A (*Orthomyxoviridae*), human respiratory syncytial virus (HRSV, *Paramyxoviridae*), and hepatitis C virus (HCV, *Flaviridae*) (Leroy et al., 2020; Su et al., 2009). This raises the fascinating possibility that recognition of cleaved multibasic CendR sequences by NRP1 could be a conserved mechanism for mediating host cell-cell fusion across highly evolutionarily distant viruses. Experimental validation of this theory could provide significant therapeutic insight into the treatment of viral infections.

6.3.5 NRP1 as a Molecular Scaffold for SARS-CoV-2 Host Factors

In addition to binding soluble extracellular ligands, NRP1 has multiple further functions at the cell surface, including lateral association with RTKs and binding and coordination of integrin complexes (Parker et al., 2012a). NRP1 can be covalently conjugated to the glycosaminoglycans heparan sulphate (HS) and chondroitin sulphate (Shintani et al., 2006). NRP1 and NRP2 also noncovalently bind to HS via a positively charged tract on the surface of the b1b2 domains, and this binding can induce dimerization of these domains (Vander Kooi et al., 2007). HS is an abundant, broadly negatively charged component of extracellular matrix

involved in myriad biological functions (Cagno et al., 2019). In addition to their CendR-dependent binding, many neuropilin ligands simultaneously bind to heparin or HS, such as VEGF-A_{165}, fibroblast growth factor and hepatocyte growth factor (Parker et al., 2012c; West et al., 2005). Addition of heparin dramatically enhances the affinity of VEGF-A_{165}-NRP1 association from 2 μM to 25 nM (Fuh et al., 2000). HS binding therefore creates an avidity effect that serves to dock neuropilin ligands within close proximity to the NRP1 b1 domain for CendR binding.

Crucially, HS is commonly exploited by a wide array of viruses, including coronaviruses, harbouring positive charge in their external glycoproteins as an attachment factor to adhere to the surface of cells (Cagno et al., 2019). The HTLV-1 SU protein behaves similarly to VEGF-A_{165} by coincidentally detecting both HS and NRP1. Moreover, HTLV-1 infection can be attenuated by incubation with the recombinant heparin binding region of VEGF-A_{165} alone, highlighting the importance of HS docking for subsequent CendR-mediated infection (Lambert et al., 2009). SARS-CoV-2 infection also depends upon HS binding, particularly through a positively charged region on the surface of the RBD that is distinct from the ACE2-binding surface (Clausen et al., 2020). Enzymatic digestion of HS or out-competition with unfractionated heparin reduces SARS-CoV-2 infection in cell culture (Clausen et al., 2020; Tree et al., 2021).

A role for integrin proteins has also been proposed in SARS-CoV-2 infection. In particular, the SARS-CoV-2 S RBD contains a RGD motif known to bind at the α-β interface of various integrin heterodimer combinations (Sigrist et al., 2020). This RGD sequence is located at the ACE2 binding interface, and thus a single RBD cannot engage both ACE2 and integrins simultaneously (Mészáros et al., 2021). However, it may be possible that different RBD subunits of the S1 trimer bind to integrins and ACE2 separately. Biochemical and structural evidence for a S1-integrin interaction is still required. Moreover, an interaction between ACE2 and integrin-β1 has been reported (Clarke et al., 2012). Various pro-protein convertase enzymes, including furin, also contain a RGD motif that may mediate their recruitment to integrins (Mészáros et al., 2021). Multiple interactions could potentially link integrins to HS, either directly, or indirectly via intermediate proteins such as fibronectin (Ballut et al., 2013; Lyon et al., 2000). Additionally, NRP1 associates with integrins through its extracellular surface domain (Hirota et al., 2015; Valdembri et al., 2009). An elegant example of interplay between integrins and NRP1 CendR binding is provided by the tumour-penetrating peptide iRGD. iRGD is a cyclic peptide with the sequence C*RGDK*GPDC. It first localises to the surface of cells via a RGD-dependent interaction with integrins (underlined in the motif), then is subsequently cleaved by furin or related proteases to reveal a CendR-conforming motif that

engages NRP1 to internalise the compound (italicised in the motif) (Ruoslahti, 2017). Transforming growth factor β1 (TGFβ1) is also an example of an endogenous NRP1 ligand that also contains an RGD motif (Glinka and Prud'homme, 2008). Taken together, a molecular scaffold can be envisaged whereby NRP1 organisation of HS and binding of integrins clusters host factors in proximity to SARS-CoV-2-S and ACE2 to enhance infection **(Figure 6.9)**.

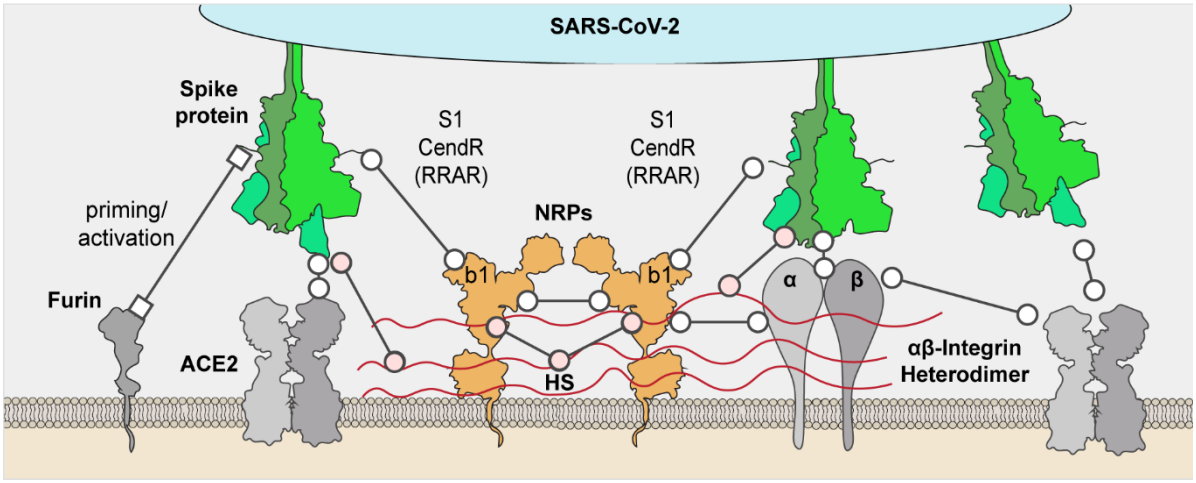

Figure 6.9 Expanded Model of NRP1 as a Molecular Scaffold for SARS-CoV-2 Infection

In addition to its role in CendR binding, NRP1 also covalently and noncovalently binds extracellular heparan sulphate (HS – red lines), which in turn is bound by S1. NRP1 also associates with integrins. S1 may also bind integrin heterodimers via an RGD motif, and ACE2 may interact with integrin-β1. Squares represent furin proteolysis, white circles represent protein-protein interactions, and pink circle represent protein-HS interactions.

6.3.6 Neuropilins as Emerging Therapeutic Targets for Infectious Disease

An accumulating body of evidence implicates neuropilins as host factors for a wide range of viruses **(Table 6.1)**. For example, viruses spanning the diverse families *Coronaviridae*, *Herpesviridae*, *Orthomyxoviridae*, *Poxviridae* and *Retroviridae* have been shown to exploit CendR binding to engage neuropilins. So far, no examples of bacterial exploitation of neuropilin binding have been reported. However, many bacterial species also exploit heparan sulphate binding for cellular attachment, and certain bacteria also depend on furin or related proprotein convertase cleavage of their pathogenic exotoxins, including the anthrax toxin, Pseudomonas exotoxin A, diphtheria toxin and shiga toxin **(Table 6.1)** (García et al., 2016; Garred et al., 1995; Gordon et al., 1995).

How can such evolutionarily distant pathogens divergently evolve to exploit the same receptor? A potential explanation could involve the intertwined biological functions of HS and

neuropilins and the sequences that bind these host factors. Regions of positive charge present on the surface of viral glycoproteins are utilised for HS adherence and are likely to be analogous to multibasic cleavage sites. Therefore, HS-binding sequences may require minimal mutagenic steps to transition to a multibasic cleavage site that produces a CendR sequence if it benefits viral fitness. Interestingly, coronaviruses appear to be able to trade furin cleavage and HS binding off against one another during cell culture adaptation, as has been reported for mouse hepatitis virus and a feline coronavirus, highlighting the dynamic mutability of these sequences (de Haan et al., 2008, 2005). The precise mechanistic role of neuropilins in infections remains unclear, but in the case of SARS-CoV-2 NRP1 enhances the rate of viral entry and appears to promote cell-cell fusion. The acquisition of CendR motifs that enhance infection and spread of viruses through host tissue may therefore be subjected to strong evolutionary pressure to become the dominant form of a viral strain. Viral exploitation of neuropilins may also promote beneficial pro-survival intracellular signalling by RTKs. In the case of Epstein-Barr virus, infection promotes EGFR, AKT and ERK phosphorylation, an effect that is attenuated by NRP1 depletion (Wang et al., 2015).

Effective vaccines are likely to be key medical interventions to abate the ongoing COVID-19 pandemic. However, due to the widespread global abundance of cases and the high transmissibility of SARS-CoV-2, it is possible that COVID-19 remains an endemic disease in various parts of the world, with threats of seasonal reintroduction (Phillips, 2021). The identification of novel therapeutic targets and effective antiviral therapies will therefore still be required to understand and treat COVID-19 in the coming years. The possibility of antiviral therapies targeting neuropilins should also be investigated for existing pathogens that may utilise CendR-dependent NRP1 binding, such as MERS-CoV and highly pathogenic avian influenza H5 and H7 variants, and the presence of putative CendR motifs in future pathogens of pandemic potential should be considered. Neuropilins also play multiple roles in the immune system, and NRP1 inhibitors display immunomodulatory effects (Powell et al., 2018; Roy et al., 2017). Therapies targeting neuropilins may therefore be particularly apt for the treatment of infectious diseases that exploit the C-end rule and concomitantly induce a hyperinflammatory response, such as COVID-19 and highly pathogenic influenza A (Tay et al., 2020; To et al., 2012).

Table 6.1 Pathogenic Proteins Containing CendR Motifs

Viral proteins are listed, alongside their potential or validated furin cleavage sites that mask a cryptic CendR motif. Literature references for CendR-dependent or -independent interaction with neuropilins are provided. Additionally, a selection of non-viral proteins is also included at the bottom of the table. It should be noted that this table is not an exhaustive list of viruses with potential CendR sequences, but rather a compilation of the known neuropilin-linked viruses, and a representation of additional significant viruses from a variety of families with unknown interactions with neuropilins.

Virus *(Protein)*	**Viral CendR Motif (* = proteolytic cleavage site)**	**Evidence of NRP Involvement**	**Interacting NRP(s)**	**Evidence of CendR-Dependent NRP Binding**	**Evidence of CendR-Independent NRP Binding**
Arenaviridae					
Lujo Virus ***(GPC)***	213-THY**KVRK*** LMK-222	(Raaben et al., 2017) (Cohen-Dvashi et al., 2018)	NRP2		✔
Coronaviridae					
Severe Acute Respiratory Syndrome Coronavirus-2 (SARS-CoV-2) ***(S)***	679-NSP**RRAR*** SVA-688	(Daly et al., 2020) (Cantuti-Castelvetri et al., 2020) (Moutal et al., 2021)	NRP1, NRP2	✔	✔
Middle Eastern Respiratory Syndrome Coronavirus (MERS-CoV) ***(S)***	745-LTP**RSVR*** SVP-754	Unknown	Unknown		
Human Coronavirus OC43 (HCoV-OC43) ***(S)***	758-SKN**RRSR*** GAI-767	Unknown	Unknown		
Human Coronavirus HKU1 (HCoV-HKU1) ***(S)***	753-SSS**RRKR*** RSI-762	Unknown	Unknown		
Herpesviridae					
Human Cytomegalovirus (HCMV) ***(gHgLpUL128-131A Pentamer)***	N/A	(Martinez-Martin et al., 2018)	NRP2		✔
Human Cytomegalovirus (HCMV) ***(gB)***	452-ITH**RTRR*** STD-461	Unknown	Unknown		

Murine Cytomegalovirus (MCMV) ***(gB)***	491-VRS**RRKR*** SFD-500	(Lane et al., 2020)	NRP1		✔
Epstein-Barr Virus ***(gB)***	425-AVL**RRRR*** RDA-434	(Wang et al., 2015)	NRP1	✔	✔
Filoviridae					
Zaire Ebolavirus ***(GP)***	594-TGG**RRTR*** REA-603	Unknown	Unknown		
Marburg Virus ***(GP)***	429-VYF**RRKR*** SIL-438	Unknown	Unknown		
Nairoviridae					
Crimean-Congo Haemorrhagic Virus ***(GP)***	241-PTN**RSKR*** NLK-250	Unknown	Unknown		
Orthomyxoviridae					
Avian Influenza A Virus ***(H5)***	340-ERR**RKKR*** GLF-349	(Yamamoto et al., 2019)	NRP1, NRP2	✔	
Avian Influenza A Virus ***(H7)***	335-IPK**RRRR*** GLF-344	(Yamamoto et al., 2019)	NRP1, NRP2	✔	
Picornaviridae					
Enterovirus A71 ***(VP3)***	N/A	(Wang et al., 2021)	NRP1		✔
Pneumoviridae					
Human Respiratory Syncytial Virus (HRSV) ***(F)***	103-TNN**RARR*** ELP-112 130-SKK**RKRR*** FLG-139	Unknown	Unknown		
Poxviridae					
Orf Strains NZ2, NZ10 **(*VEGF-E*)**	127-RPP**RRRR**-133	(Wise et al., 1999) (Wise et al., 2003) (Cébe-Suarez et al., 2008)	NRP1	✔	
Retroviridae					
Human T-cell Lymphotropic Virus Type 1 (HTLV-1) ***(SU)***	87-WIK**KPNR*** NGG-96 306-LGS**RSRR*** AVP-315	(Ghez et al., 2006) (Lambert et al., 2009) (Kusunoki et al., 2018)	NRP1	✔	
Human T-cell Lymphotropic Virus Type 2 (HTLV-2) ***(SU)***	84-WIK**KPNR*** QGL-93 302-PAT**RRRR*** AVP-311	(Ghez et al., 2006)	NRP1	✔	
Human T-cell Lymphotropic Virus Type 3 (HTLV-3) ***(SU)***	88-WIA**KPDR*** RGL-97 309-SRP**KRRR*** AVP-318	Unknown	Unknown		
Human Immunodeficiency Virus (HIV) ***(Tat)***	45-SYG**RKRR*** QRR-54 50-KKR**RQRR*** RPP-59	(Teesalu et al., 2009) (Kadonosono et al., 2015)	NRP1	✔	

Human Immunodeficiency Virus (HIV) ***(gp160)***	505-VVQ**REKR***AVG-514	Unknown	Unknown		
Other (non-virus)					
Bacillus anthracis ***(PA)***	190-SNS**RKKR***STS-190	Unknown	Unknown		
Pseudomonas aeruginosa ***(ETA)***	297-TRH**RQPR***GWE-306	Unknown	Unknown		
Cornephage beta / Cornybacterium diphtheriae ***(DT)***	219-AGN**RVRR***SVG-228	Unknown	Unknown		
Shigella dysenteriae ***(STxA)***	267-HAS**RVAR***MAS-276	Unknown	Unknown		
Vipera ammodytes Snake Venom Toxin ***(VEGF-F)***	129-PKE**KPRR***GGV-138	(Nieminen et al., 2014) (Toivanen et al., 2017)	NRP1	✔	
Charcot-Marie-Tooth disease Type 2D glycyl tRNA synthetase ***(GlyRS)***	N/A	(He et al., 2015) (Sleigh et al., 2017)	NRP1		✔

Chapter 7: General Discussion

In this thesis, I have employed quantitative proteomics as a discovery tool to highlight molecular insights into endosomal cargo sorting. In **Chapter 3**, this analysis investigated the broad role for retromer as a master regulator of endosomal biology and drew parallels between the cellular response to retromer depletion and the hallmarks of neurodegeneration. In **Chapter 4**, I aimed to develop a proteomic tool to facilitate the quantitative analysis of retrograde endosomal cargo sorting, and in **Chapter 5** I applied this methodology to identify potential novel cargoes for ESCPE-1 sequence-dependent sorting. One such newly identified cargo protein, NRP1, unexpectedly became the focus of the work in **Chapter 6**, which identified this receptor as an important host factor for SARS-CoV-2 infection. In this general discussion, I will expand on some of the models raised by the data presented in this thesis and consider outstanding questions of importance in the fields of endosomal membrane trafficking and virology.

7.1 Methodological Advances to Study Endolysosomal Biology

7.1.1 Unbiased Quantitative Proteomics as a Cargo Discovery Tool

The endosomal network is a pleiotropic collection of intracellular compartments, through which hundreds of proteins are dynamically sorted in response to a wide range of cellular cues. The foundations of our understanding of endocytic recycling are based upon the meticulous analysis of a relatively small number of cargo proteins that were conserved from model organisms and/or amenable to cell biological studies. More recently, unbiased proteomics approaches have widely expanded the range of cargoes known to be sorted through the endosomal network. Moreover, bioinformatic analysis can now classify these newly identified cargoes as substrates for recycling by endosomal sorting complexes based upon their molecular sorting signals.

Given the vast numbers of cargoes sorted through the endosomal network, perturbations to endocytic recycling have myriad, far-reaching cellular consequences. The integrated proteomic and transcriptomic approach employed in **Chapter 3** exemplifies that perturbations to the retromer complex induces multifaceted outcomes, including morphological and positional changes to the endolysosomal network, and the upregulation of genes linked to Parkinson’s and Alzheimer’s disease. Neurodegenerative diseases are by nature incredibly multivariate, complex and challenging to study. I believe that similar cell-wide, integrative proteomic and transcriptomic approaches could aid in the understanding of how the perturbation of causal proteins genetically linked to neurodegenerative disease impacts the cell. A benefit of this broad approach is the identification of proteins and genes that appear

distinct from endolysosomal biology, such as the clear enrichment of mitochondrial genes associated with Parkinson's and Alzheimer's diseases in response to the loss of retromer in **Chapter 3.2.6**. The extracellular release of lysosomal contents as a cell-to-cell transfer mechanism of pathogenic aggregate proteins is an emerging concept in the field and elucidating the protective role of retromer in counterbalancing this process could enhance our understanding of the endolysosomal network in the context of neurodegeneration. Taken together, the expanse of data provided by the proteomics and transcriptomics experiments in **Chapter 3** has served as a useful starting point for hypothesis generation that will lead to future lines of study into retromer function.

7.1.2 Towards a Global Overview of Endocytic Recycling

The HRP-TGN46 methodology established in **Chapter 4** aimed to complement the extensive analysis of endosome-to-plasma membrane recycling obtained by surface biotinylation experiments. While there are experimental drawbacks, this approach has provided additional insight into ESCPE-1-mediated retrograde recycling and could be expanded to the study of additional retrograde sorting machineries in the future. A recently described proteomic methodology involves immunoprecipitation of intact lysosomes, followed by proteomic analysis of their contents (Abu-Remaileh et al., 2017). An exciting future possibility could involve the combination of surface biotinylation, TGN biotinylation and lysosomal purification within the same cell line in response to perturbation of endosomal recycling machinery such as retromer or ESCPE-1. Such an approach may serve to provide a global overview of the shift in protein abundances across the endocytic network. For example, these approaches could integrate the decrease in surface or TGN cargo abundance with concurrent enrichment in lysosomes, highlighting those cargo proteins that are shunted toward the degradative fate upon disruption of endocytic trafficking. Through this combinatorial approach, it may soon be possible to achieve a global overview of endosomal sorting that can track the presence of hundreds of cargoes through three of the major endocytic recycling destinations.

7.1.3 Translating Basic Endosomal Cell Biology into Disease Models

Ultimately, a principle aim of fundamental research into the mechanisms and cargoes of the endolysosomal network is to better understand and potentially treat diseases in which this system is compromised. Immortalised cell culture models provide multiple benefits to the study of endosomal biology, including ease of passage, transfection and genetic manipulation, and the ability to grow sufficient material for high-coverage proteomic and transcriptomic experiments. However, to completely understand the significance of the results obtained from the experiments in this thesis, it may be necessary to study proteins of interest within more

biologically relevant systems, such as iPSCs, primary neurons or model organisms. Moreover, advances of proteomics and RNA-sequencing techniques have allowed highly sensitive integrated analysis of differential protein and transcript behaviour in iPSC systems, suggesting that it may be feasible to translate the approaches used in this thesis into iPSC cell lines derived from patient samples with mutations in genes associated with endolysosomal biology.

7.2 The Fate Decision Directing Endosomal Recycling to the Plasma Membrane or the TGN

7.2.1 A Potential Role for Posttranslational Modifications in Retrograde Sorting

In **Chapter 5.2.2**, a cohort of 39 transmembrane proteins were identified that were depleted from the HRP-TGN46-labelled proteome upon SNX5/6 depletion. In particular, NRP1 was selected and biochemically validated as an ESCPE-1 cargo. Further experimental support is required, but it appears as though NRP1 is recycled to the TGN through an ESCPE-1-dependent retrograde pathway. In addition to NRP1, a range of additional proteins that decreased in abundance upon SNX5+6 suppression, including integrin-α5, EphA2, and MET, are predominantly cell surface-localised. These proteins require further biochemical and image-based validation, but if they do indeed represent retrograde ESCPE-1 cargoes then a complicated question arises: how do the same cargoes undergo endocytic recycling to both the plasma membrane and the TGN, and what governs this fate decision?

A potential mechanism to dynamically regulate the directionality of endocytic recycling could involve posttranslational modification of cytosolic cargo tails that enhance or diminish affinity for sorting machineries. This has been established for SNX27-retromer cargoes, whereby phosphorylation of residues within the minimal C-terminal PDZbm negatively impairs SNX27 association, but phosphorylation of residues preceding the minimal PDZbm can dramatically enhance affinity for the SNX27 PDZ domain (Clairfeuille et al., 2016). A well characterised example of cargo tail phosphorylation modulating SNX27 affinity and subsequent endocytic recycling is the β2AR (Cao et al., 1999; Clairfeuille et al., 2016). At present, the most refined consensus sequence for ESCPE-1 binding is $\Phi x \Omega x \Phi x_n \Phi$ (Simonetti et al., 2019; Weeratunga et al., 2020). Given the slight deviation from this sequence in the NRP1 tail, ^{896}LENYNF^{901}, this consensus could potentially be refined to $\Phi x_{1\text{-}2} \Omega x \Phi x_n \Phi$. In the case of CI-MPR, SEMA4C and NRP1, the three cargo proteins with isothermal titration calorimetry evidence confirming direct binding to SNX5/6, a tyrosine residue comprises the central aromatic amino acid that forms a stacking interaction within the hydrophobic SNX5/6 cargo-binding groove (Simonetti

et al., 2019). It is therefore conceivable that tyrosine phosphorylation may prevent ESCPE-1 binding by introducing negative charge into the otherwise hydrophobic consensus sequence. Indeed, phosphorylation of the central Y899 residue of the ESCPE-1-interacting motif of NRP1 has been reported (Thingholm et al., 2008). Masking of the ESCPE-1 motif through phosphorylation may therefore direct cargo proteins to recycle to plasma membrane via ESCPE-1-independent mechanisms, whereas liberation of this motif by a phosphatase could encourage retrograde tubular recycling.

Spatiotemporally restricted activity of a phosphatase enzyme, for example to the late endocytic network could potentially fine-tune this mechanism to control the decision making between endosome-to-plasma membrane or endosome-to-TGN cargo sorting. In the case of activated RTKs identified in the HRP-TGN46 screen, such as EphA2, MET, CRIM1, and by extension as a RTK chaperone, NRP1, dephosphorylation to deactivate receptor signalling is likely an upstream step that precedes recycling. In response to EGF stimulation, EGFR is dephosphorylated on late endosomes by protein-tyrosine phosphatase 1B (PTP1B) at ER-endosome contact sites, prior to ESCRT-mediated internalisation into ILVs (Eden et al., 2010). Both EphA2 and MET are also reported PTP1B substrates (Haj et al., 2012; Sangwan et al., 2008). Moreover, the cytosolic tail of NRP1 is required to mediate the PTP1B-dependent dephosphorylation of VEGFR2 (Lanahan et al., 2013). The ESCPE-1 subunit SNX2 participates in the formation of ER-endosome membrane contact sites by interacting with VAPB (Dong et al., 2016). A fascinating model to explore in the future would be whether receptor dephosphorylation at membrane contact sites is coordinated with subsequent ESCPE-1-dependent tubular recycling. It is possible to envisage how a late endosomal dephosphorylation event could unmask a putative ESCPE-1 sorting motif, leading to incorporation of cargo into the same tubular carriers as CI-MPR, as seen for NRP1 in **Chapter 5.2.4**.

In addition to posttranslational modification of cargo tail sequences, it is also conceivable that endosomal sorting complexes themselves are subjected to similar spatiotemporal control. In yeast for example, Vps26 phosphorylation regulates the affinity of retromer for its cargo (Cui et al., 2017). Phosphorylation within the PX domain of SNX3 impairs its recruitment to PI(3)P-positive membranes (Lenoir et al., 2018). The S226 residue of SNX5 undergoes phosphorylation to regulate its propensity to dimerise with SNX1 and SNX2 (Itai et al., 2018). Dynamic posttranslational modifications of endosomal sorting machineries may therefore regulate their activation state, and in turn dictate which endocytic recycling route cargo may follow.

7.2.2 A Question of Polarisation?

Another cellular cue that dictates retrograde sorting could be the requirement for polarised redelivery of cargoes to a distinct subdomain of the cell surface. Integrin-β1 was demonstrated to undergo retrograde recycling in order to sustain persistent directional cell migration (Shafaq-Zadah et al., 2016). While intuitive, this model will be experimentally challenging to test for the ESCPE-1 dependent proteins identified in **Chapter 5.2.2**. HeLa cells are largely unpolarised, non-motile cells under the standard cell culture conditions utilised in this study. To observe polarisation-dependent phenotypes, different cell lines or cell culture methodologies will be required to attain clear apical-basolateral polarity. In these polarised cells, sophisticated super-resolution imaging techniques may be able to resolve the differential exit of characterised plasma membrane cargoes, and newly discovered retrograde cargoes such as NRP1 from the endocytic network. Moreover, the recently described selective biotinylation of apical and basolateral membranes of polarised cells in a transwell could be utilised to understand how perturbations to retrograde trafficking machinery influence the enrichment of plasma membrane proteins in one surface over another (Caceres et al., 2019). Neurons are highly polarised cells with distinctive intracellular organisation of endomembranes, including dendritic Golgi outposts and satellites that are large distances away from the cell soma (Wang et al., 2020). It would be particularly interesting in the future to interrogate local endosome-to-TGN trafficking within these highly specialised cells, and its impact on maintaining local proteostasis and specialised neuronal characteristics such as synaptic transmission.

An additional factor influencing the fate decision that directs cargoes to the TGN could be the requirement to associate with newly synthesised ligands. This is the case for Wntless, which undergoes SNX3-retromer-dependent retrograde trafficking from the endosomal network to facilitate Wnt secretion from the TGN (Harterink et al., 2011). As discussed in **Chapter 5.3.1**, NRP1 could potentially be involved in a similar mechanism, whereby it directs α5β1-integrin trafficking to the TGN via ESCPE-1 in order to associate with newly synthesised fibronectin molecules. This model of constitutive ligand binding and release may explain why retrograde recycling is required, rather than polarised endosome-to-plasma membrane recycling via the endocytic recycling compartment (Paul et al., 2015).

7.2.3 Additional Molecular Signals for Retrograde Cargo Sorting

Despite the advancing appreciation of the molecular codes that dictate sequence-dependent endosomal recycling, additional subtleties within the sequences of transmembrane proteins that contribute to this process undoubtedly remain to be elucidated. Experiments that exchange characterised sorting determinants between cytosolic cargo tails often observe minimal changes in the recycling route taken by the resulting chimera. For example, exchange of the SNX3-retromer-binding Øx[L/M/V] motifs within the Wntless cytosolic tail with the SNX27-retromer-binding PDZbm of the β2AR and vice versa does not alter the trafficking destination of these chimeras to the TGN and plasma membrane, respectively (Varandas et al., 2016). Instead, the kinetics of cargo enrichment and recycling appear to be altered in these mutant proteins (Varandas et al., 2016). Moreover, a chimeric construct comprising the luminal and transmembrane domains of LAMP1 fused to the cytosolic tail of TGN46 retains a lysosomal localisation, whereas, a chimeric construct comprising the luminal domain of LAMP1 with the transmembrane and cytosolic domains of TGN46 efficiently recycles retrogradely to the TGN, indicating that sequences within the transmembrane domain of cargoes can also influence subcellular localisation (Reaves et al., 1998). Together, these data indicate that while sequence recognition by endosomal sorting complexes plays a crucial role in cargo capture and enrichment on the endosomal membrane, it does not necessarily dictate the final recycling destination. Future work will be required to compare the sequence features of validated ESCPE-1 retrograde cargoes to understand whether additional molecular signals contribute to direct these proteins towards the TGN.

The endocytic network is highly fluid and dynamic, as such there is likely to be redundancy in the recycling pathways that cargoes can take, and this multiplicity of exit routes at different stages of endosomal maturation might serve as ‘fail-safes’ that can retrieve cargoes that missed earlier sequence-dependent sorting steps. For example, following surface labelling and internalisation, the well-defined retrograde cargo Wntless can be observed arriving at the plasma membrane in vesicular carriers bearing the β2AR, suggestive of direct endosome-to-plasma membrane recycling (Varandas et al., 2016). Moreover, upon WASHC2 suppression, the SNX27-retromer cargoes β2AR and GLUT1 transit to the TGN, perhaps suggestive of retrograde sorting mediating the rescue of cargoes that were not efficiently enriched for plasma membrane recycling (Lee et al., 2016; Varandas et al., 2016). This seemingly sequence-independent retrograde transport of cargo proteins may explain the depletion of cargoes lacking an ESCPE-1-binding motif from the HRP-TGN46-labelled proteome of SNX5+6 depleted cells in **Chapter 5.2.2**.

7.3 A Role for ESCPE-1 in Viral Infection

7.3.1 ESCPE-1 Mediated NRP1 Trafficking in the Context of SARS-CoV-2 Infection

In **Chapter 5**, NRP1 was identified as an ESCPE-1 cargo through an unbiased proteomic screen. The subsequent discovery of NRP1 as a host factor for SARS-CoV-2 infection through the CendR-dependent recognition of the Spike protein in **Chapter 6** raises questions about the potential involvement of ESCPE-1-mediated membrane trafficking events after viral entry. In **Chapter 6.2.3** it was demonstrated that NRP1 associates with the S1 CendR peptide peptide (^{679}NSPRRAR^{685}) with an enhanced affinity of 13.0 μM at pH 5.5, compared to 20.3 μM at pH 7.5, suggesting that the NRP1-S1 association may strengthen in acidic intracellular compartments such as the endosomal network.

An interesting possibility is that ESCPE-1 may direct the endocytic transport of S1 via NRP1 binding in infected cells. This could have various potential benefits for the virus. Cryo-electron tomography has revealed that Spike proteins vary in their structures and degrees of processing on the surface of purified SARS-CoV-2 virions, with most in a pre-fusion and post-cleaved state, some in a pre-fusion and pre-cleaved state, and a small minority in a post-fusion conformation consistent with dissociated S1 and an extended S2 structure (Ke et al., 2020). If virion and host membrane fusion occurs in the endosomal network following viral entry, ESCPE-1-mediated retrograde recycling of NRP1 could concurrently transport Spike, either in its pre-fusion form or as dissociated S1 subunits in the post-fused state, back to the TGN. This could conceivably result in re-secretion of dissociated S1, or re-delivery of pre-fusion Spike to the cell surface, where it may begin to initiate syncytia formation **(Figures 7.1A and 7.1B)**. A potential additional benefit of this retrograde model could be to transport any remaining pre-cleaved Spike molecules to the furin-rich TGN compartment to undergo proteolytic processing **(Figure 7.1C)**.

Another possibility is that ESCPE-1 engagement of NRP1 provides a mechanical force that aids viral fusion and genome release. Multiple viruses rely on host mechanical pulling forces, such as cytoskeletal machinery, the ubiquitin-proteasome system and the ER-associated degradation pathway to completely uncoat and release genomic content into the host cell (Yamauchi and Greber, 2016). In the case of influenza A virus, histone deacetylase 6 (HDAC6) recognises polyubiquitin chains within the viral capsid at the late endosomal membrane following membrane fusion. HDAC6 couples to dynein to mediate a pulling force that extrudes the M1 coat protein from the capsid, releasing the genomic contents for replication (Banerjee

et al., 2014). ESCPE-1 engages the dynein adaptor protein p150^{glued} to facilitate retrograde transport to the TGN (Wassmer et al., 2009). A S1-NRP1-ESCPE-1 axis could potentially couple the intraluminal virion membrane to cytoskeletal motors that induce membrane tension to enhance the viral fusion process **(Figure 7.1D)**.

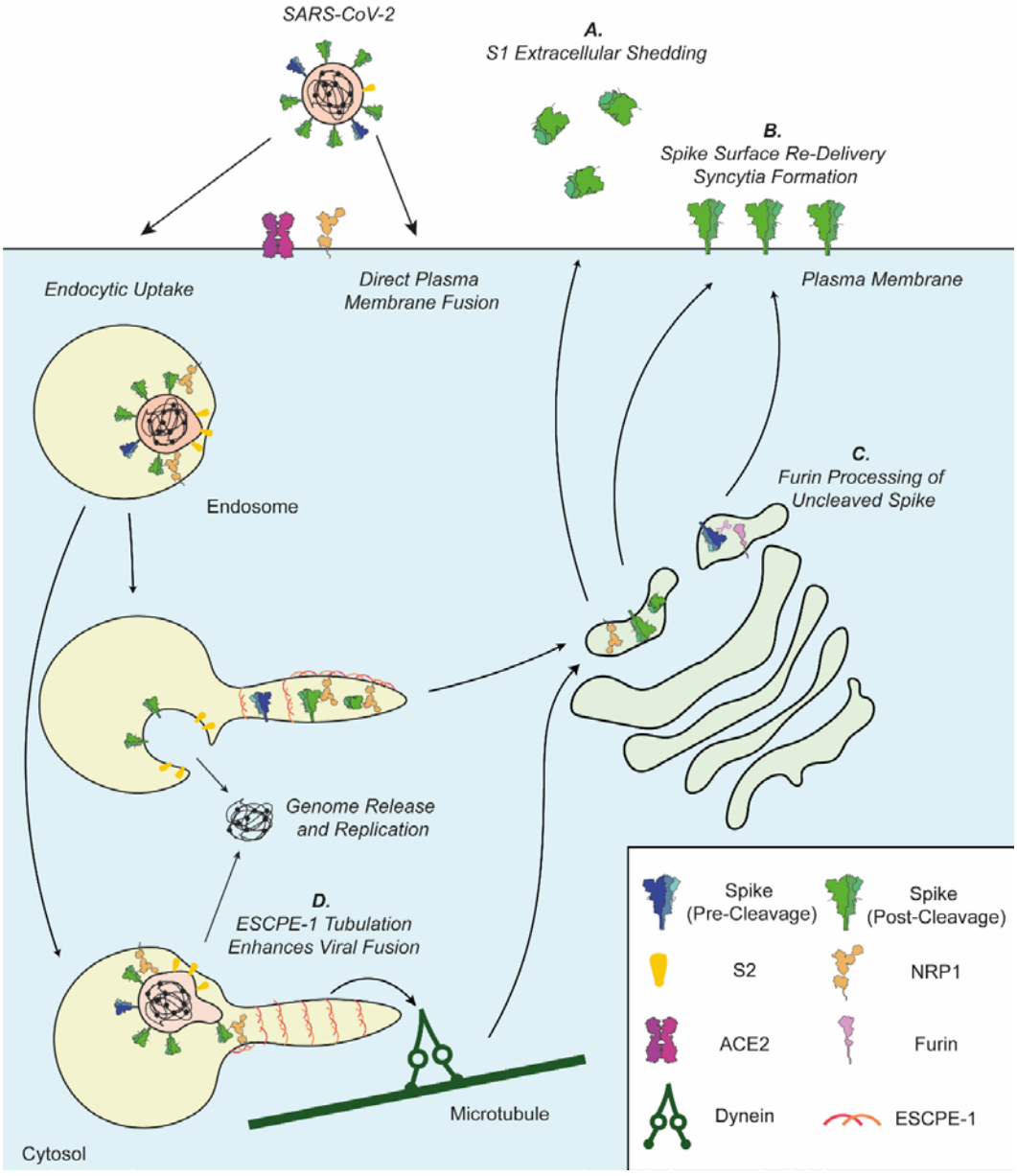

Figure 7.1 Models for ESCPE-1 Involvement in SARS-CoV-2 Infection

Following internalisation into the endocytic network, ESCPE-1 may facilitate retrograde transport of Spike proteins via NRP1. If dissociated S1 remains associated with NRP1, this may lead to secretion of the S1 ectodomain from the cell surface **(A)**. Additionally, NRP1 could chaperone any full-length Spike from endosomes to the TGN, which could be re-delivered to the cell surface **(B)**. If any Spike molecules have not undergone furin cleavage, retrograde transport could facilitate their proteolytic

processing **(C)**. Re-delivered, furin-cleaved Spike may enhance syncytia formation. Finally, through its interaction with dynein, ESCPE-1 mediated endosomal tubulation may generate a pulling force that places additional strain upon the virion and endosomal membrane, perhaps enhancing fusion and genome release **(D)**.

Retrograde transport machinery has previously been implicated in the intracellular trafficking of viral proteins, including in the cases of HIV-1 and vaccinia virus (Brass et al., 2008; Lopez-Vergès et al., 2006; Sivan et al., 2016). Retro-2, an inhibitor of retrograde transport that prevents the ER exit of the SNARE protein Syntaxin-5, has been highlighted as a protective antiviral compound against Ebola virus and Marburg virus, two filoviruses with potential CendR motifs **(Table 6.1)**, and Herpes Simplex Virus Type 2, suggesting a role for retrograde transport in the infection of these viruses (Dai et al., 2018; Forrester et al., 2020; Shtanko et al., 2018). Most recently, the antiviral activity of Retro-2 was recently confirmed for SARS-CoV-2 infection, perhaps relating to the ESCPE-1-dependent retrograde transport of NRP1 (Holwerda et al., 2020).

7.3.2 ESCPE-1 as a Regulator of Innate Cellular Defence Against Viruses

A recent study identified SNX5, and its neuronal paralogue SNX32, from a genome-wide siRNA suppression screen for factors that regulate virus-induced autophagy, a cellular defence mechanism that can mediate the degradation of internalised viruses (Dong et al., 2021). SNX5 specifically associates with virion-containing endosomes in response to infection with a range of diverse viruses, and in turn modulates membrane curvature and recruits the PI3KC3-C1 complex, which is required to generate PI(3)P for autophagosome formation. SNX5 depletion enhances susceptibility to viral infection both *in vitro* and *in vivo*. VPS29 suppression, by contrast, did not have an effect (Dong et al., 2021). This fascinating study implicates SNX5 as a key regulator of innate immunity to viral infection. The biological cue that specifically recruits SNX5 to virion-containing endosomes remains unclear. A possibility could be the sequence-dependent recognition of viral receptors, which may be clustered at high density in virion-containing compartments. In this model, SNX5 would act as an early sensor of viral entry by recognising aberrant receptor clustering and initiating a cellular clearance pathway to restrict viral infection. In addition to NRP1, multiple other proteins identified by the ESCPE-1 retrograde trafficking screen in **Chapter 5.2.2** are characterised viral entry receptors, namely CXADR, EphA2, integrin-α5, LDLR, MET, PVR and TfR. The relevance of this phenomenon to SARS-CoV-2 infection has yet to be experimentally tested. The role of ESCPE-1 in regulating the cellular response to these infections could therefore become an intriguing area of future research.

Recent genome-wide CRISPR screens have emphasised the importance of the endolysosomal network for SARS-CoV-2 infection, highlighting multiprotein complexes such as the v-ATPase, Arp2/3, retromer and the CCC complex as important regulators of infection (Daniloski et al., 2021; Zhu et al., 2021). The endolysosomal dysregulation observed upon retromer depletion in **Chapter 3** is likely consistent with inefficient viral entry and/or endosomal escape due to perturbed endosomal maturation and proteolytic activity. ESCPE-1 components were not identified in these screens, however due to the redundant nature of its subunits dual targeting of either SNX1+2 or SNX5+6 is often required to observe phenotypic consequences. Further work is therefore required to elucidate the role of ESCPE-1 in infection by SARS-CoV-2 and beyond. Over 40 years since studies of Semliki Forest virus entry led to the characterisation of endosomes, viruses clearly still have more to teach us about these dynamic compartments (Helenius et al., 1980).

Chapter 8: References

Abu-Remaileh, M., Wyant, G.A., Kim, C., Laqtom, N.N., Abbasi, M., Chan, S.H., Freinkman, E., Sabatini, D.M., 2017. Lysosomal metabolomics reveals V-ATPase- and mTOR-dependent regulation of amino acid efflux from lysosomes. Science. 358, 807–813. https://doi.org/10.1126/science.aan6298

Ackermann, M., Verleden, S.E., Kuehnel, M., Haverich, A., Welte, T., Laenger, F., Vanstapel, A., Werlein, C., Stark, H., Tzankov, A., Li, W.W., Li, V.W., Mentzer, S.J., Jonigk, D., 2020. Pulmonary Vascular Endothelialitis, Thrombosis, and Angiogenesis in Covid-19. N. Engl. J. Med. 383, 120–128. https://doi.org/10.1056/nejmoa2015432

Adell, M.A.Y., Migliano, S.M., Upadhyayula, S., Bykov, Y.S., Sprenger, S., Pakdel, M., Vogel, G.F., Jih, G., Skillern, W., Behrouzi, R., Babst, M., Schmidt, O., Hess, M.W., Briggs, J.A.G., Kirchhausen, T., Teis, D., 2017. Recruitment dynamics of ESCRT-III and Vps4 to endosomes and implications for reverse membrane budding. Elife 6. https://doi.org/10.7554/eLife.31652

Aghagoli, G., Gallo Marin, B., Katchur, N.J., Chaves-Sell, F., Asaad, W.F., Murphy, S.A., 2020. Neurological Involvement in COVID-19 and Potential Mechanisms: A Review. Neurocrit. Care 1–10. https://doi.org/10.1007/s12028-020-01049-4

Agranoff, B.W., 2009. Turtles all the way: Reflections on myo-inositol. J. Biol. Chem. 284, 21121–21126. https://doi.org/10.1074/jbc.X109.004747

Allison, R., Edgar, J.R., Pearson, G., Rizo, T., Newton, T., Günther, S., Berner, F., Hague, J., Connell, J.W., Winkler, J., Lippincott-Schwartz, J., Beetz, C., Winner, B., Reid, E., 2017. Defects in ER-endosome contacts impact lysosome function in hereditary spastic paraplegia. J. Cell Biol. 216, 1337–1355. https://doi.org/10.1083/jcb.201609033

Alvarez-Erviti, L., Seow, Y., Schapira, A.H., Gardiner, C., Sargent, I.L., Wood, M.J.A., Cooper, J.M., 2011. Lysosomal dysfunction increases exosome-mediated alpha-synuclein release and transmission. Neurobiol. Dis. 42, 360–367. https://doi.org/10.1016/j.nbd.2011.01.029

Andersen, K.G., Rambaut, A., Lipkin, W.I., Holmes, E.C., Garry, R.F., 2020. The proximal origin of SARS-CoV-2. Nat. Med. 26, 450–452. https://doi.org/10.1038/s41591-020-0820-9

Andringa, G., Lam, K.Y., Chegary, M., Wang, X., Chase, T.N., Bennett, M.C., 2004. Tissue transglutaminase catalyzes the formation of alpha-synuclein crosslinks in Parkinson's disease. FASEB J. 18, 932–934. https://doi.org/10.1096/fj.03-0829fje

Antón, Z., Betin, V.M.S., Simonetti, B., Traer, C.J., Attar, N., Cullen, P.J., Lane, J.D., 2020. A heterodimeric SNX4–SNX7 SNX-BAR autophagy complex coordinates ATG9A trafficking for efficient autophagosome assembly. J. Cell Sci. 133. https://doi.org/10.1242/jcs.246306

Arighi, C.N., Hartnell, L.M., Aguilar, R.C., Haft, C.R., Bonifacino, J.S., 2004. Role of the mammalian retromer in sorting of the cation-independent mannose 6-phosphate receptor. J. Cell Biol. 165, 123–33. https://doi.org/10.1083/jcb.200312055

Asrat, S., de Jesús, D.A., Hempstead, A.D., Ramabhadran, V., Isberg, R.R., 2014. Bacterial pathogen manipulation of host membrane trafficking. Annu. Rev. Cell Dev. Biol. 30, 79–109. https://doi.org/10.1146/annurev-cellbio-100913-013439

aTyr Pharma Inc, 2021. aTyr Pharma Announces Positive Topline Results from Phase 2 Clinical Trial of ATYR1923 in COVID-19 Patients with Severe Respiratory Complications [WWW Document]. URL https://investors.atyrpharma.com/news-releases/news-release-details/atyr-pharma-announces-positive-topline-results-phase-2-clinical

Babst, M., 2011. MVB vesicle formation: ESCRT-dependent, ESCRT-independent and everything in between. Curr. Opin. Cell Biol. 23, 452–457. https://doi.org/10.1016/j.ceb.2011.04.008

Bainton, D.F., 1981. The discovery of lysosomes. J. Cell Biol. 91. https://doi.org/10.1083/jcb.91.3.66s

Bajaj, L., Lotfi, P., Pal, R., Ronza, A. di, Sharma, J., Sardiello, M., 2019. Lysosome biogenesis in health and disease. J. Neurochem. 148, 573–589. https://doi.org/10.1111/jnc.14564

Bakker, J., Spits, M., Neefjes, J., Berlin, I., 2017. The EGFR odyssey - from activation to destruction in space and time. J. Cell Sci. 130, 4087–4096. https://doi.org/10.1242/jcs.209197

Balderhaar, H.J. klein., Ungermann, C., 2013. CORVET and HOPS tethering complexes - coordinators of endosome and lysosome fusion. J. Cell Sci. 126, 1307–1316. https://doi.org/10.1242/jcs.107805

Balla, T., 2013. Phosphoinositides: Tiny lipids with giant impact on cell regulation. Physiol. Rev. 93, 1019–1137. https://doi.org/10.1152/physrev.00028.2012

Ballabio, A., Bonifacino, J.S., 2020. Lysosomes as dynamic regulators of cell and organismal homeostasis. Nat. Rev. Mol. Cell Biol. 21, 101–118. https://doi.org/10.1038/s41580-019-0185-4

Ballut, L., Sapay, N., Chautard, É., Imberty, A., Ricard-Blum, S., 2013. Mapping of heparin/heparan sulfate binding sites on αvβ3 integrin by molecular docking. J. Mol. Recognit. 26, 76–85. https://doi.org/10.1002/jmr.2250

Banerjee, I., Miyake, Y., Philip Nobs, S., Schneider, C., Horvath, P., Kopf, M., Matthias, P., Helenius, A., Yamauchi, Y., 2014. Influenza A virus uses the aggresome processing machinery for host cell entry. Science. 346, 473–477. https://doi.org/10.1126/science.1257037

Bankaitis, V.A., Johnson, L.M., Emr, S.D., 1986. Isolation of yeast mutants defective in protein targeting to the vacuole. Proc. Natl. Acad. Sci. U. S. A. 83, 9075–9079. https://doi.org/10.1073/pnas.83.23.9075

Bärlocher, K., Hutter, C.A.J., Swart, A.L., Steiner, B., Welin, A., Hohl, M., Letourneur, F., Seeger, M.A., Hilbi, H., 2017. Structural insights into Legionella RidL-Vps29 retromer subunit interaction reveal displacement of the regulator TBC1D5. Nat. Commun. 8, 1–15. https://doi.org/10.1038/s41467-017-01512-5

Bartels, T., De Schepper, S., Hong, S., 2020. Microglia modulate neurodegeneration in Alzheimer's and Parkinson's diseases. Science. 370, 66–69. https://doi.org/10.1126/science.abb8587

Bartuzi, P., Billadeau, D.D., Favier, R., Rong, S., Dekker, D., Fedoseienko, A., Fieten, H., Wijers, M., Levels, J.H., Huijkman, N., Kloosterhuis, N., Van Der Molen, H., Brufau, G., Groen, A.K., Elliott, A.M., Kuivenhoven, J.A., Plecko, B., Grangl, G., McGaughran, J., Horton, J.D., Burstein, E., Hofker, M.H., Van De Sluis, B., 2016. CCC- and WASH-mediated endosomal sorting of LDLR is required for normal clearance of circulating LDL. Nat. Commun. 7, 1–11. https://doi.org/10.1038/ncomms10961

Bécot, A., Volgers, C., van Niel, G., 2020. Transmissible endosomal intoxication: A balance between exosomes and lysosomes at the basis of intercellular amyloid propagation. Biomedicines 8. https://doi.org/10.3390/BIOMEDICINES8080272

Behnia, R., Munro, S., 2005. Organelle identity and the signposts for membrane traffic. Nature 438, 597–604. https://doi.org/10.1038/nature04397

Beilina, A., Bonet-Ponce, L., Kumaran, R., Kordich, J.J., Ishida, M., Mamais, A., Kaganovich, A., Saez-Atienzar, S., Gershlick, D.C., Roosen, D.A., Pellegrini, L., Malkov, V., Fell, M.J., Harvey, K., Bonifacino, J.S., Moore, D.J., Cookson, M.R., 2020. The Parkinson's Disease Protein LRRK2 Interacts with the GARP Complex to Promote Retrograde Transport to the trans-Golgi Network. Cell Rep. 31. https://doi.org/10.1016/j.celrep.2020.107614

Belouzard, S., Chu, V.C., Whittaker, G.R., 2009. Activation of the SARS coronavirus spike protein via sequential proteolytic cleavage at two distinct sites. Proc. Natl. Acad. Sci. U. S. A. 106, 5871–5876. https://doi.org/10.1073/pnas.0809524106

Bendris, N., Schmid, S.L., 2017. Endocytosis, Metastasis and Beyond: Multiple Facets of SNX9. Trends Cell Biol. 27, 189–200. https://doi.org/10.1016/j.tcb.2016.11.001

Bi, F., Li, F., Huang, C., Zhou, H., 2013. Pathogenic mutation in VPS35 impairs its protection against MPP(+) cytotoxicity. Int. J. Biol. Sci. 9, 149–55. https://doi.org/10.7150/ijbs.5617

Bigay, J., Antonny, B., 2012. Curvature, Lipid Packing, and Electrostatics of Membrane Organelles: Defining Cellular Territories in Determining Specificity. Dev. Cell 23, 886–895. https://doi.org/10.1016/j.devcel.2012.10.009

Bitsikas, V., Corrêa, I.R., Nichols, B.J., 2014. Clathrin-independent pathways do not contribute

significantly to endocytic flux. Elife 2014, 1–26. https://doi.org/10.7554/eLife.03970

Blanchette, C.R., Rodal, A.A., 2020. Mechanisms for biogenesis and release of neuronal extracellular vesicles. Curr. Opin. Neurobiol. 63, 104–110. https://doi.org/10.1016/j.conb.2020.03.013

Blunsom, N.J., Cockcroft, S., 2020. Phosphatidylinositol synthesis at the endoplasmic reticulum. Biochim. Biophys. Acta - Mol. Cell Biol. Lipids 1865. https://doi.org/10.1016/j.bbalip.2019.05.015

Bonangelino, C.J., Chavez, E.M., Bonifacino, J.S., 2002. Genomic screen for vacuolar protein sorting genes in Saccharomyces cerevisiae. Mol. Biol. Cell 13, 2486–2501. https://doi.org/10.1091/mbc.02-01-0005

Bonifacino, J.S., 2014. Adaptor proteins involved in polarized sorting. J. Cell Biol. 204, 7–17. https://doi.org/10.1083/jcb.201310021

Bonifacino, J.S., Glick, B.S., 2004. The Mechanisms of Vesicle Budding and Fusion. Cell 116, 153–166. https://doi.org/10.1016/S0092-8674(03)01079-1

Bonifacino, J.S., Hierro, A., 2011. Transport according to GARP: Receiving retrograde cargo at the trans-Golgi network. Trends Cell Biol. 21, 159–167. https://doi.org/10.1016/j.tcb.2010.11.003

Bonifacino, J.S., Traub, L.M., 2003. Signals for Sorting of Transmembrane Proteins to Endosomes and Lysosomes. Annu. Rev. Biochem. 72, 395–447. https://doi.org/10.1146/annurev.biochem.72.121801.161800

Böttcher, R.T., Stremmel, C., Meves, A., Meyer, H., Widmaier, M., Tseng, H.Y., Fässler, R., 2012. Sorting nexin 17 prevents lysosomal degradation of β1 integrins by binding to the β 1-integrin tail. Nat. Cell Biol. 14, 584–592. https://doi.org/10.1038/ncb2501

Bowers, J.R., Readler, J.M., Sharma, P., Excoffon, K.J.D.A., 2017. Poliovirus Receptor: More than a simple viral receptor. Virus Res. 242, 1–6. https://doi.org/10.1016/j.virusres.2017.09.001

Bradley, B.T., Maioli, H., Johnston, R., Chaudhry, I., Fink, S.L., Xu, H., Najafian, B., Deutsch, G., Lacy, J.M., Williams, T., Yarid, N., Marshall, D.A., 2020. Histopathology and ultrastructural findings of fatal COVID-19 infections in Washington State: a case series. Lancet 396, 320–332. https://doi.org/10.1016/S0140-6736(20)31305-2

Brandhorst, D., Zwilling, D., Rizzoli, S.O., Lippert, U., Lang, T., Jahn, R., 2006. Homotypic fusion of early endosomes: SNAREs do not determine fusion specificity. Proc. Natl. Acad. Sci. U. S. A. 103, 2701–2706. https://doi.org/10.1073/pnas.0511138103

Brass, A.L., Dykxhoorn, D.M., Benita, Y., Yan, N., Engelman, A., Xavier, R.J., Lieberman, J., Elledge, S.J., 2008. Identification of host proteins required for HIV infection through a functional genomic screen. Science. 319, 921–926. https://doi.org/10.1126/science.1152725

Braulke, T., Bonifacino, J.S., 2009. Sorting of lysosomal proteins. Biochim. Biophys. Acta - Mol. Cell Res. 1793, 605–614. https://doi.org/10.1016/j.bbamcr.2008.10.016

Braun, E., Sauter, D., 2019. Furin-mediated protein processing in infectious diseases and cancer. Clin. Transl. Immunol. 8. https://doi.org/10.1002/cti2.1073

Bretscher, M.S., Munro, S., 1993. Cholesterol and the golgi apparatus. Science. 261, 1280–1281. https://doi.org/10.1126/science.8362242

Bright, N.A., Davis, L.J., Luzio, J.P., 2016. Endolysosomes Are the Principal Intracellular Sites of Acid Hydrolase Activity. Curr. Biol. 26, 2233–2245. https://doi.org/10.1016/j.cub.2016.06.046

Bright, N.A., Gratian, M.J., Luzio, J.P., 2005. Endocytic delivery to lysosomes mediated by concurrent fusion and kissing events in living cells. Curr. Biol. 15, 360–365. https://doi.org/10.1016/j.cub.2005.01.049

Brown, W.J., Goodhouse, J., Farquhar, M.G., 1986. Mannose-6-phosphate receptors for lysosomal enzymes cycle between the Golgi complex and endosomes. J. Cell Biol. 103, 1235–1247. https://doi.org/10.1083/jcb.103.4.1235

Buchrieser, J., Dufloo, J., Hubert, M., Monel, B., Planas, D., Rajah, M.M., Planchais, C., Porrot, F.,

Guivel-Benhassine, F., Van der Werf, S., Casartelli, N., Mouquet, H., Bruel, T., Schwartz, O., 2020. Syncytia formation by SARS-CoV-2-infected cells. EMBO J. 39. https://doi.org/10.15252/embj.2020106267

Bugarcic, A., Zhe, Y., Kerr, M.C., Griffin, J., Collins, B.M., Teasdale, R.D., 2011. Vps26A and Vps26B Subunits Define Distinct Retromer Complexes. Traffic 12, 1759–1773. https://doi.org/10.1111/j.1600-0854.2011.01284.x

Bulankina, A. V., Deggerich, A., Wenzel, D., Mutenda, K., Wittmann, J.G., Rudolph, M.G., Burger, K.N.J., Höning, S., 2009. TIP47 functions in the biogenesis of lipid droplets. J. Cell Biol. 185, 641–655. https://doi.org/10.1083/jcb.200812042

Burd, C., Cullen, P.J., 2014. Retromer: A master conductor of endosome sorting. Cold Spring Harb. Perspect. Biol. 6. https://doi.org/10.1101/cshperspect.a016774

Burgos, P. V., Mardones, G.A., Rojas, A.L., daSilva, L.L.P., Prabhu, Y., Hurley, J.H., Bonifacino, J.S., 2010. Sorting of the Alzheimer's Disease Amyloid Precursor Protein Mediated by the AP-4 Complex. Dev. Cell 18, 425–436. https://doi.org/10.1016/j.devcel.2010.01.015

Burguete, A.S., Fenn, T.D., Brunger, A.T., Pfeffer, S.R., 2008. Rab and Arl GTPase Family Members Cooperate in the Localization of the Golgin GCC185. Cell 132, 286–298. https://doi.org/10.1016/j.cell.2007.11.048

Buser, D.P., Schleicher, K.D., Prescianotto-Baschong, C., Spiess, M., 2018. A versatile nanobody-based toolkit to analyze retrograde transport from the cell surface. Proc. Natl. Acad. Sci. U. S. A. 115, E6227–E6236. https://doi.org/10.1073/pnas.1801865115

Buser, D.P., Spiess, M., 2019. Analysis of Endocytic Uptake and Retrograde Transport to the Trans-Golgi Network Using Functionalized Nanobodies in Cultured Cells. J. Vis. Exp. e59111. https://doi.org/10.3791/59111

Caceres, P.S., Gravotta, D., Zager, P.J., Dephoure, N., Rodriguez-Boulan, E., 2019. Quantitative proteomics of MDCK cells identify unrecognized roles of clathrin adaptor AP-1 in polarized distribution of surface proteins. Proc. Natl. Acad. Sci. U. S. A. 116, 11796–11805. https://doi.org/10.1073/pnas.1821076116

Cagno, V., Tseligka, E.D., Jones, S.T., Tapparel, C., 2019. Heparan sulfate proteoglycans and viral attachment: True receptors or adaptation bias? Viruses 11. https://doi.org/10.3390/v11070596

Cai, H., Reed, R.R., 1999. Cloning and characterization of neuropilin-1-interacting protein: A PSD-95/Dlg/ZO-1 domain-containing protein that interacts with the cytoplasmic domain of neuropilin-1. J. Neurosci. 19, 6519–6527. https://doi.org/10.1523/jneurosci.19-15-06519.1999

Cai, H., Reinisch, K., Ferro-Novick, S., 2007. Coats, Tethers, Rabs, and SNAREs Work Together to Mediate the Intracellular Destination of a Transport Vesicle. Dev. Cell 12, 671–682. https://doi.org/10.1016/j.devcel.2007.04.005

Cantuti-Castelvetri, L., Ojha, R., Pedro, L.D., Djannatian, M., Franz, J., Kuivanen, S., van der Meer, F., Kallio, K., Kaya, T., Anastasina, M., Smura, T., Levanov, L., Szirovicza, L., Tobi, A., Kallio-Kokko, H., Österlund, P., Joensuu, M., Meunier, F.A., Butcher, S.J., Winkler, M.S., Mollenhauer, B., Helenius, A., Gokce, O., Teesalu, T., Hepojoki, J., Vapalahti, O., Stadelmann, C., Balistreri, G., Simons, M., 2020. Neuropilin-1 facilitates SARS-CoV-2 cell entry and infectivity. Science. 370, 856–860. https://doi.org/10.1126/science.abd2985

Canuel, M., Korkidakis, A., Konnyu, K., Morales, C.R., 2008a. Sortilin mediates the lysosomal targeting of cathepsins D and H. Biochem. Biophys. Res. Commun. 373, 292–297. https://doi.org/10.1016/j.bbrc.2008.06.021

Canuel, M., Lefrancois, S., Zeng, J., Morales, C.R., 2008b. AP-1 and retromer play opposite roles in the trafficking of sortilin between the Golgi apparatus and the lysosomes. Biochem. Biophys. Res. Commun. 366, 724–730. https://doi.org/10.1016/j.bbrc.2007.12.015

Cao, T.T., Deacon, H.W., Reczek, D., Bretscher, A., Von Zastrow, M., 1999. A kinase-regulated PDZ-domain interaction controls endocytic sorting of the β2-adrenergic receptor. Nature 401, 286–290. https://doi.org/10.1038/45816

Caplan, M.J., Stow, J.L., Newman, A.P., Madri, J., Anderson, H.C., Farquhar, M.G., Palade, G.E., Jamieson, J.D., 1987. Dependence on pH of polarized sorting of secreted proteins. Nature 329, 632–635. https://doi.org/10.1038/329632a0

Carlton, J., Bujny, M., Peter, B.J., Oorschot, V.M.J., Rutherford, A., Mellor, H., Klumperman, J., McMahon, H.T., Cullen, P.J., 2004. Sorting nexin-1 mediates tubular endosome-to-TGN transport through coincidence sensing of high- curvature membranes and 3-phosphoinositides. Curr. Biol. 14, 1791–1800. https://doi.org/10.1016/j.cub.2004.09.077

Carlton, J.G., Cullen, P.J., 2005. Coincidence detection in phosphoinositide signaling. Trends Cell Biol. 15, 540–547. https://doi.org/10.1016/j.tcb.2005.08.005

Carosi, J.M., Denton, D., Kumar, S., Sargeant, T.J., 2021. Retromer dysfunction at the nexus of tauopathies. Cell Death Differ. 1–16. https://doi.org/10.1038/s41418-020-00727-2

Carosi, J.M., Hein, L.K., van den Hurk, M., Adams, R., Milky, B., Singh, S., Bardy, C., Denton, D., Kumar, S., Sargeant, T.J., 2020. Retromer regulates the lysosomal clearance of MAPT/tau. Autophagy 00, 1–21. https://doi.org/10.1080/15548627.2020.1821545

Carroll, B., 2020. Spatial regulation of mTORC1 signalling: Beyond the Rag GTPases. Semin. Cell Dev. Biol. https://doi.org/10.1016/j.semcdb.2020.02.007

Caswell, P.T., Chan, M., Lindsay, A.J., McCaffrey, M.W., Boettiger, D., Norman, J.C., 2008. Rab-coupling protein coordinates recycling of α5β1 integrin and EGFR1 to promote cell migration in 3D microenvironments. J. Cell Biol. 183, 143–155. https://doi.org/10.1083/jcb.200804140

Caswell, P.T., Spence, H.J., Parsons, M., White, D.P., Clark, K., Cheng, K.W., Mills, G.B., Humphries, M.J., Messent, A.J., Anderson, K.I., McCaffrey, M.W., Ozanne, B.W., Norman, J.C., 2007. Rab25 Associates with α5β1 Integrin to Promote Invasive Migration in 3D Microenvironments. Dev. Cell 13, 496–510. https://doi.org/10.1016/j.devcel.2007.08.012

Cataldo, A.M., Peterhoff, C.M., Troncoso, J.C., Gomez-Isla, T., Hyman, B.T., Nixon, R.A., 2000. Endocytic pathway abnormalities precede amyloid β deposition in sporadic alzheimer's disease and down syndrome: Differential effects of APOE genotype and presenilin mutations. Am. J. Pathol. 157, 277–286. https://doi.org/10.1016/S0002-9440(10)64538-5

Cattin-Ortolá, J., Welch, L., Maslen, S.L., Skehel, J.M., Papa, G., James, L.C., Munro, S., 2020. Sequences in the cytoplasmic tail of SARS-CoV-2 spike facilitate syncytia formation. bioRxiv 2020.10.12.335562. https://doi.org/10.1101/2020.10.12.335562

Čaval, T., Zhu, J., Tian, W., Remmelzwaal, S., Yang, Z., Clausen, H., Heck, A.J.R., 2019. Targeted Analysis of Lysosomal Directed Proteins and Their Sites of Mannose-6-phosphate Modification. Mol. Cell. Proteomics 18, 16–27. https://doi.org/10.1074/mcp.RA118.000967

Cébe-Suarez, S., Grünewald, F.S., Jaussi, R., Li, X., Claesson-Welsh, L., Spillmann, D., Mercer, A.A., Prota, A.E., Ballmer-Hofer, K., 2008. Orf virus VEGF-E NZ2 promotes paracellular NRP-1/VEGFR-2 coreceptor assembly *via* the peptide RPPR. FASEB J. 22, 3078–3086. https://doi.org/10.1096/fj.08-107219

Chan, J.F.W., Kok, K.H., Zhu, Z., Chu, H., To, K.K.W., Yuan, S., Yuen, K.Y., 2020. Genomic characterization of the 2019 novel human-pathogenic coronavirus isolated from a patient with atypical pneumonia after visiting Wuhan. Emerg. Microbes Infect. 9, 221–236. https://doi.org/10.1080/22221751.2020.1719902

Chandra, M., Chin, Y.K.Y., Mas, C., Feathers, J.R., Paul, B., Datta, S., Chen, K.E., Jia, X., Yang, Z., Norwood, S.J., Mohanty, B., Bugarcic, A., Teasdale, R.D., Henne, W.M., Mobli, M., Collins, B.M., 2019. Classification of the human phox homology (PX) domains based on their phosphoinositide binding specificities. Nat. Commun. 10, 1–14. https://doi.org/10.1038/s41467-019-09355-y

Chang, J., Lee, S., Blackstone, C., 2014. Spastic paraplegia proteins spastizin and spatacsin mediate autophagic lysosome reformation. J. Clin. Invest. 124, 5249–5262. https://doi.org/10.1172/JCI77598

Chaudhary, B., Khaled, Y.S., Ammori, B.J., Elkord, E., 2014. Neuropilin 1: Function and therapeutic

potential in cancer. Cancer Immunol. Immunother. 63, 81–99. https://doi.org/10.1007/s00262-013-1500-0

Chen, C., Garcia-Santos, D., Ishikawa, Y., Seguin, A., Li, L., Fegan, K.H., Hildick-Smith, G.J., Shah, D.I., Cooney, J.D., Chen, W., King, M.J., Yien, Y.Y., Schultz, I.J., Anderson, H., Dalton, A.J., Freedman, M.L., Kingsley, P.D., Palis, J., Hattangadi, S.M., Lodish, H.F., Ward, D.M., Kaplan, J., Maeda, T., Ponka, P., Paw, B.H., 2013. Snx3 regulates recycling of the transferrin receptor and iron assimilation. Cell Metab. 17, 343–352. https://doi.org/10.1016/j.cmet.2013.01.013

Chen, X., Laurent, S., Onur, O.A., Kleineberg, N.N., Fink, G.R., Schweitzer, F., Warnke, C., 2020. A systematic review of neurological symptoms and complications of COVID-19. J. Neurol. 268, 392. https://doi.org/10.1007/s00415-020-10067-3

Chen, Y., Gershlick, D.C., Park, S.Y., Bonifacino, J.S., 2017. Segregation in the Golgi complex precedes export of endolysosomal proteins in distinct transport carriers. J. Cell Biol. 216, 4141–4151. https://doi.org/10.1083/jcb.201707172

Chen, Y., Samaraweera, P., Sun, T.T., Kreibich, G., Orlow, S.J., 2002. Rab27b association with melanosomes: Dominant negative mutants disrupt melanosomal movement. J. Invest. Dermatol. 118, 933–940. https://doi.org/10.1046/j.1523-1747.2002.01754.x

Cheung, P.P., Pfeffer, S.R., 2016. Transport Vesicle Tethering at the Trans Golgi Network: Coiled Coil Proteins in Action. Front. Cell Dev. Biol. 4, 18. https://doi.org/10.3389/fcell.2016.00018

Chia, P.Z.C., Gasnereau, I., Lieu, Z.Z., Gleeson, P.A., 2011. Rab9-dependent retrograde transport and endosomal sorting of the endopeptidase furin. J. Cell Sci. 124, 2401–2413. https://doi.org/10.1242/jcs.083782

Chiaruttini, N., Roux, A., 2017. Dynamic and elastic shape transitions in curved ESCRT-III filaments. Curr. Opin. Cell Biol. 47, 126–135. https://doi.org/10.1016/j.ceb.2017.07.002

Christoforidis, S., Miaczynska, M., Ashman, K., Wilm, M., Zhao, L., Yip, S.C., Waterfield, M.D., Backer, J.M., Zerial, M., 1999. Phosphatidylinositol-3-OH kinases are Rab5 effectors. Nat. Cell Biol. 1, 249–252. https://doi.org/10.1038/12075

Chu, B.B., Liao, Y.C., Qi, W., Xie, C., Du, X., Wang, J., Yang, H., Miao, H.H., Li, B.L., Song, B.L., 2015. Cholesterol transport through lysosome-peroxisome membrane contacts. Cell 161, 291–306. https://doi.org/10.1016/j.cell.2015.02.019

Citron, B.A., SantaCruz, K.S., Davies, P.J.A., Festoff, B.W., 2001. Intron-Exon Swapping of Transglutaminase mRNA and Neuronal Tau Aggregation in Alzheimer's Disease. J. Biol. Chem. 276, 3295–3301. https://doi.org/10.1074/jbc.M004776200

Citron, B.A., Suo, Z., SantaCruz, K., Davies, P.J.A., Qin, F., Festoff, B.W., 2002. Protein crosslinking, tissue transglutaminase, alternative splicing and neurodegeneration. Neurochem. Int. 40, 69–78. https://doi.org/10.1016/S0197-0186(01)00062-6

Clague, M.J., Liu, H., Urbé, S., 2012. Governance of Endocytic Trafficking and Signaling by Reversible Ubiquitylation. Dev. Cell 23, 457–467. https://doi.org/10.1016/j.devcel.2012.08.011

Clairfeuille, T., Mas, C., Chan, A.S.M., Yang, Z., Tello-Lafoz, M., Chandra, M., Widagdo, J., Kerr, M.C., Paul, B., Mérida, I., Teasdale, R.D., Pavlos, N.J., Anggono, V., Collins, B.M., 2016. A molecular code for endosomal recycling of phosphorylated cargos by the SNX27-retromer complex. Nat. Struct. Mol. Biol. 23, 921–932. https://doi.org/10.1038/nsmb.3290

Clarke, N.E., Fisher, M.J., Porter, K.E., Lambert, D.W., Turner, A.J., 2012. Angiotensin Converting Enzyme (ACE) and ACE2 Bind Integrins and ACE2 Regulates Integrin Signalling. PLoS One 7, e34747. https://doi.org/10.1371/journal.pone.0034747

Clausen, T.M., Sandoval, D.R., Spliid, C.B., Pihl, J., Perrett, H.R., Painter, C.D., Narayanan, A., Majowicz, S.A., Kwong, E.M., McVicar, R.N., Thacker, B.E., Glass, C.A., Yang, Z., Torres, J.L., Golden, G.J., Bartels, P.L., Porell, R.N., Garretson, A.F., Laubach, L., Feldman, J., Yin, X., Pu, Y., Hauser, B.M., Caradonna, T.M., Kellman, B.P., Martino, C., Gordts, P.L.S.M., Chanda, S.K., Schmidt, A.G., Godula, K., Leibel, S.L., Jose, J., Corbett, K.D., Ward, A.B., Carlin, A.F., Esko, J.D., 2020. SARS-CoV-2 Infection Depends on Cellular Heparan Sulfate and ACE2. Cell 183,

1043-1057.e15. https://doi.org/10.1016/j.cell.2020.09.033

Cohen-Dvashi, H., Kilimnik, I., Diskin, R., 2018. Structural basis for receptor recognition by Lujo virus. Nat. Microbiol. 3, 1153–1160. https://doi.org/10.1038/s41564-018-0224-5

Colacurcio, D.J., Pensalfini, A., Jiang, Y., Nixon, R.A., 2018. Dysfunction of autophagy and endosomal-lysosomal pathways: Roles in pathogenesis of Down syndrome and Alzheimer's Disease. Free Radic. Biol. Med. 114, 40–51. https://doi.org/10.1016/j.freeradbiomed.2017.10.001

Collins, B.M., 2008. The Structure and Function of the Retromer Protein Complex. Traffic 9, 1811–1822. https://doi.org/10.1111/j.1600-0854.2008.00777.x

Collins, B.M., Norwood, S.J., Kerr, M.C., Mahony, D., Seaman, M.N.J., Teasdale, R.D., Owen, D.J., 2008. Structure of Vps26B and mapping of its interaction with the retromer protein complex. Traffic 9, 366–379. https://doi.org/10.1111/j.1600-0854.2007.00688.x

Collins, B.M., Skinner, C.F., Watson, P.J., Seaman, M.N.J., Owen, D.J., 2005. Vps29 has a phosphoesterase fold that acts as a protein interaction scaffold for retromer assembly. Nat. Struct. Mol. Biol. 12, 594–602. https://doi.org/10.1038/nsmb954

Connolly, C.N., Futter, C.E., Gibson, A., Hopkins, C.R., Cutler, D.F., 1994. Transport into and out of the Golgi complex studied by transfecting cells with cDNAs encoding horseradish peroxidase. J. Cell Biol. 127, 641–652. https://doi.org/10.1083/jcb.127.3.641

Cooper, A.A., Stevens, T.H., 1996. Vps10p cycles between the late-Golgi and prevacuolar compartments in its function as the sorting receptor for multiple yeast vacuolar hydrolases. J. Cell Biol. 133, 529–541. https://doi.org/10.1083/jcb.133.3.529

Costes, S. V., Daelemans, D., Cho, E.H., Dobbin, Z., Pavlakis, G., Lockett, S., 2004. Automatic and quantitative measurement of protein-protein colocalization in live cells. Biophys. J. 86, 3993–4003. https://doi.org/10.1529/biophysj.103.038422

Crevenna, A.H., Blank, B., Maiser, A., Emin, D., Prescher, J., Beck, G., Kienzle, C., Bartnik, K., Habermann, B., Pakde, M., Leonhardt, H., Lamb, D.C., von Blume, J., 2016. Secretory cargo sorting by Ca2+-dependent Cab45 oligomerization at the trans-Golgi network. J. Cell Biol. 213, 305–314. https://doi.org/10.1083/jcb.201601089

Crump, C.M., Xiang, Y., Thomas, L., Gu, F., Austin, C., Tooze, S.A., Thomas, G., 2001. PACS-1 binding to adaptors is required for acidic cluster motif-mediated protein traffic. EMBO J. 20, 2191–2201. https://doi.org/10.1093/emboj/20.9.2191

Crunfli, F., Carregari, V.C., Veras, F.P., Vendramini, P.H., Fragnani Valença, A.G., Marcelo Antunes, A.S.L., Brandão-Teles, C., Zuccoli, G. da S., Reis-De-Oliveira, G., Silva-Costa, L.C., Saia-Cereda, V.M., Codo, A.C., Parise, P.L., Toledo Teixeira, D.A., de Souza, G.F., Muraro, S.P., Silva Melo, B.M., Almeida, G.M., Silva Firmino, E.M., Ludwig, R.G., Ruiz, G.P., Knittel, T.L., Davanzo, G.G., Gerhardt, J.A., Rodrigues, P.B., Forato, J., Amorim, M.R., Silva, N.B., Martini, M.C., Benatti, M.N., Batah, S., Siyuan, L., Pereira Silva, R.E.M., João, R.B., Silva, L.S., Nogueira, M.H., Aventurato, Í.K., de Brito, M.R., Machado Alvim, M.K., da Silva, J.R., Damião, L.L., Castilho Stefano, M.E. de P., de Sousa, I.M.P., da Rocha, E.D., Gonçalves, S.M., da Silva, L.H.L., Bettini, V., de Campos, B.M., Ludwig, G., Mendes Viana, R.M., Martins, R., Vieira, A.S., Alves-Filho, J.C., Arruda, E., Sebollela, A.S., Cendes, F., Cunha, F.Q., Damásio, A., Ramirez Vinolo, M.A., Munhoz, C.D., Rehen, S.K., Mauad, T., Duarte-Neto, A.N., da Silva, L.F.F., Dolhnikoff, M., Saldiva, P., Fabro, A.T., Farias, A.S., Moraes-Vieira, P.M.M., Proença Módena, J.L., Yasuda, C.L., Mori, M.A., Cunha, T.M., Martins-De-Souza, D., 2020. SARS-CoV-2 infects brain astrocytes of COVID-19 patients and impairs neuronal viability. medRxiv 2020.10.09.20207464. https://doi.org/10.1101/2020.10.09.20207464

Cui, J., Li, F., Shi, Z.L., 2019. Origin and evolution of pathogenic coronaviruses. Nat. Rev. Microbiol. 17, 181–192. https://doi.org/10.1038/s41579-018-0118-9

Cui, T.Z., Peterson, T.A., Burd, C.G., 2017. A CDC25 family protein phosphatase gates cargo recognition by the Vps26 retromer subunit. Elife 6. https://doi.org/10.7554/eLife.24126

Cui, Y., Carosi, J.M., Yang, Z., Ariotti, N., Kerr, M.C., Parton, R.G., Sargeant, T.J., Teasdale, R.D., 2019. Retromer has a selective function in cargo sorting via endosome transport carriers. J. Cell Biol. 218, 615–631. https://doi.org/10.1083/jcb.201806153

Cullen, P.J., 2011. Phosphoinositides and the regulation of tubular-based endosomal sorting. Biochem. Soc. Trans. 39, 839–850. https://doi.org/10.1042/BST0390839

Cullen, P.J., Steinberg, F., 2018. To degrade or not to degrade: mechanisms and significance of endocytic recycling. Nat. Rev. Mol. Cell Biol. 19, 679–696. https://doi.org/10.1038/s41580-018-0053-7

Curnock, R., Calcagni, A., Ballabio, A., Cullen, P.J., 2019. TFEB controls retromer expression in response to nutrient availability. J. Cell Biol. 218, 3954–3966. https://doi.org/10.1083/JCB.201903006

Dahms, N.M., Olson, L.J., Kim, J.J.P., 2008. Strategies for carbohydrate recognition by the mannose 6-phosphate receptors. Glycobiology 18, 664–678. https://doi.org/10.1093/glycob/cwn061

Dai, J., Li, J., Bos, E., Porcionatto, M., Premont, R.T., Bourgoin, S., Peters, P.J., Hsu, V.W., 2004. ACAP1 promotes endocytic recycling by recognizing recycling sorting signals. Dev. Cell 7, 771–776. https://doi.org/10.1016/j.devcel.2004.10.002

Dai, W., Wu, Y., Bi, J., Wang, J., Wang, S., Kong, W., Barbier, J., Cintrat, J.C., Gao, F., Jiang, Z., Gillet, D., Su, W., Jiang, C., 2018. Antiviral effect of Retro-2.1 against herpes simplex Virus type 2 in Vitro. J. Microbiol. Biotechnol. 28, 849–859. https://doi.org/10.4014/jmb.1712.12052

Daly, J.L., Simonetti, B., Klein, K., Chen, K.E., Williamson, M.K., Antón-Plágaro, C., Shoemark, D.K., Simón-Gracia, L., Bauer, M., Hollandi, R., Greber, U.F., Horvath, P., Sessions, R.B., Helenius, A., Hiscox, J.A., Teesalu, T., Matthews, D.A., Davidson, A.D., Collins, B.M., Cullen, P.J., Yamauchi, Y., 2020. Neuropilin-1 is a host factor for SARS-CoV-2 infection. Science. 370, 861–865. https://doi.org/10.1126/science.abd3072

Daniloski, Z., Jordan, T.X., Wessels, H.H., Hoagland, D.A., Kasela, S., Legut, M., Maniatis, S., Mimitou, E.P., Lu, L., Geller, E., Danziger, O., Rosenberg, B.R., Phatnani, H., Smibert, P., Lappalainen, T., tenOever, B.R., Sanjana, N.E., 2021. Identification of Required Host Factors for SARS-CoV-2 Infection in Human Cells. Cell 184, 92-105.e16. https://doi.org/10.1016/j.cell.2020.10.030

Danzer, K.M., Kranich, L.R., Ruf, W.P., Cagsal-Getkin, O., Winslow, A.R., Zhu, L., Vanderburg, C.R., McLean, P.J., 2012. Exosomal cell-to-cell transmission of alpha synuclein oligomers. Mol. Neurodegener. 7, 42. https://doi.org/10.1186/1750-1326-7-42

Datta, S., Liu, Y., Hariri, H., Bowerman, J., Henne, W.M., 2019. Cerebellar ataxia disease-associated Snx14 promotes lipid droplet growth at ER-droplet contacts. J. Cell Biol. 218, 1335–1351. https://doi.org/10.1083/jcb.201808133

Davidson, A.D., Williamson, M.K., Lewis, S., Shoemark, D., Carroll, M.W., Heesom, K.J., Zambon, M., Ellis, J., Lewis, P.A., Hiscox, J.A., Matthews, D.A., 2020. Characterisation of the transcriptome and proteome of SARS-CoV-2 reveals a cell passage induced in-frame deletion of the furin-like cleavage site from the spike glycoprotein. Genome Med. 12, 68. https://doi.org/10.1186/s13073-020-00763-0

de Duve, C., 2005. The lysosome turns fifty. Nat. Cell Biol. 7, 847–849. https://doi.org/10.1038/ncb0905-847

de Haan, C.A.M., Haijema, B.J., Schellen, P., Schreur, P.W., te Lintelo, E., Vennema, H., Rottier, P.J.M., 2008. Cleavage of Group 1 Coronavirus Spike Proteins: How Furin Cleavage Is Traded Off against Heparan Sulfate Binding upon Cell Culture Adaptation. J. Virol. 82, 6078–6083. https://doi.org/10.1128/jvi.00074-08

de Haan, C.A.M., Li, Z., te Lintelo, E., Bosch, B.J., Haijema, B.J., Rottier, P.J.M., 2005. Murine Coronavirus with an Extended Host Range Uses Heparan Sulfate as an Entry Receptor. J. Virol. 79, 14451–14456. https://doi.org/10.1128/jvi.79.22.14451-14456.2005

de Haan, C.A.M., Stadler, K., Godeke, G.-J., Bosch, B.J., Rottier, P.J.M., 2004. Cleavage Inhibition of

the Murine Coronavirus Spike Protein by a Furin-Like Enzyme Affects Cell-Cell but Not Virus-Cell Fusion. J. Virol. 78, 6048–6054. https://doi.org/10.1128/jvi.78.11.6048-6054.2004

De Matteis, M.A., Godi, A., 2004. PI-loting membrane traffic. Nat. Cell Biol. 6, 487–492. https://doi.org/10.1038/ncb0604-487

Deatherage, C.L., Nikolaus, J., Karatekin, E., Burd, C.G., 2020. Retromer forms low order oligomers on supported lipid bilayers (Preprint). bioRxiv. https://doi.org/10.1101/2020.03.31.018150

Del Conte-Zerial, P., Brusch, L., Rink, J.C., Collinet, C., Kalaidzidis, Y., Zerial, M., Deutsch, A., 2008. Membrane identity and GTPase cascades regulated by toggle and cut-out switches. Mol. Syst. Biol. 4, 206. https://doi.org/10.1038/msb.2008.45

Delevoye, C., Miserey-Lenkei, S., Montagnac, G., Gilles-Marsens, F., Paul-Gilloteaux, P., Giordano, F., Waharte, F., Marks, M.S., Goud, B., Raposo, G., 2014. Recycling endosome tubule morphogenesis from sorting endosomes requires the kinesin motor KIF13A. Cell Rep. 6, 445–454. https://doi.org/10.1016/j.celrep.2014.01.002

Dell'Angelica, E.C., Bonifacino, J.S., 2019. Coatopathies: Genetic Disorders of Protein Coats. Annu. Rev. Cell Dev. Biol. 35, 131–168. https://doi.org/10.1146/annurev-cellbio-100818-125234

Deng, H.-X.X.H., Shi, Y., Yang, Y., Ahmeti, K.B., Miller, N., Huang, C., Cheng, L., Zhai, H., Deng, S., Nuytemans, K., Corbett, N.J., Kim, M.J., Deng, H.-X.X.H., Tang, B., Yang, Z., Xu, Y., Chan, P., Huang, B., Gao, X.-P.P., Song, Z., Liu, Z., Fecto, F., Siddique, N., Foroud, T., Jankovic, J., Ghetti, B., Nicholson, D.A., Krainc, D., Melen, O., Vance, J.M., Pericak-Vance, M.A., Ma, Y.-C.C., Rajput, A.H., Siddique, T., 2016. Identification of TMEM230 mutations in familial Parkinson's disease. Nat. Genet. 48, 733–739. https://doi.org/10.1038/ng.3589

Deng, Y., Pakdel, M., Blank, B., Sundberg, E.L., Burd, C.G., von Blume, J., 2018. Activity of the SPCA1 Calcium Pump Couples Sphingomyelin Synthesis to Sorting of Secretory Proteins in the Trans-Golgi Network. Dev. Cell 47, 464-478.e8. https://doi.org/10.1016/j.devcel.2018.10.012

Derivery, E., Helfer, E., Henriot, V., Gautreau, A., 2012. Actin Polymerization Controls the Organization of WASH Domains at the Surface of Endosomes. PLoS One 7, e39774. https://doi.org/10.1371/journal.pone.0039774

Derivery, E., Sousa, C., Gautier, J.J., Lombard, B., Loew, D., Gautreau, A., 2009. The Arp2/3 activator WASH controls the fission of endosomes through a large multiprotein complex. Dev. Cell 17, 712–23. https://doi.org/10.1016/j.devcel.2009.09.010

Díaz, E., Pfeffer, S.R., 1998. Tip47: A cargo selection device for mannose 6-phosphate receptor trafficking. Cell 93, 433–443. https://doi.org/10.1016/S0092-8674(00)81171-X

Dong, R., Saheki, Y., Swarup, S., Lucast, L., Harper, J.W., De Camilli, P., 2016. Endosome-ER Contacts Control Actin Nucleation and Retromer Function through VAP-Dependent Regulation of PI4P. Cell 166, 408–423. https://doi.org/10.1016/J.CELL.2016.06.037

Dong, X., Yang, Y., Zou, Z., Zhao, Y., Ci, B., Zhong, L., Bhave, M., Wang, L., Kuo, Y.C., Zang, X., Zhong, R., Aguilera, E.R., Richardson, R.B., Simonetti, B., Schoggins, J.W., Pfeiffer, J.K., Yu, L., Zhang, X., Xie, Y., Schmid, S.L., Xiao, G., Gleeson, P.A., Ktistakis, N.T., Cullen, P.J., Xavier, R.J., Levine, B., 2021. Sorting nexin 5 mediates virus-induced autophagy and immunity. Nature 589, 456–461. https://doi.org/10.1038/s41586-020-03056-z

Dores, M.R., Paing, M.M., Lin, H., Montagne, W.A., Marchese, A., Trejo, J.A., 2012. AP-3 regulates PAR1 ubiquitin-independent MVB/lysosomal sorting via an ALIX-mediated pathway. Mol. Biol. Cell 23, 3612–3623. https://doi.org/10.1091/mbc.E12-03-0251

Dudek, S.M., Johnson, G.V.W., 1994. Transglutaminase facilitates the formation of polymers of the β-amyloid peptide. Brain Res. 651, 129–133. https://doi.org/10.1016/0006-8993(94)90688-2

Dyve, A.B., Bergan, J., Utskarpen, A., Sandvig, K., 2009. Sorting nexin 8 regulates endosome-to-Golgi transport. Biochem. Biophys. Res. Commun. 390, 109–114. https://doi.org/10.1016/j.bbrc.2009.09.076

Eden, E.R., White, I.J., Tsapara, A., Futter, C.E., 2010. Membrane contacts between endosomes and

ER provide sites for PTP1B-epidermal growth factor receptor interaction. Nat. Cell Biol. 12, 267–272. https://doi.org/10.1038/ncb2026

Edgar, J.R., Eden, E.R., Futter, C.E., 2014. Hrs- and CD63-Dependent Competing Mechanisms Make Different Sized Endosomal Intraluminal Vesicles. Traffic 15, 197–211. https://doi.org/10.1111/tra.12139

Edgar, J.R., Willén, K., Gouras, G.K., Futter, C.E., 2015. ESCRTs regulate amyloid precursor protein sorting in multivesicular bodies and intracellular amyloid-β accumulation. J. Cell Sci. 128, 2520–2528. https://doi.org/10.1242/jcs.170233

Elwell, C.A., Czudnochowski, N., von Dollen, J., Johnson, J.R., Nakagawa, R., Mirrashidi, K., Krogan, N.J., Engel, J.N., Rosenberg, O.S., 2017. Chlamydia interfere with an interaction between the mannose-6-phosphate receptor and sorting nexins to counteract host restriction. Elife 6, 1–17. https://doi.org/10.7554/eLife.22709

Evans, A.J., Daly, J.L., Anuar, A.N.K., Simonetti, B., Cullen, P.J., 2020. Acute inactivation of retromer and ESCPE-1 leads to time-resolved defects in endosomal cargo sorting. J. Cell Sci. 133. https://doi.org/10.1242/JCS.246033

Evdokimova, V., Tognon, C.E., Benatar, T., Yang, W., Krutikov, K., Pollak, M., Sorensen, P.H.B., Seth, A., 2012. IGFBP7 binds to the IGF-1 receptor and blocks its activation by insulin-like growth factors. Sci. Signal. 5. https://doi.org/10.1126/scisignal.2003184

Fan, J., Ponferrada, V.G., Sato, T., Vemaraju, S., Fruttiger, M., Gerhardt, H., Ferrara, N., Lang, R.A., 2014. Crim1 maintains retinal vascular stability during development by regulating endothelial cell Vegfa autocrine signaling. Dev. 141, 448–459. https://doi.org/10.1242/dev.097949

Fehr, A.R., Perlman, S., 2015. Coronaviruses: An overview of their replication and pathogenesis. Coronaviruses Methods Protoc. 1282, 1–23. https://doi.org/10.1007/978-1-4939-2438-7_1

Feng, S., Streets, A.J., Nesin, V., Tran, U., Nie, H., Onopiuk, M., Wessely, O., Tsiokas, L., Ong, A.C.M., 2017. The sorting nexin 3 retromer pathway regulates the cell surface localization and activity of a Wnt-activated polycystin channel complex. J. Am. Soc. Nephrol. 28, 2973–2984. https://doi.org/10.1681/ASN.2016121349

Finan, G.M., Okada, H., Kim, T.W., 2011. BACE1 retrograde trafficking is uniquely regulated by the cytoplasmic domain of sortilin. J. Biol. Chem. 286, 12602–12616. https://doi.org/10.1074/jbc.M110.170217

Finsel, I., Ragaz, C., Hoffmann, C., Harrison, C.F., Weber, S., Van Rahden, V.A., Johannes, L., Hilbi, H., 2013. The legionella effector RidL inhibits retrograde trafficking to promote intracellular replication. Cell Host Microbe 14, 38–50. https://doi.org/10.1016/j.chom.2013.06.001

Fjorback, A.W., Seaman, M., Gustafsen, C., Mehmedbasic, A., Gokool, S., Wu, C., Militz, D., Schmidt, V., Madsen, P., Nyengaard, J.R., Willnow, T.E., Christensen, E.I., Mobley, W.B., Nykjær, A., Andersen, O.M., 2012. Retromer binds the FANSHY sorting motif in sorLA to regulate amyloid precursor protein sorting and processing. J. Neurosci. 32, 1467–1480. https://doi.org/10.1523/JNEUROSCI.2272-11.2012

Follett, J., Norwood, S.J., Hamilton, N.A., Mohan, M., Kovtun, O., Tay, S., Zhe, Y., Wood, S.A., Mellick, G.D., Silburn, P.A., Collins, B.M., Bugarcic, A., Teasdale, R.D., 2014. The Vps35 D620N Mutation Linked to Parkinson's Disease Disrupts the Cargo Sorting Function of Retromer. Traffic 15, 230–244. https://doi.org/10.1111/tra.12136

Forgac, M., 2007. Vacuolar ATPases: Rotary proton pumps in physiology and pathophysiology. Nat. Rev. Mol. Cell Biol. 8, 917–929. https://doi.org/10.1038/nrm2272

Forrester, A., Rathjen, S.J., Daniela Garcia-Castillo, M., Bachert, C., Couhert, A., Tepshi, L., Pichard, S., Martinez, J., Munier, M., Sierocki, R., Renard, H.F., Augusto Valades-Cruz, C., Dingli, F., Loew, D., Lamaze, C., Cintrat, J.C., Linstedt, A.D., Gillet, D., Barbier, J., Johannes, L., 2020. Functional dissection of the retrograde Shiga toxin trafficking inhibitor Retro-2. Nat. Chem. Biol. 16, 327–336. https://doi.org/10.1038/s41589-020-0474-4

Frana, M.F., Behnke, J.N., Sturman, L.S., Holmes, K. V, 1985. Proteolytic cleavage of the E2

glycoprotein of murine coronavirus: host-dependent differences in proteolytic cleavage and cell fusion. J. Virol. 56, 912–920. https://doi.org/10.1128/jvi.56.3.912-920.1985

Freeman, C.L., Hesketh, G., Seaman, M.N.J., 2014. RME-8 coordinates the activity of the WASH complex with the function of the retromer SNX dimer to control endosomal tubulation. J. Cell Sci. 127, 2053–2070. https://doi.org/10.1242/jcs.144659

Fuh, G., Garcia, K.C., de Vos, A.M., 2000. The Interaction of Neuropilin-1 with Vascular Endothelial Growth Factor and Its Receptor Flt-1. J. Biol. Chem. 275, 26690–26695. https://doi.org/10.1016/s0021-9258(19)61431-6

Gagnon, M.L., Bielenberg, D.R., Gechtman, Z., Miao, H.Q., Takashima, S., Soker, S., Klagsbrun, M., 2000. Identification of a natural soluble neuropilin-1 that binds vascular endothelial growth factor: In vivo expression and antitumor activity. Proc. Natl. Acad. Sci. U. S. A. 97, 2573–2578. https://doi.org/10.1073/pnas.040337597

Gallon, M., Clairfeuille, T., Steinberg, F., Mas, C., Ghai, R., Sessions, R.B., Teasdale, R.D., Collins, B.M., Cullen, P.J., 2014. A unique PDZ domain and arrestin-like fold interaction reveals mechanistic details of endocytic recycling by SNX27-retromer. Proc. Natl. Acad. Sci. U. S. A. 111, E3604–E3613. https://doi.org/10.1073/pnas.1410552111

Gallon, M., Cullen, P.J., 2015. Retromer and sorting nexins in endosomal sorting. Biochem. Soc. Trans. 43, 33–47. https://doi.org/10.1042/BST20140290

Galvez, T., Gilleron, J., Zerial, M., O'Sullivan, G.A., 2012. SnapShot: Mammalian Rab proteins in endocytic trafficking. Cell 151, 234-234.e2. https://doi.org/10.1016/j.cell.2012.09.013

García, B., Merayo-Lloves, J., Martin, C., Alcalde, I., Quirós, L.M., Vazquez, F., 2016. Surface proteoglycans as mediators in bacterial pathogens infections. Front. Microbiol. 7. https://doi.org/10.3389/fmicb.2016.00220

Garred, O., Van Deurs, B., Sandvig, K., 1995. Furin-induced cleavage and activation of shiga toxin. J. Biol. Chem. 270, 10817–10821. https://doi.org/10.1074/jbc.270.18.10817

Geladaki, A., Kočevar Britovšek, N., Breckels, L.M., Smith, T.S., Vennard, O.L., Mulvey, C.M., Crook, O.M., Gatto, L., Lilley, K.S., 2019. Combining LOPIT with differential ultracentrifugation for high-resolution spatial proteomics. Nat. Commun. 10, 1–15. https://doi.org/10.1038/s41467-018-08191-w

Gemmill, R.M., Nasarre, P., Nair-Menon, J., Cappuzzo, F., Landi, L., D'Incecco, A., Uramoto, H., Yoshida, T., Haura, E.B., Armeson, K., Drabkin, H.A., 2017. The neuropilin 2 isoform NRP2b uniquely supports TGFb-mediated progression in lung cancer. Sci. Signal. 10, 528. https://doi.org/10.1126/scisignal.aag0528

Ghai, R., Bugarcic, A., Liu, H., Norwood, S.J., Skeldal, S., Coulson, E.J., Li, S.S.C., Teasdale, R.D., Collins, B.M., 2013. Structural basis for endosomal trafficking of diverse transmembrane cargos by PX-FERM proteins. Proc. Natl. Acad. Sci. U. S. A. 110, E643. https://doi.org/10.1073/pnas.1216229110

Ghez, D., Lepelletier, Y., Lambert, S., Fourneau, J.-M., Blot, V., Janvier, S., Arnulf, B., van Endert, P.M., Heveker, N., Pique, C., Hermine, O., 2006. Neuropilin-1 Is Involved in Human T-Cell Lymphotropic Virus Type 1 Entry. J. Virol. 80, 6844–6854. https://doi.org/10.1128/jvi.02719-05

Gilchrist, A., Au, C.E., Hiding, J., Bell, A.W., Fernandez-Rodriguez, J., Lesimple, S., Nagaya, H., Roy, L., Gosline, S.J.C., Hallett, M., Paiement, J., Kearney, R.E.E., Nilsson, T., Bergeron, J.J.M., 2006. Quantitative Proteomics Analysis of the Secretory Pathway. Cell 127, 1265–1281. https://doi.org/10.1016/j.cell.2006.10.036

Gillingham, A.K., Munro, S., 2019. Transport carrier tethering – how vesicles are captured by organelles. Curr. Opin. Cell Biol. 59, 140–146. https://doi.org/10.1016/j.ceb.2019.04.010

Gillingham, A.K., Munro, S., 2007. The Small G Proteins of the Arf Family and Their Regulators. Annu. Rev. Cell Dev. Biol. 23, 579–611. https://doi.org/10.1146/annurev.cellbio.23.090506.123209

Glinka, Y., Prud'homme, G.J., 2008. Neuropilin-1 is a receptor for transforming growth factor β-1, activates its latent form, and promotes regulatory T cell activity. J. Leukoc. Biol. 84, 302–310. https://doi.org/10.1189/jlb.0208090

Godbold, G.D., Ahn, K., Yeyeodu, S., Lee, L.F., Ting, J.P., Erickson, A.H., 1998. Biosynthesis and intracellular targeting of the lysosomal aspartic proteinase cathepsin D. Adv. Exp. Med. Biol. 436, 153–62.

Goedhart, J., Luijsterburg, M.S., 2020. VolcaNoseR is a web app for creating, exploring, labeling and sharing volcano plots. Sci. Rep. 10, 1–5. https://doi.org/10.1038/s41598-020-76603-3

Golgi, C., 1898. Intorno alla struttura delle cellule nervose. J. Microsc. 155, 3–7. https://doi.org/10.1111/j.1365-2818.1989.tb04294.x

Gomez, T.S., Gorman, J.A., de Narvajas, A.A.M., Koenig, A.O., Billadeau, D.D., 2012. Trafficking defects in WASH-knockout fibroblasts originate from collapsed endosomal and lysosomal networks. Mol. Biol. Cell 23, 3215–3228. https://doi.org/10.1091/mbc.e12-02-0101

Gorbalenya, A.E., Baker, S.C., Baric, R.S., de Groot, R.J., Drosten, C., Gulyaeva, A.A., Haagmans, B.L., Lauber, C., Leontovich, A.M., Neuman, B.W., Penzar, D., Perlman, S., Poon, L.L.M., Samborskiy, D. V., Sidorov, I.A., Sola, I., Ziebuhr, J., 2020. The species Severe acute respiratory syndrome-related coronavirus: classifying 2019-nCoV and naming it SARS-CoV-2. Nat. Microbiol. 5, 536–544. https://doi.org/10.1038/s41564-020-0695-z

Gordon, V.M., Klimpel, K.R., Arora, N., Henderson, M.A., Leppla, S.H., 1995. Proteolytic activation of bacterial toxins by eukaryotic cells is performed by furin and by additional cellular proteases. Infect. Immun. 63.

Griffiths, G., Simons, K., 1986. The trans Golgi network: Sorting at the exit site of the Golgi complex. Science. 234, 438–443. https://doi.org/10.1126/science.2945253

Gu, F., Crump, C.M., Thomas, G., 2001. Trans-Golgi network sorting. Cell. Mol. Life Sci. 58, 1067–1084. https://doi.org/10.1007/PL00000922

Gundemir, S., Colak, G., Tucholski, J., Johnson, G.V.W., 2012. Transglutaminase 2: A molecular Swiss army knife. Biochim. Biophys. Acta - Mol. Cell Res. 1823, 406–419. https://doi.org/10.1016/j.bbamcr.2011.09.012

Gundry, C., Marco, S., Rainero, E., Miller, B., Dornier, E., Mitchell, L., Caswell, P.T., Campbell, A.D., Hogeweg, A., Sansom, O.J., Morton, J.P., Norman, J.C., 2017. Phosphorylation of Rab-coupling protein by LMTK3 controls Rab14-dependent EphA2 trafficking to promote cell:cell repulsion. Nat. Commun. 8, 1–15. https://doi.org/10.1038/ncomms14646

Guo, H.F., Li, X., Parker, M.W., Waltenberger, J., Becker, P.M., Vander Kooi, C.W., 2013. Mechanistic basis for the potent anti-angiogenic activity of Semaphorin 3f. Biochemistry 52, 7551–7558. https://doi.org/10.1021/bi401034q

Guo, H.F., Vander Kooi, C.W., 2015. Neuropilin functions as an essential cell surface receptor. J. Biol. Chem. 290, 29120–29126. https://doi.org/10.1074/jbc.R115.687327

Guo, Y., Sirkis, D.W., Schekman, R., 2014. Protein Sorting at the *trans* -Golgi Network. Annu. Rev. Cell Dev. Biol. 30, 169–206. https://doi.org/10.1146/annurev-cellbio-100913-013012

Haj, F.G., Sabet, O., Kinkhabwala, A., Wimmer-Kleikamp, S., Roukos, V., Han, H.M., Grabenbauer, M., Bierbaum, M., Antony, C., Neel, B.G., Bastiaens, P.I., 2012. Regulation of signaling at regions of cell-cell contact by endoplasmic reticulum-bound protein-tyrosine phosphatase 1B. PLoS One 7, 36633. https://doi.org/10.1371/journal.pone.0036633

Hannan, L.A., Edidin, M., 1996. Traffic, polarity, and detergent solubility of a glycosylphosphatidylinositol-anchored protein after LDL-deprivation of MDCK cells. J. Cell Biol. 133, 1265–1276. https://doi.org/10.1083/jcb.133.6.1265

Harterink, M., Port, F., Lorenowicz, M.J., McGough, I.J., Silhankova, M., Betist, M.C., Van Weering, J.R.T., Van Heesbeen, R.G.H.P., Middelkoop, T.C., Basler, K., Cullen, P.J., Korswagen, H.C., 2011. A SNX3-dependent retromer pathway mediates retrograde transport of the Wnt sorting

receptor Wntless and is required for Wnt secretion. Nat. Cell Biol. 13, 914–923. https://doi.org/10.1038/ncb2281

Hata, S., Fujishige, S., Araki, Y., Kato, N., Araseki, M., Nishimura, M., Hartmann, D., Saftig, P., Fahrenholz, F., Taniguchi, M., Urakami, K., Akatsu, H., Martins, R.N., Yamamoto, K., Maeda, M., Yamamoto, T., Nakaya, T., Gandy, S., Suzuki, T., 2009. Alcadein cleavages by amyloid β-precursor protein (APP) α- and γ-secretases generate small peptides, p3-Alcs, indicating Alzheimer disease-related γ-secretase dysfunction. J. Biol. Chem. 284, 36024–36033. https://doi.org/10.1074/jbc.M109.057497

He, W., Bai, G., Zhou, H., Wei, N., White, N.M., Lauer, J., Liu, H., Shi, Y., Dumitru, C.D., Lettieri, K., Shubayev, V., Jordanova, A., Guergueltcheva, V., Griffin, P.R., Burgess, R.W., Pfaff, S.L., Yang, X.L., 2015. CMT2D neuropathy is linked to the neomorphic binding activity of glycyl-tRNA synthetase. Nature 526, 710–714. https://doi.org/10.1038/nature15510

Heider, M.R., Munson, M., 2012. Exorcising the Exocyst Complex. Traffic 13, 898–907. https://doi.org/10.1111/j.1600-0854.2012.01353.x

Helenius, A., Marsh, M., White, J., 1980. The entry of viruses into animal cells. Trends Biochem. Sci. 5, 104–106. https://doi.org/10.1016/0968-0004(80)90260-1

Helenius, A., Mellman, I., Wall, D., Hubbard, A., 1983. Endosomes. Trends Biochem. Sci. 8, 245–250. https://doi.org/10.1016/0968-0004(83)90350-X

Henne, W.M., Buchkovich, N.J., Emr, S.D., 2011. The ESCRT Pathway. Dev. Cell 21, 77–91. https://doi.org/10.1016/J.DEVCEL.2011.05.015

Hesketh, G., Pérez-Dorado, I., Jackson, L.P., Wartosch, L., Schäfer, I.B., Gray, S.R., McCoy, A.J., Zeldin, O.B., Garman, E.F., Harbour, M.E., Evans, P.R., Seaman, M.N.J., Luzio, J.P., Owen, D.J., 2014. VARP is recruited on to endosomes by direct interaction with retromer, where together they function in export to the cell surface. Dev. Cell 29, 591–606. https://doi.org/10.1016/j.devcel.2014.04.010

Hierro, A., Rojas, A.L., Rojas, R., Murthy, N., Effantin, G., Kajava, A. V., Steven, A.C., Bonifacino, J.S., Hurley, J.H., 2007. Functional architecture of the retromer cargo-recognition complex. Nature 449, 1063–1067. https://doi.org/10.1038/nature06216

Hirota, S., Clements, T.P., Tang, L.K., Morales, J.E., Lee, H.S., Oh, S.P., Rivera, G.M., Wagner, D.S., McCarty, J.H., 2015. Neuropilin 1 balances β8 integrin-activated TGFβ signaling to control sprouting angiogenesis in the brain. Dev. 142, 4363–4373. https://doi.org/10.1242/dev.113746

Hirst, J., Edgar, J.R., Esteves, T., Darios, F., Madeo, M., Chang, J., Roda, R.H., Dürr, A., Anheim, M., Gellera, C., Li, J., Züchner, S., Mariotti, C., Stevanin, G., Blackstone, C., Kruer, M.C., Robinson, M.S., 2015. Loss of AP-5 results in accumulation of aberrant endolysosomes: Defining a new type of lysosomal storage disease. Hum. Mol. Genet. 24, 4984–4996. https://doi.org/10.1093/hmg/ddv220

Hirst, J., Miller, S.E., Taylor, M.J., von Mollard, G.F., Robinson, M.S., 2004. EpsinR is an adaptor for the SNARE protein Vti1b. Mol. Biol. Cell 15, 5593–602. https://doi.org/10.1091/mbc.e04-06-0468

Hoffmann, M., Kleine-Weber, H., Pö, S., Pö Hlmann, S., 2020a. A Multibasic Cleavage Site in the Spike Protein of SARS-CoV-2 Is Essential for Infection of Human Lung Cells. Mol. Cell 78, 779-784.e5. https://doi.org/10.1016/j.molcel.2020.04.022

Hoffmann, M., Kleine-Weber, H., Schroeder, S., Krüger, N., Herrler, T., Erichsen, S., Schiergens, T.S., Herrler, G., Wu, N.H., Nitsche, A., Müller, M.A., Drosten, C., Pöhlmann, S., 2020b. SARS-CoV-2 Cell Entry Depends on ACE2 and TMPRSS2 and Is Blocked by a Clinically Proven Protease Inhibitor. Cell 181, 271-280.e8. https://doi.org/10.1016/j.cell.2020.02.052

Hollandi, R., Szkalisity, A., Toth, T., Tasnadi, E., Molnar, C., Mathe, B., Grexa, I., Molnar, J., Balind, A., Gorbe, M., Kovacs, M., Migh, E., Goodman, A., Balassa, T., Koos, K., Wang, W., Caicedo, J.C., Bara, N., Kovacs, F., Paavolainen, L., Danka, T., Kriston, A., Carpenter, A.E., Smith, K., Horvath, P., 2020. nucleAIzer: A Parameter-free Deep Learning Framework for Nucleus Segmentation Using Image Style Transfer. Cell Syst. 10, 453-458.e6.

https://doi.org/10.1016/j.cels.2020.04.003

Holwerda, M., V'kovski, P., Wider, M., Thiel, V., Dijkman, R., 2020. Identification of an antiviral compound from the pandemic response box that efficiently inhibits sars-cov-2 infection in vitro. Microorganisms 8, 1–19. https://doi.org/10.3390/microorganisms8121872

Hopkins, C., Gibson, A., Stinchcombe, J., Futter, C., 2000. Chimeric molecules employing horseradish peroxidase as reporter enzyme for protein localization in the electron microscope. Methods Enzymol. 327, 35–45. https://doi.org/10.1016/S0076-6879(00)27265-0

Horazdovsky, B.F., Davies, B.A., Seaman, M.N.J., McLaughlin, S.A., Yoon, S.H., Emr, S.D., 1997. A sorting nexin-1 homologue, Vps5p, forms a complex with Vps17p and is required for recycling the vacuolar protein-sorting receptor. Mol. Biol. Cell 8, 1529–1541. https://doi.org/10.1091/mbc.8.8.1529

Hu, P., Liang, Y., Hu, Q., Wang, H., Cai, Z., He, J., Cai, J., Liu, M., Qin, Y., Yu, X., Jiang, C., Zhang, B., Wang, W., 2018. SNX6 predicts poor prognosis and contributes to the metastasis of pancreatic cancer cells via activating epithelial-mesenchymal transition. Acta Biochim. Biophys. Sin. (Shanghai). 50, 1075–1084. https://doi.org/10.1093/abbs/gmy110

Huang, X., Ye, Q., Chen, M., Li, A., Mi, W., Fang, Y., Zaytseva, Y.Y., O'Connor, K.L., Vander Kooi, C.W., Liu, S., She, Q.B., 2019. N-glycosylation-defective splice variants of neuropilin-1 promote metastasis by activating endosomal signals. Nat. Commun. 10, 1–16. https://doi.org/10.1038/s41467-019-11580-4

Huang, Y., Ma, T., Lau, P.K., Wang, J., Zhao, T., Du, S., Loy, M.M.T., Guo, Y., 2019. Visualization of Protein Sorting at the Trans-Golgi Network and Endosomes Through Super-Resolution Imaging. Front. Cell Dev. Biol. 7, 181. https://doi.org/10.3389/fcell.2019.00181

Hui, K.P.Y., Cheung, M.C., Perera, R.A.P.M., Ng, K.C., Bui, C.H.T., Ho, J.C.W., Ng, M.M.T., Kuok, D.I.T., Shih, K.C., Tsao, S.W., Poon, L.L.M., Peiris, M., Nicholls, J.M., Chan, M.C.W., 2020. Tropism, replication competence, and innate immune responses of the coronavirus SARS-CoV-2 in human respiratory tract and conjunctiva: an analysis in ex-vivo and in-vitro cultures. Lancet Respir. Med. 8, 687–695. https://doi.org/10.1016/S2213-2600(20)30193-4

Hung, V., Lam, S.S., Udeshi, N.D., Svinkina, T., Guzman, G., Mootha, V.K., Carr, S.A., Ting, A.Y., 2017. Proteomic mapping of cytosol-facing outer mitochondrial and ER membranes in living human cells by proximity biotinylation. Elife 6, 1–38. https://doi.org/10.7554/eLife.24463

Hung, V., Udeshi, N.D., Lam, S.S., Loh, K.H., Cox, K.J., Pedram, K., Carr, S.A., Ting, A.Y., 2016. Spatially resolved proteomic mapping in living cells with the engineered peroxidase APEX2. Nat. Protoc. 11, 456–475. https://doi.org/10.1038/nprot.2016.018

Hung, V., Zou, P., Rhee, H.-W.W., Udeshi, N.D.D., Cracan, V., Svinkina, T., Carr, S.A.A., Mootha, V.K.K., Ting, A.Y.Y., 2014. Proteomic Mapping of the Human Mitochondrial Intermembrane Space in Live Cells via Ratiometric APEX Tagging. Mol. Cell 55, 332–341. https://doi.org/10.1016/j.molcel.2014.06.003

Hunt, S.D., Townley, A.K., Danson, C.M., Cullen, P.J., Stephens, D.J., 2013. Microtubule motors mediate endosomal sorting by maintaining functional domain organization. J. Cell Sci. 126, 2493–2501. https://doi.org/10.1242/jcs.122317

Huotari, J., Helenius, A., 2011. Endosome maturation. EMBO J. 30, 3481–3500. https://doi.org/10.1038/emboj.2011.286

Hüttenrauch, M., Ogorek, I., Klafki, H., Otto, M., Stadelmann, C., Weggen, S., Wiltfang, J., Wirths, O., 2018. Glycoprotein NMB: a novel Alzheimer's disease associated marker expressed in a subset of activated microglia. Acta Neuropathol. Commun. 6, 108. https://doi.org/10.1186/s40478-018-0612-3

Imai, A., Yoshie, S., Nashida, T., Shimomura, H., Fukuda, M., 2004. The small GTPase Rab27B regulates amylase release from rat parotid acinar cells. J. Cell Sci. 117, 1945–1953. https://doi.org/10.1242/jcs.01048

Ishida, M., Bonifacino, J.S., 2019. ARFRP1 functions upstream of ARL1 and ARL5 to coordinate

recruitment of tethering factors to the trans-Golgi network. J. Cell Biol. 218, 3880–3881. https://doi.org/10.1083/jcb.20190509710072019c

Itai, N., Shimazu, T., Kimura, T., Ibe, I., Yamashita, R., Kaburagi, Y., Dohi, T., Tonozuka, T., Takao, T., Nishikawa, A., 2018. The phosphorylation of sorting nexin 5 at serine 226 regulates retrograde transport and macropinocytosis 13, e0207205. https://doi.org/10.1371/journal.pone.0207205

Izaguirre, G., 2019. The Proteolytic Regulation of Virus Cell Entry by Furin and Other Proprotein Convertases. Viruses 11. https://doi.org/10.3390/v11090837

Jaber, N., Mohd-Naim, N., Wang, Z., DeLeon, J.L., Kim, S., Zhong, H., Sheshadri, N., Dou, Z., Edinger, A.L., Du, G., Braga, V.M.M., Zong, W.X., 2016. Vps34 regulates Rab7 and late endocytic trafficking through recruitment of the GTPase-activating protein Armus. J. Cell Sci. 129, 4424–4435. https://doi.org/10.1242/jcs.192260

Jackson, C.L., Walch, L., Verbavatz, J.-M., 2016. Developmental Cell Review Lipids and Their Trafficking: An Integral Part of Cellular Organization. https://doi.org/10.1016/j.devcel.2016.09.030

Jackson, L.P., Lewis, M., Kent, H.M., Edeling, M.A., Evans, P.R., Duden, R., Owen, D.J., 2012. Molecular Basis for Recognition of Dilysine Trafficking Motifs by COPI. Dev. Cell 23, 1255–1262. https://doi.org/10.1016/j.devcel.2012.10.017

Janssen, B.J.C., Malinauskas, T., Weir, G.A., Cader, M.Z., Siebold, C., Jones, E.Y., 2012. Neuropilins lock secreted semaphorins onto plexins in a ternary signaling complex. Nat. Struct. Mol. Biol. 19, 1293–1299. https://doi.org/10.1038/nsmb.2416

Jarvis, A., Allerston, C.K., Jia, H., Herzog, B., Garza-Garcia, A., Winfield, N., Ellard, K., Aqil, R., Lynch, R., Chapman, C., Hartzoulakis, B., Nally, J., Stewart, M., Cheng, L., Menon, M., Tickner, M., Djordjevic, S., Driscoll, P.C., Zachary, I., Selwood, D.L., 2010. Small molecule inhibitors of the neuropilin-1 vascular endothelial growth factor A (VEGF-A) interaction. J. Med. Chem. 53, 2215–2226. https://doi.org/10.1021/jm901755g

Jean, S., Kiger, A.A., 2012. Coordination between RAB GTPase and phosphoinositide regulation and functions. Nat. Rev. Mol. Cell Biol. 13, 463–470. https://doi.org/10.1038/nrm3379

Jefferies, H.B.J., Cooke, F.T., Jat, P., Boucheron, C., Koizumi, T., Hayakawa, M., Kaizawa, H., Ohishi, T., Workman, P., Waterfield, M.D., Parker, P.J., 2008. A selective PIKfyve inhibitor blocks PtdIns(3,5)P2 production and disrupts endomembrane transport and retroviral budding. EMBO Rep. 9, 164–170. https://doi.org/10.1038/sj.embor.7401155

Jellett, A.P., 2018. Dissecting the molecular and functional interactions of retromer. PhD Thesis, Univ. Bristol.

Jia, D., Gomez, T.S., Billadeau, D.D., Rosen, M.K., 2012. Multiple repeat elements within the FAM21 tail link the WASH actin regulatory complex to the retromer. Mol. Biol. Cell 23, 2352–2361. https://doi.org/10.1091/mbc.E11-12-1059

Jia, D., Zhang, J.S., Li, F., Wang, J., Deng, Z., White, M.A., Osborne, D.G., Phillips-Krawczak, C., Gomez, T.S., Li, H., Singla, A., Burstein, E., Billadeau, D.D., Rosen, M.K., 2016. Structural and mechanistic insights into regulation of the retromer coat by TBC1d5. Nat. Commun. 7, 1–11. https://doi.org/10.1038/ncomms13305

Jiang, S., Hillyer, C., Du, L., 2020. Neutralizing Antibodies against SARS-CoV-2 and Other Human Coronaviruses. Trends Immunol. 41, 355–359. https://doi.org/10.1016/j.it.2020.03.007

Jimenez-Orgaz, A., Kvainickas, A., Nägele, H., Denner, J., Eimer, S., Dengjel, J., Steinberg, F., 2017. Control of RAB7 activity and localization through the retromer-TBC1D5 complex enables RAB7-dependent mitophagy. EMBO J. e201797128. https://doi.org/10.15252/embj.201797128

Jing, S., Spencer, T., Miller, K., Hopkins, C., Trowbridge, I.S., 1990. Role of the human transferrin receptor cytoplasmic domain in endocytosis: Localization of a specific signal sequence for internalization. J. Cell Biol. 110, 283–294. https://doi.org/10.1083/jcb.110.2.283

Johannes, L., Popoff, V., 2008. Tracing the Retrograde Route in Protein Trafficking. Cell 135, 1175–1187. https://doi.org/10.1016/j.cell.2008.12.009

Jordens, I., Fernandez-Borja, M., Marsman, M., Dusseljee, S., Janssen, L., Calafat, J., Janssen, H., Wubbolts, R., Neefjes, J., 2001. The Rab7 effector protein RILP controls lysosomal transport by inducing the recruitment of dynein-dynactin motors. Curr. Biol. 11, 1680–1685. https://doi.org/10.1016/S0960-9822(01)00531-0

Kadonosono, T., Yamano, A., Goto, T., Tsubaki, T., Niibori, M., Kuchimaru, T., Kizaka-Kondoh, S., 2015. Cell penetrating peptides improve tumor delivery of cargos through neuropilin-1-dependent extravasation. J. Control. Release 201, 14–21. https://doi.org/10.1016/j.jconrel.2015.01.011

Kaksonen, M., Roux, A., 2018. Mechanisms of clathrin-mediated endocytosis. Nat. Rev. Mol. Cell Biol. 19, 313–326. https://doi.org/10.1038/nrm.2017.132

Kania, A., Klein, R., 2016. Mechanisms of ephrin-Eph signalling in development, physiology and disease. Nat. Rev. Mol. Cell Biol. 17, 240–256. https://doi.org/10.1038/nrm.2015.16

Katzmann, D.J., Stefan, C.J., Babst, M., Emr, S.D., 2003. Vps27 recruits ESCRT machinery to endosomes during MVB sorting. J. Cell Biol. 162, 413–423. https://doi.org/10.1083/jcb.200302136

Ke, Z., Oton, J., Qu, K., Cortese, M., Zila, V., McKeane, L., Nakane, T., Zivanov, J., Neufeldt, C.J., Cerikan, B., Lu, J.M., Peukes, J., Xiong, X., Kräusslich, H.G., Scheres, S.H.W., Bartenschlager, R., Briggs, J.A.G., 2020. Structures and distributions of SARS-CoV-2 spike proteins on intact virions. Nature 588, 498–502. https://doi.org/10.1038/s41586-020-2665-2

Kendall, A.K., Xie, B., Xu, P., Wang, J., Burcham, R., Frazier, M.N., Binshtein, E., Wei, H., Graham, T.R., Nakagawa, T., Jackson, L.P., 2020. Mammalian Retromer Is an Adaptable Scaffold for Cargo Sorting from Endosomes. Structure 28, 393-405.e4. https://doi.org/10.1016/j.str.2020.01.009

Kerr, M.C., Bennetts, J.S., Simpson, F., Thomas, E.C., Flegg, C., Gleeson, P.A., Wicking, C., Teasdale, R.D., 2005. A novel mammalian retromer component, Vps26B. Traffic 6, 991–1001. https://doi.org/10.1111/j.1600-0854.2005.00328.x

Khakurel, A., Kudlyk, T., Bonifacino, J.S., Lupashin, V. V, 2020. The Golgi-associated retrograde protein (GARP) complex plays an essential role in the maintenance of the Golgi glycosylation machinery □-equal contribution. bioRxiv 2020.12.21.423858. https://doi.org/10.1101/2020.12.21.423858

Kim, M.J., Deng, H.X., Wong, Y.C., Siddique, T., Krainc, D., 2017. The Parkinson's disease-linked protein TMEM230 is required for Rab8a-mediated secretory vesicle trafficking and retromer trafficking. Hum. Mol. Genet. 26, 729–741. https://doi.org/10.1093/hmg/ddw413

Kirchhausen, T., Harrison, S.C., 1981. Protein organization in clathrin trimers. Cell 23, 755–761. https://doi.org/10.1016/0092-8674(81)90439-6

Klucken, J., Poehler, A.M., Ebrahimi-Fakhari, D., Schneider, J., Nuber, S., Rockenstein, E., Schlötzer-Schrehardt, U., Hyman, B.T., McLean, P.J., Masliah, E., Winkler, J., 2012. Alpha-synuclein aggregation involves a bafilomycin A1-sensitive autophagy pathway. Autophagy 8, 754–766. https://doi.org/10.4161/auto.19371

Klumperman, J., Raposo, G., 2014. The complex ultrastructure of the endolysosomal system. Cold Spring Harb. Perspect. Biol. 6, 16857–16858. https://doi.org/10.1101/cshperspect.a016857

Ko, D.C., Gordon, M.D., Jin, J.Y., Scott, M.P., 2001. Dynamic movements of organelles containing Niemann-Pick C1 protein: NPC1 involvement in late endocytic events. Mol. Biol. Cell 12, 601–614. https://doi.org/10.1091/mbc.12.3.601

Koeberl, D.D., Luo, X., Sun, B., Mcvie-Wylie, A., Dai, J., Li, S., Banugaria, S.G., Chen, Y.T., Bali, D.S., 2011. Enhanced efficacy of enzyme replacement therapy in Pompe disease through mannose-6-phosphate receptor expression in skeletal muscle. Mol. Genet. Metab. 103, 107–112. https://doi.org/10.1016/j.ymgme.2011.02.006

Koontz, L., 2014. TCA precipitation. Methods Enzymol. 541, 3–10. https://doi.org/10.1016/B978-0-12-420119-4.00001-X

Kostelansky, M.S., Sun, J., Lee, S., Kim, J., Ghirlando, R., Hierro, A., Emr, S.D., Hurley, J.H., 2006. Structural and Functional Organization of the ESCRT-I Trafficking Complex. Cell 125, 113–126. https://doi.org/10.1016/j.cell.2006.01.049

Kostelnik, K.B., Barker, A., Schultz, C., Mitchell, T.P., Rajeeve, V., White, I.J., Aurrand-Lions, M., Nourshargh, S., Cutillas, P., Nightingale, T.D., 2019. Dynamic trafficking and turnover of JAM-C is essential for endothelial cell migration. PLoS Biol. 17, e3000554. https://doi.org/10.1371/journal.pbio.3000554

Koumandou, V.L., Klute, M.J., Herman, E.K., Nunez-Miguel, R., Dacks, J.B., Field, M.C., 2011. Evolutionary reconstruction of the retromer complex and its function in Trypanosoma brucei. J. Cell Sci. 124, 1496–1509. https://doi.org/10.1242/jcs.081596

Kovtun, O., Leneva, N., Bykov, Y.S., Ariotti, N., Teasdale, R.D., Schaffer, M., Engel, B.D., Owen, D.J., Briggs, J.A.G., Collins, B.M., 2018. Structure of the membrane-assembled retromer coat determined by cryo-electron tomography. Nature 561, 561–564. https://doi.org/10.1038/s41586-018-0526-z

Krogh, A., Larsson, B., Von Heijne, G., Sonnhammer, E.L.L., 2001. Predicting transmembrane protein topology with a hidden Markov model: Application to complete genomes. J. Mol. Biol. 305, 567–580. https://doi.org/10.1006/jmbi.2000.4315

Krysan, D.J., Rockwell, N.C., Fuller, R.S., 1999. Quantitative characterization of furin specificity: Energetics of substrate discrimination using an internally consistent set of hexapeptidyl methylcoumarinamides. J. Biol. Chem. 274, 23229–23234. https://doi.org/10.1074/jbc.274.33.23229

Kucera, A., Borg Distefano, M., Berg-Larsen, A., Skjeldal, F., Repnik, U., Bakke, O., Progida, C., 2016. Spatiotemporal Resolution of Rab9 and CI-MPR Dynamics in the Endocytic Pathway. Traffic 17, 211–229. https://doi.org/10.1111/tra.12357

Kusunoki, H., Tanaka, T., Kohno, T., Matsuhashi, K., Hosoda, K., Wakamatsu, K., Hamaguchi, I., 2018. A novel neuropilin-1–binding sequence in the human T-cell lymphotropic virus type 1 envelope glycoprotein. Biochim. Biophys. Acta - Proteins Proteomics 1866, 541–548. https://doi.org/10.1016/j.bbapap.2018.02.003

Kvainickas, A., Jimenez-Orgaz, A., Nägele, H., Hu, Z., Dengjel, J., Steinberg, F., 2017. Cargo-selective SNX-BAR proteins mediate retromer trimer independent retrograde transport. J. Cell Biol. 216, 3677–3693. https://doi.org/10.1083/jcb.201702137

Kvainickas, A., Nägele, H., Qi, W., Dokládal, L., Jimenez-Orgaz, A., Stehl, L., Gangurde, D., Zhao, Q., Hu, Z., Dengjel, J., de Virgilio, C., Baumeister, R., Steinberg, F., 2019. Retromer and TBC1D5 maintain late endosomal RAB7 domains to enable amino acid–induced mTORC1 signaling. J. Cell Biol. 218, 3019–3038. https://doi.org/10.1083/JCB.201812110

Lam, S.S., Martell, J.D., Kamer, K.J., Deerinck, T.J., Ellisman, M.H., Mootha, V.K., Ting, A.Y., 2014. Directed evolution of APEX2 for electron microscopy and proximity labeling. Nat. Methods 12, 51–54. https://doi.org/10.1038/nmeth.3179

Lambert, S., Bouttier, M., Vassy, R., Seigneuret, M., Petrow-Sadowski, C., Janvier, S., Heveker, N., Ruscetti, F.W., Perret, G., Jones, K.S., Pique, C., 2009. HTLV-1 uses HSPG and neuropilin-1 for entry by molecular mimicry of VEGF165. Blood 113, 5176–5185. https://doi.org/10.1182/blood-2008-04-150342

Lanahan, A., Zhang, X., Fantin, A., Zhuang, Z., Rivera-Molina, F., Speichinger, K., Prahst, C., Zhang, J., Wang, Y., Davis, G., Toomre, D., Ruhrberg, C., Simons, M., 2013. The Neuropilin 1 Cytoplasmic Domain Is Required for VEGF-A-Dependent Arteriogenesis. Dev. Cell 25, 156–168. https://doi.org/10.1016/j.devcel.2013.03.019

Lane, R.K., Guo, H., Fisher, A.D., Diep, J., Lai, Z., Chen, Y., Upton, J.W., Carette, J., Mocarski, E.S., Kaiser, W.J., 2020. Necroptosis-based CRISPR knockout screen reveals Neuropilin-1 as a

critical host factor for early stages of murine cytomegalovirus infection. Proc. Natl. Acad. Sci. U. S. A. 117, 20109–20116. https://doi.org/10.1073/PNAS.1921315117

Lange, R., Peng, X., Wimmer, E., Lipp, M., Bernhardt, G., 2001. The poliovirus receptor CD155 mediates cell-to-matrix contacts by specifically binding to vitronectin. Virology 285, 218–227. https://doi.org/10.1006/viro.2001.0943

Lau, S.-Y., Wang, P., Mok, B.W.-Y., Zhang, A.J., Chu, H., Lee, A.C.-Y., Deng, S., Chen, P., Chan, K.-H., Song, W., Chen, Z., To, K.K.-W., Chan, J.F.-W., Yuen, K.-Y., Chen, H., 2020. Attenuated SARS-CoV-2 variants with deletions at the S1/S2 junction. Emerg. Microbes Infect. 9, 837–842. https://doi.org/10.1080/22221751.2020.1756700

Lauffer, B.E.L., Melero, C., Temkin, P., Lei, C., Hong, W., Kortemme, T., Von Zastrow, M., 2010. SNX27 mediates PDZ-directed sorting from endosomes to the plasma membrane. J. Cell Biol. 190, 565–574. https://doi.org/10.1083/jcb.201004060

Laurent-Matha, V., Derocq, D., Prébois, C., Katunuma, N., Liaudet-Coopman, E., 2006. Processing of human cathepsin D is independent of its catalytic function and auto-activation: Involvement of cathepsins L and B. J. Biochem. 139, 363–371. https://doi.org/10.1093/jb/mvj037

Law, F., Seo, J.H., Wang, Z., DeLeon, J.L., Bolis, Y., Brown, A., Zong, W.X., Du, G., Rocheleau, C.E., 2017. The VPS34 PI3K negatively regulates RAB-5 during endosome maturation. J. Cell Sci. 130, 2007–2017. https://doi.org/10.1242/jcs.194746

Lee, C.C., Kreusch, A., McMullan, D., Ng, K., Spraggon, G., 2003. Crystal structure of the human neuropilin-1 b1 domain. Structure 11, 99–108. https://doi.org/10.1016/S0969-2126(02)00941-3

Lee, S., Chang, J., Blackstone, C., 2016. FAM21 directs SNX27-retromer cargoes to the plasma membrane by preventing transport to the Golgi apparatus. Nat. Commun. 7, 1–12. https://doi.org/10.1038/ncomms10939

Lefrancois, S., Zeng, J., Hassan, A.J., Canuel, M., Morales, C.R., 2003. The lysosomal trafficking of sphingolipid activator proteins (SAPs) is mediated by sortilin. EMBO J. 22, 6430–6437. https://doi.org/10.1093/emboj/cdg629

Leneva, N., Kovtun, O., Morado, D.R., Briggs, J.A.G., Owen, D.J., 2020. Architecture and mechanism of metazoan retromer:SNX3 tubular coat assembly. bioRxiv 2020.11.28.401588. https://doi.org/10.1101/2020.11.28.401588

Lenoir, M., Ustunel, C., Rajesh, S., Kaur, J., Moreau, D., Gruenberg, J., Overduin, M., 2018. Phosphorylation of conserved phosphoinositide binding pocket regulates sorting nexin membrane targeting. Nat. Commun. 9. https://doi.org/10.1038/s41467-018-03370-1

Leroy, H., Han, M., Woottum, M., Bracq, L., Bouchet, J., Xie, M., Benichou, S., 2020. Virus-Mediated Cell-Cell Fusion. Int. J. Mol. Sci. 21, 9644. https://doi.org/10.3390/ijms21249644

Letoha, T., Hudák, A., Kusz, E., Pettkó-Szandtner, A., Domonkos, I., Jósvay, K., Hofmann-Apitius, M., Szilák, L., 2019. Contribution of syndecans to cellular internalization and fibrillation of amyloid-β(1–42). Sci. Rep. 9, 1–17. https://doi.org/10.1038/s41598-018-37476-9

Levkowitz, G., Waterman, H., Zamir, E., Kam, Z., Oved, S., Langdon, W.Y., Beguinot, L., Geiger, B., Yarden, Y., 1998. c-Cb1/Sli-1 regulates endocytic sorting and ubiquitination of the epidermal growth factor receptor. Genes Dev. 12, 3663–3674. https://doi.org/10.1101/gad.12.23.3663

Li, F., 2016. Structure, Function, and Evolution of Coronavirus Spike Proteins. Annu. Rev. Virol. 3, 237–261. https://doi.org/10.1146/annurev-virology-110615-042301

Li, Y., Xu, M., Ding, X., Yan, C., Song, Z., Chen, L., Huang, X., Wang, X., Jian, Y., Tang, G., Tang, C., Di, Y., Mu, S., Liu, X., Liu, K., Li, T., Wang, Y., Miao, L., Guo, W., Hao, X., Yang, C., 2016. Protein kinase C controls lysosome biogenesis independently of mTORC1. Nat. Cell Biol. 18, 1065–1077. https://doi.org/10.1038/ncb3407

Li, Z.-L., Buck, M., 2021. Neuropilin-1 Assists SARS-CoV-2 Infection by Stimulating the Separation of Spike Protein Domains S1 and S2. bioRxiv 2021.01.06.425627. https://doi.org/10.1101/2021.01.06.425627

Lin, D.C., Quevedo, C., Brewer, N.E., Bell, A., Testa, J.R., Grimes, M.L., Miller, F.D., Kaplan, D.R., 2006. APPL1 associates with TrkA and GIPC1 and is required for nerve growth factor-mediated signal transduction. Mol. Cell. Biol. 26, 8928–41. https://doi.org/10.1128/MCB.00228-06

Liu, C.C., Zhao, N., Yamaguchi, Y., Cirrito, J.R., Kanekiyo, T., Holtzman, D.M., Bu, G., 2016. Neuronal heparan sulfates promote amyloid pathology by modulating brain amyloid-β clearance and aggregation in Alzheimer's disease. Sci. Transl. Med. 8, 332ra44-332ra44. https://doi.org/10.1126/scitranslmed.aad3650

Lobingier, B.T., Hüttenhain, R., Eichel, K., Miller, K.B., Ting, A.Y., von Zastrow, M., Krogan, N.J., 2017. An Approach to Spatiotemporally Resolve Protein Interaction Networks in Living Cells. Cell 169, 350-360.e12. https://doi.org/10.1016/j.cell.2017.03.022

Loh, K.H., Stawski, P.S., Draycott, A.S., Udeshi, N.D., Lehrman, E.K., Wilton, D.K., Svinkina, T., Deerinck, T.J., Ellisman, M.H., Stevens, B., Carr, S.A., Ting, A.Y., 2016. Proteomic Analysis of Unbounded Cellular Compartments: Synaptic Clefts. Cell 166, 1295-1307.e21. https://doi.org/10.1016/j.cell.2016.07.041

Lombardi, D., Soldati, T., Riederer, M.A., Goda, Y., Zerial, M., Pfeffer, S.R., 1993. Rab9 functions in transport between late endosomes and the trans Golgi network. EMBO J. 12, 677–682. https://doi.org/10.1002/j.1460-2075.1993.tb05701.x

Lopez-Vergès, S., Camus, G., Blot, G., Beauvoir, R., Benarous, R., Berlioz-Torrent, C., 2006. Tail-interacting protein TIP47 is a connector between Gag and Env and is required for Env incorporation into HIV-1 virions. Proc. Natl. Acad. Sci. U. S. A. 103, 14947–14952. https://doi.org/10.1073/pnas.0602941103

Lozupone, F., Borghi, M., Marzoli, F., Azzarito, T., Matarrese, P., Iessi, E., Venturi, G., Meschini, S., Canitano, A., Bona, R., Cara, A., Fais, S., 2015. TM9SF4 is a novel V-ATPase-interacting protein that modulates tumor pH alterations associated with drug resistance and invasiveness of colon cancer cells. Oncogene 34, 5163–5174. https://doi.org/10.1038/onc.2014.437

Lu, L., Hong, W., 2003. Interaction of Arl1-GTP with GRIP domains recruits autoantigens Golgin-97 and Golgin-245/p230 onto the Golgi. Mol. Biol. Cell 14, 3767–3781. https://doi.org/10.1091/mbc.E03-01-0864

Lucas, M., Gershlick, D.C., Vidaurrazaga, A., Rojas, A.L., Bonifacino, J.S., Hierro, A., 2016. Structural Mechanism for Cargo Recognition by the Retromer Complex. Cell 167, 1623-1635.e14. https://doi.org/10.1016/j.cell.2016.10.056

Luzio, J.P., Brake, B., Banting, G., Howell, K.E., Braghetta, P., Stanley, K.K., 1990. Identification, sequencing and expression of an integral membrane protein of the trans-Golgi network (TGN38). Biochem. J. 270, 97–102. https://doi.org/10.1042/bj2700097

Luzio, J.P., Pryor, P.R., Bright, N.A., 2007. Lysosomes: Fusion and function. Nat. Rev. Mol. Cell Biol. 8, 622–632. https://doi.org/10.1038/nrm2217

Lyon, M., Rushton, G., Askari, J.A., Humphries, M.J., Gallagher, J.T., 2000. Elucidation of the structural features of heparan sulfate important for interaction with the Hep-2 domain of fibronectin. J. Biol. Chem. 275, 4599–4606. https://doi.org/10.1074/jbc.275.7.4599

Ma, M.P.C., Chircop, M., 2012. SNX9, SNX18 and SNX33 are required for progression: Through and completion of mitosis. J. Cell Sci. 125, 4372–4382. https://doi.org/10.1242/jcs.105981

Ma, W., Goldberg, J., 2013. Rules for the recognition of dilysine retrieval motifs by coatomer. EMBO J. 32, 926–937. https://doi.org/10.1038/emboj.2013.41

MacLeod, D.A., Rhinn, H., Kuwahara, T., Zolin, A., Di Paolo, G., MacCabe, B.D., Marder, K.S., Honig, L.S., Clark, L.N., Small, S.A., Abeliovich, A., 2013. RAB7L1 Interacts with LRRK2 to Modify Intraneuronal Protein Sorting and Parkinson's Disease Risk. Neuron 77, 425–439. https://doi.org/10.1016/j.neuron.2012.11.033

Maday, S., Anderson, E., Chang, H.C., Shorter, J., Satoh, A., Sfakianos, J., Fölsch, H., Anderson, J.M., Walther, Z., Mellman, I., 2008. A PDZ-Binding Motif Controls Basolateral Targeting of Syndecan-1 Along the Biosynthetic Pathway in Polarized Epithelial Cells. Traffic 9, 1915–1924.

https://doi.org/10.1111/j.1600-0854.2008.00805.x

Mallam, A.L., Marcotte, E.M., 2017. Systems-wide Studies Uncover Commander, a Multiprotein Complex Essential to Human Development. Cell Syst. 4, 483–494. https://doi.org/10.1016/j.cels.2017.04.006

Mallard, F., Antony, C., Tenza, D., Salamero, J., Goud, B., Johannes, L., 1998. Direct pathway from early/recycling endosomes to the Golgi apparatus revealed through the study of Shiga toxin B-fragment transport. J. Cell Biol. 143, 973–990. https://doi.org/10.1083/jcb.143.4.973

Mallet, W.G., Maxfield, F.R., 1999. Chimeric forms of furin and TGN38 are transported from the plasma membrane to the trans-Golgi network via distinct endosomal pathways. J. Cell Biol. 146, 345–359. https://doi.org/10.1083/jcb.146.2.345

Mana, G., Clapero, F., Panieri, E., Panero, V., Böttcher, R.T., Tseng, H.Y., Saltarin, F., Astanina, E., Wolanska, K.I., Morgan, M.R., Humphries, M.J., Santoro, M.M., Serini, G., Valdembri, D., 2016. PPFIA1 drives active α5β1 integrin recycling and controls fibronectin fibrillogenesis and vascular morphogenesis. Nat. Commun. 7, 1–20. https://doi.org/10.1038/ncomms13546

Mana, G., Valdembri, D., Serini, G., 2020. Conformationally active integrin endocytosis and traffic: Why, where, when and how? Biochem. Soc. Trans. 48, 83–93. https://doi.org/10.1042/BST20190309

Manickam, V., Tiwari, A., Jung, J.J., Bhattacharya, R., Goel, A., Mukhopadhyay, D., Choudhury, A., 2011. Regulation of vascular endothelial growth factor receptor 2 trafficking and angiogenesis by Golgi localized t-SNARE syntaxin 6. Blood 117, 1425–1435. https://doi.org/10.1182/blood-2010-06-291690

Mao, X., Kikani, C.K., Riojas, R.A., Langlais, P., Wang, L., Ramos, F.J., Fang, Q., Christ-Roberts, C.Y., Hong, J.Y., Kim, R.Y., Liu, F., Dong, L.Q., 2006. APPL1 binds to adiponectin receptors and mediates adiponectin signalling and function. Nat. Cell Biol. 8, 516–523. https://doi.org/10.1038/ncb1404

Marshansky, V., Futai, M., 2008. The V-type H+-ATPase in vesicular trafficking: targeting, regulation and function. Curr. Opin. Cell Biol. 20, 415–426. https://doi.org/10.1016/j.ceb.2008.03.015

Martell, J.D., Deerinck, T.J., Sancak, Y., Poulos, T.L., Mootha, V.K., Sosinsky, G.E., Ellisman, M.H., Ting, A.Y., 2012. Engineered ascorbate peroxidase as a genetically encoded reporter for electron microscopy. Nat. Biotechnol. 30, 1143–8. https://doi.org/10.1038/nbt.2375

Martin, T.F.J., 1998. Phosphoinositide lipids as signaling molecules: Common themes for signal transduction, cytoskeletal regulation, and membrane trafficking. Annu. Rev. Cell Dev. Biol. 14, 231–264. https://doi.org/10.1146/annurev.cellbio.14.1.231

Martina, J.A., Chen, Y., Gucek, M., Puertollano, R., 2012. MTORC1 functions as a transcriptional regulator of autophagy by preventing nuclear transport of TFEB. Autophagy 8, 903–14. https://doi.org/10.4161/auto.19653

Martinez-Martin, N., Marcandalli, J., Huang, C.S., Arthur, C.P., Perotti, M., Foglierini, M., Ho, H., Dosey, A.M., Shriver, S., Payandeh, J., Leitner, A., Lanzavecchia, A., Perez, L., Ciferri, C., 2018. An Unbiased Screen for Human Cytomegalovirus Identifies Neuropilin-2 as a Central Viral Receptor. Cell 174, 1158-1171.e19. https://doi.org/10.1016/j.cell.2018.06.028

Masters, T.A., Tumbarello, D.A., Chibalina, M. V., Buss, F., 2017. MYO6 Regulates Spatial Organization of Signaling Endosomes Driving AKT Activation and Actin Dynamics. Cell Rep. 19, 2088–2101. https://doi.org/10.1016/j.celrep.2017.05.048

Mattera, R., Park, S.Y., De Pace, R., Guardia, C.M., Bonifacino, J.S., 2017. AP-4 mediates export of ATG9A from the trans-Golgi network to promote autophagosome formation. Proc. Natl. Acad. Sci. U. S. A. 114, E10697–E10706. https://doi.org/10.1073/pnas.1717327114

Maxfield, F.R., McGraw, T.E., 2004. Endocytic recycling. Nat. Rev. Mol. Cell Biol. 5, 121–132. https://doi.org/10.1038/nrm1315

Maxfield, F.R., Yamashiro, D.J., 1987. Endosome acidification and the pathways of receptor-mediated

endocytosis. Adv. Exp. Med. Biol. 225, 189–198. https://doi.org/10.1007/978-1-4684-5442-0_16

Mayers, J.R., Fyfe, I., Schuh, A.L., Chapman, E.R., Edwardson, J.M., Audhya, A., 2011. ESCRT-0 assembles as a heterotetrameric complex on membranes and binds multiple ubiquitinylated cargoes simultaneously. J. Biol. Chem. 286, 9636–9645. https://doi.org/10.1074/jbc.M110.185363

Mayor, S., Parton, R.G., Donaldson, J.G., 2014. Clathrin-independent pathways of endocytosis. Cold Spring Harb. Perspect. Biol. 6. https://doi.org/10.1101/cshperspect.a016758

Mayor, S., Presley, J.F., Maxfield, F.R., 1993. Sorting of membrane components from endosomes and subsequent recycling to the cell surface occurs by a bulk flow process. J. Cell Biol. 121, 1257–1269. https://doi.org/10.1083/jcb.121.6.1257

McCray, B.A., Skordalakes, E., Taylor, J.P., 2010. Disease mutations in Rab7 result in unregulated nucleotide exchange and inappropriate activation. Hum. Mol. Genet. 19, 1033–1047. https://doi.org/10.1093/hmg/ddp567

McCrea, H.J., De Camilli, P., 2009. Mutations in phosphoinositide metabolizing enzymes and human disease. Physiology 24, 8–16. https://doi.org/10.1152/physiol.00035.2008

McGough, I.J., de Groot, R.E.A.A., Jellett, A.P., Betist, M.C., Varandas, K.C., Danson, C.M., Heesom, K.J., Korswagen, H.C., Cullen, P.J., 2018. SNX3-retromer requires an evolutionary conserved MON2:DOPEY2:ATP9A complex to mediate Wntless sorting and Wnt secretion. Nat. Commun. 9. https://doi.org/10.1038/s41467-018-06114-3

McGough, I.J., Steinberg, F., Jia, D., Barbuti, P.A., McMillan, K.J., Heesom, K.J., Whone, A.L., Caldwell, M.A., Billadeau, D.D., Rosen, M.K., Cullen, P.J., 2014. Retromer binding to FAM21 and the WASH complex is perturbed by the Parkinson disease-linked VPS35(D620N) mutation. Curr. Biol. 24, 1670–1676. https://doi.org/10.1016/j.cub.2014.06.024

McMillan, K.J., Gallon, M., Jellett, A.P., Clairfeuille, T., Tilley, F.C., McGough, I., Danson, C.M., Heesom, K.J., Wilkinson, K.A., Collins, B.M., Cullen, P.J., 2016. Atypical parkinsonism-associated retromer mutant alters endosomal sorting of specific cargo proteins. J. Cell Biol. 214, 389–399. https://doi.org/10.1083/jcb.201604057

McMillan, K.J., Korswagen, H.C., Cullen, P.J., 2017. The emerging role of retromer in neuroprotection. Curr. Opin. Cell Biol. 47, 72–82. https://doi.org/10.1016/J.CEB.2017.02.004

McNally, K.E., Cullen, P.J., 2018. Endosomal Retrieval of Cargo: Retromer Is Not Alone. Trends Cell Biol. 28, 807–822. https://doi.org/10.1016/j.tcb.2018.06.005

McNally, K.E., Faulkner, R., Steinberg, F., Gallon, M., Ghai, R., Pim, D., Langton, P., Pearson, N., Danson, C.M., Nägele, H., Morris, L.L., Singla, A., Overlee, B.L., Heesom, K.J., Sessions, R., Banks, L., Collins, B.M., Berger, I., Billadeau, D.D., Burstein, E., Cullen, P.J., 2017. Retriever is a multiprotein complex for retromer-independent endosomal cargo recycling. Nat. Cell Biol. 19, 1214–1225. https://doi.org/10.1038/ncb3610

Mecozzi, V.J., Berman, D.E., Simoes, S., Vetanovetz, C., Awal, M.R., Patel, V.M., Schneider, R.T., Petsko, G.A., Ringe, D., Small, S.A., 2014. Pharmacological chaperones stabilize retromer to limit APP processing. Nat. Chem. Biol. 10, 443–9. https://doi.org/10.1038/nchembio.1508

Medina, D.L., Fraldi, A., Bouche, V., Annunziata, F., Mansueto, G., Spampanato, C., Puri, C., Pignata, A., Martina, J.A., Sardiello, M., Palmieri, M., Polishchuk, R., Puertollano, R., Ballabio, A., 2011. Transcriptional activation of lysosomal exocytosis promotes cellular clearance. Dev. Cell 21, 421–30. https://doi.org/10.1016/j.devcel.2011.07.016

Merico, D., Isserlin, R., Stueker, O., Emili, A., Bader, G.D., 2010. Enrichment map: A network-based method for gene-set enrichment visualization and interpretation. PLoS One 5. https://doi.org/10.1371/journal.pone.0013984

Mészáros, B., Sámano-Sánchez, H., Alvarado-Valverde, J., Čalyševa, J., Martínez-Pérez, E., Alves, R., Shields, D.C., Kumar, M., Rippmann, F., Chemes, L.B., Gibson, T.J., 2021. Short linear motif candidates in the cell entry system used by SARS-CoV-2 and their potential therapeutic implications. Sci. Signal. 14, 334. https://doi.org/10.1126/scisignal.abd0334

Meyer, C., Zizioli, D., Lausmann, S., Eskelinen, E.L., Hamann, J., Saftig, P., Von Figura, K., Schu, P., 2000. μ1A-adaptin-deficient mice: Lethality, loss of AP-1 binding and rerouting of mannose 6-phosphate receptors. EMBO J. 19, 2193–2203. https://doi.org/10.1093/emboj/19.10.2193

Mi, H., Muruganujan, A., Huang, X., Ebert, D., Mills, C., Guo, X., Thomas, P.D., 2019. Protocol Update for large-scale genome and gene function analysis with the PANTHER classification system (v.14.0). Nat. Protoc. 14, 703–721. https://doi.org/10.1038/s41596-019-0128-8

Miaczynska, M., 2013. Effects of membrane trafficking on signaling by receptor tyrosine kinases. Cold Spring Harb. Perspect. Biol. 5, 9035–9036. https://doi.org/10.1101/cshperspect.a009035

Millet, J.K., Whittaker, G.R., 2018. Physiological and molecular triggers for SARS-CoV membrane fusion and entry into host cells. Virology 517, 3–8. https://doi.org/10.1016/j.virol.2017.12.015

Miranda, A.M., Lasiecka, Z.M., Xu, Y., Neufeld, J., Shahriar, S., Simoes, S., Chan, R.B., Oliveira, T.G., Small, S.A., Di Paolo, G., 2018. Neuronal lysosomal dysfunction releases exosomes harboring APP C-terminal fragments and unique lipid signatures. Nat. Commun. 9, 1–16. https://doi.org/10.1038/s41467-017-02533-w

Mirrashidi, K.M., Elwell, C.A., Verschueren, E., Johnson, J.R., Frando, A., Von Dollen, J., Rosenberg, O., Gulbahce, N., Jang, G., Johnson, T., Jager, S., Gopalakrishnan, A.M., Sherry, J., Dan Dunn, J., Olive, A., Penn, B., Shales, M., Cox, J.S., Starnbach, M.N., Derre, I., Valdivia, R., Krogan, N.J., Engel, J., 2015. Global mapping of the inc-human interactome reveals that retromer restricts chlamydia infection. Cell Host Microbe 18, 109–121. https://doi.org/10.1016/j.chom.2015.06.004

Mizuno, K., Tolmachova, T., Ushakov, D.S., Romao, M., Åbrink, M., Ferenczi, M.A., Raposo, G., Seabra, M.C., 2007. Rab27b Regulates Mast Cell Granule Dynamics and Secretion. Traffic 8, 883–892. https://doi.org/10.1111/j.1600-0854.2007.00571.x

Mogelsvang, S., Marsh, B.J., Ladinsky, M.S., Howell, K.E., 2004. Predicting Function from Structure: 3D Structure Studies of the Mammalian Golgi Complex. Traffic 5, 338–345. https://doi.org/10.1111/j.1398-9219.2004.00186.x

Mootha, V.K., Lindgren, C.M., Eriksson, K.F., Subramanian, A., Sihag, S., Lehar, J., Puigserver, P., Carlsson, E., Ridderstråle, M., Laurila, E., Houstis, N., Daly, M.J., Patterson, N., Mesirov, J.P., Golub, T.R., Tamayo, P., Spiegelman, B., Lander, E.S., Hirschhorn, J.N., Altshuler, D., Groop, L.C., 2003. PGC-1α-responsive genes involved in oxidative phosphorylation are coordinately downregulated in human diabetes. Nat. Genet. 34, 267–273. https://doi.org/10.1038/ng1180

Moutal, A., Martin, L.F., Boinon, L., Gomez, K., Ran, D., Zhou, Y., Stratton, H.J., Cai, S., Luo, S., Gonzalez, K.B., Perez-Miller, S., Patwardhan, A., Ibrahim, M.M., Khanna, R., 2021. SARS-CoV-2 spike protein co-opts VEGF-A/neuropilin-1 receptor signaling to induce analgesia. Pain 162, 243–252. https://doi.org/10.1097/j.pain.0000000000002097

Muhammad, A., Flores, I., Zhang, H., Yu, R., Staniszewski, A., Planel, E., Herman, M., Ho, L., Kreber, R., Honig, L.S., Ganetzky, B., Duff, K., Arancio, O., Small, S.A., 2008. Retromer deficiency observed in Alzheimer's disease causes hippocampal dysfunction, neurodegeneration, and Abeta accumulation. Proc. Natl. Acad. Sci. U. S. A. 105, 7327–32. https://doi.org/10.1073/pnas.0802545105

Mullins, C., Bonifacino, J.S., 2001. The molecular machinery for lysosome biogenesis. BioEssays 23, 333–343. https://doi.org/10.1002/bies.1048

Munro, S., 2011. The golgin coiled-coil proteins of the Golgi apparatus. Cold Spring Harb. Perspect. Biol. 3, 1–14. https://doi.org/10.1101/cshperspect.a005256

Munro, S., 1991. Sequences within and adjacent to the transmembrane segment of alpha-2,6-sialyltransferase specify Golgi retention. EMBO J. 10, 3577–3588. https://doi.org/10.1002/j.1460-2075.1991.tb04924.x

Murray, D.H., Jahnel, M., Lauer, J., Avellaneda, M.J., Brouilly, N., Cezanne, A., Morales-Navarrete, H., Perini, E.D., Ferguson, C., Lupas, A.N., Kalaidzidis, Y., Parton, R.G., Grill, S.W., Zerial, M., 2016. An endosomal tether undergoes an entropic collapse to bring vesicles together. Nature

537, 107–111. https://doi.org/10.1038/nature19326

Muzio, L., Sirtori, R., Gornati, D., Eleuteri, S., Fossaghi, A., Brancaccio, D., Manzoni, L., Ottoboni, L., Feo, L. De, Quattrini, A., Mastrangelo, E., Sorrentino, L., Scalone, E., Comi, G., Marinelli, L., Riva, N., Milani, M., Seneci, P., Martino, G., 2020. Retromer stabilization results in neuroprotection in a model of Amyotrophic Lateral Sclerosis. Nat. Commun. 11, 1–17. https://doi.org/10.1038/s41467-020-17524-7

Nakamura, F., Kalb, R.G., Strittmatter, S.M., 2000. Molecular basis of semaphorin-mediated axon guidance. J. Neurobiol. 44, 219–229. https://doi.org/10.1002/1097-4695(200008)44:2<219::AID-NEU11>3.0.CO;2-W

Nakamura, K., Ohya, W., Funakoshi, H., Sakaguchi, G., Kato, A., Takeda, M., Kudo, T., Nakamura, T., 2006. Possible role of scavenger receptor SRCL in the clearance of amyloid-βin Alzheimer's disease. J. Neurosci. Res. 84, 874–890. https://doi.org/10.1002/jnr.20992

Navarro Negredo, P., Edgar, J.R., Manna, P.T., Antrobus, R., Robinson, M.S., 2018. The WDR11 complex facilitates the tethering of AP-1-derived vesicles. Nat. Commun. 9, 1–15. https://doi.org/10.1038/s41467-018-02919-4

Nielsen, E., Christoforidis, S., Uttenweiler-Joseph, S., Miaczynska, M., Dewitte, F., Wilm, M., Hoflack, B., Zerial, M., 2000. Rabenosyn-5, a novel Rab5 effector, is complexed with hVPS45 and recruited to endosomes through a FYVE finger domain. J. Cell Biol. 151, 601–612. https://doi.org/10.1083/jcb.151.3.601

Nieminen, T., Toivanen, P.I., Rintanen, N., Heikura, T., Jauhiainen, S., Airenne, K.J., Alitalo, K., Marjomäki, V., Ylä-Herttuala, S., 2014. The impact of the receptor binding profiles of the vascular endothelial growth factors on their angiogenic features. Biochim. Biophys. Acta - Gen. Subj. 1840, 454–463. https://doi.org/10.1016/j.bbagen.2013.10.005

Niland, S., Eble, J.A., 2019. Neuropilins in the context of tumor vasculature. Int. J. Mol. Sci. 20. https://doi.org/10.3390/ijms20030639

Nilsson, T., Lucocq, J.M., Mackay, D., Warren, G., 1991. The membrane spanning domain of beta-1,4-galactosyltransferase specifies trans Golgi localization. EMBO J. 10, 3567–75.

Norris, A., Grant, B.D., 2020. Endosomal microdomains: Formation and function. Curr. Opin. Cell Biol. 65, 86–95. https://doi.org/10.1016/j.ceb.2020.02.018

Norris, A., Tammineni, P., Wang, S., Gerdes, J., Murr, A., Kwan, K.Y., Cai, Q., Grant, B.D., 2017. SNX-1 and RME-8 oppose the assembly of HGRS-1/ ESCRT-0 degradative microdomains on endosomes. Proc. Natl. Acad. Sci. U. S. A. 114, E307–E316. https://doi.org/10.1073/pnas.1612730114

Norwood, S.J., Shaw, D.J., Cowieson, N.P., Owen, D.J., Teasdale, R.D., Collins, B.M., 2011. Assembly and Solution Structure of the Core Retromer Protein Complex. Traffic 12, 56–71. https://doi.org/10.1111/j.1600-0854.2010.01124.x

Ohka, S., Ohno, H., Tohyama, K., Nomoto, A., 2001. Basolateral sorting of human poliovirus receptor α involves an interaction with the μ1B subunit of the clathrin adaptor complex in polarized epithelial cells. Biochem. Biophys. Res. Commun. 287, 941–948. https://doi.org/10.1006/bbrc.2001.5660

Organ, S.L., Tsao, M.S., 2011. An overview of the c-MET signaling pathway. Ther. Adv. Med. Oncol. 3, S7–S19. https://doi.org/10.1177/1758834011422556

Ostrowski, M., Carmo, N.B., Krumeich, S., Fanget, I., Raposo, G., Savina, A., Moita, C.F., Schauer, K., Hume, A.N., Freitas, R.P., Goud, B., Benaroch, P., Hacohen, N., Fukuda, M., Desnos, C., Seabra, M.C., Darchen, F., Amigorena, S., Moita, L.F., Thery, C., 2010. Rab27a and Rab27b control different steps of the exosome secretion pathway. Nat. Cell Biol. 12, 19–30. https://doi.org/10.1038/ncb2000

Pakdel, M., Von Blume, J., 2018. Exploring new routes for secretory protein export from the trans-Golgi network. Mol. Biol. Cell 29, 235–240. https://doi.org/10.1091/mbc.E17-02-0117

Pan, X., Zaarur, N., Singh, M., Morin, P., Kandror, K. V., 2017. Sortilin and retromer mediate retrograde transport of Glut4 in 3T3-L1 adipocytes. Mol. Biol. Cell 28, 1667–1675. https://doi.org/10.1091/mbc.E16-11-0777

Pang, H.B., Braun, G.B., Friman, T., Aza-Blanc, P., Ruidiaz, M.E., Sugahara, K.N., Teesalu, T., Ruoslahti, E., 2014. An endocytosis pathway initiated through neuropilin-1 and regulated by nutrient availability. Nat. Commun. 5, 1–12. https://doi.org/10.1038/ncomms5904

Papa, G., Mallery, D.L., Albecka, A., Welch, L.G., Cattin-Ortolá, J., Luptak, J., Paul, D., McMahon, H.T., Goodfellow, I.G., Carter, A., Munro, S., James, L.C., 2021. Furin cleavage of SARS-CoV-2 Spike promotes but is not essential for infection and cell-cell fusion. PLOS Pathog. 17, e1009246. https://doi.org/10.1371/journal.ppat.1009246

Parenti, G., Andria, G., Ballabio, A., 2015. Lysosomal Storage Diseases: From Pathophysiology to Therapy. Annu. Rev. Med. 66, 471–486. https://doi.org/10.1146/annurev-med-122313-085916

Parker, M.W., Guo, H.F., Li, X., Linkugel, A.D., Vander Kooi, C.W., 2012a. Function of members of the neuropilin family as essential pleiotropic cell surface receptors. Biochemistry 51, 9437–9446. https://doi.org/10.1021/bi3012143

Parker, M.W., Linkugel, A.D., Goel, H.L., Wu, T., Mercurio, A.M., Vander Kooi, C.W., 2015. Structural basis for VEGF-C binding to neuropilin-2 and sequestration by a soluble splice form. Structure 23, 677–687. https://doi.org/10.1016/j.str.2015.01.018

Parker, M.W., Linkugel, A.D., Vander Kooi, C.W., 2013. Effect of C-terminal sequence on competitive semaphorin binding to neuropilin-1. J. Mol. Biol. 425, 4405–4414. https://doi.org/10.1016/j.jmb.2013.07.017

Parker, M.W., Xu, P., Guo, H.-F., Vander Kooi, C.W., 2012b. Mechanism of Selective VEGF-A Binding by Neuropilin-1 Reveals a Basis for Specific Ligand Inhibition. PLoS One 7, e49177. https://doi.org/10.1371/journal.pone.0049177

Parker, M.W., Xu, P., Li, X., Vander Kooi, C.W., 2012c. Structural basis for selective vascular endothelial growth factor-A (VEGF-A) binding to neuropilin-1. J. Biol. Chem. 287, 11082–11089. https://doi.org/10.1074/jbc.M111.331140

Paroutis, P., Touret, N., Grinstein, S., 2004. The pH of the Secretory Pathway: Measurement, Determinants, and Regulation. Physiology 19, 207–215. https://doi.org/10.1152/physiol.00005.2004

Patterson, G.H., Hirschberg, K., Polishchuk, R.S., Gerlich, D., Phair, R.D., Lippincott-Schwartz, J., 2008. Transport through the Golgi Apparatus by Rapid Partitioning within a Two-Phase Membrane System. Cell 133, 1055–1067. https://doi.org/10.1016/j.cell.2008.04.044

Paul, B., Kim, H.S., Kerr, M.C., Huston, W.M., Teasdale, R.D., Collins, B.M., 2017. Structural basis for the hijacking of endosomal sorting nexin proteins by Chlamydia trachomatis. Elife 6. https://doi.org/10.7554/eLife.22311

Paul, N.R., Jacquemet, G., Caswell, P.T., 2015. Endocytic Trafficking of Integrins in Cell Migration. Curr. Biol. 25, R1092–R1105. https://doi.org/10.1016/j.cub.2015.09.049

Pereira-Leal, J.B., Hume, A.N., Seabra, M.C., 2001. Prenylation of Rab GTPases: molecular mechanisms and involvement in genetic disease. FEBS Lett. 498, 197–200. https://doi.org/10.1016/S0014-5793(01)02483-8

Pérez-Victoria, F.J., Bonifacino, J.S., 2009. Dual Roles of the Mammalian GARP Complex in Tethering and SNARE Complex Assembly at the trans-Golgi Network. Mol. Cell. Biol. 29, 5251–5263. https://doi.org/10.1128/mcb.00495-09

Pérez-Victoria, F.J., Mardones, G.A., Bonifacino, J.S., 2008. Requirement of the human GARP complex for mannose 6-phosphate-receptor- dependent sorting of cathepsin D to lysosomes. Mol. Biol. Cell 19, 2350–2362. https://doi.org/10.1091/mbc.E07-11-1189

Perini, E.D., Schaefer, R., Stöter, M., Kalaidzidis, Y., Zerial, M., 2014. Mammalian CORVET Is Required for Fusion and Conversion of Distinct Early Endosome Subpopulations. Traffic 15,

1366–1389. https://doi.org/10.1111/tra.12232

Perrin, J., Le Coadic, M., Vernay, A., Dias, M., Gopaldass, N., Ouertatani-Sakouhi, H., Cosson, P., 2015. TM9 family proteins control surface targeting of glycine-rich transmembrane domains. J. Cell Sci. 128, 2269–2277. https://doi.org/10.1242/jcs.164848

Phillips-Krawczak, C.A., Singla, A., Starokadomskyy, P., Deng, Z., Osborne, D.G., Li, H., Dick, C.J., Gomez, T.S., Koenecke, M., Zhang, J.S., Dai, H., Sifuentes-Dominguez, L.F., Geng, L.N., Kaufmann, S.H., Hein, M.Y., Wallis, M., McGaughran, J., Gecz, J., Van De Sluis, B., Billadeau, D.D., Burstein, E., 2015. COMMD1 is linked to the WASH complex and regulates endosomal trafficking of the copper transporter ATP7A. Mol. Biol. Cell 26, 91–103. https://doi.org/10.1091/mbc.E14-06-1073

Phillips, N., 2021. The coronavirus is here to stay — here's what that means. Nature 590, 382–384. https://doi.org/10.1038/d41586-021-00396-2

Polishchuk, R.S., Pietro, E.S., Pentima, A. Di, Teté, S., Bonifacino, J.S., 2006. Ultrastructure of Long-Range Transport Carriers Moving from the trans Golgi Network to Peripheral Endosomes. Traffic 7, 1092–1103. https://doi.org/10.1111/j.1600-0854.2006.00453.x

Polishchuk, R.S., Polishchuk, E. V., Marra, P., Alberti, S., Buccione, R., Luini, A., Mironov, A.A., 2000. Correlative light-electron microscopy reveals the tubular-saccular ultrastructure of carriers operating between Golgi apparatus and plasma membrane. J. Cell Biol. 148, 45–58. https://doi.org/10.1083/jcb.148.1.45

Pons, V., Ustunel, C., Rolland, C., Torti, E., Parton, R.G., Gruenberg, J., 2012. SNX12 Role in Endosome Membrane Transport. PLoS One 7, e38949. https://doi.org/10.1371/journal.pone.0038949

Powell, J., Mota, F., Steadman, D., Soudy, C., Miyauchi, J.T., Crosby, S., Jarvis, A., Reisinger, T., Winfield, N., Evans, G., Finniear, A., Yelland, T., Chou, Y.T., Chan, A.W.E., O'Leary, A., Cheng, L., Liu, D., Fotinou, C., Milagre, C., Martin, J.F., Jia, H., Frankel, P., Djordjevic, S., Tsirka, S.E., Zachary, I.C., Selwood, D.L., 2018. Small Molecule Neuropilin-1 Antagonists Combine Antiangiogenic and Antitumor Activity with Immune Modulation through Reduction of Transforming Growth Factor Beta (TGFβ) Production in Regulatory T-Cells. J. Med. Chem. 61, 4135–4154. https://doi.org/10.1021/acs.jmedchem.8b00210

Prekeris, R., Yang, B., Oorschot, V., Klumperman, J., Scheller, R.H., 1999. Differential roles of syntaxin 7 and syntaxin 8 in endosomal trafficking. Mol. Biol. Cell 10, 3891–3908. https://doi.org/10.1091/mbc.10.11.3891

Priya, A., Sugatha, J., Parveen, S., Lacas-Gervais, S., Raj, P., Gilleron, J., Datta, S., 2017. Essential and selective role of SNX12 in transport of endocytic and retrograde cargo. J. Cell Sci. 130, 2707–2721. https://doi.org/10.1242/jcs.201905

Pryor, P.R., Mullock, B.M., Bright, N.A., Lindsay, M.R., Gray, S.R., Richardson, S.C.W., Stewart, A., James, D.E., Piper, R.C., Luzio, J.P., 2004. Combinatorial SNARE complexes with VAMP7 or VAMP8 define different late endocytic fusion events. EMBO Rep. 5, 590–595. https://doi.org/10.1038/sj.embor.7400150

Pu, J., Keren-Kaplan, T., Bonifacino, J.S., 2017. A Ragulator-BORC interaction controls lysosome positioning in response to amino acid availability. J. Cell Biol. 216, 4183–4197. https://doi.org/10.1083/jcb.201703094

Pu, J., Schindler, C., Jia, R., Jarnik, M., Backlund, P., Bonifacino, J.S., 2015. BORC, a Multisubunit Complex that Regulates Lysosome Positioning. Dev. Cell 33, 176–188. https://doi.org/10.1016/j.devcel.2015.02.011

Puelles, V.G., Lütgehetmann, M., Lindenmeyer, M.T., Sperhake, J.P., Wong, M.N., Allweiss, L., Chilla, S., Heinemann, A., Wanner, N., Liu, S., Braun, F., Lu, S., Pfefferle, S., Schröder, A.S., Edler, C., Gross, O., Glatzel, M., Wichmann, D., Wiech, T., Kluge, S., Pueschel, K., Aepfelbacher, M., Huber, T.B., 2020. Multiorgan and Renal Tropism of SARS-CoV-2. N. Engl. J. Med. https://doi.org/10.1056/nejmc2011400

Puertollano, R., Aguilar, R.C., Gorshkova, I., Crouch, R.J., Bonifacino, J.S., 2001. Sorting of mannose 6-phosphate receptors mediated by the GGAs. Science. 292, 1712–1716. https://doi.org/10.1126/science.1060750

Puthenveedu, M.A., Lauffer, B., Temkin, P., Vistein, R., Carlton, P., Thorn, K., Taunton, J., Weiner, O.D., Parton, R.G., Mark Von Zastrow, 2010. Sequence-dependent sorting of recycling proteins by actin-stabilized endosomal microdomains. Cell 143, 761–773. https://doi.org/10.1016/j.cell.2010.10.003

Raaben, M., Jae, L.T., Herbert, A.S., Kuehne, A.I., Stubbs, S.H., Chou, Y. ying, Blomen, V.A., Kirchhausen, T., Dye, J.M., Brummelkamp, T.R., Whelan, S.P., 2017. NRP2 and CD63 Are Host Factors for Lujo Virus Cell Entry. Cell Host Microbe 22, 688-696.e5. https://doi.org/10.1016/j.chom.2017.10.002

Raiborg, C., Bremnes, B., Mehlum, A., Gillooly, D.J., D'Arrigo, A., Stang, E., Stenmark, H., 2001. FYVE and coiled-coil domains determine the specific localisation of Hrs to early endosomes. J. Cell Sci. 114.

Raiborg, C., Wenzel, E.M., Pedersen, N.M., Olsvik, H., Schink, K.O., Schultz, S.W., Vietri, M., Nisi, V., Bucci, C., Brech, A., Johansen, T., Stenmark, H., 2015. Repeated ER-endosome contacts promote endosome translocation and neurite outgrowth. Nature 520, 234–238. https://doi.org/10.1038/nature14359

Raiborg, C., Wesche, J., Malerød, L., Stenmark, H., 2006. Flat clathrin coats on endosomes mediate degradative protein sorting by scaffolding Hrs in dynamic microdomains. J. Cell Sci. 119, 2414–2424. https://doi.org/10.1242/jcs.02978

Ramirez, I.B.-R., Lowe, M., 2009. Golgins and GRASPs: Holding the Golgi together. Semin. Cell Dev. Biol. 20, 770–779. https://doi.org/10.1016/j.semcdb.2009.03.011

Ranneva, S. V., Maksimov, V.F., Korostyshevskaja, I.M., Lipina, T. V., 2020. Lack of synaptic protein, calsyntenin-2, impairs morphology of synaptic complexes in mice. Synapse 74. https://doi.org/10.1002/syn.22132

Ravussin, A., Brech, A., Tooze, S.A., Stenmark, H., 2021. The phosphatidylinositol 3-phosphate binding protein SNX4 controls ATG9A recycling and autophagy. J. Cell Sci. jcs.250670. https://doi.org/10.1242/jcs.250670

Reaves, B.J., Banting, G., Luzio, J.P., 1998. Lumenal and Transmembrane Domains Play a Role in Sorting Type I Membrane Proteins on Endocytic Pathways. Mol. Biol. Cell 9, 1107–1122. https://doi.org/10.1091/mbc.9.5.1107

Ren, X., Hurley, J.H., 2010. VHS domains of ESCRT-0 cooperate in high-avidity binding to polyubiquitinated cargo. EMBO J. 29, 1045–1054. https://doi.org/10.1038/emboj.2010.6

Rhee, H.W., Zou, P., Udeshi, N.D., Martell, J.D., Mootha, V.K., Carr, S.A., Ting, A.Y., 2013. Proteomic mapping of mitochondria in living cells via spatially restricted enzymatic tagging. Science. 339, 1328–1331. https://doi.org/10.1126/science.1230593

Richardson, T.G., Sanderson, E., Palmer, T.M., Ala-Korpela, M., Ference, B.A., Davey Smith, G., Holmes, M. V., 2020. Evaluating the relationship between circulating lipoprotein lipids and apolipoproteins with risk of coronary heart disease: A multivariable Mendelian randomisation analysis. PLOS Med. 17, e1003062. https://doi.org/10.1371/journal.pmed.1003062

Riederer, M.A., Soldati, T., Shapiro, A.D., Lin, J., Pfeffer, S.R., 1994. Lysosome biogenesis requires rab9 function and receptor recycling from endosomes to the trans-Golgi network. J. Cell Biol. 125, 573–582. https://doi.org/10.1083/jcb.125.3.573

Riggs, K.A., Hasan, N., Humphrey, D., Raleigh, C., Nevitt, C., Corbin, D., Hu, C., 2012. Regulation of integrin endocytic recycling and chemotactic cell migration by syntaxin 6 and VAMP3 interaction. J. Cell Sci. 125, 3827–3839. https://doi.org/10.1242/jcs.102566

Robinson, M.S., 2015. Forty Years of Clathrin-coated Vesicles. Traffic 16, 1210–1238. https://doi.org/10.1111/tra.12335

Robinson, M.S., Hirst, J., 2013. Rapid Inactivation of Proteins by Knocksideways. Curr. Protoc. Cell Biol. 61, 15.20.1-15.20.7. https://doi.org/10.1002/0471143030.cb1520s61

Rojas, R., van Vlijmen, T., Mardones, G.A., Prabhu, Y., Rojas, A.L., Mohammed, S., Heck, A.J.R., Raposo, G., van der Sluijs, P., Bonifacino, J.S., 2008. Regulation of retromer recruitment to endosomes by sequential action of Rab5 and Rab7. J. Cell Biol. 183, 513–26. https://doi.org/10.1083/jcb.200804048

Rojo Pulido, I., Nightingale, T.D., Darchen, F., Seabra, M.C., Cutler, D.F., Gerke, V., 2011. Myosin Va acts in concert with Rab27a and MyRIP to regulate acute von-Willebrand factor release from endothelial cells. Traffic 12, 1371–1382. https://doi.org/10.1111/j.1600-0854.2011.01248.x

Rosa-Ferreira, C., Christis, C., Torres, I.L., Munro, S., 2015. The small G protein Arl5 contributes to endosome-to-Golgi traffic by aiding the recruitment of the GARP complex to the Golgi. Biol. Open 4, 474–481. https://doi.org/10.1242/bio.201410975

Rose, A.A.N., Annis, M.G., Dong, Z., Pepin, F., Hallett, M., Park, M., Siegel, P.M., 2010. ADAM10 Releases a Soluble Form of the GPNMB/Osteoactivin Extracellular Domain with Angiogenic Properties. PLoS One 5, e12093. https://doi.org/10.1371/journal.pone.0012093

Rosenthal, S.L., Wang, X., Demirci, F.Y., Barmada, M.M., Ganguli, M., Lopez, O.L., Kamboh, M.I., 2012. Beta-amyloid toxicity modifier genes and the risk of Alzheimer's disease. Am. J. Neurodegener. Dis. 1, 191–198.

Rosivatz, E., Woscholski, R., 2011. Removal or masking of phosphatidylinositol(4,5)bisphosphate from the outer mitochondrial membrane causes mitochondrial fragmentation. Cell. Signal. 23, 478–486. https://doi.org/10.1016/j.cellsig.2010.10.025

Rossi, E., Bernabeu, C., Smadja, D.M., 2019. Endoglin as an Adhesion Molecule in Mature and Progenitor Endothelial Cells: A Function Beyond TGF-β. Front. Med. 6, 10. https://doi.org/10.3389/fmed.2019.00010

Rossignol, M., Gagnon, M.L., Klagsbrun, M., 2000. Genomic organization of human neuropilin-1 and neuropilin-2 genes: Identification and distribution of splice variants and soluble isoforms. Genomics 70, 211–222. https://doi.org/10.1006/geno.2000.6381

Rothman, J.E., 1994. Mechanisms of intracellular protein transport. Nature 372, 55–63. https://doi.org/10.1038/372055a0

Rothman, J.H., Howald, I., Stevens, T.H., 1989. Characterization of genes required for protein sorting and vacuolar function in the yeast Saccharomyces cerevisiae. EMBO J. 8, 2057–2065. https://doi.org/10.1002/j.1460-2075.1989.tb03614.x

Rowland, A.A.A., Chitwood, P.J.J., Phillips, M.J.J., Voeltz, G.K.K., 2014. ER contact sites define the position and timing of endosome fission. Cell 159, 1027–1041. https://doi.org/10.1016/j.cell.2014.10.023

Roy, S., Bag, A.K., Singh, R.K., Talmadge, J.E., Batra, S.K., Datta, K., 2017. Multifaceted role of neuropilins in the immune system: Potential targets for immunotherapy. Front. Immunol. 8, 1228. https://doi.org/10.3389/fimmu.2017.01228

Ruan, Q., Johnson, G.V.W., 2007. Transglutaminase 2 in neurodegenerative disorders. Front. Biosci. 12, 891–904. https://doi.org/10.2741/2111

Rubino, M., Miaczynska, M., Lippé, R., Zerial, M., 2000. Selective membrane recruitment of EEA1 suggests a role in directional transport of clathrin-coated vesicles to early endosomes. J. Biol. Chem. 275, 3745–3748. https://doi.org/10.1074/jbc.275.6.3745

Ruoslahti, E., 2017. Tumor penetrating peptides for improved drug delivery. Adv. Drug Deliv. Rev. 110–111, 3–12. https://doi.org/10.1016/j.addr.2016.03.008

Sachse, M., Urbé, S., Oorschot, V., Strous, G.J., Klumperman, J., 2002. Bilayered clathrin coats on endosomal vacuoles are involved in protein sorting toward lysosomes. Mol. Biol. Cell 13, 1313–1328. https://doi.org/10.1091/mbc.01-10-0525

Saint-Pol, A., Yélamos, B., Amessou, M., Mills, I.G., Dugast, M., Tenza, D., Schu, P., Antony, C., McMahon, H.T., Lamaze, C., Johannes, L., 2004. Clathrin adaptor epsinR is required for retrograde sorting on early endosomal membranes. Dev. Cell 6, 525–538. https://doi.org/10.1016/S1534-5807(04)00100-5

Samavarchi-Tehrani, P., Samson, R., Gingras, A.C., 2020. Proximity dependent biotinylation: Key enzymes and adaptation to proteomics approaches. Mol. Cell. Proteomics 19, 757–773. https://doi.org/10.1074/mcp.R120.001941

Sanger, A., Hirst, J., Davies, A.K., Robinson, M.S., 2019. Adaptor protein complexes and disease at a glance. J. Cell Sci. 132. https://doi.org/10.1242/jcs.222992

Sangwan, V., Paliouras, G.N., Abella, J. V., Dubé, N., Monast, A., Tremblay, M.L., Park, M., 2008. Regulation of the met receptor-tyrosine kinase by the protein-tyrosine phosphatase 1B and T-cell phosphatase. J. Biol. Chem. 283, 34374–34383. https://doi.org/10.1074/jbc.M805916200

Sarabipour, S., Mac Gabhann, F., 2018. VEGF-A121a binding to Neuropilins–A concept revisited. Cell Adhes. Migr. 12, 204–214. https://doi.org/10.1080/19336918.2017.1372878

Sardiello, M., Palmieri, M., di Ronza, A., Medina, D.L., Valenza, M., Gennarino, V.A., Di Malta, C., Donaudy, F., Embrione, V., Polishchuk, R.S., Banfi, S., Parenti, G., Cattaneo, E., Ballabio, A., 2009. A gene network regulating lysosomal biogenesis and function. Science 325, 473–7. https://doi.org/10.1126/science.1174447

Sarkar, S., Rokad, D., Malovic, E., Luo, J., Harischandra, D.S., Jin, H., Anantharam, V., Huang, X., Lewis, M., Kanthasamy, A., Kanthasamy, A.G., 2019. Manganese activates NLRP3 inflammasome signaling and propagates exosomal release of ASC in microglial cells. Sci. Signal. 12. https://doi.org/10.1126/scisignal.aat9900

Sawma, P., Roth, L., Blanchard, C., Bagnard, D., Crémel, G., Bouveret, E., Duneau, J.P., Sturgis, J.N., Hubert, P., 2014. Evidence for new homotypic and heterotypic interactions between transmembrane helices of proteins involved in receptor tyrosine kinase and neuropilin signaling. J. Mol. Biol. 426, 4099–4111. https://doi.org/10.1016/j.jmb.2014.10.007

Sbrissa, D., Ikonomov, O.C., Shisheva, A., 1999. PIKfyve, a mammalian ortholog of yeast Fab1p lipid kinase, synthesizes 5-phosphoinositides. Effect of insulin. J. Biol. Chem. 274, 21589–21597. https://doi.org/10.1074/jbc.274.31.21589

Schink, K.O., Tan, K.-W., Stenmark, H., 2016. Phosphoinositides in Control of Membrane Dynamics. Annu. Rev. Cell Dev. Biol. 32, 143–171. https://doi.org/10.1146/annurev-cellbio-111315-125349

Schnettger, L., Rodgers, A., Repnik, U., Lai, R.P., Pei, G., Verdoes, M., Wilkinson, R.J., Young, D.B., Gutierrez, M.G., 2017. A Rab20-Dependent Membrane Trafficking Pathway Controls M. tuberculosis Replication by Regulating Phagosome Spaciousness and Integrity. Cell Host Microbe 21, 619-628.e5. https://doi.org/10.1016/j.chom.2017.04.004

Schomburg, D., Salzmann, M., Stephan, D., 1994. Peroxidase. Enzym. Handb. 7 747–753. https://doi.org/10.1007/978-3-642-78521-4_142

Schöneberg, J., Lee, I.H., Iwasa, J.H., Hurley, J.H., 2016. Reverse-topology membrane scission by the ESCRT proteins. Nat. Rev. Mol. Cell Biol. 18, 5–17. https://doi.org/10.1038/nrm.2016.121

Schreij, A.M.A., Fon, E.A., McPherson, P.S., 2016. Endocytic membrane trafficking and neurodegenerative disease. Cell. Mol. Life Sci. 73, 1529–1545. https://doi.org/10.1007/s00018-015-2105-x

Schröder, B.A., Wrocklage, C., Hasilik, A., Saftig, P., 2010. The proteome of lysosomes. Proteomics 10, 4053–4076. https://doi.org/10.1002/pmic.201000196

Schulze, H., Kolter, T., Sandhoff, K., 2009. Principles of lysosomal membrane degradation. Cellular topology and biochemistry of lysosomal lipid degradation. Biochim. Biophys. Acta - Mol. Cell Res. 1793, 674–683. https://doi.org/10.1016/j.bbamcr.2008.09.020

Schwarz, Q., Ruhrberg, C., 2010. Neuropilin, you gotta let me know: Should I stay or should I go? Cell Adhes. Migr. 4, 61–66. https://doi.org/10.4161/cam.4.1.10207

Scott, G.K., Fei, H., Thomas, L., Medigeshi, G.R., Thomas, G., 2006. A PACS-1, GGA3 and CK2 complex regulates CI-MPR trafficking. EMBO J. 25, 4423–4435. https://doi.org/10.1038/sj.emboj.7601336

Seaman, M.N.J., 2021. The Retromer Complex: From Genesis to Revelations. Trends Biochem. Sci. https://doi.org/10.1016/j.tibs.2020.12.009

Seaman, M.N.J., 2012. The retromer complex - endosomal protein recycling and beyond. J. Cell Sci. 125, 4693–702. https://doi.org/10.1242/jcs.103440

Seaman, M.N.J., 2007. Identification of a novel conserved sorting motif required for retromer-mediated endosome-to-TGN retrieval. J. Cell Sci. 120, 2378–2389. https://doi.org/10.1242/jcs.009654

Seaman, M.N.J., 2004. Cargo-selective endosomal sorting for retrieval to the Golgi requires retromer. J. Cell Biol. 165, 111–122. https://doi.org/10.1083/jcb.200312034

Seaman, M.N.J., Marcusson, E.G., Cereghino, J.L., Emr, S.D., 1997. Endosome to Golgi retrieval of the vacuolar protein sorting receptor, Vps10p, requires the function of the VPS29, VPS30, and VPS35 gene products. J. Cell Biol. 137, 79–92. https://doi.org/10.1083/jcb.137.1.79

Seaman, M.N.J., McCaffery, J.M., Emr, S.D., 1998. A membrane coat complex essential for endosome-to-Golgi retrograde transport in yeast. J. Cell Biol. 142, 665–681. https://doi.org/10.1083/jcb.142.3.665

Seaman, M.N.J.J., Harbour, M.E., Tattersall, D., Read, E., Bright, N., 2009. Membrane recruitment of the cargo-selective retromer subcomplex is catalysed by the small GTPase Rab7 and inhibited by the Rab-GAP TBC1D5. J. Cell Sci. 122, 2371–2382. https://doi.org/10.1242/jcs.048686

Seaman, M.N.J.J., Harbour, M.E., Tattersall, D., Read, E., Bright, N., 2007. Identification of a novel conserved sorting motif required for retromer-mediated endosome-to-TGN retrieval. J. Cell Sci. 120, 2378–2389. https://doi.org/10.1242/jcs.009654

Sears, R.M., May, D.G., Roux, K.J., 2019. BioID as a tool for protein-proximity labeling in living cells. Methods Mol. Biol. 2012, 299–313. https://doi.org/10.1007/978-1-4939-9546-2_15

Seerapu, H.R., Borthakur, S., Kong, N., Agrawal, S., Drazba, J., Vasanji, A., Fantin, A., Ruhrberg, C., Buck, M., Horowitz, A., 2013. The cytoplasmic domain of neuropilin-1 regulates focal adhesion turnover. FEBS Lett. 587, 3392–3399. https://doi.org/10.1016/j.febslet.2013.08.040

Settembre, C., Zoncu, R., Medina, D.L., Vetrini, F., Erdin, Serkan, Erdin, SerpilUckac, Huynh, T., Ferron, M., Karsenty, G., Vellard, M.C., Facchinetti, V., Sabatini, D.M., Ballabio, A., 2012. A lysosome-to-nucleus signalling mechanism senses and regulates the lysosome via mTOR and TFEB. EMBO J. 31, 1095–108. https://doi.org/10.1038/emboj.2012.32

Sevlever, D., Jiang, P., Yen, S.H.C., 2008. Cathepsin D is the main lysosomal enzyme involved in the degradation of α-synuclein and generation of its carboxy-terminally truncated species. Biochemistry 47, 9678–9687. https://doi.org/10.1021/bi800699v

Shafaq-Zadah, M., Gomes-Santos, C.S., Bardin, S., Maiuri, P., Maurin, M., Iranzo, J., Gautreau, A., Lamaze, C., Caswell, P., Goud, B., Johannes, L., 2016. Persistent cell migration and adhesion rely on retrograde transport of β 1 integrin. Nat. Cell Biol. 18, 54–64. https://doi.org/10.1038/ncb3287

Shang, J., Wan, Y., Luo, C., Ye, G., Geng, Q., Auerbach, A., Li, F., 2020. Cell entry mechanisms of SARS-CoV-2 117. https://doi.org/10.1073/pnas.2003138117

Sharpe, H.J., Stevens, T.J., Munro, S., 2010. A Comprehensive Comparison of Transmembrane Domains Reveals Organelle-Specific Properties. Cell 142, 158–169. https://doi.org/10.1016/j.cell.2010.05.037

Shen, Y.T., Gu, Y., Su, W.F., Zhong, J. fei, Jin, Z.H., Gu, X.S., Chen, G., 2016. Rab27b is Involved in Lysosomal Exocytosis and Proteolipid Protein Trafficking in Oligodendrocytes. Neurosci. Bull. 32, 331–340. https://doi.org/10.1007/s12264-016-0045-6

Shi, F., Sottile, J., 2011. MT1-MMP regulates the turnover and endocytosis of extracellular matrix fibronectin. J. Cell Sci. 124, 4039–4050. https://doi.org/10.1242/jcs.087858

Shi, F., Sottile, J., 2008. Caveolin-1-dependent β1 integrin endocytosis is a critical regulator of fibronectin turnover. J. Cell Sci. 121, 2360–2371. https://doi.org/10.1242/jcs.014977

Shi, G., Azoulay, M., Dingli, F., Lamaze, C., Loew, D., Florent, J.-C., Johannes, L., 2012. SNAP-tag Based Proteomics Approach for the Study of the Retrograde Route. Traffic 13, 914–925. https://doi.org/10.1111/j.1600-0854.2012.01357.x

Shi, H., Rojas, R., Bonifacino, J.S., Hurley, J.H., 2006. The retromer subunit Vps26 has an arrestin fold and binds Vps35 through its C-terminal domain. Nat. Struct. Mol. Biol. 13, 540–548. https://doi.org/10.1038/nsmb1103

Shin, J.J.H., Crook, O.M., Borgeaud, A.C., Cattin-Ortolá, J., Peak-Chew, S.Y., Breckels, L.M., Gillingham, A.K., Chadwick, J., Lilley, K.S., Munro, S., 2020. Spatial proteomics defines the content of trafficking vesicles captured by golgin tethers. Nat. Commun. 11, 1–13. https://doi.org/10.1038/s41467-020-19840-4

Shin, J.J.H.H., Gillingham, A.K., Begum, F., Chadwick, J., Munro, S., 2017. TBC1D23 is a bridging factor for endosomal vesicle capture by golgins at the trans-Golgi. Nat. Cell Biol. 19, 1424–1432. https://doi.org/10.1038/ncb3627

Shintani, Y., Takashima, S., Asano, Y., Kato, H., Liao, Y., Yamazaki, S., Tsukamoto, O., Seguchi, O., Yamamoto, H., Fukushima, T., Sugahara, K., Kitakaze, M., Hori, M., 2006. Glycosaminoglycan modification of neuropilin-1 modulates VEGFR2 signaling. EMBO J. 25, 3045–3055. https://doi.org/10.1038/sj.emboj.7601188

Shtanko, O., Sakurai, Y., Reyes, A.N., Noël, R., Cintrat, J.C., Gillet, D., Barbier, J., Davey, R.A., 2018. Retro-2 and its dihydroquinazolinone derivatives inhibit filovirus infection. Antiviral Res. 149, 154–163. https://doi.org/10.1016/j.antiviral.2017.11.016

Sigrist, C.J., Bridge, A., Le Mercier, P., 2020. A potential role for integrins in host cell entry by SARS-CoV-2. Antiviral Res. 177, 104759. https://doi.org/10.1016/j.antiviral.2020.104759

Simmons, G., Gosalia, D.N., Rennekamp, A.J., Reeves, J.D., Diamond, S.L., Bates, P., 2005. Inhibitors of cathepsin L prevent severe acute respiratory syndrome coronavirus entry. Proc. Natl. Acad. Sci. U. S. A. 102, 11876–11881. https://doi.org/10.1073/pnas.0505577102

Simoes, S., Neufeld, J.L., Triana-Baltzer, G., Moughadam, S., Chen, E.I., Kothiya, M., Qureshi, Y.H., Patel, V., Honig, L.S., Kolb, H., Small, S.A., 2020. Tau and other proteins found in Alzheimer's disease spinal fluid are linked to retromer-mediated endosomal traffic in mice and humans. Sci. Transl. Med. 12. https://doi.org/10.1126/SCITRANSLMED.ABA6334

Simonetti, B., 2017. A molecular analysis of tubular-based cargo recycling by the endosome-associated SNX-BAR proteins. PhD Thesis, Univ. Bristol.

Simonetti, B., Cullen, P.J., 2019. Actin-dependent endosomal receptor recycling. Curr. Opin. Cell Biol. 56, 22–33. https://doi.org/10.1016/j.ceb.2018.08.006

Simonetti, B., Danson, C.M., Heesom, K.J., Cullen, P.J., 2017. Sequence-dependent cargo recognition by SNX-BARs mediates retromer-independent transport of CI-MPR. J. Cell Biol. 216, 3695–3712. https://doi.org/10.1083/jcb.201703015

Simonetti, B., Paul, B., Chaudhari, K., Weeratunga, S., Steinberg, F., Gorla, M., Heesom, K.J., Bashaw, G.J., Collins, B.M., Cullen, P.J., 2019. Molecular identification of a BAR domain-containing coat complex for endosomal recycling of transmembrane proteins. Nat. Cell Biol. 21, 1219–1233. https://doi.org/10.1038/s41556-019-0393-3

Simons, M., Gordon, E., Claesson-Welsh, L., 2016. Mechanisms and regulation of endothelial VEGF receptor signalling. Nat. Rev. Mol. Cell Biol. 17, 611–625. https://doi.org/10.1038/nrm.2016.87

Simonsen, A., Lippé, R., Christoforidis, S., Gaullier, J.M., Brech, A., Callaghan, J., Toh, B.H., Murphy, C., Zerial, M., Stenmark, H., 1998. EEA1 links PI(3)K function to Rab5 regulation of endosome fusion. Nature 394, 494–498. https://doi.org/10.1038/28879

Simunovic, M., Evergren, E., Callan-Jones, A., Bassereau, P., 2019. Curving Cells Inside and Out: Roles of BAR Domain Proteins in Membrane Shaping and Its Cellular Implications. Annu. Rev. Cell Dev. Biol. 35, 111–129. https://doi.org/10.1146/annurev-cellbio-100617-060558

Simunovic, M., Evergren, E., Golushko, I., Prévost, C., Renard, H.F., Johannes, L., McMahon, H.T., Lorman, V., Voth, G.A., Bassereau, P., 2016. How curvature-generating proteins build scaffolds on membrane nanotubes. Proc. Natl. Acad. Sci. U. S. A. 113, 11226–11231. https://doi.org/10.1073/pnas.1606943113

Simunovic, M., Manneville, J.-B.B., Renard, H.-F.F., Evergren, E., Raghunathan, K., Bhatia, D., Kenworthy, A.K., Voth, G.A., Prost, J., McMahon, H.T., Johannes, L., Bassereau, P., Callan-Jones, A., 2017. Friction Mediates Scission of Tubular Membranes Scaffolded by BAR Proteins. Cell 170, 172-184.e11. https://doi.org/10.1016/j.cell.2017.05.047

Singla, A., Fedoseienko, A., Giridharan, S.S.P., Overlee, B.L., Lopez, A., Jia, D., Song, J., Huff-Hardy, K., Weisman, L., Burstein, E., Billadeau, D.D., 2019. Endosomal PI(3)P regulation by the COMMD/CCDC22/CCDC93 (CCC) complex controls membrane protein recycling. Nat. Commun. 10, 1–17. https://doi.org/10.1038/s41467-019-12221-6

Sivan, G., Weisberg, A.S., Americo, J.L., Moss, B., 2016. Retrograde Transport from Early Endosomes to the trans -Golgi Network Enables Membrane Wrapping and Egress of Vaccinia Virus Virions . J. Virol. 90, 8891–8905. https://doi.org/10.1128/jvi.01114-16

Skånland, S.S., Wälchli, S., Utskarpen, A., Wandinger-Ness, A., Sandvig, K., 2007. Phosphoinositide-Regulated Retrograde Transport of Ricin: Crosstalk Between hVps34 and Sorting Nexins. Traffic 8, 297–309. https://doi.org/10.1111/j.1600-0854.2006.00527.x

Slade, L., Pulinilkunnil, T., 2017. The MiTF/TFE family of transcription factors: Master regulators of organelle signaling, metabolism, and stress adaptation. Mol. Cancer Res. 15, 1637–1643. https://doi.org/10.1158/1541-7786.MCR-17-0320

Sleigh, J.N., Gómez-Martín, A., Wei, N., Bai, G., Yang, X.L., Schiavo, G., 2017. Neuropilin 1 sequestration by neuropathogenic mutant glycyl-tRNA synthetase is permissive to vascular homeostasis. Sci. Rep. 7. https://doi.org/10.1038/s41598-017-10005-w

Small, D.H., Williamson, T., Reed, G., Clarris, H., Beyreuther, K., Masters, C.L., Nurcombe, V., 1996. The Role of Heparan Sulfate Proteoglycans in the Pathogenesis of Alzheimer's Diseasea. Ann. N. Y. Acad. Sci. 777, 316–321. https://doi.org/10.1111/j.1749-6632.1996.tb34439.x

Small, S.A., Kent, K., Pierce, A., Leung, C., Kang, M.S., Okada, H., Honig, L., Vonsattel, J.-P.P., Kim, T.-W.W., 2005. Model-guided microarray implicates the retromer complex in Alzheimer's disease. Ann. Neurol. 58, 909–919. https://doi.org/10.1002/ana.20667

Small, S.A., Petsko, G.A., 2015. Retromer in Alzheimer disease, Parkinson disease and other neurological disorders. Nat. Rev. Neurosci. 16, 126–132. https://doi.org/10.1038/nrn3896

Small, S.A., Simoes-Spassov, S., Mayeux, R., Petsko, G.A., 2017. Endosomal Traffic Jams Represent a Pathogenic Hub and Therapeutic Target in Alzheimer's Disease. Trends Neurosci. 40, 592–602. https://doi.org/10.1016/j.tins.2017.08.003

Snider, M.D., Rogers, O.C., 1985. Intracellular movement of cell surface receptors after endocytosis: Resialylation of asialo-transferrin receptor in human erythroleukemia cells. J. Cell Biol. 100, 826–834. https://doi.org/10.1083/jcb.100.3.826

Soker, S., Takashima, S., Miao, H.Q., Neufeld, G., Klagsbrun, M., 1998. Neuropilin-1 is expressed by endothelial and tumor cells as an isoform- specific receptor for vascular endothelial growth factor. Cell 92, 735–745. https://doi.org/10.1016/S0092-8674(00)81402-6

Solinger, J.A., Rashid, H.O., Prescianotto-Baschong, C., Spang, A., 2020. FERARI is required for Rab11-dependent endocytic recycling. Nat. Cell Biol. 22, 213–224. https://doi.org/10.1038/s41556-019-0456-5

Solinger, J.A., Spang, A., 2013. Tethering complexes in the endocytic pathway: CORVET and HOPS. FEBS J. 280, 2743–2757. https://doi.org/10.1111/febs.12151

Song, W., Wang, F., Savini, M., Ake, A., di Ronza, A., Sardiello, M., Segatori, L., 2013. TFEB regulates lysosomal proteostasis. Hum. Mol. Genet. 22, 1994–2009. https://doi.org/10.1093/hmg/ddt052

Stalder, D., Gershlick, D.C., 2020. Direct trafficking pathways from the Golgi apparatus to the plasma membrane 107, 112–125. https://doi.org/10.1016/j.semcdb.2020.04.001

Starling, G.P., Yip, Y.Y., Sanger, A., Morton, P.E., Eden, E.R., Dodding, M.P., 2016. Folliculin directs the formation of a Rab34– RILP complex to control the nutrient-dependent dynamic distribution of lysosomes . EMBO Rep. 17, 823–841. https://doi.org/10.15252/embr.201541382

Stechmann, B., Bai, S.K., Gobbo, E., Lopez, R., Merer, G., Pinchard, S., Panigai, L., Tenza, D., Raposo, G., Beaumelle, B., Sauvaire, D., Gillet, D., Johannes, L., Barbier, J., 2010. Inhibition of retrograde transport protects mice from lethal ricin challenge. Cell 141, 231–242. https://doi.org/10.1016/j.cell.2010.01.043

Steinberg, F., Gallon, M., Winfield, M., Thomas, E.C., Bell, A.J., Heesom, K.J., Tavaré, J.M., Cullen, P.J., 2013. A global analysis of SNX27-retromer assembly and cargo specificity reveals a function in glucose and metal ion transport. Nat. Cell Biol. 15, 461–71. https://doi.org/10.1038/ncb2721

Steinberg, F., Heesom, K.J., Bass, M.D., Cullen, P.J., 2012. SNX17 protects integrins from degradation by sorting between lysosomal and recycling pathways. J. Cell Biol. 197, 219–230. https://doi.org/10.1083/jcb.201111121

Stenmark, H., 2009. Rab GTPases as coordinators of vesicle traffic. Nat. Rev. Mol. Cell Biol. 10, 513–525. https://doi.org/10.1038/nrm2728

Stoorvogel, W., Oorschot, V., Geuze, H.J., 1996. A novel class of clathrin-coated vesicles budding from endosomes. J. Cell Biol. 132, 21–33. https://doi.org/10.1083/jcb.132.1.21

Su, B., Wurtzer, S., Rameix-Welti, M.A., Dwyer, D., van der Werf, S., Naffakh, N., Clavel, F., Labrosse, B., 2009. Enhancement of the influenza a hemagglutinin (HA)-mediated cell-cell fusion and virus entry by the viral neuraminidase (NA). PLoS One 4. https://doi.org/10.1371/journal.pone.0008495

Subramanian, A., Tamayo, P., Mootha, V.K., Mukherjee, S., Ebert, B.L., Gillette, M.A., Paulovich, A., Pomeroy, S.L., Golub, T.R., Lander, E.S., Mesirov, J.P., 2005. Gene set enrichment analysis: A knowledge-based approach for interpreting genome-wide expression profiles. Proc. Natl. Acad. Sci. U. S. A. 102, 15545–15550. https://doi.org/10.1073/pnas.0506580102

Sugiura, A., McLelland, G.-L., Fon, E.A., McBride, H.M., 2014. A new pathway for mitochondrial quality control: mitochondrial-derived vesicles. EMBO J. 33, 2142–2156. https://doi.org/10.15252/embj.201488104

Sullivan, C.P., Jay, A.G., Stack, E.C., Pakaluk, M., Wadlinger, E., Fine, R.E., Wells, J.M., Morin, P.J., 2011. Retromer disruption promotes amyloidogenic APP processing. Neurobiol. Dis. 43, 338–345. https://doi.org/10.1016/j.nbd.2011.04.002

Sun, L., Meng, Z., Zhu, Y., Lu, J., Li, Z., Zhao, Q., Huang, Y., Jiang, L., Yao, X., 2018. TM9SF4 is a novel factor promoting autophagic flux under amino acid starvation. Cell Death Differ. 25, 368–379. https://doi.org/10.1038/cdd.2017.166

Sun, P., Sleat, D.E., Lecocq, M., Hayman, A.R., Jadot, M., Lobel, P., 2008. Acid phosphatase 5 is responsible for removing the mannose 6-phosphate recognition marker from lysosomal proteins. Proc. Natl. Acad. Sci. U. S. A. 105, 16590–16595. https://doi.org/10.1073/pnas.0807472105

Surma, M.A., Klose, C., Simons, K., 2012. Lipid-dependent protein sorting at the trans-Golgi network. Biochim. Biophys. Acta - Mol. Cell Biol. Lipids 1821, 1059–1067. https://doi.org/10.1016/j.bbalip.2011.12.008

Suzuki, S.W., Emr, S.D., 2018. Membrane protein recycling from the vacuole/lysosome membrane. J. Cell Biol. 217, 1623–1632. https://doi.org/10.1083/jcb.201709162

Szondy, Z., Korponay-Szabó, I., Király, R., Sarang, Z., Tsay, G.J., 2017. Transglutaminase 2 in

human diseases. Biomed. 7, 1–13. https://doi.org/10.1051/bmdcn/2017070315

Tabuchi, M., Yanatori, I., Kawai, Y., Kishi, F., 2010. Retromer-mediated direct sorting is required for proper endosomal recycling of the mammalian iron transporter DMT1. J. Cell Sci. 123, 756–766. https://doi.org/10.1242/jcs.060574

Tang, F.L., Erion, J.R., Tian, Y., Liu, W., Yin, D.M., Ye, J., Tang, B., Mei, L., Xiong, W.C., 2015. VPS35 in dopamine neurons is required for endosome-to- golgi retrieval of Lamp2a, a receptor of chaperone- mediated autophagy that is critical for α-synuclein degradation and prevention of pathogenesis of Parkinson's disease. J. Neurosci. 35, 10613–10628. https://doi.org/10.1523/JNEUROSCI.0042-15.2015

Tay, M.Z., Poh, C.M., Rénia, L., MacAry, P.A., Ng, L.F.P., 2020. The trinity of COVID-19: immunity, inflammation and intervention. Nat. Rev. Immunol. 20, 363–374. https://doi.org/10.1038/s41577-020-0311-8

Teasdale, R.D., Collins, B.M., 2012. Insights into the PX (phox-homology) domain and SNX (sorting nexin) protein families: Structures, functions and roles in disease. Biochem. J. 441, 39–59. https://doi.org/10.1042/BJ20111226

Teasdale, R.D., Loci, D., Houghton, F., Karlsson, L., Gleeson, P.A., 2001. A large family of endosome-localized proteins related to sorting nexin 1. Biochem. J. 358, 7–16. https://doi.org/10.1042/0264-6021:3580007

Teesalu, T., Sugahara, K.N., Kotamraju, V.R., Ruoslahti, E., 2009. C-end rule peptides mediate neuropilin-1-dependent cell, vascular, and tissue penetration. Proc. Natl. Acad. Sci. U. S. A. 106, 16157–16162. https://doi.org/10.1073/pnas.0908201106

Temkin, P., Lauffer, B., Jäger, S., Cimermancic, P., Krogan, N.J., von Zastrow, M., 2011. SNX27 mediates retromer tubule entry and endosome-to-plasma membrane trafficking of signalling receptors. Nat. Cell Biol. 13. https://doi.org/10.1038/ncb2252

Thingholm, T.E., Larsen, M.R., Ingrell, C.R., Kassem, M., Jensen, O.N., 2008. TiO2-based phosphoproteomic analysis of the plasma membrane and the effects of phosphatase inhibitor treatment. J. Proteome Res. 7, 3304–3313. https://doi.org/10.1021/pr800099y

Tian, H., Mythreye, K., Golzio, C., Katsanis, N., Blobe, G.C., 2012. Endoglin mediates fibronectin/α5β1 integrin and TGF-β pathway crosstalk in endothelial cells. EMBO J. 31, 3885–3900. https://doi.org/10.1038/emboj.2012.246

Tilley, F.C., Gallon, M., Luo, C., Danson, C.M., Zhou, J., Cullen, P.J., 2018. Retromer associates with the cytoplasmic amino-terminus of polycystin-2. J. Cell Sci. 131, jcs211342. https://doi.org/10.1242/jcs.211342

Tiwari, A., Jung, J.J., Inamdar, S.M., Brown, C.O., Goel, A., Choudhury, A., 2011. Endothelial cell migration on fibronectin is regulated by syntaxin 6-mediated α5β1 integrin recycling. J. Biol. Chem. 286, 36749–36761. https://doi.org/10.1074/jbc.M111.260828

To, K.K.W., Ng, K.H.L., Que, T.L., Chan, J.M.C., Tsang, K.Y., Tsang, A.K.L., Chen, H., Yuen, K.Y., 2012. Avian influenza A H5N1 virus: A continuous threat to humans. Emerg. Microbes Infect. 1, e25. https://doi.org/10.1038/emi.2012.24

Toivanen, P.I., Nieminen, T., Laakkonen, J.P., Heikura, T., Kaikkonen, M.U., Ylä-Herttuala, S., 2017. Snake venom VEGF Vammin induces a highly efficient angiogenic response in skeletal muscle via VEGFR-2/NRP specific signaling. Sci. Rep. 7, 1–12. https://doi.org/10.1038/s41598-017-05876-y

Traer, C.J., Rutherford, A.C., Palmer, K.J., Wassmer, T., Oakley, J., Attar, N., Carlton, J.G., Kremerskothen, J., Stephens, D.J., Cullen, P.J., 2007. SNX4 coordinates endosomal sorting of TfnR with dynein-mediated transport into the endocytic recycling compartment. Nat. Cell Biol. 9, 1370–1380. https://doi.org/10.1038/ncb1656

Tree, J.A., Turnbull, J.E., Buttigieg, K.R., Elmore, M.J., Coombes, N., Hogwood, J., Mycroft-West, C.J., Lima, M.A., Skidmore, M.A., Karlsson, R., Chen, Y.H., Yang, Z., Spalluto, C.M., Staples, K.J., Yates, E.A., Gray, E., Singh, D., Wilkinson, T., Page, C.P., Carroll, M.W., 2021.

Unfractionated heparin inhibits live wild type SARS-CoV-2 cell infectivity at therapeutically relevant concentrations. Br. J. Pharmacol. 178, 626–635. https://doi.org/10.1111/bph.15304

Tremel, S., Ohashi, Y., Morado, D.R., Bertram, J., Perisic, O., Brandt, L.T.L., von Wrisberg, M.-K., Chen, Z.A., Maslen, S.L., Kovtun, O., Skehel, M., Rappsilber, J., Lang, K., Munro, S., Briggs, J.A.G., Williams, R.L., 2021. Structural basis for VPS34 kinase activation by Rab1 and Rab5 on membranes. Nat. Commun. 12, 1564. https://doi.org/10.1038/s41467-021-21695-2

Uhlen, M., Fagerberg, L., Hallstrom, B.M., Lindskog, C., Oksvold, P., Mardinoglu, A., Sivertsson, A., Kampf, C., Sjostedt, E., Asplund, A., Olsson, I., Edlund, K., Lundberg, E., Navani, S., Szigyarto, C.A.-K., Odeberg, J., Djureinovic, D., Takanen, J.O., Hober, S., Alm, T., Edqvist, P.-H., Berling, H., Tegel, H., Mulder, J., Rockberg, J., Nilsson, P., Schwenk, J.M., Hamsten, M., von Feilitzen, K., Forsberg, M., Persson, L., Johansson, F., Zwahlen, M., von Heijne, G., Nielsen, J., Ponten, F., 2015. Tissue-based map of the human proteome. Science. 347, 1260419–1260419. https://doi.org/10.1126/science.1260419, Human Protein Atlas available from http://www.proteinatlas.org

Ullrich, O., Reinsch, S., Urbé, S., Zerial, M., Parton, R.G., 1996. Rab11 regulates recycling through the pericentriolar recycling endosome. J. Cell Biol. 135, 913–924. https://doi.org/10.1083/jcb.135.4.913

Underwood, R., Wang, B., Carico, C., Whitaker, R.H., Placzek, W.J., Yacoubian, T., 2020a. The GTPase Rab27b regulates the release, autophagic clearance, and toxicity of alpha-synuclein. J. Biol. Chem. 295, 8005–8016. https://doi.org/10.1074/JBC.RA120.013337

Underwood, R., Wang, B., Pathak, A., Volpicelli-Daley, L., Yacoubian, T.A., 2020b. Rab27 GTPases regulate alpha-synuclein uptake, cell-to-cell transmission, and toxicity. bioRxiv 2020.11.17.387449. https://doi.org/10.1101/2020.11.17.387449

Valdembri, D., Caswell, P.T., Anderson, K.I., Schwarz, J.P., König, I., Astanina, E., Caccavari, F., Norman, J.C., Humphries, M.J., Bussolino, F., Serini, G., 2009. Neuropilin-1/GIPC1 signaling regulates α5β1 integrin traffic and function in endothelial cells. PLoS Biol. 7. https://doi.org/10.1371/journal.pbio.1000025

Van Breevoort, D., Snijders, A.P., Hellen, N., Weckhuysen, S., Van Hooren, K.W.E.M., Eikenboom, J., Valentijn, K., Fernandez-Borja, M., Ceulemans, B., De Jonghe, P., Voorberg, J., Hannah, M., Carter, T., Bierings, R., 2014. STXBP1 promotes Weibel-Palade body exocytosis through its interaction with the Rab27A effector Slp4-a. Blood 123, 3185–3194. https://doi.org/10.1182/blood-2013-10-535831

Van Meel, E., Klumperman, J., 2008. Imaging and imagination: Understanding the endo-lysosomal system. Histochem. Cell Biol. 129, 253–266. https://doi.org/10.1007/s00418-008-0384-0

Van Meer, G., Voelker, D.R., Feigenson, G.W., 2008. Membrane lipids: Where they are and how they behave. Nat. Rev. Mol. Cell Biol. 9, 112–124. https://doi.org/10.1038/nrm2330

Van Weering, J.R.T., Sessions, R.B., Traer, C.J., Kloer, D.P., Bhatia, V.K., Stamou, D., Carlsson, S.R., Hurley, J.H., Cullen, P.J., 2012. Molecular basis for SNX-BAR-mediated assembly of distinct endosomal sorting tubules. EMBO J. 31, 4466–4480. https://doi.org/10.1038/emboj.2012.283

van Weering, J.R.T., Verkade, P., Cullen, P.J., 2012. SNX-BAR-mediated endosome tubulation is co-ordinated with endosome maturation. Traffic 13, 94–107. https://doi.org/10.1111/j.1600-0854.2011.01297.x

van Weering, J.R.T., Verkade, P., Cullen, P.J., 2010. SNX-BAR proteins in phosphoinositide-mediated, tubular-based endosomal sorting. Semin. Cell Dev. Biol. 21, 371–80. https://doi.org/10.1016/j.semcdb.2009.11.009

Vander Kooi, C.W., Jusino, M.A., Perman, B., Neau, D.B., Bellamy, H.D., Leahy, D.J., 2007. Structural basis for ligand and heparin binding to neuropilin B domains. Proc. Natl. Acad. Sci. U. S. A. 104, 6152–6157. https://doi.org/10.1073/pnas.0700043104

Varandas, K.C., Irannejad, R., von Zastrow, M., 2016. Retromer Endosome Exit Domains Serve

Multiple Trafficking Destinations and Regulate Local G Protein Activation by GPCRs. Curr. Biol. 26, 3129–3142. https://doi.org/10.1016/j.cub.2016.09.052

Vernay, A., Lamrabet, O., Perrin, J., Cosson, P., 2018. TM9SF4 levels determine sorting of transmembrane domains in the early secretory pathway. J. Cell Sci. 131. https://doi.org/10.1242/jcs.220830

Vidyadhara, D.J., Lee, J.E., Chandra, S.S., 2019. Role of the endolysosomal system in Parkinson's disease. J. Neurochem. 150, 487–506. https://doi.org/10.1111/jnc.14820

Vilariño-Güell, C., Wider, C., Ross, O.A., Dachsel, J.C., Kachergus, J.M., Lincoln, S.J., Soto-Ortolaza, A.I., Cobb, S.A., Wilhoite, G.J., Bacon, J.A., Bahareh Behrouz, Melrose, H.L., Hentati, E., Puschmann, A., Evans, D.M., Conibear, E., Wasserman, W.W., Aasly, J.O., Burkhard, P.R., Djaldetti, R., Ghika, J., Hentati, F., Krygowska-Wajs, A., Lynch, T., Melamed, E., Rajput, A., Rajput, A.H., Solida, A., Wu, R.M., Uitti, R.J., Wszolek, Z.K., Vingerhoets, F., Farrer, M.J., 2011. VPS35 mutations in parkinson disease. Am. J. Hum. Genet. 89, 162–167. https://doi.org/10.1016/j.ajhg.2011.06.001

Villaseñor, R., Kalaidzidis, Y., Zerial, M., 2016. Signal processing by the endosomal system. Curr. Opin. Cell Biol. 39, 53–60. https://doi.org/10.1016/j.ceb.2016.02.002

Wahl, J.K., Kim, Y.J., Cullen, J.M., Johnson, K.R., Wheelock, M.J., 2003. N-cadherin-catenin complexes form prior to cleavage of the proregion and transport to the plasma membrane. J. Biol. Chem. 278, 17269–17276. https://doi.org/10.1074/jbc.M211452200

Wallroth, A., Haucke, V., 2018. Phosphoinositide conversion in endocytosis and the endolysosomal system. J. Biol. Chem. 293, 1526–1535. https://doi.org/10.1074/jbc.R117.000629

Walls, A.C., Park, Y.J., Tortorici, M.A., Wall, A., McGuire, A.T., Veesler, D., 2020. Structure, Function, and Antigenicity of the SARS-CoV-2 Spike Glycoprotein. Cell 181, 281-292.e6. https://doi.org/10.1016/j.cell.2020.02.058

Walsh, R.B., Becalska, A.N., Zunitch, M.J., Wang, S.Y., Isaac, B., Yeh, A., Koles, K., Rodal, A.A., 2020. Opposing functions for retromer and Rab11 in extracellular vesicle cargo traffic at synapses. bioRxiv 645713. https://doi.org/10.1101/645713

Wan, L., Molloy, S.S., Thomas, L., Liu, G., Xiang, Y., Rybak, S.L., Thomas, G., 1998. PACS-1 defines a novel gene family of cytosolic sorting proteins required for trans-Golgi network localization. Cell 94, 205–216. https://doi.org/10.1016/S0092-8674(00)81420-8

Wang, H.B., Zhang, H., Zhang, J.P., Li, Y., Zhao, B., Feng, G.K., Du, Y., Xiong, D., Zhong, Q., Liu, W.L., Du, H., Li, M.Z., Huang, W.L., Tsao, S.W., Hutt-Fletcher, L., Zeng, Y.X., Kieff, E., Zeng, M.S., 2015. Neuropilin 1 is an entry factor that promotes EBV infection of nasopharyngeal epithelial cells. Nat. Commun. 6, 1–13. https://doi.org/10.1038/ncomms7240

Wang, H.C., Huang, P.N., Hung, H.C., Tseng, S.N., Chang, C.C., Tsai, Y.R., Wang, Y.M., Shih, S.R., Hsu, J.T.A., 2021. Effect of a neuropilin-1-derived virus receptor trap on enterovirus a71 infection in vitro. Antimicrob. Agents Chemother. 65. https://doi.org/10.1128/AAC.00695-20

Wang, J., Fourriere, L., Gleeson, P.A., 2020. Local Secretory Trafficking Pathways in Neurons and the Role of Dendritic Golgi Outposts in Different Cell Models. Front. Mol. Neurosci. 13, 213. https://doi.org/10.3389/fnmol.2020.597391

Wang, X., Ma, D., Keski-Oja, J., Pei, D., 2004. Co-recycling of MT1-MMP and MT3-MMP through the trans-Golgi network: Identification of DKV582 as a recycling signal. J. Biol. Chem. 279, 9331–9336. https://doi.org/10.1074/jbc.M312369200

Wartosch, L., Bright, N.A., Luzio, J.P., 2015. Lysosomes. Curr. Biol. 25, R315–R316. https://doi.org/10.1016/j.cub.2015.02.027

Wassmer, T., Attar, N., Bujny, M. V., Oakley, J., Traer, C.J., Cullen, P.J., 2007. A loss-of-function screen reveals SNX5 and SNX6 as potential components of the mammalian retromer. J. Cell Sci. 120, 45–54. https://doi.org/10.1242/jcs.03302

Wassmer, T., Attar, N., Harterink, M., Van Weering, J.R.T.T., Traer, C.J., Oakley, J., Goud, B.,

Stephens, D.J., Verkade, P., Korswagen, H.C., Cullen, P.J., 2009. The Retromer Coat Complex Coordinates Endosomal Sorting and Dynein-Mediated Transport, with Carrier Recognition by the trans-Golgi Network. Dev. Cell 17, 110–122. https://doi.org/10.1016/j.devcel.2009.04.016

Waugh, M.G., Chu, K.M.E., Clayton, E.L., Minogue, S., Hsuan, J.J., 2011. Detergent-free isolation and characterization of cholesterol-rich membrane domains from trans-Golgi network vesicles. J. Lipid Res. 52, 582–589. https://doi.org/10.1194/jlr.D012807

Weeratunga, S., Paul, B., Collins, B.M., 2020. Recognising the signals for endosomal trafficking. Curr. Opin. Cell Biol. 65, 17–27. https://doi.org/10.1016/j.ceb.2020.02.005

Weixel, K.M., Blumental-Perry, A., Watkins, S.C., Aridor, M., Weisz, O.A., 2005. Distinct golgi populations of phosphatidylinositol 4-phosphate regulated by phosphatidylinositol 4-kinases. J. Biol. Chem. 280, 10501–10508. https://doi.org/10.1074/jbc.M414304200

Welz, T., Wellbourne-Wood, J., Kerkhoff, E., 2014. Orchestration of cell surface proteins by Rab11. Trends Cell Biol. 24, 407–415. https://doi.org/10.1016/j.tcb.2014.02.004

Wen, L., Tang, F.L., Hong, Y., Luo, S.W., Wang, C.L., He, W., Shen, C., Jung, J.U., Xiong, F., Lee, D. hoon, Zhang, Q.G., Brann, D., Kim, T.W., Yan, R., Mei, L., Xiong, W.C., 2011. VPS35 haploinsufficiency increases Alzheimer's disease neuropathology. J. Cell Biol. 195, 765–779. https://doi.org/10.1083/jcb.201105109

West, D.C., Rees, C.G., Duchesne, L., Patey, S.J., Terry, C.J., Turnbull, J.E., Delehedde, M., Heegaard, C.W., Allain, F., Vanpouille, C., Ron, D., Fernig, D.G., 2005. Interactions of multiple heparin binding growth factors with neuropilin-1 and potentiation of the activity of fibroblast growth factor-2. J. Biol. Chem. 280, 13457–13464. https://doi.org/10.1074/jbc.M410924200

Wilke, S., Krausze, J., Büssow, K., 2012. Crystal structure of the conserved domain of the DC lysosomal associated membrane protein: Implications for the lysosomal glycocalyx. BMC Biol. 10, 62. https://doi.org/10.1186/1741-7007-10-62

Wilkinson, L., Gilbert, T., Kinna, G., Ruta, L.A., Pennisi, D., Kett, M., Little, M.H., 2007. Crim1KST264/KST264 mice implicate Crim1 in the regulation of vascular endothelial growth factor-A activity during glomerular vascular development. J. Am. Soc. Nephrol. 18, 1697–1708. https://doi.org/10.1681/ASN.2006091012

Wingo, A.P., Liu, Y., Gerasimov, E.S., Gockley, J., Logsdon, B.A., Duong, D.M., Dammer, E.B., Robins, C., Beach, T.G., Reiman, E.M., Epstein, M.P., De Jager, P.L., Lah, J.J., Bennett, D.A., Seyfried, N.T., Levey, A.I., Wingo, T.S., 2021. Integrating human brain proteomes with genome-wide association data implicates new proteins in Alzheimer's disease pathogenesis. Nat. Genet. 53, 143–146. https://doi.org/10.1038/s41588-020-00773-z

Wingo, T.S., Cutler, D.J., Wingo, A.P., Le, N.A., Rabinovici, G.D., Miller, B.L., Lah, J.J., Levey, A.I., 2019. Association of Early-Onset Alzheimer Disease with Elevated Low-Density Lipoprotein Cholesterol Levels and Rare Genetic Coding Variants of APOB. JAMA Neurol. 76, 809–817. https://doi.org/10.1001/jamaneurol.2019.0648

Wise, L.M., Ueda, N., Dryden, N.H., Fleming, S.B., Caesar, C., Roufail, S., Achen, M.G., Stacker, S.A., Mercer, A.A., 2003. Viral vascular endothelial growth factors vary extensively in amino acid sequence, receptor-binding specificities, and the ability to induce vascular permeability yet are uniformly active mitogens. J. Biol. Chem. 278, 38004–38014. https://doi.org/10.1074/jbc.M301194200

Wise, L.M., Veikkola, T., Mercer, A.A., Savory, L.J., Fleming, S.B., Caesar, C., Vitali, A., Makinen, T., Alitalo, K., Stacker, S.A., 1999. Vascular endothelial growth factor (VEGF)-like protein from orf virus NZ2 binds to VEGFR2 and neuropilin-1. Proc. Natl. Acad. Sci. U. S. A. 96, 3071–3076. https://doi.org/10.1073/pnas.96.6.3071

Woodman, P.G., 2000. Biogenesis of the Sorting Endosome: The Role of Rab5. Traffic 1, 695–701. https://doi.org/10.1034/j.1600-0854.2000.010902.x

Worby, C.A., Dixon, J.E., 2002. Sorting out the cellular functions of sorting nexins. Nat. Rev. Mol. Cell Biol. 3, 919–931. https://doi.org/10.1038/nrm974

World Health Organization, 2021. WHO COVID-19 Weekly Epidemiological Update - 9 March 2021 [WWW Document]. URL https://www.who.int/publications/m/item/weekly-epidemiological-update---10-march-2021

Wrapp, D., Wang, N., Corbett, K.S., Goldsmith, J.A., Hsieh, C.-L., Abiona, O., Graham, B.S., Mclellan, J.S., 2020. Cryo-EM structure of the 2019-nCoV spike in the prefusion conformation. Science. 367, 1260–1263. https://doi.org/10.1126/science.abb2507

Wu, F., Zhao, S., Yu, B., Chen, Y.M., Wang, W., Song, Z.G., Hu, Y., Tao, Z.W., Tian, J.H., Pei, Y.Y., Yuan, M.L., Zhang, Y.L., Dai, F.H., Liu, Y., Wang, Q.M., Zheng, J.J., Xu, L., Holmes, E.C., Zhang, Y.Z., 2020. A new coronavirus associated with human respiratory disease in China. Nature 579, 265–269. https://doi.org/10.1038/s41586-020-2008-3

Xiao, T., Xiao, Y., Wang, W., Tang, Y.Y., Xiao, Z., Su, M., 2020. Targeting EphA2 in cancer. J. Hematol. Oncol. 13. https://doi.org/10.1186/s13045-020-00944-9

Xie, Y., Niu, M., Ji, C., Huang, T.Y., Zhang, C., Tian, Y., Shi, Z., Wang, C., Zhao, Y., Luo, H., Can, D., Xu, H., Zhang, Y., Zhang, X., 2019. SNX8 Enhances Non-amyloidogenic APP Trafficking and Attenuates Aβ Accumulation and Memory Deficits in an AD Mouse. Front. Cell. Neurosci. 13, 410. https://doi.org/10.3389/fncel.2019.00410

Xu, Y., Ren, J., He, X., Chen, H., Wei, T., Feng, W., 2019. YWHA/14-3-3 proteins recognize phosphorylated TFEB by a noncanonical mode for controlling TFEB cytoplasmic localization. Autophagy 15, 1017–1030. https://doi.org/10.1080/15548627.2019.1569928

Xu, Z., Shi, L., Wang, Y., Zhang, J., Huang, L., Zhang, C., Liu, S., Zhao, P., Liu, H., Zhu, L., Tai, Y., Bai, C., Gao, T., Song, J., Xia, P., Dong, J., Zhao, J., Wang, F.S., 2020. Pathological findings of COVID-19 associated with acute respiratory distress syndrome. Lancet Respir. Med. 8, 420–422. https://doi.org/10.1016/S2213-2600(20)30076-X

Yamamoto, Y., Tamiya, S., Shibuya, M., Nakase, I., Yoshioka, Y., 2019. Peptides with the multibasic cleavage site of the hemagglutinin from highly pathogenic influenza viruses act as cell-penetrating via binding to heparan sulfate and neuropilins. Biochem. Biophys. Res. Commun. 512, 453–459. https://doi.org/10.1016/j.bbrc.2019.03.068

Yamauchi, Y., Greber, U.F., 2016. Principles of Virus Uncoating: Cues and the Snooker Ball. Traffic 17, 569–592. https://doi.org/10.1111/tra.12387

Yan, R., Zhang, Y., Li, Y., Xia, L., Guo, Y., Zhou, Q., 2020. Structural basis for the recognition of SARS-CoV-2 by full-length human ACE2. Science. 367, 1444–1448. https://doi.org/10.1126/science.abb2762

Ye, H., Ojelade, S.A., Li-Kroeger, D., Zuo, Z., Wang, L., Li, Y., Gu, J.Y.J., Tepass, U., Rodal, A.A., Bellen, H.J., Shulman, J.M., 2020. Retromer subunit, vps29, regulates synaptic transmission and is required for endolysosomal function in the aging brain. Elife 9. https://doi.org/10.7554/eLife.51977

Yong, X., Zhao, L., Deng, W., Sun, H., Zhou, X., Mao, L., Hu, W., Shen, X., Sun, Q., Billadeau, D.D., Xue, Y., Jia, D., 2020. Mechanism of cargo recognition by retromer-linked SNX-BAR proteins. PLOS Biol. 18, e3000631. https://doi.org/10.1371/journal.pbio.3000631

Yu, J., Nagasu, H., Murakami, T., Hoang, H., Broderick, L., Hoffman, H.M., Horng, T., 2014. Inflammasome activation leads to Caspase-1-dependent mitochondrial damage and block of mitophagy. Proc. Natl. Acad. Sci. U. S. A. 111, 15514–15519. https://doi.org/10.1073/pnas.1414859111

Yu, L., McPhee, C.K., Zheng, L., Mardones, G.A., Rong, Y., Peng, J., Mi, N., Zhao, Y., Liu, Z., Wan, F., Hailey, D.W., Oorschot, V., Klumperman, J., Baehrecke, E.H., Lenardo, M.J., 2010. Termination of autophagy and reformation of lysosomes regulated by mTOR. Nature 465, 942–946. https://doi.org/10.1038/nature09076

Zerial, M., McBride, H., 2001. Rab proteins as membrane organizers. Nat. Rev. Mol. Cell Biol. 2, 107–117. https://doi.org/10.1038/35052055

Zhang, S., Zhau, H.E., Osunkoya, A.O., Iqbal, S., Yang, X., Fan, S., Chen, Z., Wang, R., Marshall,

F.F., Chung, L.W.K., Wu, D., 2010. Vascular endothelial growth factor regulates myeloid cell leukemia-1 expression through neuropilin-1-dependent activation of c-MET signaling in human prostate cancer cells. Mol. Cancer 9, 9. https://doi.org/10.1186/1476-4598-9-9

Zhang, X.M., Ellis, S., Sriratana, A., Mitchell, C.A., Rowe, T., 2004. Sec15 is an effector for the Rab11 GTPase in mammalian cells. J. Biol. Chem. 279, 43027–43034. https://doi.org/10.1074/jbc.M402264200

Zhou, P., Yang, X. Lou, Wang, X.G., Hu, B., Zhang, L., Zhang, W., Si, H.R., Zhu, Y., Li, B., Huang, C.L., Chen, H.D., Chen, J., Luo, Y., Guo, H., Jiang, R. Di, Liu, M.Q., Chen, Y., Shen, X.R., Wang, X.G., Zheng, X.S., Zhao, K., Chen, Q.J., Deng, F., Liu, L.L., Yan, B., Zhan, F.X., Wang, Y.Y., Xiao, G.F., Shi, Z.L., 2020. A pneumonia outbreak associated with a new coronavirus of probable bat origin. Nature 579, 270–273. https://doi.org/10.1038/s41586-020-2012-7

Zhou, Q., Huang, T., Jiang, Z., Ge, C., Chen, X., Zhang, L., Zhao, F., Zhu, M., Chen, T., Cui, Y., Li, H., Yao, M., Li, J., Tian, H., 2020. Upregulation of SNX5 predicts poor prognosis and promotes hepatocellular carcinoma progression by modulating the EGFR-ERK1/2 signaling pathway. Oncogene 39, 2140–2155. https://doi.org/10.1038/s41388-019-1131-9

Zhu, Yunkai, Feng, F., Hu, G., Wang, Y., Yu, Y., Zhu, Yuanfei, Xu, W., Cai, X., Sun, Z., Han, W., Ye, R., Qu, D., Ding, Q., Huang, X., Chen, H., Xu, W., Xie, Y., Cai, Q., Yuan, Z., Zhang, R., 2021. A genome-wide CRISPR screen identifies host factors that regulate SARS-CoV-2 entry. Nat. Commun. 12, 1–11. https://doi.org/10.1038/s41467-021-21213-4

Zimprich, A., Benet-Pages, A., Struhal, W., Graf, E., Eck, S.H., Offman, M.N., Haubenberger, D., Spielberger, S., Schulte, E.C., Lichtner, P., Rossle, S.C., Klopp, N., Wolf, E., Seppi, K., Pirker, W., Presslauer, S., Mollenhauer, B., Katzenschlager, R., Foki, T., Hotzy, C., Reinthaler, E., Harutyunyan, A., Kralovics, R., Peters, A., Zimprich, F., Br??cke, T., Poewe, W., Auff, E., Trenkwalder, C., Rost, B., Ransmayr, G., Winkelmann, J., Meitinger, T., Strom, T.M., Benet-Pagès, A., Struhal, W., Graf, E., Eck, S.H., Offman, M.N., Haubenberger, D., Spielberger, S., Schulte, E.C., Lichtner, P., Rossle, S.C., Klopp, N., Wolf, E., Seppi, K., Pirker, W., Presslauer, S., Mollenhauer, B., Katzenschlager, R., Foki, T., Hotzy, C., Reinthaler, E., Harutyunyan, A., Kralovics, R., Peters, A., Zimprich, F., Brucke, T., Poewe, W., Auff, E., Trenkwalder, C., Rost, B., Ransmayr, G., Winkelmann, J., Meitinger, T., Strom, T.M., 2011. A mutation in VPS35, encoding a subunit of the retromer complex, causes late-onset Parkinson disease. Am. J. Hum. Genet. 89, 168–175. https://doi.org/10.1016/j.ajhg.2011.06.008

Appendix A: Proteomics and RNA-Seq Data

Chapter 3

Table 3.1 Significantly Enriched and Depleted Proteins in the VPS35 KO Total Cell Proteome

Proteins exceeding a VPS35 KO/VPS35-GFP Log_2 fold change of ± 0.26 with a p-value of < 0.05 are displayed.

Protein Name	Coverage (%)	# Unique Peptides	VPS35 KO/VPS35-GFP Log_2 Fold Change	t-test p-value
RAB27B	13.3	2	3.05	2.06E-02
TGM2	39.7	22	2.20	8.10E-03
ERCC6	1.7	2	1.51	2.88E-02
UAP1L1	32.9	14	1.21	4.69E-02
URB1	1.5	2	1.08	2.07E-02
MYO6	40.7	46	0.95	9.40E-03
LIMCH1	25.1	6	0.95	3.83E-03
PRKG1	13.7	9	0.92	4.21E-03
AKR1B1	63.9	18	0.90	4.71E-02
SORT1	2.9	2	0.89	2.19E-02
SPTBN2	3.5	2	0.87	3.10E-02
TMEM59	7.4	2	0.86	2.19E-02
CSRP2	42.4	9	0.85	2.10E-02
MME	2.1	2	0.85	2.41E-02
GPC4	23.9	10	0.79	9.01E-03
MYLK	4.4	7	0.79	3.31E-02
CASP1	37.1	11	0.75	8.98E-03
RDH10	25.8	7	0.74	3.85E-02
RBPJ	13.0	6	0.73	1.52E-02
AMDHD2	16.4	5	0.71	1.55E-03
TSPAN4	8.6	2	0.70	2.90E-02
ANTXR1	8.9	4	0.66	2.49E-02
HACE1	7.2	6	0.63	3.08E-02
DHRS3	30.1	8	0.63	1.35E-02
SLC6A6	11.3	6	0.63	3.66E-02
CAPN2	31.8	1	0.60	4.44E-02
CMC1	25.5	2	0.59	2.31E-02
SLC14A1	9.0	4	0.58	4.40E-02
ANXA4	64.6	22	0.58	1.11E-02
KYNU	48.8	19	0.57	3.97E-02
WBP2	35.6	7	0.56	2.33E-02
SSH3	22.0	9	0.55	1.20E-02
JAK1	14.8	16	0.54	8.55E-04

PHYH	14.8	6	0.53	4.21E-02
CDK19	5.6	2	0.51	6.12E-03
GPRC5C	14.5	5	0.51	9.20E-03
VAT1	44.0	13	0.50	1.16E-02
ABCC4	25.7	31	0.50	7.70E-03
GSTM4	56.4	8	0.49	2.34E-02
TNFRSF1A	7.5	3	0.49	4.88E-02
NPC2	56.3	8	0.49	1.45E-02
APOB	2.6	7	0.48	5.67E-04
CNIH4	14.4	1	0.48	3.88E-02
PTTG1IP	3.9	1	0.48	3.90E-02
HLA-A	26.0	2	0.47	4.78E-02
ACOT13	52.9	7	0.47	2.24E-02
INTS7	3.5	3	0.47	4.54E-02
RAMAC	17.8	2	0.46	3.19E-02
RAB28	30.3	6	0.45	5.54E-03
DDX17	41.4	14	0.45	4.66E-02
TMEM132A	9.3	7	0.45	3.85E-02
ZNF518B	4.4	3	0.43	3.68E-02
MSI2	26.8	7	0.42	2.82E-02
IGF2R	35.3	72	0.42	7.50E-05
COQ8B	12.3	4	0.40	4.04E-02
T1	13.8	3	0.40	1.17E-02
TLE5	10.7	2	0.40	2.89E-02
PEPD	36.7	15	0.40	3.48E-02
EIF4A2	42.3	8	0.40	1.04E-02
FCHO2	10.5	8	0.40	3.60E-02
PRKAR2B	13.9	4	0.39	3.99E-02
GOT1	43.8	16	0.39	2.88E-02
SPG21	26.6	8	0.39	2.84E-02
SCD	18.4	7	0.38	4.79E-03
TDP2	28.5	7	0.38	4.73E-02
CWC15	29.3	7	0.37	4.32E-02
SLC38A2	14.8	5	0.37	3.62E-02
FKSG42	4.1	1	0.37	3.17E-02
MRE11	27.1	17	0.36	4.40E-03
LACTB2	50.7	11	0.35	3.52E-02
FMNL2	9.2	3	0.35	4.01E-02
NEMP1	8.3	3	0.35	3.51E-02
CAP2	35.4	13	0.35	1.85E-02
CSTB	94.9	9	0.35	1.37E-02
TRAF3IP1	5.4	4	0.34	1.32E-05
HEL-75	62.8	24	0.34	2.50E-02
ATP6V1C1	45.5	17	0.34	3.72E-02
CD46	11.0	4	0.33	3.61E-02
ZDHHC20	9.9	2	0.32	2.73E-03

HNRNPU	41.7	2	0.32	2.37E-02
PFKM	44.9	27	0.32	1.47E-02
MAP9	1.5	1	0.32	8.52E-03
CA12	7.6	2	0.32	2.07E-02
OSGEPL1	14.5	4	0.31	4.88E-03
ETFB	59.2	16	0.31	1.15E-02
REPIN1	28.9	13	0.31	3.68E-02
VPS52	15.1	8	0.31	1.70E-02
KHDRBS1	21.2	5	0.30	1.00E-02
HAGH	26.0	7	0.30	3.78E-02
RNMT	42.0	20	0.30	6.27E-04
TMEM164	12.8	3	0.30	1.25E-02
CRAT	12.0	8	0.29	3.05E-02
GTF2I	33.2	29	0.29	2.78E-02
GTF2I	38.0	29	0.29	2.78E-02
PTOV1	9.4	4	0.29	1.55E-02
PIK3R2	20.9	9	0.29	3.67E-02
RICTOR	11.0	16	0.29	2.44E-02
HDAC5	8.6	5	0.29	4.83E-02
FEN1	48.7	17	0.28	2.06E-02
MDH1	52.7	21	0.28	3.27E-02
TKT	58.1	1	0.28	4.54E-02
SYNE1	1.4	12	0.28	4.24E-02
ACAT1	39.3	16	0.28	4.16E-02
ZSCAN29	2.0	1	0.27	1.03E-02
EPHX1	47.0	19	0.27	4.64E-02
STX17	14.6	4	0.27	1.58E-02
CD59	23.4	3	0.27	1.26E-02
TCEAL3	32.0	6	0.26	2.60E-02
RDH13	27.8	9	0.26	4.73E-02
FPGT	17.1	6	0.25	3.15E-02
FNTB	7.8	3	-0.26	3.47E-02
PSMD2	53.9	46	-0.26	2.15E-02
NCOR2	25.4	47	-0.27	1.84E-02
ADRM1	26.3	3	-0.27	1.34E-02
SORBS3	25.2	8	-0.27	4.90E-02
RIC8B	10.9	5	-0.28	4.54E-02
DKFZp686F17268	54.7	1	-0.28	2.10E-02
KLF16	21.4	3	-0.29	1.47E-02
EIF2S3	52.3	22	-0.29	1.75E-02
ZNF579	11.4	4	-0.29	2.29E-02
NAGK	5.2	2	-0.29	6.42E-03
ARL8B	55.4	3	-0.29	3.07E-02
GPC1	32.3	1	-0.29	1.89E-02
TWSG1	24.2	4	-0.29	3.23E-02
PARD3	13.9	15	-0.30	2.66E-02

HYPK	39.5	3	-0.30	2.10E-02
RGS3	10.3	10	-0.30	1.24E-02
AAMP	42.2	13	-0.31	4.89E-02
AAMP	46.3	14	-0.31	4.89E-02
RNF34	17.5	6	-0.31	1.34E-02
PAK4	31.5	13	-0.31	6.43E-03
KNL1	6.3	13	-0.31	4.94E-02
PIK3CB	8.1	8	-0.31	2.92E-02
GPAT3	19.8	10	-0.31	3.50E-03
RNF25	34.2	11	-0.32	2.38E-02
VTA1	32.2	9	-0.32	3.06E-02
MGAT2	12.8	6	-0.32	6.19E-03
RUVBL1	59.6	22	-0.32	8.98E-04
DJC9	54.6	16	-0.33	1.75E-02
RUVBL2	55.1	25	-0.34	1.90E-03
DAF5	45.1	33	-0.35	2.96E-03
NUMBL	17.2	7	-0.35	4.23E-02
ITGA5	11.6	12	-0.35	7.42E-03
SLC7A1	8.9	5	-0.37	9.30E-03
SH3KBP1	30.8	20	-0.37	3.54E-02
FAM83D	17.8	9	-0.37	4.58E-02
MB21D2	23.0	10	-0.37	3.25E-02
CDC42EP1	27.1	7	-0.38	1.32E-02
SPDL1	34.7	17	-0.38	1.97E-02
OTUD5	22.4	9	-0.38	9.65E-03
DKFZp451C205	8.6	2	-0.39	3.60E-02
MELK	11.8	7	-0.39	4.56E-02
KCTD1	8.6	1	-0.40	7.82E-03
PLK1	24.2	14	-0.41	4.60E-02
STAU	43.0	1	-0.41	3.88E-02
DCAF13	12.4	5	-0.42	1.24E-02
RRM2	57.6	18	-0.42	1.25E-02
F3	16.6	5	-0.43	2.22E-02
UAP1	44.8	20	-0.44	2.30E-02
NMI	32.2	10	-0.44	2.52E-02
BCAS3	2.7	2	-0.44	6.07E-03
POLE2	4.6	2	-0.45	1.20E-02
TMLHE	3.8	2	-0.45	1.79E-02
SPAG1	6.3	4	-0.47	4.04E-03
ZNF12	9.0	1	-0.48	1.31E-02
TMSB4Y	47.7	1	-0.48	1.08E-02
MTRR	18.9	10	-0.48	1.47E-02
ET	2.0	1	-0.48	2.62E-02
TFE3	4.5	3	-0.50	1.20E-04
LNPEP	26.5	26	-0.51	2.49E-02
MICA	17.4	4	-0.51	4.25E-02

MICA	6.3	3	-0.51	4.25E-02
DPYSL3	72.4	33	-0.53	3.26E-04
CLN5	21.5	7	-0.53	3.79E-02
P4HB	65.9	1	-0.54	4.56E-02
MIOS	19.7	14	-0.54	3.01E-02
SIVA1	21.1	4	-0.54	1.31E-02
APBB2	8.4	5	-0.54	1.14E-02
GEM	5.7	2	-0.54	4.40E-03
DGKA	3.5	2	-0.55	3.51E-02
GATAD1	3.7	1	-0.56	4.32E-02
STX1A	18.1	4	-0.56	2.61E-02
TMEM192	25.5	6	-0.57	3.58E-02
DCBLD2	11.7	7	-0.59	4.32E-02
ECD	21.6	12	-0.59	7.45E-03
PTPRJ	13.8	12	-0.60	4.63E-02
SFN	24.6	2	-0.61	5.19E-03
SCARA3	6.9	4	-0.61	2.78E-02
SLC35F2	9.6	2	-0.62	3.55E-02
TRIM28	65.9	1	-0.63	4.99E-02
VPS26B	42.0	11	-0.66	1.69E-04
PDLIM5	51.1	2	-0.67	4.69E-02
NXT1	20.0	2	-0.67	1.84E-02
SH3RF1	14.0	8	-0.71	2.94E-03
AKAP12	36.4	21	-0.75	4.09E-02
CCNB1	17.8	7	-0.82	2.26E-02
STX8	30.1	6	-0.94	9.02E-03
ENPP1	25.3	22	-1.05	1.94E-02
VPS29	48.1	1	-1.05	1.09E-02
HEG1	5.2	5	-1.09	4.11E-02
ZBTB33	1.5	1	-1.10	2.64E-02
LXN	16.7	3	-1.21	2.37E-02
GDAP2	22.5	7	-1.34	2.72E-02
CFI	40.5	1	-1.40	2.37E-02
COLEC12	15.9	12	-1.79	7.45E-03
PODXL	7.3	4	-1.84	2.34E-03
VPS26A	52.6	15	-2.71	1.10E-04
VPS35	38.1	26	-4.33	3.85E-05

Table 3.2 Significantly Enriched and Depleted Proteins in the VPS35 KO 'Secretome'

Proteins exceeding a VPS35 KO/VPS35-GFP Log_2 fold change of ± 1.00 with a p-value of < 0.05 are displayed.

Protein Name	Coverage (%)	# Unique Peptides	VPS35 KO/VPS35-GFP Log_2 Fold Change	t-test p-value
GPNMB	4.4	3	5.67	5.61E-03
MMP14	14.1	8	2.80	3.44E-02
ACOT13	15.7	2	2.55	3.32E-02
CTSD	40.0	15	2.52	1.41E-02
CPQ	12.9	6	2.41	2.79E-02
EXOC3L4	1.0	1	2.39	4.42E-02
CTSB	28.3	9	2.29	1.46E-03
WFS1	9.4	8	2.22	4.67E-03
EPHX1	7.9	3	2.18	3.12E-02
DPP7	13.5	2	2.16	4.09E-02
LAMP1	8.4	4	2.13	8.63E-03
ASAH1	16.4	1	2.13	3.05E-03
IGF2R	11.1	26	2.11	9.35E-03
UPP1	26.5	8	2.09	1.38E-02
NEU1	18.8	8	2.08	3.47E-03
SCARB2	9.4	4	2.07	2.74E-02
NPC2	44.4	6	2.06	7.10E-03
GM2A	24.9	4	2.06	3.60E-02
CLSTN2	10.4	9	2.06	8.24E-03
TCEAL4	14.5	3	2.01	2.17E-02
SRP14	14.7	2	1.99	1.61E-02
CALU	48.6	3	1.99	8.74E-03
MTPN	28.0	3	1.95	3.90E-02
CAPG	16.4	5	1.90	8.92E-03
FTL	21.7	4	1.90	4.48E-03
COX4I1	19.5	3	1.89	4.59E-02
GNS	21.7	10	1.88	1.31E-02
PLD3	7.6	4	1.88	8.49E-03
ACAT1	6.3	3	1.87	2.86E-02
ACP5	18.2	5	1.86	2.56E-02
THBS1	39.5	1	1.85	7.08E-03
SRP9	31.4	3	1.84	1.74E-02
HEL-S-71	30.3	5	1.83	2.42E-02
HEL-75	36.4	14	1.83	1.44E-02
LIPA	8.5	5	1.82	3.35E-02
GRN	34.7	18	1.82	2.63E-02
IGFBP7	54.3	15	1.82	4.33E-02
CSTB	76.5	5	1.82	6.80E-03
CTGF	50.4	16	1.81	1.35E-02
PSAP	44.5	5	1.81	6.34E-03

ARSA	12.2	5	1.80	2.52E-02
PLBD2	24.1	15	1.79	2.43E-02
HEXB	37.8	20	1.78	1.70E-02
SCPEP1	11.3	4	1.74	3.27E-02
PLAU	32.7	14	1.74	2.12E-02
CTSA	20.2	10	1.74	1.57E-02
GNPDA1	31.5	6	1.71	6.88E-03
PRDX3	10.5	3	1.70	3.44E-02
AKR1B1	38.9	12	1.69	2.12E-02
CAP2	2.9	2	1.69	2.92E-03
GSN	19.1	4	1.68	1.02E-02
FDPS	14.6	7	1.68	2.91E-02
PRPF4	6.5	3	1.68	6.07E-03
LRRC59	23.8	9	1.67	9.85E-03
CBR1	74.7	12	1.67	4.34E-02
CALD1	43.3	2	1.67	1.96E-02
GDF15	20.5	7	1.65	4.26E-02
GPC4	16.4	8	1.64	3.01E-02
AP3D1	5.8	4	1.63	9.47E-05
NEDD8	46.9	5	1.63	2.22E-02
CCN1	28.6	11	1.63	3.95E-02
VGF	12.7	6	1.63	3.67E-02
VAPA	18.9	4	1.63	1.21E-02
CHCHD3	15.9	4	1.63	6.52E-03
LCP1	47.2	21	1.62	1.40E-02
EH	17.3	11	1.62	2.10E-03
SQSTM1	17.0	5	1.61	2.49E-02
HEL-S-47e	27.5	7	1.60	2.92E-02
TXN	51.4	6	1.60	1.72E-02
LETM1	12.7	7	1.60	4.27E-02
MAP1B	28.6	57	1.59	1.51E-02
MAPK1	15.0	5	1.59	3.02E-02
ATP5F1A	15.6	8	1.59	1.88E-02
REXO2	13.9	3	1.59	3.06E-02
SCP2	7.3	5	1.59	1.49E-02
PFDN1	28.7	4	1.58	1.82E-02
VAT1	23.2	7	1.57	1.88E-02
HNRNPR	30.8	13	1.57	2.80E-02
EPPK1	3.9	2	1.57	1.55E-02
KYNU	27.1	12	1.57	1.46E-02
CAPN1	10.4	7	1.57	2.14E-02
PCMT1	19.4	3	1.56	4.57E-02
HEXA	27.0	13	1.56	3.05E-02
PPT1	23.9	8	1.55	8.32E-03
TCEAL3	3.5	1	1.55	6.04E-03
TCEAL6	3.5	1	1.55	6.04E-03

CACYBP	45.6	8	1.54	6.34E-03
TFRC	42.0	29	1.53	1.27E-02
PBEF1	33.0	16	1.53	3.64E-02
HEL-S-304	39.9	8	1.53	2.46E-02
CTSL	16.5	5	1.53	1.87E-02
S100A6	43.3	5	1.53	1.32E-02
PABPN1	6.9	3	1.53	4.09E-02
PLIN3	30.6	13	1.52	4.28E-02
MACROH2A1	28.8	10	1.52	2.16E-03
ARSB	8.8	5	1.52	4.60E-02
NUMA1	21.0	40	1.51	4.27E-02
TCEA1	22.9	7	1.50	2.02E-02
UGP2	13.8	5	1.50	1.70E-02
DDX17	32.1	12	1.49	1.55E-02
DBI	50.6	3	1.49	1.59E-02
ECM1	39.6	15	1.49	2.70E-02
HEL-S-22	61.0	9	1.48	3.15E-02
PGD	42.0	20	1.48	3.58E-02
UFC1	11.4	2	1.48	2.73E-02
GOT1	34.4	15	1.48	6.86E-03
ENO2	19.4	5	1.47	2.71E-02
PTBP1	10.9	6	1.47	3.66E-02
PTBP3	4.5	3	1.47	3.66E-02
EIF2A	17.1	9	1.46	6.95E-03
HNRNPH1	22.3	4	1.46	4.88E-03
HNRNPH2	11.4	2	1.46	4.88E-03
LRPAP1	25.5	9	1.46	4.91E-02
SDCBP	3.8	2	1.45	2.44E-02
TCERG1	5.0	5	1.45	2.71E-03
CAP1	36.4	15	1.45	1.04E-02
PKIB	9.0	1	1.45	1.66E-02
ATP5F1B	10.9	2	1.45	3.64E-02
HEL-S-271	14.6	5	1.45	3.64E-02
ERH	41.3	5	1.45	1.76E-02
TGFB2	16.9	6	1.44	1.24E-02
SND1	29.3	24	1.44	2.16E-02
MAPRE1	32.5	7	1.44	2.46E-02
TBCB	26.2	6	1.44	2.07E-02
MDH1	40.7	18	1.44	1.40E-02
NUCKS1	34.2	9	1.43	2.51E-02
DNASE2	18.6	7	1.43	1.38E-03
PLS3	30.6	13	1.43	2.42E-02
HMGB2	27.8	6	1.43	2.29E-02
TXNRD2	3.0	1	1.42	9.93E-03
GLRX3	20.3	6	1.42	2.72E-02
PRKACA	5.1	2	1.42	3.17E-02

PRKACB	5.1	2	1.42	3.17E-02
HMGB1	34.4	12	1.42	2.48E-02
GMPS	21.4	13	1.42	1.24E-02
LUC7L2	10.5	3	1.41	3.86E-02
PCNP	34.3	5	1.41	5.48E-03
HMGB3	30.5	6	1.41	1.70E-02
TNFRSF11B	25.2	10	1.40	1.10E-02
HTRA1	19.0	9	1.40	3.10E-02
S100A13	49.0	6	1.40	4.94E-02
SERPINB1	10.8	5	1.40	3.36E-02
RRBP1	53.1	56	1.40	9.94E-03
PAM	10.6	11	1.40	1.75E-02
BOLA2	8.1	1	1.40	3.17E-02
BOLA2B	4.6	1	1.40	3.17E-02
H2BU1	57.1	4	1.39	3.56E-02
RAB1A	35.6	2	1.39	3.13E-02
CLIC1	73.9	13	1.39	4.21E-02
MYL6	42.9	5	1.38	2.08E-02
PFDN2	39.6	6	1.38	2.83E-02
PIN4	24.4	4	1.38	3.71E-02
HSPE1	77.5	7	1.38	3.87E-02
TCOF1	15.3	22	1.38	4.40E-02
SUPT16H	15.9	18	1.37	3.42E-02
SP100	2.5	3	1.37	4.67E-02
CTH	16.3	6	1.37	4.49E-02
GDI1	40.7	11	1.37	2.32E-02
TNPO3	5.1	5	1.37	1.01E-02
OCIAD1	8.6	2	1.37	2.47E-04
CD59	6.3	1	1.37	3.87E-02
HNRNPA2B1	49.6	13	1.37	8.44E-03
PEPD	21.3	7	1.37	1.78E-02
PLS1	7.5	2	1.37	3.07E-02
RPL26L1	28.3	1	1.36	2.21E-02
APLP2	17.6	13	1.36	2.85E-02
SON	2.2	5	1.36	3.99E-02
CORO1B	12.5	7	1.36	9.89E-03
SDC2	18.9	5	1.35	4.74E-02
PCBP1	39.6	6	1.35	3.96E-02
CLTA	21.8	7	1.35	2.31E-02
DEK	21.3	10	1.34	1.12E-02
VIM	57.1	28	1.34	1.44E-02
FEN1	16.8	5	1.34	2.68E-02
HSPB1	31.7	7	1.34	1.39E-02
ACO2	24.6	17	1.33	4.57E-02
PUF60	13.5	8	1.33	1.73E-03
TAGLN2	56.3	12	1.33	2.16E-02

HIST1H1E	48.4	5	1.33	1.11E-02
DDT	18.1	2	1.33	5.82E-03
DDT3	12.2	1	1.33	5.82E-03
NAP1L4	30.1	11	1.32	2.69E-02
CA	28.8	5	1.32	2.05E-02
GLO1	31.5	6	1.32	2.31E-02
SRI	21.2	4	1.32	2.51E-02
PLXNB2	2.9	6	1.32	1.54E-02
HDGF	59.2	1	1.32	7.31E-03
NOV	30.3	10	1.31	6.08E-03
OLA1	29.0	11	1.31	1.71E-02
VBP1	32.5	6	1.31	4.10E-02
BHMT	2.2	1	1.31	2.58E-02
PGM5	40.3	1	1.31	4.64E-02
PAICS	32.2	14	1.31	1.70E-02
ARF5	20.6	1	1.31	4.02E-02
LIN7C	19.3	4	1.31	2.47E-02
AP2M1	24.8	6	1.31	2.80E-02
RPS19	47.6	8	1.31	2.38E-02
PSME2	29.7	7	1.31	2.07E-02
GMDS	12.1	6	1.30	3.75E-02
CHMP4B	11.2	3	1.30	1.35E-02
UBAP2L	8.7	8	1.30	9.86E-03
IARS1	14.0	17	1.30	1.50E-02
AHCY	43.5	12	1.30	4.93E-02
KTN1	32.6	43	1.30	1.16E-02
FKBP3	30.8	7	1.29	2.22E-02
CHD4	11.9	18	1.29	7.43E-03
PAFAH1B1	25.0	4	1.29	1.62E-02
CSE1L	18.2	18	1.29	3.47E-02
NUDT5	36.5	7	1.29	2.80E-02
SF3B1	19.5	25	1.29	2.14E-02
SLC9A3R1	13.1	4	1.29	3.44E-02
SH3GL1	9.5	4	1.29	4.75E-03
H1-3	36.7	4	1.29	9.72E-03
APP	28.7	19	1.29	3.26E-02
GCLM	17.2	4	1.29	6.55E-03
SEPTIN2	40.4	12	1.29	3.32E-02
RECQL	15.1	10	1.29	1.31E-02
SRSF4	5.7	2	1.29	1.66E-02
ATOX1	39.7	3	1.29	4.65E-02
EEA1	21.1	30	1.28	3.14E-02
TFG	16.5	5	1.28	4.87E-02
DKC1	14.6	9	1.28	3.74E-02
API5	21.1	7	1.28	1.60E-02
AK3	14.1	3	1.28	2.34E-02

NOP16	20.8	4	1.28	1.02E-02
NIPBL	0.3	1	1.27	4.64E-02
HSPA8	95.6	1	1.27	4.04E-02
DDX6	17.4	7	1.27	4.62E-02
ACTN4	58.0	35	1.27	2.01E-02
RNH1	35.8	15	1.27	3.22E-02
ZFR	2.2	3	1.27	3.25E-02
SREK1	7.5	3	1.26	2.77E-02
CLTCL1	6.4	13	1.26	3.46E-02
KHDRBS1	22.8	9	1.26	2.58E-02
MCM4	8.8	8	1.26	4.97E-02
LMNA	55.1	34	1.26	9.12E-03
NT5C	18.9	3	1.26	7.97E-03
SIAE	15.7	8	1.26	4.79E-02
ZC3H18	7.0	7	1.26	3.69E-03
PGM1	36.7	5	1.26	3.49E-02
HDGFRP3	7.9	1	1.26	1.53E-02
MYH9	40.5	72	1.26	1.23E-02
GAA	12.3	3	1.26	2.59E-02
SRSF6	14.5	5	1.25	3.64E-02
AHCYL2	1.3	1	1.25	2.70E-02
BLVRA	35.1	11	1.25	4.43E-02
USP14	26.7	13	1.25	4.98E-02
RPLP2	85.2	5	1.25	3.98E-02
QARS1	20.9	14	1.25	1.37E-02
JPT2	30.5	4	1.25	1.01E-02
HNRPA1	36.3	9	1.25	6.37E-03
MAN2B2	11.3	11	1.25	1.81E-02
CIRBP	14.5	2	1.25	1.74E-02
PFDN5	23.4	4	1.25	3.66E-02
H1-5	41.6	11	1.24	2.40E-02
SNX2	15.0	5	1.24	2.35E-02
DSC1	6.0	4	1.24	2.72E-03
PACSIN2	20.4	10	1.24	2.21E-02
LSM2	46.3	5	1.24	3.83E-02
TKT	43.8	24	1.24	1.64E-02
RANBP1	9.7	3	1.24	1.88E-02
QARS	24.9	4	1.24	1.17E-02
PGAM1	53.9	8	1.23	3.36E-02
ALYREF	17.5	4	1.23	1.41E-02
H1-2	50.2	6	1.23	2.71E-02
ELOB	30.5	5	1.23	3.38E-02
YWHAZ	48.2	9	1.22	1.97E-02
AIFM1	14.5	7	1.22	3.26E-02
TRIP11	1.3	3	1.22	1.67E-02
U2AF2	22.9	10	1.22	2.98E-02

PARP1	28.8	32	1.22	1.70E-02
IK	5.0	3	1.22	3.46E-02
ARPC2	27.7	10	1.22	2.78E-02
EIF3H	23.0	8	1.22	2.39E-02
HEL-S-34	57.2	8	1.21	4.41E-02
TXNRD1	40.7	18	1.21	1.35E-02
CBX3	39.9	6	1.21	4.96E-02
ANKRD30B	0.5	1	1.21	1.43E-02
DKFZp686L08115	14.9	4	1.21	1.43E-02
PWP1	4.0	2	1.21	4.69E-03
HEL-S-129m	48.2	13	1.21	3.13E-02
GDI2	37.3	11	1.21	2.90E-02
CLTC	32.6	51	1.21	2.72E-02
GBA	5.0	3	1.20	2.00E-02
RPS17	22.2	3	1.20	2.26E-02
PGP	22.1	6	1.20	1.67E-02
SYNM	4.3	6	1.20	3.83E-02
ST13	28.2	14	1.20	2.89E-02
CTTN	28.2	13	1.20	3.57E-02
CHCHD4	25.2	4	1.20	1.20E-02
GSTM3	38.7	8	1.20	3.20E-02
ARPC1B	10.8	1	1.20	3.83E-02
HNRNPA3	19.6	5	1.19	1.96E-03
PARVA	17.5	6	1.19	2.02E-02
AIMP1	26.6	8	1.19	1.86E-02
SUB1	52.8	9	1.19	1.85E-02
EIF1	40.5	4	1.19	2.92E-02
C14orf166	23.4	7	1.19	9.61E-05
SNRPA	24.8	4	1.19	1.45E-02
STIP1	42.4	30	1.19	4.56E-02
KHSRP	23.1	11	1.18	2.76E-02
DLD	28.5	13	1.18	1.86E-02
ABCF1	35.7	2	1.18	7.86E-03
RPLP0	44.2	12	1.18	3.70E-02
MAP4	33.0	17	1.18	2.08E-02
AP2B1	21.1	12	1.17	3.59E-02
CAB39	14.7	6	1.17	2.94E-02
RPS21	37.3	3	1.17	4.13E-02
GPI	35.1	15	1.17	3.10E-02
SRRT	13.1	10	1.17	2.41E-02
PNN	12.7	9	1.17	2.68E-02
SEPTIN9	18.8	10	1.17	3.79E-02
LIMA1	25.0	18	1.17	7.67E-03
BZW2	33.4	13	1.17	2.72E-02
MESD	7.3	2	1.17	3.14E-02
UBB	82.2	4	1.17	2.12E-02

RPS27A	53.8	4	1.17	2.12E-02
UBA52	50.8	4	1.17	2.12E-02
NCBP2	12.2	2	1.16	2.56E-02
TBCA	47.1	9	1.16	2.43E-02
ACLY	38.9	39	1.16	3.41E-02
CCT3	33.4	17	1.16	7.12E-03
MARCKSL1	17.4	3	1.16	5.82E-03
OK/SW-cl.5	58.7	0	1.16	5.19E-03
TXNDC12	21.5	3	1.16	5.59E-03
HNRNPU	26.9	3	1.16	1.85E-02
CDC5L	6.4	5	1.16	1.23E-02
NIT2	39.1	9	1.16	3.88E-02
TPM1	43.7	4	1.16	3.96E-02
SLC39A10	7.2	7	1.16	1.71E-02
IPO9	10.2	10	1.15	3.01E-03
PRKAR1A	18.6	7	1.15	4.55E-02
TLN1	28.3	67	1.15	2.85E-02
SGTA	6.7	2	1.15	4.77E-02
XPO1	14.1	15	1.15	2.09E-02
CD109	17.4	24	1.15	3.76E-02
LDHAL6A	5.4	1	1.14	4.45E-02
PRPS2	6.3	2	1.14	4.00E-02
ACTN1	53.3	23	1.14	1.11E-02
HSP90AA2P	25.7	3	1.14	2.18E-02
RPL19	25.5	5	1.14	4.89E-02
COPB1	18.2	15	1.14	3.65E-02
HLA-C	6.1	1	1.14	3.07E-02
CDK1	17.5	4	1.13	4.02E-02
RPL9	13.0	3	1.13	2.86E-02
RPL22	23.4	3	1.13	4.31E-02
DYNC1I2	10.5	7	1.13	4.74E-02
APEX1	30.5	4	1.13	1.72E-02
PGK1	70.7	5	1.13	4.25E-02
RPL14	37.3	7	1.13	2.70E-02
SRRM2	7.1	16	1.13	8.51E-03
CIP2A	0.9	1	1.13	1.97E-02
PGM2	22.2	11	1.13	2.63E-02
LMNB2	39.0	21	1.13	4.84E-02
BCLAF1	15.8	12	1.13	1.81E-02
RPL6	39.4	14	1.13	1.46E-02
TPM4	43.7	1	1.12	2.79E-02
SHANK1	0.3	1	1.12	1.62E-02
SNRPG	25.0	2	1.12	2.30E-02
FTSJ3	4.8	4	1.12	4.20E-02
ASH2L	4.9	3	1.12	2.25E-02
HNRNPUL2	15.5	12	1.12	1.37E-02

DNCL1	20.2	1	1.12	1.83E-02
DDX39A	24.1	2	1.12	3.82E-02
HNRNPM	23.6	17	1.12	4.99E-02
MYL12B	20.9	4	1.12	4.92E-02
PPIF	26.1	6	1.12	4.51E-02
RPS2	39.9	13	1.12	2.31E-02
EIF3L	28.2	13	1.11	2.16E-02
RAP1A	10.3	2	1.11	2.25E-02
BAG3	18.4	4	1.11	1.91E-02
CAPRIN1	11.3	8	1.11	1.32E-02
PCBP2	32.9	5	1.11	3.37E-02
RPS8	46.2	9	1.11	4.93E-02
YARS	23.3	13	1.11	4.70E-02
PRPS1	9.4	3	1.11	4.37E-02
SNRPE	25.0	2	1.11	2.52E-02
PPP1R12A	16.1	14	1.11	4.22E-03
FL	47.1	21	1.11	4.88E-02
LIMS4	6.5	2	1.11	4.38E-03
DHX15	24.7	18	1.10	3.53E-02
CCDC47	1.9	1	1.10	2.27E-02
HEL-S-77	27.1	10	1.10	2.19E-02
ENO1	49.5	10	1.10	2.38E-02
MAP7D1	9.6	6	1.10	2.34E-03
TPM3	56.1	5	1.10	9.77E-03
HNRPK	24.4	12	1.09	1.24E-02
LGALS3	22.4	5	1.09	3.00E-02
EIF4G1	17.3	27	1.09	2.88E-02
RPL5	34.3	14	1.09	2.59E-02
HEL-S-64p	25.1	12	1.09	2.93E-02
SNRNP200	18.8	39	1.09	3.40E-02
TOMM70	4.9	3	1.09	1.20E-02
ATIC	33.3	16	1.09	4.74E-02
CS	23.4	11	1.09	3.98E-02
DKFZp686F17268	23.6	10	1.09	2.85E-02
BAG2	31.8	6	1.09	3.56E-03
TUBB3	28.7	1	1.08	1.55E-02
RPL36	34.3	4	1.08	3.64E-02
COPA	20.3	23	1.08	3.42E-02
SAP30	4.1	1	1.08	4.36E-02
RPL34	34.2	5	1.08	4.01E-02
MARS1	13.0	9	1.08	9.30E-03
RNPEP	38.3	22	1.08	1.93E-02
RAD23B	29.6	8	1.08	3.63E-02
SARNP	28.6	5	1.08	5.12E-03
SF3A3	21.4	9	1.08	3.33E-02
SAFB2	14.4	8	1.08	2.23E-02

SDF4	33.1	13	1.08	3.43E-02
EEF1D	32.6	5	1.08	1.63E-02
EIF3A	26.3	35	1.08	1.89E-02
LYN	1.6	1	1.08	3.36E-02
SRC	1.5	1	1.08	3.36E-02
YES1	2.9	2	1.08	3.36E-02
HEL-S-68p	74.8	9	1.07	4.12E-02
PEA15	17.7	2	1.07	8.68E-03
FAF2	7.0	4	1.07	4.74E-03
RANBP5	15.1	5	1.07	2.85E-02
YWHAE	47.6	5	1.07	3.60E-02
hCG 1821276	5.9	3	1.07	2.63E-02
TNFRSF12A	14.0	3	1.06	2.60E-02
CSRP2	24.7	5	1.06	3.26E-02
TSN	23.7	7	1.06	1.72E-02
PGM2L1	6.6	3	1.06	3.81E-02
MATR3	15.9	17	1.06	2.03E-02
DPP3	26.1	18	1.06	4.94E-02
ESD	27.0	8	1.06	4.36E-02
DHX9	26.9	32	1.06	1.44E-02
SMARCC2	9.8	7	1.05	1.79E-02
ANP32B	32.3	4	1.05	4.24E-02
AHK	38.3	103	1.05	3.06E-02
RBMX	34.3	15	1.05	2.16E-02
RAC1	16.1	4	1.05	3.00E-02
RPL3	23.8	4	1.05	2.89E-02
EL52	48.6	24	1.05	3.06E-02
NCL	31.7	32	1.05	2.08E-02
FLYWCH2	8.6	1	1.05	4.21E-02
LOC388524	43.7	7	1.05	4.52E-02
RPSA	43.7	10	1.05	4.52E-02
UBE2L6	4.6	1	1.05	3.63E-02
RPL29	23.3	5	1.05	3.14E-02
XPO7	9.3	9	1.05	2.39E-02
FXR1	15.1	5	1.05	1.65E-02
TRANK1	0.2	1	1.05	7.46E-04
LDHB	41.3	15	1.04	1.37E-02
LRRFIP1	23.0	16	1.04	3.63E-02
EIF1AY	41.0	1	1.04	1.71E-02
CPPED1	18.8	6	1.04	4.25E-02
HSP90Af	22.8	2	1.04	2.99E-02
PSMD13	26.9	10	1.04	3.77E-02
FUBP1	26.9	14	1.04	1.29E-02
SNRPB	21.7	6	1.04	3.04E-02
FKBP4	40.1	18	1.04	2.19E-03
RPS3A	40.9	13	1.03	3.19E-02

MAP1A	17.4	42	1.03	3.46E-02
GLG1	8.3	10	1.03	4.86E-02
HNRNPF	22.4	6	1.03	2.61E-02
TANC2	1.2	2	1.03	2.44E-02
SF3A1	28.4	18	1.03	1.65E-02
CTPS1	13.9	7	1.03	3.40E-02
TGOLN2	22.9	9	1.03	3.00E-02
RPL4	30.2	14	1.03	3.93E-02
CCDC58	18.1	2	1.03	6.11E-03
TPI1	60.5	16	1.03	4.21E-03
HNRNPC	41.5	18	1.02	2.53E-02
HEL103	10.1	6	1.02	2.12E-02
TAF15	16.9	3	1.02	6.94E-03
SF3B2	19.2	18	1.02	2.60E-02
SNRP70	20.6	9	1.02	2.76E-02
RPL13A	35.8	9	1.02	4.56E-02
MCM2	10.4	10	1.02	3.80E-02
ITIH2	3.5	3	1.02	2.31E-02
COPB2	17.5	15	1.02	3.55E-02
LARP1	9.5	10	1.02	9.54E-03
VCL	50.5	53	1.02	2.80E-02
PPP1R2	5.4	1	1.01	4.50E-03
SP	32.7	27	1.01	3.69E-02
NOP58	16.6	10	1.01	3.62E-02
XRCC6	37.3	27	1.01	4.25E-02
RTCB	19.4	9	1.00	2.47E-02
MARCKS	45.8	8	1.00	1.35E-02
EEF1G	31.6	17	1.00	3.79E-02
EIF5B	17.6	17	1.00	3.89E-02
WDR1	38.5	1	1.00	1.55E-02
HSP90AA5P	14.4	4	1.00	4.09E-02
PSMC5	17.7	6	1.00	2.78E-02
RSL1D1	16.9	9	1.00	3.90E-03
VARS1	23.7	12	1.00	4.76E-02
PNP	32.2	8	1.00	3.22E-02
RBM25	10.0	7	1.00	2.85E-02
EFTUD2	13.4	10	1.00	3.40E-02
MYDGF	30.6	7	1.00	3.86E-02
NSF	4.7	3	1.00	3.80E-02
COLEC12	4.6	4	-2.32	1.71E-02

Table 3.3 Gene Ontology Analysis of the VPS35 KO H4 'Secretome'

Significantly enriched proteins from **Table 2** were analysed using PANTHER gene ontology software. Significantly enriched or depleted gene ontology categories are displayed.

Gene Ontology Category	Category Size	# Proteins Identified	# Proteins Expected	Over/Under Representation	Fold Enrichment	p-Value
Unclassified (UNCLASSIFIED)	1760	3	39.05	-	0.08	0.00E+00
extracellular exosome (GO:0070062)	2098	196	46.55	+	4.21	1.80E-67
extracellular vesicle (GO:1903561)	2119	196	47.02	+	4.17	8.69E-67
extracellular organelle (GO:0043230)	2121	196	47.06	+	4.16	1.01E-66
vesicle (GO:0031982)	3928	231	87.16	+	2.65	6.27E-47
extracellular space (GO:0005615)	3389	211	75.2	+	2.81	4.53E-45
intracellular anatomical structure (GO:0005622)	14785	442	328.08	+	1.35	6.81E-41
organelle (GO:0043226)	13811	428	306.46	+	1.4	5.11E-39
cytoplasm (GO:0005737)	11873	396	263.46	+	1.5	2.36E-37
membrane-bounded organelle (GO:0043227)	12702	407	281.86	+	1.44	1.67E-35
extracellular region (GO:0005576)	4402	223	97.68	+	2.28	3.59E-34
ribonucleoprotein complex (GO:1990904)	696	85	15.44	+	5.5	1.46E-32
cytosol (GO:0005829)	5291	244	117.41	+	2.08	3.15E-32
intracellular organelle (GO:0043229)	13007	402	288.62	+	1.39	4.70E-29
intracellular organelle lumen (GO:0070013)	6101	254	135.38	+	1.88	7.90E-27
membrane-enclosed lumen (GO:0031974)	6101	254	135.38	+	1.88	7.90E-27
organelle lumen (GO:0043233)	6101	254	135.38	+	1.88	7.90E-27
cell-substrate junction (GO:0030055)	423	55	9.39	+	5.86	3.86E-21
focal adhesion (GO:0005925)	416	54	9.23	+	5.85	1.12E-20
intracellular membrane-bounded organelle (GO:0043231)	11220	351	248.97	+	1.41	2.33E-19
protein-containing complex (GO:0032991)	5532	222	122.75	+	1.81	2.77E-19
spliceosomal complex (GO:0005681)	194	35	4.3	+	8.13	1.28E-16
vacuolar lumen (GO:0005775)	172	33	3.82	+	8.65	2.88E-16
nucleus (GO:0005634)	7559	261	167.73	+	1.56	3.66E-15
secretory granule (GO:0030141)	864	67	19.17	+	3.49	6.21E-15
anchoring junction (GO:0070161)	834	65	18.51	+	3.51	1.65E-14
secretory vesicle (GO:0099503)	1031	73	22.88	+	3.19	1.73E-14

catalytic step 2 spliceosome (GO:0071013)	87	24	1.93	+	12.43	2.30E-14
secretory granule lumen (GO:0034774)	321	38	7.12	+	5.33	1.08E-12
lysosomal lumen (GO:0043202)	96	23	2.13	+	10.8	1.50E-12
cytoplasmic vesicle lumen (GO:0060205)	325	38	7.21	+	5.27	1.55E-12
vesicle lumen (GO:0031983)	327	38	7.26	+	5.24	1.86E-12
intracellular non-membrane-bounded organelle (GO:0043232)	5284	196	117.25	+	1.67	5.34E-12
non-membrane-bounded organelle (GO:0043228)	5287	196	117.32	+	1.67	5.43E-12
integral component of membrane (GO:0016021)	5762	58	127.86	-	0.45	1.84E-11
intrinsic component of membrane (GO:0031224)	5918	61	131.32	-	0.46	2.07E-11
ficolin-1-rich granule (GO:0101002)	185	28	4.11	+	6.82	3.45E-11
nucleoplasm (GO:0005654)	3983	158	88.38	+	1.79	6.57E-11
cellular_component (GO:0005575)	18835	454	417.95	+	1.09	1.08E-10
nuclear lumen (GO:0031981)	4980	183	110.51	+	1.66	2.07E-10
cytosolic ribosome (GO:0022626)	112	22	2.49	+	8.85	2.17E-10
lysosome (GO:0005764)	702	52	15.58	+	3.34	2.64E-10
lytic vacuole (GO:0000323)	702	52	15.58	+	3.34	2.64E-10
cellular anatomical entity (GO:0110165)	18695	452	414.84	+	1.09	4.99E-10
cell junction (GO:0030054)	2069	98	45.91	+	2.13	2.08E-09
supramolecular complex (GO:0099080)	1338	74	29.69	+	2.49	2.42E-09
cytoplasmic vesicle (GO:0031410)	2442	109	54.19	+	2.01	3.31E-09
intracellular vesicle (GO:0097708)	2447	109	54.3	+	2.01	3.54E-09
endomembrane system (GO:0012505)	4640	169	102.96	+	1.64	8.30E-09
vacuole (GO:0005773)	799	53	17.73	+	2.99	8.34E-09
ficolin-1-rich granule lumen (GO:1904813)	124	21	2.75	+	7.63	9.61E-09
ribosome (GO:0005840)	240	28	5.33	+	5.26	1.06E-08
nuclear speck (GO:0016607)	401	34	8.9	+	3.82	1.93E-07
azurophil granule lumen (GO:0035578)	90	17	2	+	8.51	2.24E-07
azurophil granule (GO:0042582)	154	21	3.42	+	6.15	3.59E-07
primary lysosome (GO:0005766)	154	21	3.42	+	6.15	3.59E-07
cytosolic large ribosomal subunit (GO:0022625)	59	14	1.31	+	10.69	7.18E-07
nucleolus (GO:0005730)	943	54	20.93	+	2.58	1.17E-06
nuclear body (GO:0016604)	794	48	17.62	+	2.72	1.69E-06

actin filament bundle (GO:0032432)	78	15	1.73	+	8.67	2.18E-06
ribosomal subunit (GO:0044391)	191	22	4.24	+	5.19	2.42E-06
supramolecular fiber (GO:0099512)	1009	55	22.39	+	2.46	4.79E-06
supramolecular polymer (GO:0099081)	1017	55	22.57	+	2.44	5.55E-06
melanosome (GO:0042470)	106	16	2.35	+	6.8	1.38E-05
pigment granule (GO:0048770)	106	16	2.35	+	6.8	1.38E-05
actin cytoskeleton (GO:0015629)	509	35	11.29	+	3.1	1.74E-05
U2-type spliceosomal complex (GO:0005684)	93	15	2.06	+	7.27	1.82E-05
cytoskeleton (GO:0005856)	2300	93	51.04	+	1.82	3.45E-05
spliceosomal snRNP complex (GO:0097525)	57	12	1.26	+	9.49	4.02E-05
U2-type precatalytic spliceosome (GO:0071005)	50	11	1.11	+	9.91	1.04E-04
small nuclear ribonucleoprotein complex (GO:0030532)	66	12	1.46	+	8.19	1.66E-04
precatalytic spliceosome (GO:0071011)	53	11	1.18	+	9.35	1.74E-04
ribonucleoprotein granule (GO:0035770)	248	22	5.5	+	4	1.82E-04
contractile actin filament bundle (GO:0097517)	71	12	1.58	+	7.62	3.36E-04
stress fiber (GO:0001725)	71	12	1.58	+	7.62	3.36E-04
cytoplasmic ribonucleoprotein granule (GO:0036464)	237	21	5.26	+	3.99	3.59E-04
polysome (GO:0005844)	73	12	1.62	+	7.41	4.39E-04
Sm-like protein family complex (GO:0120114)	77	12	1.71	+	7.02	7.32E-04
actomyosin (GO:0042641)	82	12	1.82	+	6.59	1.34E-03
contractile fiber (GO:0043292)	237	20	5.26	+	3.8	1.41E-03
large ribosomal subunit (GO:0015934)	118	14	2.62	+	5.35	1.66E-03
U2 snRNP (GO:0005686)	20	7	0.44	+	15.77	1.95E-03
myofibril (GO:0030016)	227	19	5.04	+	3.77	2.95E-03
polymeric cytoskeletal fiber (GO:0099513)	781	39	17.33	+	2.25	9.38E-03
perinuclear region of cytoplasm (GO:0048471)	733	37	16.27	+	2.27	9.76E-03
prespliceosome (GO:0071010)	17	6	0.38	+	15.91	1.10E-02
U2-type prespliceosome (GO:0071004)	17	6	0.38	+	15.91	1.10E-02
catalytic complex (GO:1902494)	1400	58	31.07	+	1.87	1.35E-02
nuclear chromosome, telomeric region (GO:0000784)	108	12	2.4	+	5.01	1.77E-02
podosome (GO:0002102)	30	7	0.67	+	10.52	1.88E-02

cell projection (GO:0042995)	2347	84	52.08	+	1.61	2.27E-02
aminoacyl-tRNA synthetase multienzyme complex (GO:0017101)	11	5	0.24	+	20.48	2.49E-02
plasma membrane bounded cell projection (GO:0120025)	2250	81	49.93	+	1.62	3.10E-02
polysomal ribosome (GO:0042788)	34	7	0.75	+	9.28	3.80E-02
cytosolic small ribosomal subunit (GO:0022627)	48	8	1.07	+	7.51	3.90E-02
coated vesicle membrane (GO:0030662)	182	15	4.04	+	3.71	4.14E-02
cell cortex (GO:0005938)	306	20	6.79	+	2.95	4.90E-02

Table 3.4 Significantly Enriched and Depleted RNA Transcripts in VPS35 KO H4 Cells

RNA transcripts exceeding a VPS35 KO/VPS35-GFP Log_2 fold change of ± 1.00 with an FDR value of < 0.10 are displayed.

Gene Name	Log_2 VPS35 KO/VPS35-GFP Fold Change	FDR
FABP4	3.608	0.082190692
RGS18	3.425	0.088020103
ANGPT2	3.377	0.097486596
FRY-AS1	2.984	0.037791733
MAEL	2.863	0.031570944
A2M	2.825	0.000321347
IPCEF1	2.675	0.087480709
PCP4	2.663	0.013335548
AGT	2.53	0.009163546
TBX2	2.515	1.21196E-10
FNDC1	2.502	0.082730563
SPRY1	2.495	0.008160066
MUCL1	2.427	0.077876902
CRYAB	2.382	6.01492E-06
CMKLR1	2.357	0.079095759
FAM180A	2.341	0.012528447
LINC01314	2.231	0.01746474
SEMA3F	2.208	0.000176279
CTSS	2.156	0.009657797
TGM2	2.135	0.000184007
CEMIP	2.127	0.097975587
NR4A1	2.08	0.047303591
PRUNE2	2.013	0.012774463
HSD17B2	2.004	9.68034E-06
SUN3	1.984	0.012923344
PNCK	1.964	0.021557155
ITGA8	1.923	0.004663578
GFRA2	1.898	0.012923344
ATP6V0D2	1.866	8.65585E-05
MRVI1	1.775	0.000346818
CDCP1	1.773	0.004116053
SORT1	1.761	5.31194E-07
CPED1	1.756	0.000176279
RP11-16L9.2	1.735	0.020330288
ACP5	1.631	0.013677124
IGFBP7	1.61	4.36954E-06
BMP2	1.557	0.037791733
AC002454.1	1.551	0.012528447
RAB20	1.546	6.01492E-06

PRICKLE2	1.521	0.018074545
STC1	1.508	0.000346818
SQRDL	1.49	0.017950414
AC058791.1	1.469	0.059709422
FYB	1.446	0.022776385
TBX2-AS1	1.411	0.020447135
TMSB4X	1.394	0.097934911
TMEM158	1.388	0.045300821
NPAS2	1.309	0.002304653
SCN4B	1.274	0.011442288
PAG1	1.235	4.95074E-05
SDC2	1.23	0.000130745
PTCHD1	1.218	0.001196821
CLSTN2	1.199	0.000870032
SLC16A6	1.195	0.045300821
SLC39A8	1.194	0.082027758
AKR1B10	1.156	0.041343729
KHDRBS3	1.15	0.073563413
APLN	1.137	0.014301858
PTGS2	1.135	0.021931611
RAB27B	1.121	0.081953648
CSF1	1.119	0.095097922
GPRC5B	1.115	0.030728819
IL4R	1.111	0.000798394
TMEM119	1.104	0.018903305
CCDC71L	1.104	0.081126352
MGLL	1.097	0.020447135
MCTP2	1.081	0.004505523
COL4A2	1.053	0.000191579
AMPD3	1.052	0.081732283
CASP1	1.037	0.085807318
PLPP3	1.029	0.067309341
ARHGAP42	1.022	0.003721875
PSG4	1.019	0.08599273
JAG1	1.018	0.01622935
PRKAA2	1.014	0.004248084
DAAM2	1.002	0.00013319
SPANXC	-1.002	0.095097922
ZNF311	-1.008	0.044292524
PAPOLG	-1.009	0.093513463
RP11-983P16.4	-1.018	0.014633382
ALPK1	-1.051	0.096051234
RP11-2B6.2	-1.059	0.049159777
CTC-246B18.10	-1.073	0.019692152
LFNG	-1.073	0.02375086
SYT1	-1.075	0.001551892

PLEKHG4	-1.125	0.08599273
ALCAM	-1.132	0.004248084
AMOT	-1.137	0.00462299
STAC	-1.167	0.090111034
HIST1H2BD	-1.194	0.001749042
ANKLE1	-1.223	0.081953648
RNF150	-1.236	0.003721875
LRRIQ1	-1.246	0.01513346
SEMA3E	-1.263	0.053372463
C6orf141	-1.265	0.079102327
LINC01521	-1.27	0.081126352
CSTA	-1.314	0.01531822
ARID3B	-1.363	0.025782662
RP11-46C24.7	-1.378	0.037743223
LINC00960	-1.4	0.091512362
TMEM154	-1.424	0.019230147
RP11-127B20.3	-1.431	0.081126352
KRT81	-1.444	0.000614307
UNC13D	-1.46	0.011816334
HTR7	-1.472	0.039572369
FUOM	-1.481	0.045300821
SLPI	-1.496	0.014119063
RP11-631N16.2	-1.514	0.039668091
IL11	-1.604	0.000501794
DHRS2	-1.629	0.085807318
RP5-1172A22.1	-1.679	0.01681583
AC025171.1	-1.77	0.018285842
TMEM184A	-1.787	0.014633382
CH17-360D5.2	-1.865	0.009657797
RP11-10C24.3	-1.89	0.029110532
C5orf46	-1.902	0.001705514
MMP3	-1.917	0.00369115
RP5-994D16.3	-1.922	0.063797777
STRA6	-1.966	0.000870032
TNC	-1.976	1.05493E-08
CIB2	-1.994	0.099978246
DCN	-2.003	0.006818722
LINC01583	-2.009	0.046949499
PAPPA2	-2.017	0.011816334
SFN	-2.035	0.006532274
LINC00337	-2.095	0.072483286
TSPAN10	-2.104	0.026965436
NELL2	-2.118	0.020063692
TENM2	-2.119	0.071628308
ADAMTS19	-2.144	0.003121905
SELL	-2.145	0.039668091

PLCB2	-2.283	0.013335548
LY6G5B	-2.296	0.084796417
FAM184B	-2.438	0.08599273
FAM167A	-2.461	0.00595879
SLCO1B3	-2.502	0.043969704
POSTN	-2.506	7.42143E-06
RP11-302B13.5	-2.665	0.026965436
TRIM46	-2.732	0.097486596
C9orf84	-2.84	0.020447135
RIMS1	-2.872	0.023115275
PGM5P2	-2.965	0.043969704
MMP13	-3.473	0.084013249
RP11-297D21.4	-3.506	0.005565932
LOXL3	-3.559	0.018285842
LINC01060	-3.584	0.032379819
FABP5	-3.882	0.030473319
KRT33B	-4.007	0.002304653
CD36	-4.234	0.019692152
FLG	-4.627	1.66378E-06
VPS35	-8.575	1.3094E-265

Table 3.5 RNA-Seq Enrichment Values of CLEAR Network Genes

CLEAR network genes are displayed, alongside their corresponding RNA-Seq VPS35 KO/VPS35-GFP Log_2 fold change and FDR values. Transcripts with FDR < 0.1 are labelled in green. N/A = transcript not detected.

Gene Name	Log_2 VPS35 KO/VPS35-GFP Fold Change	FDR
CTSS	2.156	0.009658
ACP5	1.631	0.013677
CTSF	1.547	0.470744
NPC2	0.911	1.05E-08
CTSB	0.903	0.000776
CTSD	0.799	6.01E-06
HEXB	0.75	0.022817
ARSB	0.731	0.40413
ASAH1	0.589	0.011939
GBA	0.588	0.604297
CD63	0.576	0.000825
GAA	0.561	0.054046
TPP1	0.545	0.032219
SLC36A1	0.515	0.392134
HEXA	0.495	0.19056
CTSL	0.49	0.438867
PSAP	0.465	0.03094
CPVL	0.463	0.118626
NPC1	0.441	0.249339
LIPA	0.438	0.445239
ARSG	0.412	0.756193
GLB1	0.405	0.391017
SGSH	0.4	0.666044
SLC17A5	0.378	0.466359
CLN5	0.345	0.615229
GGH	0.33	0.450967
MANBA	0.327	0.791843
NEU1	0.326	0.423179
PLBD2	0.326	0.317075
CLN3	0.319	0.568351
CLCN7	0.298	0.560096
NAGLU	0.259	0.657728
PPT1	0.239	0.419488
NCSTN	0.239	0.844635
HYAL2	0.22	0.754077
RNASET2	0.219	0.74025
IDUA	0.215	0.8299
GALNS	0.203	0.65535

SCPEP1	0.194	0.664634
LAMP1	0.185	0.667613
DNASE2	0.183	0.639854
GNS	0.168	0.67235
LAPTM4A	0.148	0.683048
MAN2B2	0.141	0.757241
SLC35F6	0.13	0.785705
SCARB2	0.126	0.893486
TMEM55B	0.123	0.809474
ABCA2	0.107	0.901701
ARSA	0.1	0.936029
CTSH	0.096	0.940375
GUSB	0.095	0.826656
CD68	0.081	0.900141
MCOLN1	0.066	0.965193
CTSA	0.064	0.922142
NAGA	0.027	0.977512
CTSC	0.006	0.996427
HPSE	-0.073	0.977293
ABCB9	-0.081	0.939307
SMPD1	-0.172	0.72032
PLA2G15	-0.198	0.82874
MFSD8	-0.456	0.628348
CTNS	-0.464	0.572695
IFI30	-0.697	0.698518
CTSK	N/A	N/A
CTSZ	N/A	N/A
GALC	N/A	N/A
MAN2B1	N/A	N/A
NEU4	N/A	N/A
MPO	N/A	N/A

Table 3.6 Cellular Component Gene Set Enrichments in VPS35 KO H4 Cells

The most enriched Cellular Component gene sets in VPS35 KO H4 cells based on RNA-Seq data, compared to wild-type and VPS35-GFP rescue negative control conditions are presented, ranked by net enrichment score.

Gene Set	Size	Enrichment Score	Net Enrichment Score	NOM p-value	FDR Q-value
RESPIRASOME	88	0.5311236	2.279762	0	0
RESPIRATORY CHAIN COMPLEX	76	0.5371192	2.241986	0	0.0010057
PROTON TRANSPORTING TWO SECTOR ATPASE COMPLEX	31	0.6092495	2.1214955	0	0.0020256
OXIDOREDUCTASE COMPLEX	104	0.4836435	2.1191802	0	0.0015192
PROTON TRANSPORTING V TYPE ATPASE COMPLEX	26	0.6307849	2.0935102	0	0.0034609
LYSOSOMAL LUMEN	86	0.4871098	2.0889914	0	0.0030637
INNER MITOCHONDRIAL MEMBRANE PROTEIN COMPLEX	109	0.457565	2.0519753	0	0.0036303
PLATELET DENSE GRANULE	17	0.687133	2.027283	0	0.0043298
CELL BODY MEMBRANE	28	0.594954	1.9921845	0.001792115	0.0054149
CYTOCHROME COMPLEX	28	0.5873596	1.9885879	0	0.0052761
VACUOLAR PROTON TRANSPORTING V TYPE ATPASE COMPLEX	17	0.652648	1.9555188	0	0.0076604
PHAGOCYTIC VESICLE MEMBRANE	74	0.4654095	1.9257443	0	0.0104963
APICAL DENDRITE	18	0.6506538	1.924776	0	0.0099263
CAVEOLA	69	0.4537626	1.8584299	0	0.0195216
PLASMA MEMBRANE RAFT	97	0.4152986	1.8258141	0	0.0258399
VACUOLAR MEMBRANE	388	0.3441707	1.8130313	0	0.0281755
AGGRESOME	37	0.5160706	1.8109624	0.003717472	0.0267489
VACUOLAR LUMEN	149	0.3877471	1.7877662	0	0.0322277
PIGMENT GRANULE	101	0.4009083	1.7718532	0	0.0362481
RESPIRATORY CHAIN COMPLEX IV	15	0.6177735	1.7666293	0.005660377	0.0359726
SECONDARY LYSOSOME	15	0.6076334	1.7604506	0.009920635	0.0364381
BLOC COMPLEX	19	0.5715423	1.7484857	0.009727626	0.0398197
NADH DEHYDROGENASE COMPLEX	47	0.4576909	1.7461538	0.003521127	0.0391468
LATE ENDOSOME MEMBRANE	124	0.37547	1.7081478	0	0.0532214
TERTIARY GRANULE	136	0.366011	1.6947972	0	0.0574138
ORGANELLE INNER MEMBRANE	468	0.316303	1.6924886	0	0.0567251
TERTIARY GRANULE LUMEN	43	0.4537204	1.6878431	0.011049724	0.0570708
ENDOSOME LUMEN	24	0.5122451	1.6761504	0.0078125	0.0613163
TRANS GOLGI NETWORK TRANSPORT VESICLE	29	0.4896751	1.6731333	0.010771993	0.0609591
POSTSYNAPTIC DENSITY MEMBRANE	80	0.3933807	1.6683898	0.001869159	0.0613639
POSTSYNAPTIC SPECIALIZATION MEMBRANE	102	0.3727784	1.6581385	0.001845019	0.0647051
PHAGOCYTIC VESICLE	130	0.3634637	1.6574433	0	0.0630506

MICROBODY	121	0.358184	1.6398882	0.007142857	0.0710419
INTRINSIC COMPONENT OF POSTSYNAPTIC SPECIALIZATION MEMBRANE	63	0.4013786	1.638539	0	0.069847
INTRINSIC COMPONENT OF POSTSYNAPTIC DENSITY MEMBRANE	45	0.4355008	1.6334572	0.005769231	0.071079
LEADING EDGE MEMBRANE	162	0.3455267	1.6312724	0.001739131	0.070411
MICROBODY LUMEN	47	0.4227473	1.6272035	0.015817223	0.0703339
MITOCHONDRIAL PROTEIN COMPLEX	231	0.3220201	1.5938754	0	0.0896899
LUMENAL SIDE OF MEMBRANE	27	0.4748172	1.5830117	0.02189781	0.095287
PERIKARYON	138	0.3408767	1.560827	0.001779359	0.1101135
AUTOPHAGOSOME MEMBRANE	34	0.4451662	1.5576953	0.03448276	0.1097418
ENDOSOME MEMBRANE	457	0.2938182	1.5540763	0	0.1107873
TERTIARY GRANULE MEMBRANE	62	0.3842455	1.5539292	0.017730497	0.1084256
MEMBRANE REGION	302	0.3010207	1.5468377	0.00166113	0.1115754
MITOCHONDRIAL MATRIX	433	0.2892639	1.5412025	0	0.1138477
LATE ENDOSOME	247	0.3052208	1.5297364	0.001712329	0.121565
GOLGI CISTERNA MEMBRANE	73	0.3701114	1.5293986	0.019927537	0.1192176
COSTAMERE	18	0.5132681	1.5189967	0.044145875	0.1258061
ANCHORED COMPONENT OF PLASMA MEMBRANE	54	0.3889938	1.5152311	0.018248174	0.1260572
GLIAL CELL PROJECTION	30	0.440245	1.5109177	0.028901733	0.1278259

Table 3.7 KEGG Pathway Gene Set Enrichment in VPS35 KO H4 Cells

The most enriched KEGG pathway gene sets in VPS35 KO H4 cells based on RNA-Seq data, compared to wild-type and VPS35-GFP rescue negative control conditions are presented, ranked by net enrichment score.

Gene Set	Size	Enrichment Score	Net Enrichment Score	NOM p-value	FDR Q-value
OXIDATIVE PHOSPHORYLATION	107	0.542429	2.391558	0	0
LYSOSOME	117	0.535934	2.375552	0	0
CITRATE CYCLE TCA CYCLE	29	0.655882	2.226301	0	7.84E-04
PENTOSE PHOSPHATE PATHWAY	25	0.65907	2.181652	0	8.99E-04
GALACTOSE METABOLISM	21	0.645627	2.018333	0	0.00246
GLYCOLYSIS GLUCONEOGENESIS	47	0.515562	1.972009	0	0.004125
PARKINSONS DISEASE	104	0.452879	1.959036	0	0.004581
METABOLISM OF XENOBIOTICS BY CYTOCHROME P450	37	0.508037	1.841715	0	0.017587
ARACHIDONIC ACID METABOLISM	40	0.49392	1.833832	0.001848	0.016572
BUTANOATE METABOLISM	31	0.525494	1.8249	0	0.01636
GLUTATHIONE METABOLISM	43	0.465663	1.750825	0.00365	0.034399
STEROID HORMONE BIOSYNTHESIS	33	0.493665	1.738689	0.003868	0.035112
PEROXISOME	74	0.416413	1.703001	0.005415	0.04416
AMINO SUGAR AND NUCLEOTIDE SUGAR METABOLISM	42	0.463099	1.69686	0.00367	0.043406
PYRUVATE METABOLISM	35	0.475311	1.678436	0.010619	0.047909
FRUCTOSE AND MANNOSE METABOLISM	31	0.489469	1.67376	0.007407	0.047311
OTHER GLYCAN DEGRADATION	15	0.582113	1.660796	0.013592	0.049806
ARGININE AND PROLINE METABOLISM	46	0.449322	1.659517	0.003591	0.04782
ALZHEIMERS DISEASE	139	0.358805	1.655388	0.001689	0.047192
GLYCOSPHINGOLIPID BIOSYNTHESIS GANGLIO SERIES	15	0.584873	1.650038	0.014981	0.046662
INSULIN SIGNALING PATHWAY	123	0.355762	1.619725	0	0.057548
PROXIMAL TUBULE BICARBONATE RECLAMATION	19	0.528538	1.596535	0.032567	0.065281
GLYCEROLIPID METABOLISM	45	0.414392	1.581234	0.016605	0.070684
PROPANOATE METABOLISM	29	0.453073	1.556386	0.047438	0.082088
GLYCOSAMINOGLYCAN DEGRADATION	19	0.505706	1.534865	0.032755	0.094718
VALINE LEUCINE AND ISOLEUCINE DEGRADATION	43	0.395508	1.47631	0.033088	0.142034
STEROID BIOSYNTHESIS	17	0.494422	1.463788	0.068493	0.149986
HEMATOPOIETIC CELL LINEAGE	61	0.359459	1.455806	0.027027	0.152737
FATTY ACID METABOLISM	36	0.400844	1.436564	0.048598	0.168661

Table 3.8 Ingenuity Pathway Analysis of Upstream Transcriptional Regulators Based on RNA-Seq Data

RNA-Seq data were analysed with IPA software. Upstream regulators were filtered to include 'transcriptional regulators' and are displayed alongside their enrichment in VPS35 KO H4 cells based on the RNA-Seq dataset, and their bias-corrected activation z-score. The z-score is a statistical measure of how likely an upstream regulator is to be activated, based on its downstream effector abundances in the RNA-Seq dataset. A z-score of ± 2 predicts activation or inactivation with high confidence.

Upstream Regulator	Log_2 Transcript Enrichment (VPS35 KO/VPS35-GFP Rescue)	Bias-Corrected Activation z-score	p-value of overlap
SOX7	-0.298	2.13	0.000143
SRF	0.405	1.99	0.00104
HOXA10	-0.06	1.80	0.00881
FOXA1	-0.658	1.50	0.00186
MYOD1	N/A	1.41	0.0000185
CTNNB1	0.238	1.39	1.92E-09
MITF	0.168	1.31	0.000766
TFEB	-0.647	1.20	0.000123
TP63	N/A	1.18	0.00000824
HIF1A	0.25	0.99	0.000295
USF1	N/A	0.97	0.00000071
FOXL2	-0.102	0.94	0.000123
HTT	-0.247	0.94	0.00000345
FOS	1.653	0.93	0.000887
RELA	-0.073	0.92	0.000000459
HNF1B	N/A	0.91	0.000792
CREBBP	-0.438	0.83	0.0000324
WT1	N/A	0.78	0.000532
GATA2	-0.006	0.78	0.000237
JUN	0.039	0.71	0.00191
EP300	-0.091	0.68	0.0000042
SREBF1	0.559	0.63	0.0039
TWIST1	-0.108	0.59	0.00166
Tcf7	N/A	0.54	0.00706
RUNX2	-0.928	0.51	0.00708
CEBPB	0.419	0.49	0.00222
RUNX3	0.173	0.45	0.00248
CEBPA	0.432	0.39	0.000278
IRF1	-0.074	0.36	0.00184
RBPJ	0.501	0.35	0.00146
PRDM1	0.539	0.33	0.00335

SMARCA4	0.104	0.30	1.55E-11
TCF4	0.304	0.25	0.00758
MRTFB	-0.194	0.23	0.00604
NFE2L2	0.042	0.21	0.000242
FOXC2	0.81	0.19	0.000443
EZH2	0.322	0.16	0.00315
NOTCH1	-0.129	0.16	0.000461
SATB2	-0.056	0.15	0.001
GATA4	-0.188	0.10	0.00158
MAFB	-0.173	0.08	0.0000984
MRTFA	-0.138	0.05	0.00417
TP73	-1.169	0.04	0.000324
NFKBIA	-0.006	0.03	0.0000031
NFKB2	-0.134	0.01	0.000246
NKX2-3	N/A	0.01	0.0000104
NFATC2	-0.824	-0.04	0.00175
FOXO3	-0.085	-0.10	0.00003
SPDEF	N/A	-0.11	0.00127
LEF1	-0.458	-0.20	0.000251
OTX2	N/A	-0.25	0.000491
TEAD1	0.187	-0.26	0.0082
PPRC1	0.136	-0.35	0.001
ID2	-0.232	-0.37	0.00524
TFAP2C	0.496	-0.40	0.00767
FOXO4	-0.756	-0.45	0.000000311
SMAD4	-0.337	-0.50	0.000094
SP1	-0.124	-0.53	0.000038
NFKB1	-0.004	-0.57	0.00000309
KLF11	0.153	-0.60	0.00000413
ELK1	0.494	-0.71	0.00535
SMAD3	-0.239	-0.74	0.0000841
MEF2C	0.165	-0.82	0.00000174
GLI1	-0.361	-0.85	0.0093
MYF6	N/A	-0.88	0.000673
PPARGC1A	1.317	-0.89	0.0000251
FOXO1	-0.723	-0.92	6.58E-09
TP53	-0.034	-0.97	0.00000175
HMGA1	0.158	-0.98	0.00000129
GATA1	N/A	-1.08	0.00714
ZBTB16	N/A	-1.18	0.00166
HNF1A	N/A	-1.50	0.00947
HSF1	-0.144	-1.66	0.0018
KLF2	0.637	-1.85	0.00000705
MYCN	N/A	-2.17	0.00541
IKZF1	-0.105	-2.25	0.00499

Chapter 4

Table 4.1 Proteins Identified by HRP-TGN46 Labelling

Proteins that were statistically significantly enriched ($p < 0.05$, Log_2 fold change > 2), or present in ≥ 4 medium samples but < 3 light samples are presented. L = light SILAC condition, M = medium SILAC condition.

Protein Name	Unique Peptides	Coverage (%)	L Abundance	L Repeats	M Abundance	M Repeats	Log2 M/L Fold Change	P-value
TM9SF2	4	23.83107089	21.20041109	4	30.73649168	5	9.739	3.11E-05
GLG1	47	44.86853265	20.29108231	4	29.62557416	5	9.452	1.51E-03
TM9SF4	18	28.97196262	20.29254825	4	29.6500182	5	9.334	9.51E-03
GALNT1	16	44.00715564	20.36122922	4	29.41082513	5	9.256	3.76E-03
FAM20B	16	52.81173594	19.51325364	4	28.50654793	5	9.223	5.49E-04
ALDH3A2	13	29.69072165	19.9868407	4	28.65540743	5	9.101	3.06E-03
COL12A1	103	38.09990206	21.23868933	5	30.32721112	5	9.089	2.71E-05
APP	25	42.33766234	20.27651079	4	28.85981482	5	9.048	3.35E-03
OS9	6	37.02702703	18.95404828	3	27.73289373	5	9.005	2.52E-03
LAMB2	46	32.31368187	19.49948822	5	28.44216393	5	8.943	4.09E-04
MIA3	40	53.1200839	21.35359441	5	30.25197447	5	8.898	4.90E-04
FBN2	46	23.21428571	17.48366924	3	25.84755408	5	8.805	2.32E-02
CLCC1	24	48.27586207	20.3268161	4	29.02937682	5	8.744	3.87E-04
ZMPSTE24	14	28.63157895	20.12820958	3	28.18875123	5	8.703	9.45E-03
BRI3BP	5	19.92031873	20.10980096	5	28.80859686	5	8.699	1.79E-03
PBXIP1	24	39.67168263	21.07860797	3	29.06682088	5	8.698	2.20E-02
COL5A1	42	34.11316649	20.51512187	5	29.13236957	5	8.617	6.01E-05
ITGA5	18	20.67395264	19.80730896	4	28.16410749	5	8.586	6.64E-03
RP5-1119A7	13	25	18.19791999	3	25.72661616	5	8.562	8.63E-03
MANF	15	51.89189189	20.62939221	3	28.90118168	5	8.533	2.98E-03
SCARB1	12	23.37917485	19.54568236	3	27.1432906	5	8.485	2.99E-02
MIA2	29	24.22096317	20.90841668	4	29.24599854	5	8.465	1.68E-02
HSPG2	1	28.30790253	20.70258684	3	27.9553961	5	8.462	2.09E-03
TMED4	9	49.33920705	22.18454452	5	30.6103899	5	8.426	2.65E-04
CACNA2D1	36	41.6137806	20.24246468	5	28.6410017	5	8.399	1.18E-05
BSG	7	22.07792208	19.626491	5	27.86757325	5	8.241	2.94E-06
GOLIM4	2	56.17816092	22.60672213	5	30.83631824	5	8.230	7.68E-05
FAM3C	11	51.10132159	19.38168195	3	27.6193972	5	8.229	1.02E-02
ITGB1	34	41.97994987	24.6264043	5	32.84489123	5	8.218	6.62E-03
AGRN	56	37.23404255	21.01257579	3	28.57503288	5	8.118	4.94E-04
CD44	12	44.59833795	21.18697031	5	29.28458324	5	8.098	1.14E-06
PLD3	9	25.51020408	18.99164946	5	27.04326328	5	8.052	2.51E-04
COL7A1	63	27.64945652	21.89796381	4	29.41249206	5	8.051	3.37E-04
MINPPQ	14	36.3449692	19.62459641	3	27.45889927	5	8.051	1.68E-02
MGAT5	16	27.12550607	19.66187972	3	27.05112003	5	8.024	3.62E-03
HEL-S-99n	30	66.18705036	23.97779242	5	31.98560664	5	8.008	2.03E-04

BST2	5	19.90740741	20.1942013	3	28.25437886	5	7.984	6.40E-05
GALNT7	19	47.18417047	22.93835101	5	30.88277676	5	7.944	4.00E-04
HEXB	21	34.89208633	20.06206887	5	27.99652663	5	7.934	1.43E-04
CCPG1	27	32.62879789	21.29599144	4	29.07540127	5	7.913	3.91E-03
PRKCSH	36	59.06542056	24.8953186	4	32.70789416	5	7.898	1.04E-02
MAN1A2	18	30.57722309	19.23490105	3	27.04101319	5	7.834	2.46E-02
PLOD3	28	39.83739837	22.37311824	5	30.20401529	5	7.831	9.44E-04
NUCB1	25	57.9175705	22.28218103	5	30.08668356	5	7.805	1.38E-05
MESD	14	47.86324786	22.39620102	5	30.19876324	5	7.803	1.96E-04
NCEH1	13	37.5	20.23881083	4	27.38621256	5	7.767	1.27E-03
ADAM10	28	50.53475936	21.91290507	5	29.67325946	5	7.760	5.02E-06
P3H2	26	44.91525424	20.13794297	3	27.78045674	5	7.759	2.12E-02
DSG2	27	33.45259392	19.4795909	4	27.16055666	5	7.757	8.88E-03
HEL117	22	60.04140787	20.60697293	3	27.59650576	5	7.725	2.22E-03
MAN2A1	42	43.44405594	22.4169991	5	30.14046968	5	7.723	1.09E-04
CLPTM1	20	39.01345291	22.05665152	5	29.77791129	5	7.721	2.01E-05
CRELD2	9	32.57790368	20.32133212	4	28.01382007	5	7.709	2.81E-04
ATP6AP1	11	24.46808511	20.52780096	3	27.823191	5	7.697	4.51E-03
LAMB1	63	40.71823204	23.30845087	5	30.91186867	5	7.603	9.85E-04
HSTST1	13	40.16853933	21.09207939	5	28.68118266	5	7.589	1.87E-05
P3H3	10	50.95108696	21.85831639	5	29.44215953	5	7.584	6.77E-03
POFUT1	9	35.05154639	20.45098756	3	26.84454475	5	7.573	1.62E-02
TMEM9	4	25.48076923	18.55193884	4	25.69504381	5	7.532	6.39E-04
CD109	35	28.71972318	21.18284549	5	28.68270457	5	7.500	1.19E-04
ITGA3	19	21.59847764	21.42227922	5	28.91594232	5	7.494	8.57E-05
SELENOF	7	34.54545455	20.59554259	5	28.04080439	5	7.445	7.87E-05
B3GNT6	8	21.44578313	20.06312272	4	26.94717905	5	7.414	9.26E-04
IGSF3	28	30.65326633	18.93193102	3	26.46618102	5	7.411	1.80E-02
L1CAM	37	40.33412888	24.06504606	5	31.45565262	5	7.391	1.82E-06
HEXA	15	30.18518519	21.16359957	5	28.54580982	5	7.382	2.74E-05
VASN	10	20.653789	20.27744632	3	26.94996462	5	7.373	1.90E-02
TMED9	14	47.65957447	25.56009944	5	32.8976077	5	7.338	2.51E-05
FKBP10	29	53.43642612	24.73538896	5	32.07054534	5	7.335	6.53E-05
EXT2	21	34.1997264	20.46600038	5	27.79257663	5	7.327	3.36E-05
SEL1L	24	43.19899244	22.32856471	4	29.31875367	5	7.298	9.54E-05
LRPAP1	29	54.34173669	24.15606913	5	31.45179947	5	7.296	1.31E-04
NUCB2	23	60.47619048	21.70674833	3	28.43396162	5	7.291	2.16E-02
ERP29	18	57.47126437	26.51217696	5	33.80179193	5	7.290	2.85E-04
DNAJC3	22	44.24603175	20.1350458	3	26.82163909	5	7.266	2.51E-02
GCS1	24	34.76702509	21.31911237	4	28.1312868	5	7.265	1.27E-04
MRC2	27	24.67883705	22.21049867	3	27.08870214	5	7.256694016	4.92E-02
CKAP4	47	75.74750831	25.14944678	5	32.40116287	5	7.252	1.62E-05
IGF2R	72	33.48052991	23.47174853	5	30.69425085	5	7.223	2.18E-05
COL4A1	38	38.10665069	20.35390368	3	27.58671256	5	7.216	2.04E-02
LAMC1	56	41.26786824	23.59402934	5	30.80181839	5	7.208	2.94E-05
COL4A2	46	41.29672897	22.40996729	4	29.28271684	5	7.189	3.21E-05

IKBIP	6	52.28571429	24.99449712	5	32.17800313	5	7.184	6.20E-05
NPC1	20	17.61055081	20.81565743	3	27.80770578	5	7.183	9.09E-03
Uncharacterised Protein	4	32.86713287	20.96343107	3	27.43282413	5	7.168	2.67E-03
PCYOX1	22	49.5049505	24.88634401	5	32.05387105	5	7.168	4.59E-05
EMC4	8	53.00546448	22.0561646	4	29.0299977	5	7.148	2.43E-03
CANX	32	50.50675676	26.43700661	5	33.57729823	5	7.140	8.72E-05
TMX1	16	40	22.55617974	5	29.69374544	5	7.138	5.65E-05
SEMA3C	19	32.09054594	20.35930666	4	27.48709993	5	7.130	5.56E-03
PDIA5	23	41.23314066	21.56603285	5	28.65808444	5	7.092	1.03E-02
MLEC	17	53.42465753	23.82369071	5	30.88444462	5	7.061	4.61E-06
FKBP9	4	36.66666667	23.91578838	5	30.97049855	5	7.055	5.43E-05
HTATIP2	12	46.28099174	19.13066905	3	26.02894178	5	7.044	1.77E-02
PIGS	18	39.45945946	22.78031979	5	29.80747387	5	7.027	6.91E-05
CTGF	16	52.43553009	20.21949995	4	26.80045149	5	7.013	1.54E-02
ATP1B1	10	37.95379538	19.54835746	5	26.55469159	5	7.006	2.98E-03
RCN1	28	80.66465257	26.14808386	5	33.15008642	5	7.002	6.05E-05
TMX3	20	41.85022026	23.36049526	5	30.36222719	5	7.002	4.67E-05
FSTL4	29	45.96199525	21.85791488	5	28.85792853	5	7.000	5.99E-05
ADPGK	15	42.05231388	22.59079229	3	29.24299026	5	6.989	7.71E-03
FKBP7	13	42.34234234	20.86798994	4	27.39506126	5	6.965	6.16E-04
ERP70	61	69.6124031	26.44710433	5	33.41102802	5	6.964	8.81E-05
TM9SF3	17	19.86417657	23.7578148	5	30.72000914	5	6.962	2.40E-05
ATP1B3	8	35.84229391	20.25448972	4	25.92901539	5	6.953	4.32E-04
TGFB1	15	45.38461538	21.80330829	5	28.75041984	5	6.947	3.78E-03
PDIA3	1	58.53658537	23.56892629	4	30.08298858	5	6.937	1.04E-03
TMED7	4	36.60714286	24.46411345	5	31.39613331	5	6.932	3.47E-04
SCARA3	15	25.24752475	21.72124896	5	28.65172192	5	6.930	3.06E-05
OGFOD3	4	12.53918495	18.95985876	3	25.30455194	5	6.929	8.12E-03
NPR1	25	29.12346843	19.39238718	4	26.24220663	5	6.908	3.10E-03
PGRMC2	3	22.42152466	17.52298471	3	23.78585108	5	6.902	1.38E-03
NOMO2	4	53.82794002	26.27391963	5	33.13779844	5	6.864	3.13E-05
ECE1	24	32.46753247	22.16169013	4	28.33907753	5	6.847	2.57E-04
WLS	6	18.66913124	19.93247408	5	26.77488744	5	6.842	4.55E-04
CALU	6	73.96825397	26.53276831	5	33.37286185	5	6.840	8.63E-06
EMC1	42	48.33836858	25.53898591	5	32.37409624	5	6.835	2.50E-05
UGGT1	64	52.92604502	26.93943233	5	33.74735319	5	6.808	2.97E-05
CCDC134	8	34.49781659	22.00460468	4	28.41982608	5	6.803	1.05E-03
SLC39A13	3	7.008086253	19.16670804	3	25.96402037	5	6.802	8.31E-03
LMAN2L	11	34.1954023	21.68201376	3	28.07209937	5	6.798	3.57E-03
ERP44	17	51.23152709	25.22525661	5	32.01178686	5	6.787	2.21E-05
MSRB3	6	44.79166667	19.49190851	3	26.0928005	5	6.776	1.38E-02
MAGT1	10	22.88828338	23.39556464	5	30.16307096	5	6.768	2.62E-03
ATF6	2	28.65671642	20.93113964	5	27.67197793	5	6.741	1.63E-04
TMEM43	24	63.75	25.39450245	5	32.13503027	5	6.741	8.64E-06
BCAP31	3	40.24390244	22.56810974	4	28.53419302	5	6.734	3.10E-03
EMC2	12	46.12794613	23.47534896	5	30.19631654	5	6.721	6.13E-05

NUP210	51	33.49231585	24.92448396	5	31.64467246	5	6.720	5.35E-05
CCDC47	25	50.31055901	25.14494773	5	31.85606008	5	6.711	8.85E-05
HEL-S-269	35	71.08910891	28.34912993	5	35.03370787	5	6.685	1.20E-05
SDF4	2	43.64640884	23.44476722	5	30.11815706	5	6.673	8.67E-06
P4HB	2	73.81889764	28.23969327	5	34.89787242	5	6.658	4.78E-05
ADAM17	25	38.59223301	21.5152383	5	28.1720207	5	6.657	3.49E-05
TXNDC5	23	54.16666667	27.2273168	5	33.8694084	5	6.642	7.95E-05
FBN1	82	38.38383838	23.69595959	5	30.32456757	5	6.629	8.18E-03
TMED2	6	30.84577114	20.66663663	3	27.25224938	5	6.604	4.19E-03
MAN1B1	19	38.62660944	23.27337348	4	29.66889845	5	6.577	5.91E-04
TMED10	14	48	26.06459778	4	32.18337639	5	6.575	3.47E-05
ERO1A	20	53.41880342	25.379452	5	31.93818147	5	6.559	1.08E-04
ASPH	29	56.46437995	27.61712395	5	34.16001695	5	6.543	5.29E-05
GALNT2	42	66.72504378	27.68087351	5	34.2195334	5	6.539	5.09E-06
DNAJB14	11	30.07915567	20.72861101	3	26.31574483	5	6.535	1.72E-03
GUSB	7	24.57757296	22.01187809	5	28.54398398	5	6.532	3.70E-05
SEC63	35	49.21052632	24.18624009	5	30.70241667	5	6.516	7.13E-06
P4HA2	24	50.5952381	24.35480013	5	30.86963762	5	6.515	4.14E-06
CD97	11	15.92814371	21.75146899	3	26.28480192	5	6.512605645	3.15E-02
QSOX2	19	31.51862464	21.66600502	3	26.4445711	5	6.500327973	4.50E-02
P3H1	27	47.14673913	25.45622328	5	31.95140335	5	6.495	2.57E-06
SIL1	16	34.70715835	22.98914625	5	29.48418937	5	6.495	5.70E-05
KDELC1	20	47.41035857	21.58322543	4	27.9421371	5	6.476	2.23E-03
PON2	6	39.2	21.97124954	5	28.42238654	5	6.451	3.00E-04
PLOD2	3	50.78236131	26.92445281	5	33.36004461	5	6.436	2.95E-06
B4GALT1	9	35.1758794	22.16173698	5	28.59409667	5	6.432	3.59E-05
EMC3	5	28.73563218	22.61863335	5	29.03022696	5	6.412	3.58E-07
UGGT2	59	40.50131926	24.26533229	5	30.67273441	5	6.407	3.58E-05
PDIA6	27	59.54545455	27.64735155	5	34.05137056	5	6.404	2.63E-05
CTSC	1	28.72570194	20.59792996	3	25.74022861	5	6.400	1.72E-02
SDF2	6	40.75829384	21.73223153	4	27.94551697	5	6.394	5.81E-03
VMA21	3	34.65346535	20.80576397	4	26.77316923	5	6.385	1.25E-02
GPAA1	15	23.0273752	23.48486026	5	29.85209548	5	6.367	1.07E-03
SPCS2	14	58.14977974	23.23100901	5	29.58899038	5	6.358	7.48E-06
LMAN2	14	35.6741573	23.98502044	5	30.34236908	5	6.357	1.32E-05
PGRMC1	7	42.56410256	18.64019555	3	24.48405487	5	6.355	4.31E-04
EDIL3	17	44.375	21.10545751	5	27.43313763	5	6.328	8.50E-04
HYOU1	16	57.15715716	27.56629564	5	33.89306297	5	6.327	1.18E-05
TMED3	5	17.51152074	22.25434629	3	27.96126478	5	6.326	6.82E-04
ITGA11	28	24.49494949	22.2565576	5	28.57446974	5	6.318	3.12E-04
COLGALT1	29	40.83601286	24.80867206	5	31.12018219	5	6.312	1.83E-04
TMED5	7	26.20087336	22.16271108	4	27.77920474	5	6.311	2.25E-04
CHST14	15	45.21276596	23.36347273	5	29.66999297	5	6.307	1.10E-04
HLA-C	3	31.96721311	21.31297406	4	27.26225889	5	6.303	1.56E-03
EOGT	17	31.11954459	21.68019292	4	27.82992577	5	6.303	1.63E-04
TOR1B	12	39.28571429	22.69960115	4	28.58464593	5	6.300	4.47E-05

LMAN1	2	49.80392157	27.57527498	5	33.86417783	5	6.289	4.44E-06
COX4NB	11	60	22.06878668	5	28.34358902	5	6.275	1.08E-04
CHSY3	31	44.33106576	22.13842629	4	28.43388623	5	6.268	1.39E-03
UCC1	7	23.54651163	19.78166259	4	25.87662871	5	6.268	3.34E-04
GANAB	10	52.7638191	29.94711719	5	36.20901133	5	6.262	1.46E-06
URLC10	4	38.11659193	21.81880913	5	28.07507714	5	6.256	3.07E-05
LOXL2	17	23.64341085	21.28767797	4	26.03385208	5	6.229	3.64E-04
HEL-S-125m	70	75.21793275	31.43109148	5	37.640387	5	6.209	1.47E-05
PXDN	69	56.59229209	25.57558975	5	31.77474036	5	6.199	3.58E-05
MET	32	31.00719424	22.48097303	4	28.33669058	5	6.193	3.79E-05
SLC39A7	3	7.675906183	23.01768484	5	29.20188369	5	6.184	5.64E-05
CNTNAP1	38	34.97109827	24.25602047	5	30.43053196	5	6.175	1.27E-04
TOR1A	13	41.20879121	23.77972077	5	29.92773351	5	6.148	2.88E-05
SEC11L1	8	34.07821229	22.43273184	5	28.56746788	5	6.135	1.87E-04
C15orf24	8	27.5	23.55424298	4	28.94575679	5	6.126	7.38E-05
GGH	12	37.10691824	20.94525714	5	27.05923032	5	6.114	2.03E-05
SIGMAR1	5	20.62780269	26.71608019	5	32.81267371	5	6.097	1.11E-05
CTSD	12	40.29126214	22.11968922	5	27.11033786	5	6.079650077	1.27E-05
SUN2	3	50.13297872	21.80077864	5	27.863213	5	6.062	1.63E-07
RPN1	53	71.16968699	28.60022998	5	34.66238938	5	6.062	5.74E-06
STT3B	20	24.57627119	25.456924	5	31.51190584	5	6.055	3.71E-06
TAGLN2	9	50.75376884	21.05946914	4	26.82099018	5	6.048	3.98E-04
CTSZ	8	28.05280528	21.24224984	4	27.09681194	5	6.037	1.44E-02
LEMD3	28	46.43249177	21.75525029	3	27.30638528	5	6.030	1.27E-03
EMC10	6	12.12938005	22.95159418	4	28.69435451	5	6.010	9.57E-06
CHPF2	27	41.83937824	22.88881434	5	28.89786036	5	6.009	9.63E-06
TXNDC12	8	62.79069767	23.67137399	4	29.4358853	5	6.009	1.06E-04
SSR1	5	29.02097902	25.54913979	5	31.55777143	5	6.009	6.01E-06
TXNRD1	10	21.26348228	18.05289	3	24.07713466	5	6.002	1.00E-02
UGT8	14	28.65064695	21.91734886	5	27.91659153	5	5.999	3.06E-03
PLXNB2	44	42.54624592	24.74420454	5	30.74048357	5	5.996	1.29E-05
PTGS2	23	47.35099338	23.78476565	5	29.7788985	5	5.994	1.22E-04
PRDX4	13	65.68265683	29.79972876	5	35.78529472	5	5.986	9.30E-06
SPCS3	5	22.77777778	24.21990043	5	30.20324787	5	5.983	2.41E-05
NPTX1	16	36.57407407	22.19774128	4	27.83855179	5	5.981	4.48E-04
ITGA6	36	38.2300885	21.31262944	3	27.46493881	5	5.979	1.77E-02
ITGAV	50	52.76717557	25.57817379	5	31.54412267	5	5.966	8.03E-07
PCSK9	16	32.51445087	22.58821571	5	28.54839676	5	5.960	4.54E-04
NGLY1	10	23.24159021	18.06898761	3	23.53826131	5	5.949	2.10E-02
NENF	9	66.27906977	22.0881558	4	28.09449453	5	5.941	3.57E-04
PROCR	4	21.8487395	20.54170052	3	24.00658482	5	5.891	6.35E-04
B3GALT6	12	36.47416413	20.96233358	4	26.63736997	5	5.845	1.87E-04
NCSTN	10	14.66854725	24.82515946	5	30.66969734	5	5.845	4.44E-06
PLOD1	36	60.38514443	26.52261426	5	32.36133933	5	5.839	1.37E-05
C3orf58	16	42.55813953	21.30658605	5	27.13984421	5	5.833	8.93E-04
P3H4	15	42.10526316	24.39380789	5	30.20161132	5	5.808	1.14E-04

TMEM109	5	13.16872428	24.54784881	5	30.34179166	5	5.794	1.02E-06
FUCA2	12	27.40899358	21.89044413	4	27.5438569	5	5.790	1.10E-03
ADAM15	19	29.9185099	22.03400184	5	27.82045497	5	5.786	7.71E-04
MGAT4B	12	21.71532847	19.91377315	5	25.69412885	5	5.780	1.56E-03
FKBP11	4	11.94029851	21.82647632	5	27.60449792	5	5.778	4.19E-05
HLA-C	1	58.01104972	23.11897728	5	28.89100607	5	5.772	4.40E-04
FDFT1	25	62.11031175	25.05331152	5	30.80818785	5	5.755	2.08E-06
MAP4	18	13.53939922	20.66907605	5	26.41139891	5	5.742	1.20E-03
DNAJC16	18	26.08695652	20.58483317	3	26.36403577	5	5.728	4.59E-03
ANTXR1	8	16.31205674	19.96279767	4	25.38195123	5	5.694	8.71E-03
FOLR1	7	29.57198444	24.5382944	5	30.23046167	5	5.692	7.92E-07
P4HA1	3	49.81273408	25.19845025	5	30.88045177	5	5.682	3.62E-03
LAMB3	42	45.98976109	24.21199164	5	29.89288096	5	5.681	1.29E-04
LRRC8A	20	30	20.56276885	3	25.72544436	5	5.663	2.35E-03
BMP1	26	35.69979716	22.5214735	5	28.17900511	5	5.658	1.19E-04
TOR3A	16	53.90428212	22.17408261	4	27.74670187	5	5.636	1.55E-02
HEL-S-89n	76	68.04281346	30.7771317	5	36.40076743	5	5.624	9.94E-06
HLA-A	1	33.97260274	23.10633376	5	28.72107172	5	5.615	3.09E-04
CRLF1	7	43.36492891	23.87617534	5	29.48070945	5	5.605	3.87E-05
TPM3	13	51.20967742	20.72267298	4	26.01238073	5	5.594	5.70E-03
DPY19L1	4	31.14973262	23.33487816	5	28.90211355	5	5.567	3.50E-04
CHPF	22	35.09677419	23.08196177	5	28.64140612	5	5.559	5.33E-07
C9orf125	11	34.98759305	21.60448553	5	27.11959625	5	5.515	3.57E-03
PIGT	24	36.55172414	25.75247027	5	31.26366569	5	5.511	6.67E-05
ERBB2	13	15.21912351	18.90586131	4	24.41675995	4	5.511	2.65E-04
CERCAM	10	18.31932773	19.51733254	4	25.31237665	5	5.510	1.05E-02
TMED1	6	22.02643172	21.59449294	3	25.75667544	5	5.45612138	3.12E-02
DNAJC10	11	33.03909206	25.29766938	5	30.73965759	5	5.442	2.00E-04
PPIB	14	55.09259259	26.0279596	5	31.46477673	5	5.437	2.12E-05
SLC30A7	9	24.46808511	22.08108875	5	27.47754022	5	5.396	1.80E-05
CD59	3	23.07692308	21.71188848	3	26.60782309	4	5.396	1.02E-02
ATP6AP2	10	30.57142857	24.29044567	5	29.68588756	5	5.395	6.96E-05
SDF2L1	6	22.45557351	23.07137635	5	28.4580573	5	5.387	6.33E-06
SLC39A14	3	9.146341463	21.14227447	3	25.2393555	5	5.360537689	3.30E-02
TMEM131L	25	17.96146675	20.82540166	3	25.48927741	5	5.346	3.43E-03
UNC84A	3	39.42505133	22.89146425	5	28.17736099	5	5.286	6.54E-05
CTNNB1	2	47.89272031	23.39520336	5	28.63575824	5	5.241	1.08E-04
CYR61	19	50.65616798	23.61229407	4	28.55355057	5	5.216	3.14E-03
PPT1	6	21.49253731	21.04501169	4	25.68371721	5	5.208	1.29E-03
TOR1AIP1	3	56.60377358	26.11812698	5	31.31591078	5	5.198	1.83E-05
TMTC3	22	28.41530055	23.12528689	5	28.31546429	5	5.190	9.76E-05
PIGK	16	51.39240506	25.58057109	5	30.74157737	5	5.161	1.00E-04
DNAJB12	18	45.96577017	23.16924281	4	28.22046489	5	5.161	2.65E-03
EGFR	41	43.63636364	25.43605207	5	30.59674455	5	5.161	1.40E-04
EMC9	6	43.26923077	20.47759627	3	25.05920399	5	5.114	1.05E-03
DNAJB11	17	38.26815642	27.10518842	5	32.21794648	5	5.113	1.15E-05

HLA-C	1	24.30939227	22.185344	3	26.2562646	4	5.093	1.05E-02
GLA	11	40.55944056	21.9376043	5	27.02901716	5	5.091	2.17E-04
CA5A	4	15.73770492	18.79511753	3	23.0889067	5	5.085	7.93E-03
DDOST	16	50.21929825	27.57099985	5	32.62614932	5	5.055	1.95E-06
PALLD	17	15.97975416	19.58807109	5	24.64262885	5	5.055	1.18E-02
CPD	39	35	24.54025309	4	28.48238167	5	5.042236181	3.43E-02
ARTS-1	23	28.69287991	22.61512064	4	27.34082439	5	5.013	5.29E-03
CHRNA5	2	3.846153846	18.62208883	3	23.59787283	3	4.976	2.19E-02
GGCX	15	19.92084433	24.08178622	4	28.66255118	5	4.866	4.32E-04
METTL9	7	28.93081761	20.8881331	3	24.72545489	5	4.828	1.31E-02
hCG_30600	2	11.11111111	20.35049149	3	24.98883741	4	4.806	1.51E-02
TMEM131	28	21.03027084	23.09891448	5	27.88341706	5	4.785	4.02E-05
HSPH1	5	35.8974359	22.21675342	5	26.97667704	5	4.760	9.46E-04
WNT5A	16	45.66929134	23.27544382	5	28.03108525	5	4.756	3.27E-05
OSTC	3	19.46308725	21.74159302	4	26.01197729	5	4.743	9.89E-04
ERGIC3	15	29.47103275	26.14581346	5	30.87198334	5	4.726	4.24E-05
HM13	9	24.66843501	21.80240931	5	26.5285191	5	4.726	2.10E-05
CXCR4	3	7.328605201	20.39109075	5	25.09529342	5	4.704	3.58E-05
ATP1A1	29	39.39393939	24.61417338	5	29.31374163	5	4.700	7.41E-05
NEU1	7	19.03614458	21.69568888	5	26.38372946	5	4.688	5.54E-03
TFRC	42	56.18421053	28.96641315	5	33.64903103	5	4.683	4.76E-04
IGSF10	49	25.23827678	23.32934556	5	27.97731119	5	4.648	3.89E-04
LPCAT3	8	15.19507187	21.82755962	5	26.47508009	5	4.648	3.62E-04
TMEM201	11	18.16816817	20.22426815	5	24.87115542	5	4.647	3.96E-03
CAV1	3	51.12359551	22.13149119	5	26.77653762	5	4.645	2.29E-05
B3GAT3	9	37.53665689	23.73888783	5	28.33896173	5	4.600	6.88E-06
TGM2	14	27.21979622	20.52178724	4	24.6316681	5	4.585	6.88E-03
MYH9	57	38.87755102	22.36885566	5	26.94722377	5	4.578	2.31E-03
ERGIC1	13	50.68965517	27.65216822	5	32.22049364	5	4.568	1.13E-05
NME3	7	55.62130178	21.43084985	4	25.92127146	5	4.564	2.74E-03
STT3A	20	24.53900709	27.44638388	5	31.97389698	5	4.528	9.61E-04
SREBF1	16	20.48823017	20.87231126	4	24.97424259	5	4.508	2.86E-03
TMEM165	6	22.83950617	23.76590746	5	28.25227312	5	4.486	2.29E-03
NRM	6	23.28244275	20.91613925	4	24.84121647	5	4.478	1.22E-03
RTN4	1	12.66778523	24.47104028	5	28.93072244	5	4.460	9.08E-04
LPL	14	30.52631579	24.36169944	5	28.81409221	5	4.452	7.36E-04
CRTAP	19	53.6159601	27.78441015	5	32.21555034	5	4.431	7.07E-04
EWSR1/ATF1 fusion	1	6.145251397	17.77343964	3	21.36873877	4	4.395	2.40E-02
PTDSS1	8	23.67864693	23.28400166	5	27.67361586	5	4.390	5.65E-05
BQ8482_630002	2	3.50140056	21.76263314	4	26.11357078	4	4.351	3.63E-04
TOR1AIP2	24	60.21276596	24.96649634	5	29.31641476	5	4.350	2.57E-05
UBA1	12	15.50094518	19.58312951	3	23.91775234	3	4.335	7.36E-03
ULBP2	3	27.98165138	22.45760467	4	26.40086962	5	4.331	8.11E-03
MYOF	45	28.72392043	21.00814851	5	25.33112139	5	4.323	4.35E-04
NEMP1	6	13.06306306	20.99569993	3	24.1429368	5	4.321	2.90E-02
HLA-B	1	33.14917127	21.12868865	3	23.34035798	5	4.304	7.50E-03

SEMA3B	13	21.58365262	20.80906577	3	22.8613227	5	4.292	5.61E-03
TTC17	12	31.63891323	24.99614887	5	29.27917557	5	4.283	3.58E-06
SURF4	5	17.84386617	24.95168836	5	29.22264535	5	4.271	2.53E-04
TTC13	28	37.90697674	23.71867652	5	27.97986975	5	4.261	5.44E-05
ADGRG1	13	22.7994228	24.28422008	5	28.54425769	5	4.260	5.85E-04
ERLIN2	15	48.67256637	26.85800712	5	31.08509155	5	4.227	2.12E-04
SLC33A1	8	16.21129326	22.54554493	5	26.771736	5	4.226	2.81E-04
HLA-A	2	42.19178082	24.84408752	5	29.05110753	5	4.207	2.42E-05
GPX8	1	28.70813397	26.54115514	5	30.72745707	5	4.186	5.08E-06
PRDX3	6	24.21875	20.10458915	4	24.18525066	5	4.185	6.57E-03
CSPG4	43	25.45219638	22.51541073	3	25.63212756	5	4.114	2.09E-02
TMEM87A	6	11.89189189	21.06482155	4	24.47315645	5	4.111	4.58E-04
RTN3	6	35.59322034	24.71987066	5	28.82873378	5	4.109	1.35E-04
OLFM1	7	17.5257732	22.10900489	3	25.09646669	5	4.099111764	3.19E-02
DDX1	21	36.21621622	23.43690246	5	27.50784485	5	4.071	7.72E-04
LGALS3BP	19	38.63247863	26.77931911	5	30.84709021	5	4.068	3.76E-06
CLPTM1L	1	20.26022305	25.06261917	5	29.11970533	5	4.057	1.03E-04
SLC35B2	8	19.90740741	24.36283699	5	28.41839399	5	4.056	4.39E-04
RPN2	16	45.95879556	27.31791463	5	31.37037895	5	4.052	7.27E-03
PCCA	41	56.04395604	27.09540612	5	31.13012031	5	4.035	2.54E-04
QPCTL	11	27.48691099	23.33867002	5	27.36500569	5	4.026	8.37E-05
TMEM41B	4	15.46391753	22.09476406	4	26.07516699	5	4.023	9.89E-04
DKFZp686D20222	4	38.98071625	22.69043346	3	26.17660972	5	4.011	6.92E-03
Uncharacterised Protein	11	21.25603865	23.93802019	5	27.94359194	5	4.006	2.11E-04
CHID1	6	13.87665198	22.03777503	3	24.55901457	5	4.004	1.79E-02
TMEM214	22	36.28447025	24.9415494	5	28.90787927	5	3.966	7.78E-04
LMF2	9	16.54879774	25.16801943	5	29.12521518	5	3.957	7.95E-05
KIRREL1	12	21.2681638	20.60115153	3	24.01706513	5	3.935	2.96E-02
KDELR3	3	12.14953271	20.79129913	3	23.82796031	5	3.935	1.28E-02
THEM6	10	37.98076923	22.54188409	5	26.47291546	5	3.931	1.09E-04
HNRPK	8	24.78448276	21.16516744	4	24.61891954	5	3.905	3.09E-03
SERPINE2	19	45.84382872	22.71986164	5	26.61902598	5	3.899	9.31E-04
GLT8D1	12	38.27493261	22.86292391	5	26.75771165	5	3.895	5.58E-04
HLA-A	2	11.5727003	24.30862644	4	26.78527656	5	3.880	5.83E-04
ACLY variant protein	43	45.82233949	26.3277654	5	30.19840189	5	3.871	2.02E-04
PCCB	24	50.52631579	24.33556705	5	28.19337148	5	3.858	8.04E-04
PRSS21	12	43.94904459	27.2452039	5	31.09123415	5	3.846	3.14E-05
NDC1	17	32.34421365	22.67634668	5	26.50745966	5	3.831	3.18E-03
TNLG5A	4	19.29133858	20.04606887	4	23.86227981	4	3.816	1.58E-02
ATP5PO	6	35.21126761	21.78500181	4	25.23055395	5	3.813	3.24E-03
KCTD12	8	28.92307692	18.83279971	3	22.08079081	5	3.811	2.21E-03
AXL	18	28.18791946	23.60048062	5	27.4046123	5	3.804	1.81E-04
S100A4	3	27.72277228	19.53876678	3	23.30547107	3	3.766704295	3.40E-02
EPHX1	13	34.72527473	21.24870086	4	25.16710708	5	3.756	1.76E-03
RER1	4	27.57009346	24.09283704	5	27.84722054	5	3.754	2.23E-04
SERPINE1	12	35.32338308	22.07866315	4	25.38044737	5	3.724	2.34E-03

PTPRF	14	35.44834819	24.02721278	5	27.74668837	5	3.719	6.19E-04
MCCC1	35	61.37931034	27.15881111	5	30.86162159	5	3.703	2.84E-05
ALG3	4	7.99086758	23.11260085	5	26.81488104	5	3.702	1.63E-03
TGFBI	33	58.12591508	29.21872195	5	32.89282363	5	3.674	7.95E-04
ALG11	4	8.536585366	19.82601504	4	23.68211448	5	3.666	4.37E-03
ARL6IP6	3	14.15929204	19.89978544	3	22.82506998	4	3.637	6.19E-03
SPFH1	15	52.01149425	25.70782929	5	29.31809121	5	3.610	1.93E-04
SERPINH1	28	65.55023923	31.22610431	5	34.81608503	5	3.590	8.66E-05
HACD2	1	4.724409449	21.67921582	4	25.23450154	5	3.574	1.43E-03
YIPF4	3	12.70491803	22.12728987	4	25.69659381	4	3.569	1.88E-03
CLU	25	48.77505568	28.60478694	5	32.15998535	5	3.555	3.35E-04
EBP	3	16.95652174	23.59050837	5	27.14030023	5	3.550	1.65E-03
EEF1B2	2	12.44444444	18.88493383	5	22.41847713	5	3.534	5.24E-03
Uncharacterised Protein	2	23.62869198	21.28119726	5	24.80276133	5	3.522	1.39E-04
GOPC	7	19.04761905	19.7778304	3	22.75661859	5	3.517	1.73E-02
TMEM164	2	8.417508418	20.02171332	3	22.41039622	4	3.512	1.01E-02
FBXO22	6	18.61042184	20.47718966	3	23.12215021	4	3.495	1.12E-02
PAICS	12	30.82352941	20.72937004	4	24.19008106	5	3.475	2.55E-03
UBIAD1	2	5.917159763	20.80883346	5	24.28156184	5	3.473	1.05E-03
LOX	9	28.53717026	23.34350296	4	26.3362301	5	3.465	3.97E-04
GALNS	6	14.36781609	21.5670758	3	23.89481449	5	3.465	2.50E-02
CDC37	4	15.34391534	19.03229786	3	22.15584936	4	3.439	3.56E-03
PPP6R3	11	15.80756014	20.09660599	4	23.51441715	4	3.418	2.69E-02
PRMT1	9	27.76280323	20.92451007	5	24.34058428	5	3.416	2.32E-04
LAG1	6	18.94736842	23.17112226	5	26.58077382	5	3.410	2.85E-03
SSR4	6	36.99421965	26.71376964	5	30.11545412	5	3.402	6.07E-05
CERS6	4	8.333333333	22.4700688	5	25.8302882	5	3.360	3.73E-04
SLC38A1	4	7.952286282	21.9174557	4	24.82840567	5	3.360	5.53E-03
USP48	5	6.570048309	19.65124322	3	22.99383423	3	3.343	3.24E-03
GLRX3	7	22.98507463	20.33726068	3	23.14008563	4	3.342	2.52E-02
SLC35E1	8	25.6097561	22.56141459	5	25.89708835	5	3.336	4.52E-04
CPT1A	11	18.62871928	21.84140533	3	24.62239989	5	3.336	2.89E-02
EDEM3	29	35.19313305	26.32343919	5	29.65366619	5	3.330	8.11E-04
Uncharacterised Protein	6	13.17365269	20.20295059	3	23.50823164	3	3.305	2.66E-03
PCOLCE2	7	19.51807229	20.54331667	3	23.29701492	5	3.299	5.34E-03
MAP1B	14	8.630470016	20.69486582	3	21.51883392	5	3.277152548	4.68E-02
JMJD8	4	9.880239521	22.35975548	5	25.62067668	5	3.261	3.12E-05
MTCH2	6	19.14191419	21.32777362	4	24.57475348	4	3.247	2.07E-04
HTRA1	10	21.45833333	24.59438542	5	27.83623286	5	3.242	1.43E-04
ATP5F1	10	35.9375	22.75389383	5	25.9922922	5	3.238	1.11E-03
RUFY1	10	17.79661017	20.11223226	4	22.4043465	5	3.225	2.21E-02
HTT	36	14.67218332	21.56475226	4	24.78629618	4	3.222	3.07E-03
HACD3	9	16.5	26.12990677	5	29.34599991	5	3.216	1.65E-04
CDKAL1	8	21.76165803	20.93927203	4	23.28778916	5	3.201	1.19E-02
NEDD4L	3	10.25641026	18.94229263	3	21.90053439	4	3.171	2.93E-02
MCCC2	13	49.73357016	26.16254096	5	29.32369373	5	3.161	1.26E-04

DAD1	4	36.28318584	25.16187948	5	28.29992556	5	3.138	9.27E-03
RAB14	5	45.11627907	18.91745314	3	20.65007697	5	3.125	4.97E-05
NAT14	4	23.78640777	18.45476887	4	21.57904439	4	3.124	1.44E-02
SDHB	3	11.07142857	18.10398289	3	20.75692138	4	3.120	3.75E-03
CPSF1	14	10.3950104	21.46574811	3	22.89924088	4	3.105051558	3.24E-02
BAG2	14	63.03317536	26.83236933	5	29.9231376	5	3.091	2.63E-05
HEL2	6	40	20.44588473	4	23.46459313	5	3.062	7.38E-03
KIF5B	18	26.6874351	21.99882514	5	25.05302759	5	3.054	2.26E-03
SRPRB	15	60.88560886	27.53061266	5	30.57602096	5	3.045	1.12E-04
PRDX2	5	31.31313131	22.62473074	4	25.28941382	5	3.045	2.08E-02
RABGAP1	12	13.47053321	19.8841705	3	22.40671122	4	3.044	3.46E-03
TRAM1	6	17.11229947	24.06727	5	27.10092249	5	3.034	4.13E-05
TMEM49	2	5.489260143	22.56070168	5	25.59126023	5	3.031	1.10E-04
OSBPL9	3	4.588394062	19.37776555	3	22.40488	3	3.027	1.98E-02
JAGN1	5	24.04371585	25.96684586	5	28.99331085	5	3.026	4.13E-03
SLC7A11	2	3.992015968	21.631521	5	24.65092291	5	3.019	1.44E-03
SLC38A5	5	10.80508475	24.3324283	5	27.35145283	5	3.019	3.53E-04
PC	59	61.20543294	32.49258197	5	35.50784667	5	3.015	2.30E-05
MPG	3	12.08053691	19.5922414	3	21.65957317	4	2.99939258	3.79E-02
SRPRA	22	37.46081505	25.86065393	5	28.84348195	5	2.983	6.11E-04
C16orf58	12	32.90598291	23.91321831	5	26.89161414	5	2.978	4.70E-04
ERGIC2	16	54.52196382	26.72161008	5	29.69490773	5	2.973	1.28E-04
ABCE1	9	15.19198664	20.89299063	5	23.84448532	5	2.951	1.37E-03
AIP	3	10.32608696	20.83475289	3	21.90688935	5	2.941	7.42E-03
HEL164	3	11.18012422	19.95105226	4	22.88981901	4	2.939	3.52E-03
CYB5R3	5	24.58471761	20.70656418	5	23.6394362	5	2.933	7.91E-04
TAP1	9	17.45049505	22.47590696	5	25.4002462	5	2.924	3.52E-03
CHORDC1	7	28.31325301	20.50287164	3	22.80896739	4	2.919	1.42E-02
SLC7A5	5	16.37080868	28.15772214	5	31.06942757	5	2.912	1.27E-04
FADS2	11	28.6036036	25.87149206	5	28.75938518	5	2.888	8.25E-04
PPP2R2A	5	12.52796421	20.37850684	4	23.26229298	4	2.884	3.79E-03
SLC3A2	25	54.76190476	29.80471109	5	32.6873177	5	2.883	6.44E-05
CACYBP	8	34.21052632	21.1315675	4	24.01153395	4	2.880	5.41E-03
KIAA0690	23	25.44333076	22.74247258	5	25.61122171	5	2.869	5.74E-03
KDELR1	2	14.1509434	21.26355967	4	23.43708792	5	2.861	2.54E-04
LPCAT2	9	19.11764706	20.71428117	4	23.56907095	4	2.855	1.51E-03
UTP20	42	18.13285458	24.2819739	5	27.12468937	5	2.843	9.08E-04
RRM1	14	22.22222222	22.50184735	4	24.89874814	5	2.839	5.08E-03
GTF3C1	22	13.41868184	21.69977327	5	24.52837121	5	2.829	4.23E-04
SEC24C	9	10.23765996	21.07009675	5	23.88662324	5	2.817	3.26E-04
RAB34	5	24.32432432	20.01044883	5	22.82501104	5	2.815	2.16E-02
PHGDHL1	11	40.11627907	21.97674725	5	24.78817121	5	2.811	2.42E-04
CCT8	5	10.58394161	20.2318436	4	23.03426023	4	2.802	2.72E-03
Uncharacterised Protein	5	28.19148936	24.01292863	5	26.80848941	5	2.796	2.64E-04
EEF1D	10	48.04270463	21.83142212	5	24.62689134	5	2.795	5.03E-03
FAM62A	1	26.48114901	22.56318588	4	24.70938726	5	2.795	2.07E-02

NME1	1	53.28947368	20.34374406	3	23.13751087	3	2.794	6.75E-03
ACACB	12	25.91537836	22.75257166	5	25.26229457	5	2.779988068	3.53E-02
MSMO1	4	15.01706485	22.92717649	4	25.08808028	5	2.778	5.56E-03
LPCAT4	7	18.51145038	19.68668368	3	21.64479199	4	2.767	4.98E-03
DHX15	18	23.77358491	23.17723017	5	25.91937628	5	2.742	2.12E-02
STRAP	12	43.71428571	22.69174352	5	25.43074984	5	2.739	8.31E-04
TAP2	10	15.05681818	21.79855901	4	23.82964715	5	2.730	1.75E-02
EI24	3	9.411764706	21.34919672	3	23.01219742	4	2.728	5.08E-03
GPR89B	5	12.91028446	22.82430096	5	25.54703043	5	2.723	9.14E-05
CHP	11	59.48717949	22.41350042	5	25.1306753	5	2.717	3.58E-05
CYP51A1	9	20.62868369	22.23604168	5	24.95177251	5	2.716	1.63E-03
SCRIB	10	8.277945619	20.21373413	3	22.28348655	4	2.715	1.07E-06
ELOVL5	2	12.04013378	22.27883667	4	24.98210701	4	2.703	4.44E-03
TTC26	7	16.78700361	20.77264371	3	22.05242958	3	2.702273951	3.57E-02
NCLN	11	44.93783304	28.32855211	5	31.02387648	5	2.695	1.00E-03
HSPC163	1	14.38848921	21.78240416	4	23.65021847	5	2.690	2.07E-03
DOLPP1	2	8.403361345	19.90016969	3	22.54955916	3	2.649	1.48E-02
GTF3C3	12	17.83295711	21.1235083	5	23.76877429	5	2.645	2.63E-03
SLC16A3	6	13.11827957	24.74422442	5	27.38769488	5	2.643	6.89E-03
NDUFB9	4	35.19553073	20.17227137	4	22.06171675	5	2.643	2.63E-02
SEC22B	9	39.06976744	25.19506784	5	27.83252585	5	2.637	2.27E-04
EEF2	32	41.49184149	27.14570028	5	29.77641488	5	2.631	5.31E-04
ALG12	2	3.893442623	20.87490645	4	23.50065867	4	2.626	2.71E-03
ARHGAP21	10	7.56259581	19.51765006	4	21.68426783	5	2.585	8.54E-03
ARFGEF1	9	13.57490535	20.13997472	3	21.76013519	5	2.570603416	4.68E-02
THADA	23	14.43932412	21.96842658	4	24.52331994	4	2.555	1.88E-03
LANCL1	1	2.919708029	19.83349376	5	22.3685884	5	2.535	8.44E-04
MEST	4	14.02985075	24.91779412	5	27.45260805	5	2.535	1.14E-04
ABCC1	25	19.85630307	23.99523871	5	26.49946448	5	2.504	8.47E-04
HSPBP1	7	22.00557103	21.07739592	5	23.57899469	5	2.502	7.93E-04
ATR	42	20.42360061	24.01954989	5	25.9726433	5	2.495699861	4.99E-02
Uncharacterised Protein	5	36.36363636	20.71111753	5	23.08022785	5	2.490257578	4.34E-02
DHX36	24	31.34920635	23.36189022	5	25.83785428	5	2.476	9.84E-03
HEL-75	4	11.49425287	21.45290856	3	23.92867848	3	2.476	6.42E-03
PSMG1	4	16.66666667	20.5428312	5	23.01733508	5	2.475	9.47E-04
MBOAT7	7	17.37288136	25.41910172	5	27.89180509	5	2.473	3.92E-04
R3HDM1	3	3.366696997	19.45203794	4	21.924228	4	2.472	1.00E-02
PRPF19	4	11.50793651	21.11242473	4	23.58023005	4	2.468	5.48E-03
MAT2B	3	10.17964072	17.96082154	3	20.83489599	5	2.463	2.86E-02
TBC1D4	15	14.63790447	22.75297001	4	24.28159424	5	2.460	1.83E-03
RHBDD1	3	13.96825397	21.07197051	4	23.52785964	4	2.456	1.07E-02
MGST1	4	27.09677419	25.77367584	4	27.75708715	5	2.450	5.20E-03
RCE1	2	16.71732523	21.52849071	4	22.77354088	5	2.444	1.14E-03
RECQL	7	12.78890601	21.14111596	4	23.58379962	4	2.443	6.21E-03
LRRC54	5	19.54674221	21.89933074	4	23.51725464	5	2.441	1.59E-02
ZZEF1	26	11.55015198	22.26486458	4	24.70027847	4	2.435	3.16E-03

ATM	36	14.82329843	23.29183404	3	24.2592062	4	2.428	2.41E-02
HEL-S-271	20	57.2778828	26.37799026	5	28.80456449	5	2.427	1.17E-02
TMPO	12	37.31988473	23.47094231	5	25.89058444	5	2.420	1.56E-02
BZW2	8	25.05966587	22.53226294	5	24.95145359	5	2.419	1.74E-03
ADSL	6	13.42975207	20.97187994	4	22.56046537	5	2.410	1.44E-02
RPL19	4	17.34693878	25.89552754	5	28.29849445	5	2.403	2.28E-04
TUT7	14	14.24749164	21.56718879	3	23.17955481	4	2.397	3.42E-03
SLC27A3	7	13.31689273	20.1334459	5	22.52280961	5	2.389	9.47E-03
TMEM38B	3	15.12027491	22.6489409	5	25.01874415	5	2.370	3.99E-05
THBS1	27	44.78632479	27.2253308	5	29.59220524	5	2.367	3.99E-03
DRG1	8	31.60762943	22.19519383	5	24.55906868	5	2.364	4.30E-05
Uncharacterised Protein	1	16.69902913	22.19579374	5	24.55724745	5	2.361	1.25E-03
KIF2A	5	6.451612903	19.74481867	4	22.10286667	4	2.358	3.89E-04
ATP2A2	27	37.14011516	28.75161714	5	31.10508194	5	2.353	4.28E-04
ZC3H11A	7	17.16049383	21.24633829	3	22.6385726	4	2.352	5.38E-03
SC5DL	3	7.692307692	22.05639311	5	24.39870895	5	2.342	1.04E-03
MRPS22	7	19.16666667	21.11544347	4	22.74226896	5	2.338	2.77E-02
NME1-NME2	2	45.89041096	23.84945811	5	26.17121558	5	2.322	2.16E-03
YWHAB	4	39.83739837	20.02438502	4	22.34399601	4	2.320	2.75E-02
RUVBL1	7	21.49122807	21.48781684	4	23.7921242	4	2.304	1.03E-02
SEC61A1	5	22.19917012	28.58675149	5	30.8883559	5	2.302	4.49E-05
JUP	21	47.38255034	25.20808668	5	27.50528173	5	2.297	2.09E-02
NF1	25	10.6727721	23.12716614	4	24.31804652	5	2.285	9.85E-03
CLIC1	7	33.60995851	20.70902305	4	21.8120624	5	2.285	4.75E-03
FANCA	9	7.835051546	19.07656172	4	21.34859184	4	2.272	8.55E-04
SACM1L	9	17.20613288	22.11368669	4	23.87544159	5	2.265	1.13E-03
GSTM3	7	36.44444444	21.94925742	5	24.21134111	5	2.262	3.16E-03
GPS1	5	11.20162933	21.35141927	4	22.00601305	5	2.261660875	3.82E-02
SLC35A2	1	2.709359606	21.54143569	4	23.79715873	4	2.256	5.64E-04
LTN1	21	14.55266138	22.51119486	5	24.76400794	5	2.253	1.26E-02
CLN6	2	10.28938907	22.65366962	4	24.39073372	5	2.250	6.86E-03
USP34	21	7.952622673	22.0412491	3	23.0257346	4	2.24077778	4.99E-02
RANBP6	10	15.47511312	20.88320915	5	23.11553592	5	2.232	7.18E-04
SPTLC1	15	30.23255814	23.93719632	5	26.16607995	5	2.229	5.93E-05
STOM	12	53.81944444	27.03198717	5	29.24994457	5	2.218	1.96E-04
RBBP4	3	19.52941176	22.19403967	5	24.40326541	5	2.209	9.86E-03
RAB21	3	17.77777778	19.28880838	5	21.49606851	5	2.207	6.72E-03
HSPA2	2	22.69170579	22.04622808	3	24.24886332	3	2.203	2.26E-02
PLEKHA5	7	8.030431107	20.93018418	4	22.2632687	5	2.201	3.11E-03
ARFGEF2	15	17.98319328	22.78354063	5	24.9841364	5	2.201	1.06E-03
MRPS12	2	12.31884058	20.53067767	3	22.7240654	3	2.193387732	3.09E-02
CDIPT	4	18.98734177	22.98743889	5	25.17937389	5	2.192	6.53E-04
ALG1	14	35.56034483	25.99055303	5	28.18089434	5	2.190	1.53E-04
ITPR1	48	26.4684554	25.78423342	5	27.94114151	5	2.157	1.62E-04
DDX55	9	18	21.4446242	4	23.00611187	4	2.151619022	4.63E-02
VAC14	6	7.928388747	20.10218399	4	22.25012879	4	2.148	1.55E-02

BRCC3	3	12.97468354	19.16084458	4	21.06195735	5	2.146	3.20E-04
COPA	38	37.33660131	25.70664824	5	27.84667358	5	2.140	1.79E-03
ELAC2	7	10.04842615	22.11478569	5	24.25127163	5	2.136	7.15E-03
RBM4B	2	23.9010989	21.13738427	4	22.79678681	5	2.126	1.37E-02
TSC2	19	16.49142225	21.65035886	5	23.77585675	5	2.125	2.48E-03
SLC37A4	4	13.08203991	20.09662363	4	22.21843516	4	2.122	8.73E-03
hCG_39762	3	6.313645621	21.46358943	4	23.57849164	4	2.115	3.33E-03
ATP2B1	7	19.09836066	23.02525658	5	25.13950319	5	2.114	4.76E-03
XPO6	25	23.91111111	25.89249124	5	27.99868449	5	2.106	2.07E-03
DNAJB4	5	20.63953488	20.75372373	3	21.90063371	4	2.102	8.48E-04
RRAGA	5	16.93290735	21.12865975	3	22.21368338	3	2.102009379	4.84E-02
PTPN12	7	13.33333333	20.07566849	4	21.71292329	5	2.102	2.86E-02
ELP6	2	9.77443609	18.58866766	3	20.69017622	3	2.102	2.28E-02
RAB5C	4	34.25925926	21.87702393	5	23.97808725	5	2.101	4.78E-03
CYP1B1	2	3.683241252	19.59217981	3	21.69053244	3	2.098	2.08E-02
TTI1	13	14.14141414	23.10523047	5	25.20032191	5	2.095	3.53E-03
NUDT4B	4	22.6519337	20.4948642	5	22.58815105	5	2.093	4.61E-03
RANBP1	2	7.913669065	20.49954699	5	22.59217911	5	2.093	4.20E-03
LPGAT1	8	22.97297297	23.60107573	5	25.69317452	5	2.092	2.43E-04
PES1	9	15.30612245	21.75145569	5	23.83983074	5	2.088	1.48E-02
CBX3	5	30.05464481	21.83703161	5	23.92494897	5	2.088	5.55E-04
C1QBP	4	14.89361702	21.05074519	5	23.13819411	5	2.087	1.48E-04
N-PAC	5	12.00716846	21.21189376	4	22.42759227	5	2.085	8.74E-03
KHSRP	10	22.9254571	23.20090628	4	24.5479523	5	2.083	5.91E-03
MADD	16	15.68010076	22.18030769	3	22.02253766	5	2.082	1.37E-02
TRIM28	11	17.7245509	22.04521013	3	22.81340903	5	2.081270885	3.92E-02
GNAI2	4	23.94366197	21.44507825	5	23.52278304	5	2.078	3.21E-03
NAE1	7	17.0411985	20.35733416	4	21.74309375	5	2.074	1.79E-03
MYCBP2	73	20.02992732	25.7811837	4	26.44939058	5	2.069	1.83E-02
FHOD1	12	13.61344538	20.44919565	5	22.51037801	5	2.061	3.16E-03
BOLA2	2	29.06976744	21.44474765	4	23.49706111	4	2.052313464	3.94E-02
COPE	6	22.35649547	21.55019795	5	23.59149936	5	2.041	1.19E-02
MGST3	2	16.26506024	22.54737965	3	24.24724163	4	2.038	2.77E-02
IKBKG	3	9.785202864	19.84442611	3	21.87808853	3	2.034	2.57E-02
SMAD2	6	20.98501071	21.69304665	5	23.72542921	5	2.032	3.84E-03
IPO13	10	13.91484943	22.41799409	4	23.61970544	5	2.032	1.13E-03
NCAPG2	23	22.57217848	25.16258578	5	27.1922251	5	2.030	8.76E-06
FANCI	50	44.65361446	26.23910623	5	28.26646044	5	2.027	6.89E-05
DHCR7	9	19.78947368	28.84360444	5	30.86972879	5	2.026	2.15E-04
PDF	5	25.10288066	21.23633717	4	23.26072986	4	2.024	8.58E-03
PSMC1	4	14.77272727	20.83380585	4	22.85794609	4	2.024	1.85E-02
RNF213	93	21.27092846	23.57786457	5	25.59420346	5	2.016	4.55E-03
LBR	10	15.77235772	24.9356279	5	26.9480128	5	2.012	8.95E-03
RPS12	6	53.78787879	22.61617512	3	23.45826734	4	2.012	4.69E-04
PSMD2	13	19.60569551	22.90382084	5	24.91543449	5	2.012	8.20E-03
NCAPD3	28	20.62750334	24.97704744	5	26.98860161	5	2.012	1.29E-03

ABHD14A-ACY1	2	9.215017065	20.78305494	4	22.97225024	5	2.011	1.89E-02
NPM1	5	20.74829932	24.63324532	5	26.63929606	5	2.006	7.36E-03
C2F	4	18.03278689	20.41764742	3	21.73362567	4	2.00227171	3.09E-02
ALG9	3	5.331753555	N/A	0	21.27099574	5		
GINM1	8	29.09090909	N/A	0	21.64263068	5		
DNER	5	9.633649932	N/A	0	21.83220263	5		
SYT12	6	15.67695962	N/A	0	21.71810792	5		
PPIC	3	14.62264151	21.64553544	1	27.2005872	5		
ENG	13	26.59574468	20.18947608	2	26.71857064	5		
UXS1	13	43.29411765	N/A	0	24.32177656	5		
POFUT2	14	36.36363636	N/A	0	25.14443797	5		
LGMN	6	15.01154734	19.60150102	1	23.32506075	5		
UST	6	13.30049261	N/A	0	23.46591375	5		
APOA1BP	7	28.33876221	19.24268395	1	21.97551933	5		
CREB3L2	7	20.57692308	N/A	0	23.48758559	5		
GOLGA5	35	62.92749658	22.05214243	1	27.10863592	5		
SORT1	11	17.56919374	N/A	0	23.44777561	5		
MCAM	17	30.03095975	20.37847793	1	26.70998338	5		
MIR16	7	22.65861027	19.35525863	2	25.97269897	5		
TGFB2	6	17.87439614	18.87433026	2	25.05148273	5		
COCH	4	6.666666667	N/A	0	20.57367086	5		
CTSL1	7	26.42642643	N/A	0	23.38974136	5		
DKFZp667O055	1	19.35483871	N/A	0	23.56458298	5		
Uncharacterised Protein	6	25.34722222	N/A	0	23.08791612	5		
GALNT3	11	20.06319115	18.58817473	2	26.7542349	5		
LNPEP	29	31.51219512	N/A	0	27.27811885	5		
KIAA0319L	7	8.102955195	N/A	0	23.53234027	5		
PRMT5	6	12.40188383	20.22725319	2	22.40630108	5		
HLA-B	1	6.077348066	20.50129252	2	24.09117522	5		
TIMP1	5	28.01932367	20.29628407	1	24.18241067	5		
MANBA	16	19.78378378	N/A	0	24.6842897	5		
MICAL2	11	7.102708227	N/A	0	21.68549945	5		
RFP2	7	20.39312039	N/A	0	20.68265044	5		
SGCE	3	5.8	N/A	0	23.49165158	5		
SLC29A1	4	12.28070175	N/A	0	21.12505585	5		
TNRC5	11	37.41007194	N/A	0	27.35080119	5		
TPM4	7	26.20967742	N/A	0	21.13754533	5		
ST3GAL2	3	14	N/A	0	22.37365462	5		
BTN3A2	2	21.25748503	N/A	0	21.97561353	5		
SLC38A2	3	9.486166008	N/A	0	21.16029756	5		
C1QTNF6	4	17.62589928	22.00195738	2	23.16019704	5		
IGFBP4	7	31.78294574	18.83231908	2	24.19061814	5		
TMEM2	11	9.906001446	N/A	0	23.89081759	5		
CRELD1	9	26.9047619	N/A	0	21.66629416	5		
C3orf39	9	18.44827586	N/A	0	25.07293155	5		
DAG1	19	30.83798883	20.19800687	1	24.69426674	5		

SORL1	32	16.9828365	18.68818531	1	25.94433593	5		
LOC89944	7	11.32075472	N/A	0	22.37745177	5		
COPS8	3	20.09569378	18.80509268	1	19.80241288	5		
hCG_1640809	3	12.11180124	17.64097114	1	23.17837496	5		
MTA2	5	12.7245509	21.35971897	2	22.16137186	5		
PRCP	7	16.53225806	18.86184341	1	23.37084315	5		
KTN1	36	30.06632277	22.49826696	1	24.76728108	5		
NEK9	7	9.295199183	N/A	0	22.03316181	5		
SPTLC2	15	32.91814947	N/A	0	23.52780555	5		
MMP2	4	8.636363636	N/A	0	21.17783551	5		
DNMT1	7	4.767580453	20.24216681	1	21.84978075	5		
IMPAD1	9	25.34818942	19.08939494	2	25.04428071	5		
CHST12	8	20.53140097	N/A	0	22.48334081	5		
ITGB4	39	29.79452055	18.12319596	1	25.53533131	5		
CANT1	16	45.63591022	23.94479319	1	25.38233483	5		
hCG_40889	20	20.55239643	N/A	0	23.93339318	5		
MTDH	7	16.66666667	22.36628379	1	22.14556969	5		
DPY19L4	8	11.61825726	N/A	0	24.45898805	5		
NOV	9	31.93277311	N/A	0	22.38376078	5		
B4GALNT1	1	24.95309568	N/A	0	25.91479693	5		
FURIN	9	12.84634761	N/A	0	22.80001869	5		
PTDSS2	3	8.829568789	N/A	0	22.95807009	5		
CD151	3	9.881422925	N/A	0	23.7989244	5		
TPST1	14	40.54054054	N/A	0	26.23561837	5		
TMCO3	4	6.499261448	N/A	0	23.34009402	5		
CPVL	7	19.32773109	N/A	0	21.86903365	5		
SELENOT	5	31.28205128	N/A	0	23.66654811	5		
FAT1	74	18.5620915	26.05775334	2	27.16001562	5		
ABCA2	21	14.15247364	20.40941463	1	23.87952524	5		
NOMO1	2	50.43409629	N/A	0	25.36041102	5		
HECTD1	10	5.547054323	N/A	0	21.19540052	5		
FKBP14	9	40.28436019	N/A	0	25.12586279	5		
TAPBP	5	14.48412698	19.82748123	2	24.97677001	5		
TCTN3	8	15.84	20.15767128	2	25.2849526	5		
PVR	7	20.14388489	N/A	0	24.41196241	5		
EFEMP1	12	27.78904665	N/A	0	26.80849871	5		
ECM1	13	24.07407407	18.34060966	2	23.95060244	5		
TENM3	29	14.48684698	19.81370633	2	23.97560612	5		
SARAF	10	39.5280236	18.60805681	2	25.53735572	5		
HSPA4L	13	26.340882	N/A	0	24.22181822	5		
HLA-B	2	20.44198895	20.21794369	2	23.05573738	5		
GRAMD1B	16	23.71721779	N/A	0	24.69944482	5		
PIGN	7	8.762886598	23.12024984	1	23.56981093	5		
GXYLT2	6	13.09255079	22.9455197	1	22.94002347	5		
ROR2	6	8.271474019	N/A	0	21.97937074	5		
GGT7	10	19.18429003	18.95621172	2	24.9857612	5		

C5orf51	5	23.46938776	20.59560264	2	21.21349612	5		
VKORC1L1	4	21.59090909	19.86029781	2	23.50274216	5		
NPR3	7	14.41774492	18.42139465	2	23.72568881	5		
MPZL1	3	28.2527881	19.52876287	2	25.74685506	5		
MAN2B1	11	13.35311573	N/A	0	23.44976689	5		
IL1RAP	7	11.57894737	20.53966007	1	22.66917052	5		
FUT8	10	17.73913043	21.41270115	2	25.31503665	5		
COL4A6	8	6.209724663	17.82934647	1	21.32643907	5		
CD55	9	28.6036036	N/A	0	25.64651985	5		
Uncharacterised Protein	14	34.21633554	18.24487768	2	28.28120729	5		
CERS5	1	9.743589744	N/A	0	20.6058629	5		
HIF1AN	3	10.96605744	N/A	0	19.52426576	5		
Uncharacterised Protein	3	21.63461538	19.27767781	1	20.22582006	5		
ENTPD6	6	16.56050955	N/A	0	22.25511239	5		
DNAJC10	2	30.70017953	N/A	0	19.56189429	5		
SUMF2	0	37.5	N/A	0	23.0968831	5		
CLSTN3	3	4.60251046	N/A	0	20.41837999	5		
GNS	12	21.06164384	20.45261714	1	27.38731819	5		
TM9SF1	10	13.37423313	21.35497963	2	26.75181555	5		
AIF1L	1	10.96774194	18.06878578	1	25.59807851	5		
DNASE2	5	18.89534884	N/A	0	22.15170298	5		
Uncharacterised Protein	1	7.831325301	22.93744248	2	24.44386226	5		
PSAP	19	40.75471698	18.70094408	1	27.44970531	5		
B4GALT4	6	22.09302326	N/A	0	23.91297362	5		
MGAT1	8	19.45031712	N/A	0	23.32489976	5		
DKFZp686E01144	4	4.860392968	N/A	0	21.98614757	5		
Uncharacterised Protein	3	8.478802993	21.27782332	1	24.45785299	5		
ST3GAL4	11	36.39053254	17.24899551	1	25.98240265	5		
IMT2B	5	22.93233083	N/A	0	24.00084371	5		
NECTIN2	3	7.795100223	N/A	0	21.08749522	5		
Uncharacterised Protein	4	18.55670103	N/A	0	19.80290183	5		
STIM2	15	24.45520581	20.15034462	1	24.19457278	5		
Uncharacterised Protein	1	8.26446281	20.9631951	1	21.04477292	5		
AKAP1	7	10.37037037	N/A	0	21.68661666	5		
TK1	7	41.02564103	20.50152237	2	20.65961735	5		
NELL2	5	7.043879908	N/A	0	21.5943541	5		
GLB1	15	26.89655172	20.10685907	2	26.31880751	5		
Uncharacterised Protein	13	15.76253838	N/A	0	26.27223586	5		
CDH13	7	11.97368421	N/A	0	24.09683049	5		
TMEM59	9	27.4691358	20.79561266	2	24.0063453	5		
COL1A1	2	15.70621469	N/A	0	22.64172214	5		
CANX	1	56.25	N/A	0	25.32646089	5		
BCAP29	8	27.80082988	N/A	0	24.31247322	5		
PTPRK	1	25.4076087	17.221763	1	26.73523949	5		
GANAB	3	56.10328638	22.67350905	2	27.73152485	5		
HLA-A	1	7.121661721	N/A	0	21.4028032	5		

FBLN5	7	15.89403974	N/A	0	23.76803269	5		
LAMA4	31	20.75991189	17.2596008	1	26.01023788	5		
LDLR	18	24.97354497	20.28851038	2	26.40316899	5		
SEMA4B	4	4.540023895	N/A	0	22.04066656	5		
MGRN1	7	16.83501684	N/A	0	21.10545094	5		
GRAMD1A	7	13.01115242	19.41504645	2	22.1088804	5		
ADGRE2	2	4.813477738	N/A	0	23.1657148	5		
PLOD2	2	47.62550882	20.4683693	1	26.51700119	5		
PODXL	9	22.22222222	N/A	0	25.91113116	5		
NRP1	1	19.28494041	N/A	0	24.11095585	5		
PLSCR1	3	12.57861635	N/A	0	21.84369725	5		
LAMA5	67	24.62787551	21.45117215	2	27.00255144	5		
PLXNB1	18	11.52224824	N/A	0	22.39284566	5		
ADAM12	2	17.38173817	17.29778331	2	24.53637362	5		
WDR62	3	2.56916996	N/A	0	20.86165873	5		
TGOLN2	7	20.87682672	N/A	0	23.47159679	5		
CA12	3	11.5819209	N/A	0	20.10969315	5		
EXTL3	17	19.80413493	16.96362761	1	25.30783616	5		
PCDH7	11	14.31244153	N/A	0	23.10519482	5		
NRP2	7	9.022556391	20.67775359	1	22.71037334	5		
B4GALT3	5	10.6870229	N/A	0	25.51292516	5		
TSPAN3	2	9.090909091	N/A	0	24.29562649	5		
PLIN3	5	15.66820276	N/A	0	21.31388119	5		
TPST2	8	26.52519894	18.12694672	1	25.00918554	5		
LRP4	13	8.556430446	N/A	0	21.54376652	5		
ATP9A	3	3.342884432	N/A	0	19.89158924	5		
LRP5	21	17.77089783	17.4505446	1	24.67494635	5		
B3GALNT1	5	17.82477341	N/A	0	23.2163067	5		
ATRN	12	9.587123863	N/A	0	24.45716524	5		
DGAT1	6	20.28688525	18.48568357	2	23.04175263	5		
LRIG2	9	11.64319249	N/A	0	22.57038272	5		
ENDOD1	11	27.6	N/A	0	25.51979419	5		
GLCE	15	26.74230146	N/A	0	26.68736773	5		
CLSTN1	17	19.36799185	20.5754794	2	25.56335656	5		
VAPB	1	22.22222222	18.91142662	1	22.61956778	5		
SGPL1	13	25	16.75926044	1	23.34616739	5		
CPSF4	2	33.45724907	20.14300759	1	18.9113111	5		
COL3A1	10	11.45975443	N/A	0	23.3484532	5		
STS	4	7.375643225	N/A	0	22.04287824	5		
COL6A1	13	18.19066148	N/A	0	23.90805231	5		
LAMP2	3	9.512195122	N/A	0	24.73525589	5		
PLS3	10	17.46031746	N/A	0	22.00251271	5		
NID1	21	20.04811548	21.88506093	1	24.27449591	5		
ST6GAL1	3	3.9408867	N/A	0	27.75295681	5		
STMN1	9	51.67785235	21.95305587	1	24.62938654	5		
ITGA2	3	20.99915326	N/A	0	26.06313156	5		

GJA1	5	25.91623037	N/A	0	21.73777566	5		
ITGB5	18	28.2853567	N/A	0	24.61511682	5		
PAM	14	15.93011305	20.73814321	2	26.07874256	5		
CDH2	23	39.73509934	19.2475903	2	27.1695628	5		
TNFRSF1A	3	7.692307692	19.09613679	1	21.77767776	5		
M6PR	4	15.88447653	N/A	0	24.28162596	5		
ENPP1	8	12.21621622	N/A	0	23.42560058	5		
GAL	2	13.00813008	N/A	0	22.6232009	5		
FBLN1	2	28.87624467	21.20511383	1	26.54249966	5		
PTGS1	3	10.35058431	N/A	0	23.82159196	5		
ACKR3	2	7.458563536	19.58803694	1	24.72688614	5		
LAMA1	27	10.66666667	N/A	0	22.68016726	5		
GRN	6	13.32209106	22.36876747	1	25.26536327	5		
EPHA2	19	23.25819672	18.83379642	1	26.41831423	5		
EPHB2	14	18.95734597	N/A	0	24.13846185	5		
COL4A5	6	6.646884273	19.49053744	2	24.63635562	5		
MARCKS	5	34.3373494	N/A	0	19.1782131	5		
CD70	4	27.97927461	18.47761586	1	21.45832019	5		
GPC1	13	32.97491039	22.13828762	1	26.29903828	5		
CTNNA1	21	32.1192053	20.48908508	1	25.11410814	5		
SOAT1	13	26.54545455	18.90404154	2	27.23196694	5		
COL18A1	7	5.701254276	N/A	0	23.34421792	5		
IL6ST	15	20.26143791	N/A	0	23.95344209	5		
BTD	5	11.97053407	N/A	0	20.30623383	5		
GLIPR1	4	17.66917293	N/A	0	23.33289626	5		
HSPA13	12	27.38853503	19.72142335	2	26.69605168	5		
DNASE1L1	2	8.609271523	17.47524781	1	20.51332422	5		
MAN2A2	12	13.2173913	N/A	0	24.67069757	5		
THBS3	6	9.10041841	N/A	0	22.45971096	5		
SGSH	4	9.163346614	17.91446114	1	22.51829823	5		
PLXNA3	30	25.97541422	20.00660958	2	26.48627906	5		
LUM	8	30.47337278	18.08919235	1	25.97030005	5		
NDST1	18	26.98412698	19.4483147	2	26.36158179	5		
CRIP2	3	16.82692308	17.62046968	2	22.31116761	5		
COL4A4	6	5.029585799	N/A	0	24.73839374	5		
EPHB4	7	10.94224924	N/A	0	22.14778436	5		
NAGLU	15	28.53297443	20.65271599	2	25.52170862	5		
GAS1	3	18.55072464	N/A	0	18.91503501	5		
ITGA1	13	10.6870229	20.19075238	1	24.49730088	5		
SEC61B	2	21.875	22.28085481	1	24.82365977	5		
TMEM258	1	10.12658228	N/A	0	21.07846471	5		
CXADR	11	34.79452055	N/A	0	24.79361081	5		
SLC35A1	2	6.528189911	19.39951043	2	23.22179809	5		
REEP5	4	11.64021164	N/A	0	23.4975245	5		
GCNT1	6	14.25233645	N/A	0	23.1786189	5		
PLAUR	7	32.23880597	18.79225174	1	23.41513634	5		

RELA	3	7.078039927	N/A	0	20.96621184	5		
NOTCH2	34	20.88223391	16.2107448	1	27.650327	5		
MST1R	8	7.642857143	N/A	0	21.94143065	5		
APLP2	17	32.24115334	18.46990646	1	25.95946632	5		
LRP1	107	31.33802817	20.82390036	2	28.0740252	5		
SPOCK1	7	17.08428246	N/A	0	24.61181468	5		
ST3GAL1	5	21.47058824	N/A	0	24.06294471	5		
SCAP	15	13.91712275	18.45805969	2	25.41753474	5		
FSTL1	13	40.58441558	20.28368622	2	26.25206071	5		
PTPRJ	19	19.52131638	N/A	0	23.96849448	5		
SEMA3F	2	13.12101911	N/A	0	22.79835629	5		
PTK7	19	21.12149533	N/A	0	25.3759421	5		
MSLN	13	25.55555556	N/A	0	24.05062873	5		
SLC39A6	8	10.06622517	21.00379305	1	24.66263934	5		
ADAM9	6	42.49084249	N/A	0	27.20629089	5		
SQSTM1	4	15.22727273	21.17021059	2	21.72163026	5		
STIM1	18	32.40875912	16.79451744	2	24.76409875	5		
ALCAM	15	30.53173242	N/A	0	26.46138826	5		
LRP8	15	18.06853583	N/A	0	24.10714417	5		
RCN2	15	50.78864353	20.00991146	1	27.29898594	5		
LTBP1	13	10.34282394	N/A	0	23.3647298	5		
PCOLCE	8	27.6169265	19.88273609	1	22.53612031	5		
TSN	5	19.29824561	20.40292184	2	21.78461713	5		
IGFBP7	15	56.38297872	N/A	0	26.5301273	5		
DDB1	14	15	21.72882316	2	23.23348995	5		
TMEM132A	15	21.70087977	N/A	0	23.61914702	5		
LRRFIP1	9	18.44059406	N/A	0	22.19268611	5		
GXYLT1	8	19.54545455	N/A	0	24.09591559	5		
BMP6	5	14.28571429	18.49664228	2	22.99041884	5		
CDON	4	4.817404817	N/A	0	20.05712849	5		
ANO6	8	11.42857143	N/A	0	22.65262942	5		
ITGA7 variant protein	7	6.083333333	N/A	0	22.33095985	5		
MAN2B2	6	8.424182359	17.41540774	2	22.07433572	5		
TMEM259	8	16.93548387	22.28930403	2	25.10420235	5		
FKBP2	7	57.74647887	N/A	0	24.26600488	5		
2 and 96	7	29.47019868	N/A	0	21.35022676	5		
SLC12A2	7	8.333333333	N/A	0	21.42169764	5		
ANPEP	12	15.55783009	N/A	0	21.14162712	5		
SMPD1	4	7.078313253	N/A	0	21.82154216	5		
SLC6A8	2	5.900621118	N/A	0	21.82992538	5		
SLC4A2	9	11.81672026	N/A	0	24.2277829	5		
PIGG	9	11.59715158	N/A	0	24.63473627	5		
FAM3A	6	28.69198312	17.98104992	2	24.63165301	5		
TMEM67	3	3.51758794	N/A	0	21.70748405	5		
HLA-F	7	34.97109827	N/A	0	21.48672469	5		
PPM1L	5	15	N/A	0	22.49287463	5		

MANEA	5	16.23376623	N/A	0	22.16242991	5		
FAM69A	6	16.58878505	21.7087547	1	21.97346435	5		
TGFBR1	7	18.48906561	N/A	0	22.95553231	5		
SGCB	6	21.69811321	17.1409685	1	22.2195105	5		
MANEAL	8	22.7571116	N/A	0	24.57822186	5		
CACHD1	8	7.613814757	N/A	0	22.15909671	5		
GPR107	1	9	N/A	0	21.14660056	5		
WDR25	4	7.720588235	21.28364296	2	23.72840443	5		
OLFML2A	8	15.64417178	N/A	0	25.27839795	5		
SEL1L3	12	13.95759717	15.97666254	2	24.68178881	5		
ATF6B	13	21.47937411	18.79165865	2	26.7363732	5		
STC2	2	6.622516556	N/A	0	20.97468461	5		
SLC39A1	2	5.864197531	N/A	0	21.16288384	5		
CASC4	19	42.26327945	20.69384417	1	26.74778037	5		
TXNDC11	3	23.75634518	18.73010812	2	26.26765605	5		
A4GALT	3	8.71559633	N/A	0	19.7711566	5		
B3GLCT	13	34.53815261	20.75175181	1	26.47338986	5		
MBOAT2	5	15	18.9295128	1	22.26584488	5		
LRRC8D	18	25.05827506	20.48668213	1	24.22647393	5		
CHST3	6	17.53653445	N/A	0	24.24130388	5		
ERMP1	13	16.48230088	17.74616882	1	25.96817927	5		
LYSMD3	5	27.45098039	N/A	0	21.10363849	5		
LRP10	6	11.64095372	N/A	0	24.41111492	5		
P4HA3	10	25.18382353	17.37524258	1	24.38817237	5		
GALNT10	13	29.51907131	N/A	0	25.53268168	5		
GPR180	3	8.181818182	N/A	0	23.15490248	5		
LRP11	7	21.8	N/A	0	24.05610545	5		
CHSY1	19	29.67581047	18.16565647	1	26.35601042	5		
FRAS1	36	11.55189621	22.17127456	1	24.35207767	5		
SULF2	6	7.471264368	N/A	0	21.67785888	5		
KIAA2013	11	23.97476341	19.20446285	2	25.64490831	5		
DSEL	12	12.78877888	N/A	0	24.61371355	5		
CNPY4	11	36.69354839	19.46317688	1	25.45903251	5		
ABHD12	13	33.41708543	17.50201344	1	26.43532002	5		
TMEM106B	8	32.48407643	18.2381197	1	24.19312272	5		
LARGE2	5	7.628294036	23.70349902	1	21.47928098	5		
GALNT4	7	16.0899654	N/A	0	22.02580762	5		
MMGT1	4	49.61832061	20.80695026	1	25.9278984	5		
CSGALNACT 2	12	24.90774908	N/A	0	24.05914461	5		
KRTCAP2	1	12.5	N/A	0	23.33513129	5		
DCBLD1	6	12.16783217	18.87995547	2	23.77816762	5		
XXYLT1	12	39.44020356	25.53990543	1	26.60980224	5		
GOLM1	18	40.64837905	18.88215675	1	26.57558511	5		
SUMF1	7	22.99465241	19.42287207	2	26.08895761	5		
POGLUT1	16	37.24489796	21.81679706	1	26.76890093	5		
RNF149	3	9	N/A	0	21.5576997	5		

KCT2	4	16.60377358	N/A	0	24.69300045	5		
LEMD2	10	21.86878728	19.22676356	1	24.76246194	5		
PLA2G15	6	19.41747573	N/A	0	22.93605314	5		
PLBD2	12	24.6179966	18.08644547	2	26.32586582	5		
MCFD2	2	11.64383562	N/A	0	20.94911503	5		
ITFG1	7	13.39869281	N/A	0	23.64933242	5		
LRRC8C	11	18.30635118	N/A	0	23.06541293	5		
CSGALNACT 1	12	28.7593985	N/A	0	24.04397901	5		
PIGO	5	6.427915519	19.58884868	2	22.49123278	5		
DCAKD	6	22.94372294	17.57997568	1	23.300174	5		
SELENOM	2	19.31034483	N/A	0	20.32101296	5		
POMGNT1	16	25	N/A	0	24.8189644	5		
PIEZO1	17	10.7497025	18.27107884	1	23.43824624	5		
EDEM1	7	12.78538813	20.57077074	2	22.71873524	5		
ATP2A3	14	23.68168744	18.53065944	1	24.30015141	5		
MR1	1	3.812316716	N/A	0	20.91372241	5		
MYDGF	6	33.52601156	21.84008614	2	30.96238364	5		
IGSF8	9	17.78140294	21.84753068	1	22.45851311	5		
LRRC59	7	25.40716612	20.42310981	2	25.05439096	5		
ISOC1	2	8.724832215	19.15691249	1	18.73185101	5		
RCN3	7	20.73170732	15.53572733	1	22.00996348	5		
C1GALT1C1	11	34.27672956	N/A	0	25.92993525	5		
TXNDC15	6	22.5	20.16759379	1	26.52004931	5		
RNF170	5	24.03100775	N/A	0	23.45204293	5		
DNAJC1	13	28.15884477	20.23028126	1	25.42928498	5		
SLC22A3	2	4.129263914	N/A	0	21.33680485	5		
HS6ST2	6	14.38016529	N/A	0	23.59654157	5		
SEC62	8	16.04010025	17.28923853	2	24.67572387	5		
OSMR	17	23.39121553	N/A	0	24.72565124	5		
FAM213A	7	32.31441048	17.07898615	1	20.4158575	5		
EMC6	3	20.90909091	18.73168072	2	25.72687258	5		
EDEM2	11	26.12456747	20.07224622	1	24.03989706	5		
CNTNAP3	19	19.09937888	N/A	0	25.81703186	5		
TANGO6	10	14.44241316	20.94445276	2	21.61657143	5		
XYLT2	7	9.595375723	N/A	0	24.11913777	5		
UNC93B1	3	7.035175879	N/A	0	19.67851852	5		
TMX4	8	34.67048711	N/A	0	24.0795027	5		
SLC6A15	4	6.164383562	N/A	0	19.63591305	5		
TMEM245	7	10.46643914	N/A	0	25.62189856	5		
PIGU	4	10.11494253	17.07902287	1	26.86794967	5		
ST6GALNAC4	7	28.47682119	N/A	0	24.21263705	5		
SMOC1	12	26.49769585	20.94104973	2	26.70391588	5		
POMK	9	33.71428571	N/A	0	24.78178989	5		
DNAJC18	7	25.1396648	N/A	0	21.60227534	5		
FKRP	8	19.39393939	17.21423951	1	23.59487262	5		
SIAE	3	7.456978967	N/A	0	22.5161124	5		

SCPEP1	10	27.87610619	21.50261377	1	24.2394407	5		
ENTPD7	6	14.2384106	N/A	0	22.53386664	5		
C1GALT1	10	38.29201102	N/A	0	25.54888772	5		
TMEM248	3	11.14649682	15.28560626	1	23.59904075	5		
P4HTM	10	29.6812749	19.88733084	1	24.91696704	5		
CELSR1	16	6.602521566	18.42880102	1	23.40761898	5		
EIF2AK3	1	26.61290323	19.58970096	2	26.08154825	5		
C1RL	1	2.874743326	N/A	0	20.80440671	5		
CRIM1	12	16.7953668	N/A	0	23.97311852	5		
SELENON	4	7.966101695	16.9264406	1	23.325439	5		
PTGFRN	2	33.10580205	21.88999571	1	26.48656863	5		
TXNDC16	14	19.75757576	N/A	0	25.16955719	5		
SUCO	10	10.52631579	N/A	0	22.55615079	5		
B4GALT7	7	22.93577982	19.32645291	1	25.61648384	5		
PFDN2	3	24.02597403	N/A	0	20.76059173	5		
PLXNA1	13	13.23839662	N/A	0	23.32792123	5		
GNPTG	6	24.59016393	16.20360863	1	24.0519037	5		
POMT2	6	10.4	19.56793527	1	23.7366319	5		
SLC39A10	14	21.41997593	N/A	0	25.23440673	5		
HEG1	11	12.16509776	N/A	0	20.44401755	5		
NOTCH3	31	17.44937527	N/A	0	26.77815933	5		
JAG2	6	8.319870759	N/A	0	21.69502718	5		
CNPY2	9	58.79120879	18.95084739	2	26.6219659	5		
ATP6V0A2	11	17.75700935	N/A	0	24.45827055	5		
PLXND1	14	16.05194805	N/A	0	23.87748831	5		
SNX14	6	7.505285412	20.13847805	1	21.16512269	5		
NPTN	7	18.84422111	18.65371462	2	26.51721008	5		
POMT1	12	18.07228916	18.00104888	1	23.52427101	5		
LAMC3	19	17.58730159	N/A	0	24.15253072	5		
ROBO1	25	23.62204724	17.30296217	1	25.54702089	5		
H6PD	15	21.32169576	19.62201394	1	24.25081772	5		
CD46	2	19.23076923	N/A	0	24.41090737	5		
CTSA	8	18.87550201	21.12208925	1	24.91027938	5		
eIF3a	6	6.729377713	20.38134452	2	20.67904528	4		
IKIP	1	53.93258427	20.54350975	2	25.29950688	4		
RESDA1	21	6.402293359	20.80116019	2	23.25429512	4		
RFT1	2	3.327171904	21.26161568	2	23.40013583	4		
ROCK2	7	7.997118156	N/A	0	22.24407484	4		
PRAF2	2	22.47191011	21.60021979	2	23.1464206	4		
FAM8A1	3	14.04358354	18.87349053	1	20.44387678	4		
NADK	2	6.502242152	N/A	0	19.84503203	4		
CSDE1	8	12.15538847	18.22374761	1	21.33135281	4		
FSTL3	4	23.57414449	18.82079843	1	22.53117394	4		
FVT1	3	10.54216867	N/A	0	20.67565597	4		
TREX1	4	6.573957016	19.78873174	2	20.85598726	4		
HYAL3	3	9.112709832	18.08875535	1	19.94449953	4		

DEGS1	3	10.52631579	18.69368087	1	21.3723818	4		
FBXO28	7	27.7173913	N/A	0	20.81792981	4		
ARV1	2	14.02214022	N/A	0	19.12670436	4		
ITM2C	6	27.34082397	20.164417	2	22.81741082	4		
ARSA	3	11.98428291	N/A	0	20.33111284	4		
CPSF2	7	8.31202046	20.11538868	1	19.19109901	4		
WARS	6	18.04670913	20.79606348	2	20.39537329	4		
IFI30	2	8	19.37278805	1	20.67571556	4		
TMPO	4	31.71806167	N/A	0	21.35649888	4		
LAMP1	5	14.38848921	N/A	0	25.75691382	4		
UHRF1	8	13.65227538	18.29231458	1	20.47155486	4		
SLC6A6	2	3.606102635	N/A	0	21.48190858	4		
SEZ6L2	5	8.775731311	N/A	0	20.32727937	4		
PSME2	3	12.99212598	N/A	0	20.80503261	4		
NBPF26	2	28.81355932	N/A	0	21.70832345	4		
BDNF	2	15.38461538	17.91005399	1	19.83531748	4		
C4A	5	5.561926606	N/A	0	20.10621682	4		
ABCB7	5	8.632138114	21.29597537	2	20.66510954	4		
SERPINI1	7	17.56097561	18.27419073	1	24.37948734	4		
PROS1	6	10.02824859	N/A	0	24.06280591	4		
WFS1	8	10.4494382	N/A	0	22.94801434	4		
USP5	5	9.324009324	20.23745034	2	20.39744663	4		
DPYSL3	8	17.83625731	N/A	0	21.33775216	4		
AK2	4	20.92050209	16.03376165	1	21.82955933	4		
KIF2C	6	9.931034483	N/A	0	19.94131273	4		
MATN2	1	4.811715481	N/A	0	20.64039109	4		
SCARB2	4	8.670520231	N/A	0	23.27713311	4		
ALG6	2	3.339882122	N/A	0	20.9528887	4		
FAM234B	3	5.144694534	N/A	0	20.49189328	4		
USP19	11	11.31815045	18.09285019	1	21.55808471	4		
RRBP1	24	22.53246753	21.56903074	2	22.19811404	4		
LIFR	8	8.113035552	N/A	0	22.47626074	4		
SNAP23	2	11.37440758	N/A	0	19.31126142	4		
ADAM12	2	19.18367347	N/A	0	24.07176049	4		
FAP	9	14.07894737	N/A	0	21.6075612	4		
GPD2	9	14.85557084	19.96831479	1	21.91248103	4		
DMXL1	12	5.511811024	21.28563532	2	21.77734076	4		
RNASET2	4	14.33224756	N/A	0	21.89254936	4		
NUP53	4	19.93865031	22.50691709	2	21.42377489	4		
CLGN	20	38.52459016	N/A	0	25.66344629	4		
GPRC5A	1	3.641456583	N/A	0	21.27467281	4		
BGN	4	14.67391304	N/A	0	20.51912515	4		
TRAF7	3	4.776119403	18.41939283	2	22.35598884	4		
TPCN1	4	6.862745098	N/A	0	21.73530631	4		
SPAG5	2	2.263202012	N/A	0	20.54162549	4		
BMPR2	4	5.973025048	N/A	0	21.15191214	4		

HMGCR	9	12.83783784	N/A	0	21.53506121	4		
KIF18A	8	12.36080178	22.25583555	2	21.22712953	4		
IFNGR1	5	13.29243354	N/A	0	22.48056461	4		
MAP7	6	10.81441923	22.82694011	2	22.70098116	4		
TXNDC14	4	13.17567568	19.24850819	2	21.82205729	4		
TXNL1	7	32.1799308	22.48264499	2	22.02460801	4		
FZD6	7	11.04815864	N/A	0	22.53449955	4		
Uncharacterised Protein	1	4.269662921	21.00557782	1	22.76498985	4		
RINT1	1	1.515151515	20.86730127	2	21.95808572	4		
PRSS23	6	21.40992167	N/A	0	22.81955066	4		
GLA	1	26.06635071	N/A	0	21.45071974	4		
APOL2	5	12.24944321	18.88346178	2	21.52126406	4		
SYMPK	3	3.453689168	22.81577476	1	19.42917795	4		
SSR2	1	2.97029703	N/A	0	27.26711175	4		
FKP8	5	15.87301587	N/A	0	22.28321584	4		
FKTN	4	9.057971014	N/A	0	21.37904399	4		
BMPR1A	4	18.98496241	N/A	0	20.93780096	4		
hCG_1984214	4	25.77777778	20.01547242	2	20.42266107	4		
TLL1	11	15.54054054	N/A	0	23.35520397	4		
COPS4	6	18.57142857	19.45621731	2	21.19464879	4		
CANX	1	21.79487179	N/A	0	21.77020864	4		
ITGA2	1	24.41613588	N/A	0	22.26044209	4		
GOSR1	4	21.37096774	N/A	0	20.72001791	4		
THY1	3	23.63636364	N/A	0	19.68469516	4		
NR2C2	3	6.341463415	20.40586225	2	19.84711425	4		
HLA-B	1	2.37388724	N/A	0	22.54995208	4		
DGCR2	3	7.636363636	N/A	0	21.05606988	4		
NPC2	3	15.83710407	N/A	0	20.27940894	4		
CLPTM1L	1	33.33333333	21.08883999	1	21.58533666	4		
PIGX	4	14.49275362	18.17443648	2	23.06925179	4		
IFITM3	2	30.82706767	N/A	0	22.69236479	4		
TOR1AIP1	1	53.92320534	N/A	0	21.86391636	4		
CYB5B	4	37.33333333	19.43901651	1	25.10034343	4		
BSCL2	2	3.663793103	17.05840889	1	22.8631226	4		
MICA	2	4.6875	N/A	0	24.54058649	4		
P2RX5	7	19.2575406	17.96353343	1	23.60855442	4		
ABCC4	5	4.452830189	20.02423381	2	22.08776311	4		
B4GALT5	3	12.88659794	N/A	0	21.6486762	4		
C21orf2	2	10.546875	18.38339106	1	19.04025556	4		
MARCH6	3	3.846153846	N/A	0	21.31566857	4		
CUTA	1	7.82122905	N/A	0	20.89021338	4		
PPP6R2	3	4.554865424	N/A	0	19.99215019	4		
LRP6	11	10.84934904	N/A	0	21.78132685	4		
PRNP	5	18.94736842	N/A	0	21.66505665	4		
ATP5H	11	55.27950311	18.11455688	1	23.69527227	4		
SLITRK5	6	7.724425887	N/A	0	22.85518109	4		

SVIL	4	2.619692864	N/A	0	19.21087217	4		
ECEL1	7	12.38709677	18.39447617	1	23.42582898	4		
CST3	2	18.49315068	N/A	0	23.05001749	4		
COL1A1	2	9.972677596	N/A	0	22.65295371	4		
AGT	3	8.146639511	N/A	0	17.79371204	4		
FGFR4	1	2.804642166	N/A	0	20.21009114	4		
SLPI	1	9.090909091	N/A	0	22.55139507	4		
ABCC3	8	8.349641226	N/A	0	20.15797362	4		
PON2	2	39.26940639	19.04317195	2	23.59013648	4		
GNAI3	2	16.94915254	N/A	0	20.86458356	4		
CD46	7	18.62244898	N/A	0	25.18990107	4		
NAGA	3	8.272506083	N/A	0	21.041352	4		
GM2A	2	8.808290155	N/A	0	22.8161904	4		
CD58	3	8	16.20617923	1	23.60363368	4		
EIF2AK2	3	5.807622505	20.22202544	2	20.32897453	4		
ITGB8	5	7.802340702	N/A	0	22.4361066	4		
MAN1A1	4	8.575803982	23.20739725	1	22.08996505	4		
LTBR	3	12.87356322	N/A	0	22.0474529	4		
COL15A1	10	8.501440922	N/A	0	24.28331337	4		
ECI1	4	15.23178808	21.92576723	2	20.21221754	4		
NOTCH1	4	3.052837573	N/A	0	20.78901282	4		
TFPI2	5	29.36170213	N/A	0	22.49002331	4		
CAMLG	5	20.94594595	N/A	0	21.34366822	4		
CAV2	3	28.39506173	N/A	0	21.09279105	4		
NEK4	5	6.77764566	19.53137516	2	20.60777044	4		
MTPN	1	14.40677966	18.89703044	1	20.29052989	4		
NAAA	7	19.22005571	N/A	0	20.95502479	4		
CALD1	6	11.09709962	N/A	0	20.99274441	4		
EXTL2	3	8.761329305	N/A	0	22.92243746	4		
GOLGA2	7	7.784431138	N/A	0	20.16001399	4		
LOXL1	3	8.18815331	N/A	0	21.86231134	4		
CD47	1	2.476780186	N/A	0	21.81784622	4		
GRIK2	8	12.7753304	N/A	0	21.7423357	4		
PLA2R1	8	8.612440191	N/A	0	21.8127014	4		
PTPRS	8	10.21560575	N/A	0	22.35303156	4		
PKD2	5	6.198347107	N/A	0	20.70519733	4		
SEMA3A	6	8.949416342	N/A	0	22.69534667	4		
MBTPS1	11	14.35361217	N/A	0	22.36327009	4		
LTBP2	2	1.372872048	N/A	0	19.11802073	4		
EXT1	9	13.13672922	19.3784224	1	23.74491064	4		
HNRNPUL2	4	7.49665328	N/A	0	19.65103926	4		
HFE	2	7.471264368	N/A	0	19.65309882	4		
ITPRIPL2	3	7.85046729	19.58597605	2	20.37904728	4		
LGR4	6	4.748062016	20.19453972	2	22.88575555	4		
EIF4G3	12	10.28089888	20.51041151	2	20.88189743	4		
KIF4A	14	12.87449393	18.86241976	1	21.85652667	4		

RNFT1	2	8.045977011	N/A	0	20.08436278	4		
NT5DC1	4	9.89010989	N/A	0	21.12262557	4		
APEX1	2	10.06289308	18.64503086	1	18.79223376	4		
MARC1	3	9.495548961	N/A	0	18.64950318	4		
CD276	2	27.52808989	18.62796212	1	25.87051104	4		
HCTP4	7	10.9772423	20.35482704	1	21.78688061	4		
LMBRD2	6	10.79136691	N/A	0	20.84351867	4		
HLA-E	4	25.69832402	21.84693946	1	22.85153181	4		
CIAPIN1	6	19.87179487	19.14587292	1	22.45728744	4		
C14orf1	2	10.71428571	N/A	0	22.64537113	4		
NCAPH2	1	1.652892562	N/A	0	21.15947117	4		
MFSD5	5	15.33333333	N/A	0	23.46456208	4		
MYORG	11	15.82633053	18.23240906	2	23.2666695	4		
SPINK6	1	20	N/A	0	24.04705181	4		
ARSK	4	6.902985075	N/A	0	23.08691613	4		
B3GNT9	3	7.711442786	18.66877111	1	23.5101181	4		
FAT4	20	5.541056013	N/A	0	22.64471419	4		
DPY19L3	3	4.469273743	N/A	0	22.05606057	4		
PGAP1	5	6.399132321	N/A	0	22.2394733	4		
BTN2A1	4	8.159392789	N/A	0	21.76026424	4		
NEGR1	4	16.66666667	N/A	0	22.06782675	4		
FRMD5	5	12.28070175	N/A	0	21.6914451	4		
MEGF8	10	5.588752197	N/A	0	22.83489407	4		
AMIGO2	3	10.91954023	N/A	0	19.66887065	4		
OAF	3	10.62271062	17.47878498	1	20.59497508	4		
ERO1B	9	25.91006424	N/A	0	20.79295164	4		
SLITRK4	8	12.78375149	N/A	0	22.27828017	4		
ADGRA3	5	4.617713853	N/A	0	21.10884082	4		
UBR2	6	4.216524217	20.77571516	1	19.76808635	4		
ABCA7	6	3.541472507	N/A	0	21.28693537	4		
TMTC2	2	2.272727273	N/A	0	20.89376489	4		
CISD2	5	42.22222222	17.0741676	1	23.03120069	4		
BMPER	3	5.547445255	N/A	0	20.20360344	4		
PCYOX1L	6	13.36032389	20.1209684	1	25.13767421	4		
NETO2	5	13.71428571	N/A	0	18.70039037	4		
B3GALNT2	7	15.4	N/A	0	24.55218404	4		
TMEM161B	6	14.37371663	N/A	0	21.2312651	4		
CNNM3	12	23.05516266	N/A	0	23.65048024	4		
ABCF1	8	12.30769231	21.86172573	2	22.25622523	4		
FLCN	5	10.88082902	21.14962862	2	20.01425832	4		
MOSPD2	8	16.98841699	N/A	0	23.14604435	4		
CHPT1	2	5.911330049	N/A	0	21.4969626	4		
AGPAT2	5	21.86379928	21.70043584	2	21.56632882	4		
CKAP2	3	5.710102489	18.99986808	2	19.56365331	4		
SUSD6	1	4.620462046	N/A	0	18.05361822	4		
ATP6V0A1	6	10.75268817	N/A	0	22.08858018	4		

SMARCE1	2	6.082725061	19.3992129	2	20.23044007	4		
PMEPA1	3	15.67944251	N/A	0	21.61730868	4		
NXPE3	3	6.797853309	N/A	0	19.25125681	4		
EDC3	5	12.00787402	19.85633344	2	19.34297613	4		
DCBLD2	7	12.25806452	N/A	0	21.38299385	4		
VPS35	4	6.909547739	20.29293866	1	19.08936514	4		
CGREF1	5	23.58803987	N/A	0	21.81784777	4		
TSG101	2	6.923076923	19.61742373	2	20.90233856	4		
TM2D3	3	11.74089069	19.31828924	2	23.92269985	4		
TMEM106C	1	6.8	N/A	0	20.5608841	4		
KLF16	1	10.31746032	N/A	0	17.52309135	4		
SCAPER	4	3.785714286	19.25619808	2	19.69110154	4		
TNKS1BP1	20	17.17755928	20.55799525	2	22.17426805	4		
SELENOI	2	4.785894207	N/A	0	21.23796301	4		
DERL2	2	7.531380753	22.28303835	1	20.8268938	4		
TWSG1	2	10.76233184	N/A	0	21.08856899	4		
FAM234A	2	3.985507246	N/A	0	19.75745917	4		
TMEM231	3	11.39240506	N/A	0	21.88433323	4		
ZDHHC6	1	2.905569007	N/A	0	21.50760619	4		
TMEM206	3	10.57142857	N/A	0	21.05655826	4		
GORASP2	2	6.194690265	N/A	0	18.79013221	4		
SPC25	4	19.19642857	21.12575911	2	20.05495082	4		
KIAA1549	9	5.948717949	N/A	0	21.75620151	4		
CELSR2	8	3.729045501	N/A	0	21.50173842	4		
CD320	5	20.56737589	N/A	0	23.63606461	4		
DMAP1	2	5.995717345	19.4565268	2	20.38882234	4		
NECTIN3	3	7.103825137	N/A	0	20.23112643	4		
LTBP3	10	12.27935533	N/A	0	21.84315995	4		
TYW1	2	4.234972678	N/A	0	19.31363092	4		
KLHL11	4	5.508474576	20.59619772	2	20.04118285	4		
NDUFB11	3	29.41176471	19.93877784	1	20.30435225	4		
TMEM161A	4	10.02087683	N/A	0	20.05601845	4		
PODXL2	7	17.68595041	N/A	0	22.31724801	4		
LRP1B	21	5.957816917	22.90851614	1	23.78557409	4		
ADAM22	5	7.06401766	N/A	0	21.823947	4		
NAGPA	3	7.766990291	N/A	0	21.13434023	4		
TIMELESS	9	8.112582781	N/A	0	20.70697948	4		
PPP6R1	4	5.561861521	20.01296346	1	20.38855726	4		
SLC5A6	2	4.094488189	17.78305313	1	21.60670554	4		
RXYLT1	5	9.706546275	N/A	0	21.00698434	4		
UBE2J1	3	13.20754717	N/A	0	21.99435093	4		
USP15	7	9.174311927	19.44326976	2	21.55973468	4		
LRP12	7	10.82654249	N/A	0	21.05273482	4		
BACE2	2	4.633204633	N/A	0	20.78042433	4		
SPCS1	2	26.47058824	N/A	0	24.13273263	4		
SLC30A1	3	7.100591716	N/A	0	20.90073451	4		

HEL-S-112	4	14.89361702	N/A	0	18.95762407	4		
CADM1	2	8.280254777	N/A	0	21.09506091	4		
DCAF12	2	14.97797357	N/A	0	21.43598555	4		
IGF1R	25	26.40819312	20.61586101	2	26.80057291	5		
TFPI	9	37.17105263	19.20748597	2	25.00421337	5		
HMOX2	11	39.87341772	21.10064053	2	24.77253379	5		
VCP	19	29.65260546	23.73411545	2	23.74865907	5		
YWHAG	3	34.81781377	21.06313605	2	22.19835743	5		
ITPR2	27	17.21584598	21.28491359	2	23.1071964	5		
GNPTAB	21	19.42675159	20.30846513	2	26.38513409	5		
CSTB	4	55.10204082	21.67451931	2	22.80782541	5		
GPAT4	5	9.868421053	21.46598454	2	23.30229714	5		
ZDHHC13	4	9.807073955	19.56359207	2	21.61074449	5		
TMEM30A	13	34.07202216	19.21988112	2	26.10521853	5		

Table 4.2 Gene Ontology Cellular Components Enriched in the HRP-TGN46-Labelled Proteome

The list of proteins labelled by HRP-TGN46 **(Table 4.1)** was analysed with PANTHER gene ontology software. The top 50 significantly enriched/depleted cellular component categories are displayed, ranked by p-value. + = significant overrepresentation, - = significant underrepresentation of categories.

Gene Ontology Category	Category Size	# Proteins Identified	# Proteins Expected	Over/Under Representation	Fold Enrichment	p-Value
endomembrane system (GO:0012505)	4585	819	345.47	+	2.37	7.52E-137
endoplasmic reticulum (GO:0005783)	1447	386	109.03	+	3.54	5.10E-95
organelle membrane (GO:0031090)	3576	605	269.44	+	2.25	7.96E-82
endoplasmic reticulum membrane (GO:0005789)	1097	306	82.66	+	3.7	1.48E-77
nuclear outer membrane-endoplasmic reticulum membrane network (GO:0042175)	1119	308	84.31	+	3.65	6.30E-77
membrane (GO:0016020)	9898	1122	745.79	+	1.5	3.71E-76
intrinsic component of membrane (GO:0031224)	5940	800	447.57	+	1.79	1.26E-71
integral component of membrane (GO:0016021)	5787	784	436.04	+	1.8	1.32E-70
membrane-bounded organelle (GO:0043227)	12661	1256	953.98	+	1.32	2.04E-55
vesicle (GO:0031982)	3889	564	293.03	+	1.92	1.67E-53
extracellular vesicle (GO:1903561)	2119	370	159.66	+	2.32	3.83E-48
extracellular organelle (GO:0043230)	2124	370	160.04	+	2.31	4.82E-48
extracellular region (GO:0005576)	4391	595	330.85	+	1.8	6.98E-48
extracellular exosome (GO:0070062)	2098	366	158.08	+	2.32	1.18E-47
Golgi apparatus (GO:0005794)	1602	308	120.71	+	2.55	1.04E-46
organelle (GO:0043226)	13794	1304	1039.35	+	1.25	1.43E-46
extracellular space (GO:0005615)	3358	492	253.02	+	1.94	3.08E-46
endoplasmic reticulum lumen (GO:0005788)	310	128	23.36	+	5.48	4.29E-46
cytoplasm (GO:0005737)	11544	1154	869.81	+	1.33	1.03E-45
cellular anatomical entity (GO:0110165)	18739	1554	1411.94	+	1.1	3.81E-42
bounding membrane of organelle (GO:0098588)	2117	353	159.51	+	2.21	8.37E-42
cellular_component (GO:0005575)	18929	1558	1426.26	+	1.09	9.54E-40
Unclassified (UNCLASSIFIED)	2067	24	155.74	-	0.15	9.54E-40
Golgi membrane (GO:0000139)	761	186	57.34	+	3.24	2.62E-39
intracellular vesicle (GO:0097708)	2396	348	180.53	+	1.93	2.48E-30
intracellular membrane-bounded organelle (GO:0043231)	10959	1058	825.74	+	1.28	3.94E-30
cytoplasmic vesicle (GO:0031410)	2393	347	180.31	+	1.92	5.31E-30
intracellular organelle (GO:0043229)	12761	1170	961.51	+	1.22	1.77E-26
collagen-containing extracellular matrix (GO:0062023)	410	107	30.89	+	3.46	1.11E-24
integral component of organelle membrane (GO:0031301)	379	98	28.56	+	3.43	1.92E-22

intrinsic component of organelle membrane (GO:0031300)	410	102	30.89	+	3.3	2.95E-22
cell surface (GO:0009986)	948	169	71.43	+	2.37	4.38E-22
integral component of endoplasmic reticulum membrane (GO:0030176)	163	62	12.28	+	5.05	2.28E-21
intrinsic component of endoplasmic reticulum membrane (GO:0031227)	171	63	12.88	+	4.89	4.10E-21
extracellular matrix (GO:0031012)	538	115	40.54	+	2.84	2.22E-20
lysosome (GO:0005764)	702	133	52.89	+	2.51	1.91E-19
lytic vacuole (GO:0000323)	702	133	52.89	+	2.51	1.91E-19
vacuole (GO:0005773)	805	145	60.65	+	2.39	2.51E-19
intracellular (GO:0005622)	14571	1261	1097.89	+	1.15	4.57E-19
secretory granule (GO:0030141)	846	146	63.74	+	2.29	5.35E-18
endoplasmic reticulum-Golgi intermediate compartment (GO:0005793)	133	51	10.02	+	5.09	6.15E-18
whole membrane (GO:0098805)	1715	234	129.22	+	1.81	6.94E-17
focal adhesion (GO:0005925)	409	90	30.82	+	2.92	7.16E-17
Golgi cisterna (GO:0031985)	116	46	8.74	+	5.26	9.24E-17
Golgi stack (GO:0005795)	150	52	11.3	+	4.6	9.31E-17
organelle subcompartment (GO:0031984)	394	87	29.69	+	2.93	2.00E-16
cell-substrate junction (GO:0030055)	416	90	31.34	+	2.87	2.46E-16
cell (GO:0005623)	1117	169	84.16	+	2.01	8.56E-16
secretory vesicle (GO:0099503)	1016	157	76.55	+	2.05	2.12E-15
basement membrane (GO:0005604)	99	40	7.46	+	5.36	5.65E-15

Table 4.3 Gene Ontology Biological Processes Enriched in the HRP-TGN46-Labelled Proteome

The list of proteins labelled by HRP-TGN46 **(Table 4.1)** was analysed with PANTHER gene ontology software. The top 50 significantly enriched/depleted biological process categories are displayed, ranked by p-value. + = significant overrepresentation, - = significant underrepresentation of categories.

Gene Ontology Category	Category Size	# Proteins Identified	# Proteins Expected	Over/Under Representation	Fold Enrichment	p-Value
protein glycosylation (GO:0006486)	95	46	7.16	+	6.43	2.00E-19
glycoprotein biosynthetic process (GO:0009101)	101	47	7.61	+	6.18	2.83E-19
carbohydrate derivative biosynthetic process (GO:1901137)	129	49	9.72	+	5.04	3.73E-17
carbohydrate derivative metabolic process (GO:1901135)	282	72	21.25	+	3.39	1.46E-16
Unclassified (UNCLASSIFIED)	10588	636	797.78	-	0.8	4.38E-15
cell adhesion (GO:0007155)	373	67	28.1	+	2.38	2.03E-09
biological adhesion (GO:0022610)	373	67	28.1	+	2.38	2.03E-09
glycoprotein metabolic process (GO:0009100)	31	17	2.34	+	7.28	1.14E-08
protein N-linked glycosylation (GO:0006487)	29	16	2.19	+	7.32	2.88E-08
protein folding (GO:0006457)	117	30	8.82	+	3.4	9.46E-08
ER to Golgi vesicle-mediated transport (GO:0006888)	84	25	6.33	+	3.95	1.03E-07
cellular process (GO:0009987)	6070	558	457.36	+	1.22	1.34E-07
Golgi vesicle transport (GO:0048193)	124	29	9.34	+	3.1	7.88E-07
carbohydrate metabolic process (GO:0005975)	185	37	13.94	+	2.65	8.33E-07
sensory perception of chemical stimulus (GO:0007606)	224	1	16.88	-	0.06	2.37E-06
cellular metabolic process (GO:0044237)	1744	185	131.41	+	1.41	8.85E-06
cell-matrix adhesion (GO:0007160)	50	16	3.77	+	4.25	9.36E-06
cell-substrate adhesion (GO:0031589)	54	16	4.07	+	3.93	2.08E-05
response to organonitrogen compound (GO:0010243)	37	13	2.79	+	4.66	2.86E-05
transcription, DNA-templated (GO:0006351)	1251	56	94.26	-	0.59	3.37E-05
detection of chemical stimulus involved in sensory perception (GO:0050907)	184	1	13.86	-	0.07	3.47E-05
neuron development (GO:0048666)	172	31	12.96	+	2.39	4.00E-05
organonitrogen compound metabolic process (GO:1901564)	191	33	14.39	+	2.29	5.33E-05
cellular modified amino acid metabolic process (GO:0006575)	54	15	4.07	+	3.69	6.95E-05
sterol metabolic process (GO:0016125)	35	12	2.64	+	4.55	7.01E-05
neuron differentiation (GO:0030182)	224	36	16.88	+	2.13	1.14E-04
inorganic ion homeostasis (GO:0098771)	247	38	18.61	+	2.04	1.46E-04
regulation of metabolic process (GO:0019222)	1347	65	101.49	-	0.64	1.57E-04
response to nitrogen compound (GO:1901698)	52	14	3.92	+	3.57	1.59E-04
response to topologically incorrect protein (GO:0035966)	33	11	2.49	+	4.42	1.71E-04
ion homeostasis (GO:0050801)	252	38	18.99	+	2	1.79E-04
localization (GO:0051179)	2059	203	155.14	+	1.31	1.84E-04

generation of neurons (GO:0048699)	240	37	18.08	+	2.05	1.90E-04
cell morphogenesis involved in neuron differentiation (GO:0048667)	110	22	8.29	+	2.65	1.90E-04
axonogenesis (GO:0007409)	98	20	7.38	+	2.71	1.95E-04
primary metabolic process (GO:0044238)	547	68	41.22	+	1.65	2.07E-04
polysaccharide metabolic process (GO:0005976)	62	15	4.67	+	3.21	2.55E-04
neurogenesis (GO:0022008)	255	38	19.21	+	1.98	2.90E-04
multicellular organism development (GO:0007275)	609	73	45.89	+	1.59	3.18E-04
ubiquitin-dependent ERAD pathway (GO:0030433)	24	9	1.81	+	4.98	3.29E-04
endomembrane system organization (GO:0010256)	112	21	8.44	+	2.49	4.37E-04
system development (GO:0048731)	474	59	35.71	+	1.65	5.42E-04
axon guidance (GO:0007411)	75	16	5.65	+	2.83	5.42E-04
peptide metabolic process (GO:0006518)	39	11	2.94	+	3.74	5.66E-04
gene expression (GO:0010467)	1842	100	138.79	-	0.72	5.71E-04
organic hydroxy compound metabolic process (GO:1901615)	46	12	3.47	+	3.46	5.84E-04
regulation of cellular biosynthetic process (GO:0031326)	752	32	56.66	-	0.56	6.06E-04
regulation of biosynthetic process (GO:0009889)	753	32	56.74	-	0.56	6.07E-04
chemical homeostasis (GO:0048878)	299	41	22.53	+	1.82	7.93E-04
positive regulation of neuron projection development (GO:0010976)	22	8	1.66	+	4.83	8.29E-04

Table 4.4 Mannose-6-Phosphate Proteins Enriched in the HRP-TGN46-Labelled Proteome

M6P-tagged proteins identified in (Čaval et al., 2019) that were significantly enriched, or not detected in the control 'light' SILAC condition are displayed.

Protein Name	Unique Peptides	Coverage (%)	Mean L Abundance	Mean M Abundance	Log_2 Medium/Light	t-test *p*-value
CPVL	7	19.32773109	N/A	21.86903365	N/A	N/A
CTSA	8	18.87550201	N/A	24.91027938	N/A	N/A
CTSC	1	28.72570194	20.59792996	25.74022861	6.400	1.72E-02
CTSD	12	40.29126214	21.03068779	27.11033786	6.080	1.27E-05
CTSL1	7	26.42642643	N/A	23.38974136	N/A	N/A
CTSZ	8	28.05280528	21.24224984	27.09681194	6.037	1.44E-02
DNASE2	5	18.89534884	N/A	22.15170298	N/A	N/A
GBA	11	21.25603865	23.93802019	27.94359194	4.006	2.11E-04
GGH	12	37.10691824	20.94525714	27.05923032	6.114	2.03E-05
GLA	11	40.55944056	21.9376043	27.02901716	5.091	2.17E-04
GLB1	15	26.89655172	N/A	26.31880751	N/A	N/A
GNS	12	21.06164384	N/A	27.38731819	N/A	N/A
HEXA	15	30.18518519	21.16359957	28.54580982	7.382	2.74E-05
LGMN	6	15.01154734	N/A	23.32506075	N/A	N/A
MAN2A1	42	43.44405594	22.4169991	30.14046968	7.723	1.09E-04
MAN2B1	11	13.35311573	N/A	21.64603886	N/A	N/A
NAAA	7	19.22005571	N/A	20.95502479	N/A	N/A
NPC2	3	15.83710407	N/A	20.27940894	N/A	N/A
PLBD2	12	24.6179966	N/A	26.32586582	N/A	N/A
PLOD1	36	60.38514443	26.52261426	32.36133933	5.839	1.37E-05
PLOD2	3	50.78236131	26.92445281	33.36004461	6.436	2.95E-06
PPT1	6	21.49253731	21.04501169	25.68371721	5.208	1.29E-03
PRCP	7	16.53225806	N/A	23.37084315	N/A	N/A
PSAP	19	40.75471698	N/A	27.44970531	N/A	N/A
RNASET2	4	14.33224756	N/A	21.89254936	N/A	N/A
SMPD1	4	7.078313253	N/A	21.82154216	N/A	N/A

Chapter 5

Table 5.1 Depleted Proteins in the SNX5+6 siRNA HRP-TGN46-Labelled Proteome

Proteins with a fold change of $Log_2 \pm 0.26$ and a p-value of < 0.1 are displayed. Proteins that were depleted from the SNX5+6 siRNA proteome relative to the Scr siRNA proteome are classified by the presence of a transmembrane domain, and putative cytosolic SNX5/6 interacting motifs. Proteins that were either identified as ESCPE-1 interactors (Simonetti et al., 2017) or depleted from a SNX5+6 KO surface proteome (unpublished) are also indicated.

Protein Name	Soluble/ TM	Cytosolic ϕxΩxϕ Motif(s)	ESCPE-1 Interactions	Depleted from SNX5+6 KO Surfaceome?	Coverage	# Unique Peptides	Log_2 Fold Change SNX5+6 siRNA/Scr siRNA	T test
IL1RAP	TM	**AHFGT FGYKL IKWKG**		**YES**	11.22807	6	-1.303988884	0.000199
PROCR	TM			**YES**	5.462185	1	-1.300925457	0.021589
ITGB8	TM				6.762029	5	-1.233701692	0.016394
CXADR	TM				22.73973	6	-1.164760219	0.008272
ZDHHC13	TM	**GRYGI AGYDV LHWAA VKFYI LHWAI IAYLI LHWAV IAFLG GCFGL**			8.360129	4	-1.13925609	0.060167
EPHA2	TM	**LKFTT VDFLG MKYLA WSFGI AIYQL AGYTA IAYSLL**	**SNX32**		23.05328	19	-0.988161284	0.023433
NPR3	TM			**YES**	12.19963	6	-0.964880167	0.088488
RNFT1	TM	**PSYGV**			5.287356	2	-0.848606568	0.072779
PTPRJ	TM	**ANYMP PKYAA FRYLV GTFIA LIYQI**		**YES**	12.78983	14	-0.794385554	0.016798
CD44	TM		**SNX2 SNX5 SNX32**		41.55125	11	-0.710864416	0.002809

MYORG	TM	**GCYAY AMYTF**			1.540616	1	-0.708290603	0.083225
ST6GALNAC4	TM				16.55629	4	-0.681947779	0.094193
SLC43A3	TM	**IPYPL YSYGL WSYAF**			3.05499	2	-0.675102257	0.002764
RCE1	TM				7.294833	2	-0.644922654	0.003181
ADGRE2	TM	**LAFKA**			3.008424	1	-0.630171285	0.046569
ALCAM	TM				18.35334	8	-0.616119106	7.07E-05
NRP1	TM	**YNFEL**	**SNX6 SNX32**		10.07584	6	-0.599253497	0.005762
CDKAL1	TM				20.55268	8	-0.591687978	0.003697
TFRC	TM			**YES**	54.73684	40	-0.576910916	0.045573
BTN2A1	TM	**IEWTV GQYRA PFFRL LDYEA**			6.451613	3	-0.572438944	0.079746
TM9SF4	TM	**IGFYA GFYAA AAYMF YMFVR**			23.36449	5	-0.558197177	0.06253
TMEM41B	TM				14.77663	4	-0.500675232	0.009646
KIRREL1	TM	**GYYNC PTYRL ADYRA**	**SNX32**		12.15324	7	-0.485973715	0.050746
GXYLT1	TM				4.545455	2	-0.483162544	0.049718
MET	TM	**VRYDA VQYPL MKYLA**			23.09353	27	-0.4820057	0.026963
LDLR	TM			**YES**	24.02116	17	-0.477514601	0.04715
ITGA5	TM		**SNX5**	**YES**	17.75956	16	-0.475708709	0.012
LPCAT2	TM	**ASFFP**			13.78676	7	-0.467278315	0.072859
B4GALT1	TM				9.547739	3	-0.464611229	0.098502
DSEL	TM				6.60066	7	-0.463491395	0.035151
CRIM1	TM	**ARFSG GFYSM**		**YES**	20.3668	15	-0.449362753	0.069731
LRRC8A	TM	**IAYIP**			23.20988	16	-0.370678509	0.014787
SORL1	TM				14.09214	27	-0.3591256	0.05392
PTPRK	TM	**AYFDM**			19.83696	22	-0.357061304	0.043376
PVR	TM	**VSYSA**		**YES**	13.18945	5	-0.345456621	0.052992
SLC35A1	TM	**GRFKA**			4.154303	1	-0.328701315	0.016238
SLC35E1	TM	**LWYAL**			17.56098	6	-0.322785893	0.039432
LAMP2	TM			**YES**	9.512195	3	-0.321689929	0.025391
ENG	TM				27.05167	3	-0.282256536	0.067118
COPS4	Soluble				21.90476	8	-2.838174292	0.033993
SQSTM1	Soluble				60.90909	5	-1.952011967	0.049421

GOPC	Soluble				24.02597	9	-1.049709481	0.01487
PRCP	Soluble				11.08871	4	-1.026308022	0.051223
NGLY1	Soluble				11.92661	6	-0.982366185	0.047672
CCN3	Soluble				31.37255	8	-0.965479559	0.014019
TSN	Soluble				23.24561	6	-0.819044376	0.061675
CTSD	Soluble			**YES**	25.72816	8	-0.792954727	0.019872
TGFBI	Soluble				38.06735	25	-0.752242263	0.000676
ABCE1	Soluble		**SNX5 SNX6 SNX32**		23.87312	14	-0.688365582	0.096243
NCAPH2	Soluble				8.595041	4	-0.686480156	0.006851
DPYSL3	Soluble				34.79532	15	-0.66327734	0.045717
HTATIP2	Soluble				21.4876	5	-0.636996471	0.067132
PLEKHA5	Soluble			**YES**	15.80727	13	-0.591558254	0.033508
SVIL	Soluble				6.142728	10	-0.581159898	0.002314
R3HDM1	Soluble				8.462238	7	-0.576998892	0.065329
NID1	Soluble				14.11387	15	-0.552092478	0.081039
ACLY	Soluble				45.47054	46	-0.544609949	0.097642
GLYR1	Soluble				16.66667	7	-0.527586359	0.011768
FAM3C	Soluble			**YES**	43.17181	9	-0.510846483	0.013312
CHORDC 1	Soluble				38.55422	11	-0.486289511	0.062988
RELA	Soluble				13.43013	6	-0.433472258	0.084589
DHX15	Soluble		**SNX32**		38.23899	30	-0.424071453	0.0224
TPX2	Soluble				20.88353	14	-0.414889836	0.01222
CD59	Soluble				15.38462	2	-0.398099819	0.074382
ATP5F1	Soluble				30.46875	7	-0.391759945	0.025367
XPO6	Soluble				19.64444	22	-0.391661968	0.028538
NEK9	Soluble				20.53115	15	-0.391418419	0.07718
ZZEF1	Soluble				5.471125	13	-0.377167112	0.05747
PDF	Soluble				8.641975	2	-0.374415151	0.05565
SCRIB	Soluble				7.673716	12	-0.360143407	0.035656
CTNNB1	Soluble		**SNX32**		18.26309	9	-0.356288457	0.08766
KIF18A	Soluble				11.24722	6	-0.33855183	0.013766
C1QBP	Soluble			**YES**	9.929078	2	-0.321709672	0.014869
THBS1	Soluble		**SNX1 SNX2**		46.49573	32	-0.319369841	0.023594
FOLR1	Soluble				19.84436	5	-0.312573984	0.085812
UHRF1	Soluble				15.986	13	-0.275697289	0.069894
COX4NB					25.71429	6	-0.245538502	0.016758
TAPBP					4.563492	2	-0.235323722	0.006618
PTGES					5.555556	1	-0.227432027	0.087436
POMT2					4.4	3	-0.212144853	0.079528
DHX36					26.98413	20	-0.206619081	0.051206
NADK					11.65919	4	-0.19008033	0.023728
CACHD1					1.491366	2	-0.166812832	0.019044
SEC62					12.03008	5	0.237111049	0.014631

MEGF8					1.476274	3	0.304943091	0.069464
SUMF1					10.42781	3	0.346134794	0.063921
OSTC					13.42282	2	0.370455931	0.031362
PC					61.12054	65	0.37095081	0.030562
ADGRG1					15.44012	8	0.373361444	0.089443
P3H3					31.25	6	0.394638268	0.092831
TMX4					12.03438	3	0.395853969	0.063324
ABHD14A-ACY1					12.28669	6	0.39910521	0.055888
CHST14					30.05319	11	0.403671971	0.041264
EXTL3					14.14581	11	0.484446878	0.057355
PPP6R1					4.31328	3	0.495739084	0.056748
P3H4					31.57895	12	0.496605593	0.097914
FBN1					28.03901	65	0.502511272	0.072297
LRPAP1					34.73389	15	0.506762272	0.092188
PPM1L					18.05556	6	0.509418582	0.042713
SART3					13.30604	11	0.510874608	0.076681
XXYLT1					9.669211	3	0.511705993	0.043631
FAT4					1.525798	7	0.533998013	0.081055
TXNDC11					18.37563	15	0.537567458	0.037919
P4HA2					40.6746	20	0.578675902	0.084473
FADS2					25.9009	10	0.607664245	0.064226
UGT8					16.08133	8	0.612779019	0.067751
FKBP10					41.75258	21	0.653110956	0.096169
CALU					54.92063	4	0.660324102	0.080225
ECE1					18.57143	13	0.673629299	0.085295
NUP210					28.03392	47	0.712470652	0.056245
SLC27A3					13.4402	7	0.747152194	0.088848
UGGT2					28.82586	43	0.749524472	0.094144
ERLIN2					48.67257	15	0.789169906	0.02914
LTBP1					6.856479	8	0.815789795	0.005383
CNTNAP1					25.28902	32	0.836592798	0.062462
MIA3					28.26429	51	0.841969246	0.083219
FSTL4					27.19715	12	0.877493547	0.094114
DCAKD					12.55411	3	0.985286061	0.09747
SPFH1					37.35632	11	1.040203211	0.050601
IGSF10					11.97103	26	1.115827005	0.046999
RCN2					32.17666	8	1.146198112	0.068525
COL4A1					17.49551	16	1.15226552	0.072168
NPTX1					21.06481	10	1.164888297	0.01626
SLITRK5					6.5762	5	1.303725256	0.071655
ATP9A					1.241643	1	1.425430909	0.031084
C1QTNF6					8.992806	2	1.446109319	0.001116
SUN2					32.71277	18	1.455060198	0.052624
NAGLU					15.88156	9	1.474400847	0.085114
DKFZp667O055					19.35484	1	1.69111812	0.022544

FAM69A					2.803738	1	1.979125045	0.093632
TNRC5					24.82014	6	2.405854658	0.091294

Table 5.2 Gene Ontology Cellular Components Depleted in the SNX5+6 siRNA HRP-TGN46-Labelled Proteome

The list of proteins significantly depleted in the SNX5+6 siRNA HRP-TGN46 proteome **(Table 5.1)** were analysed with PANTHER gene ontology software. Significantly enriched/depleted biological process categories are displayed, ranked by p-value. + = significant overrepresentation, - = significant underrepresentation of categories.

Gene Ontology Category	Category Size	# Proteins Identified	# Proteins Expected	Over/Under Representation	Fold Enrichment	p-Value
Unclassified (UNCLASSIFIED)	1756	2	6.65	-	0.3	0.00E+00
cell surface (GO:0009986)	918	22	3.48	+	6.33	4.27E-09
anchoring junction (GO:0070161)	833	19	3.15	+	6.02	3.95E-07
cell junction (GO:0030054)	2097	27	7.94	+	3.4	9.32E-06
intrinsic component of plasma membrane (GO:0031226)	1746	24	6.61	+	3.63	2.54E-05
focal adhesion (GO:0005925)	419	12	1.59	+	7.56	1.07E-04
cell-substrate junction (GO:0030055)	426	12	1.61	+	7.44	1.27E-04
integral component of plasma membrane (GO:0005887)	1665	22	6.31	+	3.49	2.38E-04
extracellular region (GO:0005576)	4323	37	16.37	+	2.26	2.95E-04
membrane (GO:0016020)	9907	60	37.52	+	1.6	4.27E-04
endomembrane system (GO:0012505)	4654	38	17.63	+	2.16	6.57E-04
intrinsic component of membrane (GO:0031224)	5923	44	22.43	+	1.96	6.65E-04
basolateral plasma membrane (GO:0016323)	246	9	0.93	+	9.66	7.33E-04
cell periphery (GO:0071944)	6313	45	23.91	+	1.88	1.30E-03
integral component of membrane (GO:0016021)	5764	42	21.83	+	1.92	2.51E-03
extracellular exosome (GO:0070062)	2098	23	7.95	+	2.89	3.02E-03
extracellular vesicle (GO:1903561)	2118	23	8.02	+	2.87	3.54E-03
extracellular organelle (GO:0043230)	2120	23	8.03	+	2.86	3.60E-03
cell-cell junction (GO:0005911)	493	11	1.87	+	5.89	4.24E-03
plasma membrane (GO:0005886)	5823	42	22.05	+	1.9	4.60E-03
extracellular space (GO:0005615)	3389	30	12.84	+	2.34	5.27E-03
cell leading edge (GO:0031252)	422	10	1.6	+	6.26	7.44E-03
external side of plasma membrane (GO:0009897)	429	10	1.62	+	6.15	8.57E-03
receptor complex (GO:0043235)	544	11	2.06	+	5.34	1.06E-02
cell projection membrane (GO:0031253)	346	9	1.31	+	6.87	1.11E-02
vesicle (GO:0031982)	3919	32	14.84	+	2.16	1.12E-02

Golgi apparatus (GO:0005794)	1627	19	6.16	+	3.08	1.23E-02
plasma membrane region (GO:0098590)	1241	16	4.7	+	3.4	2.23E-02
cytoplasmic vesicle (GO:0031410)	2429	23	9.2	+	2.5	3.40E-02
intracellular vesicle (GO:0097708)	2434	23	9.22	+	2.5	3.51E-02

Table 5.3 Gene Ontology Molecular Function Depleted in the SNX5+6 siRNA HRP-TGN46-Labelled Proteome

The list of proteins significantly depleted in the SNX5+6 siRNA HRP-TGN46 proteome **(Table 5.1)** were analysed with PANTHER gene ontology software. Significantly enriched/depleted molecular function categories are displayed, ranked by p-value. + = significant overrepresentation, - = significant underrepresentation of categories.

Gene Ontology Category	Category Size	# Proteins Identified	# Proteins Expected	Over/Under Representation	Fold Enrichment	p-Value
protein-containing complex binding (GO:0044877)	1277	20	4.84	+	4.14	1.33E-04
glycosaminoglycan binding (GO:0005539)	234	9	0.89	+	10.16	9.57E-04
virus receptor activity (GO:0001618)	76	6	0.29	+	20.85	1.90E-03
exogenous protein binding (GO:0140272)	77	6	0.29	+	20.57	2.04E-03
transmembrane receptor protein kinase activity (GO:0019199)	81	6	0.31	+	19.56	2.70E-03
cell adhesion molecule binding (GO:0050839)	538	12	2.04	+	5.89	2.82E-03
transmembrane receptor protein tyrosine kinase activity (GO:0004714)	62	5	0.23	+	21.29	1.55E-02

Table 5.4 Gene Ontology Biological Processes Depleted in the SNX5+6 siRNA HRP-TGN46-Labelled Proteome

The list of proteins significantly depleted in the SNX5+6 siRNA HRP-TGN46 proteome **(Table 5.1)** were analysed with PANTHER gene ontology software. Significantly enriched/depleted biological process categories are displayed, ranked by p-value. + = significant overrepresentation, - = significant underrepresentation of categories.

Gene Ontology Category	Category Size	# Proteins Identified	# Proteins Expected	Over/Under Representation	Fold Enrichment	p-Value
Unclassified (UNCLASSIFIED)	2746	2	10.4	-	0.19	0.00E+00
cell adhesion (GO:0007155)	951	22	3.6	+	6.11	5.17E-08
biological adhesion (GO:0022610)	957	22	3.62	+	6.07	5.84E-08
blood vessel morphogenesis (GO:0048514)	405	15	1.53	+	9.78	3.97E-07
tube morphogenesis (GO:0035239)	644	17	2.44	+	6.97	2.87E-06
blood vessel development (GO:0001568)	488	15	1.85	+	8.12	4.87E-06
entry into host (GO:0044409)	110	9	0.42	+	21.6	6.03E-06
movement in host environment (GO:0052126)	115	9	0.44	+	20.66	8.72E-06
vasculature development (GO:0001944)	511	15	1.94	+	7.75	8.99E-06
biological process involved in interaction with host (GO:0051701)	177	10	0.67	+	14.92	1.92E-05
tube development (GO:0035295)	840	18	3.18	+	5.66	2.05E-05
angiogenesis (GO:0001525)	313	12	1.19	+	10.12	2.89E-05
cell migration (GO:0016477)	962	17	3.64	+	4.67	9.76E-04
circulatory system development (GO:0072359)	852	16	3.23	+	4.96	1.10E-03
system development (GO:0048731)	4275	37	16.19	+	2.29	1.39E-03
viral entry into host cell (GO:0046718)	102	7	0.39	+	18.12	1.64E-03
locomotion (GO:0040011)	1336	19	5.06	+	3.76	4.24E-03
localization of cell (GO:0051674)	1100	17	4.17	+	4.08	6.27E-03

cell motility (GO:0048870)	1100	17	4.17	+	4.08	6.27E-03
immune system process (GO:0002376)	2849	28	10.79	+	2.59	8.35E-03
response to wounding (GO:0009611)	543	12	2.06	+	5.84	9.74E-03
multicellular organism development (GO:0007275)	4875	38	18.46	+	2.06	1.42E-02
cellular component organization (GO:0016043)	5776	42	21.88	+	1.92	1.61E-02
leukocyte activation (GO:0045321)	935	15	3.54	+	4.24	2.02E-02
biological process involved in symbiotic interaction (GO:0044403)	937	15	3.55	+	4.23	2.07E-02
regulation of cell adhesion (GO:0030155)	726	13	2.75	+	4.73	3.27E-02
viral process (GO:0016032)	849	14	3.22	+	4.35	3.38E-02
positive regulation of protein metabolic process (GO:0051247)	1539	19	5.83	+	3.26	3.42E-02
regulation of protein kinase B signaling (GO:0051896)	237	8	0.9	+	8.91	3.60E-02
anatomical structure formation involved in morphogenesis (GO:0048646)	869	14	3.29	+	4.25	4.40E-02

Appendix B: Publications

Daly, J.L., and Cullen, P.J. Endoplasmic Reticulum-Endosome Contact Sites: Specialized Interfaces for Endosomal Tubule Fission? *Biochemistry*. 2018, 57(49), 6738-6740.

Evans, A.J., **Daly, J.L**., Anuar, A.N.K., Simonetti, B., Cullen, P.J. Acute inactivation of retromer and ESCPE-1 leads to time-resolved defects in endosomal cargo sorting. *Journal of Cell Science*. 2020, 133(5)

Daly J.L.*, Simonetti, B.*, Klein, K.*, Chen, K.E. ‡, Williamson, M.K. ‡, Antón-Plágaro, C. ‡, Shomark, D.K., Simón-Gracia, L., Bauer, M., Hollandi, R., Greber, U.F., Horvath, P., Sessions, R.B., Helenius, A., Hiscox, J.A., Teesalu, T., Matthews, D.A., Davidson, A.D., Collins, B.M., Cullen, P.J., Yamauchi, Y. Neuropilin-1 is a host factor for SARS-CoV-2 infection. *Science*. 370(6518), 861-865.

* contributed equally.

‡ contributed equally.

Biochemistry
Viewpoint
Cite This: Biochemistry 2018, 57, 6738−6740
pubs.acs.org/biochemistry

Endoplasmic Reticulum−Endosome Contact Sites: Specialized Interfaces for Orchestrating Endosomal Tubule Fission?

James L. Daly and Peter J. Cullen*

School of Biochemistry, University of Bristol, Biomedical Sciences Building, Bristol BS8 1TD, U.K.

The endomembrane system enables the delegation of separate biological processes to spatially distinct organelles within eukaryotic cells. While it is imperative that the unique biochemical compositions of these compartments are maintained, interorganellar communication provides a means to dynamically exchange proteins, lipids, and ions, allowing eukaryotic cells to achieve a level of complexity that supersedes the sum of its parts. Recently, membrane contact sites (MCSs) have emerged as a novel mechanism for crosstalk between organelles, in addition to canonical processes of vesicular membrane trafficking. Most notably, tubules of the endoplasmic reticulum (ER) have been demonstrated to contact the plasma membrane, mitochondria, and endosomes, among other organelles. ER MCSs tether the opposing organelle membrane within 30 nm without the occurrence of membrane fusion. A range of functions of ER MCSs have thus far been established, including bidirectional lipid transfer, Ca^{2+} exchange, and fine-tuned control over organelle transport and positioning. A fascinating emerging concept is the potential role for tubular ER projections in the regulation of organelle fission. In a recent publication in *Cell*, Hoyer et al. investigated the role of ER−endosome MCSs in the regulation and timing of endosomal fission by developing a proximity-dependent labeling strategy with the biotin ligase enzyme BioID to identify novel ER proteins within the vicinity of dynamic endosomal tubules.[1]

Endosomal recycling is an essential process whereby transmembrane proteins (termed "cargoes") are recognized by their cytosolic sequence motifs and sorted away from a degradative fate as endosomes mature and fuse with lysosomes. This recognition is achieved by an array of evolutionarily conserved protein complexes, such as the retromer or retriever complexes, that integrate into higher-order coat structures.[2] These multiprotein assemblies corral cargo into a retrieval subdomain on the endosomal membrane and mediate the biogenesis of tubular structures that ultimately separate and traffic to an acceptor compartment such as the plasma membrane or trans-Golgi network (TGN). Despite the molecular details of this sequence-based cargo recognition and tubule formation becoming clearer, the final stages of tubule scission remain ambiguous. ER−endosome contact sites have been suggested to influence the process of endosomal sorting and trafficking by imposing a tight diffusion barrier on endosomal buds and defining the sites of tubule fission.[1]

The WASH complex, which is the major activator of the branched actin-nucleating Arp2/3 complex on endosomes, localizes to budding retrieval subdomains and plays an orchestrating role in the clustering of recycling complexes along the tubule.[2] By tagging BioID to the WASH complex subunit FAM21, Hoyer et al. establish a system for biotinylating vicinal proteins to this transient subdomain. Mass spectrometric analysis of labeled proteins revealed the ER transmembrane protein TMCC1 as a proximal protein to FAM21, in addition to a previously established ER MCS protein, VAPA/B. When expressed as a GFP fusion protein, TMCC1 (and its paralogues, TMCC2 and TMCC3) localized to discrete domains in the peripheral ER that colocalize with Rab7-positive budding endosomal tubules prior to fission. This represents a distinct distribution to other markers of ER−endosome MCSs, such as Protrudin that primarily contacts the vacuolar portion of the endosome, suggesting that the specific location of MCS formation is governed by precise protein−protein interactions that contribute to its function. Moreover, silencing of TMCC1 induced an impaired endosomal fission phenotype, whereby FAM21-positive endosomal buds form as usual but ultimately collapse back into the endosome following unsuccessful fission. Accordingly, TMCC1 knockdown resulted in dispersal of the prototypical endosome-to-TGN cargo CI-MPR, suggesting a defect in endosomal recycling.[1] These data are in agreement with the model of ER−endosome contact comprising a late step in endosomal fission.

On endosomes, Coronin 1C was also identified as a requisite for MCS formation at budding profiles. Coronin 1C is an actin-binding regulatory protein that mediates the turnover of actin filaments through Arp2/3 disassembly. Like FAM21, Coronin 1C localizes to budding Rab7-positive endosomal tubules. Depletion of Coronin 1C reduced the frequency of ER−endosome contacts and the efficiency of tubule fission, in a manner comparable to that of the phenotype observed upon TMCC1 knockdown.[1] Given the known function of Coronin 1C, this raises the intriguing possibility of actin dynamics playing an intimate role in the formation and/or stabilization of ER−endosome MCSs.

With the identification of two novel proteins that are required for the formation and maintenance of ER−endosome MCSs, the molecular landscape of these dynamic events is becoming clearer (Figure 1). However, the precise functions of these proteins in this process remain ambiguous, and a biochemical model that describes the order of events leading from MCS formation to tubule fission remains to be established. Recently, a mechanism was proposed whereby SNX2, a component of the cargo-selective SNX−BAR complex that localizes to endosomal tubules, directly contacts VAPA/B along with the endosomal lipid transfer protein OSBP.[3] Given the fact that SNX2 localizes to the same retrieval subdomains as FAM21 on endosomes, this pathway provides a potential clue as to how ER−endosome MCSs at these sites of fission

Received: November 12, 2018
Published: November 30, 2018

DOI: 10.1021/acs.biochem.8b01176
Biochemistry 2018, 57, 6738−6740

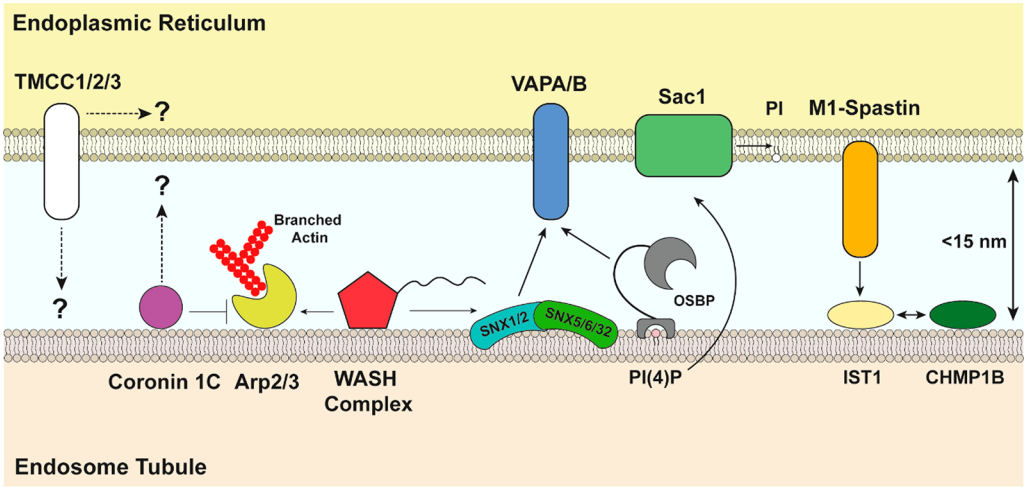

Figure 1. Mechanistic details of protein−protein interactions at the ER−endosomal tubule interface. The specific process of tubule recognition may be achieved by a combination of the validated VAPA/B−SNX2 interaction, association of TMCC1/2/3 with a currently unknown partner, or further as yet unidentified proteins. The role of Coronin 1C in the formation and stabilization of MCSs is unknown but may involve its actin-regulating activity. The interaction of M1-Spastin with IST1 has also been highlighted as a key interaction in the regulation of tubule fission. It should be noted that this is not an exhaustive representation of all proteins involved at ER−endosome MCSs but rather those associated specifically with tubular subdomains. PI denotes phosphatidylinositol; PI(4)P denotes phosphatidylinositol 4-phosphate.

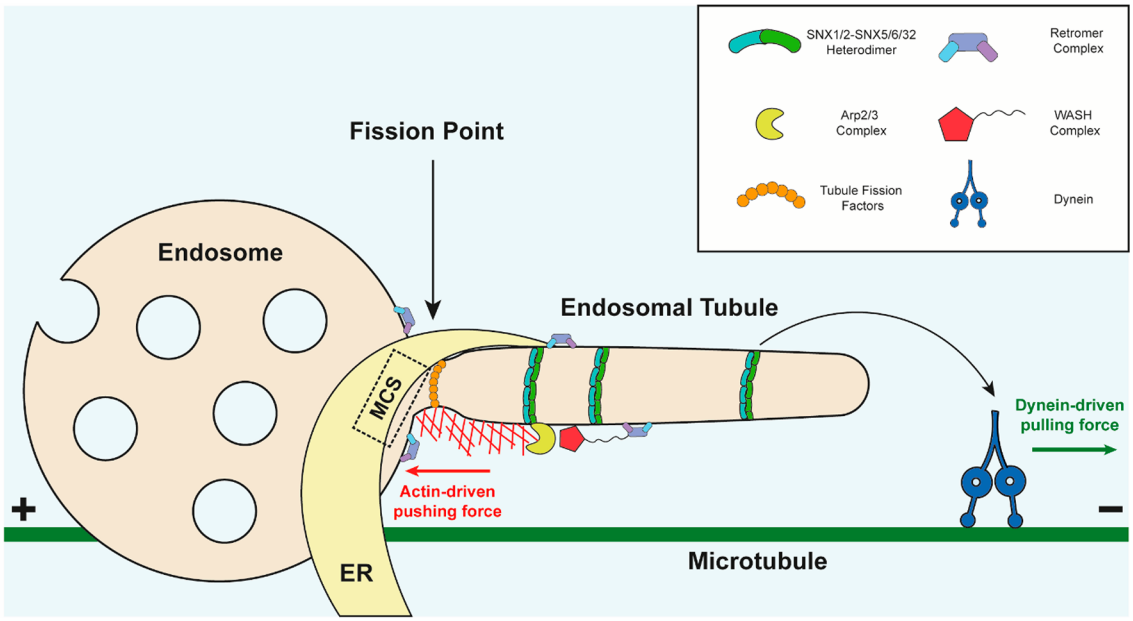

Figure 2. Overview of ER−endosome membrane contacts at endosomal tubules. Following tubule biogenesis and cargo enrichment, which is independent of ER contact, an ER−endosome MCS is proposed to form as a late stage in the fission process. From a biophysical viewpoint, this contact may serve to constrict the tubule membrane, aiding the process of tubule fission. A "pushing" force at the base of the tubule generated by branched actin polymerization and an opposite "pulling" force produced by dynein-dependent microtubule transport may also contribute to fission efficiency. It is also possible that constriction of the tubule membrane facilitates the recruitment of curvature-sensing fission factors to catalyze this process.

may be initiated. A variety of candidate fission factors on endosomal tubules have been proposed, including dynamins, EHD proteins, and ESCRT-III components IST1 and CHMP1B, but without definitive mechanisms. Furthermore, a biophysical hypothesis posits that frictional force generated as BAR-coated tubules elongate, combined with opposing "pushing" forces from branched actin polymerization and a mechanical "pulling" force from cytoskeletal motors, drives tubule scission (Figure 2).[4] An intriguing recent study demonstrated that artificially applied mechanical forces are sufficient to induce mitochondrial fission independently of ER MCSs, suggesting that the broad role of the ER in organelle fission may be to constrict the target membrane to a point by which curvature-sensing adaptors for fission machinery may assemble. Could it be possible that an analogous mechanism governs endosomal tubule fission? It is tempting to speculate that an initial constriction induced by ER contact serves to recruit fission factors or more generally imposes local tension that aids the process of friction-driven scission.

The functional consequences of ER−endosome MCSs for global cellular health are beginning to be determined. Recently, it was demonstrated that mutations in the ER-localized protein

DOI: 10.1021/acs.biochem.8b01176
Biochemistry 2018, 57, 6738−6740

M1-spastin that disrupt its ability to interact with IST1 on endosomes also induce a perturbed endosomal tubule fission phenotype that leads to pronounced lysosomal defects.[5] The process of tubular endosomal budding and trafficking is responsible for the dynamic subcellular localization of hundreds of cargo proteins.[2] For example, the β2-adrenergic receptor (β2AR) is a validated SNX27-retromer cargo for endosome-to-plasma membrane recycling that localizes to FAM21-positive, actin-rich endosomal tubules. A direct readout of the functional importance of these ER−endosome MCSs may therefore be achieved by analyzing the consequence of TMCC1 depletion for cell surface β2AR levels. Moreover, it will be interesting to investigate whether ER−endosome MCSs are required for all instances of endosomal tubule fission or solely in the fission of actin-rich, cargo retrieval tubules decorated with recycling complexes.

Mutations affecting endosomal cargo recognition and recycling have been linked to a range of diseases, most of which are neurological in their etiology.[2] In the future, it will be interesting to investigate the impact of MCSs at the level of model organisms and whether the effects of perturbing these contacts resemble the phenotypes observed following the disruption of endosomal recycling. As demonstrated in this most recent study, the continued partnership of spatiotemporally resolved live imaging and protein labeling will likely provide the key to discovering additional candidates that function at this dynamic membrane interface in the future.

AUTHOR INFORMATION

Corresponding Author

*E-mail: pete.cullen@bristol.ac.uk.

ORCID

James L. Daly: 0000-0002-4551-1256

Funding

J.L.D. was supported by a Wellcome Trust studentship for the Dynamic Molecular Cell Biology Ph.D. programme (203959/Z/16/Z). P.J.C. was supported by the Wellcome Trust (104568/Z/14/Z) and the Medical Research Council (MR/L007363/1 and MR/P018807/1).

Notes

The authors declare no competing financial interest.

REFERENCES

(1) Hoyer, M. J., Chitwood, P. J., Ebmeier, C. C., Striepen, J. F., Qi, R. Z., Old, W. M., and Voeltz, G. K. (2018) A Novel Class of ER Membrane Proteins Regulates ER-Associated Endosome Fission. *Cell 175*, 254−265.e14.

(2) Cullen, P. J., and Steinberg, F. (2018) To degrade or not to degrade: mechanisms and significance of endocytic recycling. *Nat. Rev. Mol. Cell Biol. 19*, 679−696.

(3) Dong, R., Saheki, Y., Swarup, S., Lucast, L., Harper, J. W., and De Camilli, P. (2016) Endosome-ER Contacts Control Actin Nucleation and Retromer Function through VAP-Dependent Regulation of PI4P. *Cell 166*, 408−423.

(4) Simunovic, M., Manneville, J. B., Renard, H. F., Evergren, E., Raghunathan, K., Bhatia, D., Kenworthy, A. K., Voth, G. A., Prost, J., McMahon, H. T., Johannes, L., Bassereau, P., and Callan-Jones, A. (2017) Friction Mediates Scission of Tubular Membranes Scaffolded by BAR Proteins. *Cell 170*, 172−184.e11.

(5) Allison, R., Edgar, J. R., Pearson, G., Rizo, T., Newton, T., Günther, S., Berner, F., Hague, J., Connell, J. W., Winkler, J., Lippincott-Schwartz, J., Beetz, C., Winner, B., and Reid, E. (2017) Defects in ER-endosome contacts impact lysosome function in hereditary spastic paraplegia. *J. Cell Biol. 216*, 1337−1355.

DOI: 10.1021/acs.biochem.8b01176
Biochemistry 2018, 57, 6738−6740

© 2020. Published by The Company of Biologists Ltd | Journal of Cell Science (2020) 133, jcs246033. doi:10.1242/jcs.246033

RESEARCH ARTICLE

Acute inactivation of retromer and ESCPE-1 leads to time-resolved defects in endosomal cargo sorting

Ashley J. Evans*,‡, James L. Daly, Anis N. K. Anuar, Boris Simonetti and Peter J. Cullen‡

ABSTRACT

Human retromer, a heterotrimer of VPS26 (VPS26A or VPS26B), VPS35 and VPS29, orchestrates the endosomal retrieval of internalised cargo and promotes their cell surface recycling, a prototypical cargo being the glucose transporter GLUT1 (also known as SLC2A1). The role of retromer in the retrograde sorting of the cation-independent mannose 6-phosphate receptor (CI-MPR, also known as IGF2R) from endosomes back to the *trans*-Golgi network remains controversial. Here, by applying knocksideways technology, we develop a method for acute retromer inactivation. While retromer knocksideways in HeLa and H4 human neuroglioma cells resulted in time-resolved defects in cell surface sorting of GLUT1, we failed to observe a quantifiable defect in CI-MPR sorting. In contrast, knocksideways of the ESCPE-1 complex – a key regulator of retrograde CI-MPR sorting – revealed time-resolved defects in CI-MPR sorting. Together, these data are consistent with a comparatively limited role for retromer in ESCPE-1-mediated CI-MPR retrograde sorting, and establish a methodology for acute retromer and ESCPE-1 inactivation that will aid the time-resolved dissection of their functional roles in endosomal cargo sorting.

KEY WORDS: ESCPE-1, VPS35, Endosome, Retromer, Knocksideways, GLUT1, CI-MPR, SNX5

INTRODUCTION

The endosomal pathway functions as a major intracellular hub for the sorting of numerous integral proteins, which include signalling receptors, adhesion molecules, nutrient transporters, ion channels, and their associated proteins and lipids (collectively termed 'cargoes') (Maxfield and McGraw, 2004; Grant and Donaldson, 2009; Cullen and Steinberg, 2018). On entering the pathway, cargoes are sorted between two fates: they are either selected for degradation within the lysosome, or retrieved from this fate and promoted for recycling to the plasma membrane and the *trans*-Golgi network (TGN) (Cullen and Steinberg, 2018). The efficient sorting of cargo is essential for normal cellular homeostasis, and defects in sorting are increasingly linked with human physiology and pathophysiology (Schreij et al., 2016; Cullen and Steinberg, 2018).

School of Biochemistry, Biomedical Sciences Building, University of Bristol, Bristol BS8 1TD, UK.
*Present address: Drug Discovery Unit, Cancer Research UK Manchester Institute, University of Manchester, Alderley Park, Macclesfield SK10 4TG, UK.

‡Authors for correspondence (pete.cullen@bristol.ac.uk, ae13237@bristol.ac.uk)

P.J.C., 0000-0002-9070-8349

Handling Editor: Daniel Billadeau
Received 9 March 2020; Accepted 5 June 2020

Sequence-dependent cargo sorting for retrieval and recycling is orchestrated by highly conserved multi-protein complexes that include the retromer and retriever complexes, the COMMD/CCDC22/CCDC93 (CCC) complex, and the endosomal SNX-BAR sorting complex for promoting exit-1 (ESCPE-1) complex (Seaman et al., 1998; Carlton et al., 2004; Phillips-Krawczak et al., 2015; McNally et al., 2017; Simonetti et al., 2019). These bind to sorting motifs present within the intracellular cytoplasmic domains of cargo either directly (Fjorback et al., 2012; Phillips-Krawczak et al., 2015; Bartuzi et al., 2016; Lucas et al., 2016; Kvainickas et al., 2017; Simonetti et al., 2019) or indirectly via cargo adaptors (Lauffer et al., 2010; Harterink et al., 2011; Temkin et al., 2011; Steinberg et al., 2012, 2013; Gallon et al., 2014; McNally et al., 2017). Working alongside these complexes, the endosome-associated Wiscott–Aldrich syndrome protein and SCAR homologue (WASH) complex drives the ARP2/3-mediated formation of branched F-actin networks (Derivery et al., 2009; Gomez and Billadeau, 2009). Together, cargo recognition and organisation of a localised F-actin network leads to the formation of one or more retrieval sub-domains on the cytosolic face of the endosomal membrane that provide platforms for the co-ordinated biogenesis of cargo-enriched transport carriers (Puthenveedu et al., 2010).

In higher metazoans, retromer is defined as a stable heterotrimer of VPS35, VPS29 and VPS26 (mammals express two paralogs, VPS26A and VPS26B) (Burd and Cullen, 2014). Retromer is associated to endosomes through binding to sorting nexin-3 (SNX3) (Harterink et al., 2011), RAB7-GTP (paralogs RAB7A and RAB7B) (Rojas et al., 2008; Seaman et al., 2009) and by association to cargo (Harrison et al., 2014; Lucas et al., 2016). Retromer also binds to sorting nexin-27 (SNX27), a cargo adaptor for the sequence-dependent recognition of around 400 cargo proteins that contain a specific type of C-terminal PDZ-binding motif (Temkin et al., 2011; Steinberg et al., 2013; Gallon et al., 2014; Clairfeuille et al., 2016). The principal role of retromer is therefore is to orchestrate the retrieval of hundreds of internalised cargo and to promote their recycling to the cell surface (Temkin et al., 2011; Steinberg et al., 2013). That being said, controversy remains as to the role of retromer in a distinct retrieval pathway, the retrograde endosome-to-TGN sorting of the cation-independent mannose 6-phosphate receptor (CI-MPR, also known as IGF2R) (reviewed in Seaman, 2018).

At steady state, CI-MPR is predominantly enriched at the TGN where it associates with newly synthesised hydrolase precursors (Braulke and Bonifacino, 2009). The resulting CI-MPR–hydrolase complex is transported to the endosomal pathway, where the acidified endosomal lumen induces the release of the hydrolase. While the hydrolase precursors are delivered to the lysosome, where they contribute to the degradative capacity of this organelle, the unoccupied CI-MPR is retrieved and recycled to the TGN for further rounds of hydrolase delivery. Many studies in mammalian

Journal of Cell Science (2020) 133, jcs246033. doi:10.1242/jcs.246033

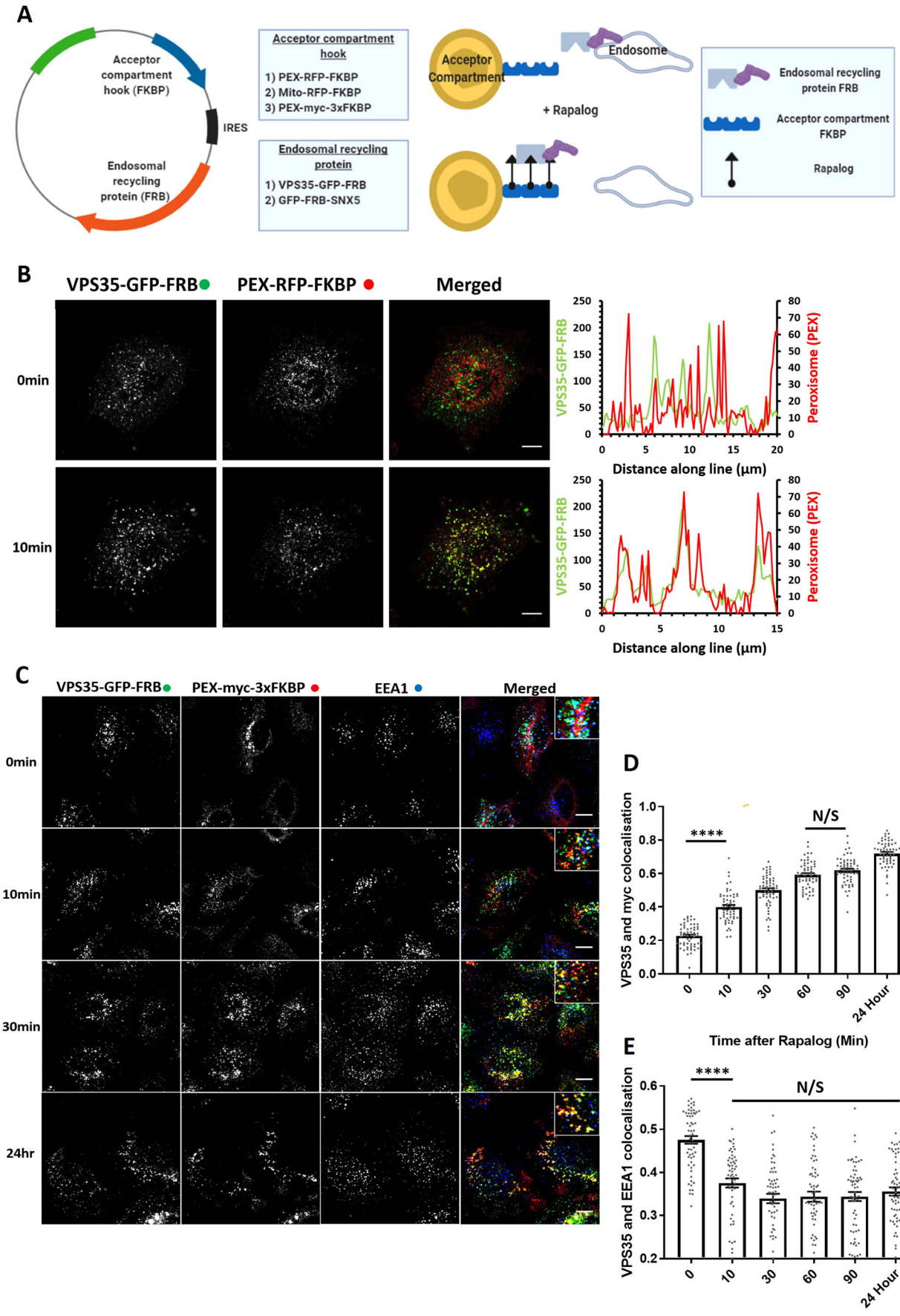

Fig. 1. See next page for legend.

Journal of Cell Science (2020) 133, jcs246033. doi:10.1242/jcs.246033

Fig. 1. Knocksideways can rapidly mislocalise retromer from endosomes. (A) Schematic showing the design of the endosomal knocksideways system. (B) HeLa cells transfected with retromer knocksideways (PEX–RFP–FKBP and VPS35–GFP–FRB). Still frames are shown from a movie (Movie 1A) at either 0 min or 10 min after the addition of rapalog. Line scans were generated using ImageJ by drawing a line through peroxisome structures, and represent the colocalisation between VPS35–GFP–FRB and PEX–RFP–FKBP at each time point. The merged panel displays both channels. (C) Retromer knocksideways HeLa cells were fixed at multiple time points after the addition of rapalog. Anti-Myc and anti-EEA1 antibodies were used to label PEX–Myc–3×FKBP and early endosomes, respectively, and the merged panel displays triple colocalisation between three channels. Magnified images are displayed in the insets at the top right of the merged image. (D) Pearson's colocalisation between VPS35–GFP–FRB and PEX–Myc–3×FKBP (peroxisomal targeting sequence) at multiple time points after the addition of rapalog. n_{exp}=3, n_{cell}=60 with all data points being displayed. (E) Pearson's colocalisation between VPS35–GFP–FRB and EEA1 (early endosome marker) at multiple time points after the addition of rapalog. n_{exp}=3, n=60 with all data points being displayed. ****P<0.0001; N/S, not significant (P>0.05) (ordinary one-way ANOVA with multiple comparisons). Error bars show the s.e.m. Scale bars: 10 µm.

cells are consistent with a role for retromer in CI-MPR transport (Arighi et al., 2004; Seaman, 2004, 2007; Wassmer et al., 2007; Bulankina et al., 2009; Harbour et al., 2010; Hao et al., 2013; Breusegem and Seaman, 2014; McGough et al., 2014; Cui et al., 2019). However, we, and others, have recently questioned the precise role of retromer in this pathway (Kvainickas et al., 2017; Simonetti et al., 2017). Rather, structural, biochemical and functional evidence has associated ESCPE-1 in sequence-dependent endosome-to-TGN sorting of the CI-MPR through direct recognition of a bipartite sorting motif localised within the unstructured cytosplasmic tail of this receptor (Kvainickas et al., 2017; Simonetti et al., 2017, 2019).

Part of this controversy may stem from technical variability and in particular the reliance on the generation of retromer knockdown and knockout cells (Seaman, 2018). These procedures induce the gradual loss of retromer expression over the course of hours and days, a time window that has the potential to initiate the activation of compensatory pathways that suppress phenotypes or result in variable and subtle phenotypes. Here, we have applied the 'knocksideways' methodology (Robinson et al., 2010) to acutely remove retromer and trap this complex on an organelle not implicated in retromer function. Using time-resolved analysis of cargo trafficking, we show that while acute retromer inactivation leads to robust defects in the endosomal recycling of the prototypical retromer cargo GLUT1 (also known as SLC2A1), we failed to detect a quantifiable perturbation in the distribution of the CI-MPR. In contrast, acute knocksideways-mediated inactivation of ESCPE-1 led to a time-resolved perturbation in CI-MPR endosome-to-TGN sorting. Our study therefore defines a method for the acute inactivation of endosomal retrieval and recycling complexes, and provides further data to support the need to reflect on the central role of retromer in the retrograde sorting of the CI-MPR.

RESULTS

Retromer knocksideways – design and temporal dynamics

To design the retromer knocksideways, we first engineered a cassette encoding the core VPS35 subunit fused through a C-terminal flexible linker to green fluorescent protein (GFP), which was itself linked to the N-terminus of rapamycin-binding (FRB) domain (resultant construct encoding VPS35–GFP–FRB, Fig. 1A). In light of evidence linking retromer to aspects of lysosomal function (e.g. Kvainickas et al., 2019), we utilised a modified version of FRB (T2098L) that enables the induction of heterodimerisation by rapalog (AP21967), a compound that has a lower affinity to endogenous mTOR than rapamycin (Clackson et al., 1998). To validate that the VPS35–GFP–FRB chimera was functional, we expressed the construct in a previously characterised VPS35-knockout HeLa cell line (Kvainickas et al., 2017). The VPS35–GFP–FRB chimera localised to cytosolic puncta that were identified as endosomes by means of colocalisation with the endosome marker EEA1 (Fig. S1A). Consistent with VPS35–GFP–FRB assembling into a functional retromer, expression of the VPS35–GFP–FRB chimera in the VPS35-knockout HeLa cells reverted the observed lysosomal missorting of GLUT1 and allowed recycling of the transporter back to the cell surface (Fig. S1B,C). The designed VPS35–GFP–FRB chimera is therefore correctly localised to endosomes and retains its function in endosomal cargo retrieval and recycling.

To engineer the acceptor compartment, we fused red fluorescent protein (RFP) to FKBP and linked this to either a mitochondrial targeting sequence [yeast Tom70p, forming Mito–RFP–FKBP (Robinson et al., 2010)] or a peroxisomal targeting sequence [PEX3 (residues 1–42), forming PEX–RFP–FKBP (Kapitein et al., 2010)]. To ensure a balanced co-expression, we cloned the genes encoding Mito–RFP–FKBP and VPS35–GFP–FRB into a bicistronic vector, and generated a corresponding bicistronic vector for PEX–RFP–FKBP and VSP35–GFP–FRB (Fig. 1A). To visualise the temporal dynamics of retromer knocksideways, we performed live imaging immediately after the application of rapalog. For both the mitochondrial and peroxisomal knocksideways systems, we observed dynamic accumulation of VPS35–GFP–FRB onto the corresponding acceptor compartment (Movies 1A and B), such that ∼10 min after induction of dimerisation there was clear colocalisation between retromer and the acceptor compartment (Fig. 1B; Fig. S1D).

Considering that retromer has been implicated in mitochondrial function (Braschi et al., 2010), we decided to focus on developing the peroxisomal acceptor compartment system; to date, peroxisomes have not been implicated in retromer biology. To increase the capacity of the acceptor compartment, we converted PEX–RFP–FKBP to PEX–Myc–3×FKBP (each FKBP separated by a flexible linker of GGSGGGSGGAP) (Fig. 1A). In transiently transfected HeLa cells, the PEX–Myc–3×FKBP chimera displayed colocalisation with the known peroxisome marker PMP70 (Fig. S1E).

In VPS35-knockout HeLa cells transiently transfected to express PEX–Myc–3×FKBP and VPS35–GFP–FRB, the addition of 100 nM of rapalog established that rerouting of VPS35–GFP–FRB from EEA1-positive endosomes to peroxisomes was achieved within 10 min and was complete by 30 min (Fig. 1C–E) – in the continued presence of rapalog the peroxisome rerouted VPS35–GFP–FRB was retained on this organelle (maximum time studied 24 h). Together, these data establish a method for the acute knocksideways of a functional VPS35–GFP–FRB construct.

Using knocksideways to examine retromer assembly in cells

GFP–nanotrap immunoisolation is an established method for identifying protein–protein interactions, including those of the retromer complex (McGough et al., 2014; McMillan et al., 2016). Here, we used knocksideways to analyse protein–protein interactions in living cells. Consistent with the assembly of VPS35–GFP–FRB into a functional complex (Fig. S2A), analysis of the endogenous localisation of VPS26 revealed that it too was rerouted to peroxisomes with a similar kinetic profile to that observed for VPS35–GFP–FRB (the lack of a suitable antibody

Journal of Cell Science (2020) 133, jcs246033. doi:10.1242/jcs.246033

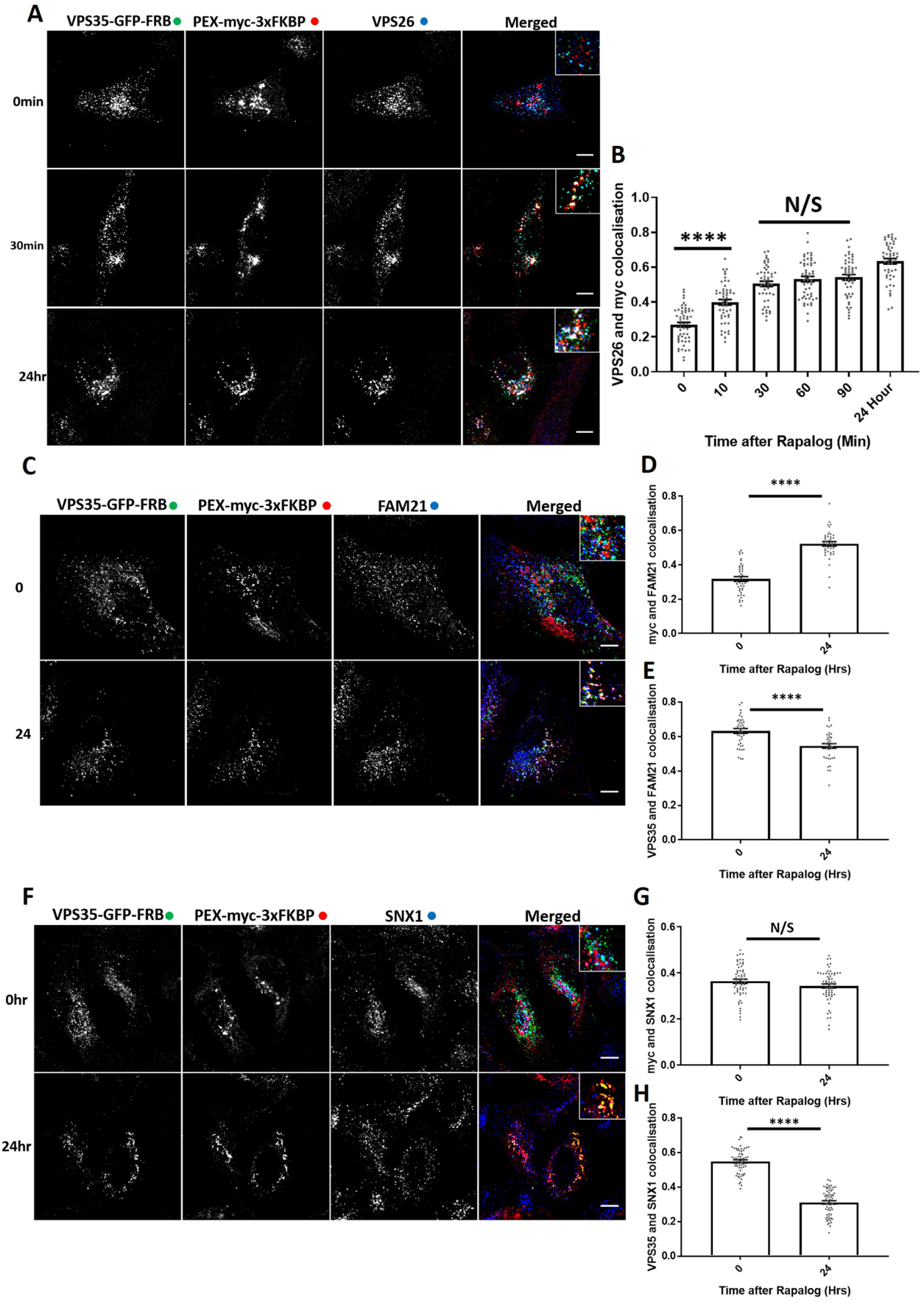

Fig. 2. See next page for legend.

Fig. 2. Retromer knocksideways 'drags' biochemically validated interacting proteins onto peroxisomes. (A) Retromer knocksideways HeLa cells were fixed before or at multiple time points after the addition of rapalog and labelled for Myc and VPS26. A merged panel displays all three channels combined with a magnified image (inset). (B) Pearson's colocalisation between VPS26 and Myc at multiple timepoints after the addition of rapalog. n_{exp}=3, n_{cell}=49-54 with all datapoints being displayed. ****P<0.0001; N/S, not significant (P>0.05) (ordinary one-way ANOVA with multiple comparisons). (C) Retromer knocksideways HeLa cells were fixed before or after 24 h of rapalog addition and then labelled with anti-myc and anti-FAM21 antibodies. The merged panel displays all three channels with a magnified image (inset). (D) Pearson's colocalisation between Myc and FAM21 before and after 24 h of rapalog treatment. n_{exp}=2, n_{cell}=40 with all data points being displayed. ****P<0.0001 (Welch's t-test). (E) Pearson's colocalisation between anti-VPS35 and anti-FAM21 antibodies before and after 24 h of rapalog treatment. n_{exp}=2, n_{cell}=40 with all data points being displayed. ****P<0.0001 (Welch's t-test). (F) Retromer knocksideways HeLa cells were fixed before or after 24 h of rapalog treatment and then labelled for Myc and SNX1. The merged panel displays the PEX–Myc–3×FKBP and SNX1 channels combined and with a magnified image (inset). (G) Pearson's colocalisation between Myc and SNX1 before and after the addition of rapalog for 24 h. n_{exp}=3, n_{cell}=60 with all datapoints being displayed. N/S, not significant (P>0.05) (Welch's t-test). (H) Pearson's colocalisation between VPS35–GFP–FRB and SNX1 before and after the addition of rapalog for 24 h. n_{exp}=3, n_{cell}=60 with all datapoints being displayed. ****P<0.0001 (Welch's t-test). Error bars show the s.e.m. Scale bars: 10 µm.

precluded the equivalent analysis of VPS29) (Fig. 2A,B). In addition, the major retromer accessory complex, the FAM21-containing WASH complex (Derivery et al., 2009; Gomez and Billadeau, 2009; Harbour et al., 2010; Jia et al., 2012) was also rerouted to peroxisomes upon retromer knocksideways (Fig. 2C,D; Fig. S2B,C). Supporting evidence that a sub-population of the WASH complex is associated with endosomes independently of retromer (McNally et al., 2017; MacDonald et al., 2018), a significant amount of the WASH complex was retained on endosomes even after retromer knocksideways (Fig. 2C,E; Fig. S2B,D,E). Retromer knocksideways was selective in that VPS35L, the core component of the functionally distinct retriever complex (McNally et al., 2017), retained endosome association and was not recruited to peroxisomes upon retromer knocksideways (Fig. S2F–H).

Given the selectivity of retromer knocksideways, we also decided to apply this methodology to examine the relationship between retromer and the SNX-BAR proteins that assemble to form the ESCPE-1 complex in cells (Simonetti et al., 2019). In yeast, these SNX-BAR proteins associate with the Vps26–Vps35–Vps29 heterotrimer to form the stable pentameric retromer complex (Seaman et al., 1998). In metazoans, however, retromer and ESCPE-1 appear to function independently, which is inconsistent with the formation of a long-lived and stable pentameric complex (Kvainickas et al., 2017; Simonetti et al., 2017). Indeed, we failed to observe the rerouting of endogenous SNX1, a component of the ESCPE-1 complex, onto peroxisomes after 24 h of rapalog treatment (Fig. 2F–H). These data therefore support the *in vivo* evidence that in metazoans retromer and ESCPE-1 have evolved into functionally distinct complexes (Kvainickas et al., 2017; Simonetti et al., 2017, 2019; Strutt et al., 2019). Overall, the designed VPS35 knocksideways provides a method for the acute and selective rerouting of retromer (and its functionally coupled accessory proteins) away from endosomes to neighbouring peroxisomes.

Acute retromer knocksideways leads to a time-resolved GLUT1 sorting defect

Retromer and retromer-associated cargo adaptors have been shown to control the endosomal retrieval and recycling of numerous cell surface proteins including the glucose transporter GLUT1 (Steinberg et al., 2013). To define the functional consequence of retromer knocksideways, we examined the steady-state distribution of GLUT1 in VPS35-knockout HeLa cells rescued by expression of the VPS35–GFP–FRB knocksideways construct. Following the addition of rapalog for 24 h, fixed cell confocal imaging revealed a GLUT1 missorting phenotype, defined by the steady-state loss of GLUT1 at the cell surface and the enrichment of GLUT1 with LAMP1-positive late endosomes/lysosomes (Fig. 3A,B). To time-resolve the appearance of the GLUT1 trafficking phenotype, we fixed cells at various points following rapalog addition. Quantification established that a statistically significant GLUT1 missorting phenotype began to emerge after 1–3 h of retromer knocksideways and reached a maximum penetrance after 10 h (Fig. 3C,D). The difference between the time scales of retromer knocksideways (Fig. 1C–E) compared with the appearance of the GLUT1 missorting phenotype is entirely consistent with the known rate of GLUT1 lysosomal-mediated degradation observed upon retromer suppression and reflects the relatively slow rate of endocytosis of this transporter (Steinberg et al., 2013).

The missorting of GLUT1 upon retromer knocksideways was not the result of a global effect on endosomal sorting, as the endosomal retrieval and recycling of the retriever-dependent cargo $\alpha_5\beta_1$-integrin (McNally et al., 2017) was not affected upon retromer knocksideways (Fig. S3A,B) – consistent with the lack of effect of retromer knocksideways on the endosomal association of the retriever complex (Fig. S2F–H). Moreover, the development of the GLUT1 missorting did not stem from the recruiting of 'foreign' proteins to peroxisomes as retromer knocksideways performed in wild-type HeLa cells, which retain expression of endogenous VPS35 that is not subject to knocksideways, did not elicit the development of a GLUT1 missorting phenotype (Fig. S3C,D). Together, these data support that it is the specific removal and inactivation of retromer that causes the time-resolved development of the observed GLUT1 missorting phenotype.

Retromer-independent CI-MPR retrograde trafficking

Next, we investigated the role of retromer in the retrograde trafficking of CI-MPR from endosomes to the TGN (Arighi et al., 2004; Seaman, 2004; Kvainickas et al., 2017; Simonetti et al., 2017; Cui et al., 2019). In VPS35-knockout HeLa cells rescued through expression of VPS35–GFP–FRB, the CI-MPR is chiefly localised to the perinuclear TGN, as defined through colocalisation with TGN markers Golgin97 and TGN46 (also known as GOLGA1 and TGOLN2, respectively) (Fig. 4A,B). After the addition of rapalog and initiation of retromer knocksideways, we failed to observe a quantifiable alteration in the steady-state distribution of the CI-MPR (Fig. 4A–D) over a time frame where the endosomal missorting of internalised GLUT1 was readily observed (Fig. 3C,D). Given that the endosome-to-TGN transport of the CI-MPR is considered to occur over a period of ∼20 to 30 min (Seaman, 2004), the acute perturbation of retromer function does not appear to lead to a detectable defect in the endosomal sorting of the CI-MPR (Kvainickas et al., 2017; Simonetti et al., 2017).

Knocksideways of ESCPE-1 leads to a time-resolved defect in CI-MPR sorting

The ESCPE-1 complex regulates sequence-dependent endosome-to-TGN transport of the CI-MPR (Simonetti et al., 2019). ESCPE-1 comprises a heterodimer of SNX1 or SNX2 (these proteins are functionally redundant) associated with either SNX5 or SNX6, which are also functionally redundant (Wassmer et al., 2007). Of

Journal of Cell Science (2020) 133, jcs246033. doi:10.1242/jcs.246033

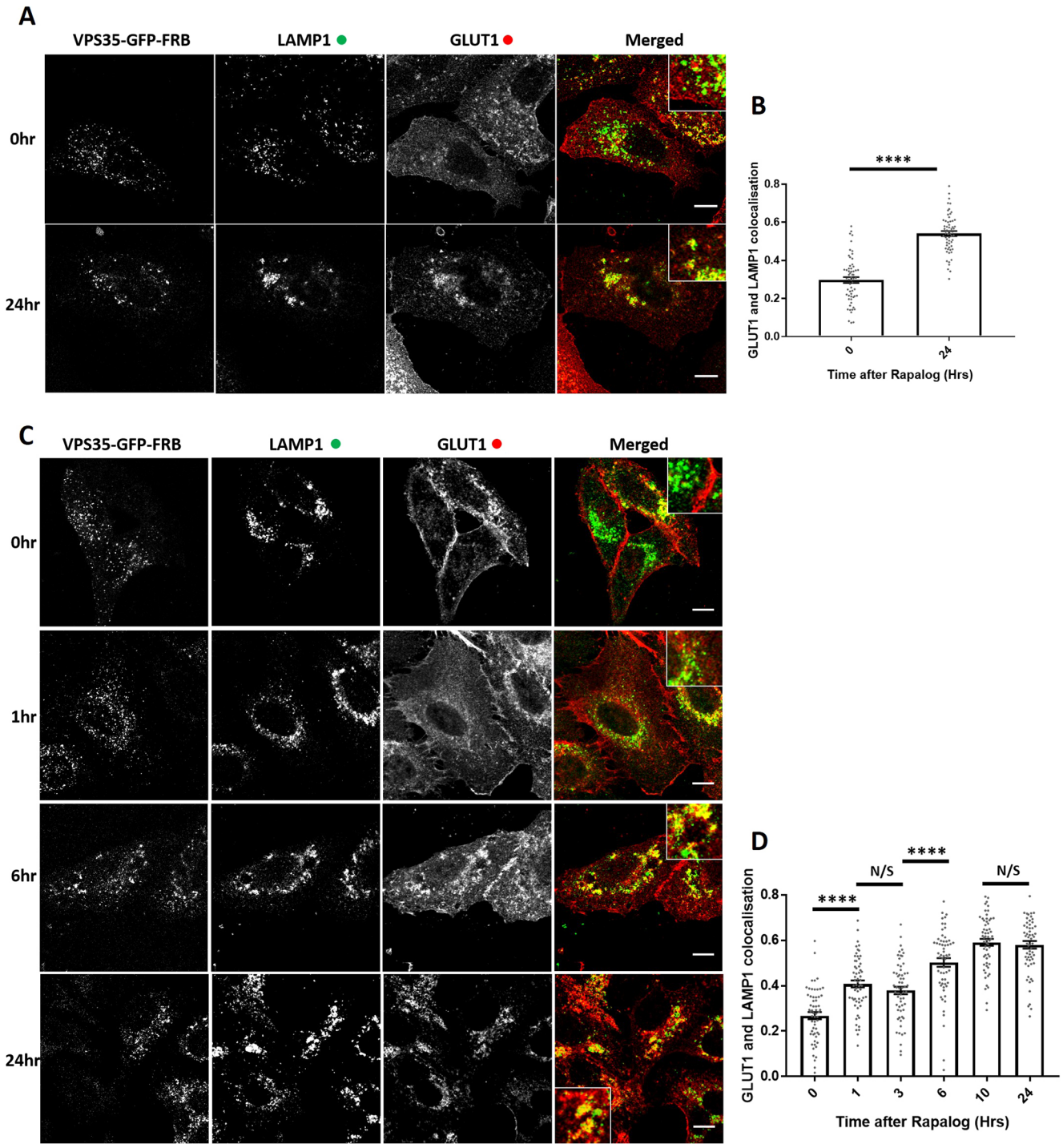

Fig. 3. Retromer knocksideways results in the rapid functional inactivation of retromer and the temporal resolution of the accumulation of retromer-depleted phenotypes. (A) Retromer knocksideways HeLa cells were fixed before or after 24 h of rapalog addition. Anti-LAMP1 and anti-GLUT1 were then used to label the late endosome/lysosome and retromer cargo, respectively. The merge panel displays both the LAMP1 (green) and the GLUT1 (red) channels with a magnified image (inset). (B) Pearson's colocalisation between GLUT1 and LAMP1 before and after 24 h of rapalog treatment. n_{exp}=3, n_{cell}=60 with all data points being displayed. ****P<0.0001 (Welch's t-test). (C) Retromer knocksideways HeLa cells were fixed before and after the indicated time of rapalog treatment. Anti-LAMP1 and anti-GLUT1 were then used to label late endosome/lysosome and retromer cargo, respectively. The merge panels display both the LAMP1 and GLUT1 labelling with a magnified image (inset). (D) Pearson's colocalisation between GLUT1 and LAMP1 before and at multiple time points after the addition of rapalog. n_{exp}=3, n_{cell}=60 with all data points being displayed. ****P<0.0001; N/S, not significant (P>0.05) (ordinary one-way ANOVA with multiple comparisons). Error bars show the s.e.m. Scale bars: 10 µm.

these proteins, it is the PX domains of SNX5 and SNX6 that directly bind to the ΦxΩxΦ(x)nΦ sorting motif (where Φ represents hydrophobic amino acids) in CI-MPR to mediate endosome-to-TGN transport (Simonetti et al., 2019). To provide a positive control for the lack of detectable effect of retromer knocksideways on CI-MPR trafficking, we therefore constructed a bicistronic vector

Journal of Cell Science (2020) 133, jcs246033. doi:10.1242/jcs.246033

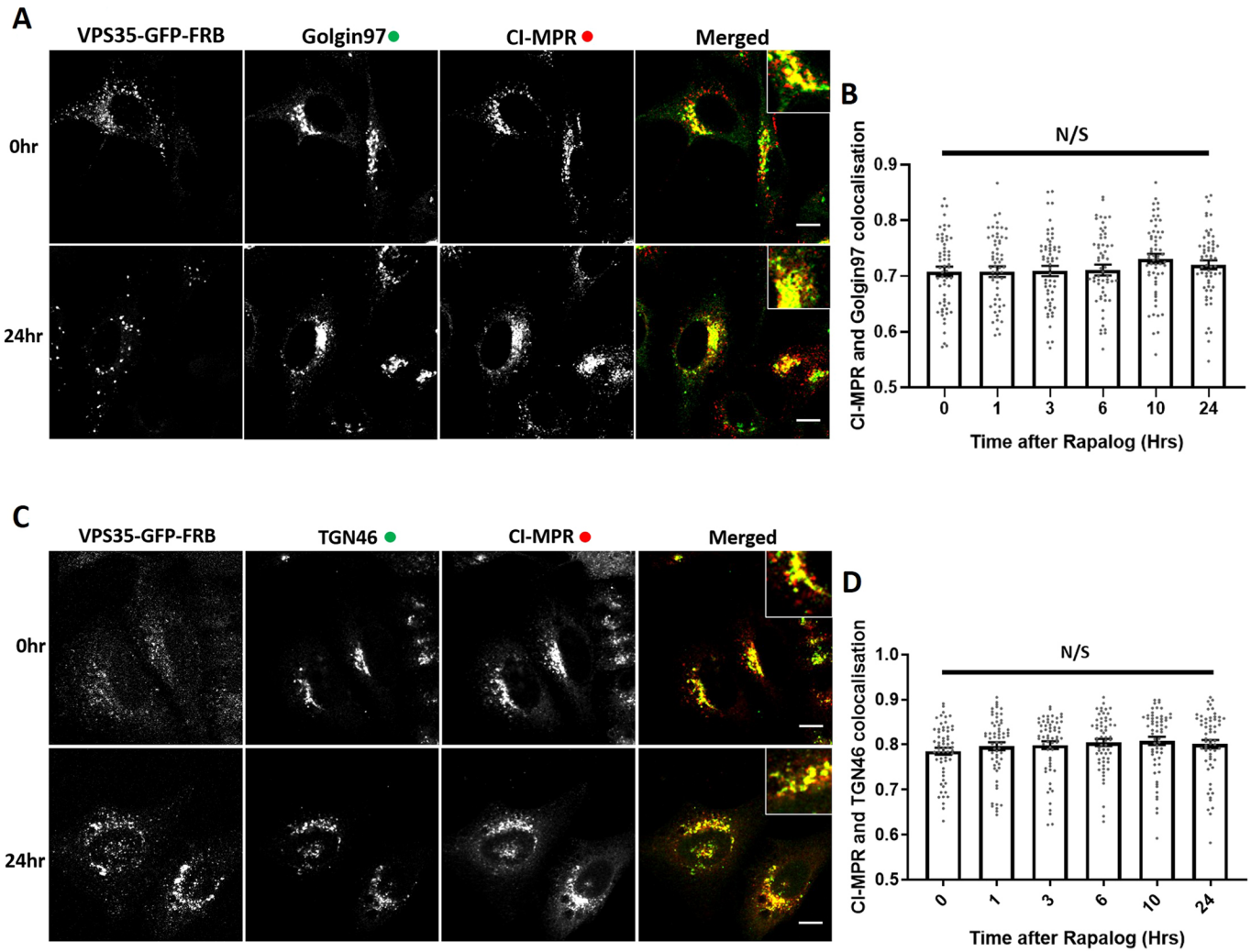

Fig. 4. Knocksideways indicates no visible role for retromer in SNX-BAR mediated retrograde transport of CI-MPR. (A) Retromer knocksideways HeLa cells were fixed before or at multiple time points after the addition of rapalog and labelled for Golgin97 and CI-MPR. A merged panel displays both the anti-Golgin97 and anti-CI-MPR channels with a magnified image (inset). (B) Pearson's colocalisation between CI-MPR and Golgin97 at multiple timepoints after the addition of rapalog. n_{exp}=3, n_{cell}=60 with all datapoints being displayed. (C) Retromer knocksideways HeLa cells were fixed before or at multiple time points after the addition of rapalog and labelled for TGN46 and CI-MPR. A merged panel displays both the TGN46 and CI-MPR channels with a magnified image (inset). (D) Pearson's colocalisation between CI-MPR and TGN46 at multiple timepoints after the addition of rapalog. n_{exp}=3, n_{cell}=60 with all datapoints being displayed. N/S, not significant (P>0.05) (ordinary one-way ANOVA with multiple comparisons). Error bars show the s.e.m. Scale bars: 10 µm.

encoding PEX–Myc–3×FKBP and GFP–FRB–SNX5 (Fig. 1A). When expressed in HeLa cells, GFP–FRB–SNX5 localised to endosomes as defined by colocalisation with EEA1 (Fig. 5A). Interestingly, after rapalog addition, we observed a slight recruitment of EEA1 to the peroxisomal hook, indicating a movement of the endosomal compartment to the peroxisomal compartment (Fig. 5B,C). However, this endosomal 'dragging' was not complete, as there was still a loss of colocalisation between GFP–FRB–SNX5 and EEA1 (Fig. 5B,D). In GFP–FRB–SNX5 knocksideways cells, endogenous SNX1 was recruited to peroxisomes after rapalog treatment with no loss of colocalisation between SNX5 and SNX1, indicating a recruitment of the functional ESCPE-1 complex (Fig. 5E–G).

Next, we used the GFP–FRB–SNX5 knocksideways system to time-resolve CI-MPR endosome-to-TGN trafficking. Expression of the GFP–FRB–SNX5 chimera in a previously isolated and characterised SNX5/SNX6 double-knockout HeLa cell line (Simonetti et al., 2017) reverted the observed missorting of the CI-MPR and allowed the receptor to return to its normal steady-state localisation (Fig. S4A,B). Consistent with the role of SNX5 in the ESCPE-1-mediated endosome-to-TGN transport of the CI-MPR (Kvainickas et al., 2017; Simonetti et al., 2017, 2019), SNX5 knocksideways in SNX5/SNX6 double-knockout HeLa cells led to the time-resolved appearance of a CI-MPR missorting phenotype as defined by a reduced enrichment of the CI-MPR at the Golgin97 or TGN46-labelled TGN with a maximum penetrance at 6 h (Fig. 6A, B; Fig. S4C,D). There was no observed defect in $\alpha_5\beta_1$-integrin recycling during GFP–FRB–SNX5 knocksideways, indicating the selective nature of this procedure (Fig. 6C,D). Together, these data establish that acute perturbation of the ESCPE-1 complex leads to a missorting of CI-MPR.

Establishing knocksideways in a human H4 neuroglioma cell line

Our study of endosomal cargo sorting associated with depletion or knocksideways of sorting machinery has so far been limited to a single non-neuronal cell type. To extend these observations, we therefore turned to H4 neuroglioma cells and generated both

Journal of Cell Science (2020) 133, jcs246033. doi:10.1242/jcs.246033

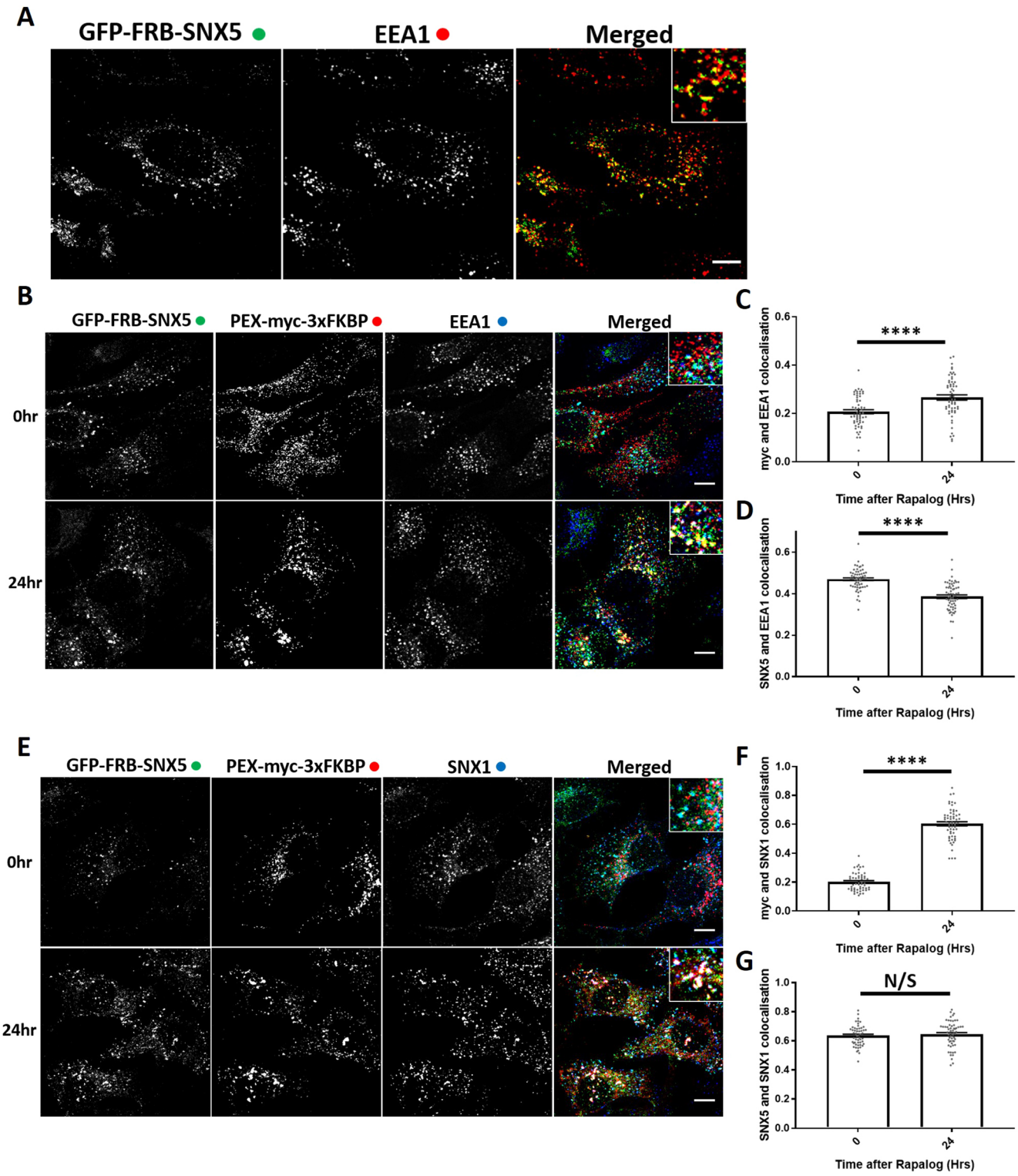

Fig. 5. ESCPE-1 knocksideways results in the dragging of a small population of endosomes and peroxisomes together while still removing ESCPE-1 from endosomes. (A) SNX-BAR knocksideways cells were fixed and then labelled with anti-EEA1 antibody. Both the GFP–FRB–SNX5 and EEA1 channels are shown in the merged panel with a magnified image (inset). (B) ESCPE-1 knocksideways HeLa cells were fixed before and after the addition of rapalog for 24 h and then labelled for Myc and EEA1. The merged panel shows all three channels with a magnified image (inset). (C) Pearson's colocalisation between Myc and EEA1 before and after 24 h of rapalog treatment. n_{exp}=3, n_{cell}=60 with all data points being displayed. (D) Pearson's colocalisation between GFP–FRB–SNX5 and EEA1 before and after 24 h of rapalog treatment. n_{exp}=3, n_{cell}=60 with all data points being displayed. (E) ESCPE-1 knocksideways HeLa cells were fixed before and after the addition of rapalog for 24 h and then labelled for Myc and SNX1. The merged panel shows all three channels with a magnified image (inset). (F) Pearson's colocalisation between Myc and SNX1 before and after 24 h of rapalog treatment. n_{exp}=3, n_{cell}=53-60 with all data points being displayed. (G) Pearson's colocalisation between GFP–FRB–SNX5 and SNX1 before and after 24 h of rapalog treatment. n_{exp}=3, n_{cell}=53–60 with all data points being displayed. ****P<0.0001; N/S, not significant (P>0.05) (Welch's t-test). Error bars show the s.e.m. Scale bars: 10 µm.

Journal of Cell Science (2020) 133, jcs246033. doi:10.1242/jcs.246033

retromer knockout (targeting VPS35) and ESCPE-1-knockout cells (dual targeting of SNX5 and SNX6). Interestingly, confocal imaging of the retromer-knockout cells revealed an enhanced intensity in the staining of endogenous CI-MPR that was not observed in the ESCPE-1-knockout cells (Fig. 7A,B). Despite the increase in the CI-MPR signal intensity, retromer-knockout cells did not display a significant change in the quantified Pearson's correlation coefficient between CI-MPR and Golgin97 (Fig. 7A, C). In contrast, the ESCPE-1 knockout H4 neuroglioma cells displayed a clear redistribution of CI-MPR to peripheral dispersed puncta (Fig. 7A,D; Fig. S5A).

To extend these data, we isolated individual clonal retromer and ESCPE-1-knockout H4 cell lines. Biochemical analysis of three independent clonal lines revealed that retromer knockout resulted in a pronounced upregulation of CI-MPR protein levels (Fig. S5B). Moreover, the abundance of another lysosomal hydrolase receptor, sortilin, was also increased across all three independent lines, as was the immature and mature forms of the lysosomal hydrolase cathepsin D (Fig. 7E–I). These increases in protein levels were not observed across three independent ESCPE-1-knockout H4 cell lines (Fig. 7E–I).

To examine whether the increased protein abundance of CI-MPR, sortilin and cathepsin D arose from a retromer-dependent trafficking

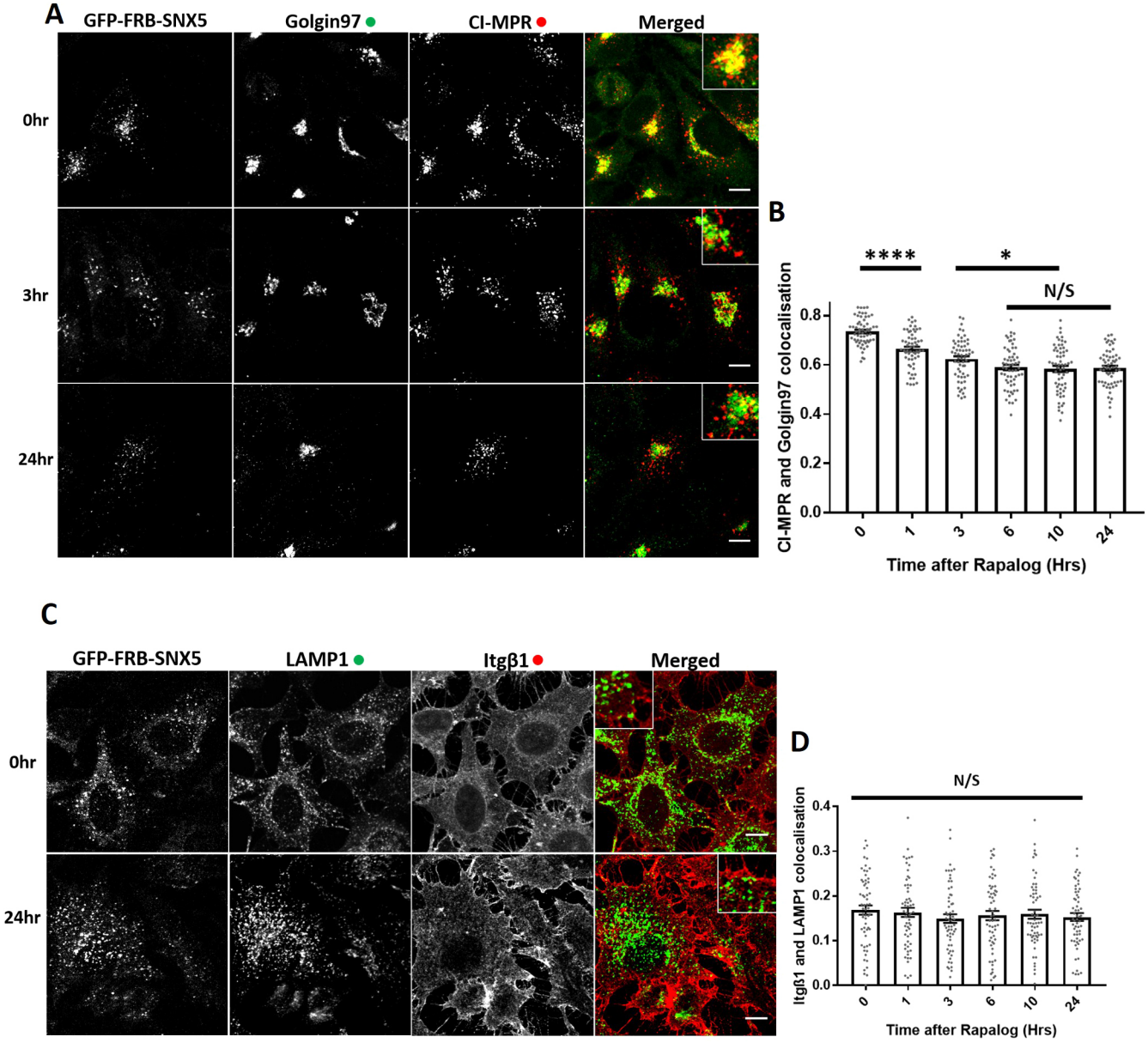

Fig. 6. ESCPE-1 knocksideways inactivates ESCPE-1 and results in a temporally resolved CI-MPR redistribution away from the TGN. (A) SNX-BAR knocksideways HeLa cells were fixed before or at multiple time points after the addition of rapalog and then labelled for Golgin97 and CI-MPR. The merged panel shows both the anti-Golgin97 and anti-CI-MPR channels with a magnified image (inset). (B) Pearson's colocalisation between Golgin97 and CI-MPR before or at multiple time points after the addition of rapalog. n_{exp}=3, n_{cell}=60 with all data points being displayed. (C) SNX-BAR knocksideways HeLa cells were fixed before or at multiple time points after the addition of rapalog and then labelled for LAMP1 and Itgβ1. The merged panel shows both the LAMP1 and Itgβ1 channels with a zoom panel. (D) Pearson's colocalisation between LAMP1 and Itgβ1 before or at multiple time points after the addition of rapalog. n_{exp}=3, n_{cell}=60 with all data points being displayed. *P<0.05; ****P<0.0001; N/S, not significant (P>0.05) (ordinary one-way ANOVA with multiple comparisons). Error bars show the s.e.m. Scale bars: 10 µm.

Journal of Cell Science (2020) 133, jcs246033. doi:10.1242/jcs.246033

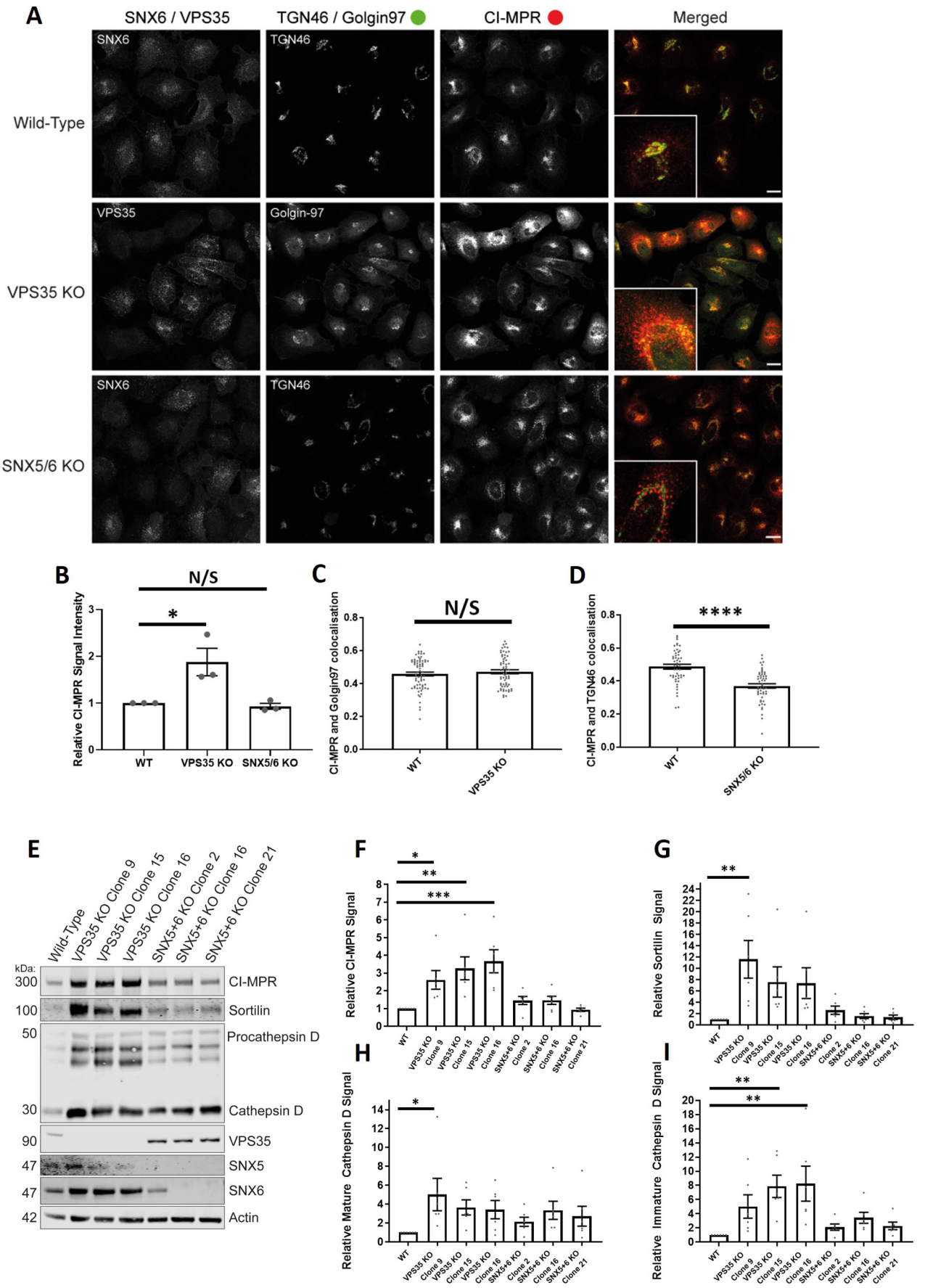

Fig. 7. See next page for legend.

Journal of Cell Science

Fig. 7. VPS35-knockout H4 neuroglioma cells display an upregulation of lysosomal hydrolases and lysosomal hydrolase receptors. (A) VPS35 and SNX5/SNX6 dual-knockout mixed population H4 neuroglioma cells were generated and then fixed. Cells were stained with either anti-VPS35 or anti-SNX6 antibodies to confirm which cells were knocked out in the mixed population. Cells were also co-stained with both anti-CI-MPR and either anti-TGN46 (SNX5/SNX6 dual knockout) or anti-Golgin97 (VPS35 knockout) antibodies. The merged panel displays both the CI-MPR and TGN46 or Golgin97 channels. Scale bars: 20 µm. (B) Normalised values for relative CI-MPR signal intensity between conditions. n_{exp}=3, n_{cell}=44–68 with average value data being shown for each experiment. P<0.05; N/S, not significant (P>0.05) (Student's t-test). (C) Pearson's colocalisation between CI-MPR and Golgin97 in wild-type and VPS35-knockout cells. n_{exp}=3, n_{cell}=64–69 with all data points being displayed. N/S, not significant (P>0.05) (Welch's t-test). (D) Pearson's colocalisation between CI-MPR and TGN46 in wild-type and SNX5/SNX6 knockout cells. n_{exp}=3, n_{cell}=49–53 with all data points being displayed. ****P<0.0001 (Welch's t-test). (E) Representative western blot analysis of wild-type and VPS35-knockout or SNX5/SNX6 knockout clonal cell lines using anti-CI-MPR, anti-sortilin, anti-cathepsin D, anti-VPS35, anti-SNX5, anti-SNX6 amd anti-actin antibodies. (F–I) Relative (actin) measured signals for wild-type and VPS35-knockout or SNX5/SNX6 dual-knockout clonal cell lines for CI-MPR, sortilin, mature cathepsin D and immature cathepsin D. n=7. *P<0.05; **P<0.01; ***P<0.001 (ordinary one-way ANOVA with multiple comparisons). Error bars show the s.e.m.

defect or reflected a longer-term compensatory mechanism, we established the acute VPS35 knocksideways methodology in H4 cells. Expression of VPS35–GFP–FRB rescued the GLUT1 missorting phenotype in retromer-knockout cells. Initiation of VPS35 knocksideways resulted in a time-resolved missorting and accumulation of GLUT1 to LAMP1-positive late endosomes and lysosomes (Fig. 8A,B) confirming an acute perturbation in retromer function (Fig. 3C,D). In a parallel time-resolved retromer knocksideways experiments, we failed to detect a significant redistribution of CI-MPR away from TGN markers Golgin97 and TGN46 (Fig. 8C–F). These data in H4 cells therefore corroborates our observation in HeLa cells, and does not appear to explain the increased protein abundance of CI-MPR, sortilin and cathepsin D.

DISCUSSION

Here, we have developed and applied knocksideways to acutely inactivate retromer and the ESCPE-1 complex (Fig. 1A). Previously developed to inactivate the AP1 and AP2 clathrin adaptors (Robinson et al., 2010; Hirst et al., 2012), this approach provides a method to acutely perturb the function of sorting complexes in a time frame that better aligns with the dynamic nature of endosomal membrane trafficking. By visualising the sorting of endogenous GLUT1 and CI-MPR, our data provide insight into the temporal dynamics of endosomal cargo sorting and support the established role of retromer in cell surface recycling (Temkin et al., 2011; Steinberg et al., 2013).

In applying knocksideways, we have established that retromer and ESCPE-1 can be specifically and rapidly inactivated, leading to the time-resolved development of selective cargo sorting defects through the endosomal pathway. Interestingly, in examining CI-MPR phenotypes in H4 neuroglioma cells, we observed a clear distinction between acute retromer knocksideways and the long-term effects of retromer knockout. Only in the latter did we observe an increase in the steady-state expression of CI-MPR, sortilin and cathepsin D (Fig. S5C). In part, this phenotype may reflect the role of retromer as a master regulator (Jimenez-Orgaz et al., 2018) of the activity state of endosomal RAB7 through binding to the RAB7 GAP TBC1D5 (Seaman et al., 2009, 2018; Jimenez-Orgaz et al., 2018; Kvainickas et al., 2019). In the absence of retromer, RAB7 loses its dynamic organisation on endosomes and lysosomes and becomes hyperactivated and immobile on lysosomes (Jimenez-Orgaz et al., 2018; Seaman et al., 2018). This leads to impaired mTORC1 activity and the induction of autophagy, and the appearance of swollen and evenly dispersed lysosomes (Jimenez-Orgaz et al., 2018; Cui et al., 2019; Curnock et al., 2019; Kvainickas et al., 2019). Moreover, retromer-knockout cells display activation of the TFEB transcription factors (Curnock et al., 2019), master regulators of cellular nutrient sensing and energy metabolism (Sardiello et al., 2009; Settembre et al., 2011). Thus, besides its role in cargo retrieval and recycling within the endosomal pathway (Steinberg et al., 2013), retromer has emerged as a master regulator of RAB7 in nutrient sensing and signalling (Jimenez-Orgaz et al., 2018; Curnock et al., 2019; Kvainickas et al., 2019). The observed upregulation of CI-MPR, sortilin and cathepsin D expression in H4 neuroglioma cells therefore likely reflects this regulatory role, through a complex compensation in lysosomal function induced by long-term retromer knockout.

In yeast, retromer is a pentameric assembly (Seaman et al., 1998). An increasing body of biochemical, cellular and *in vivo* functional data are consistent with the equivalent metazoan assembly having evolved into two functionally distinct complexes, the retromer (VPS26–VPS35–VPS29) and the ESCPE-1 (SNX1/SNX2 and SNX5/SNX6) complexes (Norwood et al., 2011; Swarbrick et al., 2011; Kvainickas et al., 2017; Simonetti et al., 2017, 2019; Strutt et al., 2019). In utilising knocksideways as an interaction assay in living cells, we have provided further supporting evidence of the distinct nature of the retromer and ESCPE-1 complexes. Specifically, acute knocksideways of the core VPS35 retromer component results in the equivalent time-resolved knocksideways of the endogenous population of VPS26 but has no detectable effect on the endosomal localisation of ESCPE-1. This technically distinct approach therefore provides further data to support the diversification of retromer and ESCPE-1 into two functionally distinct sorting complexes.

The development of retromer knocksideways has added to our understanding of the endosomal association of the actin polymerising WASH complex. Direct binding of FAM21 to VPS35 is a major mechanism for the retromer-dependent association of the WASH complex to endosomes (Gomez and Billadeau, 2009; Harbour et al., 2010; Jia et al., 2012). That said, increasing evidence suggests that a subpopulation of the WASH complex is associated to endosomes independently of retromer (McNally et al., 2017; Kvainickas et al., 2017; Simonetti et al., 2017; MacDonald et al., 2018). Consistent with these data, acute knocksideways of retromer induces a redistribution of a major proportion of endogenous WASH, but a significant subpopulation retains an endosomal association.

In summary, by applying knocksideways, we have acutely inactivated retromer and ESCPE-1 and, through quantification of the resulting temporal development of cargo-sorting defects, provided clarification of the role of these complexes in the sorting of CI-MPR and GLUT1 (Fig. S5C). While not excluding a role for retromer in the known complexities of CI-MPR sorting (Seaman, 2018), our time-resolved analysis establishes that the ESCPE-1 complex is the primary mediator of sequence-dependent endosome-to-TGN sorting of this receptor.

MATERIALS AND METHODS

Antibodies

Antibodies used in this study are as follows: SNX1 [clone 51; 611482; BD Bioscience; immunofluorescence (IF) 1:200], GLUT1 (ab40084; Abcam; IF 1:200), Golgin97 (clone CDF4; A-21270; Thermo Fisher Scientific; IF 1:400), VPS26 (ab23892; Abcam; IF 1:200), VPS35 (ab10099; Abcam; IF

Journal of Cell Science (2020) 133, jcs246033. doi:10.1242/jcs.246033

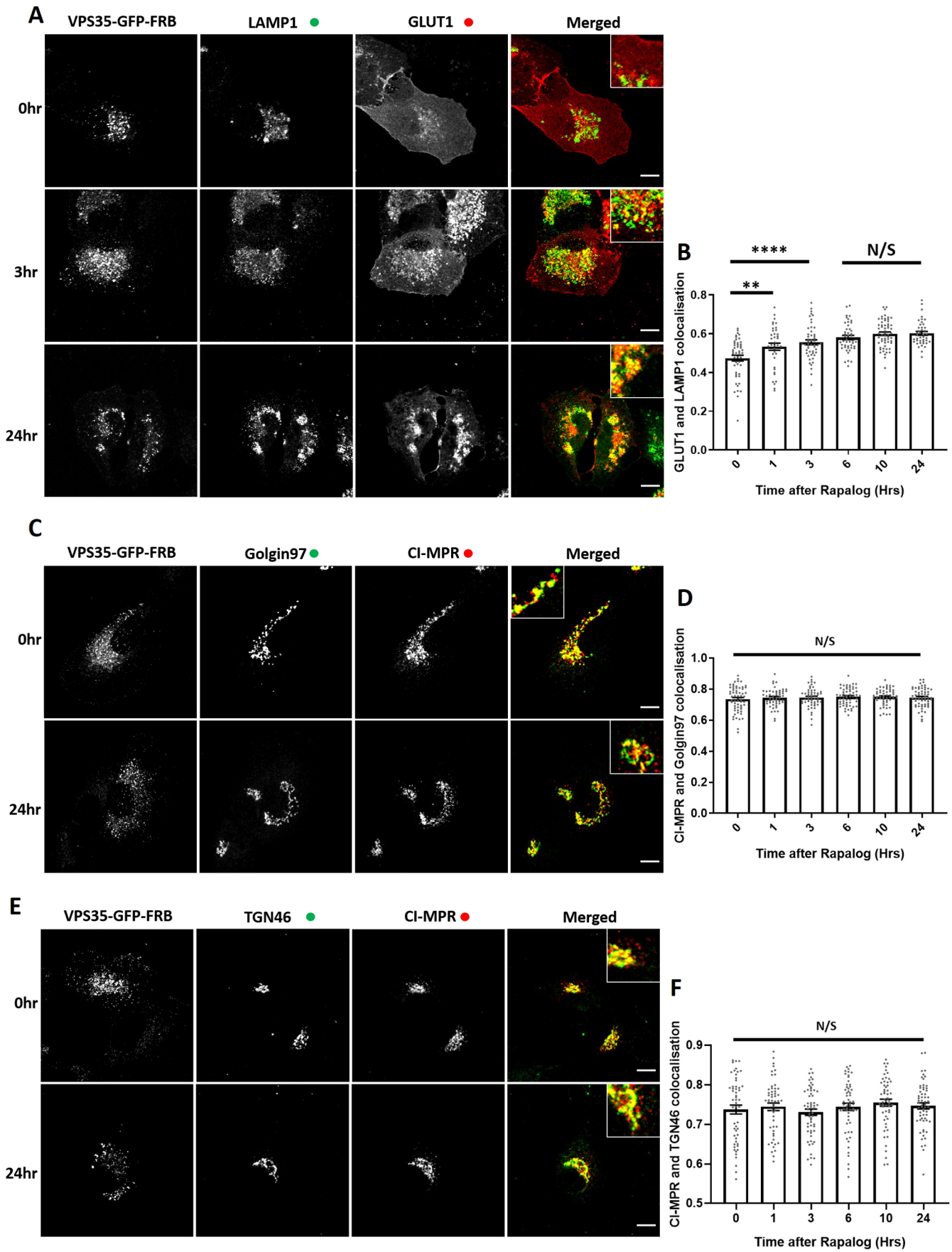

Fig. 8. See next page for legend.

Journal of Cell Science (2020) 133, jcs246033. doi:10.1242/jcs.246033

Fig. 8. VPS35 knocksideways in H4 neuroglioma cells confirms a role for retromer in recycling of GLUT1 but no visible role for retromer in the retrograde CI-MPR trafficking. (A) Retromer knocksideways H4 neuroglioma cells were fixed before or at multiple time points after the addition of rapalog. Antibodies towards anti-LAMP1 and anti-GLUT1 were then used to label late endosome/lysosome and retromer cargo, respectively. The merge panels display both the LAMP1 and GLUT1 labelling with a magnified image (inset). (B) Pearson's colocalisation between GLUT1 and LAMP1 before or at multiple time points after the addition of rapalog. n_{exp}=3, n_{cell}=37–58 with all data points being displayed. (C) Retromer knocksideways H4 neuroglioma cells were fixed before or or at multiple time points after the addition of rapalog and labelled with anti-Golgin97 and anti-CI-MPR antibodies. A merged panel displays both the Golgin97 and CI-MPR channels with a magnified image (inset). (D) Pearson's colocalisation between CI-MPR and Golgin97 at multiple timepoints after the addition of rapalog. n_{exp}=3, n_{cell}=52–60 with all data points being displayed. (E) Retromer knocksideways H4 neuroblastoma cells were fixed before or at multiple time points after the addition of rapalog and labelled with anti-TGN46 and anti-CI-MPR antibodies. A merged panel displays both the TGN46 and CI-MPR channels. (F) Pearson's colocalisation between CI-MPR and TGN46 at multiple time points after the addition of rapalog. n_{exp}=3, n_{cell}=52–56 with all datapoints being displayed. $^{**}P<0.01$; $^{****}P<0.0001$; N/S, not significant ($P>0.05$) (ordinary one-way ANOVA with multiple comparisons). Error bars show the s.e.m. Scale bars: 10 µm.

1:200), VPS35 [ab97545; Abcam; IF 1:200), VPS35 [ab157220; Abcam; western blotting (WB) 1:1000], VPS29 (ab98929; Abcam; WB 1:200), FAM21 (gift from Daniel D. Billadeau, Mayo Clinic, Rochester, MN; IF 1:400), EEA1 (N-19; sc-6415; Santa Cruz Biotechnology; IF 1:200), TGN46 (AHP500G; Bio-Rad Laboratories; IF 1:200), anti-Myc (gift from Harry Mellor, The University of Bristol, UK; IF 1:500), LAMP1 (DSHB Hybridoma Product; H4A3; deposited to the DSHB by August, J.T./Hildreth, J.E.K.; IF 1:500), LAMP1 (ab24170; Abcam; IF 1:200), mouse EEA1 (610457; BD Bioscience; IF 1:200), CI-MPR (ab124767; Abcam; WB 1:1000, IF 1:200), Itgβ1 (TS2/16; IF 1:200), SNX6 (Clone D-5; 365965; Santa Cruz Biotechnology; WB 1:500), PMP70 (PA1-650; Invitrogen; IF 1:200), WASH1 (gift from Daniel D. Billadeau; IF 1:400), C16orf62 (PA5-28553; Pierce; IF 1:200), sortilin (ab16640; Abcam; WB 1:1000), cathepsin D (21327-1-AP, Proteintech; WB 1:1000), SNX5 (ab180520; Abcam; WB 1:500) and β-actin (A1978; Sigma-Aldrich; WB 1:2000).

Plasmids

A pIRESneo3 vector was adapted to generate the bicistronic knocksideways system. First, VPS35–GFP and FRB (PCR from the Kinesin-FRB template (gift from Lukas Kapetein, Utrecht University, Netherlands) were PCR overlapped together inserting a XhoI site between VPS35–GRP and FRB and then ligated downstream of the IRES component between the SmaI and PacI sites. PEX–RFP–FKBP was amplified from the template (gift from Lukas Kapetein) and ligated into the MCS downstream of the CMV promoter in pIRESNEO3 using EcoRV and NotI. The mitochondrial targeting sequence (gift from Scottie Robinson CIMR, UK) was inserted in place of the PEX targeting sequence using the EcoRV and AgeI restriction sites. To create GFP–FRB–SNX5, first, GFP–FRB was amplified and inserted between the SmaI and PacI sites to generate a new FseI site upstream of the PacI restriction site. The new FseI and PacI site was used to insert SNX5. The PEX–RFP–FKBP was converted to PEX–Myc–3×FKBP by PCR of Myc–FKBP and inserted between the AgeI and NotI sites to generate PEX–Myc–FKBP. The AscI site (upstream of FKBP in the PEX–RFP–FKBP) was used to sequential insert two FKBP cassettes using a MluI-AscI insertion (MluI compatible with AscI but destroying the AscI site allowing the second insertion). CRISPR Cas9 plasmids were obtained from Addgene (#62988, pSpCas9(BB)-2A-Puro PX459 V2.0).

Cell culture and DNA transfection

HeLa (American Type Culture Association) and H4 neuroglioma cells (we thank Dr Helen Scott and Professor James Uney for providing this cell line) were cultured in DMEM (Sigma) supplemented with 10% (v/v) FCS (Sigma) and grown using standard conditions. Lipofectamine LTX was used in DNA transfections. For each six well dish, 2 µg of DNA was mixed with 4 µl of the LTX supplement into 100 µl of Opti-Mem (Thermo Fisher). In another incubation, 100 µl of Opti-Mem was mixed with 8 µl of Lipofectamine LTX. After a 5-min incubation, the two 100 µl Opti-Mem mixes were combined and incubated for a further 20 min. The 200 µl mix was then added dropwise onto 60–80% confluent HeLa cells and transfected cells were left for 48 h for DNA expression. VPS35-knockout HeLa cells and SNX5/SNX6 double knockout was generated as previously described and cultured as stated above for wild-type HeLa cells (Simonetti et al., 2017).

Generation of H4 clonal cells

H4 cells were seeded the day prior to transfection, then transiently transfected with CRISPR plasmids encoding the Cas9 enzyme, a puromycin-resistance marker and specific gRNA guides against VPS35, SNX5 or SNX6 (Kvainickas et al., 2017; Simonetti et al., 2017) using FuGENE® 6 (Promega). The day after transfection, cells are incubated with 1 µg/ml puromycin for 24 h to select for knockout cells. Following puromycin selection, H4 cells were seeded into a 96-well plate at a density of 1 cell per well in 200 µl Iscove's modified Dulbecco's medium (Thermo Fisher). Clones were grown to confluency then expanded and screened for successful knockout deletion by western blotting.

GFP trap and western blot analysis

Cells were lysed in GFP trap buffer (50 mM Tris-HCl, 0.5% NP-40 and Roche protease inhibitor cocktail) and the lysate was added to pre-equilibrated GFP trap beads (ChromoTek). Beads were washed three times in the GFP trap buffer and then lysates were diluted in 2× sample buffer and boiled for 10 min. Proteins were resolved on a NuPAGE 4-12% gels (Invitrogen) and transferred onto polyvinylidene fluoride membrane (EMD Millipore). Once transferred membranes were blocked in TBS 5% milk and the primary antibody (see antibody section) was diluted in Tris-buffered saline (TBS) with 0.1% (v/v) Tween-20 (TBS-T) and 5% (w/v) milk and incubated with the membrane for 1 h at room temperature or overnight at 4°C. Membranes were washed three times in TBS-T. Secondary antibodies (see antibody section) were diluted into TBS-T with 5% milk and 0.01% SDS and incubated with the washed membrane for 1 h at room temperature. TBS-T was used to wash the membrane (three times) prior to quantitative imaging using an Odyssey scanning system (LI-COR Biosciences). Analysis was performed on Image Studio Lite (LI-COR Biosciences).

Knocksideways

pIRESneo3 bicistronic vectors encoding the knocksideways peroxisomal/mitochondrial acceptor compartment and either VPS35–GFP–FRB or GFP–FRB–SNX5 were transfected into cells. Either 0.1% (v/v) ethanol vehicle or rapalog (Takara, Cat. #635056, 100 nM) was added at the 0 timepoint and cells were cultured for a further 24 h. The following day rapalog was added for a further period as indicated, and then cells were fixed and stained.

Immunofluorescence staining

Cells were washed once in PBS before fixation for 8 min in 4% PFA (16% PFA stock diluted in PBS). Three washes in PBS were performed, and then a 5-min incubation with PBS 100 mM glycine was used to quench the PFA. After three more PBS washes, cells were left in PBS overnight. Cells were incubated with PBS plus 3% BSA and 0.1% Triton X-100 for 10 min and then with PBS plus 3% BSA for a further 10 min. Primary antibodies (see antibody section) were diluted in PBS plus 3% BSA and incubated for 1 h. Cells were washed three times with PBS with the secondary antibody (see antibody section) being diluted into PBS plus 3% BSA and incubated for 1 h. Cells were washed three times with PBS and washed once with distilled water before mounting the coverslips in Fluoromount-G (Thermo Fisher).

Microscopy and image analysis

For image acquisition, a Leica SP5-AOBS confocal laser scanning confocal microscope was used attached to a Leica DM I6000 inverted epifluorescence microscope. A 63× HCX PL APO oil lens and standard acquisition software

and detectors were used. Once acquired, Pearson's correlation colocalisation and signal intensity analyses were quantified using Volocity 6.3 software (PerkinElmer). Image and line scan analysis was completed using ImageJ FIJI software. GraphPad Prism 7 was used for presentation and statistical analysis of data.

Live-cell imaging was performed using a Leica SP8 AOBS confocal laser scanning microscope attached to a Leica DM I6000 inverted epifluorescence microscope. The adaptive focus control was used to prevent drift of the *Z*-plane over time. The two hybrid GaAsP detectors were used to enable low laser settings. Images were acquired using the 63× HC PL APO CS2 lens and a speed of one image per 10 s. Imaging was performed at 37°C and 2× rapalog DMEM complete media was added to the pre-selected cell.

Competing interests

The authors declare no competing or financial interests.

Author contributions

Conceptualization: A.J.E., J.L.D., P.J.C.; Methodology: A.J.E., P.J.C.; Formal analysis: A.J.E., J.L.D.; Investigation: A.J.E., J.L.D., A.N.K.A., B.S.; Resources: A.J.E.; Writing - original draft: A.J.E., P.J.C.; Writing - review & editing: A.J.E., J.L.D., A.N.K.A., B.S., P.J.C.; Supervision: P.J.C.; Funding acquisition: P.J.C.

Funding

This work was funded through Wellcome Trust (104568/Z/14/Z) and the Medical Research Council (MR/L007363/1 and MR/P018807/1) awards to P.J.C. Deposited in PMC for immediate release.

Supplementary information

Supplementary information available online at
https://jcs.biologists.org/lookup/doi/10.1242/jcs.246033.supplemental

References

Arighi, C. N., Hartnell, L. M., Aguilar, R. C., Haft, C. R. and Bonifacino, J. S. (2004). Role of the mammalian retromer in sorting of the cation-independent mannose 6-phosphate receptor. *J. Cell Biol.* **165**, 123-133. doi:10.1083/jcb.200312055

Bartuzi, P., Billadeau, D. D., Favier, R., Rong, S., Dekker, D., Fedoseienko, A., Fieten, H., Wijers, M., Levels, J. H., Huijkman, N. et al. (2016). CCC- and WASH-mediated endosomal sorting of LDLR is required for normal clearance of circulating LDL. *Nat. Commun.* **7**, 10961. doi:10.1038/ncomms10961

Braschi, E., Goyon, V., Zunino, R., Mohanty, A., Xu, L. and McBride, H. M. (2010). Vps35 mediates vesicle transport between the mitochondria and peroxisomes. *Curr. Biol.* **20**, 1310-1315. doi:10.1016/j.cub.2010.05.066

Braulke, T. and Bonifacino, J. S. (2009). Sorting of lysosomal proteins. *Biochim. Biophys. Acta* **1793**, 605-614. doi:10.1016/j.bbamcr.2008.10.016

Breusegem, S. Y. and Seaman, M. N. J. (2014). Genome-wide RNAi screen reveals a role for multipass membrane proteins in endosome-to-Golgi retrieval. *Cell Rep.* **9**, 1931-1945. doi:10.1016/j.celrep.2014.10.053

Bulankina, A. V., Deggerich, A., Wenzel, D., Mutenda, K., Wittmann, J. G., Rudolph, M. G., Burger, K. N. J. and Höning, S. (2009). TIP47 functions in the biogenesis of lipid droplets. *J. Cell Biol.* **185**, 641-655. doi:10.1083/jcb.200812042

Burd, C. and Cullen, P. J. (2014). Retromer: a master conductor of endosome sorting. *Cold Spring Harb. Perspect. Biol.* **6**, a016774. doi:10.1101/cshperspect.a016774

Carlton, J., Bujny, M., Peter, B. J., Oorschot, V. M. J., Rutherford, A., Mellor, H., Klumperman, J., McMahon, H. T. and Cullen, P. J. (2004). Sorting nexin-1 mediates tubular endosome-to-TGN transport through coincidence sensing of high-curvature membranes and 3-phosphoinositides. *Curr. Biol.* **14**, 1791-1800. doi:10.1016/j.cub.2004.09.077

Clackson, T., Yang, W., Rozamus, L. W., Hatada, M., Amara, J. F., Rollins, C. T., Stevenson, L. F., Magari, S. R., Wood, S. A., Courage, N. L. et al. (1998). Redesigning an FKBP-ligand interface to generate chemical dimerizers with novel specificity. *Proc. Natl. Acad. Sci. USA* **95**, 10437-10442. doi:10.1073/pnas.95.18.10437

Clairfeuille, T., Mas, C., Chan, A. S. M., Yang, Z., Tello-Lafoz, M., Chandra, M., Widagdo, J., Kerr, M. C., Paul, B., Mérida, I. et al. (2016). A molecular code for endosomal recycling of phosphorylated cargos by the SNX27-retromer complex. *Nat. Struct. Mol. Biol.* **23**, 921-932. doi:10.1038/nsmb.3290

Cui, Y., Carosi, J. M., Yang, Z., Ariotti, N., Kerr, M. C., Parton, R. G., Sargeant, T. J. and Teasdale, R. D. (2019). Retromer has a selective function in cargo sorting via endosome transport carriers. *J. Cell Biol.* **218**, 615-631. doi:10.1083/jcb.201806153

Cullen, P. J. and Steinberg, F. (2018). To degrade or not to degrade: mechanisms and significance of endocytic recycling. *Nat. Rev. Mol. Cell Biol.* **19**, 679-696. doi:10.1038/s41580-018-0053-7

Curnock, R., Calcagni, A., Ballabio, A. and Cullen P.J. (2019). TFEB controls retromer expression in response to nutrient availability. *J. Cell Biol.* **218**, 3954-3966. doi:10.1083/jcb.201903006

Derivery, E., Sousa, C., Gautier, J. J., Lombard, B., Loew, D. and Gautreau, A. (2009). The Arp2/3 activator WASH controls the fission of endosomes through a large multiprotein complex. *Dev. Cell* **17**, 712-723. doi:10.1016/j.devcel.2009.09.010

Fjorback, A. W., Seaman, M., Gustafsen, C., Mehmedbasic, A., Gokool, S., Wu, C., Militz, D., Schmidt, V., Madsen, P., Nyengaard, J. R. et al. (2012). Retromer binds the FANSHY sorting motif in SorLA to regulte amyloid precursos protein sorting and processing. *J. Neurosci.* **32**, 1467-1480. doi:0.1523/jneurosci.2272-11.2012

Gallon, M., Clairfeuille, T., Steinberg, F., Mas, C., Ghai, R., Sessions, R. B., Teasdale, R. D., Collins, B. M. and Cullen, P. J. (2014). A unique PDZ domain and arrestin-like fold interaction reveals mechanistic details of endocytic recycling by SNX27-retromer. *Proc. Natl. Acad. Sci. USA* **111**, E3604-E3613. doi:10.1073/pnas.1410552111

Gomez, T. S. and Billadeau, D. D. (2009). A FAM21-containing WASH complex regulates retromer-dependent sorting. *Dev. Cell* **17**, 699-711. doi:10.1016/j.devcel.2009.09.009

Grant, B. D. and Donaldson, J. G. (2009). Pathways and mechanisms of endocytic recycling. *Nat. Rev. Mol. Cell Biol.* **10**, 597-608. doi:10.1038/nrm2755

Hao, Y.-H., Doyle, J. M., Ramanathan, S., Gomez, T. S., Jia, D., Xu, M., Chen, Z. J., Billadeau, D. D., Rosen, M. K. and Potts, P. R. (2013). Regulation of WASH-dependent actin polymerization and protein trafficking by ubiquitination. *Cell* **152**, 1051-1064. doi:10.1016/j.cell.2013.01.051

Harbour, M. E., Breusegem, S. Y. A., Antrobus, R., Freeman, C., Reid, E. and Seaman, M. N. J. (2010). The cargo-selective retromer complex is a recruiting hub for protein complexes that regulate endosomal tubule dynamics. *J. Cell Sci.* **123**, 3703-3717. doi:10.1242/jcs.071472

Harrison, M. S., Hung, C.-S., Liu, T.-T., Christiano, R., Walther, T. C. and Burd, C. G. (2014). A mechanism for retromer endosomal coat complex assembly with cargo. *Proc. Natl. Acad. Sci. USA* **111**, 267-272. doi:10.1073/pnas.1316482111

Harterink, M., Port, F., Lorenowicz, M. J., McGough, I. J., Silhankova, M., Betist, M. C., van Weering, J. R. T., van Heesbeen, R. G. H. P., Middelkoop, T. C., Basler, K. et al. (2011). A SNX3-dependent retromer pathway mediates retrograde transport of the Wnt sorting receptor Wntless and is required for Wnt secretion. *Nat. Cell Biol.* **13**, 914-923. doi:10.1038/ncb2281

Hirst, J., Borner, G. H., Antrobus, R., Peden, A. A., Hodson, N. A., Sahlender, D. A. and Robinson, M. S. (2012). Distinct and overlapping roles for AP-1 and GGAs revealed by the 'knocksideways' system. *Curr. Biol.* **22**, 1711-1716. doi:10.1016/j.cub.2012.07.012

Jia, D., Gomez, T. S., Billadeau, D. D. and Rosen, M. K. (2012). Multiple repeat elements within the FAM21 tail link the WASH actin regulatory complex to the retromer. *Mol. Biol. Cell* **23**, 2352-2361. doi:10.1091/mbc.e11-12-1059

Jimenez-Orgaz, A., Kvainickas, A., Nägele, H., Denner, J., Eimer, S., Dengjel, J. and Steinberg, F. (2018). Control of RAB7 activity and localization through the retromer-TBC1D5 complex enables RAB7-dependent mitophagy. *EMBO J.* **37**, 235-254. doi:10.15252/embj.201797128

Kapitein, L. C., Schlager, M. A., van der Zwan, W. A., Wulf, P. S., Keijzer, N. and Hoogenraad, C. C. (2010). Probing intracellular motor protein activity using an inducible cargo trafficking assay. *Biophys. J.* **99**, 2143-2152. doi:10.1016/j.bpj.2010.07.055

Kvainickas, A., Jimenez-Orgaz, A., Nägele, H., Hu, Z., Dengjel, J. and Steinberg, F. (2017). Cargo-selective SNX-BAR proteins mediate retromer trimer independent retrograde transport. *J. Cell Biol.* **216**, 3677-3693. doi:10.1083/jcb.201702137

Kvainickas, A., Nägele, H., Qi, W., Dokládal, L., Jimenez-Orgaz, A., Stehl, L., Gangurde, D., Zhao, Q., Hu, Z., Dengjel, J. et al. (2019). Retromer and TBC1D5 maintain late endosomal RAB7 domains to enable amino acid-induced mTORC1 signaling. *J. Cell Biol.* **218**, 3019-3038. doi:10.1083/jcb.201812110

Lauffer, B. E. L., Melero, C., Temkin, P., Lei, C., Hong, W., Kortemme, T. and von Zastrow, M. (2010). SNX27 mediates PDZ-directed sorting from endosomes to the plasma membrane. *J. Cell Biol.* **190**, 565-574. doi:10.1083/jcb.201004060

Lucas, M., Gershlick, D. C., Vidaurrazaga, A., Rojas, A. L., Bonifacino, J. S. and Hierro, A. (2016). Structural mechanism for cargo recognition by the retromer complex. *Cell* **167**, 1623-1635.e14. doi:10.1016/j.cell.2016.10.056

MacDonald, E., Brown, L., Selvais, A., Liu, H., Waring, T., Newman, D., Bithell, J., Grimes, D., Urbe, S., Clague, M. J. et al. (2018). HRS-WASH axis governs actin-mediated endosomal recycling and cell invasion. *J. Cell Biol.* **217**, 2549-2564. doi:10.1083/jcb.201710051

Maxfield, F. R. and McGraw, T. E. (2004). Endocytic recycling. *Nat. Rev. Mol. Cell Biol.* **5**, 121-132. doi:10.1038/nrm1315

McGough, I. J., Steinberg, F., Jia, D., Barbuti, P. A., McMillan, K. J., Heesom, K. J., Whone, A. L., Caldwell, M. A., Billadeau, D. D., Rosen, M. K. et al. (2014). Retromer binding to FAM21 and the WASH complex is perturbed by the Parkinson

disease-linked VPS35(D620N) mutation. *Curr. Biol.* **24**, 1678. doi:10.1016/j.cub.2014.07.004

McMillan, K. J., Gallon, M., Jellett, A. P., Clairfeuille, T., Tilley, F. C., McGough, I., Danson, C. M., Heesom, K. J., Wilkinson, K. A., Collins, B. M. et al. (2016). Atypical parkinsonism-associated retromer mutant alters endosomal sorting of specific cargo proteins. *J. Cell Biol.* **214**, 389-399. doi:10.1083/jcb.201604057

McNally, K. E., Faulkner, R., Steinberg, F., Gallon, M., Ghai, R., Pim, D., Langton, P., Pearson, N., Danson, C. M., Nägele, H. et al. (2017). Retriever is a multiprotein complex for retromer-independent endosomal cargo recycling. *Nat. Cell Biol.* **19**, 1214-1225. doi:10.1038/ncb3610

Norwood, S. J., Shaw, D. J., Cowieson, N. P., Owen, D. J., Teasdale, R. D. and Collins, B. M. (2011). Assembly and solution structure of the core retromer protein complex. *Traffic* **12**, 56-71. doi:10.1111/j.1600-0854.2010.01124.x

Phillips-Krawczak, C. A., Singla, A., Starokadomskyy, P., Deng, Z., Osborne, D. G., Li, H., Dick, C. J., Gomez, T. S., Koenecke, M., Zhang, J.-S. et al. (2015). COMMD1 is linked to the WASH complex and regulates endosomal trafficking of the copper transporter ATP7A. *Mol. Biol. Cell* **26**, 91-103. doi:10.1091/mbc.e14-06-1073

Puthenveedu, M. A., Lauffer, B., Temkin, P., Vistein, R., Carlton, P., Thorn, K., Taunton, J., Weiner, O. D., Parton, R. G. and von Zastrow, M. (2010). Sequence-dependent sorting of recycling proteins by actin-stabilized endosomal microdomains. *Cell* **143**, 761-773. doi:10.1016/j.cell.2010.10.003

Robinson, M. S., Sahlender, D. A. and Foster, S. D. (2010). Rapid inactivation of proteins by rapamycin-induced rerouting to mitochondria. *Dev. Cell* **18**, 324-331. doi:10.1016/j.devcel.2009.12.015

Rojas, R., van Vlijmen, T., Mardones, G. A., Prabhu, Y., Rojas, A. L., Mohammed, S., Heck, A. J. R., Raposo, G., van der Sluijs, P. and Bonifacino, J. S. (2008). Regulation of retromer recruitment to endosomes by sequential action of Rab5 and Rab7. *J. Cell Biol.* **183**, 513-526. doi:10.1083/jcb.200804048

Sardiello, M., Palmieri, M., di Ronza, A., Medina, D. L., Valenza, M., Gennarino, V. A., Di Malta, C., Donaudy, F., Embrione, V., Polishchuk, R. S. et al. (2009). A gene network regulating lysosomal biogenesis and function. *Science* **325**, 473-477. doi:10.1126/science.1174447

Schreij, A. M. A., Fon, E. A. and McPherson, P. S. (2016). Endocytic membrane trafficking and neurodegenerative disease. *Cell Mol. Life Sci.* **73**, 1529-1545. doi:10.1007/s00018-015-2105-x

Seaman, M. N. J. (2004). Cargo-selective endosomal sorting for retrieval to the Golgi requires retromer. *J. Cell Biol.* **165**, 111-122. doi:10.1083/jcb.200312034

Seaman, M. N. J. (2007). Identification of a novel conserved sorting motif required for retromer-mediated endosome-to-TGN retrieval. *J. Cell Sci.* **120**, 2378-2389. doi:10.1242/jcs.009654

Seaman, M. N. J. (2018). Retromer and the cation-independent mannose 6-phosphate receptor–time for a trail separation. *Traffic* **19**, 150-152. doi:10.1111/tra.12542

Seaman, M. N. J., McCaffery, J. M. and Emr, S. D. (1998). A membrane coat complex essential for endosome-to-Golgi retrograde transport in yeast. *J. Cell Biol.* **142**, 665-681. doi:10.1083/jcb.142.3.665

Seaman, M. N. J., Harbour, M. E., Tattersall, D., Read, E. and Bright, N. (2009). Membrane recruitment of the cargo-selective retromer subcomplex is catalysed by the small GTPase Rab7 and inhibited by the Rab-GAP TBC1D5. *J. Cell Sci.* **122**, 2371-2382. doi:10.1242/jcs.048686

Seaman, M. N. J., Mukadam, A. S. and Breusegem, S. Y. (2018). Inhibition of TBC1D5 activates Rab7a and can enhance the function of the retromer cargo-selective complex. *J. Cell Sci.* **131**, jcs217398. doi:10.1242/jcs.217398

Settembre, C., Di Malta, C., Polito, V. A., Garcia Arencibia, M., Vetrini, F., Erdin, S., Erdin, S. U., Huynh, T., Medina, D., Colella, P. et al. (2011). TFEB links autophagy to lysosomal biogenesis. *Science* **332**, 1429-1433. doi:10.1126/science.1204592

Simonetti, B., Danson, C. M., Heesom, K. J. and Cullen, P. J. (2017). Sequence-dependent cargo recognition by SNX-BARs mediates retromer-independent transport of CI-MPR. *J. Cell Biol.* **216**, 3695-3712. doi:10.1083/jcb.201703015

Simonetti, B., Paul, B., Chaudhari, K., Weeratunga, S., Steinberg, F., Gorla, M., Heesom, K. J., Bashaw, G. J., Collins, B. M. and Cullen, P. J. (2019). Molecular identification of a BAR domain-containing coat complex for endosomal recycling of transmembrane proteins. *Nat. Cell Biol.* **21**, 1219-1233. doi:10.1038/s41556-019-0393-3

Steinberg, F., Heesom, K. J., Bass, M. D. and Cullen, P. J. (2012). SNX17 protects integrins from degradation by sorting between lysosomal and recycling pathways. *J. Cell Biol.* **197**, 219-230. doi:10.1083/jcb.201111121

Steinberg, F., Gallon, M., Winfield, M., Thomas, E. C., Bell, A. J., Heesom, K. J., Tavaré, J. M. and Cullen, P. J. (2013). A global analysis of SNX27-retromer assembly and cargo specificity reveals a function in glucose and metal ion transport. *Nat. Cell Biol.* **15**, 461-471. doi:10.1038/ncb2721

Strutt, H., Langton, P. F., Pearson, N., McMillan, K. J., Strutt, D. and Cullen, P. J. (2019). Retromer controls planar polarity protein levels and asymmetric localization at intercellular junctions. *Curr. Biol.* 29, 484-491.e6. doi:10.1016/j.cub.2018.12.027

Swarbrick, J. D., Shaw, D. J., Chhabra, S., Ghai, R., Valkov, E., Norwood, S. J., Seaman, M. N. and Collins, B. M. (2011). VPS29 is not an active metallophosphatase but is a rigid scaffold required for retromer interaction with accessory proteins. *PLoS ONE* **6**, e20420. doi:10.1371/journal.pone.0020420

Temkin, P., Lauffer, B., Jäger, S., Cimermancic, P., Krogan, N. J. and von Zastrow, M. (2011). SNX27 mediates retromer tubule entry and endosome-to-plasma membrane trafficking of signalling receptors. *Nat. Cell Biol.* **13**, 715-721. doi:10.1038/ncb2252

Wassmer, T., Attar, N., Bujny, M. V., Oakley, J., Traer, C. J. and Cullen, P. J. (2007). A loss-of-function screen reveals SNX5 and SNX6 as potential components of the mammalian retromer. *J. Cell Sci.* **120**, 45-54. doi:10.1242/jcs.03302

CORONAVIRUS

Neuropilin-1 is a host factor for SARS-CoV-2 infection

James L. Daly[1]*, Boris Simonetti[1]*†, Katja Klein[2]*, Kai-En Chen[3]‡, Maia Kavanagh Williamson[2]‡, Carlos Antón-Plágaro[1]‡, Deborah K. Shoemark[4], Lorena Simón-Gracia[5], Michael Bauer[6], Reka Hollandi[7], Urs F. Greber[6], Peter Horvath[7,8], Richard B. Sessions[1], Ari Helenius[9], Julian A. Hiscox[10,11], Tambet Teesalu[5], David A. Matthews[2], Andrew D. Davidson[2], Brett M. Collins[3], Peter J. Cullen[1]†, Yohei Yamauchi[2,12]†

Severe acute respiratory syndrome coronavirus 2 (SARS-CoV-2), the causative agent of coronavirus disease 2019 (COVID-19), uses the viral spike (S) protein for host cell attachment and entry. The host protease furin cleaves the full-length precursor S glycoprotein into two associated polypeptides: S1 and S2. Cleavage of S generates a polybasic Arg-Arg-Ala-Arg carboxyl-terminal sequence on S1, which conforms to a C-end rule (CendR) motif that binds to cell surface neuropilin-1 (NRP1) and NRP2 receptors. We used x-ray crystallography and biochemical approaches to show that the S1 CendR motif directly bound NRP1. Blocking this interaction by RNA interference or selective inhibitors reduced SARS-CoV-2 entry and infectivity in cell culture. NRP1 thus serves as a host factor for SARS-CoV-2 infection and may potentially provide a therapeutic target for COVID-19.

Severe acute respiratory syndrome coronavirus 2 (SARS-CoV-2) is the coronavirus responsible for the current coronavirus disease 2019 (COVID-19) pandemic (*1*, *2*). A marked difference between the spike (S) protein of SARS-CoV-2 and SARS-CoV is the presence, in the former, of a polybasic sequence motif, Arg-Arg-Ala-Arg (RRAR), at the S1/S2 boundary. It provides a cleavage site for a host proprotein convertase, furin (*3*–*5*) (fig. S1A). The resulting two proteins, S1 and S2, remain noncovalently associated, with the serine protease TMPRSS2 further priming S2 (*6*). Furin-mediated processing increases infectivity and affects the tropism of SARS-CoV-2, whereas furin inhibition diminishes SARS-CoV-2 entry, and deletion of the polybasic site in the S protein reduces syncytia formation in cell culture (*3*–*5*, *7*).

The C terminus of the S1 protein generated by furin cleavage has an amino acid sequence (^{682}RRAR^{685}) that conforms to a [R/K]XX[R/K] motif, termed the "C-end rule" (CendR) (fig. S1B) (*8*). CendR peptides bind to neuropilin-1 (NRP1) and NRP2, transmembrane receptors that regulate pleiotropic biological processes, including axon guidance, angiogenesis, and vascular permeability (*8*–*10*). To explore the possibility that the SARS-CoV-2 S1 protein may associate with neuropilins, we generated a green fluorescent protein (GFP)–tagged S1 construct (GFP-S1) (fig. S1C). When expressed in human embryonic kidney 293T (HEK293T) cells engineered to express the SARS-CoV-2 receptor angiotensin-converting enzyme 2 (ACE2), GFP-S1 immunoprecipitated endogenous NRP1 and ACE2 (Fig. 1A). We transiently coexpressed NRP1-mCherry and either GFP-S1 or GFP-S1 ΔRRAR (a deletion of the terminal ^{682}RRAR^{685} residues) in HEK293T cells. NRP1 immunoprecipitated the S1 protein, and deletion of the CendR motif reduced this association (Fig. 1B). Comparable binding was also observed with mCherry-NRP2, a receptor with high homology to NRP1 (fig. S1, D and E). In both cases, residual binding was observed with the ΔRRAR mutant, indicating an additional CendR-independent association between neuropilins and the S1 protein.

To probe the functional relevance of this interaction, we generated HeLa wild-type and NRP1 knockout (KO) cell lines stably expressing ACE2, designated as HeLa^{wt}+ACE2 and HeLa^{NRP1KO}+ACE2, respectively (the level of ACE2 expression was comparable between these lines) (fig. S1F). Using a clinical isolate SARS-CoV-2 (SARS-CoV-2/human/Liverpool/REMRQ001/2020), we performed viral infection assays and fixed the cells at 6 and 16 hours postinfection (hpi). SARS-CoV-2 infection was reduced in HeLa^{NRP1KO}+ACE2 relative to HeLa^{wt}+ACE2 (Fig. 1C). HeLa cells lacking ACE2 expression were not infected (fig. S1G). In Caco-2 cells, a human colon adenocarcinoma cell line endogenously expressing ACE2 and widely used in COVID-19 studies, the suppression of NRP1 expression by short hairpin RNA (shRNA) greatly reduced SARS-CoV-2 infection at both 7 and 16 hpi, respectively, whereas that of vesicular stomatitis virus (VSV) pseudotyped with VSV-G was unaffected (Fig. 1D and figs. S1H and S2A). To determine if NRP1 was required for early virus infection, we established a sequential staining procedure using antibodies against SARS-CoV-2 S and N proteins to distinguish extracellular and intracellular viral particles (fig. S2B). Although NRP1 depletion did not affect SARS-CoV-2 binding to the Caco-2 cell surface (Fig. 1E), virus uptake was halved in NRP1-depleted cells compared to control cells after 30 min of internalization (Fig. 1F). Thus, NRP1 enhances SARS-CoV-2 entry and infection.

We also observed that SARS-CoV-2–infected HeLa^{wt}+ACE2 cells displayed a multinucleated syncytia cell pattern, as reported by others (Fig. 1C) (*5*). Using an image analysis algorithm and supervised machine learning (fig. S2, C to F) (*11*), we quantified syncytia of infected HeLa^{wt}+ACE2 and HeLa^{NRP1KO}+ACE2 cells. At 16 hpi, the majority of HeLa^{wt}+ACE2 cells formed syncytia, whereas in HeLa^{NRP1KO}+ACE2 cells, this phenotype was reduced (fig. S2G). When infected with a SARS-CoV-2 isolate lacking the furin cleavage site (SARS-CoV-2 ΔS1/S2) (fig. S1A), the differences in infection and syncytia formation were less pronounced (fig. S2, H and I). However, a significant decrease in infection of HeLa^{NRP1KO}+ACE2 was still observed at 16 hpi, indicating that NRP1 may additionally influence infection through a CendR-independent mechanism (fig. S2H).

The extracellular regions of NRP1 and NRP2 are composed of two CUB domains (a1 and a2), two coagulation factor domains (b1 and b2), and a MAM domain (*9*). Of these, the b1 domain contains the specific binding site for CendR peptides (fig. S3A) (*12*). Accordingly, the mCherry-b1 domain of NRP1 immunoprecipitated GFP-S1, and a shortened GFP-S1 construct spanning residues 493 to 685 (figs. S1C and S3B). Isothermal titration calorimetry (ITC) established that the b1 domain of NRP1 directly bound a synthetic S1 CendR peptide (^{679}NSPRRAR^{685}) with an affinity of 20.3 μM at pH 7.5, which was enhanced to 13.0 μM at pH 5.5 (Fig. 2A). Binding was not observed to an S1 CendR peptide in which the C-terminal arginine was mutated to alanine (^{679}NSPRRAA^{685}) (Fig. 2A). We cocrystallized the NRP1 b1 domain in complex with the S1 CendR peptide (Fig. 2B). The resolved 2.35-Å structure revealed four molecules of b1 with electron density of the S1 CendR peptide clearly visible in the asymmetric unit (fig. S3C). S1 CendR peptide binding displayed strong similarity to the previously solved structure of NRP1 b1 domain in complex with

[1]School of Biochemistry, Faculty of Life Sciences, Biomedical Sciences Building, University of Bristol, Bristol BS8 1TD, UK. [2]School of Cellular and Molecular Medicine, Faculty of Life Sciences, Biomedical Sciences Building, University of Bristol, Bristol BS8 1TD, UK. [3]Institute for Molecular Bioscience, the University of Queensland, St. Lucia, QLD 4072, Australia. [4]School of Biochemistry and BrisSynBio Centre, Faculty of Life Sciences, Biomedical Sciences Building, University of Bristol, Bristol BS8 1TD, UK. [5]Laboratory of Cancer Biology, Institute of Biomedicine and Translational Medicine, University of Tartu, Tartu, Estonia. [6]Department of Molecular Life Sciences, University of Zurich, Winterthurerstrasse 190, 8057 Zürich, Switzerland. [7]Synthetic and Systems Biology Unit, Biological Research Centre (BRC), Szeged, Hungary. [8]Institute for Molecular Medicine Finland, University of Helsinki, Helsinki, Finland. [9]Institute of Biochemistry, ETH Zurich, Zurich, Switzerland. [10]Institute of Infection, Veterinary and Ecological Sciences, University of Liverpool, Liverpool, UK. [11]Singapore Immunology Network, Agency for Science, Technology, and Research, 138648, Singapore. [12]Division of Biological Science, Graduate School of Science, Nagoya University, Furo-cho, Chikusa-ku, Nagoya, 464-8601, Japan.
*These authors contributed equally to this work.
†Corresponding author. Email: bs13866@bristol.ac.uk (B.S.); pete.cullen@bristol.ac.uk (P.J.C.); yohei.yamauchi@bristol.ac.uk (Y.Y.)
‡These authors contributed equally to this work.

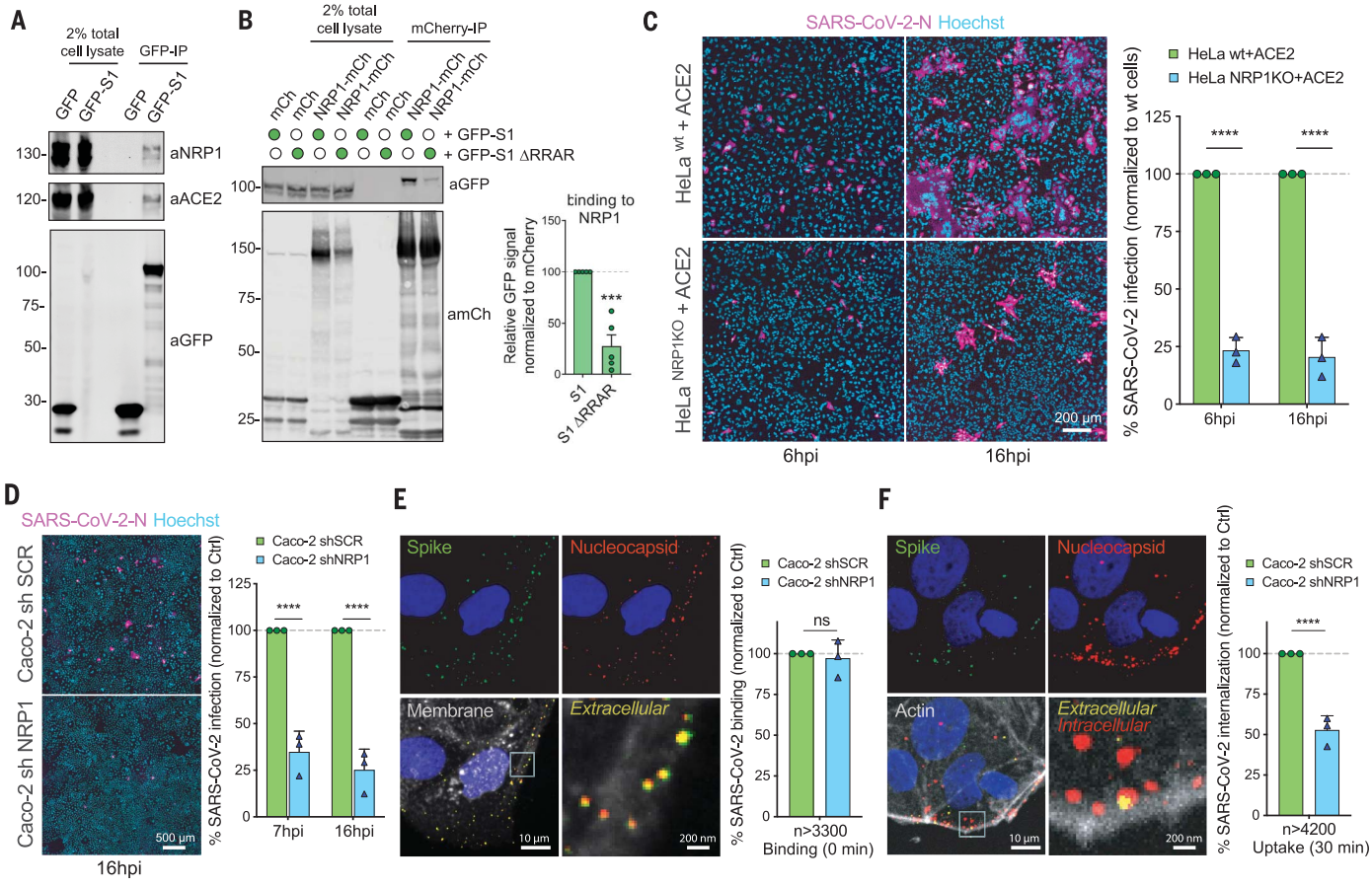

Fig. 1. NRP1 Interacts with S1 and enhances SARS-CoV-2 infection. (**A**) HEK293T cells transduced to express ACE2 were transfected to express GFP or GFP-tagged S1 and lysed after 24 hours. The lysates were subjected to GFP-nanotrap, and the immune isolates were blotted for ACE2 and NRP1 (N = 3 independent experiments). (**B**) HEK293T cells were cotransfected to express GFP-tagged S1 or GFP-S1 ΔRRAR and mCherry or mCherry-tagged NRP1 and subjected to GFP-nanotrap (N = 5 independent experiments). Two-tailed unpaired t test; P = 0.0002. (**C**) HeLa^{wt}+ACE2 and HeLa$^{NRP1\ KO}$+ACE2 cells were infected with SARS-CoV-2. Cells were fixed at 6 or 16 hpi and stained for N protein (magenta) and Hoechst (cyan), and virus infectivity was quantified (N = 3 independent experiments). Two-tailed unpaired t test; P = 0.00002 and 0.00088. Scale bar, 200 μm. (**D**) Caco-2 cells expressing shRNA against NRP1 or a nontargeting control (SCR) were infected with SARS-CoV-2 and fixed at 7 or 16 hpi. The cells were stained for N protein (magenta) and Hoechst (cyan), and infectivity was quantified (N = 3 independent experiments). Two-tailed unpaired t test; P = 0.0005 and 0.00032. Scale bar, 500 μm. (**E**) Caco-2 shSCR or shNRP1 cells were inoculated with a multiplicity of infection (MOI) = 50 of SARS-CoV-2 and incubated in the cold for 60 min, and fixed. A two-step antibody staining procedure was performed with antibodies against S and N to distinguish external (green) and total (red) virus particles, and the binding of particles per cell was quantified for >3300 particles per condition (N = 3 independent experiments). Two-tailed unpaired t test; P = 0.6859. (**F**) Caco-2 shSCR or shNRP1 cells were bound with SARS-CoV-2 as in (E), followed by incubation at 37°C for 30 min. The cells were fixed and stained as in (E). Viral uptake was quantified for >4200 particles per condition (N = 3 independent experiments). Two-tailed unpaired t test; P = 0.00079. Scale bars [(E) and (F)], 10 μm and 200 nm (magnified panels). The square regions were enlarged. The bars, error bars, and circles and triangles represent the mean, SEM (B) and SD [(C) to (F)], and individual data points, respectively. ***P < 0.001, ****P < 0.0001. ns, not signficant.

its endogenous ligand VEGF-A$_{164}$ (Fig. 2B and fig. S3D) (*12*). The key residues responsible for contacting the C-terminal R685 of the CendR peptide —Y297, W301, T316, D320, S346, T349 and Y353—are almost identical between the two structures (Fig. 2B and fig. S3D). The R682 and R685 side chains together engage NRP1 via stacked cation-π interactions with NRP1 side chains of Y297 and Y353. By projecting these findings onto the structure of the NRP1 ectodomain, the b1 CendR binding pocket appears to be freely accessible to the S1 CendR peptide (fig. S3E) (*13*).

Site-directed mutagenesis of the S1 R685 residue to aspartic acid drastically reduced GFP-S1$^{493\text{-}685}$ immunoprecipitation by mCherry-b1, confirming the critical role of the C-terminal arginine (Fig. 2C). Mutagenesis of the T316 residue within the mCherry-b1 domain of NRP1 to arginine also reduced association with GFP-S1$^{493\text{-}685}$, consistent with its inhibitory impact on VEGF-A$_{164}$ binding (*12*) (Fig. 2D). Accordingly, incubation of mCherry-b1 with VSV particles pseudotyped with trimeric S resulted in immunoprecipitation of processed forms of S1, which was dependent on the T316 residue (fig. S3F). Next, we transiently expressed either GFP, full-length NRP1 wt-GFP, or full length NRP1-GFP harboring the T316R mutation in HeLa^{NRP1KO}+ACE2 cells. GFP expression and ACE2 expression levels were comparable and both constructs retained similar cell surface localization (fig. S3, G and H). SARS-CoV-2 infection was significantly enhanced in cells expressing NRP1 wt-GFP compared to GFP control, whereas it was not enhanced in cells expressing the T316R mutant (Fig. 2E). Thus, the SARS-CoV-2 S1 CendR and NRP1 interaction promotes infection.

To establish the functional relevance of the S1 CendR-NRP1 interaction, we screened monoclonal antibodies (mAb#1, mAb#2, mAb#3) raised against the NRP1 b1b2 ectodomain. All three bound to the NRP1 b1b2 domain, displayed staining by immunofluorescence

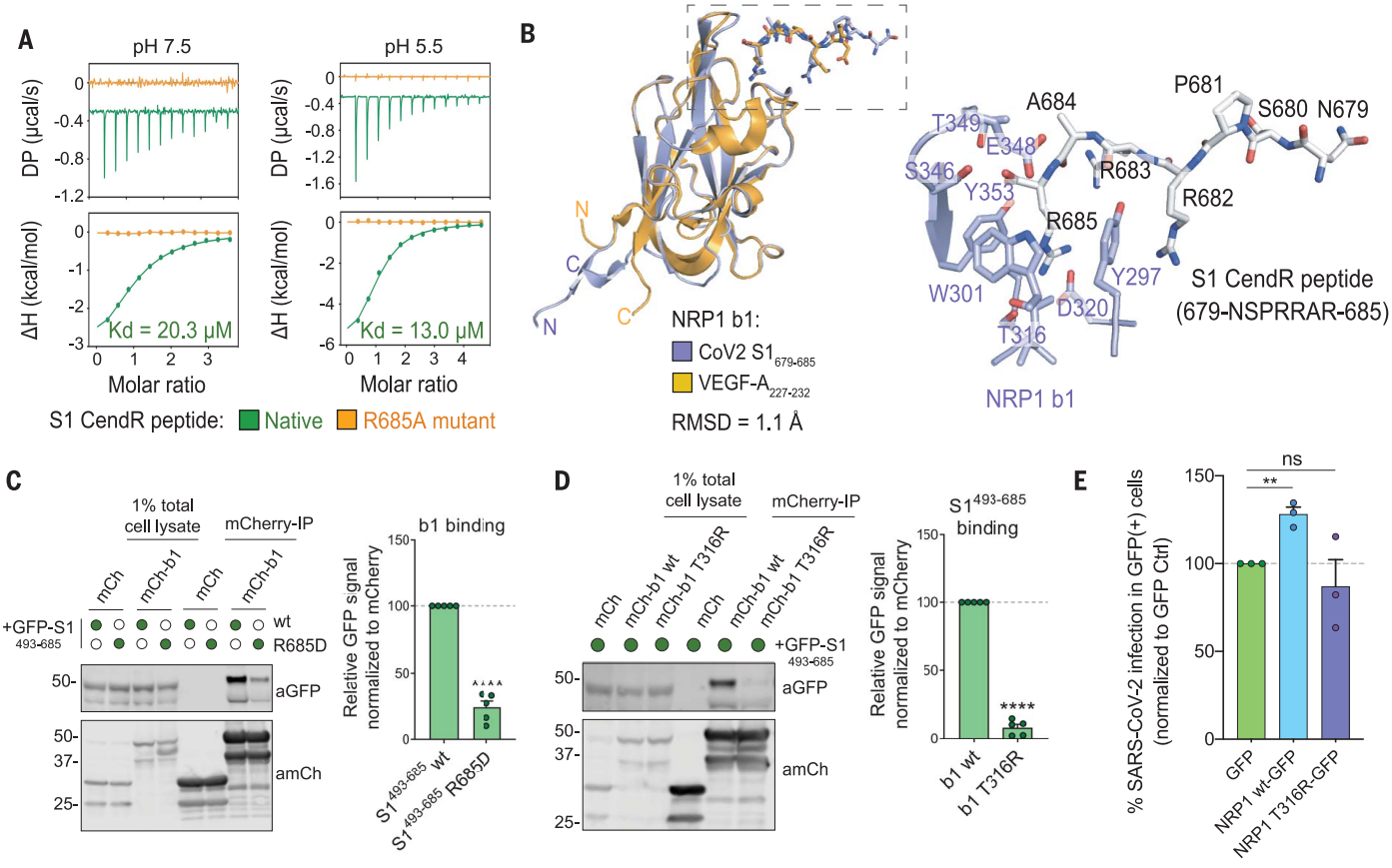

Fig. 2. Molecular basis for CendR binding of SARS-CoV-2 S1 with NRP1. (**A**) Binding of NRP1 b1 with native (green line) and mutant (orange line) form of S1 CendR peptide (corresponding to residues 679 to 685) by ITC at two different pH conditions (N = 3 independent experiments). All ITC graphs represents the integrated and normalized data fit with 1-to-1 ratio binding. (**B**) (Left) NRP1 b1–S1 CendR peptide complex superposed with NRP1 b1–VEGF-A fusion complex (PDB ID: 4DEQ). Bound peptides are shown in stick representation. RMSD, root mean square deviation. (Right) Enlarged view highlighting the binding of S1 CendR peptide b1. Key binding residues on b1 are shown in stick representation. Abbreviations for the amino acid residues are as follows: A, Ala; D, Asp; E, Glu; N, Asn; P, Pro; R, Arg; S, Ser; T, Thr; W, Trp; and Y, Tyr. (**C**). HEK293T cells were cotransfected with combinations of GFP-tagged $S1^{493-685}$ and $S1^{493-685}$ R685D, and mCherry or mCherry-NRP1 b1, and subjected to mCherry-nanotrap (N = 5 independent experiments). Two-tailed unpaired t test; $P < 0.0001$. (**D**). HEK293T cells were cotransfected with combinations of GFP-tagged $S1^{493-685}$ and mCherry, mCherry-NRP1 b1 or mCherry-NRP1 b1 T316R mutant, and subjected to mCherry-nanotrap (N = 5 independent experiments). Two-tailed unpaired t test; $P < 0.0001$. (**E**) $HeLa^{NRP1KO}$ + ACE2 cells transfected with GFP, NRP1 wt-GFP, or NRP1 T316R-GFP constructs were infected 24 hours later with SARS-CoV-2. At 16 hpi, the cells were fixed and stained for SARS-CoV-2-N, and viral infection was quantified in the GFP-positive subpopulation of cells (N = 3 independent experiments). The percentage of infection was normalized to that of GFP-transfected cells. Two-tailed unpaired t test; $P = 0.002$. The bars, error bars, and circles represent the mean, SEM [(C) and (D)] and SD (E), and individual data points, respectively. $^{**}P < 0.01$, $^{****}P < 0.0001$. ns, not signficant.

in NRP1-expressing PPC-1 (human primary prostate cancer) cells but not in M21 (human melanoma) cells that do not express NRP1 (fig. S4A) (*8*), and stained the extracellular domain of NRP1-GFP expressed in cells (fig. S4B). Of these antibodies, mAb#3, and to a lesser extent mAb#1, bound to the CendR-binding pocket with high specificity, as defined by reduced ability to bind to a b1b2 mutant that targets residues (S346, E348, T349) at the opening of the binding pocket (Fig. 3A) (*12*). Incubation of Caco-2 cells with mAbs#1 and 3 reduced SARS-CoV-2 infection compared to a control mAb targeting avian influenza A virus (H11N3) hemagglutinin (Fig. 3B). Consistent with this, mAb#3 inhibited binding of GFP-$S1^{493-685}$ and mCherry-b1 (Fig. 3C). As a comparison, Caco-2 and Calu-3 cells were incubated with soluble ACE2, which inhibited SARS-CoV-2 infection in both cases (fig. S4C).

Next, we turned to the small molecule EG00229, a selective NRP1 antagonist that binds the b1 CendR binding pocket and inhibits VEGF-A binding (Fig. 3D) (*14*). ITC established that EG00229 bound to the NRP1 b1 domain with a dissociation constant (K_d) of 5.1 and 11.0 µM at pH 7.5 and 5.5, respectively (Fig. 3E). EG00229 inhibited the direct binding between b1 and the S1 CendR peptide, and the immunoprecipitation of GFP-$S1^{493-685}$ by mCherry-b1 (Fig. 3E and fig. S4D). Finally, incubation of Caco-2 cells with EG00229 reduced the efficiency of SARS-CoV-2 infection at 7 and 16 hpi (Fig. 3F). Thus, the SARS-CoV-2 interaction with NRP1 can be targeted to reduce viral infectivity in relevant human cell lines (fig. S5).

Cell entry of SARS-CoV-2 depends on priming by host cell proteases (*5*, *6*, *15*). Our data indicate that a component of SARS-CoV-2 S protein binding to cell surface neuropilins occurs via the S1 CendR motif generated by the furin cleavage of S1/S2. Though not affecting cell surface attachment, this interaction promotes entry and infection by SARS-CoV-2 in physiologically relevant cell lines widely used in the study of COVID-19. The molecular basis for the effect is unclear, but neuropilins are known to mediate the internalization of CendR ligands through an endocytic process resembling macropinocytosis,

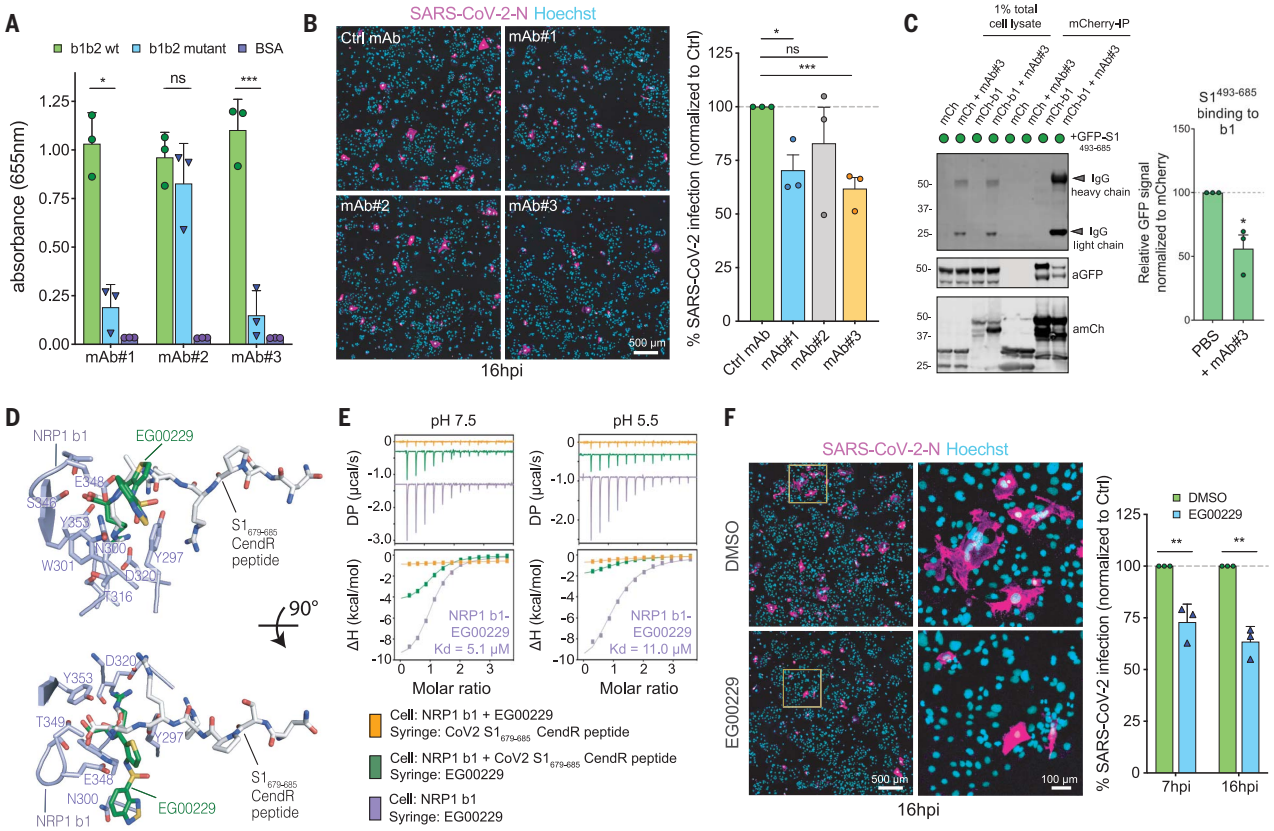

Fig. 3. Selective inhibition of the S1-NRP1 interaction reduces SARS-CoV-2 infection. (**A**) Enzyme-linked immunosorbent assay of anti-NRP1 monoclonal antibodies (mAb#1, mAb#2, mAb#3) at 3 µg/ml using plates coated with NRP1 b1b2 wild type, b1b2 mutant (S346A, E348A, T349A), or bovine serum albumin (BSA), used as a control (N = 3 independent experiments). Binding is represented as arbitrary units of absorbance at 655 nm. Two-tailed unpaired t test; P = 0.0207, 0.2430, 0.0007. (**B**) Cells were first treated with anti-H11N3 (100 µg/ml) (Ctrl) mAb, mAb#1, mAb#2, or mAb#3 for 1 hour before infection with SARS-CoV-2. Cells were fixed at 16 hpi and stained for N protein (magenta) and Hoechst (cyan) (N = 3 independent experiments). Two-tailed unpaired t test; P = 0.015, 0.36, 0.0003. Scale bar, 500 µm. (**C**) HEK293T cells were cotransfected with combinations of mCherry or mCherry-b1 and GFP-tagged S1$^{493-685}$ and subjected to mCherry-nanotrap with or without coincubation with mAb#3 (N = 3 independent experiments). Two-tailed unpaired t test; P = 0.0143. (**D**) NRP1 b1–S1 CendR peptide complex superimposed with NRP1 b1–EG00229 inhibitor complex (PDB ID:3I97). Key binding residues on b1, bound peptides, and EG00229 are shown in stick representation. (**E**) ITC analysis of EG00229 binding to b1 domain of NRP1 at two different pH conditions. Preincubation with EG00229 blocks S1 CendR peptide binding (orange line), and the CendR peptide can reduce binding of EG00229 (green line) (N = 3 independent experiments). All ITC graphs represent the integrated and normalized data fit with 1-to-1 ratio binding. (**F**). Cells were first treated with 100 µM EG00229 or dimethyl sulfoxide before infection with SARS-CoV-2. Cells were fixed at 7 and 16 hpi and stained for N protein (magenta) and Hoechst (cyan) (N = 3 independent experiments). The square regions were enlarged. Scale bars, 500 µm and 100 µm (magnified panels). Two-tailed unpaired t test; P = 0.0059 and 0.0013. The bars, error bars, and circles and triangles represent the mean, SEM (C) and SD [(A), (B), and (F)], and individual data points, respectively. *P < 0.05, **P < 0.01, ***P < 0.001.

(*8*, *16*, *17*). Notably, gene expression analysis has revealed an up-regulation of NRP1 and NRP2 in lung tissue from COVID-19 patients (*18*). A SARS-CoV-2 virus with a natural deletion of the S1/S2 furin cleavage site demonstrated attenuated pathogenicity in hamster models (*19*). NRP1 binding to the CendR peptide in S1 is thus likely to play a role in the increased infectivity of SARS-CoV-2 compared with SARS-CoV. The ability to target this specific interaction may provide a route for COVID-19 therapies.

REFERENCES AND NOTES

1. WHO Coronavirus disease, 2019 (COVID-19) Weekly Epidemiological Update – 31 August 2020. https://www.who.int/docs/default-source/coronaviruse/situation-reports/20200831-weekly-epi-update-3.pdf?sfvrsn=d7032a2a_4
2. E. Dong, H. Du, L. Gardner, *Lancet Infect. Dis.* **20**, 533–534 (2020).
3. D. Wrapp *et al.*, *Science* **367**, 1260–1263 (2020).
4. A. C. Walls *et al.*, *Cell* **181**, 281–292.e6 (2020).
5. M. Hoffmann, H. Kleine-Weber, S. Pöhlmann, *Mol. Cell* **78**, 779–784.e5 (2020).
6. M. Hoffmann *et al.*, *Cell* **181**, 271–280.e8 (2020).
7. J. Shang *et al.*, *Proc. Natl. Acad. Sci. U.S.A.* **117**, 11727–11734 (2020).
8. T. Teesalu, K. N. Sugahara, V. R. Kotamraju, E. Ruoslahti, *Proc. Natl. Acad. Sci. U.S.A.* **106**, 16157–16162 (2009).
9. H. F. Guo, C. W. Vander Kooi, *J. Biol. Chem.* **290**, 29120–29126 (2015).
10. A. Plein, A. Fantin, C. Ruhrberg, *Microcirculation* **21**, 315–323 (2014).
11. R. Hollandi *et al.*, *Cell Syst.* **10**, 453–458.e6 (2020).
12. M. W. Parker, P. Xu, X. Li, C. W. Vander Kooi, *J. Biol. Chem.* **287**, 11082–11089 (2012).
13. B. J. Janssen *et al.*, *Nat. Struct. Mol. Biol.* **19**, 1293–1299 (2012).
14. A. Jarvis *et al.*, *J. Med. Chem.* **53**, 2215–2226 (2010).
15. J. K. Millet, G. R. Whittaker, *Virology* **517**, 3–8 (2018).
16. M. Simons, E. Gordon, L. Claesson-Welsh, *Nat. Rev. Mol. Cell Biol.* **17**, 611–625 (2016).
17. H. B. Pang *et al.*, *Nat. Commun.* **5**, 4904 (2014).
18. M. Ackermann *et al.*, *N. Engl. J. Med.* **383**, 120–128 (2020).
19. S.-Y. Lau *et al.*, *Emerg. Microbes Infect.* **9**, 837–842 (2020).

ACKNOWLEDGMENTS

We thank the Bristol Synthetic Biology Centre and the Advanced Computing Research Centre for provision of HPC (Bluegem), and the University of Bristol Wolfson Bioimaging Facility. We thank the University of Queensland Remote Operation Crystallisation and X-ray facility (UQ-ROCX) and the staff for their support with the crystallization experiments, and the staff of the Australian Synchrotron for assistance with x-ray diffraction data collection.
Funding: J.L.D. was supported by a Wellcome Trust studentship from the Dynamic Molecular Cell Biology Ph.D. program (203959/Z/16/Z), C.A.P. was supported by Beca Fundación Ramón Areces Estudios Postdoctorales en el Extranjero, and M.K.W. was supported by an MRC grant (MR/R020566/1) awarded to A.D.D. This project has received funding from the MRC (MR/P018807/1), Wellcome Trust (104568/Z/14/2), Lister Institute of Preventive Medicine, and Elizabeth Blackwell Institute for Health Research Rapid Response Call (COVID-19) awarded to P.J.C, the European Research Council under the European Union's Horizon 2020

research and innovation program (No 856581 - CHUbVi), and from MRC-AMED (MR/T028769/1) awarded to Y.Y., the Swiss National Science Foundation and Kanton Zurich awarded to U.F.G. B.M.C. is supported by an Australian National Health and Medical Research Council (NHMRC) Senior Research Fellowship (APP1136021) and Project Grant (APP1156493), and the United States Food and Drug Administration grant no. HHSF2232015101O4C "Ebola Virus Disease: correlates of protection, determinants of outcome and clinical management" amended to incorporate urgent COVID-19 studies awarded to J.A.H., A.D.D., and D.A.M. R.H. and P.H. acknowledge support from the LENDULET-BIOMAG Grant (2018-342), from H2020-discovAIR (874656), and from Chan Zuckerberg Initiative, Seed Networks for the HCA-DVP. T.T. was supported by the European Regional Development Fund (Project no. 2014-2020.4.01.15-0012), by European Research Council grant GLIOGUIDE and Estonian Research Council (grants PRG230 and EAG79, to T.T.). **Author contributions:** J.L.D., B.S., A.H., P.J.C., and Y.Y. conceived the study. J.L.D., B.S., K.K, and Y.Y. performed most of the experiments. K.K., M.K.W., D.A.M., and A.D.D. performed all work with infectious SARS-CoV-2 supervised by A.D.D. M.K.W. and A.D.D. isolated SARS-CoV-2 strains used for the work. K.C., C.A.P., M.B., L.S.G., U.F.G., K.K., R.B.S., D.K.S., J.A.H., and T.T. did experimental work and/or provided essential reagents. R.H. and P.H. performed image analysis. B.S., A.D.D., B.M.C., P.J.C., and Y.Y. supervised the research. J.L.D., B.S., A.D.D., P.J.C., and Y.Y. wrote the manuscript and made the figures. All authors read and approved the final manuscript. **Competing interests:** T.T. is an inventor of patents on CendR peptides and a shareholder of Cend Therapeutics Inc., a company that holds a license for the CendR peptides and is developing the peptides for cancer therapy. J.A.H. is a member of the Department of Health, New and Emerging Respiratory Virus Threats Advisory Group (NERVTAG) and the Department of Health, Testing Advisory Group. U.F.G. is a consultant to F. Hoffmann–La Roche Ltd, Switzerland. All other authors declare no competing interests. **Data and materials availability:** Coordinates and structure factors for the NRP1 b1-S1 CendR peptide complex have been deposited at the Protein Data Bank (PDB) with accession code 7JJC. All other data are available in the manuscript or the supplementary materials.

SUPPLEMENTARY MATERIALS

science.sciencemag.org/content/370/6518/861/suppl/DC1
Materials and Methods
Figs. S1 to S5
Tables S1 to S3
References (*20*–*33*)
MDAR Reproducibility Checklist

View/request a protocol for this paper from *Bio-protocol*.

14 June 2020; accepted 12 October 2020
Published online 20 October 2020
10.1126/science.abd3072

Science

Neuropilin-1 is a host factor for SARS-CoV-2 infection

James L. Daly, Boris Simonetti, Katja Klein, Kai-En Chen, Maia Kavanagh Williamson, Carlos Antón-Plágaro, Deborah K. Shoemark, Lorena Simón-Gracia, Michael Bauer, Reka Hollandi, Urs F. Greber, Peter Horvath, Richard B. Sessions, Ari Helenius, Julian A. Hiscox, Tambet Teesalu, David A. Matthews, Andrew D. Davidson, Brett M. Collins, Peter J. Cullen and Yohei Yamauchi

Science **370** (6518), 861-865.
DOI: 10.1126/science.abd3072originally published online October 20, 2020

Another host factor for SARS-CoV-2

Virus-host interactions determine cellular entry and spreading in tissues. Severe acute respiratory syndrome coronavirus 2 (SARS-CoV-2) and the earlier SARS-CoV use angiotensin-converting enzyme 2 (ACE2) as a receptor; however, their tissue tropism differs, raising the possibility that additional host factors are involved. The spike protein of SARS-CoV-2 contains a cleavage site for the protease furin that is absent from SARS-CoV (see the Perspective by Kielian). Cantuti-Castelvetri *et al.* now show that neuropilin-1 (NRP1), which is known to bind furin-cleaved substrates, potentiates SARS-CoV-2 infectivity. NRP1 is abundantly expressed in the respiratory and olfactory epithelium, with highest expression in endothelial and epithelial cells. Daly *et al.* found that the furin-cleaved S1 fragment of the spike protein binds directly to cell surface NRP1 and blocking this interaction with a small-molecule inhibitor or monoclonal antibodies reduced viral infection in cell culture. Understanding the role of NRP1 in SARS-CoV-2 infection may suggest potential targets for future antiviral therapeutics.

Science, this issue p. 856, p. 861; see also p. 765

Science (print ISSN 0036-8075; online ISSN 1095-9203) is published by the American Association for the Advancement of Science, 1200 New York Avenue NW, Washington, DC 20005. The title *Science* is a registered trademark of AAAS.